# SYNTHESIS, CHARACTERIZATION AND APPLICATION OF A NOVEL BIOSORBENT-MAGNETIC NANOMATERIAL CROSS-LINKED WITH CYCLODEXTRIN USING EPICHLOROHYDRIN AND HEXAMETHYLENE DIISOCYANATE AS ADSORBENTS FOR HEAVY METALS AND ORGANICS.

Thesis submitted to the Vaal University of Technology

in fulfilment of the requirement for the award of

the degree of Doctor of Technology in

Chemistry

by

Agnes Pholosi

Student number: 209103108

(M Tech Chemistry)

Promoter                    : Prof. A. E Ofomaja

Co-promoter                 : Prof. E. B Naidoo

March 2019

## DECLARATION

I declare that this thesis is my own, unaided work. It is being submitted for the Degree, Doctoris

Technologiae to the Department of Chemistry, Vaal University of Technology, Vanderbijlpark.

It has not been submitted before for any degree or examination to any other University.

# DEDICATION

I dedicate this work to parents, my late grandfather and my mentors who made it possible for me to get this far, May God bless you abundantly.

Jeremiah 29: 11

"For I know the plans I have for you". Declares the LORD, plans to prosper you and not to harm you, plans to give you hope and future…

# ACKNOWLEDGEMENTS

# PRESENTATIONS AND PUBLICATIONS

The work presented in this dissertation has been published in peer-viewed journal and presented at both national and international conferences.

**Conference contributions**

**Agnes Pholosi**, Eliazer B. Naidoo, Augustine E. Ofomaja. Cyclodextrin cross-linked magnetic nanocomposite for efficient adsorption of 4-nitrophenol from aqueous solution, The 43rd National Convention of the South African Chemical Institute, CSIR-ICC, Pretoria, South Africa. 2-7 Dec 2018 (Poster).

**Agnes Pholosi**, Augustine E. Ofomaja, Eliazer B. Naidoo. Synthesis of magnetite-cyclodextrin nano-biocomposite for removal of 4-Nitrophenol: response surface methodology. International Conference on Pure and Applied Chemistry, Flic en Flac, Mauritius. 1-6 July 2018 (Oral).

**Agnes Pholosi,** Eliazer B. Naidoo, Augustine E. Ofomaja, Removal of 4-Nitrophenol using ($Fe_3O_4$) nano-biocomposite- crosslinked cyclodextrin from aqueous solution. 9th International conference of the Africa Materials Research Society, Gaborone, Botswana. 11-14 Dec 2017 (Poster).

**Agnes Pholosi,** Eliazer B. Naidoo. Augustine E. Ofomaja, Magnetite coated pine cone powder for Cr(VI) removal from aqueous solution. International Conference on Pure and Applied Chemistry, Flic en Flac, Mauritius. 18-22 July 2016 (Oral).

**Agnes Pholosi**, Augustine E. Ofomaja, Eliazer B. Naidoo, Insight into the mechanism of toxic chromium (VI) from wastewater using magnetite coated pine powder, 2016 Spring Meeting and 12th Global Congress on Process Safety, Houston, Texas. 10-14 April 2016 (Poster).

**Agnes Pholosi**, Augustine E. Ofomaja, Eliazer B. Naidoo. Biosorption of Cr (VI) from waste water using pine cone powder and iron oxide-pine cone powder nanocomposite. The 42nd National Convention of the South African Chemical Institute, Durban, South Africa. 29 Nov– 2 Dec 2015 (Oral).

**Agnes Pholosi**, Augustine E. Ofomaja, Eliazer B. Naidoo. Overcoming kinetic limitations of Cr(VI) adsorption onto biosorbents: biomass-magnetite bio-nanocomposite. 2015 AIChE Spring Meeting and 11th Global Congress on Process Safety, Austin, Texas. 26-30 April 2015 (Poster).

**Agnes Pholosi**, Augustine E. Ofomaja, Eliazer B. Naidoo, Pine cone-iron magnetic nanoparticles composite: an effective biomaterial composite for Cr(VI) removal from aqueous solution, Fourth International Conference on Multifunctional, Hybrid and Nanomaterials. Sitges (near Barcelona), Spain, 9-13 Match 2015 (Poster).

**Agnes Pholosi**, Eliazer B. Naidoo, Augustine E. Ofomaja, Iron oxide-biomass magnetic composite for chromium adsorption, Analitika 2014. Parys, South Africa,7-11 September 2014 (Oral).

**Agnes Pholosi**, Augustine E. Ofomaja, Eliazer B. Naidoo. Synthesis and characterization of iron magnetite nanoparticles coated pine cone, 5th International conference on nanoscience and nanotechnology, Vanderbijlpark, South Africa. 30 March-02 April 2014 (Poster).

## Peer reviewed articles

1. **Agnes Pholosi**, Eliazer B. Naidoo, Augustine E. Ofomaja (2018) Clean application of magnetic biomaterial for the removal of As(III) from water, Environmental Science and Pollution Research, 25: 30348-30365.

2. **Agnes Pholosi**, Eliazer B. Naidoo, Augustine E. Ofomaja (2019) Enhanced Arsenic(III) adsorption from aqueous solution by magnetic pine cone biomass, Materials Chemistry and Physics, 222:20-30.

3. **Agnes Pholosi**, Eliazer B. Naidoo, Augustine E. Ofomaja (2019) Sequestration of As(III) adsorption from aqueous solution using chemically activated pine cone biomass: evaluation of interaction and mechanism, International Journal of Environmental Science and Technology, https://doi.org/10.1007/s13762-019-02283-w.

# ABSTRACT

In the present era of water resources scarcity, efficient treatment of wastewater is a major prerequisite especially for growing economy. Numerous approaches have been studied for the development of cheaper and more effective adsorbents for removal of both organic and inorganic pollutants from wastewater. The present study seeks to harness the potential of biosorption and nanotechnology by producing more efficient, selective, mechanically stable and effective adsorbents for removal of organic and inorganic pollutants. The biosorbent-magnetic nanomaterial was synthesized by coating magnetite nanoparticles with sodium hydroxide treated pine cone by co-precipitation method. Magnetite coated pine bio-composite was then modified by cross-linking with hexamethylene diisocyanate and epichlorohydrin to the molecular recognition compound "cyclodextrin". These novel biosorbent-magnetic nanoparticle materials were explored in overcoming the drawbacks of the biosorbent alone and selectively remove inorganic and organic pollutants from complex matrices.

The synthesized materials were characterized by several analytical techniques including, Fourier Transformed Infrared Spectroscopy (FTIR), Thermogravimetric analysis (TGA), X-Ray Diffraction (XRD), Scanning Electron Microscopy-Energy Dispersive X-Ray (SEM–EDX), Transmission Electron Microscopy (TEM), Brunauer, Emmett and Teller Isotherm (BET) surface area analysis, X-ray Photoelectron Spectroscopy (XPS), Vibrating Sample Magnetometer (VSM) and pH at point of zero charge ($pH_{pzc}$). Sodium hydroxide treated pine cone and magnetite coated pine cone were applied for both chromium(VI) and arsenic(III) adsorption while the magnetite coated pine cone, magnetite coated pine cone crosslinked to cyclodextrin using both epichlorohydrin and hexamethylene diisocyanate were applied for 4-nitrophenol removal from aqueous solution. Batch adsorption studies were performed to optimize operating parameters such as solution pH, adsorbent dose, contact time, temperature and initial concentration. Pseudo first, pseudo second, intraparticle diffusion, pore and film diffusion kinetic models were determined to investigate the mechanism of adsorption process. Coefficient of correlation, $r^2$, and variable error, methods were also applied in the determination of the best fit of the kinetic method.

Structural characterization of magnetite coated pine cone and the magnetite coated pine crosslinked to cyclodextrin using 1,6-hexamethylene diisocyanate and epichlorohydrin were confirmed by characterization techniques applied. The adsorption of Cr(VI), As(III) and 4-nitrophenol was found to be dependent on the solution pH, adsorbent dose, initial

concentration, temperature and ionic strength. Kinetic modelling revealed that the adsorption of Cr(VI), As(III) and 4-nitrophenol is controlled by pseudo second order kinetic model suggesting surface adsorption and intraparticle diffusion model. Intraparticle, pore and film diffusion models gave further insight into the controlling diffusion mechanism involved in the adsorption process for all pollutants investigated. Equilibrium studies indicated that the adsorption of all pollutants followed Langmuir isotherm indicating that adsorption sites are homogeneous in nature. The obtained thermodynamic parameters demonstrated that the adsorption of Cr(VI), As(III) and 4-nitrophenol were spontaneous, favourable and endothermic in nature. Anionic effect positively affected Cr(VI) and As(III) removal but had a negative effect on the 4-nitrophenol adsorption. Adsorption of 4-nitrophenol onto the nanocomposite adsorbents was attributed to multiple adsorbent-adsorbate interactions such as hydrogen bonding, hydrophobic attraction and guest host interaction. Magnetite coated pine better removed Cr(VI) and As(III) from aqueous solution than NaOH treated pine cone biomaterial while the magnetite coated pine crosslinked to cyclodextrin using 1,6-hexamethylene diisocyanate exhibited better adsorption performance for 4-nitrophenol removal than the nanocomposite crosslinked using epichlorohydrin and the magnetite coated pine cone.

# TABLE OF CONTENTS

## Contents

# LIST OF ABBREVIATION AND SYMBOLS

**Abbreviations**

| | |
|---|---|
| PCP | Pine cone powder |
| NTP | Sodium hydroxide treated pine cone |
| MNP | Magnetite nanoparticles |
| NTP-NC | Magnetite coated pine cone |
| EPI | Epichlorohydrin |
| HMDI | Hexamethylene diisocyanate |
| CM-βCD-EPI | Carboxymethyl-beta cyclodextrin-epichlorohydrin |
| CD | Cyclodextrin |
| β-CD | beta-Cyclodextrin |
| NTPNC-EPI-CD | Magnetite coated pine cone crosslinked to cyclodextrin using epichlorohydrin |
| NTPNC-HMDI-CD | Magnetite coated pine cone crosslinked to cyclodextrin using hexamethylene diisocyanate |
| DBTDL | Dibutyltin dilaurate |
| 4-NP | 4-Nitrophenol |
| WHO | World Health Organization |
| EPA | Environmental Protection Agency |
| USEPA | United State Environmental Protection Agency |
| RSM | Response surface methodology |
| FTIR | Fourier Transformed Infrared Spectroscopy |
| BET | Brunauer, Emmett and Teller Isotherm |
| TGA | Thermogravimetric analysis |
| DTA | Derivative thermal analysis |
| XRD | X-Ray Diffraction |
| AAS | Atomic Absorption Spectrophotometer |
| ICP-OES | Inductively Coupled Plasma-Optical Emission Spectrometer |
| UV/Vis | Ultra Violet/ Visible spectroscopy |
| VSM | Vibrating Sample Magnetometer |
| XPS | X-ray Photoelectron Spectroscopy |

| | |
|---|---|
| TEM | Transmission Electron Microscopy |
| SEM | Scanning Electron Microscopy |
| $pH_{pzc}$ | pH at point of zero charge |

**Nomenclature**

| | |
|---|---|
| $q_e$ | Equilibrium capacity. |
| $q_t$ | Equilibrium capacity at time t. |
| $q_m$ | Langmuir Monolayer capacity. |
| $k_1$ | Pseudo-first order rate constant. |
| $k_2$ | Pseudo-second order rate constant. |
| $k_i$ | Intraparticle diffusion rate constant |
| $r^2$ | Correlation coefficient. |
| $K_a$ | Langmuir equilibrium constant. |
| $K_F$ | Freundlich capacity constant. |
| n | Freundlich affinity constant. |
| $C_o$ | Initial Concentration. |
| $C_e$ | Equilibrium concentration. |
| $h$ | the initial sorption rate. |
| $C_s$ | Saturation concentration of solute |
| C | Boundary layer constant |
| $D_1$ | Film diffusion coefficient |
| $D_2$ | Pore diffusion coefficient |
| $B_t$ | Boyd constant |
| $K_B$ | Constant expressive of energy of interaction with the surface. |
| $q_{e,m}$ | Equilibrium capacity obtained by calculating from model |
| $\Delta G$ | Change of Gibbs free energy |
| $\Delta H$ | Change of enthalpy |
| $\Delta S$ | Change of entropy |
| Ea | Activation energy |
| $t$ | time |

# LIST OF FIGURES

# LIST OF TABLES

**CHAPTER 1**

# 1    INTRODUCTION

## 1.1    BACKGROUND

With the rapid development of industrialization and urbanization, a variety of inorganic and organic molecules are discharged into the environment, causing many serious environmental problems such as water pollution. Due to the toxic and carcinogenic properties of both inorganic and organic pollutants, it is necessary to treat the pollutant containing water before being released into the environment. Despite their presence at low concentration range, environmental pollutants possess serious threats to freshwater supply, living organisms, and public health (Brezonik and Arnold, 2012). Water researchers have estimated that by 2025, more than half of the world population will be facing water-based vulnerability or a water crisis (Kulshreshtha, 1998, Rijsberman, 2006). To combat this increasing burden on our aquatic environment, increasingly strict regulation on pollution discharge need to be implemented by various government bodies, with focus primarily on waste reduction. The treatment system used by industries is frequently regarded as a regulatory obligation, increasing capital and running costs and yielding negative economic returns (Chan et al., 2009). Pollutants are produced in large quantities especially in developed countries therefore, good reliable methods are necessary to treat effluents before discharge.

Recently, numerous approaches have been studied for the development of cheaper and more effective technologies, both to decrease the amount of wastewater produced and to improve the quality of the treated effluent. Biological treatment, membrane process, advanced oxidation processes, chemical and electrochemical techniques and adsorption procedures are the most widely used for removing metals and organic compounds from industrial effluents (Crini, 2005b, Yao et al., 2009). However, the application of some of these methods may be impractical due to economic constraints or may be insufficient to meet strict regulatory requirements. Most of these techniques suffer from drawbacks such as incomplete metal removal, requirements of expensive equipment and monitoring system, high reagent and energy requirements, generation of toxic sludge, other waste products that require disposal, membrane scaling, fouling and blocking (Demiral et al., 2008, Hu et al., 2003). Adsorption

process offer many advantages over other conventional methods due to its feasibility, low cost, efficiency and less time and energy consumption (Xu et al., 2015).

Various materials have been explored as efficient and effective adsorbents for both heavy metals and organic pollutants from aqueous solutions. The use of non-conventional, low-cost biosorbents prepared from agricultural wastes is increasing because of its availability in large quantities, low cost and simplicity of design. However, their commercial application has been hindered by problems associated with physical characteristics such as separation of small particle size with low density, low porosity and internal surface, poor mechanical strength and rigidity (Volesky and Holan, 1995). Incorporating agricultural wastes with a suitable matrix such as magnetic nanoparticles may overcome the problems by offering ideal size, mechanical strength, rigidity, and porous characteristics to the biological material (Trujillo et al., 1995). Magnetic nanoparticles offer advantages such as high surface area, greater active sites, easy separation and ease of modification. However, because they are susceptible to air oxidation, they tend to agglomerate in large clusters.

Among natural compounds applied in surface modification of $Fe_3O_4$, β-Cyclodextrin (β-CD) have attracted significant attention because of its exceptional structure and unique properties such as specific affinity, simple design, low cost, availability and the presence of various reactive groups on the backbone chain (Crini, 2005b). Cyclodextrin has the ability to form guest-host interaction with wide range of organics due to binding forces between itself and the guest molecules (Kumari and Parashara, 2018, Cifuentes et al., 2016). However, their application as adsorbents in wastewater treatment is limited by the fact that they are soluble in water, which can be overcome by grafting onto water-insoluble matrix or polymerize into cross-linked polymers by reacting with coupling agents. A step further in developing adsorbents with superior properties would be the inclusion of magnetic nanoparticles and agricultural waste into natural polymers, thus combining the advantages of all materials.

## 1.2    PROBLEM STATEMENT

There has been a rapid expansion in the chemical industry which leads to the discharge of toxic chemicals into the environment affecting plants, water and soil quality. Water generated by industrial sectors contains a complex and time-dependent mixture of organic and inorganic pollutants. Hence the water quality in South Africa is drastically deteriorating due to heavy metals and organic pollutant contamination. Treatment of industrial wastewater is a complex

problem due to the wide variety of compounds present in different concentrations. Heavy metals and aromatic organic compounds that contaminate water have been a critical problem mainly because they tend to persist and accumulate in the environment. The presence of dyes in water, even at very low concentrations, is highly visible and undesirable. Most of the used dyes are stable to photodegradation, bio-degradation and oxidizing agents.

The wastewater treatment methods proposed and used by industrial sectors do not remove the spectrum of pollutant load. In practice, a combination of different processes is often used for pollutant removal to achieve the desired water quality in the most economical way. This is due to the fact that there is, as yet, no single water treatment process that simultaneously removes all pollutants from water to desirable levels. Another difficulty is the treatment of wastewater containing low concentrations of molecules and/or ions. Thus, there is a need to develop new treatment methods acceptable for industrial use which are effective for a wide range of pollutants from multicomponent mixtures, even at very low concentrations.

There have been efforts by researchers to produce several efficient and cost-effective materials as adsorbents from local sources in South Africa and the world over to combat the issue of ever-increasing disposal of contaminated effluents into surface and ground water. These biomaterials often have their limitation which include, low surface area, low mechanical strength in packed column, low filtration rate and low adsorption capacity. The incorporation of nanotechnology into the field of biosorption may be applied in addressing the problems highlighted. The high surface to volume ratio of nanomaterials, the excellent mechanical strength, low internal diffusion resistance and the possibility of magnetic separation can be impacted by incorporating nanomaterials into biosorbents. The unique properties of cyclodextrins, such as chemical stability, high reactivity, hydrophobic cavity, hydrophilic interior, and excellent selectivity towards aromatic compounds and metals strengthen their application in water treatment.

## 1.3 AIMS AND OBJECTIVES

Aim: Synthesizing a magnetic nano-biosorbents by surface modification of $Fe_3O_4$ nanoparticles (MNP) with pine cone powder (PCP) cross-linked to β-cyclodextrin using hexamethylene diisocyanate (HMDI) and epichlorohydrin (EPI) as cross-linking agents.

The research aim of the study was achieved through the following objectives:

1. To prepare NaOH treated pine cone powder.
2. To synthesize and optimize ($Fe_3O_4$) magnetite coated pine cone bio-composite by co-precipitation method.
3. To cross-link β-cyclodextrin onto magnetite coated pine cone nanocomposite using epichlorohydrin and 1,6-Hexamethylene diisocyanate.
4. To apply response surface methodology in optimizing the working conditions of the cross-linked magnetite coated pine cone-cyclodextrin nanocomposites.
5. To characterize the synthesized Magnetite coated pine cone, magnetite coated pine cone crosslinked to beta-cyclodextrin using EPI and magnetite coated pine cone crosslinked to beta-cyclodextrin using HMDI using different analytical tools i.e. FTIR, TEM, TGA, SEM, XRD, XPS, VSM, BET surface area and $pH_{pzc,}$
6. To compare batch adsorption study of the adsorbent for heavy metals and organic pollutants removal from wastewater.
7. To determine the kinetic, equilibrium and thermodynamic parameters for the biosorption process.
8. To determine the mechanism of uptake and recovery of heavy metals and organic pollutants from solution.
9. To study the effect of competing ions and anionic strength for the removal of both heavy metals and organic pollutants.

## 1.4    OUTLINE OF THE RESEARCH

The thesis consists of a total of 7 chapters, where chapter 1 and 2 discuss introduction and literature review, chapter 3 gives the detailed experimental procedure, chapter 4, 5 and 6 present the preparation of nanocomposites, characterization and batch adsorption studies for heavy metals and organic pollutant removal.

Chapter 1
This chapter covers the introduction and problem statement. It gives an insight into the research project. The aim and objectives are also presented in this chapter.

Chapter 2

This chapter covers literature review of biosorbents, magnetic nanoparticles, cyclodextrin polymers, their synthesis and application in waste water treatment. Adsorption process as an alternative method for removal of pollutant from aqueous solution and factors affecting pollutants removal is also discussed in the chapter.

Chapter 3:

The experimental procedure for the synthesis of the adsorbent materials, characterization and their application for heavy metals (As(III) and Cr(VI)) and organic pollutant (4-nitrophenol) adsorption.

Chapter 4

This chapter discusses the optimization of the synthesis procedure and characterization of the magnetite coated pine cone bio-composite.

Chapter 5

This chapter discusses the application of the NaOH treated pine cone and magnetite bio-composite material for Cr(VI) and As(III) adsorption from aqueous solutions. Batch adsorption studies, kinetics, equilibrium isotherms and insight into the mechanism of Cr(VI) and As(III) adsorption using both NaOH treated pine cone and magnetite bio-composite material are also discussed.

Chapter 6

This chapter discusses the crosslinking of magnetite coated pine cone with beta cyclodextrin using epichlorohydrin and hexamethylene diisocyanate using response surface methodology (RSM). Characterization and application of the adsorbents for 4-nitrophenol (4-NP) adsorption from aqueous solution.

Chapter 7

This chapter gives a general conclusion of the research and recommendations for future work.

## 1.5  REFERENCES

BREZONIK, P. L. & ARNOLD, W. A. 2012. Water chemistry: Fifty years of change and progress. *Environmental Science and Technology,* 46**,** 5650-5657.

CHAN, Y. J., CHONG, M. F., LAW, C. L. & HASSELL, D. G. 2009. A review on anaerobic-aerobic treatment of industrial and municipal wastewater. *Chemical Engineering Journal,* 155**,** 1-18.

CIFUENTES, T., CAYUPI, J., CELIS-BARROS, C., ZAPATA-TORRES, G., BALLESTEROS, R. & BALLESTEROSGARRIDO, R. 2016. Spectroscopic studies of the interaction of 3-(2-thienyl)-[1,2,3]triazolo[1,5-a]pyridine with 2,6-dimethyl-beta-cyclodextrin and ctDNA. *Organic & Biomolecular Chemistry,* 14**,** 9760-9767.

CRINI, G. 2005. Recent developments in polysaccharide-based materials used as adsorbents in wastewater treatment. *Progress in Polymer Science,* 30**,** 38-70.

DEMIRAL, H., DEMIRAL, I., TUMSEK, F. & KARABACAKOGLU, B. 2008. Adsorption of chromium (VI) from aqueous solution by activated carbon derived from olive bagasse and applicability of different adsorption models, *Chemical Engineering Journal,* 144**,** 188-196.

HU, Z., LEI, L., YIJIU, L. I. & NI, Y. 2003. Chromium adsorption on high performance activated carbons from aqueous solution. *Separation and Purification Technology,* 31**,** 13-18.

KULSHRESHTHA, S. N. 1998. A global outlook for water resources to the year 2025. *Water Resources Management,* 12**,** 167-184.

KUMARI, P. & PARASHARA, S. H. 2018. β-cyclodextrin modified magnetite nanoparticles for efficient removal of eosin and phloxine dyes from aqueous solution. *Materials Today: Proceedings,* 5**,** 15473-15480.

RIJSBERMAN, F. R. 2006. Water scarcity: Fact or fiction? . *Agricultural Water Management,* 80**,** 5-22.

TRUJILLO, E. M., SPRINTI, M. & ZHUANG, H. 1995. Immobilized biomass: a new class of heavy metal bioexchangers. In: Senguptal, A.K. *ed. Ion Exchange Technology: Advances in Pollution Control. Technomic Publishing Company Inc***,** 225-271.

VOLESKY, B. & HOLAN, Z. R. 1995. Biosorption of heavy metals. *Biotechnology Progress,* 11**,** 235-250.

XU, X., SONG, W., HUANG, D., GAO, B., SUN, Y., YUE, Q. & FU, K. 2015. Performance of novel biopolymer-based activated carbon and resin on phosphate elimination from stream,. *Colloids and Surfaces A,* 476**,** 68-75.

YAO, Z., WANG, L. & QI, J. 2009. Biosorption of methylene blue from aqueous solution using a bioenergy forest waste: Xanthoceras sorbifolia seed coat. *Clean Soil Air Water,* 37**,** 642-648.

# 2 CHAPTER 2

## LITERATURE REVIEW

Literature review on the existing adsorbents, agricultural waste materials, pine cone, magnetic nanoparticle, cyclodextrin, their synthesis and applications for both organic and inorganic pollutants from aqueous solution is presented in this chapter.

## 2.1 ADSORBENTS

An adsorbent is defined as a material that is porous in nature with a high surface area that can adsorb substances onto its surface by intermolecular forces. Adsorbents may be of mineral, organic or biological origin, zeolites, industrial by-products, agricultural wastes, biomass, and polymeric materials (Kurniawan and Babel, 2003). According to Bailey et al. (1999) an adsorbent can be considered low-cost if it requires little processing, is abundant in nature or is a by-product or waste material from another industry. In recent years, the search for low-cost adsorbents that have metal-binding capacities has intensified (Leung et al., 2000). The success of an adsorption process starts with the choice of the adsorbent. Technical applicability and cost-effectiveness are the key factors that play major roles in the selection of the most suitable adsorbent to treat effluent. Certain factors should also be considered when choosing a suitable adsorbent for adsorption processes which includes: high capacity and rate of adsorption, efficiency for removal of a wide variety of target pollutants, selectivity for different concentrations, granular nature with high surface area, high physical strength, kinetics, non-toxic, regenerable, tolerance for a wide range of wastewater parameters, and low cost.

## 2.2 TYPES OF ADSORBENTS

Low cost adsorbents can be categorized as natural materials, industrial waste and agricultural waste materials. A number of materials have been extensively investigated as adsorbents in water pollution control including: silica gel (Cao et al., 2014), activated carbon (Li et al., 2014), zeolite (Jin et al., 2014, Kong et al., 2014, Yang et al., 2014), clay minerals (Mouzdahir et al., 2010, Ugochukwu et al., 2014) etc. Activated carbon has certainly been the most popular and widely used adsorbent in wastewater treatment applications throughout the world (Jais et al., 2016, Gawande and Kaware, 2016).

## 2.3 NATURAL MATERIALS

A number of natural materials such as chitin, clays, zeolites and activated carbon have been extensively studied for different pollutants removal from aqueous solution and are described below.

### 2.3.1 Activated carbon

Activated carbon is a carbonaceous material with a high surface area and a very porous structure, a great adsorption capacity and an effective regeneration (Momčilović et al., 2011). It is the most widely used adsorbent because of its large capacity and a wide variety of adsorbates. Activated carbon manufacturing consists of a charring or carbonization step in which most of the non-carbon material is volatilized by pyrolysis (usually between 500 and 750 °C). However, it remains an expensive material since the higher the quality the greater its cost. A complexing agent is required to improve its removal performance for inorganic matters. It also has poor mechanical rigidity and low selectivity when applied to real environmental pollution. Activated carbon becomes exhausted after several uses and needs to be separated from the aquatic system by filtration using traditional methods. However, the traditional method for separating the spent adsorbent has been found to be a tedious process resulting in the blockage in filters and loss of carbon in the sludge (Zhang et al., 2007). Therefore, this situation makes it no longer attractive to be widely applied in small-scale industries.

### 2.3.2 Clays

Three basic species of clay exist, namely: smectites (such as montmorillonite), kaolinite, and micas; out of which montmorillonite has the highest cation exchange capacity. The negative charge on the structure of clay minerals gives clay the capability to attract metal ions. Clays can be modified to enhance its efficiency for the removal of pollutants from water and wastewaters. Number of studies have been conducted using clays, mainly montmorillonite and bentonite to show their effectiveness for removing metal ions such as $Zn^{2+}$, $Pb^{2+}$, and $Al^{3+}$ from aqueous solutions (Ozdes et al., 2011). Putra et al. (2009) investigated the removal of amoxicillin from aqueous solutions by adsorption on bentonite.

### 2.3.3 Zeolite

Zeolites are a naturally occurring crystalline alumina silicates consisting of a framework of tetrahedral molecules, linked with each other by shared oxygen atoms. They are generally white, opaque and chalk like in appearance. They are internally inherently crystalline and exhibits micropores within the crystals that have uniform dimensions. Zeolites have high ion exchange capacity and size selective adsorption capacities, relatively high specific surface areas as well as thermal and mechanical stabilities (Wang et al., 2009). Bhatnagara and Sillanpää (2011) reported that there are 40 natural and over 100 synthetic zeolites which are also considered as selective adsorbents. Zeolites have been mostly attractive adsorbents in recent years because of its relatively cheap prices of about US$ 0.03–0.12/kg, depending on the quality of the mineral (Babel and Kurniawan, 2003). However, zeolites become unstable at high pH (Basu et al., 2006), hence solution pH need to be adjusted making this process expensive. Mthombeni et al. (2015) reported that natural zeolites are stable over wide environmental conditions, however, they have poor capacity for most contaminants. A number of researchers tested the surfactant modified zeolites and metal modified zeolites (Jiménez-Cedillo et al., 2011, Swarnkar et al., 2012, Simsek et al., 2013) in order to overcome the natural limitation and enhance arsenic removal.

### 2.3.4 Chitin and chitosan

Chitin is a naturally occurring muco polysaccharide which is found in a wide range of natural sources such as crustaceans, molluscs, insects, fungi and annelids. Chitosan is produced by alkaline *N*-deacetylation of chitin, which is widely found in the exoskeleton of shellfish and crustaceans. Chitin and chitosan are abundant, renewable and biodegradable resources. Studies have been conducted on application of Chitin and chitosan as low cost biosorbents and it has been demonstrated that chitosan-based biosorbents are efficient materials and have an extremely high affinity for dyes (Crini, 2006). Chitosan recently received considerable interest for heavy metals removal due to its excellent metal-binding capacities and low cost as compared to activated carbon. However, these materials have been found to be soluble in acidic media and cannot be used as an insoluble sorbent under these conditions. Physical and chemical modification may be applied to overcome this problem. Dai et al. (2012) chemically modified chitosan with 2-hydroxyethyltrimethyl ammonium chloride and applied it for Cr(VI) reduction and removal from aqueous solution.

## 2.4 BIOLOGICAL ADSORBENTS

A great interest has recently been directed to the biosorption of contaminants from solutions using different biomaterials as adsorbents. Biosorption is defined as the removal of pollutants by the passive binding to non-living biomass from an aqueous solution. From last few decades, biosorption process has emerged as a cost effective and efficient alternative for water and wastewater treatment utilizing naturally occurring and agricultural waste materials as biosorbents as these are cheaper, renewable and abundantly available. Biosorption has several advantages including low cost due to abundance of biomass, high selectivity, regenerable, required less sophisticated operation skill, limited sludge generation and generally have performance comparable to that of conventional techniques (Grassi et al., 2012, Park et al., 2010, Wang et al., 2015).

### 2.4.1 Industrial waste materials

Industrial waste is regarded as the potential low-cost adsorbent for the removal of pollutants. These materials are generally generated as by-products, hence locally available in large quantities. Various types of industrial wastes such as fly ash, waste slurry, lignin, red mud, coffee husks, blast furnace sludge, tea factory waste, sugar beet pulp, waste pomace of olive oil factory waste have been explored for their technical feasibility to remove toxic heavy metals from contaminated water (Alaba et al., 2018, Singh et al., 2018, Ahmaruzzaman, 2008, Anastopoulos et al., 2017).

#### 2.4.1.1 Fly ash

Fly ash is a waste material originating in great amount in combustion processes. It is a mineral residue resulting from the coal combustion in electricity generating plants. Fly ash consists mainly of carbon, oxides of silica, alumina and iron. Raw fly ash has generally been reported to have low adsorption capacity which may be enhanced by physical or chemical treatment, thereby increasing the value for application. It is widely used in industries as a low-cost adsorbent, even though it contains heavy metals. Removal of dyes, phenols and heavy metals such as Cr(VI), Cr(III), Hg, Pb, Cd, Cu, As(III) and As(V) have been reported by different researchers (banerjee et al., 2004, Feng et al., 2004, Gupta and Suha, 2009). Sun et al. (2010) studied the adsorption of anionic dyes on fly ash and reported that an increase in the initial dye concentration enhanced the adsorption capacity but failed to increase the removal efficiency.

## 2.4.1.2  Red mud

Red mud is a waste material formed during the production of alumina. It is mainly composed of fine particles of silica, iron, aluminum, calcium and hydroxides and titanium oxides, which are responsible for its high surface reactivity. It has been explored as an alternate adsorbent for different heavy metals. Altundogan et al. (2002) applied red mud for As removal. The authors reported that alkaline aqueous medium (pH 9.5) favored As(III) removal, whereas the acidic pH range (1.1–3.2) was effective for As(V) removal.

## 2.4.1.3  Blast furnace slag

Steel plants have been reported to produce a large volume of granular blast furnace slag as a byproduct, which causes serious disposal problem. This slag may be converted into an effective and economical adsorbent for the removal of some toxic heavy metals and organic pollutants from aqueous solution. The removal of various metals dyes have been studied using blast furnace slag in recent years (Zhao et al., 2016).

## 2.4.2  Agricultural waste materials

Natural materials and agricultural wastes have been recently explored as potential biosorbents by many researchers due to their cost effectiveness, local availability, and the added economic value associated with avoiding disposal routes such as landfill and incineration  (Crini, 2006, Babel and Kurniawan, 2003). Various agricultural waste materials have been examined for the removal of diverse type of pollutants from water. Agricultural wastes such as, sawdust (Gupta and Babu, 2009), coffee (Utomo and Hunter, 2010), yeast (Moyo et al., 2012), coffee resin (Mulani et al., 2013), tannin resin (Huang et al., 2013), palm branches (Shouman et al., 2013), tea waste (Lunge et al., 2014), pine cone (Ofomaja et al., 2015), straw (Salem and Yakoot, 2016), coconut shell (Tang et al., 2017), avocado shell (Palma et al., 2016), bagasse (Rattanachueskul et al., 2016) and olive powder (Lopez-Cabeza et al., 2017) among others have attracted attention for the removal of different contaminants from aqueous solution.

### 2.4.2.1    Algae

Algae include a large and diverse assemblage of organisms that contain chlorophyll and carry out oxygenic photosynthesis. Algae are classified on the nature of the chlorophyll(s), the cell wall chemistry, and flagellation. All types of algae contain chlorophyll *a*. The microorganism's cell wall mainly consists of polysaccharides, lipids and proteins, which offer many functional groups such as carboxylate, hydroxyl, sulphate, phosphate, amide and amino groups which have many binding sites for metals. Main advantages on application of algae as a biosorbent include low cost, high metal adsorption capacity and their wide availability (Sharma and Garg, 2014).

### 2.4.2.2    Coconut waste

The coconut (Cocos nucifera) is highly nutritious and rich in fiber, vitamins, and minerals. Coconut wastes such as coir pith, coconut bunch waste, coconut husk, copra meal, male flowers of coconut tree, etc. have been widely explored as adsorbents for the removal of various pollutants from wastewater. Isah et al. (2015) studied the removal of Reactive Blue 19 dye on coconut shell based activated carbon. The authors reported that the process was more efficient in alkaline medium than in acidic medium and also at higher temperatures.

## 2.5    CHEMICAL COMPOSITION OF AGRICULTURAL ADSORBENTS

Agricultural by-products usually are composed of lignin, cellulose and hemicellulose as major constituents which consists of other polar functional groups of lignin, which includes extractives, alcohols, aldehydes, ketones, carboxylic, phenolic, and ether groups. These groups have high affinity for heavy metals and can bind metal ions by donation of an electron pair from these groups to form complexes or chelates with the metal ions in solution (Pagnanelli et al., 2003, Zhou et al., 2015). Lignin is a macromolecule, which consists of alkylphenols and has a complex three-dimensional structure as shown in Fig. 2.1. This matrix comprises a variety of functional groups, such as hydroxyl, methoxyl and carbonyl, which impart a high polarity to the lignin macromolecule. Lignin is a polymer of aromatic compounds which provide structural strength, provide sealing of water conducting system that links roots with leaves, and protect plants against degradation. Lignin is a major component of wood, accounting for 23–33% of softwood mass and 16–25% of hardwood mass (Bridgwater, 2004).
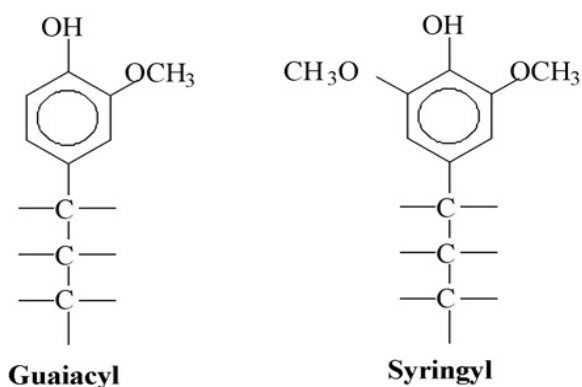
Figure 2. 1: Schematic illustration of building units of lignin (Demirbas, 2008).

Cellulose is a remarkable pure organic polymer, consisting solely of units of anhydroglucose held together in a giant straight chain molecule that are bound together by β-(1,4)-glycosidic linkages as shown in Fig. 2.2.
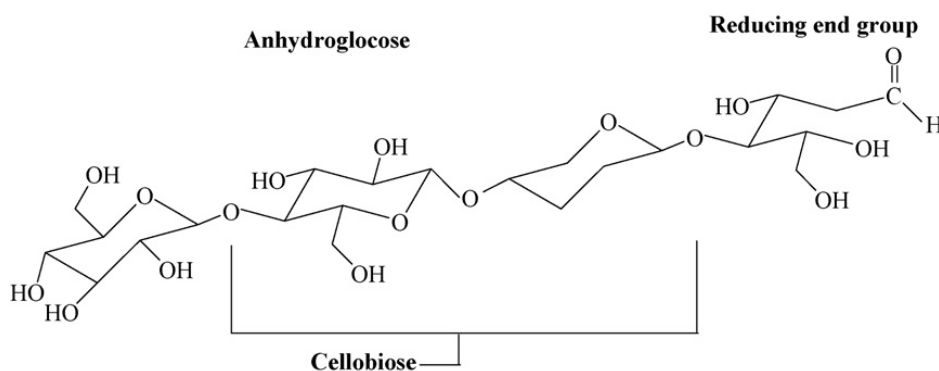


Figure 2.2: The structure of cellulose. Anhydroglucose is the monomer of cellulose, cellolbiose is the dimer (Ravikumar et al., 2005).

## 2.6 BIOSORBENTS IN WATER AND WASTEWATER TREATMENTS

The biological materials, also known as biosorbents, contain special surface properties and functional groups which enable them to adsorb different kinds of pollutants by metal binding (Ofomaja and Ho, 2007). Biosorbents offer advantages over other adsorbents in wastewater treatment which includes selective adsorption of heavy metal ions, little processing, low cost and easy regeneration (Wan Ngah and Hanafiah, 2008). However, their use is limited by low sorption capacity, low filtration rates and low surface area. Recently different kinds of low cost materials such as by-products or waste materials have been reported as potential adsorbents for various pollutants from aqueous solution. Gupta and co-workers have reviewed the details of treatment methods for various pollutants in water using low-cost adsorbents (Gupta et al.,

2009). To eliminate the disadvantages of the biosorbent, several modifications can be applied which includes grinding particles to a very small size, grafting or cross-linking to a synthetic polymer or fixing onto an inorganic support material. The biosorbent particles can be packed in columns which are the most effective devices for continuous removal of pollutants, although mechanical strength of the biosorbent is low in packed columns.

## 2.7   SURFACE MODIFICATION OF BIOSORBENT

The application of untreated plant wastes as biosorbents is accompanied with several problems such as low adsorption capacity and leaching of soluble organic compounds contained in the plant material onto the solution thereby increasing the total oxygen carbon (TOC), biological oxygen demand (BOD and high chemical oxygen demand (COD). Pretreatment of biosorbents will extract plant water soluble or organic soluble constituents which may leach into treated water, improve the adsorption capacity of the biosorbent by swelling the material so as to increase the internal and external surfaces (Sciban et al., 2006) and modify the biosorbent surface to allow for penetration of polyfunctional organic compounds into the matrix of the biosorbent (Wartelle and Marshall, 2000). Chemical modification liberates new adsorption sites and enhances mechanical stability and protonation (Anastopoulos et al., 2013, Velazquez-Jimenez, 2013, Yargıç et al., 2014).

Several researchers have investigated the use of numerous chemical agents/extractants for modifying plant materials in their application as biosorbents and some of these include bases (sodium hydroxide, calcium hydroxide, sodium carbonate), acetone and ethanol (Montazer-rahmati et al., 2011), acids, (hydrochloric acid, tartaric acid, nitric acid, sulphuric acid, citric acid), minerals, organic acid solutions and organic compounds (ethylenediamine, formaldehyde, epichlorohydrin, methanol, glutaraldehyde and polyethylene imine) (Feng et al., 2011, Martínez-Cabanas et al., 2016), dye and oxidizing agents (hydrogen peroxide) (Wan Ngah, 2008). Several investigations have been performed on the citric modification of agricultural wastes products. Wartelle and Marshall (2000) modified several common agricultural wastes (soybeans, rice hulls, sugarcane bagasse, cottonseed, rice straw and rice bran) with citric acid and determined their ability to adsorb copper ions. Sciban et al. (2006) applied formaldehyde–sodium hydroxide treatment of oak and black locust sawdust before applying it as an adsorbent for removing copper and zinc from aqueous solution. It has been

shown that treating agricultural materials with polyacids (citric, tartaric, phosphoric) at a mildly elevated temperature enhanced their metal ion sorption capacity. Recently, Ramrakhiani et al. (2017) treated dried activated tannery industry sludge with NaOH, EDTA and n-hexane and observed the significant increase in the Co(II) biosorption efficiency of up to 6–8% than the control biosorbent. NaOH treatment was conducted for this study because of the possibility of the hydrolysis reactions that can lead to the formation of more hydroxyl (–OH) and carboxylic (–COOH) groups both in undissociated and dissociated forms and enhanced the metal binding properties of the biosorbent.

## 2.8    PINE CONE

Pine trees are evergreen, coniferous, and fast-growing resinous trees which are widely grown in most temperate regions in relatively dense stands. There are about 115 species of pine which come in male and female varieties. Male and female cones grow on the same tree but male pine cones are smaller, not more than 5 cm long, more herbaceous and are short lived (lives for only few months). They are covered with pollen sacs and after they are released, they then fall off the trees. Female pine cones on the other hand are woody with scaled structure, typically 3-60 cm long and are much harder than the male pine cones. Pine cone is composed of epidermal and sclerenchyma cells which contain cellulose, hemicellulose, lignin, resin, and tannins in their cell walls which contains polar functional groups such as alcohols, aldehydes, ketones, carboxylic, phenolic and ether groups (Ucun et al., 2003). They also contain little amounts of xylose, arabinose, some extractable compounds and resins which is a sticky residue that is deposited on hands and fingers when pine cones are handled. Lignin strengthens the cell walls and protects the microfibrils of the cell wall from chemical, physical and biological attack (Ofomaja et al., 2009). Some properties of pine cone are shown in Table 2.1. Pine tree cones are produced in large quantities at forest industries as a litter and their popular uses include decoration, wood, making coffins and resins.

Table 2.1: Properties of pine cone (Brebu et al., 2010; Nagata et al., 1990)

| Properties of pine cone. | Proximate analysis wt% |
|---|---|
| **Moisture** | 9.6 |
| **Ash** | 0.9 |
| **Volatile** | 77.8 |
| **Elemental analysis wt%** | |
| **C** | 42.62 |
| **H** | 5.56 |
| **N** | 0.76 |
| **S** | 0.05 |
| **O** | 51.01 |
| **Main constituents wt %** | |
| **Lignin** | 37.4 |
| **Hemicellulose** | 46.5 |
| **Cellulose** | 18.8 |
| **Ethanol/toluene extractives** | 15.4 |

## 2.8.1 Pine cone as a biosorbent

Considering the fact that South Africa is an agricultural and industrial country, it will be much logical and cost effective to use the abundant agricultural wastes as adsorbents. Large quantities of pine cones are produced annually as agricultural by-product throughout the world. Each pine cone is composed of an axis upon which are borne, in a spiral fashion, a large number of woody scales. The use of pine cone as a biosorbent material presents strong potential due to its high content of cellulose, hemicellulose and lignin. Pine cone is one of the adsorbents widely used to treat industrial wastewater since it possesses impressive biosorption capacities for the removal of heavy metal ions and dyes. Pine cone has been extensively studied as an efficient biosorbent in the removal of textile dye (Mahmoodi et al., 2011), phosphate ion (Benyoucef and Amrani, 2011), phenol (Vazquez et al., 2006), copper (Ofomaja et al., 2009), cesium (Ofomaja et al., 2013), lead (Pholosi et al., 2013, Ofomaja et al., 2010b), chromium (VI) (Ucun et al., 2003) and arsenic (Saqib et al., 2013, Vinh et al., 2015).

Pine cone has been applied for various pollutants removal on its modified and unmodified form. Several modifying agents have been studied to reduce organic components of pine cone thereby increasing its adsorption capacity. Modified pine cone powder as biosorbent has been shown to have high affinity for many metal ions. For example, Ofomaja and Naidoo (2010) treated pine cone powder surface with potassium hydroxide and applied it for copper(II) and lead(II) removal from solution. Dawood and Sen (2012) treated pine cone with hydrochloric acid before applying it for anionic dye Congo red adsorption from aqueous solution. As a potential biosorbent, pine cone has the advantage of achieving maximum metal removal at short contact time. For example, Malkoc (2006) achieved equilibrium for nickel (II) in 3 minutes while Ucun et al. (2002) removed chromium(IV) from aqueous solution in 20 minutes. Literature research revealed that initial solution pH strongly affects metal sorption on to pine cone powder. Oguz. (2005) showed that pine cone powder capacity for chromium(VI) increased from 10.00 to 16.60 mg/g when solution pH decreased from 5.4 to 1.5 while Ucun et al. (2003) observed an increase from 6.73 to 53.6 % for lead ion adsorption as solution pH was increased from 2.0 to 4.0.

Pine cone like other biosorbents, possesses some limitations in wastewater treatment such as low biosorption capacity, low filtration rates and low surface area. A major drawback in its application as a biosorbent is the discolouration of the treated water due to the presence of organic components. However, this may be overcome by incorporating pine cone with a material that contains such properties. Magnetic nanoparticle is one material that has recently been coated on biosorbents to improve its adsorption capacity. Magnetic biosorbents such as magnetic sugarcane bagasse (Yamamura et al., 2011), magnetically modified spent coffee ground (Safarik et al., 2012), slow pyrolysis magnetic biochar (Zhang et al., 2013), magnetic tea waste (Lunge et al., 2014) and iron coated seaweed (Vieira et al., 2017a) amongst others have been explored for wastewater treatment.

## 2.9 MAGNETIC NANOPARTICLES

Magnetic nanoparticles are materials made up of a magnetic core and polymeric shell (Rakhshaee and Panahandeh, 2011). Magnetic nanoparticles have been recently applied in water and wastewater treatment because of their ease of synthesis, high surface area, large amounts of active sites for interaction with metallic and organic species, separation after use by an external magnetic field and the absence of internal diffusion resistance (Panneerselvam

et al., 2011a). Magnetic nanoparticles can be reused after magnetic separation by desorbing the adsorbed contaminants (Huber, 2005). Iron magnetic particles have gained popularity in recent years for numerous applications (Jiang et al., 2011). Several types of iron magnetic particles such as $Fe_2O_3$ (Mornet et al., 2002), maghemite (Hu et al., 2005), $Fe_3O_4$ (Shen et al., 2009b), $CuFe_2O_4$ (Tu et al., 2012) and $\alpha$-$Fe_2O_3$ (Liu et al., 2018b) have been explored for their ability to perform as adsorbents for metallic and organic pollutants from water. According to Rakhshaee and Panahandeh (2011), these magnetic particles contain zerovalent iron $Fe^0$ nano-iron material ($Fe^0$ NPs) which are active for remediating contaminants that are susceptible to reductive transformation like heavy metals of high valences (Manning et al., 2007), azo dyes (Fan et al., 2009), halogenated organics and toxic inorganic anions (Yang and Lee, 2005). Nanomagnetic materials have the advantage of being easily synthesized and manipulated through coating and functionalization, environmentally friendly and display high adsorption performances due to their large surface to volume ratio (Gupta and Nayak, 2012b).

## 2.10 IRON NANOPARTICLES

The intensively studied nanosized ferric oxides for heavy metals removal from wastewater include goethite ($\alpha$-FeOOH), hematite ($\alpha$-$Fe_2O_3$) (Al-Ahmari et al., 2018), amorphous hydrous Fe oxides, maghemite ($\gamma$-$Fe_2O_3$) (Talbot et al., 2018), and magnetite ($Fe_3O_4$) (Feng et al., 2012). These nanoparticles have different chemical properties originating from the oxidation states of iron. They exist in a rich variety of structures (polymorphs) and hydration states. Iron oxides have several advantages which includes; better oxidative stability, compatibility in non-aqueous systems, and nontoxicity over other metal nanoparticles. These iron nanoparticles have been widely used as materials for drug carrier (Yang et al., 2006), hyperthermia (Ghosh et al., 2011), magnetic resonance imaging (MRI) (Ma and Liu, 2007), proton exchange membrane (Brijmohan and Shaw, 2007), sensor (Pankhurst et al., 2003, Sun, 2006) and cancer therapy (Hu et al., 2006).

### 2.10.1 Magnetite ($Fe_3O_4$)

Magnetite ($Fe_3O_4$) phase arises from the inverse spinel structure with Fe(III) ions which is distributed randomly between octahedral and tetrahedral sites, while Fe(II) ions exists only in octahedral sites. It exhibits the unique electrical and magnetic properties based on the transfer

of electrons between $Fe^{2+}$ and $Fe^{3+}$ in the cubic sites (Geng et al., 2008). Among all iron oxides, magnetite $Fe_3O_4$ possess the most interesting properties because of the presence of iron cations in two valence states, $Fe^{2+}$ and $Fe^{3+}$, in the inverse spinel structure. Magnetite can be found naturally as the mineral that is commonly known as lodestone, which is a black and ferromagnetic material. Magnetite nanoparticles are however the most studied materials due to their response to magnetic field through the superparamagnetic behaviour at room temperature with high saturation magnetization.

### 2.10.2  Hematite ($\alpha$-Fe$_2$O$_3$)

Hematite, ferric oxide, can be found naturally as the mineral hematite in rocks and soils. It has the corundum structure where the oxides ions form a hexagonal close packing lattice and $Fe^{III}$ ions occupying octahedral holes (Butler et al., 2003). Two thirds of the holes are occupied with $Fe^{III}$ ions and this arrangement produces pairs of $Fe(O)_6$ octahedra. In the structure, each octahedra shares edges with three other neighbors in the same plane and shares a face with another one from an adjacent plane. Hematite has been applied for treatment of both heavy metals and dyes from aqueous solution (Al-Ahmari et al., 2018).

### 2.10.3  Zero-valent iron

Nano zero-valent iron (nZVI) has been shown to be a strong reducing agent useful for removing several pollutants from aqueous solution. The nZVI has been reported to have the ability to reduce Cr(VI) to Cr(III), and also adsorb and co-precipitate the chromium (III) in solution (O'Carroll et al., 2013). Different types of nZVI processes also have been used to treat various pollutants, including chlorinated hydrocarbons, nitrochlorobenzene, nitrites, dyes, and textile wastewaters due to the strong redox potential and large specific surface area of the nZVI particles (Liu et al., 2012)

### 2.11  COATING OF MAGNETIC NANOPARTICLES

One major issue in the use of nano particles is agglomeration which occurs primarily by direct interparticle interactions via Van der Waals forces and magnetic interaction (Cushing et al., 2004). This phenomenon of agglomeration causes a reduction of specific surface area, interfacial free energy and ultimately particle reactivity (Rakhshaee and Panahandeh, 2011).

Iron magnetic nanoparticles especially $Fe_3O_4$ are also known to show poor selectivity and stability under acidic conditions (Liu et al., 2013). Surface modification using a stabilizer is therefore of great importance in determining the nanoparticle stability under physiochemical conditions. These stabilizers are capable of increasing dispersion of the nanoparticles by electrostatic repulsion and steric hindrance (Yang and Lee, 2005). Magnetic nanoparticles can therefore be coated on solid matrix such as polymers, silica, organic coating agents, carbon, zeolites and biomaterials to make separation from the effluent simple (Zhang, 2003).

### 2.11.1 Coating of magnetic nanoparticles onto biomaterials

Magnetic nanomaterial's applied as adsorbents in water treatment are usually injected directly into the effluent stream and subsequent separation of the nanoparticles from aqueous solution is usually difficult and time consuming and may lead to clogging in continuous systems (López-Téllez et al., 2011). Coating magnetic nanoparticles with biomaterials combines the relatively large numbers of active sites, the high specific surface area and the convenience of separation offered by the magnetic species, with the adsorption properties of the biomaterial due to the presence of the functional groups it contains. Iron magnetic nanoparticles have been coated or functionalized and stabilized by biological materials such as seaweed (Vieira et al., 2017b), orange peel powder (Gupta and Nayak, 2012b), Shellac (Gong et al., 2012), tea waste (Panneerselvam et al., 2011b), orange peel pith (López-Téllez et al., 2011), cross-linked pectin (Rakhshaee and Panahandeh, 2011), polyacrylic acid (Huang and Chen, 2009), humic acid (Liu et al., 2008), gum arabic (Banerjee and Chen, 2007), and chitosan (Chang and Chen, 2005). The prepared magnetic nanomaterial-biosorbents have been applied for the removal of heavy metals and organic pollutants from aqueous solution. The addition of chelating organic anions, such as carboxylate ions (e.g. citric, gluconic, or oleic acid) or polymer surface complexing agents (e.g. dextran, carboxydextran, starch, or polyvinyl alcohol) during the formation of magnetite can help to control the size of the nanoparticles (Laurent et al., 2008).

### 2.12 APPLICATION OF MAGNETIC NANOPARTICLES FOR POLLUTANTS REMOVAL

Recently, nanosized magnetic material have gained special attention as adsorbents for pollutants removal based on their numerous advantages such as high separation efficiency,

simple manipulation process, kind operation conditions (Lu and Astru, 2018) and ease of functional modifications. They also possess high surface area and optimal magnetic properties, which lead to high adsorption efficiency, high removal rate of contaminants, easy and rapid separation of adsorbent from solution via magnetic field. Magnetic nanoparticles can be reusable after magnetic separation by removing the adsorbed toxic contaminants (Chen et al., 2009). Their basic properties, extremely small size, high surface-area-to volume ratio and the absence of internal diffusion resistance provides better kinetics for adsorption of metal ions from aqueous solution. Magnetite nanoparticles with superparamagnetism can be easily magnetized with an external magnetic field and demagnetized immediately once the external magnetic field is removed, not retaining any magnetism. Magnetic nanoparticles are susceptible to air oxidation and due to high specific surface energy and anisotropic dipolar attraction, magnetite nanoparticles tend to aggregate together into larger clusters which lead to a possible loss of superparamagnetism and limit their applications. Modification of the surface of MNPs not only prevents aggregation/agglomeration of the particles, leading to colloidal stability, but also renders them with water-solubility, biocompatibility, non-toxicity, nonspecific adsorption to cells, and bioconjugation.

## 2.13  SYNTHESIS OF $Fe_3O_4$ NANOPARTICLES

Due to unique size, biocompatibility, low toxicity and superparamagnetic properties, magnetic nanoparticles are emerging as promising tools in various fields such as physics, medicine, biology, environment and material science. Most of these applications require the nanoparticle to be of uniform in shape and size, and be well dispersed in a solvent (Jang and Lim, 2010). The optimization of properties can be achieved by choosing appropriate synthesis method or by varying preparation conditions. For different applications, various methods have been reported to synthesize iron oxide nanoparticles including co-precipitation, thermal decomposition, sol-gel synthesis, hydrothermal reaction, micro emulsion synthesis, solvothermal synthesis, sonochemical reaction, laser pyrolysis and high temperature organic phase decomposition (Daou et al., 2006, Zhang et al., 2007, GhanbarI, 2014, Aphesteguy et al., 2015, Baier et al., 2007). These studies provided many useful preparation technologies for the preparation of $Fe_3O_4$ with different shapes. Among these reported methods, the chemical co-precipitation has been found to be the most promising method because of its simplicity, productivity and spherical shaped $Fe_3O_4$ has been obtained (Mohsen et al., 2014). A brief

description of the methods most widely used for preparing materials with applications in metal removals is given in the following section:

### 2.13.1 Micro emulsion method

Microemulsion is defined as a thermodynamically stable isotropic dispersion of two immiscible liquids consisting of nano-size domains of one or both liquids in the other, stabilized by an interfacial film of surface-active molecules. Microemulsions may be classified as water-in-oil (w/o) or oil-in-water (o/w) depending on the dispersed and continuous phases (Pestana et al., 2008). Water and oil (w/o) microemulsion is a method consisting of nano sized water droplets dispersed in an oil phase and stabilized by surfactant molecules at the water/oil interface. The major advantage of the microemulsion systems is that the size of nanoparticles can be controlled by varying their composition and by modulating the size of the aqueous micellar core. However, there are several disadvantages of using microemulsions for the synthesis of magnetic nanoparticles. First, extensively agglomerated nanoparticles are often generated. Second, the nanoparticles are poorly crystalline for the procedure is usually performed at a relatively low temperature. Third, the yield of the nanoparticles is often very low (Zhang et al., 2007).

### 2.13.2 Hydrothermal

Hydrothermal reactions are aqueous reactions carried out using autoclaves or high-pressure reactors where the pressure can be over 2000 psi at temperatures above 200 ℃. High temperatures result in rapid nucleation and faster growth of the newly formed particles, leading to the formation of small-sized nanoparticles (NPs). There are two main routes for the formation of magnetite via hydrothermal conditions: (1) hydrolysis and oxidation (2) neutralization of mixed metal hydroxides. These two reactions are very similar, except that only ferrous salts are used in the first method. In this process, the reaction conditions, such as solvent, temperature, and time, usually have important effects on the products. In the hydrothermal process, the particle size is controlled mainly through the rate processes of nucleation and grain growth. Size and morphological control in hydrothermal reactions is achieved by controlling time and temperature whereas the reaction conditions of precursor material and pH have an impact on phase purity of the nanoparticles. Daou et al. (2006) have described the hydrothermal synthesis of monodisperse magnetite nanoparticles of average size 39 nm.

### 2.13.3 Co-precipitation method

Co-precipitation method has been by far the most commonly used method for the preparation of magnetic iron oxide nanoparticles. In coprecipitation method, magnetite nanoparticles are precipitated from a mixed ferrous and ferric salt solution by adding NaOH or $NH_4OH$ as a precipitating agent. The advantage of this method is that it is fast, simple, cost effective, versatile and diverse surface modification can be carried out at the same time during the preparation and large quantities of particles can be synthesized. The size, composition and shape of nanoparticles depend on the type of salts used (chlorides, sulphates, nitrates, perchlorates), temperature, solution pH, $Fe^{2+}$ and $Fe^{3+}$ ratio and ionic strength of the precipitation medium (Liu, 2004). Particles with sizes ranging from 5 to 100 nm have been obtained using this method. In general, the magnetite reaction may be written as follows:

$$Fe^{2+} + 2Fe^{3+} + 8OH \rightarrow Fe_3O_4 + 4H_2O \tag{2.1}$$

### 2.14 MOLECULAR RECOGNITION COMPOUNDS

Molecular recognition involves a specific interaction between two or more molecules via non-covalent bonding e.g. metal coordination, hydrogen bonding, hydrophobic interaction, halogen bonding, $\pi$-$\pi$ interaction, electrostatic effects, electromagnetic effect and van der Waals forces (Cosic, 1994). In the application of molecular recognition to the separation processes, a chemical compound with high species selectivity attached to a solid support is used to accomplish the required chemical separation. The recognition compound called the "host" possesses a high degree of recognition to specific elements or compounds called the "guest" (Rahman et al., 2013). The recognition property of the compound should be effective even at low concentrations of the "guest" or when the guest is present in complex matrices (Izatt, 1994). The "host" compound is usually the larger molecule which encompasses the smaller "guest" molecule. Some known "host" molecules include cyclodextrin, calixarenes, pillararenes, cucurbiturils, porhyrins, crown ethers, cryptophanes etc. The thermodynamic benefits of the host-guest chemistry are derived from the idea that there is a lower overall Gibbs free energy due to the interaction between host and guest molecules. One important recognition compound applied in water and wastewater treatment for host-guest interaction is cyclodextrin (CD), which are cyclic oligosaccharides formed by monomers of D-glucopyranose bound together by means of α-1,4-glycocidc linkages and closed in a ring to form a hollow structure

of a truncated cone (Paolino, 2013). Host-guest supramolecular complexes involving an amphiphilic compound and a cyclodextrin ring is driven by non-covalent interactions, including van der Waals, hydrophobic, electrostatic and charge transfer interactions, metal coordination, hydrogen bonding and steric effects (Zhang and Wang, 2011). In aqueous solution, the inclusion of (dehydrated) guest into the non-polar cavity of the CD is accompanied by the release of water from the CD cavity as shown in Fig. 2.3. The latter process is strongly dependent on the interactions between water-water and water-cyclodextrin occurring inside the cyclodextrin cavity (Pajzderska et al., 2011), and it also depends on other factors, including the size of the cyclodextrin cavity and guest as well as the structure (geometry) of guest molecules (Garcia-Rio et al., 2010).
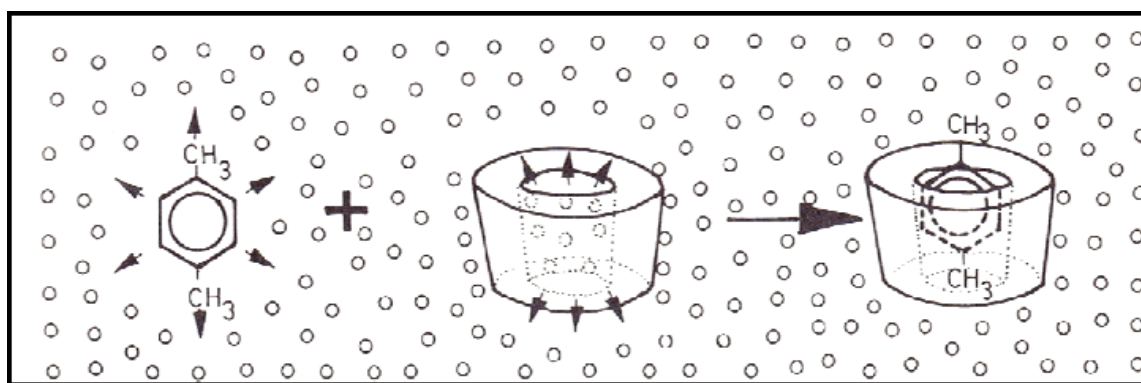


Figure 2.3: Cyclodextrin inclusion complex formation using xylene as the guest molecule. Small circles represent the water molecules


## 2.15  CYCLODEXTRIN

Cyclodextrins (CDs) are a family of compound made of sugar (starch) molecules bound together in a cyclic ring. They are a group of naturally cyclic oligosaccharides, with six, seven, or eight glucose sub-units linked by α-(1,4) glycosidic bonds in a torus shaped structure and are denominated as α-, β-, and γ-CD, respectively. The three-dimensional structures formed in CD keeps the hydroxyl groups on the outer edges, while hydrogen atoms and oxygen bridges exist in the internal cavity. This structure therefore, makes cyclodextrin possess an internal hydrophilic surface and a hydrophobic central cavity (Meyer et al., 2000, Mallard et al., 2015). Non-polar pollutant can be trapped on the internal cavity while the outer surface remains hydrophilic. Cyclodextrin-based polymers could remove both organic and inorganic pollutants from water to desirable levels because of their efficiency in pollutant removal from poly-contaminated mixtures, even at low trace concentrations. Attention has recently been focused

on cyclodextrin based polymeric materials in a wide variety of applications due to their unique sorption properties. Due to the properties and size of the cavity, CD's are able to form inclusion complexes either in solution or in the solid state with a wide variety of guest molecules differing in their chemical and physical properties (Braibanti et al., 1998). CDs represent an interesting and attractive alternative as adsorbents because of their particular structure, physico-chemical characteristics, chemical stability, high reactivity and excellent selectivity towards aromatic compounds and metals, resulting from the presence of chemical reactive groups (hydroxyl, acetamido or amino functions) in polymer chains (Crini, 2005a). The α-, β-, and γ-CD chemical structures are shown in Fig. 2.4 and their properties are demonstrated in table 2.2.
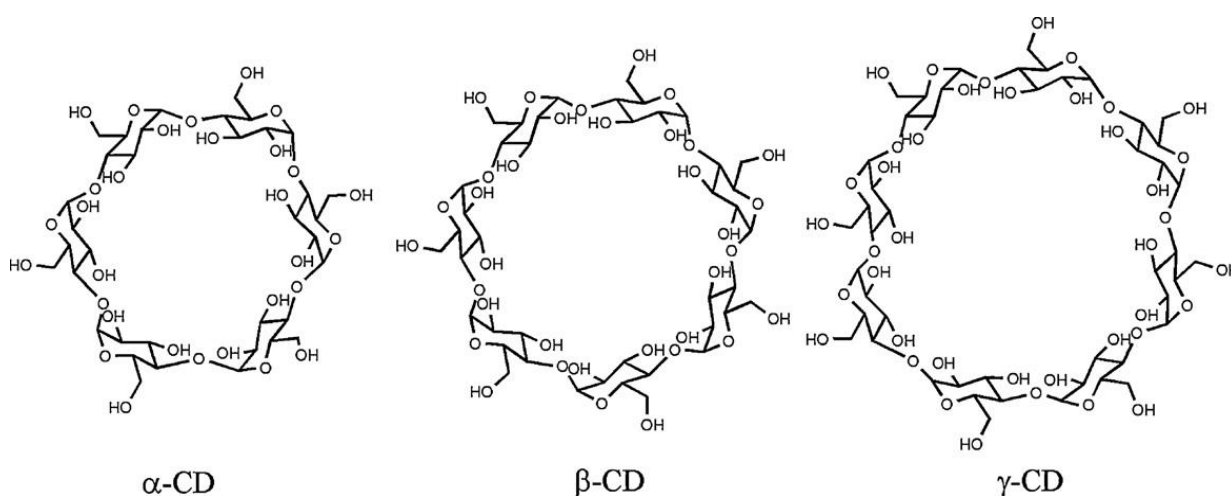


Figure 2.4: Chemical structure of alpha- (α-CD), beta- (β-CD) and gamma- (γ-CD) cyclodextrins.

Table 2.2: Properties of natural cyclodextrins. Adapted from: Cyclodextrins and their complexes; (Dodziuk, 2006)

| *Property* | α-Cyclodextrin | β-Cyclodextrin | γ-Cyclodextrin |
|---|---|---|---|
| Number of glucose units | 6 | 7 | 8 |
| Molecular weight | 972 | 1134 | 1296 |
| Approximate inner cavity diameter (pm) | 500 | 620 | 800 |
| Approximate outer diameter (pm) | 1460 | 1540 | 1750 |
| Approximate volume of cavity (106 pm3) | 174 | 262 | 427 |
| Solubility in water at 25ºC (g/100 mL) | 14.5 | 1.85 | 23.2 |
| Surface tension (MN/m) | 71 | 71 | 71 |

| Melting temperature range (°C) | 255-260 | 255-265 | 240-245 |
|---|---|---|---|
| Crystal water content (wt.%) | 10.2 | 13-15 | 8-18 |
| Water molecules in cavity | 6 | 11 | 17 |

## 2.16 BETA-CYCLODEXTRIN

Among the three types of cyclodextrin, β-CD has a rather rigid structure, complete with a secondary belt formed by hydrogen bonds (Szejtli, 2004). β-CD has 21 hydroxyl groups present at the 2-, 3- and 6-positions in the glucose unit which are very reactive and available to form a number of linkages. Furthermore, β-CD shows excellent intermolecular interaction due to its hydrophobic cavity, which can accommodate and recognize various types of compounds. β-CD is the most commonly applied due to the relative ease of synthesis, low price and the presence of internal cavity into which large number of molecules will fit. However, their main disadvantage which limits its application in pollutants removal from wastewater is the fact that they are very soluble in water. Numerous studies on the preparation of water-insoluble β-cyclodextrin polymer (β-CDP) has been conducted to overcome the solubility problem (Morin-Crini and Crini, 2013).
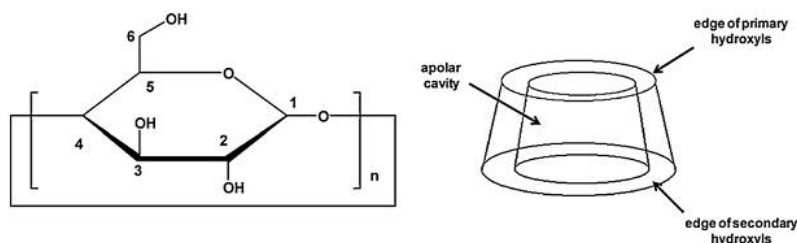


Figure 2.5: Chemical structure and shape of the β-cyclodextrin molecule (Crini and Crini, 2013).

## 2.17 CROSS-LINKING

Cross-linking occurs when a reagent (namely a crosslinking agent) introduces intermolecular bridges and/or crosslinks between polysaccharide macromolecules thus forming a three-dimensional network. Chemical cross-linkers used for carbohydrate molecules are polyfunctional compounds with electrophilic functions that can form covalent bonds with the free reactive hydroxyl groups of the carbohydrate molecules (Gallego et al., 2013a). Several types of cross-linkers for carbohydrate molecules have been studied and applied, some of which include epichlorohydrin (1-chloro-2,3-epoxypropane) (Chen et al., 2011), diisocyanate

(Mohamed et al., 2011b), glutaraldehyde (Mera et al., 2008) and dicarboxylic acids (Sarkar and Kochak, 2005). The cross-linker when applied usually produce branching across the carbohydrate molecules leading to three-dimensional network which converts the carbohydrate molecule from being water-soluble into an insoluble and re-generable network shaped polymer suitable for variety of applications (Liu et al., 2011).

Cross-linkers have been used to form links between biomaterials and specific molecular recognition compounds as in the case of composites formed between cotton and cyclodextrin (CD) using vinyl monomer as cross-linker (Lee et al., 2001), starch and cyclodextrin (CD) using hexamethylene diisocyanate (HMDI) as cross-linker (Ozmen et al., 2008) and chitosan beads and cyclodextrin using hexamethylene diisocyanate (HMDI) as cross-linkers (Zha et al., 2008). In the case of epichlorohydrin (EPI), lone pairs of electrons on the oxygen of –OH on the carbohydrate and/or molecular recognition compound interact with the electron efficient carbon ($-CH_2-$) of the epoxide. Due to the unique structure of the molecules combined with their polyfunctionality, β-CD molecules can form cross-linked networks. β-CD can be cross-linked by direct reaction between its hydroxyl groups with a coupling agent to form water-soluble or water-insoluble polymeric structures. The primary product of the reaction of CD with a coupling agent such as epichlorohydrin (EPI) or hexamethylene diisocyanate (HMDI) in an alkaline medium is a heterogeneous mixture of various CD glyceryl ethers. Cross-linked beads have advantages such as faster kinetics, increased ease of operation (Bailey et al., 1999) and interesting diffusion properties. After adsorption, the cross-linked materials can be easily regenerated by washing using a solvent or by solvent extraction. Cross-linked materials retain their original properties even though crystallinity changes and are not affected by acidic or basic solutions.

### 2.17.1 Epichlorohydrin as a cross-linking agent

Epichlorohydrin is a bifunctional cross-linking agent containing two reactive functional groups, which can form bonds with β-CD molecules (cross-linking step) and/or itself (polymerization step). EPI (1-chloro-2,3-epoxypropane) is the most common cross-linker used in polysaccharide chemistry (Morin-Crini and Crini, 2013). It is a short molecule with an epoxy group which is highly reactive with hydroxyl groups. Although this cross-linking reaction was developed 60 years ago, it is well known and relatively easy to apply for the preparation of

water-insoluble β–cyclodextrin-epichlorohydrin based networks. Modified CDs have recently received attention for their ability to efficiently remove both toxic heavy metals and organic pollutants. Delval and co-workers prepared β-CD polymer by polymerization using EPI as a cross linking agent for aromatic pollutants removal (Delval et al., 2002). Sikder et al. (2014) modified all three types of CD with epichlorohydrin to reduce their solubility in water before applying them for Cu(II) ions removal from aqueous solution. The authors achieved an increase in Cu(II) adsorption capacity after modification.

### 2.17.2 Hexamethylene diisocyanate as a cross-linking agent

Diisocyanate are interesting for environmental purposes because they are highly cross-linked and possess high surface areas and a heterogeneous non-polar network. When diisocyanates are applied as cross-linkers, for example, the isocyanate group (-N=C=O) reacts favourably and specifically with the –OH nucleophile on the carbohydrate and/or molecular recognition compound because of its ability to coordinate with hydrogen of the nucleophile and in the process, form two amide linkages (-CO-NH-) between the biomaterials or biomaterial and molecular recognition compound (Gallego et al., 2013b). Yamasaki et al. 2008, prepared a series of cross-linked cyclodextrin particles using diisocyanate-based cross-linkers. Choubey (2018) recently crosslinked hexamethylene diisocyanate with pine cone and applied it for removal of 2-nitrophenol from aqueous solution. The authors observed an increase in 2-nitrophenol adsorption capacity after crosslinking with hexamethylene diisocyanate.

### 2.17.3 Cross-linking cyclodextrin to magnetic nanoparticles

Recently studies have been conducted on crosslinking or modifying the soluble cyclodextrin with different materials for different pollutants removal from aqueous solution. A step further in developing adsorbents with superior properties would be the inclusion of magnetite coated nanoparticles into cyclodextrin, thus combining the advantages of both materials. Badruddoza et al. (2011) developed a nano-sorbent with carboxymethyl-β-CD modified $Fe_3O_4$ nanoparticles (CM-CD-MNPs) for the removal of copper ions and methylene dye from aqueous solution. CM-β-CD was suspected to form metal complexes, which play an important role in its ability to mitigate metal toxicity. The adsorption of methylene blue reached equilibrium within 50 min with 85–90% being adsorbed within 20 min of contact. Abdolmaleki et al. (2015)

reported a simple, cost-effective, and environmentally friendly synthesis of a novel nano-sorbent using triazinyl-β-CD-modified magnetic nanoparticle (T-β-CD–MNPs). In this work, a novel magnetite coated pine cone was cross-linked to carboxymethyl cyclodextrin and cyclodextrin using hexamethylene diisocyanate.

## 2.18  ADSORPTION PROCESS

Adsorption is a mass transfer process by which a substance is transferred from the liquid phase to the surface of a solid, and becomes bound by physical and or chemical interactions (Kurniawan and Babel, 2003). Compared with conventional or some biological methods for removing pollutants from industrial effluent, the adsorption process offers significant advantages such as cost effectiveness, profitability, high removal efficiency, minimization of chemical or biological sludge, regeneration of adsorbents, possibility of metal recovery, simplicity of operation, no metal toxicity issues and simplicity of design (Hashem et al., 2007, Mittal et al., 2005, Mohammad et al., 2010, Yao et al., 2009, MM et al., 2010). The main motivation for the use of adsorption process for wastewater treatment includes: (1) the difficulty to remove certain pollutants via conventionally secondary treatment, (2) the toxic or hazardous nature of the pollutants, (3) the high volatility which creates harmful vapours or odours, and (4) their presence in very low concentrations that make their removal via other methods difficult (Kumar et al., 2011, Sud et al., 2008).

### 2.18.1  Adsorption mechanism

Due to high affinity of the sorbent for the metal ion species, the latter is attracted and bound by rather complex process affected by several mechanisms involving chemisorption, complexation, adsorption on surface and pores, ion exchange, chelation, adsorption by physical forces, entrapment in inter and intrafibrillar capillaries (Basso et al., 2002, Qaiser et al., 2007).

### 2.18.2  Factors affecting adsorption

Adsorption process has been reported to be mostly affected by certain factors including; initial concentration of pollutants, solution pH, surface area of adsorbent, temperature, ionic strength, competing ions, contact time and particle size of the adsorbent (Chibban et al., 2012, Ihsanullah et al., 2016). The percentage removal of most various pollutants have been reported to usually

increase with increase in the adsorbent dose, initial concentration, contact time, and stirring speed (Bisht et al., 2016). Some factors affecting the adsorption of pollutants by different adsorbents are discussed in the following sub section.

### 2.18.2.1 Solution pH

Previous reports have shown that the solution pH is one important parameter affecting the adsorption process (Pholosi et al., 2013). Solution pH significantly affects the ionization degree, the metal chemistry and the mineral's surface properties (Ansari et al., 2011). Hamdaoui. (2006) showed that adsorption of methylene blue on sawdust and crushed brick increased by increasing solution pH (until solution pH of 9). For pH values lower than 5, both adsorbents were positively charged, hence a decrease in adsorption capacity was observed because methylene blue is a cationic dye. Cesium uptake by pine cone modified hexacyanoferrate was also revealed to have increased with increasing initial solution pH (Ofomaja et al., 2015). At low solution pH, the solution is acidic having high $H^+$ ion concentration which will compete with $Cs^+$ ions for adsorption sites leading to lower $Cs^+$ uptake. Whereas, as solution pH increases, an increase in $Cs^+$ uptake was due to the decrease in $H^+$ ion concentration in solution and the ionization of surface acid groups. El-Said et al. (2011) studied the effect of solution pH between pH 2 to 8 on the adsorption of Zn(II) onto rice husk. They observed that the removal of Zn(II) increased with increasing pH, and the maximum removal occurred at pH 6 (El-Said et al., 2011). It has also been demonstrated that the adsorption of cations is higher at pH values higher than the point of zero charge ($pH_{PZC}$) and lower at low pH values (Ihsanullah et al., 2016, Chibban et al., 2012). This is due to electrostatic interactions between the cation ions and negative surface charge at higher solution pH.

### 2.18.2.2 Adsorbent dose

Adsorption of heavy metals was found to be highly affected by the adsorbent dose. It has been investigated that the percentage removal of pollutants increases with an increase in adsorbent dosage. This can be justified due to the extra availability of vacant sites at higher adsorbent dosage (Gupta et al., 2015). Kumar et al. (2012) explored modified agricultural waste for metal ion adsorption. The authors reported that the metal ion removal increases with increase in adsorbent dose due to the availability of high surface area.

*2.18.2.3 Temperature*

Effect of temperature on the adsorption studies have also been investigated by many researchers. Variations in temperature cause changes in the thermodynamic parameters. Adsorption of pollutants may increase with an increase in temperature resulting in an endothermic process or decrease with an increase in temperature resulting in exothermic process. From various reports, adsorption of most pollutants or heavy metals have been observed to be an endothermic process. An increase in temperature subsequently results in an increase in the diffusion rate of the adsorbate. High temperature normally increases molecular activity at boundary layer interface which may increase the rate of diffusion of solute. Increasing temperature increases the surface activity and kinetic energy of adsorbate. However, it has been reported that the physical structure of the adsorbent may also be affected (Fomina and Gadd, 2014). Saha et al. (2013) studied the uptake of Cr(VI) metal ions by *mosambi (*Citrus limetta) peel and observed an increase in Cr(VI) removal with increasing temperature leading to an endothermic process.

*2.18.2.4 Initial concentration of pollutant*

Studies have shown that the initial concentration of the pollutant in the liquid phase significantly affects the adsorption process. However, at low initial concentration the ratio of pollutants to adsorbent mass is low and thus adsorption does not depend on initial concentration. Increasing the initial concentration means that more pollutants are available and thus, more are adsorbed for constant adsorbent mass. At higher initial concentration the driving force to overcome the mass transfer resistance for the migration of the pollutants from the bulk solution to the mineral surface increases (Arief et al., 2008). In several studies, the increase of initial concentration has been found to result in an increase in the adsorption capacity and a decrease of the percentage removal.

### 2.18.3 Modelling of Adsorption experimental data

Predicting the rate at which adsorption takes place for a given system and understanding how adsorbates interact with adsorbents are the most important factor in adsorption system design. The kinetic parameters describe the solute uptake rate which in turn controls the residence time of adsorbate uptake at the solid–solution interface. In addition, predicting the rate of pollutants

removal from aqueous solution is important in kinetics as it gives information for designing and modelling the processes. While on the other hand, the adsorption isotherms are so critical in optimizing the use of adsorbents. Thus, the correlation of equilibrium data by either theoretical or empirical equations is essential to the practical design and operation of adsorption systems. Several isotherms and kinetic equations are well explained and applied to fit experimental data.

### 2.18.3.1 Equilibrium Isotherm models

Adsorption isotherm is basically important to describe how solutes interact with adsorbents and is critical in optimizing the use of adsorbents. Equilibrium condition is attained when the concentration of the solute remains constant, as a result of zero net transfer of solute adsorbed and desorbed from adsorbent surface. The equilibrium adsorption isotherms describe the relationships between the equilibrium concentration of the adsorbate in the solid and liquid phase at constant temperature (Nadeem et al., 2006; Gökmen et al., 2002; Wang and Qin. 2005), and also propose the involved interactive forces in the process. The process at constant temperature, can be described by an adsorption isotherm according to the general equation:

$$q = \frac{(C_o - C_e)}{m} V \tag{2.2}$$

where q is the equilibrium sorption capacity (mg/g), $C_o$, the initial adsorbate concentration (mg/dm$^3$) $C_e$, the equilibrium adsorbate concentration (mg/dm$^3$), V the solution volume (dm$^3$) and m is the mass of the adsorbent (g). The percentage removal is calculated using the following equation:

$$\%R = \frac{(C_o - C_e)}{C_o} x100 \tag{2.3}$$

Considering that the adsorption process can be more complex, several adsorption isotherms were proposed. Among these, the most commonly used models to describe the process in water and wastewater applications were developed by Langmuir and Freundlich (Ho, 2004; Basha *et al.*, 2008). Equilibrium isotherms such as the Temkin, Langmuir- Freundlich (Sips isotherm), Redlich-Peterson, Tooth, and Dubinin-Radushkevich have also be used to model experimental data.

Table 2.3 Equation of isotherm models for Adsorption Equilibrium

| Isotherm | Equation |
|---|---|
| Freundlich | $q_e = K_f C_e^{1/n}$ |
| Langmuir | $q_e = \dfrac{q_m K_a C_e}{1 + K_a C_e}$ |
| BET | $q = \dfrac{K_B C_e q_m}{(C_s - C_e)\left[1 + \left(K_B - 1\left(\dfrac{C_e}{C_s}\right)\right)\right]}$ |
| Langmuir-Freundlich (Sips) | $q_e = \dfrac{q_m b C_e^{\beta}}{1 + b C_e^{\beta}}$ |
| Redlich-Peterson | $q_e = \dfrac{A C_e}{1 + B C_e^{g}}$ |
| Temkin | $q = \dfrac{RT}{b_T} \ln A_T C_e$ |
| Dubinin-Radushkevich | $q_e = (q_s)\exp(-K_d \varepsilon^2)$ |

## 2.18.4 Freundlich isotherm

The isotherm developed by Freundlich is one of the earliest empirical equations used to describe equilibrium data. The isotherm assumes a heterogeneous surface with a non-uniform distribution of heat of adsorption, where the total amount of adsorbed material is the summation of adsorption on all sites. It describes reversible adsorption and is not restricted to the formation of monolayer. The isotherm can be derived assuming a logarithmic decrease in the enthalpy of biosorption with the increase in the fraction of occupied sites and is given by:

$$q_e = K_f C_e^{1/n} \tag{2.4}$$

Where $K_F$ and $\frac{1}{n}$ are the Freundlich constants characteristics of the system, indicating the biosorption capacity and biosorption intensity, respectively. Eq. (2.3) can be linearized in logarithmic form to give Eq. (2.4) and the Freundlich constants can be determined.

$$\log q_e = \log K_f + \frac{1}{n} \log C_e \qquad\qquad (2.5)$$

### 2.18.5 Langmuir isotherm

The Langmuir isotherm is a theoretical isotherm developed in 1916 (Coulson and Richardson, 1991) by Langmuir to relate the amount of gas adsorbed on a surface due to the pressure of the gas. It is the simplest theoretical isotherm for monolayer adsorption onto a surface with finite number of identical sites. At constant temperature, metal ions held onto the biosorbent will be in equilibrium with metal ions in bulk solution. The equation is applicable to homogeneous adsorption where adsorption process has equal activation energy. This model is based on the following assumptions; (i) Adsorption cannot proceed beyond monolayer coverage, (ii) All sites are equivalent and the surface is uniform (that is, the surface is perfectly flat on a microscopic scale), (iii) The ability of a molecule to adsorb at a given site in independent of the occupation of neighbouring sites. The saturated monolayer isotherm can then be represented as:

$$q_e = \frac{q_m K_a C_e}{1 + K_a C_e} \qquad\qquad (2.6)$$

Where $C_e$ is the equilibrium concentration (mg/dm$^3$); $q_e$ is the amount of metal ion adsorbed (mg g$^{-1}$); $q_m$ is the $q_e$ for a complete monolayer (mg g$^{-1}$), $K_a$ is the biosorption equilibrium constant (dm$^3$/mg).

### 2.18.6 BET isotherm

The BET model is an extension of the Langmuir model for multilayer biosorption (Bruanuer et al., 1938). It assumes that if the initial adsorbed layer can act as an adsorbent for further adsorption, then, instead of the isotherm levelling off to some saturated value at high pressure, it can be expected to rise indefinitely. The original form of the BET equation is given as:

$$q = \frac{K_B C_e q_m}{(C_s - C_e)\left[1 + \left(K_B - 1\left(\frac{C_e}{C_s}\right)\right)\right]} \qquad\qquad (2.7)$$

Where $C_e$ is the concentration of solute remaining in solution equilibrium (mg/dm$^{3)}$), Cs the saturation concentration of solute (mg/dm$^3$), q the amount of solute adsorbed per unit weigh of adsorbent (mg g$^{-1}$), $q_m$ the amount of solute adsorbed per unit weigh of biosorbent in forming a complete monolayer on the surface (mg g$^{-1}$) and $K_B$ is the constant expressive of energy of interaction with the surface. The equation can be written in the linearized form:

$$\frac{C_e}{(C_s - C_e)q} = \frac{1}{K_B q_m} + \left(\frac{K_B - 1}{K_B q_m}\right)\left(\frac{C_e}{C_s}\right) \tag{2.8}$$

A plot of $C_e$/(C$_s$-C$_e$)q against (C$_e$/C$_s$) should give a straight line and from the slope and intercept the values of $K_B$ and $q_m$ can be calculated.

### 2.18.7 Temkin Isotherm

The Temkin isotherm model assumes that the adsorption energy decreases linearly with the surface coverage due to adsorbent–adsorbate interactions and the adsorption is characterized by a uniform distribution of binding energies, up to some maximum binding energy (Temkin and Pyzhev, 1940). The nonlinear form of Temkin isotherm model is given by the equation:

$$q_e = \frac{RT}{b}\ln(K_T C_e) \tag{2.9}$$

where $b$ (J/mol) is the Temkin constant related to the heat of sorption and $K_T$ (dm$^3$/g) is the equilibrium binding constant related to the maximum binding energy. The free energy change associated with the maximum binding energy is given as:

$$K_T = Exp(-\Delta G_{max} / RT) \tag{2.10}$$

The corresponding enthalpy ($\Delta H$) and entropy ($\Delta S$) associated with the maximum binding energies can be obtained from the equation:

$$\Delta G_{max} = \Delta H_{max} - T \Delta S_{max} \tag{2.11}$$

### 2.18.8 Dubinin-Radushkevich

Dubinin-Radushkevich model is generally applied to express the nature of biosorption as physical and chemical. In Dubinin-Radushkevich isotherm, the magnitude of $E$ can be related to the reaction mechanism. If $E$ is in the range of 8–16 kJ/mol, sorption is governed by ion exchange (EL-Kamash et al., 2005). In the case of $E < 8$ kJ/mol, physical forces may affect the sorption mechanism. The Dubinin–Radushkevich (D–R) isotherm has the linear form of:

$$\ln q_e = \ln q_m - \beta \varepsilon^2 \tag{2.12}$$

where $q_m$ is the Dubinin–Radushkevich monolayer biosorption capacity (mg/g), $\beta$ a constant related to biosorption energy ($mol^2/kJ^2$), and $\varepsilon$ is the Polanyi potential which is related to the equilibrium concentration as follows

$$\varepsilon = RT \ln \left( 1 + \frac{1}{C_e} \right) \tag{2.13}$$

where R is the gas constant (8.314 J/mol K) and T is the absolute temperature. The constant $\beta$ gives the mean free energy, $E$ (kJ/mol), mean free energy change when 1 mol of the ion is transferred to the surface of the solid from infinity in the solution and can be computed using the relationship:

$$E = \frac{1}{\sqrt{2\beta}} \tag{2.14}$$

### 2.18.9  Langmuir-Freundlich (Sips)

Langmuir-Freundlich (Sips) model is the combination of Langmuir and Freundlich models, developed by Sips in (1948). The model is mostly used to study the equilibrium of multicomponent systems and it is obtained by introducing a power law expression of the Freundlich isotherm into the Langmuir isotherm. The non-linearized form of Sips isotherm model can be given as follows:

$$q_e = \frac{q_m b C_e^\beta}{1 + b C_e^\beta} \tag{2.15}$$

where, $q_m$ (mg/g) is the maximum monolayer adsorption capacity, b [(L/mg) m s] is the Sips isotherm constant representing the energy of adsorption. $\beta$ is the empirical constant. When the value of $\beta = 1$ or closer to 1, the Sips isotherm equation reduces to the Langmuir equation and if the value of either $C_e$ or b approaches 0, the Sips isotherm reduces to Freundlich isotherm.

## 2.19   KINETIC MODELS TO PREDICT THE RATE OF ADSORPTION

Adsorption kinetics involves the study of the rate at which pollutants are removed from aqueous solution onto adsorbent surface, which in turn controls the residence time of the adsorbate uptake at the solid solution interface. It essentially provides valuable insight into the reaction pathways and mechanisms of the adsorption processes. Numerous kinetic models have been used to express the mechanism of solute adsorption onto adsorbent and to describe the reaction order of adsorption systems based on solution concentration. Reaction orders based on the capacity of the adsorbent have been presented, such as Lagergren's first-order equation (Lagergren, 1898), Pseudo second-order expression (Ho and MCkay, 2000) and diffusion chemisorption model (Sutherland, 2004).

### 2.19.1   Lagergren Pseudo first order model

The first order rate equation was presented by Lagergren in 1898 for the adsorption of oxalic acid and malonic acid onto charcoal (Lagergren, 1898).  This Lagergren first order rate equation has been called Pseudo first order (Ho and MCkay, 1998). Lagergren distinguished kinetics equation based on the solution concentration and adsorption capacity of solids. Ever since this kinetic equation has been widely applied for adsorption of different kinds of pollutants including heavy metals and organic compounds. The pseudo-first order kinetic model can be used to follow adsorption kinetics which proceeds by diffusion through a boundary (Lagergren, 1898) and it is expressed as:

$$\log(q_e - q_t) = \log(q_e) - \frac{k_1}{2.303} t \qquad (2.16)$$

The nonlinear form of the pseudo-first order model is given as:

$$q_t = q_e\left(1 - e^{-kt}\right) \qquad (2.17)$$

Where $q_t$ and $q_e$ are the amount adsorbed at time $t$ and at equilibrium, respectively, and $k_1$ is the rate constant of the pseudo-first-order kinetic model (min$^{-1}$). Plots of log ($q_e$-$q_t$) versus t gives a straight line for pseudo-first-order kinetics, $k_1$ and $q_e$ can be determined from the slope and intercept of the graph respectively.

## 2.19.2 Ho second order reaction model

The pseudo-second order model is based on the assumption that the rate limiting step may be chemical adsorption, involving valence forces through sharing or exchange of electrons between the adsorbent and adsorbate (Ho and MCkay, 2000). The pseudo-second-order accounts for adsorption processes that proceeds for surface chemisorption (Ho and MCkay, 1998):

$$\frac{dq_t}{dt} = k_2(q_e - q_t)^2$$ (2.18)

Where $k$ is the rate constant of adsorption, (g mg$^{-1}$ min$^{-1}$), $q_e$ is the amount adsorbed at equilibrium, (mg g$^{-1}$), $q_t$ is amount adsorbed on the surface of the adsorbent at any time, $t$, (mg g$^{-1}$). Eq. (2.18) integrated and rearranged to give Eq. (2.19) below:

$$\frac{t}{q_t} = \frac{1}{k_2 q_e^2} + \frac{1}{q_e} t$$ (2.19)

On re-arrangement, the non-linear form of the pseudo-second-order model was obtained:

$$q_t = \frac{k_2 q_e^2 t}{1 + k_2 q_e t}$$ (2.20)

Where the initial adsorption rate, h, is given by:

$$h = k_2 q_e^2$$ (2.21)

The plot of $t/q_t$ versus $t$ should give a linear relationship which allows the computation of a second-order rate constant, $k_2$ and $q_e$.

### 2.19.3   Intraparticle diffusion model

The intraparticle diffusion model is based on the theory proposed by Weber and Morris (1963) to determine the mechanism involved in the adsorption process.  The Weber and Morris equation is:

$$q_t = k_i t^{0.5} + C \tag{2.22}$$

where $k_i$ is the intraparticle diffusion rate constant (mgg$^{-1}$ min$^{-0.5}$) and the intercept C, obtained by extrapolation of the linear portion of the plot of $q_t$ versus $t^{0.5}$, back to the axis is taken to be proportional to the extent of the boundary layer thickness. According to Weber and Morris (1963), if the intra-particle diffusion is the rate-limiting step in the adsorption process, the graph of $q_t$ vs. $t_{0.5}$ should yield a straight line passing through the origin.

### 2.19.4  Diffusion chemisorption model

Sutherland (2004) developed an empirical diffusion chemisorption kinetic model to simulate adsorption of heavy metals unto heterogeneous surfaces. Sutherland's expression is as follows:

$$\frac{t^{0.5}}{q_t} = \frac{t^{0.5}}{q_e} + \frac{1}{K_{DC}} \tag{2.23}$$

where $q_t$ (mg/g), the rate of change of concentration of the solid phase is equated as a function of the rate of mass transfer from the liquid phase to the adsorption site ($K_{DC}$ (mg/g t$^{0.5}$) and $q_e$ (mg/g) is the equilibrium capacity, while $t^{0.5}$, is the time in min raised to the power of $0.5$. Therefore, the plot of $t^{0.5}/q_t$ versus $t^{0.5}$ will yield a straight line with slope equal to $1/q_e$ and intercept equal to the diffusion-chemisorption constant, $K_{DC}$.

### 2.20  CONCLUSION

Adsorption using agricultural waste materials, nano-sized adsorbents and natural polymers such as polysaccharides and their derivatives have gained significant interest because of their particular properties. Literature on these materials have been reviewed.

## 2.21 REFERENCES

ABDOLMALEKI, A., MALLAKPOUR, S. & BORANDEH, S. 2015. Efficient heavy metal ion removal by triazinyl-bcyclodextrin functionalized iron nanoparticles. *RSC Advances,* 5**,** 90602-90608.

AHMARUZZAMAN, M. 2008. Adsorption of phenolic compounds on low-cost adsorbents: a review *Advances in Colloid and Interface Science,* 143**,** 48-67.

AL-AHMARI , S. D., WATSON, K., FONG, B. N., RUYONGA, R. M. & ALI, H. 2018. Adsorption kinetics of 4-n-nonylphenol on hematite and goethite. *Journal of Environmental Chemical Engineering,* 6**,** 4030-4036.

ALABA, P. A., OLADOJA, N. A., SANI, Y. M., AYODELE, O. B., MOHAMMED, I. Y., OLUPINLA, S. F. & DAUD, W. M. W. 2018. Insight into wastewater decontamination using polymeric adsorbents. *Journal of Environmental Chemical Engineering,* 6**,** 1651-1672.

ALTUNDOGAN, H. S., ALTUNDOGAN, S., TUMEN, F. & BILDIK, M. 2002. Arsenic adsorption from aqueous solutions by activated red mud. *Waste management,* 22**,** 357-363.

ANASTOPOULOS, I., KARAMESOUTI, M., MITROPOULOS, A. C. & KYZAS, G. Z. 2017. A review for coffee adsorbents. *Journal of Molecular Liquids,* 229**,** 555-565.

ANASTOPOULOS, I., MASSAS, I. & EHALIOTIS, C. 2013. Composting improves biosorption of,Pb2+ and Ni2+ by renewable lignocellulosic materials. Characteristics and mechanisms involved. *Chemical Engineering Journal,* 231**,** 245-254.

ANSARI, M. I., MASOOD, F. & MALIK, A. 2011. Bacterial biosorption: a technique for remediation of heavy metals in microbes and microbial technology, in: I. Ahmad, F. Ahmad, J. Pichtel (Eds.). *Agricultural Environmental Applications*.

APHESTEGUY, J. C., KURLYANDSKAYA, G. V., DE CELIS, J. P., SAFRONOV, A. P. & SCHEGOLEVA, N. N. 2015. Magnetite nanoparticles prepared by co-precipitation method in different conditions, Materials Chemistry and Physics. *Materials Chemistry and Physics,* 161**,** 243-249.

ARIEF, V. O., TRILESTARI, K., SUNARSO, J., INDRASWATI, N. & ISMADJI, S. 2008. Recent progress on biosorption of heavy metals from liquids using low cost biosorbents: characterization, biosorption parameters and mechanism studies, . *Clean Soil Air Water* 36**,** 937-962.

BABEL, S. & KURNIAWAN, T. A. 2003. Low-cost adsorbents for heavy metals uptake from contaminated water: a review. *Journal of Hazardous Material,* 97**,** 219-243.

BADRUDDOZA, A. Z. M., TAY, A. S. H., TAN, P. Y., HIDAJAT, K. & UDDIN, M. S. 2011. Carboxymethyl--cyclodextrin conjugated magnetic nanoparticles as nano-adsorbents for removal of copper ions: synthesis and adsorption studies. *Journal of Hazardous Material,* 185**,** 1177-1186.

BAIER, J., KOETZ, J., KOSMELLA, S., TIERSCH, B. & REHAGE, H. 2007. Polyelectrolyte-Modified Inverse Microemulsions and Their Use as Templates for the Formation of Magnetite Nanoparticles. *Journal of Physical Chemistry,* 111**,** 8612-1816.

BAILEY, S. E., OLIN, T. J., BRICKA, R. M. & ADRIAN, D. D. 1999. A review of potentially low-cost sorbents for heavy metals, . *Water Research,* 33**,** 2469-2479.

BANERJEE, S. S. & CHEN, D. H. 2007. Fast removal of copper ions by gum arabic modified magnetic nano-adsorbent, . *Journal of Hazardous Material,* 147**,** 174-179.

BANERJEE S.S, JOSHI. M. V. & JAYARAM RV, J. 2004. Removal of Cr(VI) and Hg(II) from aqueous solution using Fly Ash and impregnated Fly Ash. *Separation and Purification Technology,* 39**,** 1611-.

BASSO, M. C., CERRELLA, E. G. & CUKIERMAN, A. L. 2002. Lignocellulosic materials as potential biosorbents of trace toxic metals from wastewater. *Chemical Resources,* 41**,** 3580-3585.

BASU, A., MUSTAFIZ, S., ISLAM, M. R., BJORNDALEN, N., RAHAMAN, M. S. & CHAALAL, O. 2006. A Comprehensive Approach for Modelling Sorption of Lead and Cobalt Ions through Fish Scales as an Adsorbent. *Chemical Engineering Communications,* 193**,** 580-605.

BENYOUCEF, S. & AMRANI, M. 2011. Adsorption of Phosphate Ions Onto Low Cost Aleppo Pine Adsorbent. *Desalination,* 275**,** 231-236.

BHATNAGARA, A. & SILLANPÄÄ, M. 2011. A review of emerging adsorbents for nitrate removal from water. *Chemical Engineering Journal***,** 493-504.

BISHT, R., AGARWAL, M. & SINGH, K. 2016. Heavy metal removal from wastewater using various adsorbents: a review. *Journal of water Reuse and Desalination,* 7**,** 387-419.

BRAIBANTI, A., PISICARO, E., GHIOZZI, A., COMPARI, C. & BOVIS, G. 1998. Host-guest interactions between β-cyclodextrin and piroxicam. *Reactive and Functional Polymers,* 36**,** 251-255.

BREBU, M., UCAR, S., VASILE, C. & YANIK, J. 2010. Co-pyrolysis of pine cone with synthetic polymers, Fuel, 89, 1911-1918.

BRIDGWATER, A .V. 2004. Biomass fast pyrolysis, Thermal science, 8, 21-50.

BRIJMOHAN, S. B. & SHAW, M. T. 2007. Magnetic ion-exchange nanoparticles and their application in proton exchange membranes. *Journal of Membrane Science,* 303**,** 64-71.

BRUANUER, S., EMMETT, P.H., TELLER. E. 1938, Adsorption of gases in multimolecular layers, Journal of American Chemical Society, 60 (1938) 309–316.

CAO, F., YIN, P., LIU, X., LIU, C. & QU, R. 2014. Mercury adsorption from fuel ethanol onto phosphonated silica gel prepared by heterogeneous method. *Renewable Energy***,** 61-68.

CHANG, Y. C. & CHEN, D. H. 2005. Preparation and adsorption properties of monodisperse chitosan-bound $Fe_3O_4$ magnetic nanoparticles for the removal of Cu(II) ions,. *Journal of Colloid Interface Science,* 283**,** 446-451.

CHEN, C. Y., YANG, C. Y. & CHEN, A. H. 2011. Biosorption of Cu(II), Zn(II), Ni(II) and Pb(II) ions by cross-linked metal-imprinted chitosans with epichlorohydrin. *Journal of Environmental Management,* 92**,** 796-802.

CHEN, J., WANG, Y. G., LI, Z. Q., WANG, C., LI, J. F. & GU, Y. J. 2009. Synthesis and characterization of magnetic nanocomposites with $Fe_3O_4$ core.  Journal of Physics: Conference Series, IOP Publishing, 012-041.

CHERN, J. M. & CHIEN, Y. W. 2002. Adsorption of nitrophenol onto activated carbon: isotherms and breakthrough curves, Water Res. 36 (2002) 647–655.

CHIBBAN, M., ZERBET, M., CARJA, G. & SINAN, F. 2012. Application of low cost adsorbents for Arsenic removal-A review. *Journal of Environmental Chemistry and Ecotoxicology,* 4**,** 91-102.

CHOUBEY, S. 2018. Kinetics and equilibrium study of 2-nitrophenol adsorption onto polyurethane cross-linked pine cone biomass. *Journal of Cleaner Production* 179**,** 191-209.

COSIC, I. 1994. Macromolecular bioactivity: is it resonant interaction between macromolecules? Theory and application. *IEEE Transactions On Biomedical Engineering,* 41**,** 1101-1114.

CRINI, G. 2005. Recent developments in polysaccharide-based materials used as adsorbents in wastewater treatment. *Progress in Polymer Science,* 30**,** 38-70.

CRINI, G. 2006. Non-conventional low-cost adsorbents for dye removal: a review. *Bioresource Technology,* 97**,** 1061-1085.

CUSHING, B. L., KOLESNICHHENKO, V. L. & O'CONNOR, C. J. 2004. Recent advances in the liquid phase synthesis of inorganic nanoparticles. *Chemical Reviews,* 104**,** 3893-3946.

DAI, J., REN, F., TAO, C. & 2012. Adsorption of Cr(VI) and speciation of Cr(VI) and Cr(III) in aqueous solutions using chemically modified chitosan, . *Internation Journal of Environmental Research and Public Health,* 9**,** 1757-1770.

DAOU, T. J., POURROY, G., COLIN, S. B., GRENECHE, J. M., BOUILLET, C. U., LEGARE, P., BERNHARDT, P., LEUVREY, C. & ROGEZ, G. 2006. Hydrothermal Synthesis of Monodisperse Magnetite Nanoparticles. *Chemistry of Materials,* 18**,** 4399-4404.

DAWOOD, S. & SEN, T. K. 2012. Removal of anionic dye Congo red from aqueous solution by raw pine and acid-treated pine cone powder as adsorbent: Equilibrium, thermodynamic, kinetics, mechanism and process design. *Water research* 46**,** 1933-1946.

DELVAL, F., CRINI, G., MORIN, N. O., VEBREL, J., BERTINI, S. & TORRI, G. 2002. The sorption of several types of dye on crosslinked polysaccharides derivatives. *Dyes and Pigments* 53**,** 79-92.

DEMIRBAS, E. 2008. Heavy metal adsorption onto agro-based waste materials: A review. *Journal of Hazardous Materials* 157**,** 220-229.

DODZIUK, H. 2006. Cyclodextrins and Their Complexes. *Ed.; Wiley-VCH: Weinheim.*

EL-KAMASH, A. M., ZAKI, A. A. & ABED EL GELEEL, M. A. 2005. Modeling batch kinetics and thermodynamics of zinc and cadmium ions removal from waste solutions using synthetic zeolite. *Journal of Hazardous Material,* B127**,** 211-220.

EL-SAID, A. G., BADAWAY, N. A., ABDEL-AAL, A. & GARAMAN, S. E. 2011. Optimization parameters for adsorption and desorption of Zn(II) and Se(IV) using rice husk:kinetic and equilibrium. *Ionics* 17**,** 263-270.

FAN, J., GUO, Y., WANG, J. & FAN, M. 2009. Rapid decolonization of azo dye methyl orange in aqueous solution by nanoscale zerovalent iron. *Journal of Hazardous Material,* 166**,** 904-910.

FENG, L., CAO, M., MA, X., ZHU, Y. & HU, C. 2012. Superparamagnetic high-surface-area $Fe_3O_4$ nanoparticles as adsorbents for arsenic removal. *Journal of Hazardous Material,* 227-228**,** 439-446.

FENG, N., GUO , X., LIANG, S., ZHU, Y. & LIU, J. 2011. Biosorption of heavy metals from aqueous solutions by chemically modified orange peel. *Journal of Hazardous Material,* 185**,** 49-54.

FENG, Q., LIN, Q., GONG, F., SUGITA, S. & SHOYA, M. J. 2004. *Journal of colloid Interface Science,* 278**,** 1.

FOMINA, M. & GADD, G. M. 2014. Biosorption: Current perspective on concept, definition and application. . *Bioresource Technology,* 160**,** 3-14.

GALLEGO, R., ARTEAGA, J. F., VALENCIA, C. & FRANCO, J. M. 2013a. Chemical modification of methyl cellulose with HMDI to modulate the thickening properties in castor oil. *Cellulose,* 21**,** 495-507.

GALLEGO, R., ARTEAGA, J. F., VALENCIA, C. & FRANCO, J. M. 2013b. Isocyanate-Functionalized Chitin and Chitosan as Gelling Agents of Castor Oil**.** *Molecules* 18**,** 6532-6549.

GARCIA-RIO, L., MEJUTO, J. C., RODRIGUEZ-DAFONTE, P. & HALL, R. W. 2010. The role of water release from the cyclodextrin cavity in the complexation of benzoyl chlorides by dimethyl-beta-cyclodextrin. *Tetrahedron,* 66**,** 2529-2537.

GAWANDE, P.& KAWARE J. 2016. Review on Low Cost Adsorbents for Desulphurization of Liquid Fuels. *IJSRSET Engineering Technology*, 2, 108-112.

GENG, B. Y., MA, J. Z. & YOU, J. H. 2008. Controllable synthesis of single-crystalline Fe3O4 polyhedra possessing the active basal facets,. *Crystal Growth and Design,* 8**,** 1443-1447.

GHANBARI, D. S.-N., MASOUD GHASEMI-KOOCH, MAJID 2014. A sonochemical method for synthesis of Fe3O4 nanoparticles and thermal stable PVA-based magnetic nanocomposite. *Journal of Industrial and Engineering Chemistry,* 20**,** 3970-3974.

GHOSH, R., PRADHAN, L., DEVI, Y. P., MEENA, S. S., TEWARI, R. K. & UMAR, A. 2011. Induction heating studies of Fe3O4 magnetic nanoparticles capped with oleic acid and polyethylene glycol for hyperthermia. *Journal of Material Chemistry,* 21**,** 13388-13398.

GONG, J., CHEN, L., ZENG, G., LONG, F., DENG, J., NIU, Q. & HE, X. 2012. Shellac-coated iron oxide nanoparticles for the removal of cadmium(II) ions from aqueous solution. *Journal of environmental Sciences,* 24**,** 1165-1173.

GRASSI, M., KAYKIOGLU, G., BELGIORNO, V. & LOFRANO, G. 2012. Removal of emerging contaminants from water and wastewater by adsorption process. In: Lofrano,

G. (Ed.), Emerging Compounds Removal from Wastewater,. *Springer Briefs in Green Chemistry for Sustainability.*

GUPTA, S. & BABU, B. V. 2009. Removal of toxic metal Cr(VI) from aqueous solutions using sawdust as adsorbent: equilibrium, kinetics and regeneration studies. *Chemical Engineering Journal,* 150**,** 352-365.

GUPTA, V. K., CARROTT, P. J. M., RIBEIRO CARROTT, M. M. M. & SUHAS 2009. Low cost adsorbents: growing approach to wastewater treatment - a review. *Critical Reviews in Environmental Science and Technology,* 39**,** 783-842.

GUPTA, V. K., MORADI, O., TYAGI, I., AGARWAL, S., SADEGH, H., GHOSHEKANDI, R. S., MAKHLOUF, A. S. H., GOODARZI, M. & GARSHASBI, A. 2015. Study on the removal of heavy metal ions from industry waste by carbon nanotubes: effect of the surface modification: a review,. *Critical Reviews in Environmental Science and Technology.*

GUPTA, V. K. & NAYAK, A. 2012. Cadmium removal and recovery from aqueous solutions by novel adsorbents prepared from orange peel and $Fe_2O_3$ nanoparticles. *Chemical Engineering Journal,* 180**,** 81-90.

GUPTA, V. K. & SUHA, S. 2009. Application of low-cost adsorbents for dye removal - a review. *Journal of Environmental Management,* 90**,** 2313-2342.

HASHEM, A., AKASHA, R. A., GHITH, A. & HUSSEIN, D. A. 2007. Adsorbent based on agricultural wastes for heavy metal and dye removal: A Review,. *Energy Education Science and Technology,* 19**,** 69-86.

HO, Y. S. & MCKAY, G. 1998. Kinetic models for the sorption of dye from aqueous solution by wood. *Process Safety and Environmental Protection,* 76 B**,** 183-191.

HO, Y. S. & MCKAY, G. 2000. The kinetics of sorption of divalent metal ions onto sphagnum moss peat. *Water Research,* 34**,** 735-742.

HU, F. X., NEOH, K. G. & KANG, E. T. 2006. Synthesis and in vitro anti-cancer evaluation of tamoxifen-loaded magnetite/PLLA composite nanoparticles. *Biomaterials,* 27**,** 5725-5733.

HU, J., CHEN, G. & LO, I. M. C. 2005. Removal and recovery of Cr(VI) from wastewater by maghaemite nanoparticles. *Water Research,* 39**,** 4528-4536.

HUANG, S. H. & CHEN, D. H. 2009. Rapid removal of heavy metal cations and anions from aqueous solutions by an amino-functionalized magnetic nano-adsorbent. *Journal of Hazardous Material,* 163**,** 174-179.

HUANG, Z., ZHANG, B. & FANG, G. 2013. Adsorption behavior of Cr(VI) from aqueous solutions by microwave modified porous larch tannin resin. *Bioresources,* 8**,** 4593-4609.

HUBER, D. L. 2005. Synthesis, properties and application of iron nanoparticles. S*mall,* 1**,** 482-501.

IHSANULLAH, A. A., AL-AMER, A. M., LAOUI, T., AL-MARRI, M. J., NASSER, M. S. & ATIEH, M. A. 2016. Heavy metal removal from aqueous solution by advanced carbon nanotubes: Critical review on adsorption applications. *Separation and Purification Technology,* 157**,** 141-161.

ISAH, A. U., GIWA, A., SALISU, B., SALLAHUDEEN, M. & MUSTAPHA, A. 2015. Kinetics, equilibrium and thermodynamics studies of C.I. Reactive Blue 19 dye adsorption on coconut shell based activated carbon. *International Biodeterioration & Biodegradation,* 102**,** 262-273.

IZATT, R. M., BRADSHAW, J.S., BRUENING, R.L. AND BRUENING, M.L 1994. Solid phase extraction of ions of analytical interest using molecular recognition technology. *American Laboratory,* 26, 28-38.

JAIS, F M., IBRAHIM, S., YOON, Y. & JANG, M. 2016. Enhanced arsenate removal by lanthanum and nano–magnetite composite incorporated palm shell waste–based activated carbon. *Separation and Purification Technology,* 169, 93–102.

JANG, J. H. & LIM, H. B. 2010. Characterization and analytical application of surface modified magnetic nanoparticles. *Microchemical Journal,* 94**,** 148-158.

JIANG, C., LIU, R., SHEN, X., ZHU, L. & SONG, F. 2011. Ni0.5Zn0.5Fe2O4 nanoparticles and their magnetic properties and adsorption of bovine serum albumin,. *Powder Technology,* 211**,** 90-94.

JIMÉNEZ-CEDILLO, M. J., OLGUÍN, M. T., FALL, C. H. & COLÍN, A. 2011. Adsorption capacity of iron- or iron–manganese-modified zeolite-rich tuffs for As(III) and As(V) water pollutants. *Applied Clay Science,* 54**,** 206-216.

JIN, X., YU , B., CHEN, Z., AROCENA, J. M. & THRING, R. W. 2014. Adsorption of Orange II dyein aqueous solution onto surfactant-coated zeolite: characterization, kineticand thermodynamic studies. *Journal of Colloid Interface Science***,** 15-20.

KONG, S., WANG, Y., ZHAN, H., LIU, M., LIANG, L. & HU, Q. 2014. Competitive adsorption ofhumic acid and arsenate on nanoscale iron-manganese binary oxide-loadedzeolite in groundwater. *Journal of Geochemical Exploration,* 87**,** 220-225.

KUMAR, P. S., RAMALINGAM, S., DINESH KIRUPHA, S., MURUGESAN, A., VIDHYADEVI, T. & SIVANESAN, S. 2011. Adsorption behavior of nickel(II) onto cashew nut shell: Equilibrium, thermodynamics, kinetics, mechanism and process design. *Chemical Engineering Journal,* 167**,** 122-131.

KURNIAWAN, T. A. & BABEL, S. 2003. A research study on Cr(VI) removal from contaminated wastewater using low-cost adsorbents and commercial activated carbon. In: Second Int. Conf. on Energy Technology towards a Clean Environment (RCETE). *Thailand,* 2**,** 1110-1117.

LAGERGREN, S. 1898. Zur theorie der sogenannten adsorption gelöster stoffe, Kungliga Svenska. Vetenskapsakademiens. *Handlingar,* 24**,** 1-39.

LAURENT, S., FORGE, D., PORT, M., ROCH, A., ROBIC, C., L, V. E. & MULLER, R. N. 2008. Magnetic iron oxide nanoparticles: Synthesis, stabilization, vectorization, physicochemical characterizations and biological applications. *Chemical Rewiews,* 108**,** 2064-2110.

LEE, M. H., YOON, K. J. & KO, S. W. 2001. Synthesis of a vinyl monomer containing β-cyclodextrin and grafting onto cotton. *Journal of Applied Polymer and Science,* 80**,** 438-446.

LEUNG, W. C., WONG, M. F., CHUA, H., LO, W. & LEUNG, C. K. 2000. Removal and recovery of heavy metals by bacteria isolated from activated sludge treating industrial effluents and municipal wastewater. *Water Science and Technology* 41**,** 233-240.

LI, W. G., GONG, X. J., WANG, K., ZHANG, X. R. & FAN, W. B. 2014. Adsorption characteristics of arsenic from micro-polluted water by an innovative coal-based mesoporous activated carbon. *Bioresource Technology***,** 166-173.

LIU, H. B., CHEN, T. H., CHANG, D. Y., CHEN, D. H., LIU, Y., HE, H. P., YUAN, P. & FROST, R. 2012. Nitrate reduction over nanoscale zero-valent iron prepared by hydrogen reduction of goethite. *Materials Chemistry and Physics,* 133**,** 205-211.

LIU, J., GUO, D., ZHOU, Y., WU, Z., LI, W., ZHAO, F. & ZHENG, X. 2011. Identification of ancient textiles from Yingpan, Xinjiang, by multiple analytical techniques,. *Journal of Archaeology Sciences* 38**,** 1763-1770.

LIU, J. F., ZHAO, Z. S. & JIANG, G. B. 2008. Coating $Fe_3O_4$ magnetic nanoparticles with humic acid for high efficiency removal of heavy metals in water,. *Environmental Science and Technology,* 42**,** 6949-6954.

LIU, X., MA, Z., XING, J., AND LIU, H 2004. Preparation and characterization of amino-silane modified superparamagnetic silica nanospheres. *Journal of Magnetism and Magnetic Materials,* 270**,** 1-6.

LIU, Y., CHEN, M. & HAO, Y. 2013. Study of the adsorption of Cu(II) by EDTA functionalized $Fe_2O_4$ magnetic nano-particles. *Chemical Engineering Journal,* 218**,** 46-54.

LIU, Z., CHEN, J., WU, Y., LI, Y., ZHOO, J. & NA, P. 2018. Synthesis of magnetic orderly mesoporous $\alpha$-$Fe_2O_3$ nanocluster derived from MIL-100 (Fe) for rapid and efficient arsenic(III,V) removal *Journal of Hazardous Material,* 343**,** 304-314.

LOPEZ-CABEZA, R., GAMIZ, B., CORNEJO, J. & CELIS, R. 2017. Behavior of the enantiomers of the herbicide imazaquin in agricultural soils under different application regimes. *Geoderma,* 293**,** 64-72.

LÓPEZ-TÉLLEZ, G., BARRERA-DÍAZ, C. E., BALDERAS-HERNÁNDEZ, P., ROA-MORALES, G. & BILYEU, B. 2011. Removal of hexavalent chromium in aquatic by iron nanoparticles embedded in orange peel pith. *Industrial Engineering Chemical Resources,* 50**,** 2488-2494.

LU, F. & ASTRU, D. 2018. Nanomaterials for removal of toxic elements from water. *Coordination Chemistry Reviews,* 356**,** 147-164.

LUNGE, S., SINGH, S. & SINHA, A. 2014. Magnetic iron oxide ($Fe_3O_4$) nanoparticles from tea waste for arsenic removal. *Journal of Magnetism and Magnetic Materials,* 356**,** 21-31.

MA, Z. & LIU, H. 2007. Synthesis and surface modification of magnetic particles for application in biotechnology and biomedicine. *China Particuology,* 5**,** 1-10.

MAHMOODI, N. M., HAYATI, B., ARAMI, M. & LAN, C. 2011. Adsorption of Textile Dyes on Pine Cone From Colored Wastewater: Kinetic, Equilibrium and Thermodynamic Studies. *Desalination,* 268**,** 117-125.

MALKOC, E. 2006. Ni(II) removal from aqueous solutions using cone biomass of Thuja orientalis. *Journal of Hazardous Material,* B137**,** 899-908.

MALLARD, I., STADE, L. W., RUELLAN, S., JACOBSEN, P. A. L., LARSEN, K. L. & FOURMENTIN, S. 2015. Sythesis, characterization and sorption capacities toward organic pollutants of new cyclodexrin modified zeolite derivatives, . *Colloids and Surfaces A Physicochemical and Engineering Aspects,* 482**,** 50-57.

MANNING, B. A., KISER, J. R., KWON, H. & KANEL, S. R. 2007. Spectroscopic investigation of Cr(III)- and Cr(VI)-treated nanoscale zerovalent iron. *Environmental Science and Technology,* 41**,** 586-592.

MARTÍNEZ-CABANAS, M., LÓPEZ-GARCÍA, M., BARRIADA, J. L., HERRERO, R. & SASTRE DE VICENTE, M. E. 2016. Green synthesis of iron oxide nanoparticles. Development of magnetic hybrid materials for efficient As(V) removal. *Chemical Engineering Journal,* 301**,** 83-91.

MERA, K., NAGAI, M., BROCK, J. W. C., FUJIWARA, Y., MURATA, T., MARUYAMA, T., BAYNES, J. W., OTAGIRI, M. & NAGAI, R. 2008. Glutaraldehyde is an effective cross-linker for production of antibodies against advanced glycation end-products,. *Journal of Immunological Methods,* 334**,** 82-90.

MEYER, E. E., ISLAM, M. F., LAU, W. & OU-YANG, H. D. 2000. Complexation kinetics of cyclodextrin with hydrophobic molecules confined in an isolated droplet in water. *Langmuir,* 16**,** 5519-5522.

MITTAL, A., KRISHNAN, L. & GUPTA, V. K. 2005. Removal and recovery of malachite green from wastewater using an agricultural waste material, de-oiled soya. *Separation and Purification Technology,* 43**,** 125-133.

ABD El-LATIF, M.M., IBRAHIM, A. & EI-KADY, M. 2010. Adsorption equilibrium, kinetics and thermodynamics of methylene blue from aqueous solutions using biopolymer oak sawdust composite. *Journal of American Science,* 6**,** 267-283.

MOHAMED, M. H., WILSON, L. D. & HEADLEY, J. V. 2011. Design and characterization of novel β-cyclodextrin based copolymer materials. *Carbohydrate Research,* 346**,** 219-229.

MOHAMMAD, M., MAITRA, S., AHMAD, N., BUSTAM, A., SEN, T. K. & DUTTA, B. K. 2010. Metal ion removal from aqueous solution using physic seed hull. *Journal of Hazardous Material,* 179**,** 363-372.

MOHSEN, E., JABER, J., MEHDI, M A. & FATEMEH, N. D. 2014. Synthesis and characterization of $Fe_3O_4$@$SiO_2$–polymer-imid–Pd magnetic porous nanospheres and their application as a novel recyclable catalyst for Sonogashira–Hagihara coupling reactions. *Journal of Iran Chemical Society*, 11:499–510.

MOMČILOVIĆ, M., PURENOVIĆ, M., BOJIĆ, A., ZARUBICA, A. & RANĐELOVIĆ, M. 2011. Removal of lead(II) ions from aqueous solutions by adsorption onto pine cone activated carbon. *Desalination,* 276**,** 53-59.

MONTAZER-RAHMATI, M. M., RABBANI, P., ABDOLALI, A. & KESHTKAR, A. R. 2011. Kinetics and equilibrium studies on biosorption of cadmium, lead, and nickel ions from aqueous solutions by intact and chemically modified brown algae. *Journal of Hazardous Material,* 185**,** 401-407.

MORIN-CRINI, N. & CRINI, G. 2013. Environmental applications of water-insoluble β-cyclodextrin–epichlorohydrin polymers. *Progress in Polymer Science,* 38**,** 344-368.

MORNET, S., GRASSET, F. & PORTIER, J. 2002. Maghemite @silica nanoparticle for nanoparticle for biological applications. *European Cells and Materials,* 3**,** 10-113.

MOUZDAHIR, Y. E., ELMCHAOURI, A., MAHBOUB, R., GIL, A. & KORILI, S. 2010. Equilibrium modeling for the adsorption of methylene blue from aqueous solutions on activated clay minerals. *Desalination***,** 335-338.

MOYO, C. M., MUTARE, E., CHIGONDO, F. & NYAMUNDA, B. C. 2012. Removal of phenol from aqueous solution by adsorption on yeast, sacchromyces cerevisiae. *International journal of Recent Research and Applied Studies,* 11**,** 486-494.

MTHOMBENI, N. H., ONYANGO, M. S. & AOYI, O. 2015. Adsorption of hexavalent chromium onto magnetic natural zeolite-polymer composite. *Journal of the Taiwan Institute of Chemical Engineers***,** 242-251.

MULANI, K., DANIELS, S., RAJDEO, K., TAMBE, S. & CHAVAN, N. 2013. Adsorption of chromium (VI) from aqueous solutions by coffee polyphenol-formaldehyde/acetaldehyde resins. *Journal of Polymer,* 2013**,** 1-11.

NAGATA, K., SALAGMI, H., HARADA, H., MONOYOMA, M., ISHIHAMA, A. & KONNO K. 1990. Inhibition of influenza virus infection by pine cone antitumor substances. *Antiviral Research*, 13,11-21.

NOURI, S. & HAGHSERESH, F. 2004. Adsorption of *p*-nitrophenol in untreated and treated activated carbon, Adsorption 10, 79–86.

O'CARROLL, D., SLEEP, B., KROL, M., BOPARAI, H. K. & KOCUR, C. 2013. Nanoscale zero valent iron and bimetallic particles for contaminated site remediation. *Advanced Water Resources,* 51**,** 104-122.

OFOMAJA, A. E. 2010. Intraparticle diffusion process for lead(II) biosorption onto mansonia wood sawdust. *Bioresource Technology,* 101**,** 5868-76.

OFOMAJA, A. E. & HO, Y. S. 2007. Effect of pH on cadmium biosorption by coconut copra meal. *Journal of Hazardous Material,* B139**,** 356-362.

OFOMAJA, A. E. & NAIDOO, E. B. 2010. Biosorption of lead(II) onto pine cone powder: Studies on biosorption performance and process design to minimize biosorbent mass. *Carbohydrate Polymers,* 82**,** 1031-1042.

OFOMAJA, A. E., NAIDOO, E. B. & MODISE, S. J. 2009. Removal of copper (II) from aqueous solution by pine and base modified pine cone powder as biosorbent. *Journal of Hazardous Material,* 168**,** 909-917.

OFOMAJA, A. E., PHOLOSI, A. & NAIDOO, E. B. 2013. Kinetics and competitive modeling of cesium biosortion onto chemically modified pine cone powder. *Journal of the Taiwan Institute of Chemical Engineers* 44**,** 943-951.

OFOMAJA, A. E., PHOLOSI, A. & NAIDOO, E. B. 2015. Application of raw and modified pine biomass material for cesium removal from aqueous solution. *Ecological Engineering* 82**,** 258-266.

OFOMAJA, A. E., UNUABONAH, E. I. & OLADOJA, N. A. 2010. Competitive modeling for the biosorptive removal of copper and lead ions from aqueous solution by Mansonia wood sawdust. *Bioresource Technology,* 101**,** 3844-3852.

OGUZ, E. 2005. Adsorption characteristics and the kinetics of the Cr(VI) on the Thuja oriantalis. *Colloids and Surfaces A: Physicochemical and Engineering Aspects,* 252**,** 121-128.

OZDES, D., DURAN, C., & SENTURK, H. B. 2011. Adsorptive removal of Cd(II) and Pb(II) ions from aqueous solutions by using Turkish illitic clay. *Journal of Environmental Management*, 92, 3082–3090.

OZMEN, E. Y., SEZGIN, M., YILMAZ, A. & YILMAZ, M. 2008. Synthesis of β-cyclodextrin and starch based polymers for sorption of azo dyes from aqueous solutions. *Bioresource Technology,* 99**,** 526-531.

PAGNANELLI, F., MAINELLI, S., VEGLI, F. & TORO, L. 2003. Heavy metal removal by olive pomace: biosorbent characterization and equilibrium modelling. *Chemical Engineering Science,* 58**,** 4709-4717.

PAJZDERSKA, A., CZARNECKI, P., MIELCAREK, J. & WASICKI, J. 2011. H-1 NMR study of rehydration/dehydration and water mobility in beta-cyclodextrin. *Carbohydrate Polymers,* 346**,** 659-663.

PALMA, C., LLORET, L., PUEN, A., TOBAR, M. & CONTRERAS, E. 2016. Production of carbonaceous material from avocado peel for its application as alternative adsorbent for dyes removal. *Chinese Journal of Chemical Engineering,* 24**,** 521-528.

PANKHURST, Q. A., CONNOLLY, J., JONES, S. K. & DOBSON, J. 2003. Applications of magnetic nanoparticles in biomedicine. *Journal of Physics D: Applied Physics,* 36**,** 167-181.

PANNEERSELVAM, P., MORAD, N. & TAN, K. A. 2011a. Magnetic nanoparticle ($Fe_3O_4$) impregnated onto tea waste for the removal of nickel(II) from aqueous solution. *Journal of Hazardous Material,* 186**,** 160-168.

PAOLINO, M., ENNEN, F., LAMONI, S., CERNESCU, M., VOIT, B., CAPPELLI, A., APPELHANS, D. AND KOMBER, H 2013. Cyclodextrin-Adamantane host-guest interactions on the surface of biocompatible Adamantyl-modified glycodendrimers,. *Macromole,* 46**,** 3215-3227.

PARK, Y. D., PARK, Y. S. & MOON, J. 2010. The past, present, and future trends of biosorption. *Biotechnology and Bioprocess Engineering,* 15**,** 86-102.

PESTANA, K. C., FORMARIZ, T. P., FRANZINI, C. M., SARMENTO, V. H. V., CHIAVACCI, L. A., SCARPAA, M. V., EGITOC, E.S.T., OLIVEIRA, A.G. 2008. Oil-in-water lecithin-based microemulsions as a potential delivery system for amphotericin B. *Colloids and Surfaces B: Biointerfaces,* 66, 253–259.

PHOLOSI, A., OFOMAJA, A. E. & NAIDOO, E. B. 2013. Effect of chemical extractants on the biosorptive properties of pine cone powder: Influence on lead(II) removal mechanism. *Journal of Saudi Chemical Society,* 17**,** 77-86.

PUTRA, E. K., PRANOWO, R., SUNARSO, J., INDRASWATI, N. & ISMADJI, S. 2009. Performance of activated carbon and bentonite for adsorption of amoxicillin from wastewater: Mechanisms, isotherms and kinetics. *Water Research,* 43**,** 2419-2430.

QAISER, S., SALEEMI, A. R. & AHMAD, M. M. 2007. Heavy metal uptake by agro based waste materials. *Environmental Biotechnology,* 10**,** 409-416.

RAHMAN, I. M. M., BEGUM, Z. A. & HASEGAWA, H. 2013. Selective separation of elements from complex solution matrix with molecular recognition plus macrocycles attached to a solid,. *Microchemical Journal,* 110**,** 485-493.

RAKHSHAEE, R. & PANAHANDEH, M. 2011. Stabilization of a magnetic nano-adsorbent by extracted pectin to remove methylene blue from aqueous solution: A comparative study between two kinds of cross-linked pectin. *Journal of Hazardous Material,* 189**,** 158-166.

RAMRAKHIANI, L., HALDER, A., MAJUMDER, A., MANDAL, A. K., MAJUMDAR, S. & GHOSH, S. 2017. Industrial waste derived biosorbent for toxic metal remediation:

Mechanism studies and spent biosorbent management. *Chemical Engineering Journal,* 308**,** 1048-1064.

RATTANACHUESKUL, N., SANING, A., KAOWPHONG, S., CHUMHA, N. & CHUENCHOM, L. 2016. Magnetic carbon composites with a hierarchical structure for adsorption of tetracycline, prepared from sugarcane bagasse via hydrothermal carbonization coupled with simple heat treatment process. *Bioresource Technology,* 226**,** 164-172.

RAVIKUMAR, K., DEEBIKA, B. & BALU, K. 2005. Decolourization of aqueous dye solutions by a novel adsorbent: application of statistical designs and surface plots for the optimization and regression analysis. *Journal of Hazardous Material,* 122**,** 75-83.

SAFARIK, I., HORSKA, K., SVOBODOVA, B. & SAFARIKOVA, M. 2012. Magnetically modified spent coffee grounds for dyes removal. *Eur Food Research Technology* 234**,** 345-350.

SAHA, R., MUKHERJEE, K., SAHA, I., GHOSH, A., GHOSH, S. K. & SAHA, B. 2013. Removal of hexavalent chromium from water by adsorption on mosambi (Citrus limetta) peel. 39**,** 2245-2257.

SALEM, N. A. & YAKOOT, S. M. 2016. Research article non-steroidal anti-inflammatory drug, ibuprofen Adsorption using rice straw based biochar. *Internation Journal of Pharmacy***,** 729-736.

SAQIB, A. N. S., WASEEM, A., KHAN, A. F., MAHMOOD, Q., KHAN, A., HABIB, A. & KHAN, A. R. 2013. Arsenic bioremediation by low cost materials derived from Blue Pine (Pinus wallichiana) and Walnut (Juglans regia). *Ecological Engineering* 51**,** 88-94.

SARKAR, A. B. & KOCHAK, G. M. 2005. HPLC analysis of aliphatic and aromatic dicarboxylic acid cross-linkers hydrolyzed from carbohydrate polyesters for estimation of the molar degree of substitution. *Carbohydrate Polymers,* 59**,** 305-312.

SCIBAN, M., KLASNJA, M. & SKRBIC, B. 2006. Modified hardwood sawdust as adsorbent of heavy metal ions from water. . *Wood Science Techmology,* 40**,** 217-027.

SHARMA, S. & GARG, S. 2014. A brief study of various adsorbents for removal of Ni metal ions from waste water. *International Journal of Engineering study***,** 201-208

SHEN, Y. F., TANG, J., NIE, Z. H., WANG, Y. D., REN, Y. & ZUO, L. 2009. Preparation and application of magnetic Fe304 nanoparticles for wastewater purification. *Separation and Purification Technology,* 66**,** 312-319.

SHOUMAN, M. M., FATHY, N. A., KHEDR, S. A. & ATTIA, A. A. 2013. Comparative biosorption studies of hexavalent chromium ion onto raw and modified branches. *Advanced Physical Chemistry,* 2013**,** 1-9.

SIKDER, M. T., ISLAM, M. S., KIKUCHI, T., SUZUKI, J., SAITO, T. & KURASAKI, M. 2014. Removal of copper ions from water using epichlorohydrin cross-linked β-cyclodextrin polymer: characterization, isotherms and kinetics. *Water Environment Research,* 86**,** 296-304.

SIMSEK, E. B., OZDEMIR, E. & BEKER, U. 2013. Zeolite supported mono- and bimetallic oxides: promising adsorbents for removal of As(V) in aqueous solutions. *Chemical Engineering Journal,* 220**,** 402-411.

SINGH, N. B., NAGPAL, G., AGRAWAL, S. & RACHNA, A. 2018, Water purification by using Adsorbents: A Review. *Environmental Technology & Innovation*

SUD, D., MAHAJAN, G. & KAUR, M. P. 2008. Agricultural waste material as potential adsorbent for sequestering heavy metal ions from aqueous solutions - A review. *Bioresource Technology,* 14**,** 6017-6027.

SUN, D., ZHANG, X., WU, Y. & LIU, X. 2010. Adsorption of anionic dyes from aqueous solution on fly ash. *Journal of Hazardous Material,* 181**,** 335-342.

SUN, S. 2006. Recent Advances in Chemical Synthesis, Self-Assembly, and Applications of FePt Nanoparticles. *Advanced Materilals,* 18**,** 393-403.

SUTHERLAND, C. 2004. Removal of heavy metals from waters using low cost adsorbents process development. . *PhD Thesis. The University of the West Indies, Trinidad***,** 150-164.

SWARNKAR, V., AGRAWAL, N. & TOMAR, R. 2012. Sorption of chromate and arsenate by Surfactant Modified Erionite (E-SMZ). *Journal of Dispersion Science and Technology,* 33**,** 919-927.

SZEJTLI, J. 2004. Past, present and futute of cyclodextrin research. *Pure Applied Chemistry,* 76**,** 1825-1845.

TALBOT, D., ABRAMSON, S., GRIFFETE, N. & BÉE, A. 2018. pH-sensitive magnetic alginate/γ-Fe2O3 nanoparticles for adsorption/desorption of a cationic dye from water. *Journal of Water Process Engineering,* 25**,** 301-308.

TANG, R. X., DAI, C., LI, C., LIU, W. H., GAO, S. T. & WANG, C. 2017. Removal of methylene blue from aqueous solution using agricultural residue walnut shell: equilibrium, kinetic, and thermodynamic studies. *Journal of Chemistry***,** 1-10.

TEMPKIN, M.I. & PYZHEV, V. 1940, Kinetics of ammonia synthesis on promoted iron catalyst, *Acta Physichochimica USSR* 12, 327–356.

TU, Y. J., YOU, C. F. & CHANG, C. K. 2012. Kinetics and thermodynamics of adsorption of Cd on green manufactured nano-particles. *Journal of Hazardous Material,* 235**,** 116-122.

UCUN, H., BAYHAN, Y. K., KAYA, Y., CAKICI, A. & ALGUR, O. F. 2003. Biosorption of lead (II) from aqueous solution by cone biomass of pinussylvestris. *Desalination,* 154**,** 233-238.

UCUN, H., BAYHAN, Y. K., KAYA, Y., CAKICI, A. & F, A. O. 2002. Biosorption of chromium(VI) from aqueous solution by cone biomass of Pinus *Bioresource Technology,* 85**,** 155-158.

UGOCHUKWU, U. C., JONES, M. D., HEAD, I. M., MANNING, D. A. & FIALIPS, C. I. 2014. Biodegradation and adsorption of crude oil hydrocarbons supported on homo ionic montmorillonite clay minerals. *Applied Clay Science***,** 84-86.

UTOMO, H. D. & HUNTER, K. A. 2010. Particle concentration effect: adsorption of divalent metal ions on coffee grounds. *Bioresource Technology,* 101**,** 1482-1486.

VAZQUEZ, G., ALONSO, R., FREIRE, S., GONZALEZ-ALVAREZ, J. & ANTORRENA, G. 2006. Uptake of Phenol From Aqueous Solutions by Adsorption in a Pinus pinaster Bark Bed. *Journal of Hazardous Material,* 133**,** 61-67.

VELAZQUEZ-JIMENEZ, L. H. 2013. Chemical characterization of raw and treated agave bagasse and its potential as adsorbent of metal cations from water. *Water Research,* 41.

VIEIRA, B. R. C., PINTOR, A. M. A., BAVENTURA, R. A. R., BOTELHO, C. M. S. & SANTOS, S. C. R. 2017a. Arsenic removal from water using iron-coated seaweeds. *Journal of Environmental Management,* 192**,** 224-233.

VINH, N. V., ZAFAR, M., BAHERA, S. K. & PARK, H. S. 2015. Arsenic(III) removal from aqueous solution by raw and zinc-loaded pine cone char: equilibrium, kinetics and thermodynamic studies. *International Journal of Environmental Science and Technology,* 12**,** 1283-1294.

WAN NGAH, W. S. & HANAFIAH, M. A. K. M. 2008. Removal of heavy metal ions from wastewater by chemically modified plant waste as adsorbents: A review. *Bioresource Technology,* 99**,** 3935-3948.

WANG, C., LI, J., SUN, X., WANG, L. & X, S. 2009. Evaluation of zeolites synthesized from fly ash as potential adsorbents for wastewater containing heavy metals. *Journal of environmental Sciences,* 21**,** 127-136.

WANG, S. J., ZHANG, M. X. & YAO, Q. L. 2015. A novel biosorbent formed of marine-derived Penicillium janthinellum mycelial pellets for removing dyes from dye-containing wastewater. *Chemical Engineering Journal,* 259**,** 837-844.

WARTELLE, L. H. & MARSHALL, W. E. 2000. Citric acid modified agricultural by-products as copper ion adsorbents,. *Advances in Environmental Research,* 4**,** 1-7.

YAMAMURA, A. P. G., YAMAURAM, M. & COSTA, C. H. 2011. Magnetic biosorbent for removal of uranyl ions. *International Journal of Nuclear Energy Science and Technology,* 6**,** 8-16.

YANG, G. C. C. & LEE, H. L. 2005. Chemical reduction of nitrate by nanosized iron: kinetics and pathways,. *Water Research,* 39**,** 884-894.

YANG, J., PARK, S. B., YOON, H.-G. H., Y M & HAAM, S. 2006. Preparation of poly ε-caprolactone nanoparticles containing magnetite for magnetic drug carrier. *International Journal of Pharmaceutics,* 324**,** 185-190.

YANG, M., LIN, J., ZHAN, Y. & ZHANG, H. 2014. Adsorption of phosphate from water onlake sediments amended with zirconium-modified zeolites in batch mode. *Ecological Engineering***,** 223-233.

YAO, Z., WANG, L. & QI, J. 2009. Biosorption of methylene blue from aqueous solution using a bioenergy forest waste: Xanthoceras sorbifolia seed coat. *Clean Soil Air Water,* 37**,** 642-648.

YARGıÇ, A. S., YARBAY SAHIN, R. Z., OZBAY, N. & ONAL, E. 2014. Assessment of toxic copper(II) biosorption from aqueous solution by chemically-treated tomato waste (Solanum lycopersicum). *Journal of clean Production*.

ZHA, L. F., CHANG, S. & YUE YAN, J. 2008. Preparation and adsorption kinetics of porous γ-glycidoxypropyltrimethoxysilane crosslinked chitosan–β-cyclodextrin membranes. *Journal of Membrane Science,* 321**,** 316-323.

ZHANG, G., QU, J., LIU, H., COOPER, A. T. & WU, R. 2007. CuFe2O4/activated carbon composite: a novel magnetic adsorbent for the removal of acid orange II and catalytic regeneration. *Chemosphere,* 68**,** 1058-1066.

ZHANG, W., QIAO, X., CHEN, J. 2007 Synthesis of silver nanoparticles-Effects of concerned parameters in water/oil microemulsion, *Materials Science and Engineering B*, 142, 1–15.

ZHANG, M., GAO, B., VARNOOSFADERANI, S., HEBARD, A., YAO, Y. & INYANG, M. 2013. Preparation and characterization of a novel magnetic biochar for arsenic removal. *Bioresource Technology,* 130**,** 457-462.

ZHANG, W. 2003. Nanoscaleiron particles for environmental remediation: an overview. *Journal of Nanoparticles Reseach,* 5**,** 323-332.

ZHANG, X. & WANG, C. 2011. Supra molecular amphiphiles. *Chemical Society Reviews,* 40**,** 94-101.

ZHAO, D., QIU, Q., WANG, Y., HUANG, M., WU, Y., LIU, X. & JIANG, T. 2016. Efficient removal of acid dye from aqueous solutions via adsorption using low-cost blast-furnace slag. *Desalination Water Trreatment,* 57**,** http://dx.doi.org/10.1080/19443994.2016.1179225.

ZHOU, Y., ZHANG, L. & CHENG, Z. J. 2015. Removal of organic pollutants from aqueous solution using agricultural wastes: a review. *Journal of Molecular Liquids,* 212**,** 739-762.

# CHAPTER 3

## 3    EXPERIMENTAL METHODOLOGY

## 3.1    INTRODUCTION

This chapter is divided into four sections. The first section describes sample collection, preparation and characterization. Section two involved the application of the prepared nano $Fe_3O_4$-pine cone bio-composite in section 1 for chromium(VI) and arsenic(III) adsorption from aqueous solution. Section three and four involved the cross-linking of the synthesized nano $Fe_3O_4$-pine cone bio-composite with cyclodextrin using epichlorohydrin and hexamethylene diisocyanate by Response Surface Methodology (RSM), respectively.

## 3.2    EXPERIMENTAL

### 3.2.1    Chemicals and reagents

Sodium hydroxide (NaOH > 98.5 %) and ammonium hydroxide ($NH_4OH$, 25 %) were supplied by Labchem (South Africa). Hydrochloric acid (32 %), Dibutyltin dilaurate ($C_{32}H_{64}O_4Sn$ > 96 %), Hexane ($C_6H_{14}$ > 99 %), 4-nitrophenol ($C_6H_5NO_3$) and Ferrous sulphate ($FeSO_4.7H_2O$ > 98 %) were supplied by Merck. Ferric chloride ($FeCl_3.6H_2O$ > 99 %), sodium arsenite ($NaAsO_2$ > 90 %), β-cyclodextrin (β-CD > 97 %), Hexamethylene diisocyanate [$(CH_2)_6(NCO)_2$ > 99 %], Epichlorohydrin ($C_3H_5ClO$ > 99 %) were purchased from Sigma-Aldrich. Potassium dichromate ($K_2Cr_2O_7$) was purchased from Associated Chemical Enterprises. All syntheses were carried out under nitrogen atmosphere with vigorous stirring to ensure uniform dispersions.

### 3.2.2    Collection of pine tree cones

Pine tree cones were collected from a plantation in Vanderbijlpark, South Africa. The cones were washed to remove impurities such as sand and leaves. The washed cones were dried at 90 ºC for 48 hours in the oven. The scales on the cones were removed and crushed by a pulveriser. The pine cone powder was then sieved and particles between 90 and 45 µm were collected and applied (Ofomaja and Naidoo, 2010).

### 3.2.3 Preparation of pine tree cones

#### 3.2.3.1 Preparation of NaOH treated pine biomass (NTP)

A weighed amount of 50 g of pine cone powder was contacted with 500 $cm^3$ of 0.15 mol/$dm^3$ sodium hydroxide solution and the slurry was stirred for 18 hrs at room temperature. After 18 hrs of contact, the pine cone powder was allowed to settle, NaOH was decanted and the remaining pine cone powder was washed with 500 $cm^3$ of distilled water. The procedure was repeated five more times to ensure removal of sodium hydroxide from the pine biomass. The residue was then dried overnight at 90 $^{\circ}C$.

#### 3.2.3.2 Preparation of nano-$Fe_3O_4$-pine cone bio-composite (NTP-NC)

Nano-$Fe_3O_4$-pine cone bio-composite were obtained from dissolving different mass (2.1:3.1, 1.05:1.55, 0.55:0.78, 0.27:0.39 and 0.143 g: 0.203 g of $FeSO_4.7H_2O$: $FeCl_3.6H_2O$ ratio in 60 $cm^3$ of ultrapure water that was previously degassed with nitrogen and heated at 80 $^{\circ}C$. An amount of 30 $cm^3$ of 20 % ammonium hydroxide and different amounts (1.0, 1.5, 2.0, 2.5, and 3.0 g) of pine biomass were added. The reaction was carried out for another 30 minutes (min) at 60 $^{\circ}C$ under constant stirring to ensure the complete growth of the nanoparticle crystals. The resulting black particles were washed with ultrapure water followed by ethanol to remove any unreacted chemicals, separated by magnetic separation and dried in a vacuum oven at 60 $^{\circ}C$ overnight before use.

### 3.2.4 Sample characterization

#### 3.2.4.1 Point of zero charge

The pH at point zero charge (pH$_{pzc}$) of the NaOH treated pine cone powder (NTP) and Nano-$Fe_3O_4$-pine cone bio-composite (NTP-NC) were determined by the solid addition method (Srivastava et al., 2006). To a series of 100 $cm^3$ conical flasks, 45 $cm^3$ of 0.01 mol $dm^{-3}$ of $KNO_3$ solution was transferred. The pH$_i$ values of the solution were roughly adjusted from pH 2 to 12 by adding either 0.10 mol $dm^{-3}$ HCl or NaOH on a pH meter. The total volume of the solution in each flask was made up to 50 $cm^3$ by adding the $KNO_3$ solution of the same strength. The pH$_i$ of the solution was accurately noted, and 0.10 g of pine cone powder was added to the flask, which was securely capped immediately. The suspensions were then manually shaken and allowed to equilibrate for 48 hrs with intermittent manual shaking. The pH values of the

supernatant liquids were noted. The difference between the initial and final pH values ($pH=pH_i - pH_f$) was plotted against the $pH_i$. The point of intersection of the resulting curve at which $pH = 0$ gave the $pH_{pzc}$.

### 3.2.4.2   Fourier transform infrared spectroscopy (FTIR)

The FTIR spectra of the synthesised Nano-$Fe_3O_4$-pine cone bio-composite before and after adsorption were recorded on a Fourier Transform Infrared Spectrometer (Perkin-Elmer infrared spectrophotometer) to elucidate the functional groups present.

### 3.2.4.3   X-ray diffraction (XRD)

The crystallographic structure of the NTP and NTP-NC were analyzed by X-ray diffraction. XRD patterns were obtained with an X'Pert PRO X-ray diffractometer (PANalytical, PW3040/60 XRD; CuKα anode; λ = 0.154 nm). The samples were gently consolidated in an aluminium holder and scanned at 45 kV and 40 mA from 10◦ to 70◦ 2θ, the exposure time for each sample was 20 min and a step size of 0.02◦.

### 3.2.4.4   Scanning electron microscopy (SEM) and EDX analysis

Scanning electron microscopy (SEM) was used to observe the microstructure and surface morphology of NTP and NTP-NC. The SEM images were obtained on a Cerl-Zeiss Sigma instrument (Germany) that uses a tungsten filament source. The samples were Pd-Au coated and imaging was done at 5 kV.

### 3.2.4.5   Transmission electron microscopy (TEM) Measurement

A bright field transmission electron microscopy (TEM) was used for the size measurement and size distribution of the adsorbent.

### 3.2.4.6   Thermogravimetric analysis (TGA)

To measure the changes in the weight loss of the sample as a function of temperature, simultaneous thermal analyser (Perkin Elmer STA 6000) was used. This instrument is capable

of obtaining DSC and TGA measurements simultaneously. The NTP and NTP-NC adsorbents were weighed into quartz crucibles. Thermal scans were performed from 30 to 700 °C at a heating rate of 10 ºC/min and an empty crucible was used as a reference.

### 3.2.4.7   Brunauer-Emmett-Teller (BET) Method

The specific surface area of the NTP and NTP-NC adsorbents were measured by BET analyzer. The BET surface area and pore size distribution were determined using computer-controlled nitrogen gas adsorption analyzer. Degassing was carried out for 1 hr at 90 $^{\circ}$C and increased to 120 $^{\circ}$C for 2 hrs. A mass of 0.2 g of the NTP and NTP-NC adsorbent material was applied for analysis.

### 3.2.4.8   X-ray photoelectron spectroscopy

X-ray photoelectron spectroscopy (XPS) analysis was carried out on PHI 5000 scanning ESCA microprobe with a 100 μm diameter monochromatic Al Kα x-ray beam (hν = 1486.6 eV) generated by a 25 W, 15 kV electron beam to analyze different binding energy peaks. Multipack version 9 software was utilized to analyse the spectra to identify the chemical compounds and their electronic states using Gaussian–Lorentz fits.

### 3.2.4.9   Vibrating sample magnetometer

Magnetic properties of powder samples were characterized with a Quantum Design MPMS-7, by measuring the applied field dependence of magnetization between -15 and 15 kOe.

## 3.2.5   Experimental Procedure for Cr(VI) removal

### 3.2.5.1   Processes for Cr(VI) removal

Batch adsorption experiments for Cr(VI) removal from NaOH treated pine cone (NTP) and Nano-$Fe_3O_4$-pine cone nanocomposite (NTP-NC) were conducted in order to determine the optimum adsorbent dose, solution pH, temperature, solution volume and equilibrium time, to generate adsorption equilibrium data and kinetics data. Cr(VI) stock solution was prepared by dissolving a weighed amount of $K_2Cr_2O_7$ in deionized water.

### 3.2.5.2  Effect of initial solution pH

The effect of initial solution pH of Cr(VI) adsorption was studied in a batch adsorption system in which 100 cm$^3$ of 100 mg/dm$^3$ of Cr(VI) were added to six 250 cm$^3$ beakers and the initial solution pH varied from 1.0 to 10.0 using 0.1 mol/dm$^3$ of either HCl or NaOH solution. An amount of 0.1 g of NTP and NTP-NC nanocomposite were added to each beaker and agitated for 2 hrs at room temperature. At the end of agitation, the mixture was centrifuged and filtered. The amount of Cr(VI) left in solution after contacting with 1,5-Diphenyl carbazide was then determined by Perkin-Elmer (USA) Lambda 25 Ultra Violet-Visible (UV/Vis) spectrometer at 540 nm.

### 3.2.5.3  Effect of adsorbent dose

The effect of adsorbent dose on the equilibrium uptake of Cr(VI)) was investigated by adding the NTP and NTP-NC adsorbent masses of 0.05; 0.10; 0.50; 1.0; and 1.5 g to five 250 cm$^3$ beakers containing 100 cm$^3$ of 100 mg/dm$^3$ solution at pH 3. The flasks were shaken at 145 rpm and 291 K for 2 hrs and the equilibrium concentration of Cr(VI) remaining was determined by UV/Vis spectrophotometry.

### 3.2.5.4  Effect of initial concentration

The effect of adsorbent concentration on the equilibrium uptake of Cr(VI) was investigated with adsorbent concentrations of 25; 50; 75; 100; 125; and 150 mg/dm$^3$. The experiments were performed by adding 0.5 g of NTP and NTP-NC into 250 cm$^3$ beakers containing 100 cm$^3$ of Cr(VI) solution at pH 3. The flasks were shaken at 145 rpm and 291 K for 2 hrs and the equilibrium concentration of Cr(VI) remaining in solution was determined by UV/Vis spectrophotometry.

### 3.2.5.5  Equilibrium studies

A volume of 75 cm$^3$ of different Cr(VI) ion solution with concentration ranging from 25 to 150 mg/dm$^3$ set at pH 2 were placed in 250 cm$^3$ conical flask. Accurately weighed amount (0.5 g) of NTP and NTP-NC was then added to the solutions. The conical flasks were then shaken at a constant speed of 145 rpm in a shaker at different temperature from (299, 304, 309, 314 and

319 K). After shaking the flasks for 2 hrs, the NTP biomaterial was filtered and NTP-NC was separated by magnetic separation. The filtrate was then analyzed with UV/Vis spectrophotometry to determine the amount of Cr(VI) ions left in solution.

### 3.2.5.6   Kinetics studies

Batch contact kinetic experiments were performed by contacting 0.5 g of the adsorbent materials with 75 cm$^3$ of Cr(VI) solution of concentrations 25, 75 100, 125 and 150 mg/dm$^3$ in five conical flasks agitated at 200 rpm for 2 hrs at different temperatures from (299, 304, 309, 314 and 319 K) set to pH 3. Aliquots (0.1 cm$^3$) of sample was withdrawn at different interval (0.5; 1; 2; 3; 5; 20; 30; 60 and 120 min), filtered and diluted appropriately and analysed for Cr(VI) left using UV-Vis spectrophotometry.

### 3.2.5.7   Effect of ionic strength

The effect of ionic strength on Cr(VI) adsorption onto NTP and NTP-NC was examined by contacting 0.5 g of the adsorbents with 100 cm$^3$ of 100 mg/dm$^3$ Cr(VI) solution containing 0.01, 0.05, 0.10, 0.15 and 0.20 mg/dm$^3$ of NaNO$_3$. After shaking the flasks for 2 hrs, the adsorbents were filtered off or magnetically separated. The filtrate was then analysed for Cr(VI) remaining by UV-Vis spectrophotometry.

### 3.2.5.8   Effect of competing anions

For the effect of anion competition, 0.5 g of the (NTP and NTP-NC) adsorbents were contacted with 100 cm$^3$ of 0.1 mol/dm$^3$ of NaCl, Na$_2$SO$_4$, Na$_2$CO$_3$, NaNO$_3$ and NaHPO$_4$ set at pH 3, 299 K and shaken for 2 hrs. After shaking the flasks for 2 hrs, the adsorbents were filtered off or magnetically separated. The filtrate was then analysed for Cr(VI) remaining by UV-Vis spectrophotometry.

### 3.2.5.9   Desorption studies

Desorption characteristics of an adsorbent is evaluated by extracting adsorbed metal ions by different solvents. Biosorbent residue used in the system of 1.0 g of NTP and NTP-NC in contact with 100 cm$^3$ of 200 mg/dm$^3$ of Cr(VI) solution was separated by centrifugation and

washed with distilled water. The washed residue solid was then dried overnight and stirred in 100 $cm^3$ of 0.5 $mol/dm^3$ of each of the desorbing solvents (HCl, NaOH, $CH_3COOH$) and $H_2O$. After shaking the flask for 2 hrs at 200 rpm, the NTP and NTP-NC solids were separated by filtration and the leached amount of Cr(VI) ions in the filtrate were analyzed by UV-Vis spectrophotometry.

### 3.2.6    Experimental process for As(III) removal

Batch adsorption experiments for As(III) removal from NaOH treated pine cone (NTP) and Nano-$Fe_3O_4$-pine cone bio-composite (NTP-NC) were conducted in order to determine the optimum adsorbent dose, solution pH, temperature, concentration and equilibrium time, to generate adsorption equilibrium data and kinetics data. As(III) stock solution was prepared by dissolving a weighed amount of $NaAsO_2$ in deionized water.

### 3.2.6.1    *Effect of initial solution pH*

The effect of initial solution pH of As(III) adsorption was studied in a batch adsorption system in which 100 $cm^3$ of 100 $mg/dm^3$ of As(III) were added to six 250 $cm^3$ beakers and the initial solution pH varied from 1.0 to 10.0 using 0.1 $mol/dm^3$ of either HCl or NaOH solution. An amount of 0.1 g of NTP and NTP-NC biosorbents was added to each beaker and agitated for 2 hrs at room temperature. At the end of agitation, the mixture was then magnetically separated. Concentration of As(III) left in solution was then determined by Inductively Coupled Plasma-Optical Emission Spectrometry (ICP-OES). About 50 $cm^3$ aliquots were sampled from the suspension and passed through an arsenic speciation cartridge (Metalsoft Center, Highland Park, NJ) packed with a 2.5 g highly selective absorbent. The cartridge removed all As(V) but allowed As(III) to pass through in the pH range 4 to 9. Then, As(III) in the filtered solution was also determined using ICP-OES.

### 3.2.6.2    *Effect of adsorbent dose*

The effect of adsorbent dose on the equilibrium uptake of As(III) was investigated by adding the NTP and NTP-NC adsorbent masses of 0.05; 0.1; 0.5; 1.0 and 1.5 g to five 250 $cm^3$ beakers

containing 100 cm$^3$ of 100 mg/dm$^3$ solution at pH 8. The flasks were shaken at 200 rpm for 2 hrs and the equilibrium concentration of As(III) remaining was determined ICP-OES.

### 3.2.6.3 Equilibrium studies

A volume of 100 cm$^3$ of different As(III) concentrations ranging from 25 to 150 mg/dm$^3$ set at pH 8 were placed in 250 cm$^3$ conical flask. Accurately weighed amount (0.5 g) of NTP and NTP-NC were then added to the solutions. The conical flasks were then shaken at a constant speed of 200 rpm in a shaker at different temperatures from (299, 304, 309, 314 and 319 K). After shaking the flasks for 2 hrs, the adsorbents were filtered off or magnetically separated. The filtrate was then analysed for As(III) remaining by ICP-OES.

### 3.2.6.4 Kinetics studies

Batch contact kinetic experiments were performed by contacting 0.5 g of the adsorbent materials with 100 cm$^3$ of As(III) solution of concentrations 25, 75 100, 125 and 150 mg/dm$^3$ in five conical flasks agitated at 200 rpm for 2 hrs at different temperatures from (299, 304, 309, 314 and 319 K) set to pH 8. Aliquots (0.1 cm$^3$) of samples were withdrawn at different time intervals (0.5; 1; 2; 3; 5; 20; 30; 60 and 120 min), filtered and diluted appropriately. The samples were then analysed for As(III) left in solution using ICP-OES.

### 3.2.6.5 Effect of ionic strength

The effect of ionic strength on As(III) adsorption onto NTP and NTP-NC was examined by contacting 0.5 g of the adsorbents with 100 cm$^3$ of 100 mg/dm$^3$ As(III) solution containing 0.01, 0.05, 0.10, 0.15 and 0.20 mg/dm$^3$ of NaNO$_3$. After shaking the flasks for 2 hrs, the adsorbents were filtered off or magnetically separated. The filtrate was then analysed for As(III) remaining by ICP-OES.

### 3.2.6.6 Effect of competing anions

For the effect of anion competition, 0.5 g of the adsorbents (NTP and NTP-NC) were contacted with 100 cm$^3$ of 0.1 mol/dm$^3$ of NaCl, Na$_2$SO$_4$, Na$_2$CO$_3$, NaNO$_3$ and NaHPO$_4$ set at pH 8 and

shaken for 2 hrs. After shaking the flasks for 2 hrs, the adsorbents were filtered off or magnetically separated. The filtrate was then analysed for As(III) remaining by ICP-OES.

### 3.2.6.7 As(III)/$NO_3^-$ exchange on $NO_3^-$-loaded NTP and NTP-NC

NTP and NTP-NC (5.0 g) were dispersed in 100 mg/dm$^3$ NaNO$_3$ solution and stirred at 200 rpm for 5 hrs at pH 5 at 299 K. After 5 hrs of stirring, the solid was washed to remove excess NaNO$_3$ and dried overnight at 363 K. An amount of 0.5 g of the $NO_3^-$-loaded adsorbent was added to 100 cm$^3$ solutions of 0, 5, 25, 50 and 100 mg/dm$^3$ As(III) solutions set at pH 8 and stirred at 200 rpm 299 K. The amounts of $NO_3^-$ ions released in solution and As(III) remaining were determined using an Ion selective electrode and ICP-OES, respectively.

### 3.2.6.8 Desorption and reuse

Desorption characteristics of an adsorbent can be evaluated by extracting adsorbed metal ions by different solvents. Adsorbent residue used in the system of 0.5 g of NTP and NTP-NC in contact with 100 cm$^3$ of 100 mg/dm$^3$ of As(III) solution was separated by centrifugation and washed with distilled water. The washed residue solid was then dried overnight and stirred in 100 cm$^3$ of 0.5 mg/dm$^3$ of each of the desorbing solvents (HCl, NaOH and H$_2$O). After shaking the flask for 2 hrs at 200 rpm, adsorbent solids were separated by filtration and the leached amount of As(III) in the filtrate were analysed by ICP-OES.

## 3.2.7 Cross linking of cyclodextrin with nano-Fe$_3$O$_4$-pine cone bio-composite (NTP-NC) using epichlorohydrin as a cross linking agent

### 3.2.7.1 Synthesis of carboxymethyl-cyclodextrin-epichlorohydrin (CM-CD-EPI) polymer

CM-CD polymer was prepared following the procedure of literature (Fernández et al., 2004). β-Cyclodextrin (5 g) was dissolved in 50 cm$^3$ of 10% (w/v) NaOH and 10 ml of epichlorohydrin was added. The system was vigorously stirred for 8 hrs, excess 5 ml of epichlorohydrin was added with stirring and the mixture kept overnight at room temperature. The solution was concentrated to about 15 cm$^3$ and precipitated by addition of cold ethanol (500 cm$^3$). The gummy precipitate was crushed several times with ethanol until a fine precipitate was obtained.

The precipitate was then washed again with ethanol and acetone and dried overnight at 60 ºC in a high vacuum oven.

Two grams of the above polymer was further dissolved in 50 cm$^3$ 5% (w/v) NaOH and 2 g of monochloroacetic acid was added. The system was vigorously stirred for 24 h, neutralized with 2 mol/dm$^3$ HCl, concentrated to about 15 cm$^3$ and cooled to 4 ºC. The precipitated NaCl was filtered off and the supernatant was precipitated by addition of cold ethanol (500 cm$^3$). The gummy precipitate was crushed several times with ethanol in a mortar until a fine precipitate was obtained. The precipitate was then washed two more times with ethanol and acetone and dried under high vacuum at 60 ºC overnight.

### 3.2.7.2 *Response surface methodology for the synthesized CM-CD-EPI polymer with magnetite-pine cone bio-composite (NTP-NC)*

A reduced central composite design (CCD) was used in the experimental procedure to investigate the effects of NTP-NC dose (0.5-2.0 g), CM-CD-EPI dosage (0.5–2.0 g), reaction time (3-24 hrs) and reaction temperature (30-90 ºC) on the crosslinking of CM-CD onto NTP-NC biosorbent. The full model equation with quadratic terms for predicting the optical response was given as independent variables and their coded levels for the quadratic model design in Table 3.1. Design Expert Version 6.0.6 (Stat-Ease, USA) was used to optimize the levels of the independent variables and to evaluate the interactions of the process parameters.

NTPNC-EPI-CD nanocomposite was synthesized by one step method where the known amount of NTP-NC and a known amount of CM-CD-EPI polymer were dissolved in 40 cm$^3$ of ultrapure water with vigorous stirring at a speed of 1200 rpm. The reaction was heated for 1 hr at 90 ºC under constant stirring and an inert environment. The resulting nanoparticles were washed with ultrapure water several times to remove any unreacted chemicals and dried in a vacuum oven overnight.

Table 3.1: Design model for the cross linking of the synthesized CM-CD-EPI polymer with nano-$Fe_3O_4$-pine cone bio-composite (NTP-NC)

| Factor | Name | Units | Type | Low actual | High actual | Low coded | High coded |
|--------|------|-------|------|-----------|-------------|-----------|------------|
| A | NTP-NC mass | g | Numeric | 0.50 | 2.00 | -1.000 | 1.000 |
| B | CM-CD-EPI mass | g | Numeric | 0.50 | 2.00 | -1.000 | 1.000 |
| C | Temp | $^o$C | Numeric | 30.00 | 90.00 | -1.000 | 1.000 |
| D | Time | hours | Numeric | 3.00 | 24.00 | -1.000 | 1.00 |

### 3.2.8 Cross linking of cyclodextrin with $Fe_3O_4$-pine cone bio-composite (NTP-NC) using hexamethylene diisocyanate as a crosslinking agent

NTP-NC (0.1 g) and cyclodextrin (0.1g) were dispersed in anhydrous hexane (10 cm$^3$), in which dibutyltin dilaurate (1 cm$^3$) was added as catalyst in a 250 cm$^3$ three-necked round-bottomed flask with a magnetic stirrer and an inlet for $N_2$ gas. The mixture was heated in a reflux set up at 50 °C for 15 min to complete the process of activation. A separate volume of HMDI (2.5 cm$^3$) was dissolved in anhydrous hexane (10 cm$^3$) and added drop wise to the activated pine cone biomass. The mixture was heated under reflux in a nitrogen atmosphere for 1 hr with continuous stirring. The HMDI cross-linked NTP-NC-CD produced was rinsed with fresh hexane several times, followed by drying in a vacuum oven at 60 °C for 8 hrs. A reduced central composite design (CCD) was used in the experimental procedure to investigate the effects of CD mass (0.05-0.15 g), dibutyltin dilaurate volume (0.5–1.5 cm$^3$), hexamethylene diisocyanate volume (2-3 cm$^3$) and reaction temperature (40-60 °C) on the crosslinking of CD onto NTP-NC biosorbent using hexamethylene diisocyanate.

Table 3.2: Design model for the cross linking of the CD polymer with nano-$Fe_3O_4$-pine cone bio-composite (NTP-NC) using hexamethylene diisocyanate

| Factor | Name | Units | Type | Low Actual | High Actual | Low Coded | High Coded |
|--------|------|-------|------|------------|-------------|-----------|------------|
| A | A DBTDL volume | $cm^3$ | Numeric | 0.50 | 1.50 | -1.000 | 1.000 |
| B | CD mass | g | Numeric | 0.05 | 0.15 | 1000 | 1000 |
| C | temp | $^oC$ | Numeric | 40.00 | 60.00 | -1.000 | 1.000 |
| D | HMDI volume | $cm^3$ | Numeric | 2.00 | 3.00 | -1.000 | 1.000 |

### 3.2.9 Characterization of the NTP-NC crosslinked to CD by epichlorohydrin (NTPNC-EPI-CD) and hexamethylene diisocyanate (NTP-NC-CD-HMDI)

#### 3.2.9.1 Fourier Transform Infrared spectroscopy (FTIR)

The FTIR spectra of the synthesised NTPNC-EPI-CD and NTPNC-HMDI-CD nanocomposite were recorded on a Fourier Transform Infrared Spectrometer (Perkin-Elmer infrared spectrophotometer) to confirm crosslinking of magnetite coated pine onto cyclodextrin.

#### 3.2.9.2 X-ray Diffraction (XRD)

The structural properties and crystallographic structure of the NTPNC-EPI-CD and NTPNC-HMDI-CD nanocomposites were analyzed by X-ray diffraction. XRD patterns were obtained with an X'Pert PRO X-ray diffractometer (PANalytical, PW3040/60 XRD; CuKα anode; λ = 0.154 nm). The samples were gently consolidated in an aluminium holder and scanned at 45 kV and 40 mA from 10∘ to 70∘ 2θ, the exposure time for each sample was 20 min and a step size of 0.02∘.

#### 3.2.9.3 Thermogravimetric Analysis (TGA)

To measure the changes in the weight loss of the NTPNC-EPI-CD and NTPNC-HMDI-CD nanocomposites as a function of temperature, simultaneous thermal analyser (Perkin Elmer STA 6000) was used. This instrument can obtain DSC and TGA measurements simultaneously.

The biosorbent were weighed into quartz crucibles. Thermal scans performed from 30 to 700 °C at a heating rate of 10 °C/min. An empty crucible was used as a reference.

### 3.2.9.4  Brunauer-Emmett-Teller (BET) Method

The specific surface area of NTPNC-EPI-CD and NTPNC-HMDI-CD nanocomposites were measured by BET analyzer. The BET surface area and pore size distribution were determined using computer-controlled nitrogen gas adsorption analyzer. Degassing was carried out for 1 hr at 90 °C and increased to 120 °C for 2 hrs. A mass of 0.2 g of the adsorbent material was applied for analysis.

### 3.2.9.5  Vibrating Sample Magnetometer (VSM)

Magnetic properties of the NTPNC-EPI-CD and NTPNC-HMDI-CD nanocomposites were characterized with a Quantum Design MPMS-7, by measuring the applied field dependence of magnetization between -15 and 15 kOe.

### 3.2.9.6  Point of zero charge

The pH at point zero charge ($pH_{pzc}$) of the NTPNC-EPI-CD and NTPNC-HMDI-CD were determined by the solid addition method (Srivastava et al., 2006). To a series of 100 cm$^3$ conical flasks, 45 cm$^3$ of 0.01 mol dm$^{-3}$ of KNO$_3$ solution was transferred. The $pH_i$ values of the solution were roughly adjusted from pH 2 to 12 by adding either 0.10 mol dm$^{-3}$ HCl or NaOH on a pH meter. The total volume of the solution in each flask was made up to 50 cm$^3$ by adding the KNO$_3$ solution of the same strength. The $pH_i$ of the solution was accurately noted, and 0.10 g of the nanocomposite was added to the flask, which was securely capped immediately. The suspensions were then manually shaken and allowed to equilibrate for 48 hrs with intermittent manual shaking. The pH values of the supernatant liquids were noted. The difference between the initial and final pH values ($pH=pH_i - pH_f$) was plotted against the $pH_i$. The point of intersection of the resulting curve at which pH= 0 gave the $pH_{pzc}$.

*3.2.9.7 Transmission Electron Microscopy (TEM) Measurement*

A bright field transmission electron microscopy (TEM) was used for the size measurement and size distribution of the adsorbent.

## 3.2.10 Experimental process for 4-nitrophenol removal by NTPNC, NTPNC-EPI-CD, NTPNC-HMDI-CD nanocomposite

Batch adsorption experiments for 4-Nitrophenol using NTP-NC, NTPNC-EPI-CD and NTPNC-HMDI-CD nanocomposites were conducted to determine the optimum adsorbent dose, solution pH, temperature, adsorbent concentration and equilibrium time, to generate adsorption equilibrium data and kinetics data.

*3.2.10.1 Effect of initial solution pH*

The effect of initial solution pH on the 4-Nitrophenol (4-NP) adsorption was studied in a batch adsorption system in which 100 cm$^3$ of 100 mg/dm$^3$ of 4-NP was added to six 250 cm$^3$ beakers and the initial solution pH varied from 1.0 to 10.0 using 0.1 mol/dm$^3$ of either HCl or NaOH solution. An amount of 0.1 g of NTP-NC, NTPNC-EPI-CD and NTPNC-HMDI-CD nanocomposite adsorbents was added to each beaker and agitated for 2 hrs at room temperature. The samples were then filtered and analysed using a (UV/Vis) spectrometer to determine the amounts of 4-Nitrophenol left in the solution at 460 nm.

*3.2.10.2 Effect of adsorbent dose*

The effect of biosorbent dose on the equilibrium uptake of 4-NP was investigated by adding the NTP-NC, NTPNC-EPI-CD and NTPNC-HMDI-CD nanocomposite biosorbents masses of 0.05; 0.10; 0.50; 1.0; and 1.5 g to five 250 cm$^3$ beakers containing 100 cm$^3$ of 100 mg/dm$^3$ solution at pH 3 and pH 7 for NTPNC-HMDI-CD. The flasks were shaken at 145 rpm and 291 K for 2 hrs and the equilibrium concentration of 4-NP remaining was determined by UV/Vis spectrophotometry.

### 3.2.10.3 Effect of initial concentration

The effect of adsorbent concentration on the equilibrium uptake of 4-Nitrophenol was investigated with adsorbent concentrations of 25; 50; 75; 100; 125; and 150 mg/dm$^3$. The experiments were performed by adding 0.1 g of NTP-NC, NTPNC-EPI-CD and NTPNC-HMDI-CD nanocomposite biosorbents to 250 cm$^3$ beakers containing 100 cm$^3$ of 4-NP solution at pH 3 for NTPNC and NTPNC-EPI-CD and pH 7 for NTPNC-HMDI-CD nanocomposite. The flasks were shaken at 145 rpm and 299 K for 2 hrs and the equilibrium concentration of 4-NP remaining in solution was determined by UV/Vis spectrophotometry.

### 3.2.10.4 Equilibrium studies

A volume of 100 cm$^3$ of different 4-NP ion solutions with concentration ranging from 25 to 150 mg/dm$^3$ set at pH 3 and pH 7 were placed in 250 cm$^3$ conical flask. Accurately weighed amount (0.1 g) of NTP-NC, NTPNC-EPI-CD and NTPNC-HMDI-CD nanocomposites were then added to the solutions. The conical flask was then shaken at a constant speed of 145 rpm in a shaker at different temperature (299, 304, 309, 314 and 319 K). After shaking the flasks for 2 hrs, the biomaterials were filtered and separated by magnetic separation. The filtrate was then analyzed for the 4-NP ions remaining by UV/Vis spectrophotometer.

### 3.2.10.5 Kinetics studies

Batch contact kinetic experiments were performed by contacting 0.1 g of the NTP-NC, NTPNC-EPI-CD and NTPNC-HMDI-CD nanocomposite adsorbent materials with 100 cm$^3$ of 4-NP solution of concentrations 25, 75 100, 125 and 150 mg/dm$^3$ in five conical flasks agitated at 200 rpm for 2 hrs at different temperature (299, 304, 309, 314 and 319 K). Aliquot (0.1 cm$^3$) of sample was withdrawn at different interval (0.5; 1; 2; 3; 5; 20; 30; 60 and 120 min), filtered and diluted appropriately and analysed for the amount of 4-NP left in solution using UV-Vis spectrophotometer.

### 3.2.10.6 Desorption studies

Adsorbent residue used in the system of 1.0 g of NTP-NC, NTPNC-EPI-CD and NTPNC-HMDI-CD in contact with 100 cm$^3$ of 200 mg/dm$^3$ of 4-NP solution was separated by

centrifugation and washed with distilled water. The washed residue solid was then dried overnight and stirred in 100 cm$^3$ of ethanol. After shaking the flask for 2 hrs at 200 rpm, the solids were separated by filtration and the leached amount of 4-Nitrophenol in the filtrate were analyzed by UV-Vis spectrophotometry.

### 3.2.10.7 Effect of ionic strength

The effect of ionic strength on 4-NP adsorption onto NTP-NC, NTPNC-EPI-CD and NTPNC-HMDI-CD nanocomposites was examined by contacting 0.1 g of the adsorbents with 100 cm$^3$ of 100 mg/dm$^3$ 4-NP solution containing 0.01, 0.05, 0.10, 0.15 and 0.20 mg/dm$^3$ of NaNO$_3$. After shaking the flasks for 2 hrs, the adsorbents were filtered off or magnetically separated. The filtrate was then analysed for 4-NP remaining by UV-Vis spectrophotometry.

### 3.2.10.8 Effect of competing anions

For the effect of anion competition, 0.1 g of the NTP-NC, NTPNC-EPI-CD and NTPNC-HMDI-CD nanocomposites were contacted with 100 cm$^3$ of 0.1 mol/dm$^3$ of NaCl, Na$_2$SO$_4$, Na$_2$CO$_3$, NaNO$_3$ and NaHPO$_4$ set at pH 8 and shaken for 2 hrs. After shaking the flasks for 2 hrs, the adsorbents were filtered off or magnetically separated. The filtrate was then analysed for 4-nitrophenol remaining by UV-Vis spectrophotometry.

REFERENCES

FERNÁNDEZ, M., VILLALONGA, M. L., FRAGOSO, A., CAOB, B. N., M & VILLALONGA, R. 2004. α-Chymotrypsin stabilization by chemical conjugation with O-carboxymethyl- poly-cyclodextrin. *Process Biochemistry,* 39**,** 535-539.

OFOMAJA, A. E. & NAIDOO, E. B. 2010. Biosorption of lead(II) onto pine cone powder: Studies on biosorption performance and process design to minimize biosorbent mass. *Carbohydrate Polymers,* 82**,** 1031-1042.

SRIVASTAVA, V. C., MALL, I. D. & M, M. I. 2006. Characterization of mesoporous rice husk ash (RHA) and adsorption kinetics of metal ions from aqueous solution onto RHA *Journal of Hazardous Material,* B134**,** 257-267.

**CHAPTER 4**

## 4 RESULTS AND DISCUSSION

## 4.1 INTRODUCTION

This chapter covers the optimization and characterization of the magnetite bio-composite (NTP-NC). The first part covers optimization of the working parameters for the synthesis of the magnetite bio-composite material by co-precipitation method, such as the amount of the $Fe^{2+}$: $Fe^{3+}$ mass ratio and the biomaterial (pine cone powder) mass. The optimum reaction conditions of the magnetite bio-composite produced was monitored using FTIR to elucidate functional groups present on magnetite and pine biomass, XRD for the crystalline structure, particle size and morphology using TEM and magnetic property using VSM instrument. Further characterization of the optimum magnetite bio-composite material was conducted using different analytical tools such as SEM-EDX, BET surface area, XPS and $pH_{pzc}$ are reported in the second part.

## 4.2 OPTIMIZATION AND CHARACTERIZATION OF MAGNETITE BIOCOMPOSITE

### 4.2.1 Optimization of working conditions

Magnetic nanoparticles are considered for pollutants removal due to their unique properties such as strong magnetism, small particle size, chemical stability, good biocompatibility, high surface area, resulting in high adsorption capacity. Chemical "co-precipitation" is the most common method for magnetite synthesis, yielding small size particles that are spherical in shape. The method includes: (1) Co-precipitation of $Fe^{2+}$ and $Fe^{3+}$, (2) Partial reduction of $Fe^{3+}$, (3) Partial oxidation of $Fe^{2+}$ and co precipitation. of $Fe^{3+}$ and $Fe^{2+}$ at molar ratio of 2:1 in the presence of a base under inert environment. Magnetite synthesis is highly sensitive as magnetite is susceptible to air oxidation and can easily agglomerate, hence surface modification is one crucial step for their application as adsorbents. NaOH treated pine cone, a low-cost agricultural waste material was used as a coating agent with the aim of preventing magnetite aggregation, enhance stability and improve surface properties by adding significant amount of low cost material without compromising the adsorbent surface. Because magnetite properties strongly depend on their dimension, shape, saturation magnetization and mono dispersion,

different analytical tools were conducted to determine the effect of varying pine cone mass and $Fe^{2+}$: $Fe^{3+}$ mass ratio on magnetite coated pine cone synthesis.

## 4.2.2   Effect of Fe(II)/Fe(III) mass ratio on magnetite bio-composite synthesis.

The effect of Fe(II)/Fe(III) mass ratio on the synthesis of NTP-NC by co-precipitation method was conducted by varying $Fe^{2+}$: $Fe^{3+}$ (2.1:3.1, 1.05:1.55, 0.55:0.78, 0.27:0.39, and 0.14:0.2) mass ratio, using 1.0 g of pine cone at 60 ºC for 30 min under inert environment.

### *4.2.2.1   Fourier Transformed Infra-Red (FTIR)*

To examine the effect of varying $Fe^{2+}$: $Fe^{3+}$ (2.1:3.1, 1.05:1.55, 0.55:0.78, 0.27:0.39, and 0.14:0.2) mass ratio on NTP-NC bio-composite functional groups, FTIR analysis was conducted and the results are reported in Fig. 4.1. From Fig. 4.1, all spectra show relevant bands at 3307, 2888, 1591 $cm^{-1}$ characteristics of O-H stretching vibration, symmetric C-H band and C-O vibration, respectively (Acisli et al., 2017, Subramanian et al., 2005). Magnetite was observed by the strong Fe-O stretching vibration at 548 $cm^{-1}$(Chen et al., 2009). While the C-O-C peak was observed at 1052 $cm^{-1}$ for all samples. The sample with mass ratio of 2.1:3.1 and 1.05:1.55 g of $Fe^{2+}$: $Fe^{3+}$ were observed to have a broad peak between 1022-1052 $cm^{-1}$ which may be due to the C-O-C and Fe-OH present in the bio-composite. The peak was observed to sharpen and increase in intensity with the reduction in Fe(II)/Fe(III) mass ratio from 2.1:3.1 g to 0.143:0.203 g of $Fe^{2+}$: $Fe^{3+}$ mass ratio indicating the increase in the C-O-C groups from the excess pine cone present in the material. The increase in this group was confirmed by the increase and sharpening of the C-O group at 1591$cm^{-1}$. The Fe-O peak at 548 $cm^{-1}$ on the other hand was observed to increase slightly with a reduction in $Fe^{2+}$: $Fe^{3+}$ mass ratio from 2.1:3.1 to 0.27:0.391, and reduce as $Fe^{2+}$: $Fe^{3+}$ mass ratio was further reduced to 0.143:0.203 g.
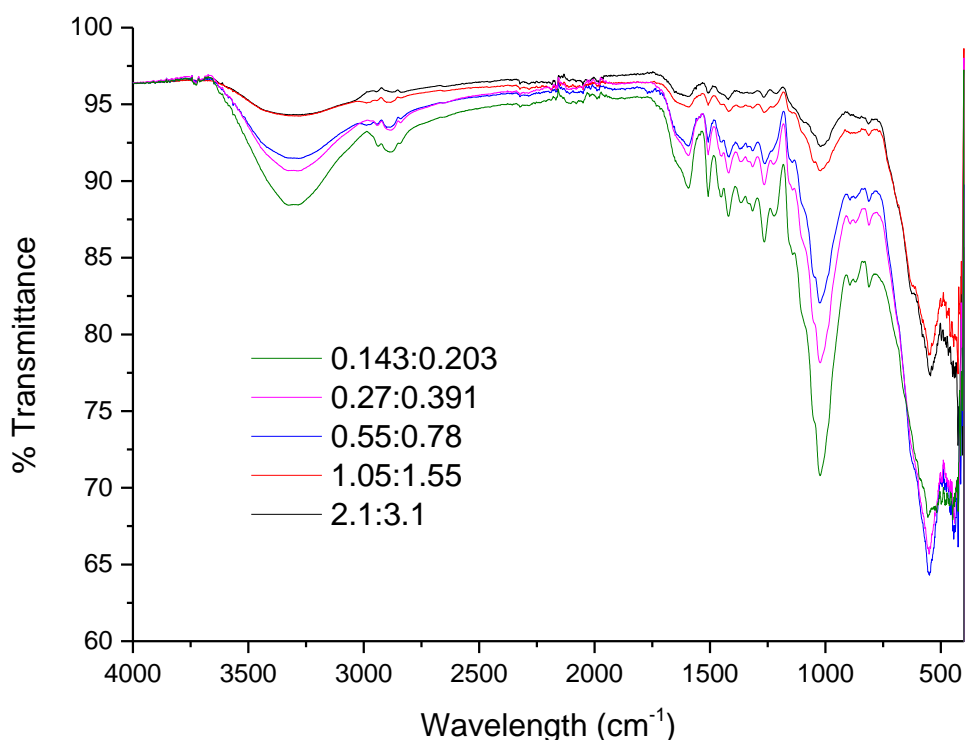
**Figure *4.1:* FTIR spectra of the effect of $Fe^{2+}$/$Fe^{3+}$ mass ratio on the synthesis of magnetite bio-composite.**

*4.2.2.2   Thermal gravimetric analysis (TGA)*

In an attempt to study the effect of $Fe^{2+}$: $Fe^{3+}$ mass ratio (2.1:3.1, 1.05:1.55, 0.55:0.78, 0.27:0.39, and 0.14:0.2) on thermal stability of the NTP-NC bio-composite, TGA measurements were conducted from room temperature to 700 $^{o}$C under nitrogen environment. Three stages of weight loss were observed for all samples. The initial weight loss can be observed at temperature below 100 $^{o}$C which is attributed to the loss of adsorbed water and water molecules that may have been trapped in the adsorbent matrix (Simões dos Reis et al., 2016). The second step of weight loss is observed in the temperature range of 260 to 400 °C due to the decomposition of cellulose and hemicellulose (Subhedar et al., 2018). The third weight loss was observed at 680-700 °C which is due to the phase transition from $Fe_3O_4$ to FeO (Mahdavi et al., 2013). The 2.1:3.1 g ($Fe^{2+}$: $Fe^{3+}$) sample was observed to be more stable than other samples, and the stability was shown to reduce with reduction in $Fe^{2+}$: $Fe^{3+}$ mass ratio. This may be due to the small amount of iron present in the sample as the $Fe^{2+}$: $Fe^{3+}$ mass ratio reduces and the larger amount of pine cone which dominated the sample.
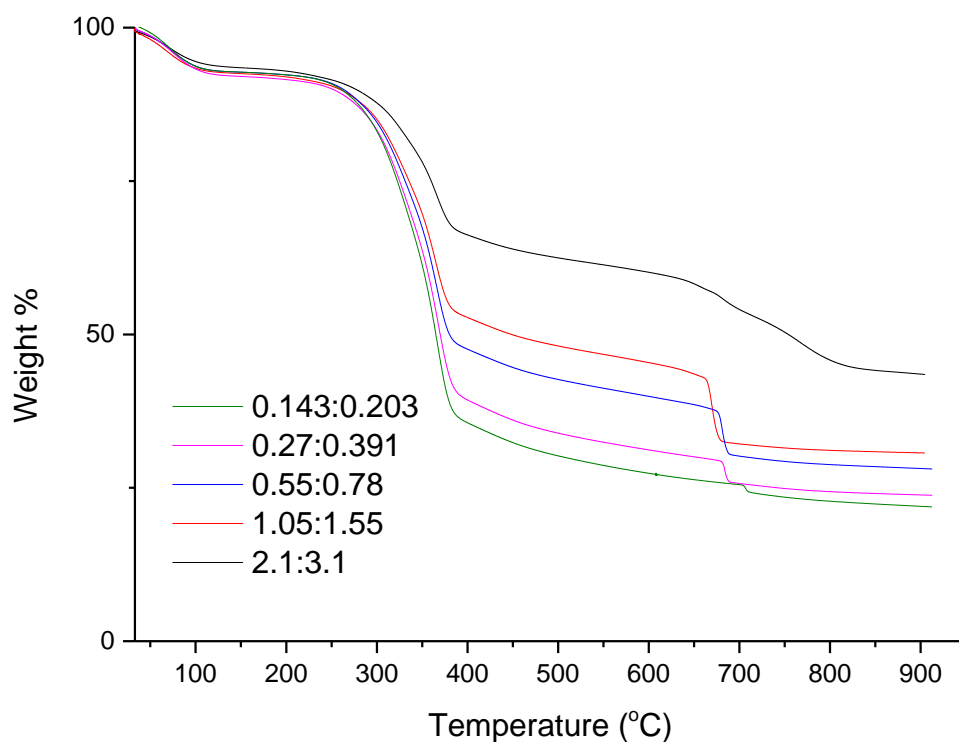
Figure 4.2: TGA curves of different $Fe^{2+}$: $Fe^{3+}$ mass ratio on the synthesis of NTP-NC bio-composite

*4.2.2.3   Vibrating Scanning Magnetometer (VSM)*

The magnetic property of the synthesized NTP-NC bio-composite with different mass of $Fe^{2+}$: $Fe^{3+}$ were investigated by VSM analysis at room temperature. All the samples have similar magnetization curve, therefore only the (2.1:3.1) $Fe^{2+}$: $Fe^{3+}$ sample is presented. The saturation magnetization of the NTP-NC bio-composite was observed to be 37.50 emu/g with coercivity value of 11.29 indicating superparamagnetic behavior (Lida et al., 2007).
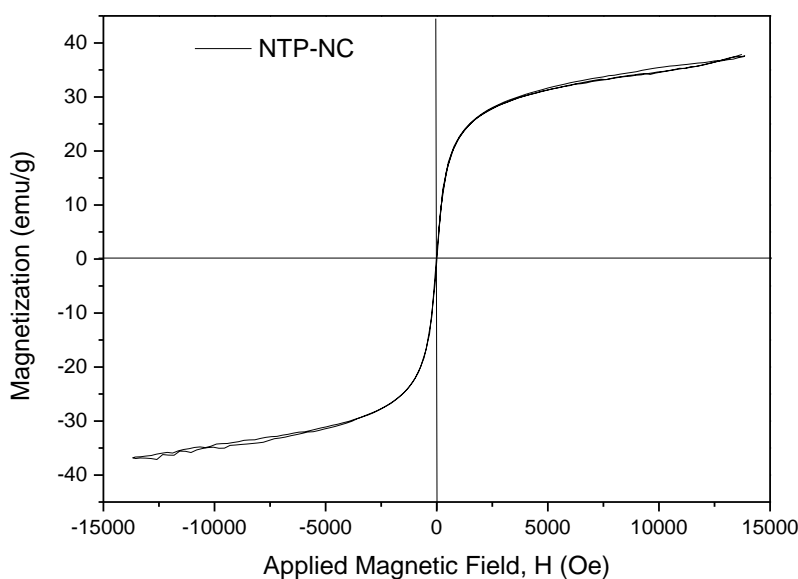
Figure 4.3: Magnetization curve of the magnetite bio-composite.

### 4.2.2.4 X-Ray Diffraction (XRD)

XRD patterns of 2:1 molar ratios of $Fe^{2+}$: $Fe^{3+}$ with different mass of Fe(II)/Fe(III) was conducted to determine the effect of varying the mass of $Fe^{2+}$: $Fe^{3+}$ while keeping pine cone mass constant on crystallinity of NTP-NC bio-composite. The XRD pattern of $Fe^{2+}$: $Fe^{3+}$ (2.1:3.1, 1.05:1.55, 0.55:0.78, 0.27:0.39, and 0.14:0.2) mass where plotted against magnetite peak in Fig.4.4a and maghemite peak in Fig.4.4b. From the Fig, all XRD patterns depicts iron oxide phases with five characteristic peaks at 30.09°, 35.42°, 43.05°, 56.94° and 62.51° corresponding to (220), (311), (400), (511) and (440) of magnetite crystalline structure (JCPDS Card no. 19-0629). The crystalline structure of cellulose I peak at 2 theta 22.84° due to the presence of pine cone was observed to appear as the mass of $Fe^{2+}$: $Fe^{3+}$ reduces from 0.55:0.78 and became visible at 0.14:0.2 mass ratio (Rehan et al., 2018). Generally, maghemite and magnetite have similar crystal structure and lattice spacing, hence it is not easy to distinguish their XRD pattern. The sample prepared by weighing 2.1:3.1 mass of $Fe^{2+}$: $Fe^{3+}$ was observed to match magnetite peak than all other samples which showed slight shift from all magnetite peaks. However, these samples (of mass ratio of 1.05:1.55, 0.55:0.78, 0.27:0.39, and 0.14:0.2) were observed to match the maghemite peak well indicating that the prepared sample may be a combination of magnetite and maghemite. The 2.1:3.1 mass ratio of $Fe^{2+}$: $Fe^{3+}$ sample was found to have a slight shift when compared to the maghemite peak.
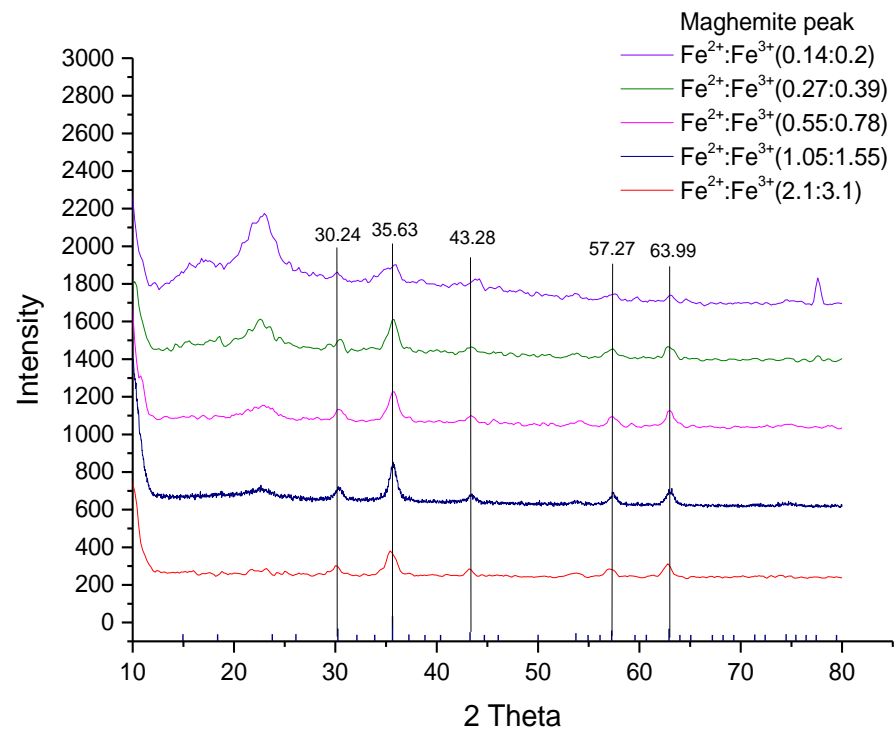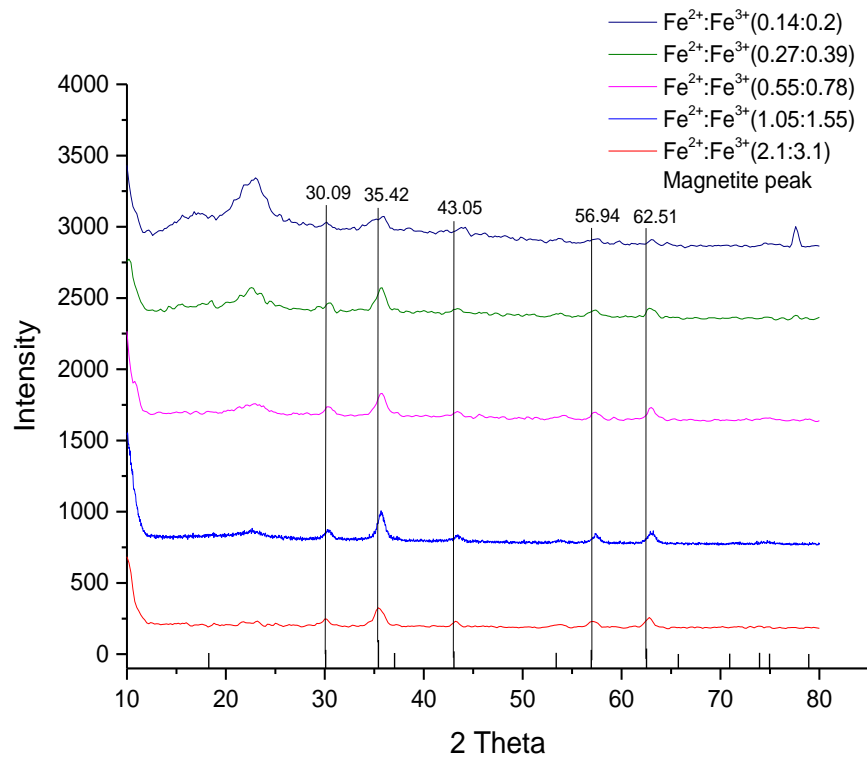
Figure 4.4: XRD pattern of NTP-NC bio-composite of 2:1 molar ratio of different mass of $Fe^{2+}$: $Fe^{3+}$ with (A) magnetite peak shown by solid bars (B) with maghemite peak shown by solid bars.

*4.2.2.5   Transmission Electron Microscopy (TEM)*

TEM analysis was performed to study the effect of varying $Fe^{2+}$: $Fe^{3+}$ mass ratio (2.1:3.1, 1.05:1.55, 0.55:0.78, 0.27:0.39, and 0.14:0.2) of 2:1 molar ratio on the morphology and particle size of the NTP-NC bio-composite. The TEM micrograph and histograms of the size distribution are given in Fig 4.5 (A-E) and Fig 4.6 (A-E), respectively. From Fig 4.5, the surface morphology of NTP-NC bio-composite of 2.1:3.1 g mass ratio of $Fe^{2+}$: $Fe^{3+}$ was seen to have spherical uniform morphology with a slight agglomeration which may be due to the magnetic interaction of nanoparticles. On reducing the mass of $Fe^{2+}$: $Fe^{3+}$ to 1.05:1.55 g and 0.55:0.78 g in Fig 4.5 B and C, respectively, particle size agglomeration increased with large uniform particles forming. On further reducing the mass of $Fe^{2+}$: $Fe^{3+}$ to 0.27:0.39 (Fig. 4.5 D) and 0.143:0.203 g (Fig 4.5 E), well dispersed larger spherical particles were observed. The histogram of the sample synthesized by 2.1:3.1 g of $Fe^{2+}$: $Fe^{3+}$ in Fig 4.6 a display a relatively narrow particle size distribution between 6-14 nm with an average particle size of 10.04 nm. Reduction in $Fe^{2+}$: $Fe^{3+}$ mass from 1.05:1.55g to 0.14:0.2 g resulted in broadening of particle size distribution leading to an increase in nanoparticle size from 10.49 to 12.68 nm.
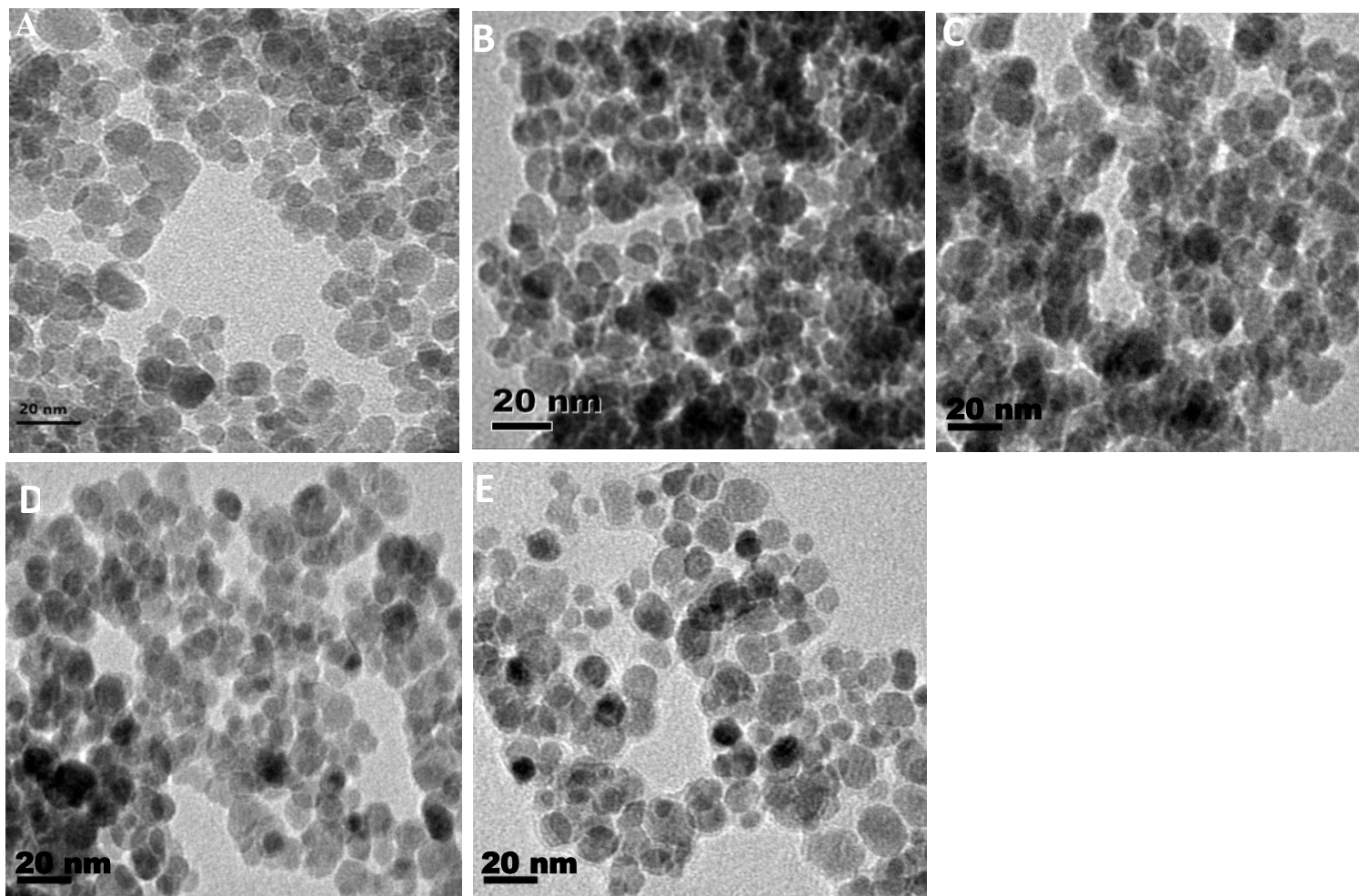
Figure 4.5: TEM images of NTP-NC bio-composite of different mass rations (A) 2.1:3.1, (B) 1.05:1.55, (C) 0.55:0.78, (D) 0.27:0.39, and (E) 0.14:0.2 of 2:1 molar ratio of $Fe^{2+}$: $Fe^{3+}$
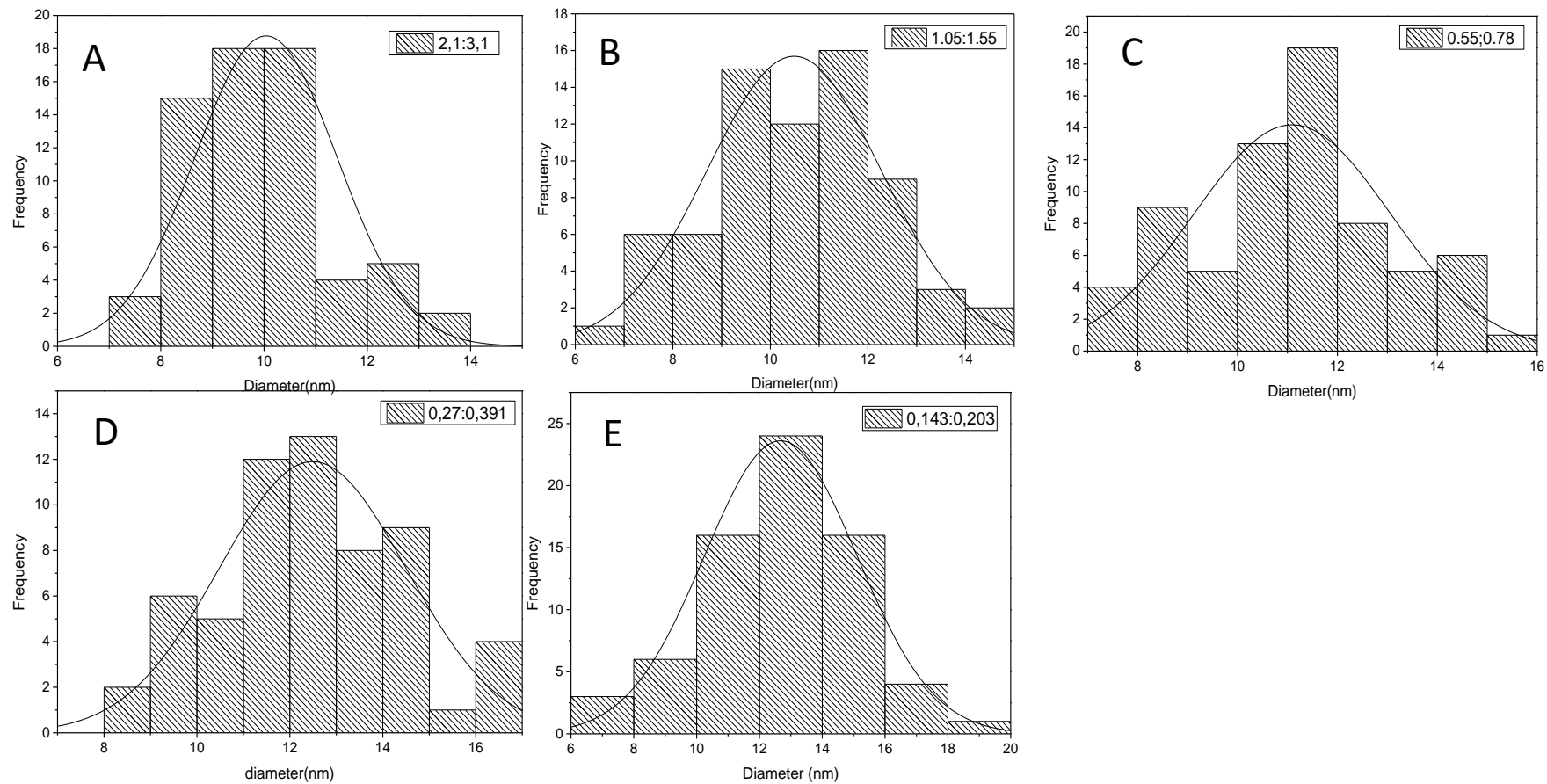
Figure 4.6: Size distribution of NTP-NC bio-composite of different mass ratio (A) 2.1:3.1, (B) 1.05:1.55, (C) 0.55:0.78, (D) 0.27:0.39, and (E) 0.14:0.2 of 2:1 molar ratio of $Fe^{2+}$: $Fe^{3+}$

### 4.2.3 Effect of pine mass on magnetite bio-composite synthesis

*4.2.3.1 Transmission Electron Microscopy (TEM)*

To improve magnetite agglomeration and examine the difference in particle size among NTP-NC samples synthesized by different pine cone mass, TEM analysis was conducted. Figs.4.7 A to F. show the TEM images of bare magnetite (MNP) and MNP immobilized on different pine cone (NTP) masses from 1.0 to 3.0 g. TEM of bare MNP Fig.4.7 A reveals the particles are spherical and slightly agglomerated. The TEM micrograph of MNP on 1.0 g NTP is shown in Fig.4.7 B, the micrograph shows that the magnetite nanoparticles are spherical in shape and are closely packed on the surface of the biomass support. As the mass of pine cone was increased to 1.5 g (Fig.4.7 C), the spherical magnetite particles became better dispersed on the NTP support. As the mass of NTP was increased from 2.0 to 2.5 and 3.0 g, agglomeration of magnetite nanoparticles increased and the NTP particles became visible in the TEM micrograph appearing as a separate phase (Fig.4.7 D to F).
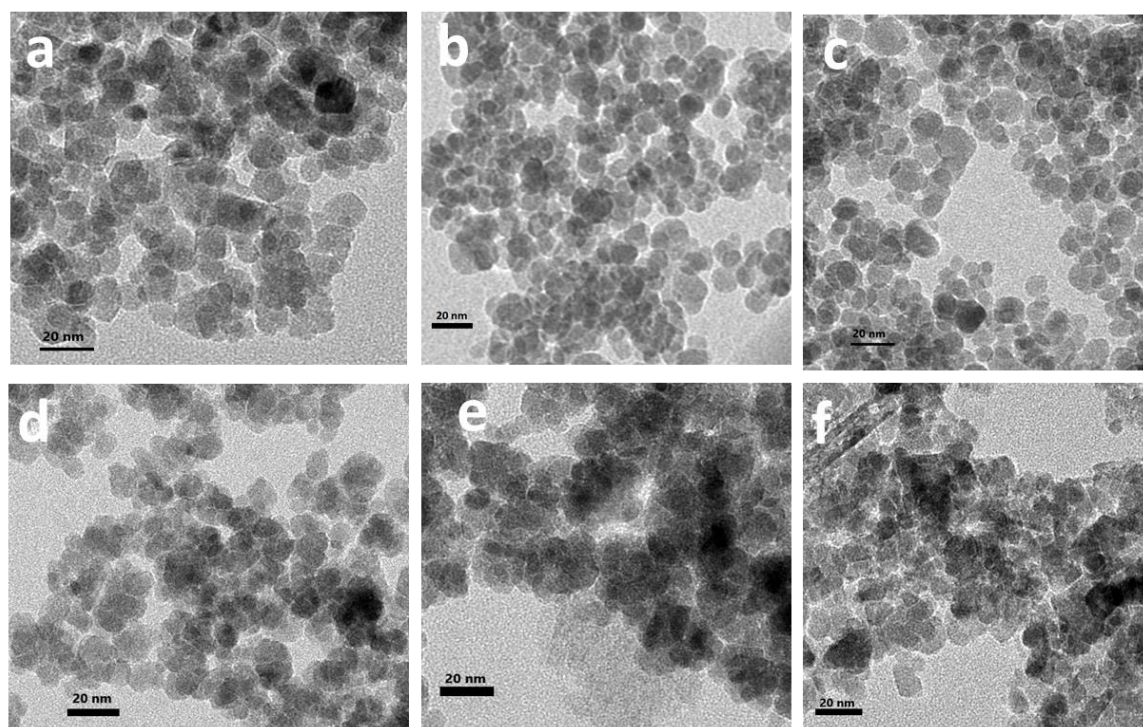


Figure 4.7: TEM images of (A) MNP, (B) MNP immobilized on 1.0 g PCP, (C) MNP immobilized on 1.5 g PCP, (D) MNP immobilized on 2.0 g PCP, (E) MNP immobilized on 2.5 g PCP, and (F) MNP immobilized on 3.0 g PCP.
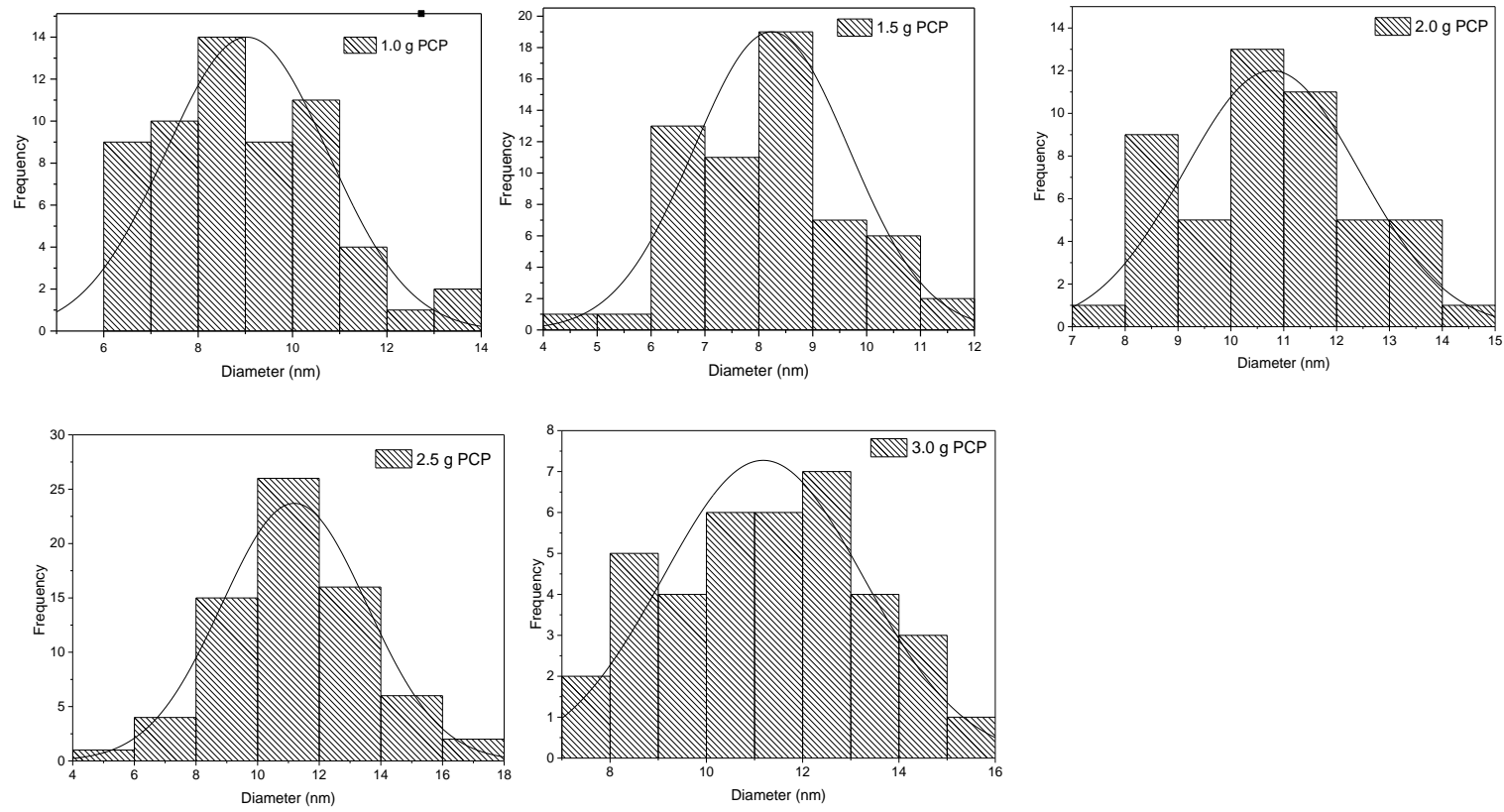
Figure 4.8: Size distribution of NTP-NC bio-composite for different pine cone mass.

The effect of the increased interaction between pine cone and the nanoparticles led to the smaller particle size (1.0 g pine: 9.03 nm and 1.5 g pine: 8.23 nm) and narrow size distribution in the 1.5 g samples as compared to the 1.0 g sample shown in Fig 4.8. The increase in mass of pine to 2.0, 2.5 and 3.0 g was observed to broaden the particle size distribution and increased the nanoparticle sizes from 10.77, 11.19 to 11.18 nm, respectively.

### 4.2.3.2   *Fourier Transformed Infra-Red (FTIR) analysis*

FTIR analysis of magnetite bio-composite (NTP-NC) with different pine cone masses were conducted to determine the effect of increasing pine mass on the functional groups present in the material, and the results are shown in Fig. 4.9. The spectra in Fig. 4.9 show peaks related to both NTP and NTP-NC. The spectra show similarity in the peaks for all samples but with variation in intensities of some peaks. Peaks at 3338 and 2881 cm$^{-1}$ are typical of hydrogen bond stretching of $\alpha$-cellulose and -CH$_3$, -CH$_2$-, groups cellulose (Santra and Sarkar, 2016). Peaks at 1633, 1598, and 1052 cm$^{-1}$ on the spectra can be attributed to C=O, C-O, C-O-C in lignin (Gupta and Nayak, 2012a). On the other hand, magnetite can be seen at FTIR peaks of 1027, 548 and 477 cm$^{-1}$ attributed to Fe-O and Fe-OH groups (Reza and Ahmaruzzaman, 2015a).

On comparing the FTIR spectra of different NTP mass, it was observed that the major differences were in the peaks at 1052, 1027, 548 and 477 cm$^{-1}$. It was observed that with 1.0 and 1.5 g of pine, the peaks at 1052 and 1027 cm$^{-1}$ attributed to C-O-C of lignin and Fe-O of magnetite were sharp and distinct. The difference between both peaks were the low intensity of the 1.5 g peak as compared to the 1.0 g of pine. It is known that iron oxides magnetic particles interact with oxygenated functional groups of biomaterials (Barbu et al., 2010). Therefore, an increase in the pine content increased the interaction between functional groups of pine cone and magnetite which resulted in the appearance of the C-O-C and Fe-O peaks and the Fe-OH peak at 477 cm$^{-1}$ in the FTIR spectrum. As the pine mass was increased to 2.0 g and above, the peaks at 1027 and 1052 cm$^{-1}$ became broadened and both peaks merged at 1052 cm$^{-1}$ while the peaks at 548 and 477 cm$^{-1}$ reduce in intensity.
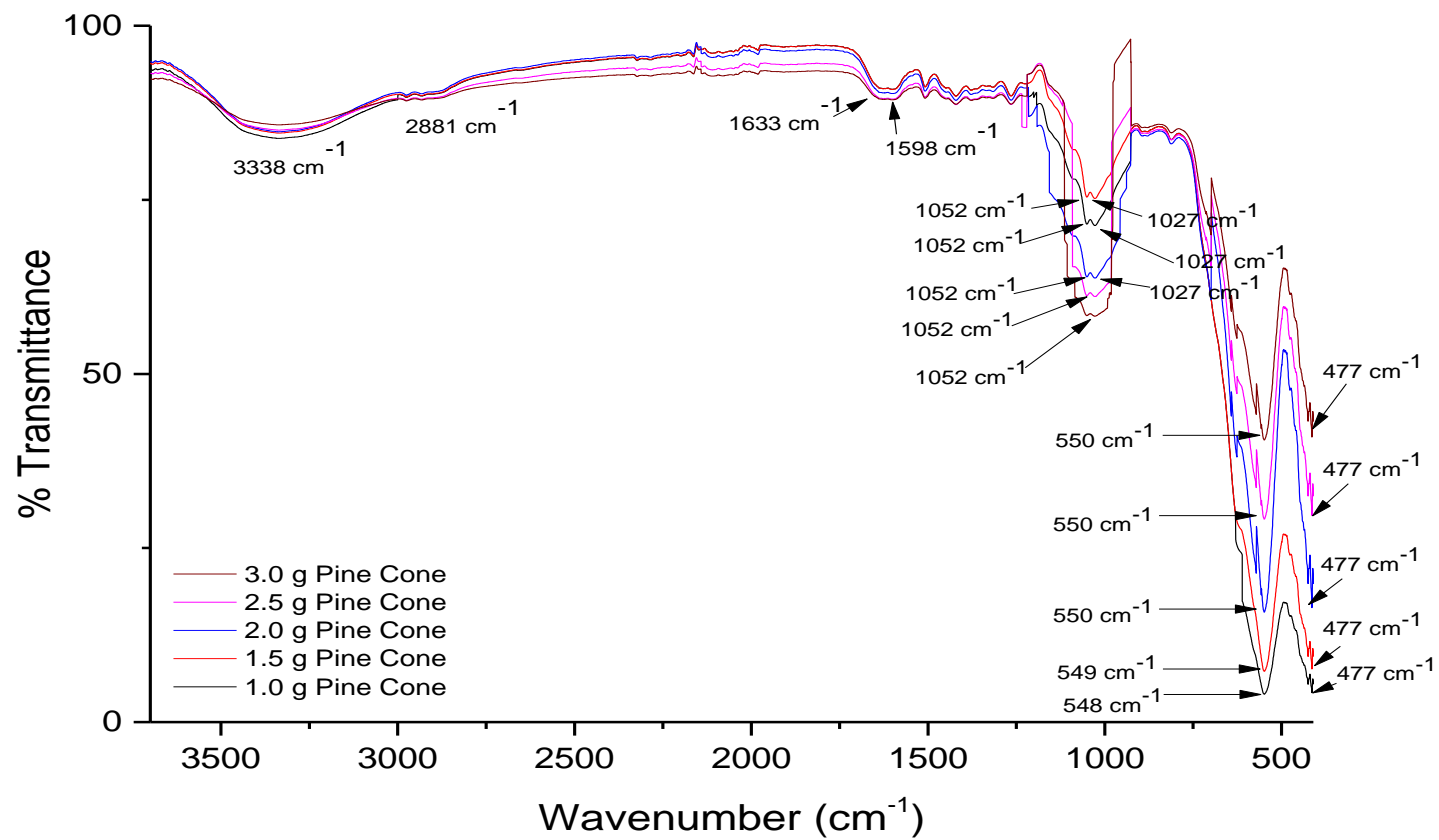
Figure 4.9: FTIR spectra of NTP-NC on the effect of pine mass

*4.2.3.3   Thermal Gravimetric Analysis (TGA)*

The TGA thermogram of magnetite immobilized on different masses of pine cone are shown in Fig. 4.10. The thermogram showing the decomposition of NTP-NC with different pine cone content perform in the temperature range of 26 to 700 °C. The results revealed that the degradation pattern for all samples were similar and some samples were more stable than others. The first region of weight loss of about 1.2, 1.9, 2.4, 2.7 and 3.1 % was observed between 26 and 100 °C for 1.0, 1.5, 2.0, 2.5 and 3.0 g of pine cone, respectively, which was attributed to loss of physical or chemical adsorbed water (Daneshfozoun et al., 2017). A second rapid weight loss in the temperature range of 260 to 400 °C indicating the decomposition of cellulose and hemicellulose was also observed (Subhedar et al., 2018). The percentage decomposition in the temperature range where 30.5, 27.6, 39.0, 41.1 and 42.3 % for magnetite immobilized on 1.0, 1.5, 2.0, 2.5 and 3.0 g of pine cone respectively.
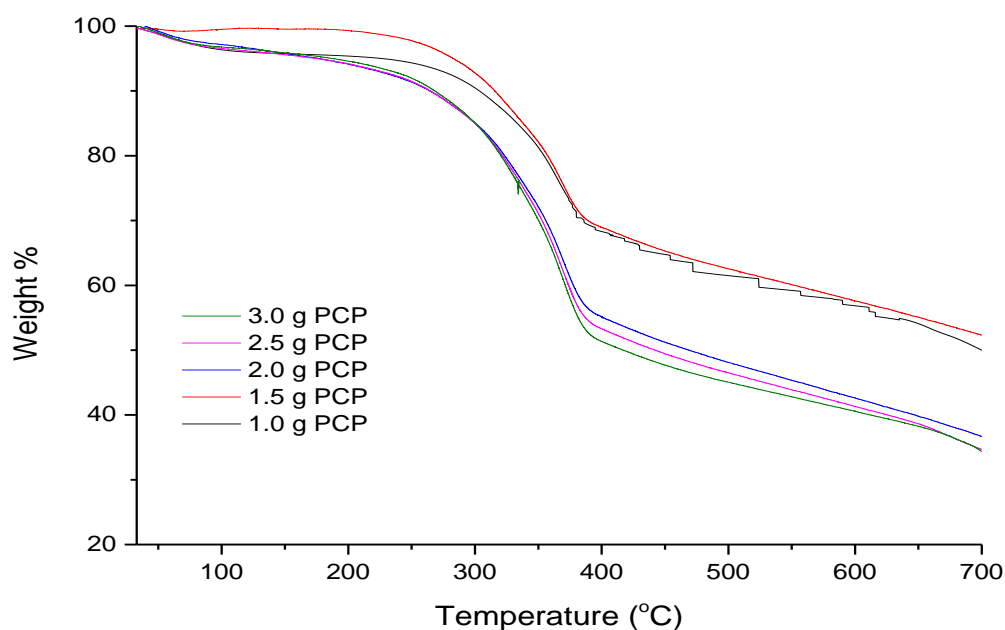


Figure 4.10: TGA analysis of the effect of pine mass on the magnetite bio-composite synthesis

The final stage of decomposition was observed at temperature range of 430 and 700 °C, which had lower weight losses and consisting of stable phenolic lignin residue (Esmeraldo et al., 2010). The variation in the decomposition pattern was therefore due to the magnetite-pine cone interaction (Zhu et al., 2010). The thermal stabilities of the samples with lower amounts of pine cone were observed to be higher than those with higher amounts of pine cone. Sample with 1.5 g of pine cone had better thermal stability than 1.0 g of pine cone

sample. The reason for this observation is attributed to the interaction between magnetite and pine cone. The 1.5 g pine cone sample gave a smaller size range and particle size as compared to other samples and therefore is expected to have better interaction.

### 4.2.3.4 Vibrating Scanning Magnetometer (VSM)

The NTP-NC composites produced were then tested for their magnetic properties using VSM analysis. The magnetic response of NTP-NC with various masses of pine (1.0, 1.5, 2.0, 2.5 and 3.0 g) were performed by measuring the applied field dependence of magnetization cycled between -15 and 15 kOe at room temperature. The values of saturation magnetization and coercivity read from the magnetization curve in Fig.4.4 are tabulated in table 4.1 below. The results show saturation magnetization of 34.34 for 1.0 g of pine cone and increased to 37.50 emu/g as pine cone mass increases to 1.5 g. As the NTP mass was increased above 1.5 g, there was a reduction in saturation magnetization down to 17.15 emu/g at NTP mass of 3.0 g. On the other hand, the coercivity was observed to decrease with decreasing particle size. The coercivity values reduced from 11.82 to 11.29 as mass of pine increased from 1.0 to 1.5 g and increase above 1.5 g. Immobilization of NTP-NC onto NTP was observed to reduce the saturation magnetism of magnetite. The increase in saturation magnetism reached its optimum value with 1.5 g of pine.
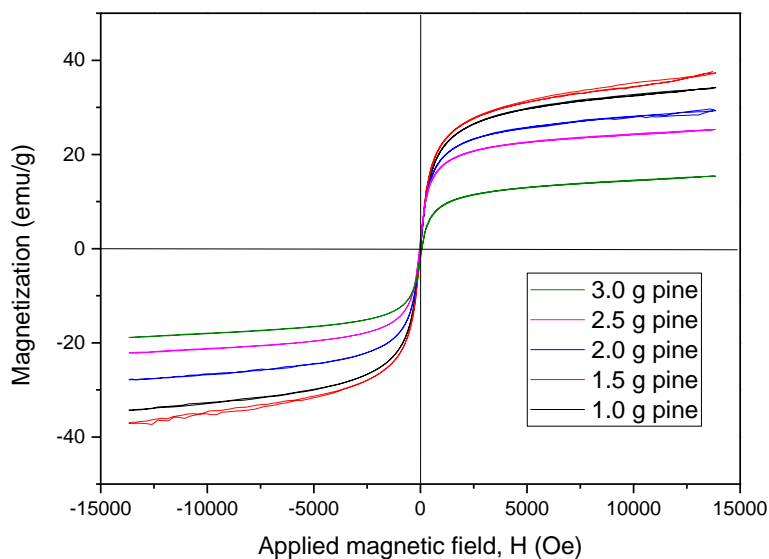


Figure 4.11: Magnetization curve of the effect of pine mass on the synthesis of magnetite bio-composite at room temperature.

Table 4.1: Adsorption capacities, Saturation magnetization and coercivity and particle size on the effect of pine cone mass on NTP-NC bio-composite synthesis.

| Sample | Cr(VI) Adsorption Capacity (mg/g) | As(III) Adsorption Capacity (mg/g) | Saturation magnetization (emu/g) | Coercivity (G) | Particle size (nm) |
|---|---|---|---|---|---|
| MNP on 1.0 g PCP | 38.2 | 8.33 | 34.24 | 11.82 | 9.03 |
| MNP on 1.5 g PCP | 38.7 | 13.86 | 37.50 | 11.29 | 8.23 |
| MNP on 2.0 g PCP | 34.0 | 10.48 | 28.76 | 12.72 | 10.77 |
| MNP on 2.5 g PCP | 32.3 | 8.54 | 23.75 | 12.98 | 11.19 |
| MNP on 3.0 g PCP | 32.0 | 8.48 | 17.15 | 13.16 | 11.18 |

*4.2.3.5   As(III) and Cr(VI) adsorption studies*

Finally, the NTP-NC composites produced were tested for their ability to remove As(III) and Cr(VI) from aqueous solution. It was observed that the As(III) capacity of the sample with 1.0 g pine was 8.33 mg/g while Cr(VI) capacity was 38.2 mg/g. As the mass of pine cone in the composite was increased to 1.5 g, As(III) and Cr(VI) adsorption reached maximum values at 13.86 mg/g and 38.7 mg/g, respectively. Further increase in pine mass led to reduction in As(III) capacity to 8.48 mg/g and Cr(VI) capacity to 32.0 mg/g when 3.0 g of pine cone was added. The results of these experiments suggest that both Cr(VI) and As(III) adsorption capacity can be related to the particle size of the nano-biocomposite produced. The smaller the sizes of the particles, the higher the surface available for adsorption and the higher the charge density of the adsorbent material. Shen et al. (Shen et al., 2009a) also observed an increase in the amounts of Ni(II), Cu(II), Cd(II) and Cr(VI) adsorbed with decreasing particles size of $Fe_3O_4$ nanoparticles produced.

## 4.3 FURTHER CHARACTERIZATION OF THE OPTIMUM NANO-BIO COMPOSITE MATERIAL

### 4.3.1 Scanning Electron Microscopy- Energy Dispersive X-ray spectroscopy (SEM-EDX)

Scanning electron microscopy has been a primary tool for characterizing the surface morphology and fundamental physical properties of the adsorbent surface. The surface morphology of the NTP and NTP-NC samples are shown in Figs.4.12 A and B. From Fig.4.12 A, pine cone surface can be seen to be rough with considerable number of large pores which provide access and large surface area for adsorption of pollutants. The morphology of NTP-NC in Fig.4.12 B revealed that the particles are also spherical in shape. It was observed that the particles exist in the same phase suggesting that the pine cone particles are coated with nano-$Fe_3O_4$. The EDX images (Fig.4.12 C and D) reveals that the NTP consist of carbon and oxygen as the main constituents while NTP-NC consists of carbon, oxygen and iron. Gold and palladium detected in the NTP sample were from the gold/palladium coating of the sample prior to analysis.
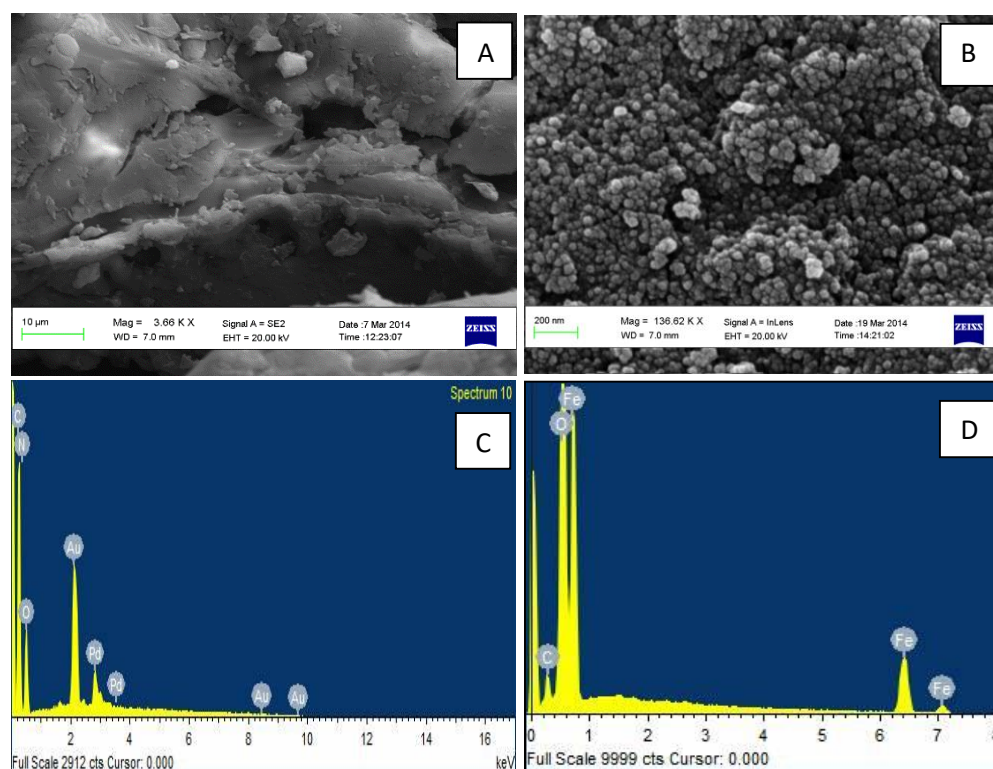


Figure 4.12: SEM images of (A) Pine cone, (B) magnetite bio-composite, EDX of (C) Pine cone and (D) magnetite bio-composite.

## 4.3.2  Elemental mapping

The dispersion of Fe, O and C on both NTP and NTP-NC is shown in Figs.4.13 A–E. Figs.4.13 A and B shows the distribution of C on the NTP and NTP-NC surfaces. The pictures show that the surface of carbon on NTP-NC (purple colour) was not as clear as that of NTP, indicating an introduction of another element on the surface. Figs.4.13 C and D shows the distribution of O atoms on the NTP and NTP-NC surface (green colour). The increased intensity and the wider dispersion of the green colour on the NTP-NC as compared to the NTP sample suggests the presence of a well dispersed oxide immobilized on the surface of NTP-NC. The picture in Fig.4.13 E present the distribution of Fe on the surface of NTP-NC. It can be observed that the Fe atoms are well distributed over the NTP-NC surface suggesting that both materials are compactible and do not exist as two separate phases. The distribution of the Fe atoms was similar to the O atoms as seen in Fig.4.13 D, this suggests that the Fe atoms are associated with the O atoms and the compound is likely iron oxide.
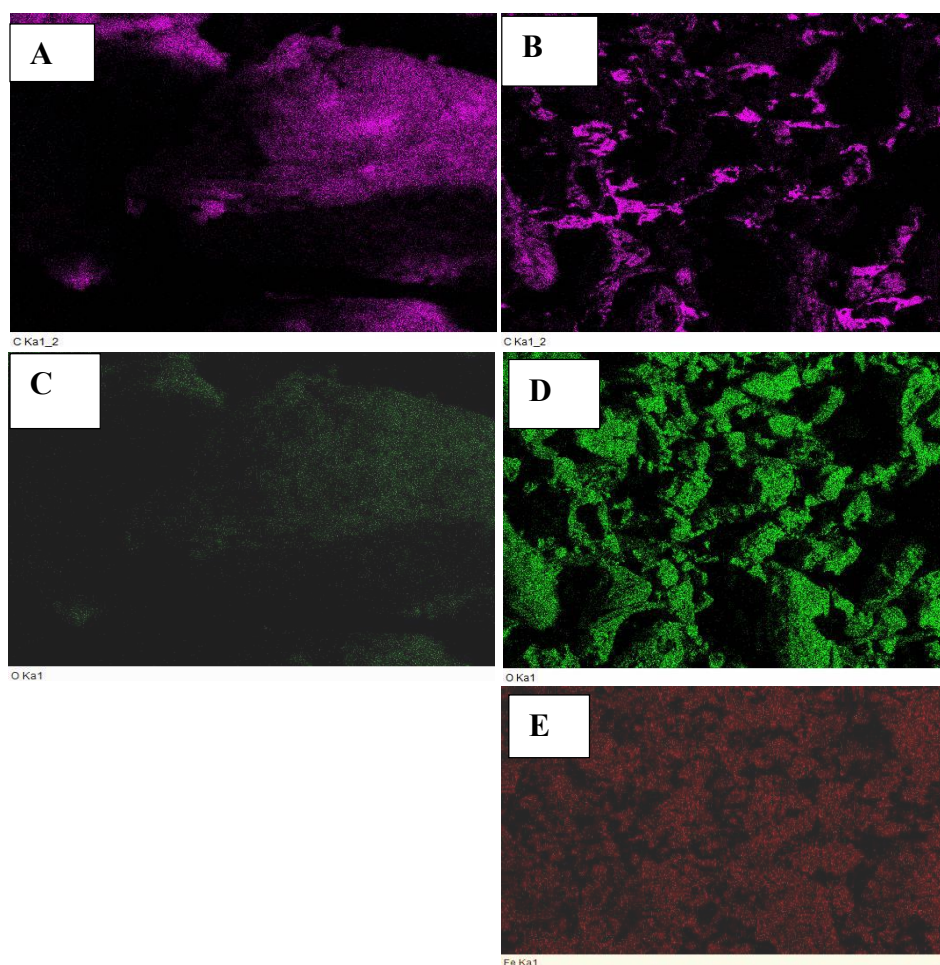


Figure 4.13: Elemental mapping of distribution of carbon in (A) NTP and (B) NTP-NC, distribution of O in (C) NTP and (D) NTP-NC and (E) distribution of Fe in NTP-NC.

### 4.3.3 Thermal gravimetric Analysis (TGA)

TGA analysis was conducted to determine the thermal stability and the decomposition profile of the NaOH treated pine cone, magnetite and nano bio-composite as a function of temperature. The TGA analysis were performed under nitrogen atmosphere to minimize the mass increase which may be caused by the oxidation of ferrous ions and the results are recorded in Fig. 4.12 A. The NTP curve shows two weight loss processes. The initial weight loss can be observed at temperature below 100 ºC which is attributed to the loss of water. The second weight loss was observed at 220 ºC which is due to the decomposition cellulose and hemicellulose materials on the pine cone biomass. The NTP-NC bio-composite shows four weight loss processes. The first weight loss is due to loss of moisture, the second weight loss was observed to be attributed to the decomposition of the cellulose and hemicellulose from the pine cone biomass. The third weight loss at 670 °C has been attributed to the phase transition from $Fe_3O_4$ to FeO, and the last weight loss was observed at around 786 because of the deoxidation of FeO since the TGA/DTA analysis was achieved under the nitrogen atmosphere (Zhao et al., 2006). It can be seen that pine cone has the lowest thermal stability and pure magnetite was seen to be more thermally stable. Incorporating pine cone onto magnetite nanoparticle enhanced the nano bio-composite thermal stability.

The derivative weight % versus temperature curves for NTP, magnetite and NTP-NC are shown in Fig.4.14 B. The NaOH treated pine cone curve indicates a single decomposition peaks between 300-350 ºC, which is due to the hemicelluloses and lignin degradation (Wan et al., 2011). Four derivative peaks are observed in the DTA curve of nano bio-composite which related to the four mass losses in the TGA curve. The peak at 350 ºC on the nano bio-composite, is due to the decomposition of cellulose and hemicellulose in the TGA curve from pine cone biomass, confirms the strong binding between pine cone molecules and magnetite. The two peaks around 670 and 780 ºC confirm the phase transition from $Fe_3O_4$ to FeO.
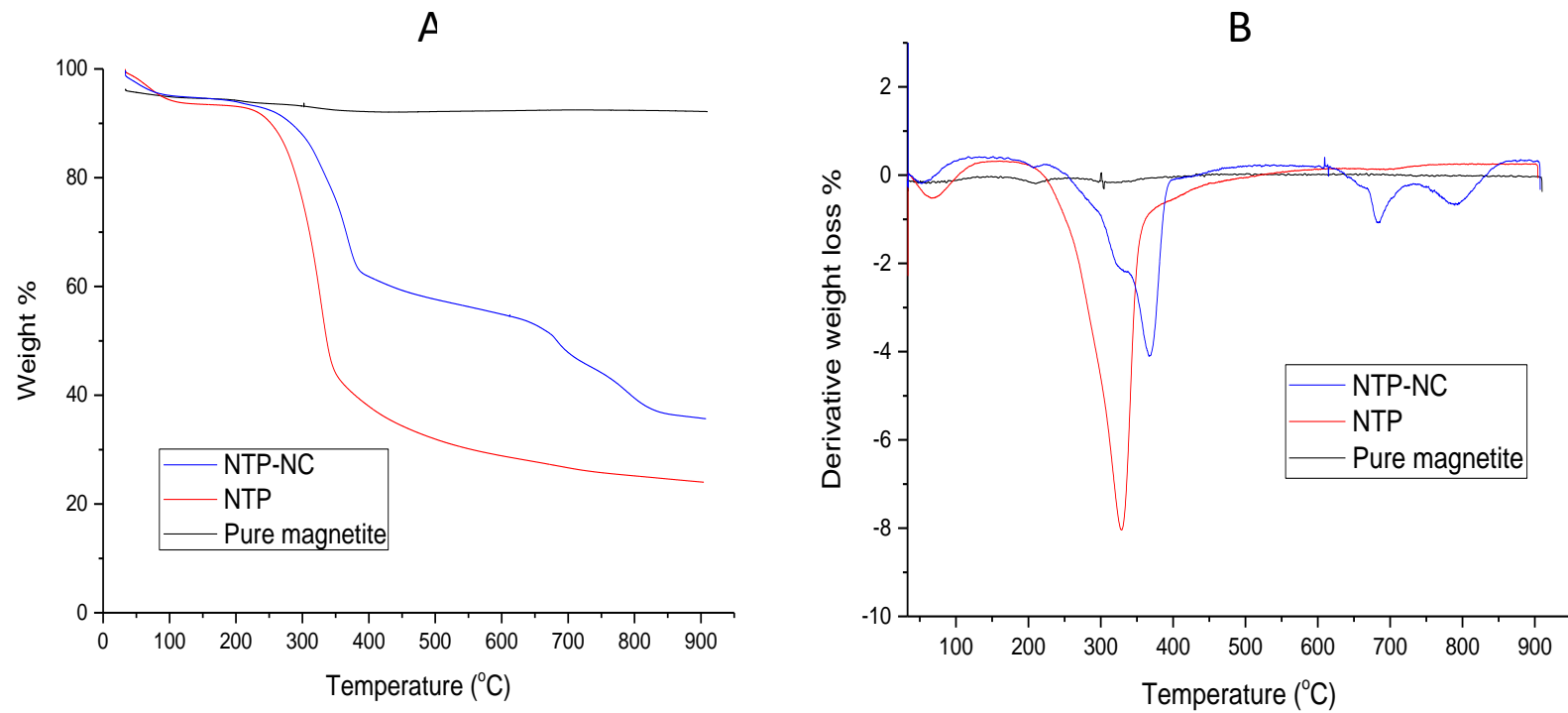
Figure 4.14: (A) TGA and (B) DTA curves of NaOH treated pine cone, magnetite and magnetic bio-composite nanoparticles.

### 4.3.4  X-ray Photoelectron Spectroscopy (XPS) analysis

X-ray photoelectron spectroscopy (XPS) is a versatile surface analysis technique that can be used to analyse elements composition and chemical state of elements present on the NaOH treated pine cone (NTP) and nano bio-composite magnetite pine cone (NTP-NC) and the full range is shown in Fig.4.15a. The XPS survey spectrum of NTP indicated the presence of oxygen and carbon. The spectrum consists of two major peaks at 282 and 530 eV, corresponding to C 1s and O 1s, respectively. The spectrum for NTP-NC shows three peaks at 284, 530 and 710 eV corresponding to C 1s, O 1s and Fe 2p photoemissions. The C 1s and O 1s spectra of NTP are shown in Fig.4.15b and c. The C 1s spectrum can be curve-fitted into three components with binding energies of 282.6, 284.3, and 285.9, eV, attributed to the carbon atoms in the form of C-C (aromatic) and C-O alcoholic hydroxyl and ether (Zheng et al., 2009). The O 1s peak shows that the broad peak at 530.5 eV, attributed to the C-O group of alcoholic hydroxyl and ether can be fitted to two sub peaks at 529.1eV attributed to the (C=O functional group) (Zheng et al., 2009) and 531.7 eV attributed to the C=O bonds (Toupin and Bélanger, 2008). These peaks are characteristic peaks of lignin, cellulose and hemicellulose confirming that pine cone is made up of different functional groups.

The C 1s, O 1s and Fe 2p spectra for NTP-NC are shown in Fig.4.15d-f. The C1s peak can be curve-fitted into three components with binding energy of 283.2, 285.15 and 286.4 eV, attributed to the carbon atoms in the forms of C-C (aromatic) and C-O (carbonyl) (Zheng et al., 2009). The O 1s XPS spectrum for NTP-NC presented in Fig.4.15e can be curve fitted into three peaks with binding energies of 530, 531.5 and 532.7 eV. The sharpest peak is the peak at 530 eV resulting from lattice oxygen in $Fe_3O_4$ while the peak at 532.7 eV is associated with OH of water on the surface (Önsten et al., 2010). The O 1s peaks were found to have shifted to a higher binding energy after incorporating magnetite with NaOH pine cone. The shift in the binding energy when magnetite is incorporated onto NTP may be due to the interaction between the $Fe_3O_4$ particles and oxygenated groups of lignin thus reducing its electron density. Pratt et al. (1994) reported that $O^{2-}$ oxygen shift to higher binding energies when $OH^-$ is structurally incorporated into ferric oxide. The authors suggested that interaction between the proton on the hydroxyl oxygen and the oxide oxygen produces the binding energy shift to higher binding energies.
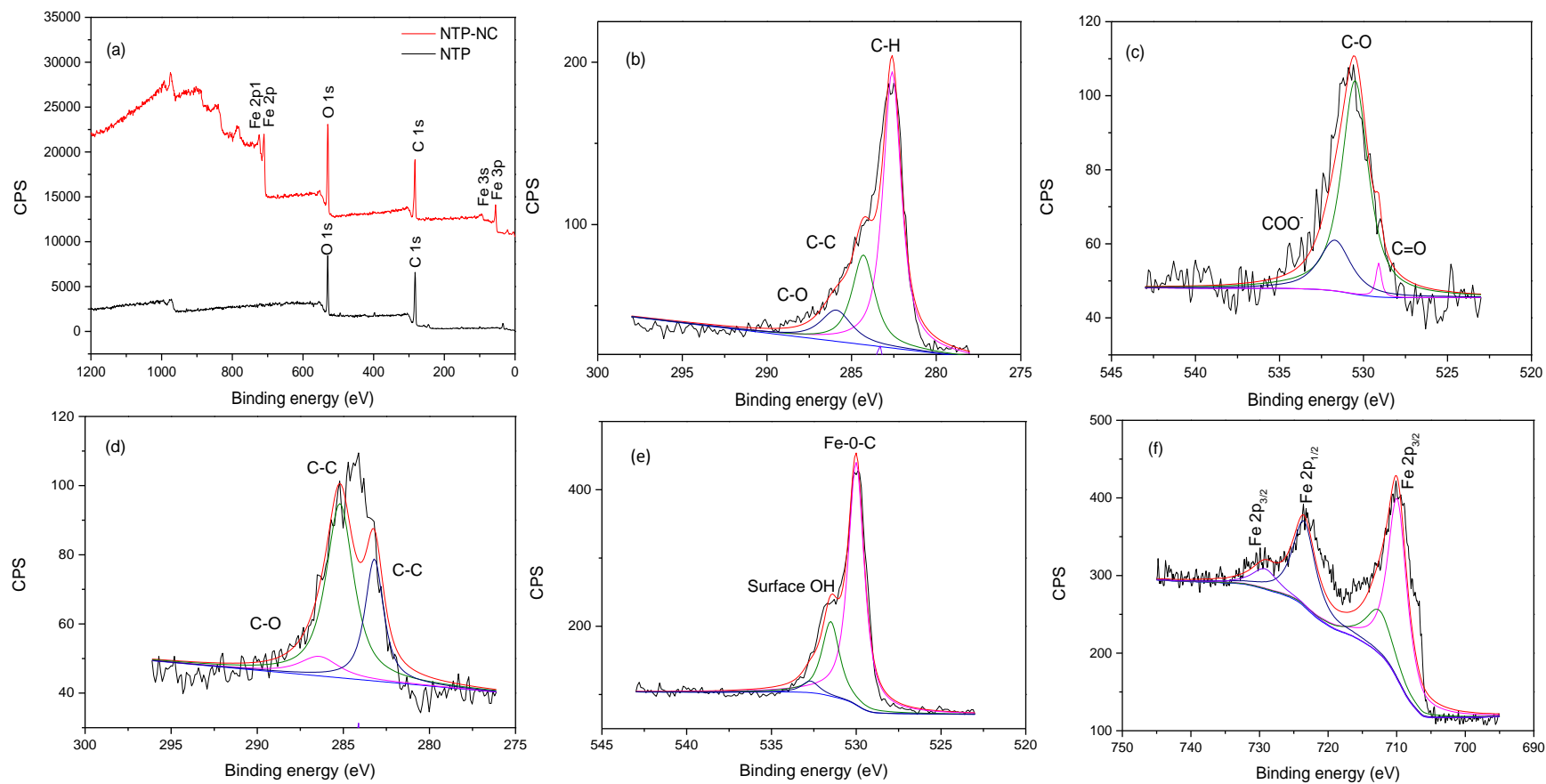
Figure 4.15: (a) Full XPS spectra of NTP and NTP-NC, (b) NTP C 1s, (c) NTP O 1s, (d) NTP-NC C 1s, (e) NTP-NC O 1s, (f) NTP-NC Fe 2p

Fig.4.15 f shows Fe 2p spectrum which shows three peaks at binding energy of 709.9, 723.5, and 729.2 eV corresponding to Fe $2p_{3/2}$, Fe $2p_{1/2}$ and Fe $2p_{3/2}$, respectively, which can be attributed to magnetite. The presence of Fe 2p peak confirm the incorporation of magnetite and NaOH treated pine cone. Furthermore the % atomic concentration of Fe (II) and Fe (III) are 74.2104 % and 25.789 %, respectively.

### 4.3.5 pH at point zero charge (pH$_{pzc}$)

pH at point zero charge (pH$_{pzc}$) is the point where the net charge of the adsorbent material is zero. pH$_{pzc}$ of the NTP and NTP-NC bio-composite was determined by solid addition method and the results are given in Fig 4.16. The pH$_{pzc}$ of NTP was observed to be 5.69 while that of NTP-NC was found to be 5.86. The pH$_{pzc}$ values of NTP and NTP-NC reveal that the adsorbents surface carry net positive charge below pH$_{pzc}$, and it is positively charged above the pH$_{pzc}$.
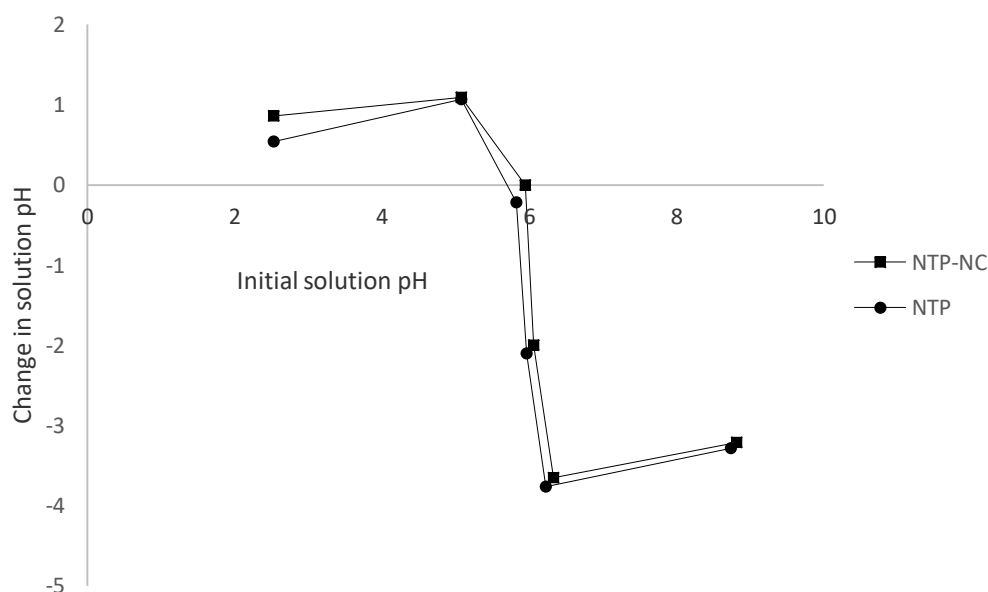


Figure 4.16: pH$_{pzc}$ graph of NaOH treated pine cone and magnetite bio-composite.

### 4.3.6 Vibrating Scanning Magnetometer (VSM)

To further understand the magnetic properties of magnetite, NaOH treated pine cone (NTP), and optimum nano-biocomposite (NTP-NC), magnetization measurements were performed by measuring the applied field dependence of magnetization cycled between 15 and 15 kOe at room temperature. The value of saturation magnetization of pure magnetite was observed to be 64.66 emu/g which is slightly lower than the value reported for bulk $Fe_3O_4$ (92 emu/g) (Mürbe et al., 2008). The decrease in saturation magnetization observed with the pure magnetite samples synthesized have been reported to be due to the effect of the increased thermal fluctuation near the surface of $Fe_3O_4$ nanoparticles or that of the magnetically disordered surface formed resulting in the large surface-to-volume ratio associated with the fine particle size (Goya et al., 2003, Kim et al., 2001, Lin et al., 2006). The magnetization curve of pure magnetite, NaOH treated pine cone and nano bio-composite samples are shown in Fig.4.15. The magnetic hysteresis loop of pure magnetite and nano bio-composite materials indicates no remanence and reveals its superparamagnetic nature.
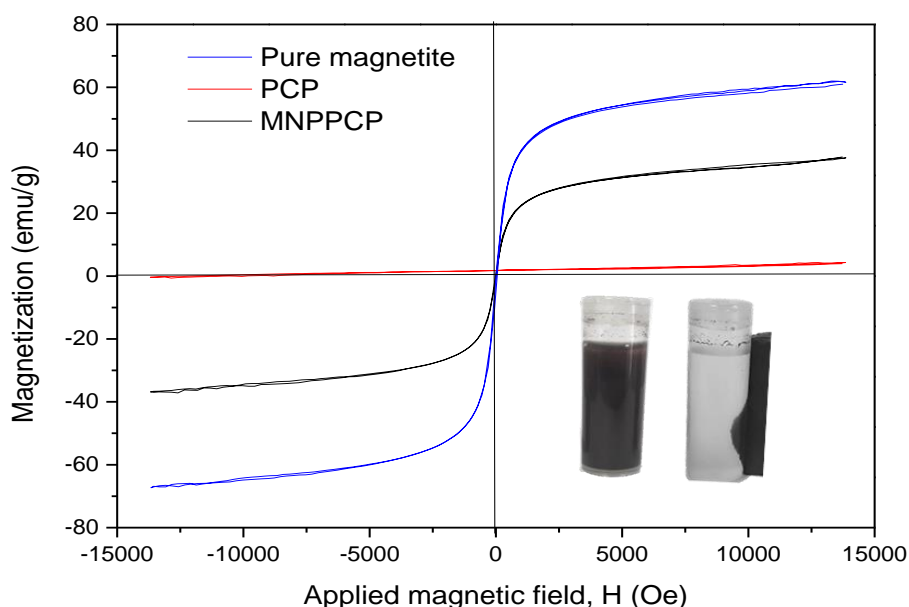


Figure 4.17: Magnetization curve of pure magnetite, NaOH treated pine cone and magnetite coated pine bio-composite sample.

The optimum nano bio-composite have the saturation magnetization of 37.50 emu/g. The saturation magnetization was observed to reduce from 64.66 emu/g to 37.50 emu/g and coercivity reduced from 24.92 G to 10.64 G, when pine cone biomass reacted with magnetite. Low coercivity shows that nano bio-composite is superparamagnetic. The reduction in saturation magnetization may be due to the interaction of organics from the pine cone with iron oxide and the reduced primary size of the magnetite material. NaOH treated pine cone was observed to have a paramagnetic nature with saturation magnetization of 2.47 emu/g and coercivity of 66.14 G, implying the material can only exist with an applied magnetic field and do not retain permanent magnetization without an applied magnetic field

### 4.3.7    Surface area

Adsorption-desorption isotherms using $N_2$ and corresponding pore-size distribution curves of NTP and NTP-NC are shown in Fig.4.18 a and b and the surface properties are presented in Table 4.2. From Table 4.2, the BET surface area for pure MNP, NTP-NC and NTP were 113.60, 54.80 and 2.25 $m^2$/g. The pore volume and pore size were found to be 0.6231, 0.1522 and 0.0177 $cm^3$/g and 25.86, 23.10 and 10.17 nm respectively. As seen from the results, NTP had very low surface area and pore volume which is typical of most lignocellulosic materials (Huang et al., 2015). The higher surface area of NTP-NC over NTP can be attributed to the smaller size of NTP-NC in the composite. According to the classification of IUPAC, the isotherms for MNP, NTP and NTP-NC were Type IV as indicated by the hysteresis loop at $P/P_0 = 0.72 – 0.99$ for MNP, $P/P_0 = 0.34 – 0.99$ for NTP and $P/P_0 = 0.35 – 0.99$ for NTP-NC, respectively (Sing et al., 1985). The presence of hysteresis loops at high relative pressure is indicative of the formation of multilayer adsorption with a solid mesopore structure (Jaramillo et al., 2010). The hysteresis loop exhibited by three samples were observed to be different, indicating significant changes in the pore structures in the formation of the composite. The characteristic feature of the isotherm for MNP was H1 hysteresis loop which describes agglomerated spherically shaped nanoparticles organised in a uniform manner with cylindrical pore geometry exhibiting high pore size uniformity (Sing et al., 1985). It was also observed that MNP exhibits an additional small hysteresis loop at $P/P_0 = 0.15–0.65$ which attributed to mesoporosity confined in the framework of the material (Tzvetkov et al., 2017).
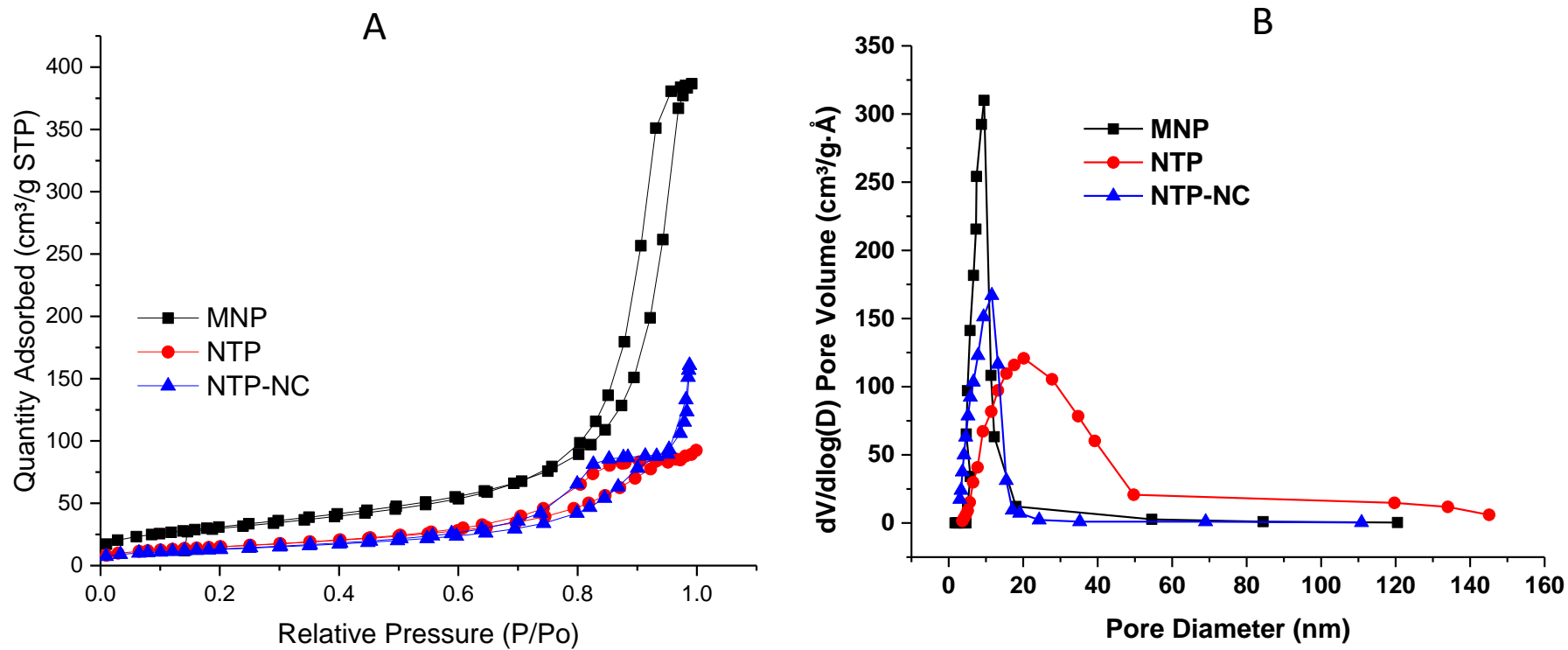
Figure 4.18: (A) Nitrogen adsorption isotherms and (B) Pore size distribution of pure magnetite, NaOH treated pine cone and magnetite coated pine cone bio-composite.

For NTP and NTP-NC, the characteristic feature of the isotherm was H3 hysteresis loop which describes narrow slit-like pores, particles with internal voids of irregular shape and broad size distribution (Sing et al., 1985). The particle size diameter curve of MNP, NTP and NTP-NC is shown in Fig.4.18 b. The results show that the pore diameters of MNP and NTP were 9.38 and 20.08 nm while the composite (NTP-NC) had particle size diameter at 11.40 nm.

Table 4.2: Surface properties of adsorbents

| Properties | Pure MNP | NTP | NTP-NC |
|---|---|---|---|
| Surface area ($m^2/g$) | 113.60 | 2.25 | 54.80 |
| Pore volume ($cm^3/g$) | 0.6321 | 0.0177 | 0.1522 |
| Ave. pore width (nm) | 25.86 | 10.17 | 23.10 |

## 4.4  CONCLUSION

Magnetite-coated pine cone bio-composite was successfully synthesized by co-precipitation method using $Fe^{3+}$: $Fe^{2+}$ salt by maintaining 2:1 molar ratio under alkaline condition at inert environment. The amount of $Fe^{2+}$: $Fe^{3+}$ mass ratio and pine cone dose were successfully optimised and characterized using different analytical tools. FTIR, XRD and TGA analysis confirmed surface coating of magnetite by pine cone. XRD pattern indicated that the magnetite coated pine cone bio-composite was formed and coating with pine cone did not change the $Fe_3O_4$ phase. Spherically shaped magnetite nanoparticles were packed on the surface of pine cone mass. Nanoparticles became better dispersed with increasing pine cone mass from 1 to 1.5 g and agglomeration occurred when pine cone mass was increased to 2 g and more. Nanoparticle size was observed to reduce with pine cone mass from 1 to 1.5 and broadened as pine cone mass was further increased from 2 to 3 g, and increased with a reduction in the amount of $Fe^{2+}$: $Fe^{3+}$ mass ratio. Magnetic nanoparticles of average particle size of 8.1 nm were observed when 1.5 g of pine and 2:1 mass ratio of $Fe^{3+}$: $Fe^{2+}$ was applied. VSM results showed that magnetite coated pine cone exhibit superparamagnetic behaviour and responded well to an externally applied magnetic field which increased its separation from aqueous solution. The presence of Fe 2p peak on the XPS spectra of magnetite coated pine cone confirmed the incorporation of magnetite and NaOH treated pine cone. Higher Cr(VI) and As(III) adsorption of 13.86 and 38.7 mg/g were observed at 1.5 g of pine cone and 2:1 $Fe^{3+}$: $Fe^{2+}$ mass ratio, respectively.

## 4.5 REFERENCE

ACISLI, O., KHATAEE, A., KARACA, S., KARIMI, A. & DOGAN, E. 2017. Combination of ultrasonic and fenton processes in the presence of magnetite nanostructures prepared by high energy planetary ball mill *Ultrason Sonochemistry,* 34**,** 754-762.

BARBU, M., STOIA, M., STEFANESCU, O. & STEFANESCU, M. 2010. Thermal and FT-IR studies on the interaction between $Cr(NO_3)_3.9H_2O$ and some diols. *Chem. Bull. "Polltehnica" Uni. (Timisoara),* 55**,** 180-185.

CHEN, J., WANG, Y. G., LI, Z. Q., WANG, C., LI, J. F. & GU, Y. J. Synthesis and characterization of magnetic nanocomposites with $Fe_3O_4$ core. Journal of Physics: Conference Series, 2009. IOP Publishing, 012-041.

DANESHFOZOUN, S., ABDULLAH, M. A. & ABDULLAH, B. 2017. Preparation and characterization of magnetic biosorbent based on oil palm empty fruit bunch fibers, cellulose and Ceiba pentandra for heavy metal ions removal. *Industrial Crops & Products,* 105**,** 93-103.

ESMERALDO, M. A., BARRETO, A. C. H., FREITAS, J. E. B., FECHINE, P. B. A., SOMBRA, A. S. B., CORRADINI, E., MELE, G., MAFFEZZOLI, A. & MAZZETTO, S. E. 2010. Dwarf-green coconut fibers: a versatile natural renewable raw bioresource. Treatment, morphology, and physicochemical properties. *BioResources,* 5**,** 2478-2501.

FERNÁNDEZ, M., VILLALONGA, M. L., FRAGOSO, A., CAOB, B. N., M & VILLALONGA, R. 2004. α-Chymotrypsin stabilization by chemical conjugation with O-carboxymethyl- poly-cyclodextrin. *Process Biochemistry,* 39**,** 535-539.

GOYA, G., BERQUO, T., FONSECA, F. & MORALES, M. 2003. Static and dynamic magnetic properties of spherical magnetite nanoparticles. *Journal of Applied Physics,* 94**,** 3520-3528.

GUPTA, V. & NAYAK, A. 2012. Cadmium removal and recovery from aqueous solutions by novel adsorbents prepared from orange peel and Fe2O3 nanoparticles. *Chemical Engineering Journal,* 180**,** 81-90.

JARAMILLO, J., ALVAREZ, P. M. & GOMEZ-SERRANO, V. 2010. Oxidation of activated carbon by dry and wet methods: Surface chemistry and textural modifications. *Fuel Processing Technology,* 91**,** 1768-1775.

KIM, D., ZHANG, Y., VOIT, W., RAO, K. & MUHAMMED, M. 2001. Synthesis and characterization of surfactant-coated superparamagnetic monodispersed iron oxide nanoparticles. *Journal of Magnetism and Magnetic Materials,* 225**,** 30-36.

LIDA, H., TAKAYANAGI, K., NAKANISHI, T. & OSAKA, T. 2007. Synthesis of Fe3O4 nanoparticles with various sizes and magnetic properties by controlled hydrolysis. *Journal of Colloid and Interface Science* 314, 274-280.

LIN, C.-R., CHU, Y.-M. & WANG, S.-C. 2006. Magnetic properties of magnetite nanoparticles prepared by mechanochemical reaction. *Materials Letters,* 60, 447-450.

MAHDAVI, M., AHMAD, M., HARON, M. J., NAMVAR, F., NADI, B., RAHMAN, M. Z. & AMIN, J. 2013. Synthesis, Surface Modification and Characterisation of Biocompatible Magnetic Iron Oxide Nanoparticles for Biomedical Applications. *Molecules*, 7533-7548.

MÜRBE, J., RECHTENBACH, A. & TÖPFER, J. 2008. Synthesis and physical characterization of magnetite nanoparticles for biomedical applications. *Materials Chemistry and Physics,* 110, 426-433.

OFOMAJA, A. E. & NAIDOO, E. B. 2010. Biosorption of lead(II) onto pine cone powder: Studies on biosorption performance and process design to minimize biosorbent mass. *Carbohydrate Polymers,* 82, 1031-1042.

ÖNSTEN, A., STOLTZ, D., PALMGREN, P., YU, S., GÖTHELID, M. & KARLSSON, U. O. 2010. Water adsorption on ZnO (0001): Transition from triangular surface structures to a disordered hydroxyl terminated phase. *The Journal of Physical Chemistry C,* 114, 11157-11161.

PRATT, A., MUIR, I. & NESBITT, H. 1994. X-ray photoelectron and Auger electron spectroscopic studies of pyrrhotite and mechanism of air oxidation. *Geochimica et Cosmochimica Acta,* 58, 827-841.

REHAN, M., ABDEL-WAHED, N. A. M., FAROUK, A. & EL-ZAWAHRY, M. M. 2018. Extraction of Valuable Compounds from Orange Peel Waste for Advanced Functionalization of Cellulosic Surfaces. *ACS Sustainable Chem. Eng*.

REZA, R. A. & AHMARUZZAMAN, M. 2015. A novel synthesis of Fe2O3@ activated carbon composite and its exploitation for the elimination of carcinogenic textile dye from an aqueous phase. *RSC Advances,* 5, 10575-10586.

SANTRA, D. & SARKAR, M. 2016. Optimization of process variables and mechanism of arsenic (V) adsorption onto cellulose nanocomposite. *Journal of Molecular Liquids,* 224, 290-302.

SHEN, Y., TANG, J., NIE, Z., WANG, Y., REN, Y. & ZUO, L. 2009. Preparation and application of magnetic Fe 3 O 4 nanoparticles for wastewater purification. *Separation and Purification Technology,* 68, 312-319.

SIMÕES DOS REIS, G., HOFFMANN SAMPAIO, C. H., LIMA, E. C. & WILHELM, M. 2016. Preparation of novel adsorbents based on combinations of polysiloxanes and sewage sludge to remove pharmaceuticals from aqueous solutions. *Colloids and Surfaces A: Physicochem. Eng. Aspects* 497**,** 304-315.

SING, K. S. W., HAUL, R. A. W., PIEROTTI, R. A. & SIEMIENIEWSKA, T. 1985. Reporting physisorption data for gas/solid systems with special reference to the determination of surface area and porosity. . *Pure & Applied Chemistry,* 57**,** 603-619.

SRIVASTAVA, V. C., MALL, I. D. & M, M. I. 2006. Characterization of mesoporous rice husk ash (RHA) and adsorption kinetics of metal ions from aqueous solution onto RHA *Journal of Hazardous Material,* B134**,** 257-267.

SUBHEDAR, P. B., RAY, P. & GOGATE, P. R. 2018. Intensification of delignification and subsequent hydrolysis for the fermentable sugar production from lignocellulosic biomass using ultrasonic irradiation. *Ultras. Sonochem,* 40**,** 140-150.

SUBRAMANIAN, K., KUMAR, P. S., JEYAPAL, P. & VENKATESH, N. 2005. Characterization of ligno-cellulosic seed fibre from Wrightia Tinctoria plant for textile applications—an exploratory investigation. *European Polymer Journal,* 41**,** 853-861.

TOUPIN, M. & BÉLANGER, D. 2008. Spontaneous functionalization of carbon black by reaction with 4-nitrophenyldiazonium cations. *Langmuir,* 24**,** 1910-1917.

TZVETKOV, G., KANEVA, N. & SPASSOV, T. 2017. Room-temperature fabrication of core-shell nano-ZnO/pollen grain biocomposite for adsorptive removal of organic dye from water. *Applied Surface Science,* 400**,** 481-491.

ZHENG, J.-C., FENG, H.-M., LAM, M. H.-W., LAM, P. K.-S., DING, Y.-W. & YU, H.-Q. 2009. Removal of Cu (II) in aqueous media by biosorption using water hyacinth roots as a biosorbent material. *Journal of Hazardous Materials,* 171**,** 780-785.

ZHU, J., WEI, S., RYU, J., SUN, L., LUO, Z. & GUO, Z. 2010. Magnetic epoxy resin nanocomposites reinforced with core- shell structured Fe@FeO nanoparticles: fabrication and property analysis. *ACS Appl. Mater. Interfaces,* 2**,** 2100-2107.

## CHAPTER 5

## 5    RESULTS AND DISCUSSION

## 5.1    INTRODUCTION

This chapter covers the application of the NaOH treated pine cone (NTP) and magnetite coated pine cone bio-composite (NTP-NC) material for Cr(VI) and As(III) adsorption from aqueous solutions. Batch adsorption studies such as effect of solution pH and adsorbent dose were conducted. Different kinetic models such as the Lagergen's pseudo-first order equation, second-order equation and intraparticle diffusion were employed in modelling the uptake of Cr(VI) and As(III) onto the NaOH treated pine cone and bio-nano composite material. The activation energies, enthalpies and entropies of activation for the kinetic and diffusion processes were calculated for each process to determine the adsorption mechanism and the participation of the different processes in the adsorption mechanism. Evidence of the mechanism of Cr(VI) and As(III) removal by both NaOH treated pine cone and magnetite coated pine cone bio-composite material from FTIR and XPS analysis after both metals adsorption was also presented.

## 5.2    BATCH ADSORPTION STUDIES FOR CR(VI) REMOVAL

### 5.2.1    Effect of solution pH on Cr(VI) removal

The first approach to evaluate the adsorption capacity of adsorbents towards metals is the determination of the solution pH, since it has a significant influence on the adsorption of heavy metals, due to metal sorption, surface charge and functional group chemistry of the adsorbent (Kim et al., 2013). The effect of solution pH on the adsorption of Cr(VI) by NaOH treated pine cone and magnetite coated pine cone are shown in Fig 5.1. The results indicate that the removal of Cr(VI) from aqueous solution is highly pH-dependent. For both adsorbent samples, it was observed that higher amount of Cr(VI) was removed at low solution pH. The amount of Cr(VI) removal increased slightly as solution pH increases from pH 1 to 3 and decreased steadily as solution pH increases from 3 to 10. Cr(VI) in solution exists mainly in three forms, ($Cr_2O_7^{2-}$, $HCrO_4^-$ and $CrO_4^{2-}$) and exists as $Cr_2O_7^{2-}$ and $HCrO_4^-$ under acidic conditions. The results show that higher Cr(VI) removal is observed for NTP-NC than NTP.
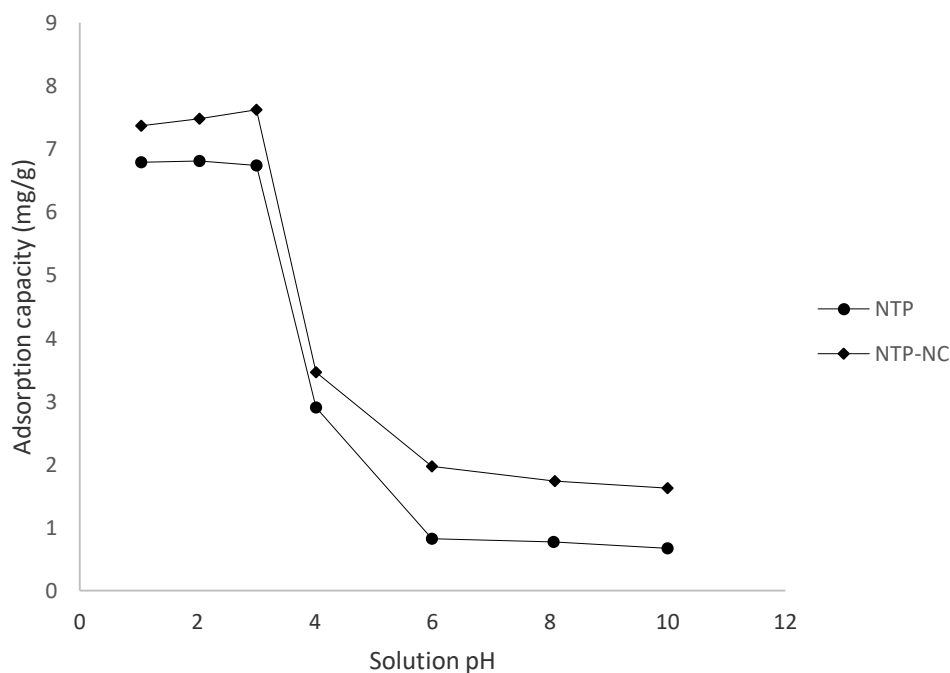
Figure 5.1: Effect of solution pH on the uptake of Cr(VI) from aqueous solution using NTP and NTPNC

 At high solution pH, lower amount of Cr(VI) was found to be removed. The decrease in amount of Cr(VI) removal may be due to the abundance of $OH^-$ ions which enhances electrostatic repulsion forces between Cr(VI) anions and negatively charged groups on the surface of both biosorbents (Fathy et al., 2015). At low solution pH, there is a large number of $H^+$ ions, which protonate the negatively charged groups on the biosorbent surface that easily bind to the chromate through electrostatic attraction as shown in equation 5.1 (Kratochvil et al., 1998, Park et al., 2008).

$$COO^- + H^+ + Cr_2O_7^{2-} \rightarrow COOH^+\text{-}Cr \qquad\qquad (5.1)$$

Similar results were obtained by Kumari et al, (2015) using mesoporous magnetite nanospheres as adsorbent. Large number of $H^+$ ions present in the Cr(VI) metal oxides will protonate the negatively charged groups (amines or carboxylic group) on the biosorbent or Fe(II) surface creating an electron donor group which may transfer electrons to the Cr(VI) thereby reducing it to Cr(III). Cr(III) ions remain in aqueous solution or form complexes on the Cr binding groups on the biosorbent surface. These two methods are possible for removal of Cr(VI) from

aqueous solution. The chromium reduction can take place through various reactions, mainly the following:

$$Cr_2O_7{}^{2-} + 14H^+ + 6e \rightarrow 2Cr^{3+} + 7H_2O \tag{5.2}$$

$$HCrO_4{}^- + 7H^+ + 3e \rightarrow Cr^{3+} + 4H_2O \tag{5.3}$$
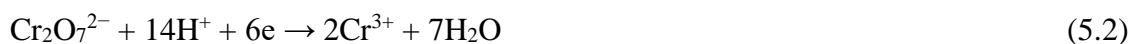
Aqueous Fe(II) has been explored to be one of the potential reducing agents that can reduce Cr(VI) in the Cr(VI) containing wastes to Cr(III) under acidic conditions. Magnetite ($Fe_2O_3$) is an iron oxide mineral in which Fe is found in two oxidation states: $Fe^{2+}$ and $Fe^{3+}$. Fe (II) in the magnetite is used as the potential reducing agent according to the following reaction:

$$2Fe_3O_4 + 10\,H^+ + 2CrO_4^{2-} \rightarrow 9\gamma - 3Fe_2O_3 + 2Cr^{3+} + 5H_2O \tag{5.4}$$
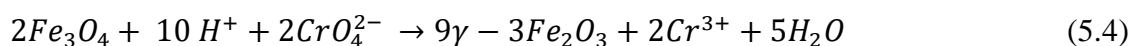
## 5.2.2  Effect of adsorbent dose

Adsorbent dosage is a significant parameter in the removal of Cr(VI) in aqueous solution, since it could change the adsorbent–adsorbate equilibrium of the system. The effect of NTP and NTPNC dose on the Cr(VI) adsorption n was studied at the initial concentration of 75 mg/dm$^3$ and solution pH set at pH 3 at 26 °C and agitated at 200 rpm for 2 h and it is shown in Fig.5.2 A and B. From the results, an increase in adsorbent dose from 0.05 to 1.5 g resulted in a decrease in adsorption capacity from 10.4 to 5.19 mg/g and 31 to 6.55 mg/g for NTP and NTPNC, respectively. However, Cr(VI) percentage removal sharply increased with an increase in adsorbent dosage from 5.2 to 77.9 % and 15.5 to 98.3 % for NTP and NTPNC respectively. At low adsorbent dose, active sites of the adsorbents are fully exposed and are occupied by Cr(VI) ions excess in solution, causing saturation of the surface and yielding a higher adsorption capacity (Albadarin et al., 2011). As adsorbent dose increases, more surface area is available resulting in the insufficient availability of Cr(VI) ions to occupy all the active adsorption sites hence adsorption capacity reduces (Chen et al., 2011).
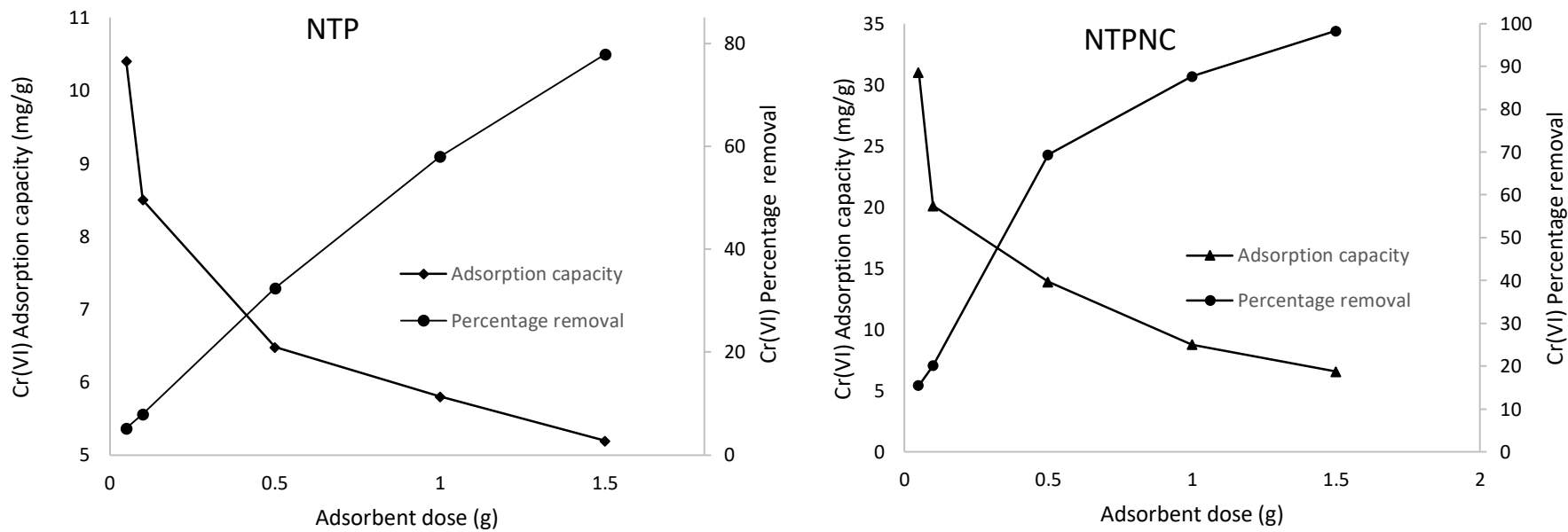
Figure 5.2: The effect of adsorbent dose on (a) NTP and (b) NTPNC for Cr(VI) removal.

The increase in Cr(VI) percentage removal with an increase in adsorbent dose is due to more available active sites of the adsorbents. Thus, choosing a rational adsorbent dose with a comprehensive consideration is necessary. Therefore, the amount of 0.5 g was taken as the optimum dose for further Cr(VI) adsorption studies.

### 5.2.3   Kinetic studies - Effect of concentration

Kinetic studies were conducted to establish the rate of adsorbate-adsorbent interactions so as to understand the mechanism by which pollutants are accumulated and how they get adsorbed on the adsorbents surface. The study involves monitoring the experimental conditions which influence the rate of chemical reaction and assist in attaining equilibrium in a reasonable time. The known dependant factors and rate can be used in developing the adsorbent material for industrial application. The kinetics of the uptake of Cr(VI) by NTP and NTP-NC will depend on whether the slowest step of adsorption proceeds by diffusion through a boundary, adsorption of the adsorbate by sites on the adsorbent surface or diffusion into the internal surface and are discussed below:

#### *5.2.3.1   Kinetics modelling*

Adsorption kinetics gives insight into the reaction pathway between adsorbate and adsorbent and eventually the mechanism of adsorbate uptake on the adsorbent. The pseudo-first order and pseudo second order kinetic model were applied for Cr(VI) adsorption onto both NTP and NTP-NC and the results are discussed.

5.2.3.1.1  Pseudo first and pseudo second order kinetic models

The pseudo-first order kinetic model can be used to follow adsorption kinetics which proceeds by diffusion through a boundary (Lagergren, 1898). Plots of log ($q_e$-$q_t$) versus t from the pseudo-first order model gives a straight line, which allows computation of the adsorption rate constant, $k_1$ and the equilibrium capacity, $q_e$. On the other hand, the pseudo-second-order accounts for adsorption processes that proceeds for surface chemisorption (Ho, 1995). The experimental kinetic data for the batch contact adsorption between 0.5 g of NTP and NTP-NC and various concentrations of (25, 75, 100, 125 and 150 mg/dm$^3$) Cr(VI) solutions were obtained and plotted according to the pseudo-first and pseudo-second kinetic models and the kinetic parameters calculated and given in Table 5.1a and b. The results of the batch kinetic

experiments revealed that Cr(VI) removal by NTP was lower than the removal by NTP-NC for all the concentrations of Cr(VI) applied in this study. The capacities for NTP ranged between 0.87 to 7.01 mg/g and that for NTP-NC ranged between 1.41 to 9.38 mg/g as initial concentration of Cr(VI) solution was increased from 25 to 150 mg/dm$^3$. The higher capacities of the NTP-NC over NTP can be attributed to its greater ability to reduce Cr(VI) to Cr(III) and to complex Cr(III) from aqueous solution. It was observed that the pseudo-second-order model predicted the experimental adsorption capacities more accurately than the pseudo-first order model for both NTP and NTP-NC.

Table 5.1a: Kinetic data for the adsorption of Cr(VI) onto NTP

| Kinetic model | 25 mg/dm$^3$ | 75 g/dm$^3$ | 100 g/dm$^3$ | 125 mg/dm$^3$ | 150 mg/dm$^3$ |
|---|---|---|---|---|---|
| NTP | | | | | |
| **Pseudo-first order** | | | | | |
| *Exp. q* (mg/g) | 0.87 | 2.20 | 3.39 | 5.22 | 7.01 |
| *Model q* (mg/g) | 0.80 | 2.07 | 3.19 | 4.88 | 6.58 |
| $k_1$ (min$^{-1}$) | 0.1620 | 0.3386 | 0.5144 | 0.8160 | 1.0934 |
| $r^2$ | 0.9931 | 0.9931 | 0.9889 | 0.9931 | 0.9885 |
| Variable Error | 0.0017 | 0.0096 | 0.0333 | 0.0096 | 0.1358 |
| | | | | | |
| **Pseudo-second order** | | | | | |
| *Exp. q* (mg/g) | 0.87 | 2.20 | 3.39 | 5.22 | 7.01 |
| *Model q* (mg/g) | 0.87 | 2.25 | 3.40 | 5.23 | 7.01 |
| $k_2$ (g/mg min) | 0.1788 | 0.1975 | 0.2220 | 0.2336 | 0.2435 |
| *h* (mg/g min) | 0.1353 | 0.9998 | 2.5663 | 6,3896 | 11,9656 |
| $r^2$ | 0.9975 | 0.9986 | 0.9966 | 0.9990 | 0.9990 |
| Variable Error | 0.00061 | 0.0019 | 0.0103 | 0.0067 | 0.0114 |

Table 5.1b: Kinetic data for the adsorption of Cr(VI) onto NTP-NC

| Kinetic model | 25 mg/dm$^3$ | 75 g/dm$^3$ | 100 g/dm$^3$ | 125 mg/dm$^3$ | 150 mg/dm$^3$ |
|---|---|---|---|---|---|
| **NTP-NC** | | | | | |
| **Pseudo-first order** | | | | | |
| *Exp. q* (mg/g) | 1.41 | 3.67 | 5.50 | 7.48 | 9.38 |
| *Model q* (mg/g) | 1.23 | 3.48 | 5.20 | 7.07 | 8.90 |
| $k_1$ (min$^{-1}$) | 0.2361 | 0.5216 | 0.8118 | 1.1514 | 1.4459 |
| $r^2$ | 0.9928 | 0.9861 | 0.9875 | 0.9873 | 0.9910 |
| Variable Error | 0.0043 | 0.0495 | 0.0940 | 0.1701 | 0.1879 |
| | | | | | |
| **Pseudo-second order** | | | | | |
| *Exp. q* (mg/g) | 1.41 | 3.67 | 5.50 | 7.48 | 9.38 |
| *Model q* (mg/g) | 1.48 | 3.71 | 5.53 | 7.50 | 9.40 |
| $k_2$ (g/mg min) | 0.1875 | 0.2081 | 0.2281 | 0.2497 | 0.2561 |
| *h* (mg/g min) | 0.4107 | 2.8643 | 6.9755 | 14.0456 | 22,6290 |
| $r^2$ | 0.9960 | 0.9933 | 0.9990 | 0.9982 | 0.9997 |
| Variable Error | 0.0024 | 0.0242 | 0.0080 | 0.0249 | 0.0069 |

The pseudo-first order rate constant, $k_1$, was observed to increase with increasing initial concentration of Cr(VI) in solution indicating that concentration gradient between the bulk solution and the adsorbent surface is a major driving force for the adsorption process. The pseudo-second-order rate constant, $k_2$, was also found to increase with increasing Cr(VI) concentration in solution and its values for NTP was lower than for NTP-NC, signifying that Cr(VI) removal was based not only on the concentration gradient, but on the surface area and the availability of active sites on the adsorbent surface. Finally, initial sorption rate, $h$, of the pseudo-second-order model was observed to increase with increasing Cr(VI) concentration in solution and its values were higher for NTP-NC than for NTP. These results again confirm the effect of surface area and variety of surface functionality on the removal of Cr(VI) by NTP and NTP-NC respectively. The fit of the kinetic model to the experimental data was compared using the correlation coefficient and variable error for Cr(VI) adsorption onto NTP and NTP-NC. The correlation coefficient, $r^2$, values were high for Cr(VI) adsorption onto both adsorbents, but the pseudo second order model had the higher $r^2$ values as compared with the pseudo first order model for both adsorbents. The values of variable error for the pseudo second-order model was found to be lower than that of the pseudo first order. The predicted equilibrium capacities for the pseudo second-order model for both NTP and NTP-NC were closer to the experimental equilibrium capacities than the pseudo first-order model.

### 5.2.3.2 Diffusion modelling

Diffusion of pollutant from aqueous solution onto porous materials play a vital role in the adsorption process since pollutants may need to reach active sites or surfaces via diffusion processes. Diffusion across the thin film of liquid surrounding the adsorbent particles (external or film diffusion) and diffusion into the liquid contained in the pores (pore or intraparticle diffusion) are common means through which pollutant species may be removed from solution. The inclusion of $Fe_3O_4$ in the NTP-NC sample may change the overall surface of the adsorbent which could alter the diffusion kinetics of Cr(VI) removal by NTP.

### 5.2.3.2.1 Intraparticle Diffusion

The effect of $Fe_3O_4$ modification of NTP on the intraparticle diffusion of Cr(VI) into NTP and NTP-NC particles was studied using the intraparticle diffusion model. According to Weber and Morris, if the rate limiting step is intraparticle diffusion, a plot of Cr(VI) adsorbed against the

square root of the contact time should yield a straight line passing through the origin. The larger the intercept, the greater the contribution of the surface biosorption in the rate-limiting step. The intraparticle diffusion plot of $q_t$ versus $t^{0.5}$ for Cr(VI)) adsorption onto NTP and NTP-NC is presented in Fig. 5.3 A and B, respectively. Figs. 5.3a and b show that the intraparticle diffusion curve for Cr(VI) adsorption onto NTP and NTP-NC did not pass through the origin, indicating that intraparticle diffusion is not solely rate limiting but can be separated into two stages. The first rapid step represents external surface adsorption in which surface adsorption is rate-determining while the second almost horizontal step represents the adsorption equilibrium stage.

The intraparticle diffusion rate constant, $k_i$, was calculated at different initial Cr(VI) concentrations and the results are presented in Table 5.2. The intraparticle diffusion rate has been shown to be affected by several factors such as (i) boundary layer diffusion, which measures the thickness of the liquid film covering the adsorbent surface and (ii) the rate of surface adsorption (Ofomaja et al., 2010). These factors along with the intraparticle diffusion rate are dependent on surface characteristics of the adsorbent. The results in Table 5.2 show that the intraparticle diffusion rate, $k_i$, were found to increase with increasing initial concentration of Cr(VI) ions for both NTP and NTP-NC and the values of $k_i$ for NTP-NC were higher than for NTP at lower concentrations. The increase in $k_i$ with initial concentration can be attributed to increased external mass transfer of Cr(VI) ions from aqueous solution to the adsorbent surface. Therefore NTP-NC with higher external mass transfer rates gave higher values for intraparticle diffusion rates. The intercept of the intraparticle diffusion plot reflects the boundary layer effect and the greater its value, the greater the contribution of surface adsorption in the rate-limiting step (Vadivelan and Kumar, 2005). The value of the intercept, $C$, increased with increasing initial Cr(VI) ion concentration for both adsorbents but NTP-NC had higher intercept values than NTP. This means that the contribution of surface adsorption to the rate limiting step increased for both adsorbents but surface adsorption contributed more to the adsorption of Cr(VI) onto NTP-NC than onto NTP. Therefore, the strong surface adsorption of Cr(VI) onto NTP-NC may have led to the lower intraparticle diffusion rates.
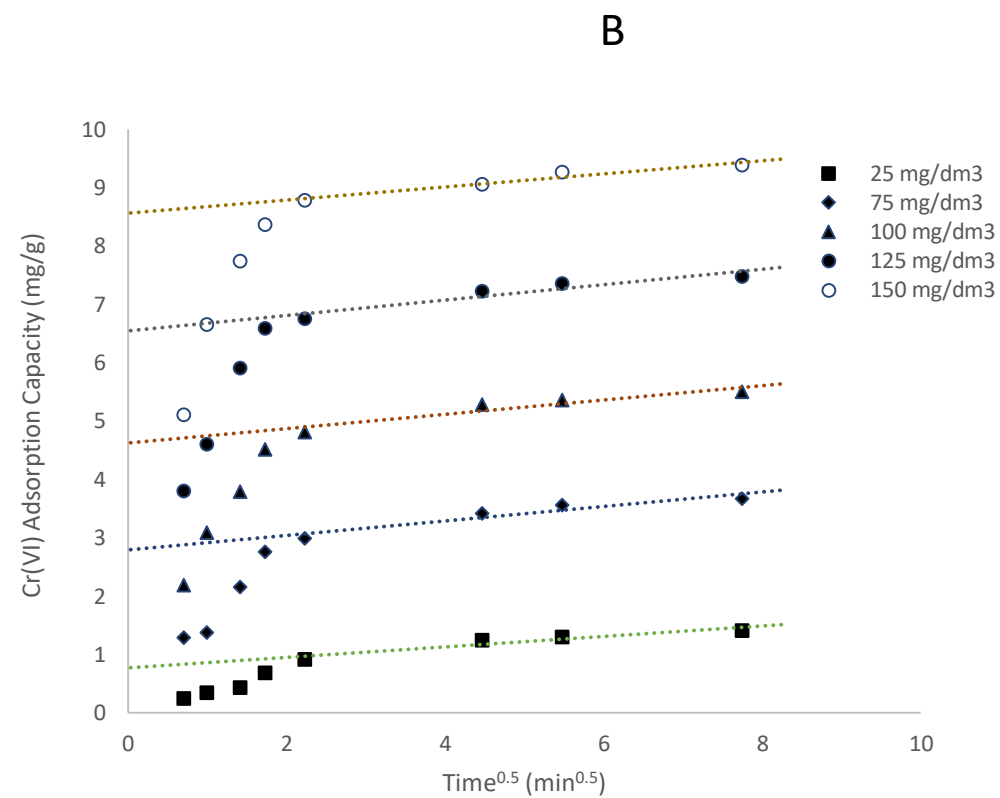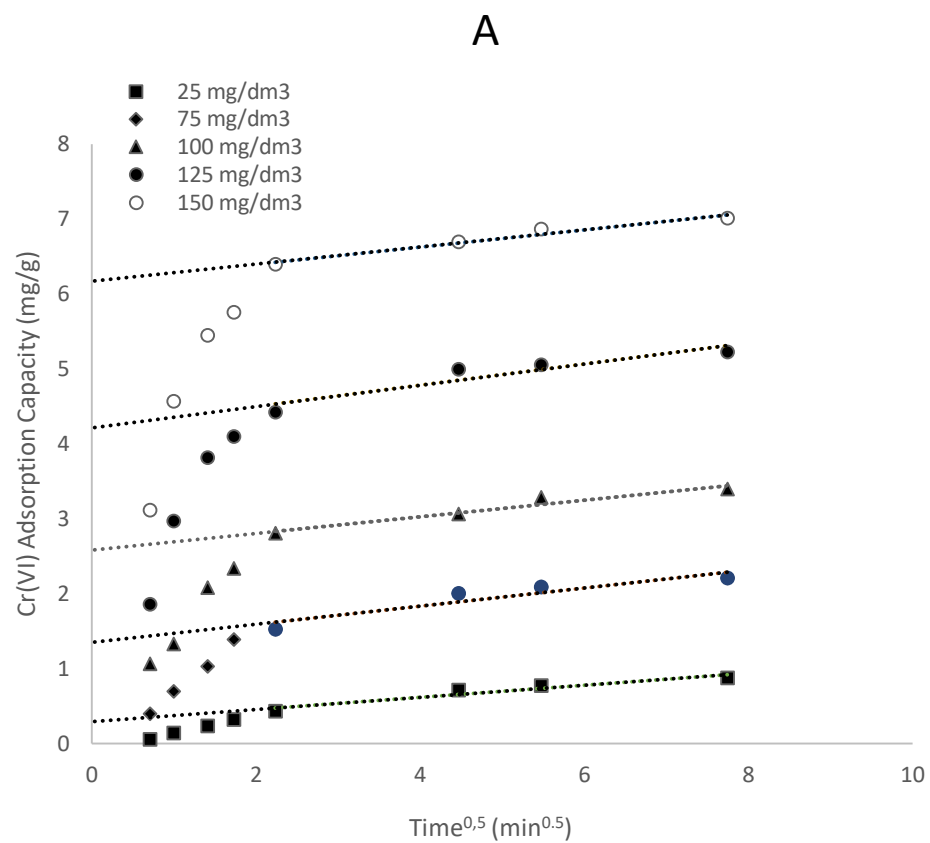
Figure 5.3: Intraparticle diffusion of Cr(VI) adsorption onto (A) NTP and (B) NTP-NC at different concentration.

Table 5.2: Intraparticle models data for the diffusion of Cr(VI) onto NTP and NTP-NC.

| Diffusion model | 25 mg/dm$^3$ | 75 g/dm$^3$ | 100 g/dm$^3$ | 125 mg/dm$^3$ | 150 mg/dm$^3$ |
|---|---|---|---|---|---|
| **NTP** | | | | | |
| **Intraparticle Diffusion model** | | | | | |
| $k_i$ (mg g$^{-1}$ min$^{-0.5}$) | 0.0809 | 0.1218 | 0.1106 | 0.1422 | 0.1143 |
| $C$ | 0.2896 | 1.3430 | 2.814 | 4.2113 | 6.1681 |
| $r^2$ | 0.9151 | 0.8723 | 0.9411 | 0.8770 | 0.9648 |
| **Film Diffusion** | | | | | |
| $D_1$ (cm$^2$/s) | 2.36 x10$^{-7}$ | 2.91 x10$^{-7}$ | 3.21 x10$^{-6}$ | 4.38 x10$^{-6}$ | 5.20 x10$^{-6}$ |
| $r^2$ | 0.9477 | 0.9956 | 0.9882 | 0.9507 | 0.9228 |
| **Pore Diffusion** | | | | | |
| $D_2$ (cm$^2$/s) | 4.40 x10$^{-7}$ | 5.20 x10$^{-6}$ | 5.41 x10$^{-6}$ | 5.57 x10$^{-6}$ | 6.72 x10$^{-6}$ |
| $r^2$ | 0.9640 | 0.9776 | 0.9825 | 0.9955 | 0.9995 |
| **NTP-NC** | | | | | |
| **Intraparticle Diffusion model** | | | | | |
| $k_i$ (mg g$^{-1}$ min$^{-0.5}$) | 0.0896 | 0.1241 | 0.1236 | 0.1322 | 0.1117 |
| $C$ | 0.7689 | 2.7892 | 4.6211 | 6.5412 | 8.5654 |
| $r^2$ | 0.9072 | 0.9062 | 0.8923 | 0.9024 | 0.9483 |
| **Film Diffusion** | | | | | |
| $D_1$ (cm$^2$/s) | 1.51 x10$^{-13}$ | 1.71 x10$^{-13}$ | 2.43 x10$^{-13}$ | 2.33 x10$^{-13}$ | 3.10 x10$^{-13}$ |
| $r^2$ | 0.9312 | 0.9912 | 0.9255 | 0.9342 | 0.9811 |
| **Pore Diffusion** | | | | | |
| $D_2$ (cm$^2$/s) | 7.51 x10$^{-13}$ | 7.91 x10$^{-13}$ | 8.21 x10$^{-13}$ | 9.38 x10$^{-13}$ | 9.60 x10$^{-13}$ |
| $r^2$ | 0.9655 | 0.9956 | 0.9882 | 0.9507 | 0.9228 |

### 5.2.3.2.2 Pore and film diffusion

Intraparticle diffusion process is known to be controlled by both film and pore diffusion (Ofomaja et al., 2010). The film diffusion coefficients, $D_l$, can be calculated assuming the adsorbents particle to be a sphere of radius 'a' and that the diffusion follows Fick's law, the relationship between uptake times is given by (Crank, 1975):

$$\frac{q_t}{q_e} = 6\left(\frac{D_t}{a^2}\right)^{0.5}\left[\pi^{-0.5} + 2\sum\sum_{n=1}^{\infty} ierfc\frac{na}{D_t t^{0.5}}\right] - 3\frac{D_t}{a^2} \tag{5.5}$$

At small times, $D_t$ is replaced by $D_l$ and Eq.(5.5) reduces to:

$$\frac{q_t}{q_e} = 6\left(\frac{D_l}{\pi a^2}\right)^{0.5} t^{0.5} \tag{5.6}$$

The fractional uptake of Cr(VI) was shown to be a function of the square root of time, $t^{0.5}$. The plots of fractional uptake of Cr(VI) versus $t^{0.5}$ for NTP and NTP-NC is shown in Fig. 5.4 A and B, respectively. The plot is observed to have sections that represents a very fast initial stage followed by a slow final uptake of Cr(VI) ions into the pores which was similar to the trend obtained in the intraparticle diffusion plot. The film diffusion coefficient ($D_l$) values for Cr(VI) adsorption onto NTP and NTP-NC at different concentrations were calculated from the slope of the plots of $q_t/q_e$ versus $t$ and are shown in Tables 5.2.

For moderate and large times, the relation between weight uptake and diffusion equation is:

$$\frac{q_t}{q_e} = 1 - \frac{6}{\pi^2}\sum_{n=1}^{\infty}\frac{1}{n^2}\exp\left(\frac{-Dn^2\pi^2 t}{a^2}\right) \tag{5.7}$$

As t tends to large at times, Eq.(5.7) can be written in the form:

$$\left(1 - \frac{q_t}{q_e}\right) = \frac{6}{\pi^2}\exp\left(\frac{-D_2\pi^2 t}{a^2}\right) \tag{5.8}$$

If B = ($D_2\pi^2/a^2$) Eq.(5.8) can be simplified as:

$$\left(1 - \frac{q_t}{q_e}\right) = \frac{6}{\pi^2}\exp(-Bt) \tag{5.9}$$

$$Bt = -0.4997 - \ln\left(1 - \frac{q_t}{q_e}\right) \tag{5.10}$$

*Eq.* (5.10) is used to calculate $B_t$ values at different initial Cr(VI) concentrations and calculated $B_t$ values were then plotted against time, $t$ for Cr(VI) adsorption onto NTP and NTP-NC and is given in Fig. 5.5 A and B. From these plots, it is possible to identify whether external transport or intraparticle diffusion controls the rate of adsorption. The plot of $B_t$ against time, $t$ for NTP and NTP-NC show linear relationships which do not pass through the origin in the initial stage of Cr(VI) adsorption. The plots were observed to cut the y-axis between -0.5 and 0.25 for NTP and between -0.3 and 0.25 for NTP-NC. The intercept values became more positive after coating magnetite with pine cone and was shown to increase with increase in initial concentration of Cr(VI). The results show that external mass transfer process increased due to surface coating and it is the controlling step in the initial stage of the adsorption.

The slope (B) of the plots of $Bt$ versus t, at different initial Cr(VI) concentrations were used to calculate the pore diffusion coefficient ($D_2$) from the equation below:

$$B = \pi^2 \frac{D_2}{r^2} \tag{5.11}$$

The calculated values of both film diffusion coefficient ($D_1$) and pore diffusion coefficient ($D_2$) for NTP and NTP-NC are presented in Table 5.2 and were observed to increased with an increase in initial Cr(VI) concentration. This may be attributed to an increase in concentration gradient between the bulk solution and adsorbent surface resulting in an increase in both film and pore diffusion. The values of the pore diffusion coefficient, ($D_2$) were seen to be higher than those of film diffusion coefficient, ($D_1$) for both NTP and NTP-NC bio-composite suggesting that there was stronger resistance for Cr(VI) getting to the thin liquid film than it is to diffusing into pores.
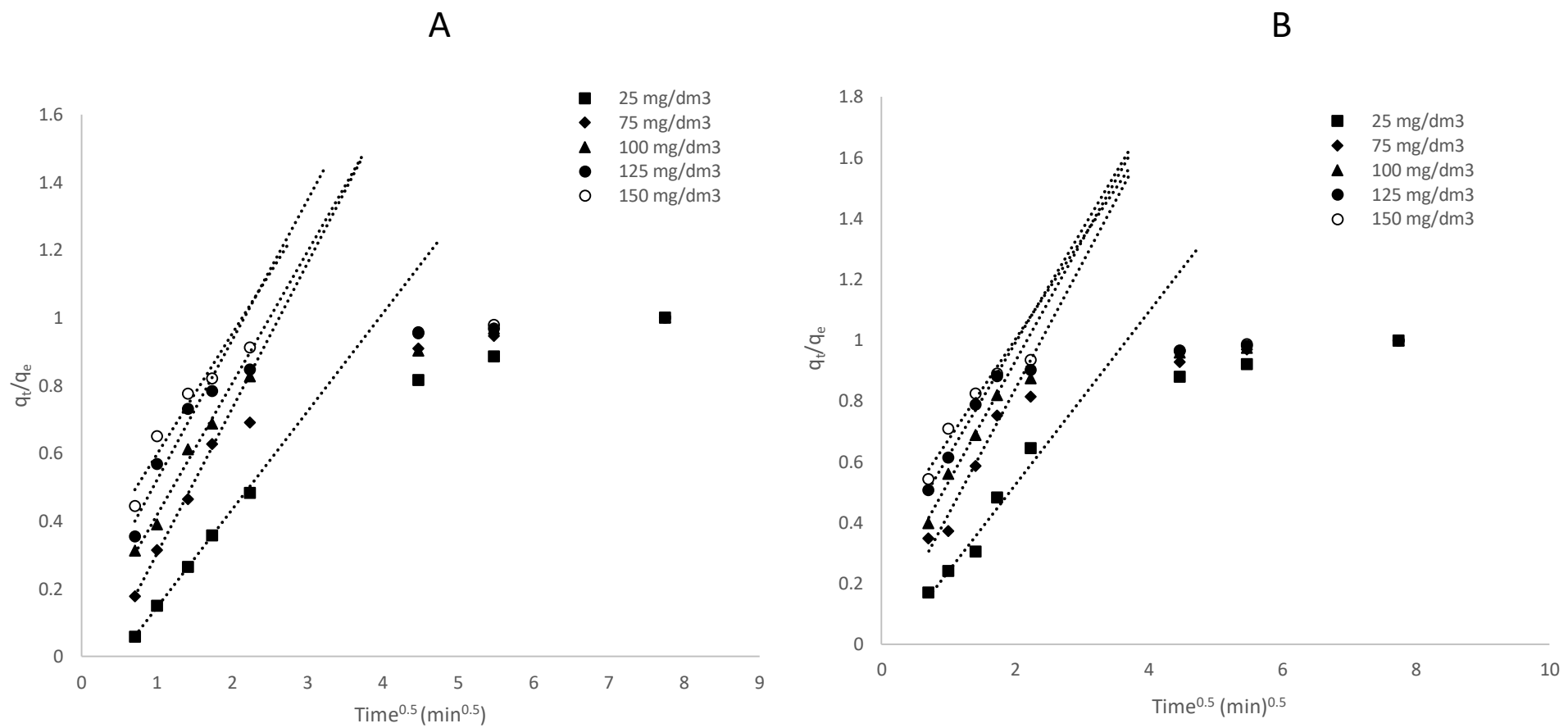
Figure 5.4: Fractional uptake of Cr(VI) onto (A) NTP and (B) NTP-NC at different concentrations.
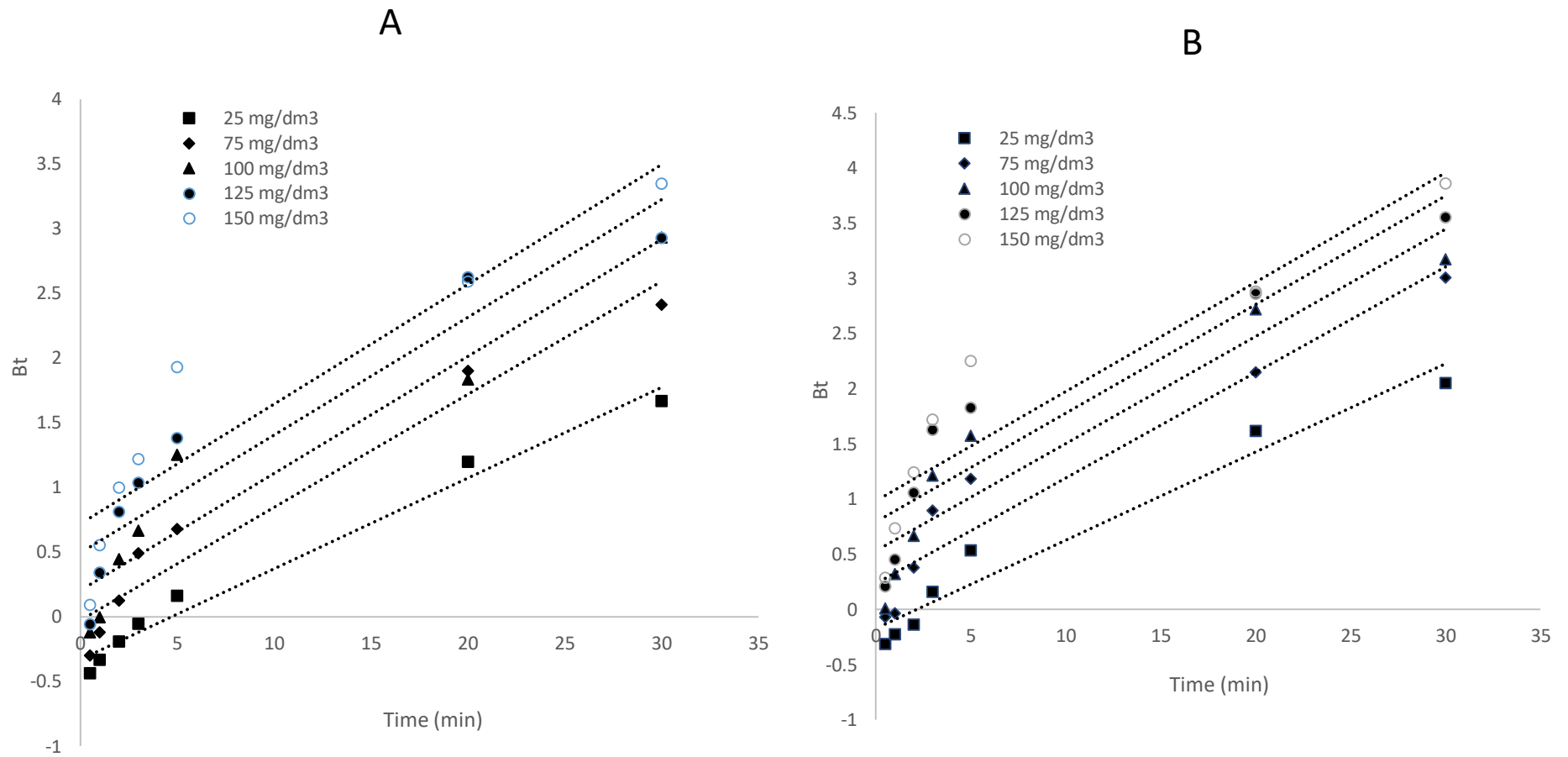
Figure 5.5: Boyd's diffusion of Cr(VI) onto (A) NTP and (B) NTP-NC at different concentrations.

### 5.2.4 Kinetic studies – Effect of temperature

*5.2.4.1 Kinetic modelling*

5.2.4.1.1 Pseudo first and pseudo second order model

The values of the kinetic rate parameters for pseudo first and pseudo second order model for Cr(VI) adsorption onto NTP and NTP-NC with increasing solution temperature along with the correlation coefficients and the variables errors are shown in Table 5.3a and b. The results of the pseudo-first order modelling of the NTP and NTP-NC adsorption kinetic data revealed that NTP-NC had a higher adsorption capacity for Cr(VI) than NTP. The pseudo-first-order model predicted adsorption capacities, $q_1$, and rate constants, $k_1$, for both adsorbents were found to increase with increasing solution temperature indicating that boundary diffusion is promoted by temperature increase. The rate constant, $k_1$, was observed to be higher for NTP-NC than for NTP suggesting a more rapid kinetic uptake for NTP-NC than for NTP. Comparing results for the pseudo-second order modelling of Cr(VI) adsorption onto NTP and NTP-NC, it was also observed that the predicted model capacities values, $q_2$, initial sorption rates, $h$, and the pseudo-second rate constants, $k_2$, increased with increasing temperature. These results suggest that the adsorption process is chemically activated by temperature.

The fit of the kinetic model to the experimental data was compared using the correlation coefficient and variable error for Cr(VI) adsorption onto NTP and NTP-NC. The correlation coefficient, $r^2$, values for pseudo first order were in the range 0.9771 to 0.9865 for NTP and 0.9797 to 0.9920 for NTP-NC while the variable error was in the range 0.1360 to 0.1572 for NTP and 0.1176 to 0.2359 for NTP-NC. On the other hand, the correlation coefficient, $r^2$, values for pseudo second order were in the range 0.9971 to 0.9996 for NTP and 0.9938 to 0.9997 for NTP-NC while the variable error was in the range 0.0038 to 0.0202 for NTP and 0.0050 to 0.0212 for NTP-NC. The pseudo second order model had the higher $r^2$ values and the lowest variable error values as compared with the pseudo first order model for both adsorbents. The predicted equilibrium capacities for the pseudo second-order model for both NTP and NTP-NC were closer to the experimental equilibrium capacities than the pseudo first-order model. The results show that the pseudo second order kinetic model better fitted the kinetic data that the pseudo first order model.

Table 5.3 a: Kinetic parameters for the adsorption of Cr(VI) onto NTP.

| Kinetic model | 299 K | 304 K | 309 K | 314 K | 319 K |
|---|---|---|---|---|---|
| NTP | | | | | |
| **Pseudo-first order** | | | | | |
| *Exp. q* (mg/g) | 7.01 | 7.70 | 8.06 | 8.82 | 9.41 |
| *Model q* (mg/g) | 6.58 | 7.22 | 7.69 | 8.45 | 9.09 |
| $k_1$ (min$^{-1}$) | 1.0934 | 1.3401 | 1.9119 | 2.2606 | 2.4500 |
| $r^2$ | 0.9771 | 0.9775 | 0.9792 | 0.9839 | 0.9865 |
| Variable Error | 0.1360 | 0.1554 | 0.1572 | 0.1451 | 0.1401 |
| | | | | | |
| **Pseudo-second order** | | | | | |
| *Exp. q* (mg/g) | 7.01 | 7.70 | 8.06 | 8.82 | 9.41 |
| *Model q* (mg/g) | 7.03 | 7.64 | 8.04 | 8.86 | 9.43 |
| $k_2$ (g/ mg min) | 0.2454 | 0.2910 | 0.4363 | 0.4928 | 0.5276 |
| $h$ (mg/g min) | 12.12 | 16.99 | 28.20 | 38.68 | 46.92 |
| $r^2$ | 0.9981 | 0.9971 | 0.9976 | 0.9996 | 0.9993 |
| Variable Error | 0.0098 | 0.0202 | 0.0180 | 0.0038 | 0.0034 |

Table 5.3 b: Kinetic parameters for the adsorption of Cr(VI) onto NTP-NC.

| Kinetic model | 299 K | 304 K | 309 K | 314 K | 319 K |
|---|---|---|---|---|---|
| NTP-NC | | | | | |
| **Pseudo-first order** | | | | | |
| *Exp. q* (mg/g) | 9.38 | 9.98 | 10.44 | 10.71 | 11.16 |
| *Model q* (mg/g) | 8.90 | 9.50 | 10.04 | 10.35 | 10.84 |
| $k_1$ (min$^{-1}$) | 1.4454 | 1.8182 | 2.3595 | 2.6566 | 2.7988 |
| $r^2$ | 0.9880 | 0.9797 | 0.9839 | 0.9886 | 0.9920 |
| Variable Error | 0.1879 | 0.2359 | 0.2045 | 0.1532 | 0.1176 |
| | | | | | |
| **Pseudo-second order** | | | | | |
| *Exp. q* (mg/g) | 9.38 | 9.98 | 10.44 | 10.71 | 11.16 |
| *Model q* (mg/g) | 9.40 | 9.98 | 10.45 | 10.72 | 11.21 |
| $k_2$ (g/mg min) | 0.2561 | 0.3190 | 0.4527 | 0.5272 | 0.5512 |
| $h$ (mg/g min) | 22.63 | 31.77 | 49.44 | 60.58 | 69.27 |
| $r^2$ | 0.9993 | 0.9985 | 0.9938 | 0.9994 | 0.9997 |
| Variable Error | 0.0069 | 0.0164 | 0.0212 | 0.0076 | 0.0050 |

### 5.2.4.1.2 Activation energy

Since the rate constants of the different kinetic applied for the modelling of Cr(VI) uptake onto NTP and NTP-NC showed linear relationships with the adsorption temperatures, the adsorption rate constant was expressed as a function of solution temperature by relationship:

$$\ln k_2 = lnk_o - \frac{E_a}{RT} \tag{5.12}$$

Where $k_2$ is the pseudo-second order rate constant of adsorption (g mg/min), $k_0$ is the temperature-independent factor (g/mg min), $E_a$ is the activation energy (kJ/mol), $R$ is the Arrhenius constant (8.314 J/mol K) and T is the solution temperature (K). The activation energy was then obtained from the slope of the plot of $\ln(k_2)$ versus 1/T and it gives an indication of the diffusion path of the adsorption kinetic process whether to be film diffusion or pore diffusion (Zulfikar et al., 2013). Adsorption kinetic processes controlled by film diffusion have typical activation energy in the range of 17–21 kJ/mol while typical values of activation energy for pore diffusion-controlled adsorption process is in the range of 21 to 42 kJ/mol (Namasivayam and Sangeetha, 2006). In this study, the values of activation energies for Cr(VI) adsorption onto NTP and NTP-NC for second-order model were 32.75 for NTP and 32.41 for NTP-NC. The values were observed to fall within the range of 21 to 42 kJ/mol signifying the adsorption kinetic process was controlled by pore diffusion. The results confirm the higher pore diffusion coefficients for both NTP and NTPNC bio-composite.

### 5.2.4.2 Diffusion modelling

### 5.2.4.2.1 Intraparticle diffusion

Intraparticle diffusion is rate limiting in the adsorption process if a plot of metal ions adsorbed against the square root of the contact time yields a straight line. When the kinetic data was analysed using the intraparticle diffusion model, it was observed that the plot in Fig. 5.6 did not pass through the origin indicating that intraparticle diffusion was not the only rate-limiting step. The intraparticle diffusion parameters for Cr(VI) adsorption onto both NTP and NTP-NC were calculated and presented in Table 5.4 a and b, respectively. From the table, the intraparticle diffusion rate constant, $k_i$, for the adsorption of Cr(VI) onto NTP and NTP-NC decreased while the intercept, $C$, representing the boundary layer effect increased with increasing solution temperature.
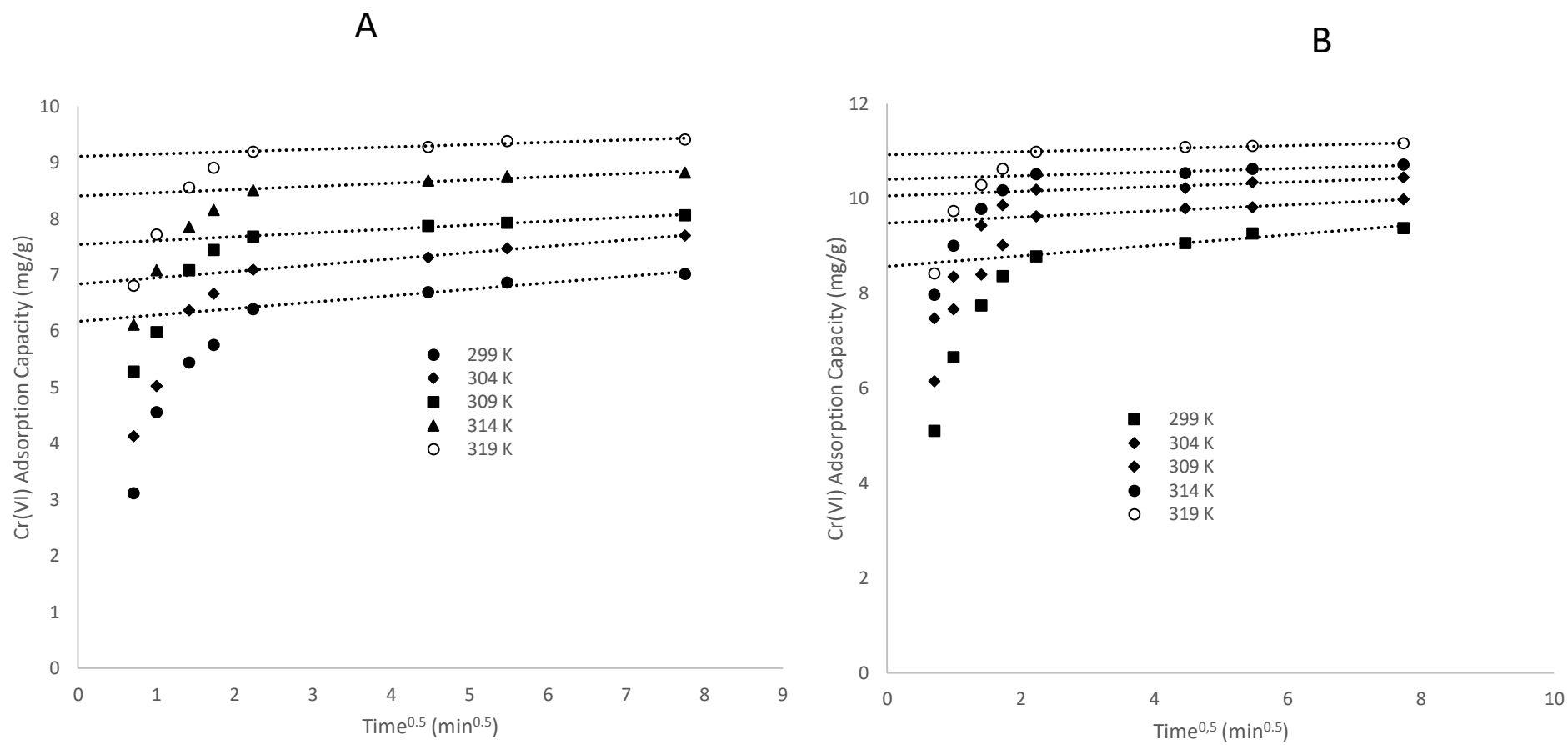
Figure 5.6: Intraparticle diffusion of Cr(VI) adsorption onto (A) NTP and (B) NTP-NC at different temperature.

Table 5.4 a: Diffusion parameters for the adsorption of Cr(VI) onto NTP.

| Diffusion model | 299 K | 304 K | 309 K | 314 K | 319 K |
|---|---|---|---|---|---|
| NTP | | | | | |
| **Intraparticle Diffusion** | | | | | |
| $k_i$ (g/ mg min$^{0.5}$) | 0.1143 | 0.1123 | 0.0686 | 0.0566 | 0.0421 |
| $C$ | 6.1681 | 6.8331 | 7.5430 | 8.4078 | 9.1025 |
| $D_i$ | $1.26 \times 10^{-5}$ | $1.49 \times 10^{-5}$ | $2.24 \times 10^{-5}$ | $2.53 \times 10^{-5}$ | $2.70 \times 10^{-5}$ |
| $R_i$ | 0.1201 | 0.1370 | 0.1435 | 0.1739 | 0.2732 |
| $C/q_{ref}$ | 0.8799 | 0.8630 | 0.8565 | 0.8261 | 0.7268 |
| $r^2$ | 0.9648 | 0.9942 | 0.9865 | 0.9494 | 0.9021 |
| **Film Diffusion** | | | | | |
| $D_1$ (cm$^2$/s) | $2.36 \times 10^{-7}$ | $2.54 \times 10^{-7}$ | $2.75 \times 10^{-7}$ | $2.79 \times 10^{-7}$ | $2.94 \times 10^{-7}$ |
| $r^2$ | 0.9477 | 0.9388 | 0.8893 | 0.8505 | 0.8425 |
| **Pore Diffusion** | | | | | |
| $D_2$ (cm$^2$/s) | $4.40 \times 10^{-7}$ | $4.47 \times 10^{-7}$ | $5.16 \times 10^{-7}$ | $5.36 \times 10^{-7}$ | $6.23 \times 10^{-7}$ |
| $r^2$ | 0.9640 | 0.9412 | 0.9407 | 0.9756 | 0.9809 |

Table 5.4 b: Diffusion parameters for the adsorption of Cr(VI) onto NTP-NC

| Diffusion model | 299 K | 304 K | 309 K | 314 K | 319 K |
|---|---|---|---|---|---|
| NTP-NC | | | | | |
| **Intraparticle Diffusion** | | | | | |
| $k_i$ (g/ mg min$^{0.5}$) | 0.1117 | 0.0639 | 0.0478 | 0.0377 | 0.0322 |
| $C$ | 8.5634 | 9.4817 | 10.0590 | 10.4070 | 10.9240 |
| $D_i$ | 1.89 x10$^{-13}$ | 2.35 x10$^{-13}$ | 3.34 x10$^{-13}$ | 3.89 x10$^{-13}$ | 4.07 x10$^{-13}$ |
| $R_i$ | 0.0871 | 0.0499 | 0.0365 | 0.0283 | 0.0211 |
| $C/q_{ref}$ | 0.9129 | 0.9501 | 0.9635 | 0.9717 | 0.9789 |
| $r^2$ | 0.9483 | 0.9845 | 0.9030 | 0.9261 | 0.9415 |
| | | | | | |
| **Film Diffusion** | | | | | |
| $D_1$ (cm$^2$/s) | 1.51 x10$^{-13}$ | 1.52 x10$^{-13}$ | 1.54 x10$^{-13}$ | 1.55 x10$^{-13}$ | 1.56 x10$^{-13}$ |
| $r^2$ | 0.9312 | 0.8857 | 0.893 | 0.8261 | 0.8111 |
| | | | | | |
| **Pore Diffusion** | | | | | |
| $D_2$ (cm$^2$/s) | 7.51 x10$^{-13}$ | 8.34 x10$^{-13}$ | 9.13 x10$^{-13}$ | 9.42 x10$^{-13}$ | 9.56 x10$^{-13}$ |
| $r^2$ | 0.9655 | 0.9899 | 0.9830 | 0.9903 | 0.9811 |

Results from kinetic modelling has so far shown that adsorption capacity increased with temperature which suggests chemisorption reaction between the active sites on the adsorbent and the Cr(VI) ions. As adsorption temperature increased, the mobility of the Cr(VI) ions decreases due to chemisorption reaction with active sites therefore reducing the diffusion of Cr(VI) ions into the inner surface of the adsorbent, this will account for the reduction of intraparticle diffusion rate constant with temperature. On the other hand, the values of intercept, *C*, indicating boundary diffusion or surface adsorption increased with temperature for both NTP and NTP-NC suggesting that surface adsorption became prominent as temperature was increased. Similar results of decreasing intraparticle diffusion rates and increasing surface adsorption with temperature have been reported for the adsorption of cadmium ions onto nano-zerovalent iron particles.

### 5.2.4.2.2  Pore and film diffusion

The values of film diffusion coefficient for Cr(VI) adsorption by NTP and NTP-NC were found to reduce with increasing solution temperature at constant initial Cr(VI) concentration of 150 mg/dm$^3$. The magnitude of film diffusion coefficient, $D_1$ was higher for NTP than for NTP-NC signifying that film diffusion was faster for NTP than for NTP-NC. Two reasons can be suggested for the higher $D_1$ values for NTP: (i) the repulsion experienced by the positively charged Cr(III) produced in larger percentage for the NTP-NC/Cr(VI) system as it crosses through the liquid film to the positively charged adsorbent surface at pH, and (ii) the roughness impacted on the surface introduced by modification by $Fe_3O_4$ (Mao et al., 2012). The values of $D_1$ was also found to reduce with increasing reaction temperature for both NTP and NTP-NC. The reduction in $D_1$ with increasing temperature can be attributed to rapid saturation of active sites on the adsorbent surface leading to the reduction of mass transfer across the thin liquid film and due to random motion of Cr(VI) ions in solution which is associated with increased thermal energy (Kamins, 1998). Film diffusion coefficient, $D_1$ was found to also decrease with increasing reaction temperature for the adsorption of Cr(VI) onto maize barns (Hasan et al., 2008). Michelsen et al. (1975) showed that film diffusion coefficient in the range of $10^{-6} - 10^{-8}$ cm$^2$s$^1$ indicates that film diffusion is active in the adsorption mechanism. In this study, the magnitude of film diffusion coefficient was in the range of $10^{-7}$ for NTP and $10^{-13}$ for NTP-NC suggesting that film diffusion was active in the mechanism for Cr(VI) adsorption onto NTP but not for NTP-NC.

The plots of $Bt$ vs. t for the adsorption of Cr(VI) onto NTP and NTP-NC in Fig.5.8 a and b, respectively, were found to be linear at the initial stage of the adsorption process (up to 5 min of contact) and did not pass through the origin at all temperatures investigated indicating that external mass transfer of Cr(VI) ions is rate limiting at the initial stages (Ofomaja et al., 2010). The intercepts of the plots cut the y-axis between 0.08 to 0.67 for NTP and 0.27 to 0.83 for NTP-NC as temperature increased from 299 to 319 K, indicating that NTP lines were closer to origin than those of NTP-NC and the curves shifted away from origin with increase in temperature. This observation suggests that a stronger participation of external mass transfer in the rate determining step for NTP and that as temperature increases the participation of external mass transfer reduces giving way to intraparticle diffusion control.

The slope (B) of the plots of $Bt$ vs. t at different temperatures for Cr(VI) adsorption onto NTP and NTP-NC were employed in calculation of pore diffusion coefficient using the Eq.(5.18): The values of pore diffusion coefficient, $D_2$, for the adsorption of Cr(VI) onto NTP and NTP-NC were calculated and displayed in Tables 5.4 a and b, respectively. The results revealed that the values of $D_2$ increased with increasing temperature for both NTP and NTP-NC and its magnitude was higher for NTP than for NTP-NC. Lower magnitude of $D_2$ for NTP-NC can be attributed to the restriction of Cr(VI) ions into the internal surface of the adsorbent due to its modification with $Fe_3O_4$ nanoparticles. The increase in the values of $D_2$ with increasing temperature can be attributed to increased mobility of the Cr(VI) ions in solution with increase in temperature (McKay and Poots, 1980, Önal et al., 2007). The results obtained revealed that the values of $D_2$ are in the range of $10^{-7}$ for NTP and $10^{-13}$ for NTP-NC suggesting that pore diffusion was rate controlling for NTP-NC and for NTP adsorbents.
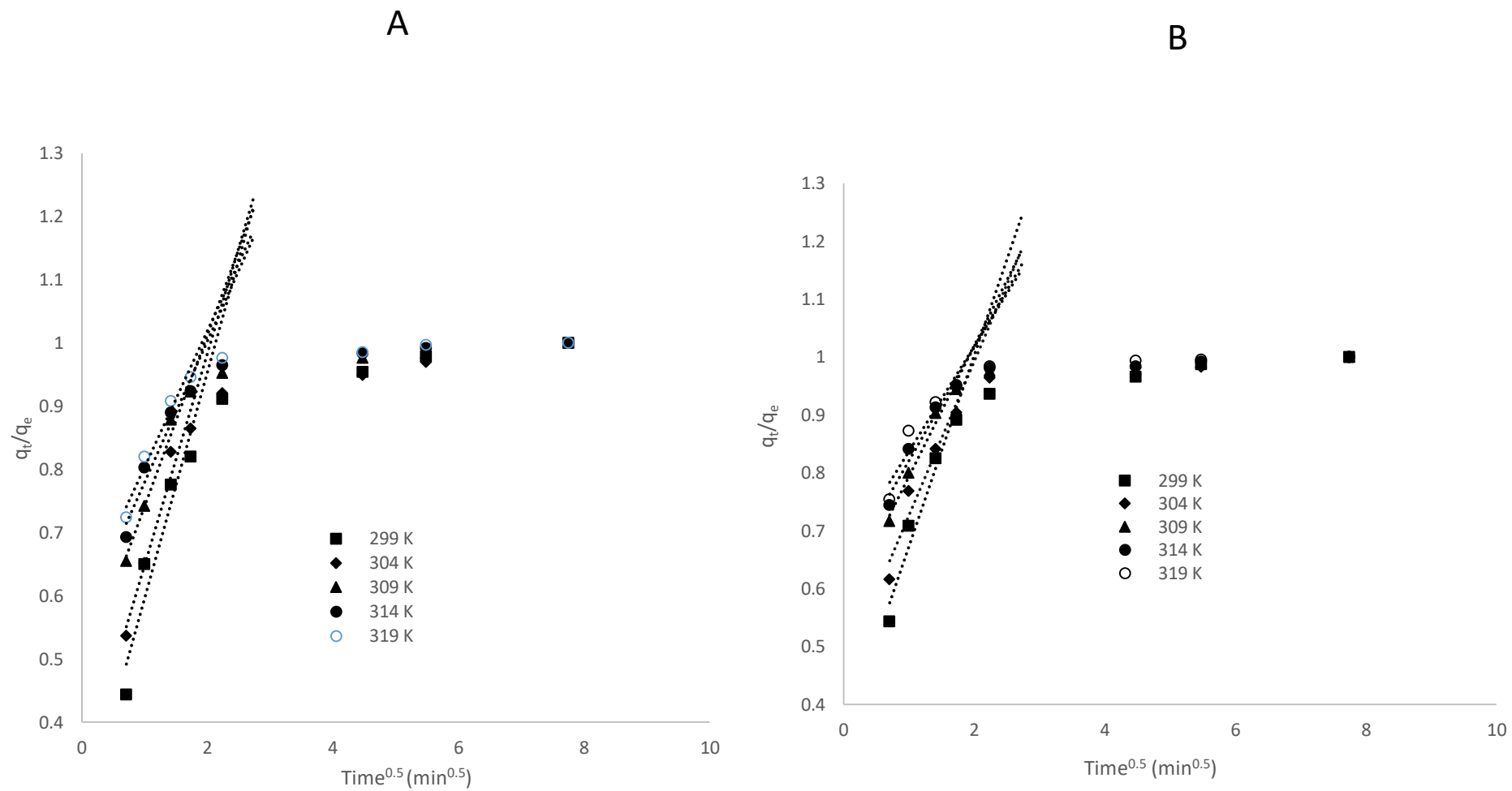
Figure 5.7: Fractional uptake of Cr(VI) onto (A) NTP and (B) NTP-NC at different temperatures.
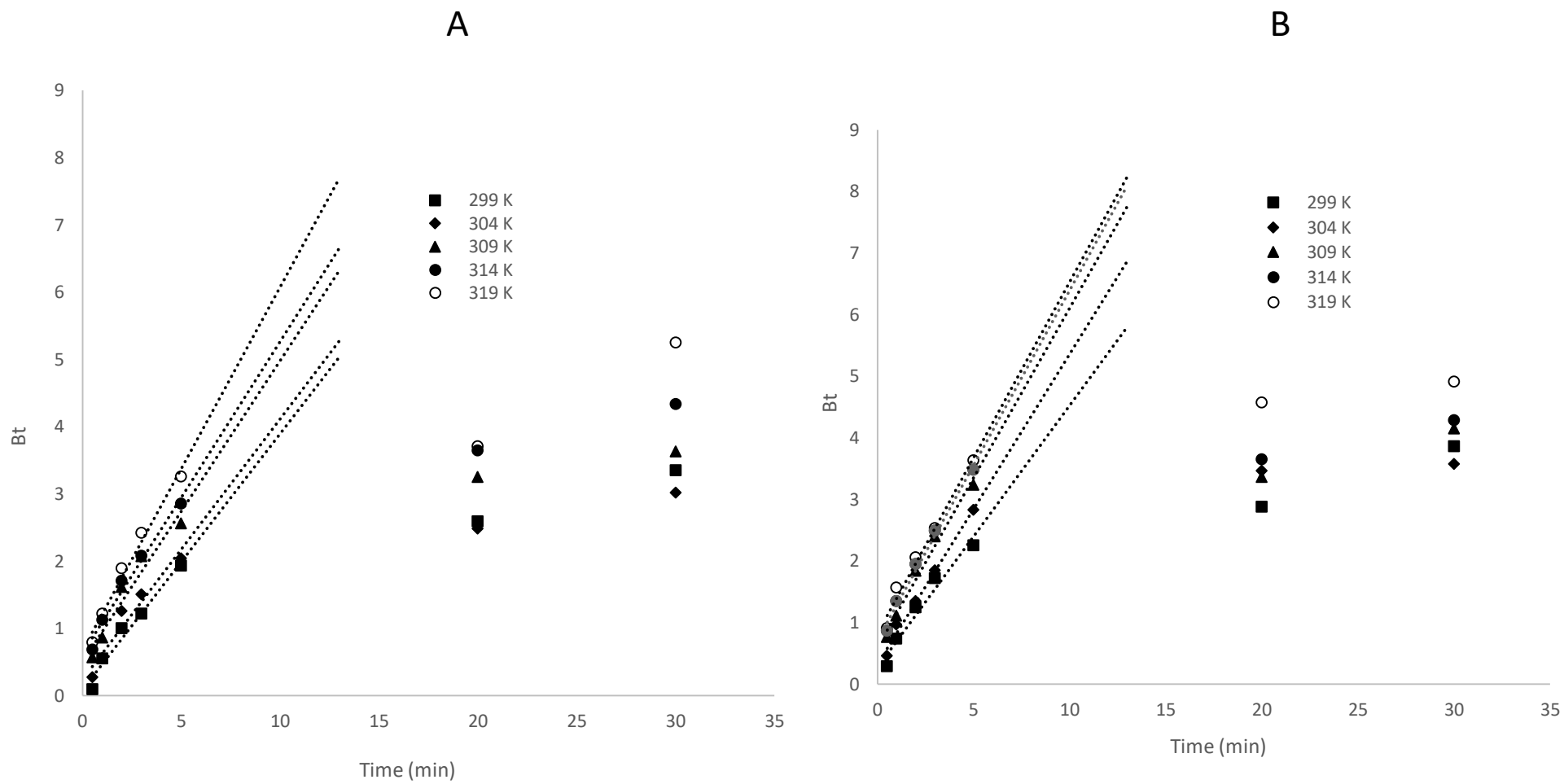
Figure 5.8: Boyd's diffusion of Cr(VI) onto (A) NTP and (B) NTP-NC at different temperatures

131

### 5.2.5   Equilibrium Isotherm

Equilibrium isotherm modelling can be used to characterize an adsorption system for the sequestration of pollutant from aqueous solution. Parameters obtained from the relationship between the quantities of pollutant concentrated on the adsorbent surface and that remaining in the bulk solution at a given temperature can give an indication of the affinity of the adsorbent for the adsorbate. The equilibrium system in this study was modelled using three equilibrium isotherm models namely the Langmuir, Freundlich and the Dubinin-Radushkevish (D-R) isotherm models.

Equilibrium isotherm parameters of the chosen isotherm models along with values of error measurement taken from the correlation coefficient, $r^2$ and percentage variable error for NTP and NTP-NC are shown in Table 5.5a and b. The best fitting isotherm model to the experimental data was observed to be the Langmuir isotherm as can be seen from the higher values of $r^2$ and the least values of percentage variable error for both adsorbents. The values error determination for Langmuir model where within the range of 0.9944 to 0.9994 and 1.01 to 9.03 % for NTP and 0.9983 to 0.9997 and 0.31 to 7.08 % for NTP-NC. The good fit to the Langmuir model suggests that the adsorption sites on the adsorbent are homogenous, forming a monolayer coverage of adsorbed Cr(VI) ions on the surface. The values of monolayer capacity and equilibrium constant were observed to increase as the adsorption temperature increased from 299 to 319 K. The NTP and NTP-NC efficiency for Cr(VI) removal from solution was also examined by applying the dimensionless constant separation factor for the equilibrium parameter ($R_L$) with the form:

$$R_L = \frac{1}{1 + K_a C_0}$$  (5.13)

The parameter $K_a$ in Eq. (5.12) is the Langmuir isotherm equilibrium capacity and $C_0$ is the initial concentration of the Cr(VI) in solution. The value of $R_L$ was observed to decrease from 0.1605 to 0.0551 for NTP and from 0.0459 to 0.0073 for NTP-NC as adsorption temperature was increased from 299 to 319 K. This result confirms that adsorption efficiency increased with temperature for both adsorbents. The Freundlich isotherm also showed a good fit with the experimental data with values of $r^2$ and percentage variable error in the range of 0.9927 to 0.9998. and 0.49 to 11.94 % and from 0.9927 to 0.9978 and 8.26 to 49.88 % for NTP and NTP-NC, respectively. The parameter, $n$ indicating adsorption affinity and the adsorption capacity indicating parameter, $K_F$, were seen to increase in magnitude suggesting that both affinity for

132

Cr(VI) ions and adsorption capacity were favoured by increasing temperature. Error determination was also performed on the equilibrium data modelled using the D-R isotherm and the results shown in Table 5.5a and b. It was observed that both $r^2$ and percentage variable error values were reasonably good ranging from 0.9049 to 0.9972 and 9.74 to 19.68 for NTP and from 0.9072 to 0.9767 and 22.54 to 37.33 % for NTP-NC. Values of saturation capacity, $q_s$ (mol/g) was observed to be close to the Langmuir isotherm monolayer capacities when converted to mg/g. The saturation capacity was also found to increase with increasing adsorption temperature. The adsorption energy parameter, $\beta$ decreased from 3.15 x $10^{-9}$ to 2.64 x $10^{-9}$ mol$^2$/kJ$^2$ for NTP and from 2.00 x $10^{-9}$ to 1.62 x $10^{-9}$ mol$^2$/kJ$^2$ for NTP-NC as temperature was increased from 299 to 319 K. The mean free energy of adsorption, $E$, which gives an indication of the adsorption mechanism increased with adsorption temperature from 12.60 to 13.80 kJ/mol for NTP and from 15.80 to 16.80 kJ/mol for NTP-NC. The value of $E$ can be used to determine the adsorption type. For example, $E$ values < 8 kJ/mol will indicate physical processes, $E$ values between 8 and 16 kJ/mol indicates ion-exchange processes, while E values > 16 kJ/mol indicates chemical adsorption (Lunge et al., 2014). The range of the mean free energy of adsorption obtained in this study suggests that the adsorption mechanism for Cr(VI) onto both NTP and NTP-NC is by ligand-ion exchange (Lunge et al., 2014).

Table 5.5 a: Equilibrium data for Cr(VI) adsorption onto NTP

| Isotherm model | 299 K | 304 K | 309 K | 314 K | 319 K |
|---|---|---|---|---|---|
| **NTP** | | | | | |
| **Langmuir** | | | | | |
| $q$ (mg/g) | 11.56 | 12.01 | 13.10 | 14.19 | 15.61 |
| $K_a$ (dm$^3$/mg) | 0.0436 | 0.0506 | 0.0585 | 0.0787 | 0.0857 |
| $r^2$ | 0.9944 | 0.9989 | 0.9990 | 0.9996 | 0.9994 |
| %Variable Error | 9.03 | 2.91 | 3.80 | 1.01 | 1.79 |
| | | | | | |
| **Separation factor** | 0.1605 | 0.1157 | 0.0965 | 0.0660 | .0.0551 |
| | | | | | |
| **Freundlich** | | | | | |
| $n$ | 3.07 | 3.65 | 3.78 | 4.73 | 5.03 |
| $K_F (mg / g)(dm^3 / mg)^{1/n}$ | 4.113 | 4.846 | 4.137 | 4.554 | 4.286 |
| $r^2$ | 0.9927 | 0.9966 | 0.9998 | 0.9982 | 0.9971 |
| %Variable Error | 11.94 | 6.23 | 0.49 | 4.70 | 8.92 |
| | | | | | |
| **Dubinin–Radushkevich** | | | | | |
| $q_s$ (mol/g) | $1.43 \times 10^{-4}$ | $1.62 \times 10^{-4}$ | $1.95 \times 10^{-4}$ | $1.97 \times 10^{-4}$ | $2.03 \times 10^{-4}$ |
| $\beta$ (mol$^2$/J$^2$) | $3.15 \times 10^{-9}$ | $2.73 \times 10^{-9}$ | $2.72 \times 10^{-9}$ | $2.52 \times 10^{-9}$ | $2.64 \times 10^{-9}$ |
| $E$ (kJ/mol) | 12.60 | 12.1 | 13.60 | 14.10 | 13.80 |
| $r^2$ | 0.9049 | 0.9180 | 0.9972 | 0.9726 | 0.9619 |
| %Variable Error | 19.68 | 11.54 | 9.74 | 9.97 | 10.32 |

Table 5.5 b: Equilibrium data for Cr(VI) adsorption onto NTP-NC

| Isotherm model | 299 K | 304 K | 309 K | 314 K | 319 K |
|---|---|---|---|---|---|
| **NTP-NC** | | | | | |
| **Langmuir** | | | | | |
| $q$ (mg/g) | 15.24 | 16.46 | 17.06 | 18.13 | 19.11 |
| $K_a$ (dm$^3$/mg) | 0.1731 | 0.1954 | 0.2584 | 0.4109 | 0.6838 |
| $r^2$ | 0.9983 | 0.9994 | 0.9997 | 0.9985 | 0.9996 |
| %Variable Error | 3.73 | 0.31 | 1.43 | 7.08 | 1.86 |
| | | | | | |
| **Separation factor** | 0.0459 | 0.0353 | 0.0236 | 0.0133 | 0.0073 |
| | | | | | |
| **Freundlich** | | | | | |
| $n$ | 7.26 | 7.34 | 8.13 | 9.82 | 10.83 |
| $K_F (mg\,/\,g)(dm^3\,/\,mg)^{1/n}$ | 6.223 | 5.383 | 5.571 | 6.156 | 5.793 |
| $r^2$ | 0.9941 | 0.9978 | 0.9466 | 0.9898 | 0.9927 |
| %Variable Error | 20.94 | 8.62 | 14.57 | 49.88 | 46.30 |
| | | | | | |
| **Dubinin–Radushkevich** | | | | | |
| $q_s$ (mol/g) | $1.68 \times 10^{-4}$ | $1.93 \times 10^{-4}$ | $2.06 \times 10^{-4}$ | $2.18 \times 10^{-4}$ | $2.49 \times 10^{-4}$ |
| $\beta$ (mol$^2$/J$^2$) | $2.00 \times 10^{-9}$ | $1.95 \times 10^{-9}$ | $1.85 \times 10^{-9}$ | $1.65 \times 10^{-9}$ | $1.62 \times 10^{-9}$ |
| $E$ (kJ/mol) | 15.80 | 16.00 | 16.50 | 16.70 | 16.80 |
| $r^2$ | 0.9335 | 0.9767 | 0.9707 | 0.9072 | 0.9432 |
| %Variable Error | 37.33 | 22.54 | 27.42 | 28.97 | 26.65 |

### 5.2.6 Thermodynamic parameters of adsorption

To evaluate the influence of temperature on the adsorption process of Cr(VI) onto NTP and NTP-NC, thermodynamic parameters such as change in free energy ΔG*, enthalpy *ΔH** and entropy *ΔS** were calculated from the following equations:

$$\Delta G^* = -RT \ln K_L \tag{5.14}$$

where $K_L$ is calculated from the ratio of Cr(VI) on the adsorbent surface at equilibrium to the Cr(VI) left in solution.

$$\ln K_L = -\frac{\Delta G^*}{RT} = -\frac{\Delta H^*}{RT} + \frac{\Delta S^*}{R} \tag{5.15}$$

Multiply Eq.(5.15) with - *RT*:

$$\Delta G^* = \Delta H^* - T\Delta S^* \tag{5.16}$$

where *R* is the gas constant (8.314 J/mol K), *T* is the absolute temperature (K), *ΔH** and *ΔS** could be obtained from the slope and intercept of *ΔG** versus *1/T*. Thermodynamic analysis was investigated at five different temperatures (299, 304, 309, 314 and 319 K). The values of the thermodynamic parameters for Cr(VI) adsorption onto NTP and NTP-NC are given in Table 5.6. The values of free energy change, *ΔG** for NTP and NTP-NC were calculated to range from -37.86 to -40.42 kJ/mol for NTP and from -39.08 to -41.72 kJ/mol for NTP-NC as adsorption temperature was increased from 299 to 319 K. The negative sign of free energy change suggests that the adsorption of Cr(VI) onto NTP and NTP-NC is spontaneous, and the spontaneity increases with temperature. The results also show that the adsorption of Cr(VI) onto NTP-NC was more spontaneous than that of NTP. The positive values of *ΔH** which were calculated to be 37.68 kJ/mol for NTP and 29.21 kJ/mol for NTP-NC confirmed the endothermic nature of adsorption and further supported the increase of adsorption capacity with the increase in temperature. The higher value of *ΔH** for NTP as compared to that of NTP-NC showed that Cr(VI) adsorption by NTP-NC needed less energy adsorbed than that of NTP. Finally, the entropy values were calculated as 12.79 J/mol K for NTP and 13.17 J/mol K for NTP-NC. The positive values of the entropy suggest that increasing randomness during the adsorption process (Xu et al., 2012). The higher values of entropy of NTP-NC over NTP suggests that the randomness is higher in NTP-NC than in NTP.

Table 5.6: Thermodynamic parameters of Cr(VI) adsorption onto NTP and NTP-NC

| Sample | Temp. (K) | $\Delta G^*$(kJ/mol) | $\Delta H^*$(kJ/mol) | $\Delta S^*$(J/ K mol) |
|---|---|---|---|---|
| NTP | 299 | -37.86 | | |
| | 304 | -38.50 | | |
| | 309 | -39.14 | 37.68 | 12.79 |
| | 314 | -39.28 | | |
| | 319 | -40.42 | | |
| NTP-NC | 299 | -39.08 | | |
| | 304 | -39.74 | | |
| | 309 | -40.40 | 29.21 | 13.17 |
| | 314 | -41.06 | | |
| | 319 | -41.72 | | |

### 5.2.7 Mechanism evidence

To prove which mechanism is predominant for Cr(VI) removal using NTP and NTP-NC, the amount of Cr concentration left in solution (total chromium, Cr(VI) and Cr(III)) and changes in $H^+$ concentration were plotted against different solution pH and the results are shown in Fig. 5.9. It is known that the reduction of Cr(VI) to Cr(III) consumes $H^+$ and release $OH^-$ which rises the solution pH. The results showed that the change in $[H^+]$ concentrations at the end of the adsorption process where higher for lower initial solution pH's (where lower amounts of Cr was found in solution) than for higher initial solution pH's (where higher amounts of Cr was found in solution) and the change in $[H^+]$ concentration became small and almost constant after initial solution pH 4. This is consistent with the assumption that the removal of Cr from solution is associated with $[H^+]$ ion consumption and that as the concentration of $[H^+]$ ions reduce in solution; the Cr removal reduces.

It can be observed that the change in $H^+$ concentration for NTP increases as the solution pH increases from pH 1 to 4. At solution pH of 1, higher change in $H^+$ concentration is observed which resulted in higher amount of Cr(VI) being reduced to Cr(III). Cr concentration left in solution was observed to be 28.256 $mg/dm^3$, 27.956 $mg/dm^3$ and 0.400 $mg/dm^3$ for total Cr, Cr(III) and Cr(VI) for NTP, respectively. The results show that a higher amount of Cr(VI) was reduced to Cr(III) and less amount of Cr(VI) was left in solution. The NTP-NC sample was found to have followed the same trend. The Cr concentration left in solution was 21.559 $mg/dm^3$, 10.899 $mg/dm^3$ and 10.600 $mg/dm^3$ for total Cr, Cr(III) and Cr(VI), respectively. Almost half of the Cr(VI) was reduced to Cr(III) and stayed in solution. NTP was found to have reduced Cr(VI) to Cr(III) more than NTP-NC, but higher Cr concentration was left in solution for NTP than for NTP-NC sample. At solution pH (pH 1), higher amount of $H^+$ are present in the solution causing protonation of negatively charged functional groups on the biosorbent causing a change in the surface charge. The reduced Cr(III) will therefore repel the protonated functional groups on the biosorbent and stay in solution. At solution pH 2, the change in $H^+$ concentration decreased for both samples, causing less reduction of Cr(VI) to Cr(III).
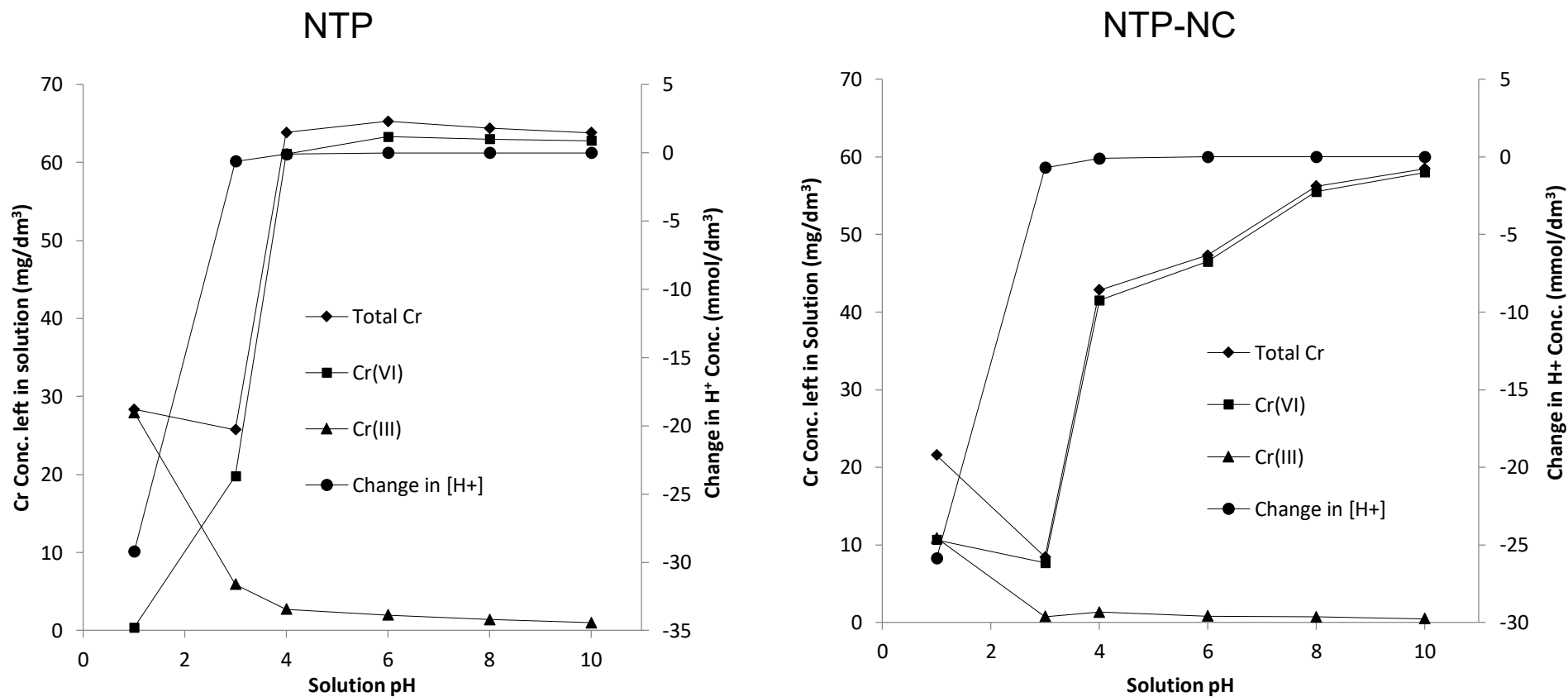
Figure 5.9: The plot of the amount of Cr concentration left in solution and the changes in H$^+$ concentration at different solution pH for (A) NTP and (B) NTP-NC.

Cr concentration left in solution was found to decrease to 25.737 mg/dm$^3$ and 5.397 mg/dm$^3$ for total Cr and Cr(III), respectively, while Cr(VI) increased to 19.8 mg/dm$^3$, for NTP. The results show that less amount of Cr(VI) was reduced to Cr(III). For NTP-NC, the concentration of Cr left in solution was found to decrease to 8.446 mg/dm$^3$, 7.7 mg/dm$^3$ and 0.746 mg/dm$^3$ for total Cr, Cr(VI) and Cr(III), respectively. The results indicate that less amount of Cr(VI) was reduced to Cr(III) for both samples. As solution pH increases from 1 to 3, less amount of H$^+$ is present. Less amount of Cr(III) will be repelled.

The amount of total Cr and Cr(VI) left in solution was found to increase at solution pH 4 until reaching an almost constant state at solution pH of 10 for NTP. For the NTP-NC sample, the amount of total Cr and Cr(VI) increased sharply as pH increases from 4 to 10. From solution pH 4 to 10, there is a smaller change in H$^+$ concentration causing a small reduction of Cr(VI) to Cr(III). The amount of total Cr and Cr(VI) increased sharply as pH increases from 4 to 10. Less amount of Cr concentration was left in solution for NTP-NC than for NTP. The amount of Cr(III) reduced gradually and was completely removed from the solution for both biosorbent materials but the reduction was more for NTP-NC than for NTP. This may be due to the fact that the reduced Cr(III) was adsorbed from the solution by the carbonyl group from the biosorbent material. As the pH increases more OH$^-$ are present in the solution and interact with the Cr(III) thereby removing it from the solution. The results also show that the removal of Cr(VI) and its reduction to Cr(III) requires a large number of protons in the acidic medium.

To further examine the Cr(VI) adsorption characteristics from aqueous solution by NTP and NTP-NC, the profile of Cr concentration and ORP were investigated at solution pH of 3 and the results are shown in Fig. 5.10 A and B. From the graphs, the values of ORP was found to decrease from 339 to 255 for both biosorbent materials. The total Cr and Cr(VI) concentration was found to decrease sharply with contact time from 0 to 120 minutes and was lower for NTP-NC than NTP with maximum concentration of 26.494 mg/dm$^3$ and 24.1 mg/dm$^3$ for NTP-NC and 33.824 mg/dm$^3$ and 30.4 mg/dm$^3$ for NTP. Cr(III) appeared in acidic solution and was found to increase gradually with contact time. The results reveal the reduction of Cr(VI) to Cr(III) when brought into contact with the NTP and NTP-NC biosorbent materials. The results show that the reduction of Cr(VI) to Cr(III) is highly dependent on the redox potential.
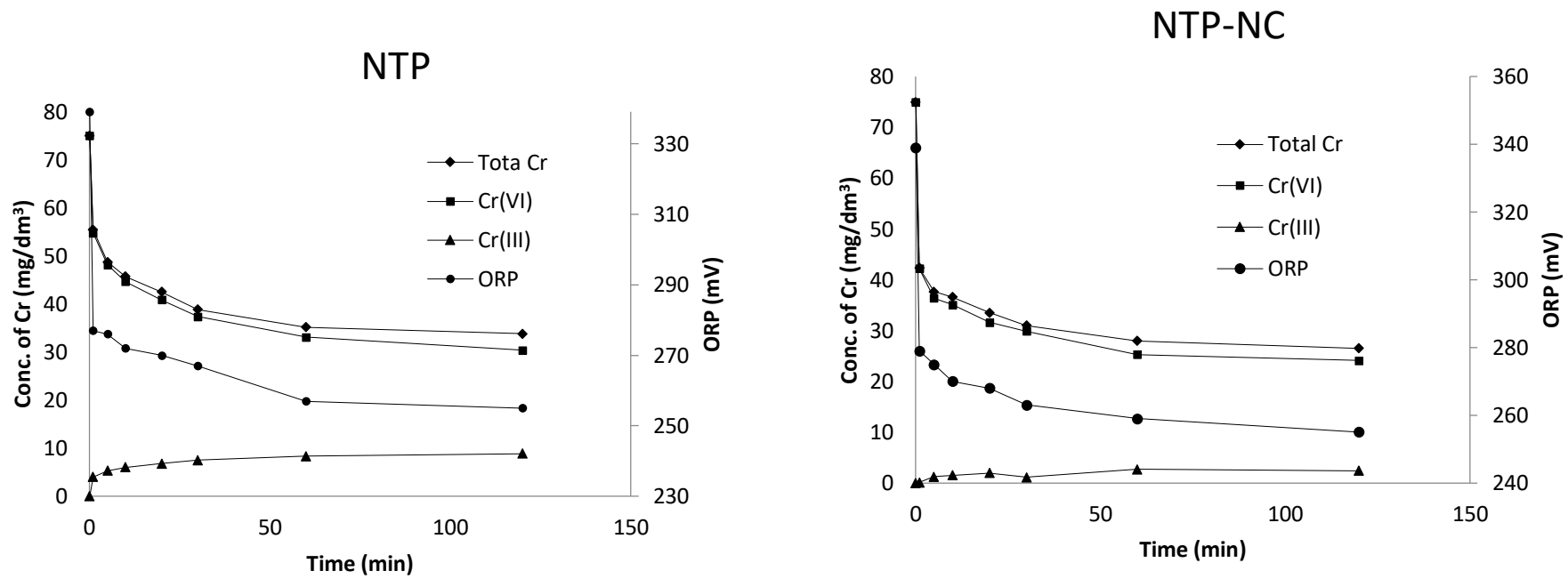
Figure 5.10: The profile of Cr concentration left in solution and ORP with time (A) NTP and (B) NTP-NC

*5.2.7.1 Fourier Transformed Infrared (FTIR) analysis after Cr(VI) adsorption*

FTIR analysis was conducted to explore the possible mechanism involved in the adsorption of Cr(VI) by NTP and NTP-NC. According to Park et al. (2011), Cr(VI) can be spontaneously reduced to Cr(III) when in contact with biomaterials or reducing agents especially in an acidic solution, since Cr(VI) has a high redox potential (above +1.3 V). It has been reported from literature that the main functional groups responsible for Cr adsorption and reduction on the biosorbents are the hydroxyl group, carboxyl group and amino groups (Sukumar et al., 2014). Cr(VI) reduction to Cr(III) using biosorbents may be shown as follows (Altungdogan, 2005):

$$H_2CrO_4^- + organic\ matter + H^+ \rightarrow Cr^{3+} + H_2O + CO_2 \qquad (5.17)$$
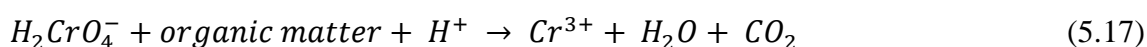
The functional group elucidation is one of the key factors to understand the mechanism and binding process on biosorbents. The FTIR of NaOH treated pine before and after Cr(VI) biosorption is shown in Fig.5.11. From the results, the FTIR spectrum of NaOH treated pine cone shows a number of absorption peaks, indicating the complex nature of the biosorbent. The main characteristics peaks include the peak representing the unbounded -OH group at 3334.04 cm$^{-1}$, the peak representing the aliphatic C-H group at 2897.86 cm$^{-1}$, the peak representing C-O and vibration of C=C at 1602.99 cm$^{-1}$ and the peak at 1223.00 cm$^{-1}$ and 658.85 cm$^{-1}$ which are due to O-H deformation of phenolic group (Subramanian et al., 2005). The peak at 1022 cm$^{-1}$ representing the C-O stretching of secondary alcohol in cellulose is observed.
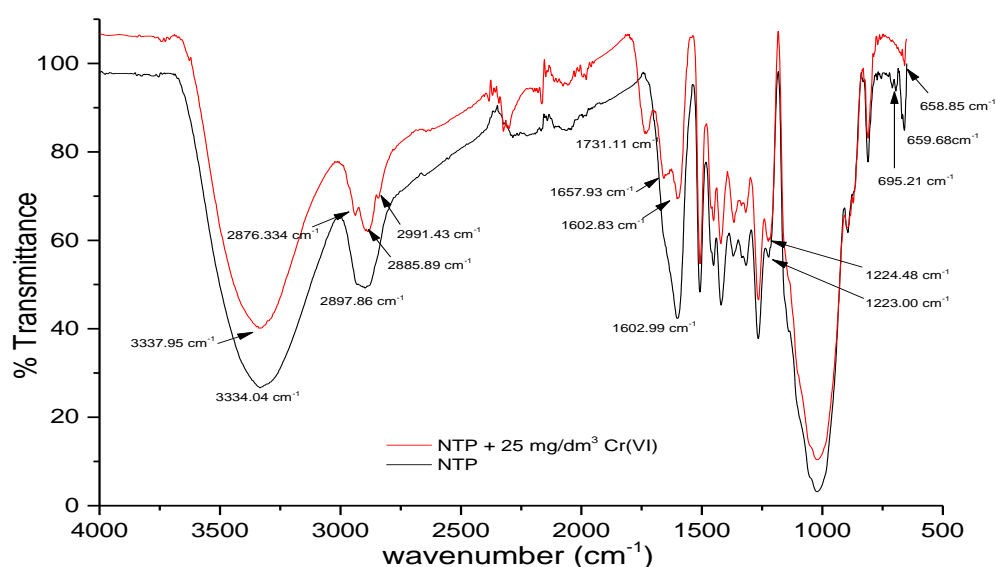


Figure 5.11: FTIR spectra of NTP before and after Cr(VI) adsorption

After Cr(VI) adsorption, changes in intensities and shift in the peaks position were noted. A broad hydroxyl peak at 3334.04 cm$^{-1}$ was found to have reduced in intensity and shifted to 3337.95 cm$^{-1}$. The aliphatic C-H group at 2897.86 cm$^{-1}$ was observed to have reduced in intensity and splitted into three small peaks, indicating that C-H group was lost in the reduction of Cr(VI) to Cr(III). A new peak appeared at 1730.11 cm$^{-1}$ which represent the C=O stretch of a lignin (Gupta and Nayak, 2012a). These show that the Cr(VI) biosorption onto NaOH treated pine cone led to the formation of carboxylic group on the surface which resulted from oxidation of C-OH group by Cr(VI) (Wang and Lee, 2011). The C-OH groups act as the reductant for Cr(VI) in solution. A sharp peak at 1602.99 cm$^{-1}$ was shown to have reduced and splitted into two peaks at 1602.83cm$^{-1}$ and 1657.93cm$^{-1}$. The peaks representing the O-H deformation of phenolic group at 1223.00 cm$^{-1}$ was found to have shifted slightly to 1224.48 cm$^{-1}$ and 658.85 cm$^{-1}$ splitted to 659.68 cm$^{-1}$ and 695.21 cm$^{-1}$ and reduced in intensity. The decrease in intensities of the peaks implies the loss of these groups on the biosorbent surface as a result of reaction of Cr(VI). The results also show that the functional groups with oxygen mainly the hydroxyl and carboxylate groups are the most probable site for Cr biosorption. Similar observations were reported by Sen et al (2012) when they used cork and heat-treated cork samples from quercus cerris and quercus suber for removal of chromium (VI) in aqueous environments. The author observed that lignin plays a significant role in adsorption of Cr(VI) onto both samples. Results are also in agreement with other studies which concluded that hydroxyl and carboxylate groups are the main functional groups amongst others for adsorption of Cr(VI) (Dong et al., 2011, Singha et al., 2011).

Fig.5.12 shows FTIR spectra of NTP-NC before and after Cr(VI) biosorption. The broad absorption peak at 3256.99 cm$^{-1}$ is due to unbounded -OH group, the peak representing the asymmetric and symmetric C-H stretching in the organic carbon chain at 2913.79 cm$^{-1}$ (Sukumar et al., 2014), the sharp peak at 1627.69 cm$^{-1}$ is attributed to the Fe-OH band (Xing et al., 2011). The peak at 1507.69 is indicative of the C=C vibration of aromatic lignin (Subramanian et al., 2005), the peak at 1264.77 cm$^{-1}$ and 1223.92 cm$^{-1}$ are indicative of O-H deformation of phenolic group (Subramanian et al., 2005). The peak at 1022 represent the C-O stretching of secondary alcohol in cellulose. The peak at 806. 86 cm$^{-1}$ is indicative of β-(1,4)-glycosidic linkage of cellulose. The presence of Fe$_3$O$_4$ could be demonstrated by the strong peak at 564 cm$^{-1}$ which is indicative of stretch vibrational mode of Fe-O bonds in the tetrahedral sites and the octahedral sites (Bastami and Entezari, 2012). The peaks revealed that magnetite has been successfully modified with pine cone.
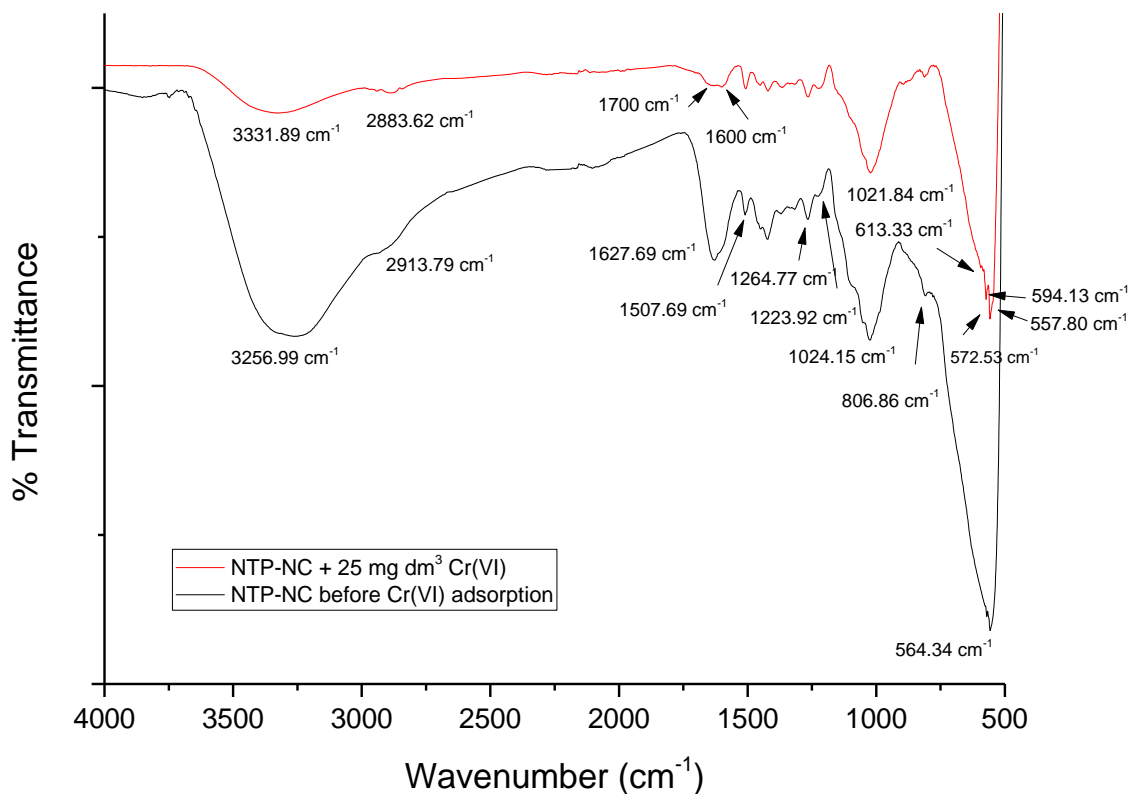
Figure 5.12. FTIR spectra of NTP-NC before and after Cr(VI) adsorption

After Cr (VI) biosorption, changes in functional groups were visible. Several peaks decreased in intensities and shifted. The broad hydroxyl group at 3256.99 cm$^{-1}$ decreased in intensity and shifted to 3331.89cm$^{-1}$. The aliphatic C-H group shifted from 2913.79 cm$^{-1}$ to 2883.62 cm$^{-1}$. The Fe-OH peak at 1627.69 cm$^{-1}$ reduced in intensity and splitted into two at 1600.13 cm$^{-1}$ and 1700 cm$^{-1}$. The peak at 564 cm$^{-1}$ was found to have splitted into four peaks at 557.80, 572.52, 594.13, and 613.33 cm$^{-1}$. This shift and splitting of the peak at 564 cm$^{-1}$ indicate that the deformation vibration of Fe-O was involved in the reduction of Cr(VI) to Cr(III) resulting in the conversion of magnetite to maghemite. The formation of maghemite prove the fact that Cr(VI) reduction reaction takes place on the surface of biosorbent nanomaterial and consumes all surface Fe(II) available, which oxidizes to Fe(III). The reduction in peak intensities and shifting in the peaks was due to the interaction of the hydroxyl group, carboxylate, Fe and Cr(VI) on the reduction of Cr(VI) to Cr(III).

*5.2.7.2  X-ray photoelectron spectroscopy (XPS) analysis after Cr(VI) adsorption*

XPS profiles of NTP before and after Cr(VI) adsorption and the Cr 2p core level before and after Cr(VI) adsorption are shown in Fig 5.13 a-c, while the XPS profile of NTP-NC before and after Cr(VI) adsorption, Fe 2p core level before and after Cr(VI) adsorption and Cr 2p core level before and after Cr(VI) adsorption are shown in Fig 5.14 a-d. Two new peaks emerged at binding energies of 575.8 and 582.5 eV for NTP and 575.5 and 585.6 eV for NTP-NC after Cr(VI) adsorption, which are characteristic peaks of Cr $2p_{3/2}$ and Cr $2p_{1/2}$, respectively. These peaks can be assigned to Cr(III) species (Moulder et al., 1992; Biesinger et al., 2011). Cr (VI) is characterized by higher binding energy than Cr(III) since hexavalent form draws electrons more strongly than the trivalent form (Park et al., 2007). Dambies et al. (2000) conducted XPS to study chemical interactions between Cr(VI) and chitosan from crab shells. The authors observed significant bands appearing at binding energies of 577.3 and 579.8 eV which can be attributed to Cr(III) and Cr(VI) after grinding the sample. The results indicate that toxic Cr(VI) was reduced to less toxic Cr(III) when NTP biosorbent and NTP-NC nanocomposite were in contact with 75 mg/dm$^3$ Cr(VI) solutions. Similar observation was made by Ren et al. (2016) in the adsorption of Cr(VI) onto amine cross linked biosorbent. The authors observed broad peaks at 576.2 eV and 585.9 eV which were characteristics of Cr $2p_{3/2}$ and Cr $2p_{½}$. Results implies that Cr bound to the surface of both NTP and NTP-NC were through trivalent form. Thus, the adsorption mechanism of Cr(VI) onto NTP and NTP-NC surface is suggested to be adsorption coupled reduction mechanism.
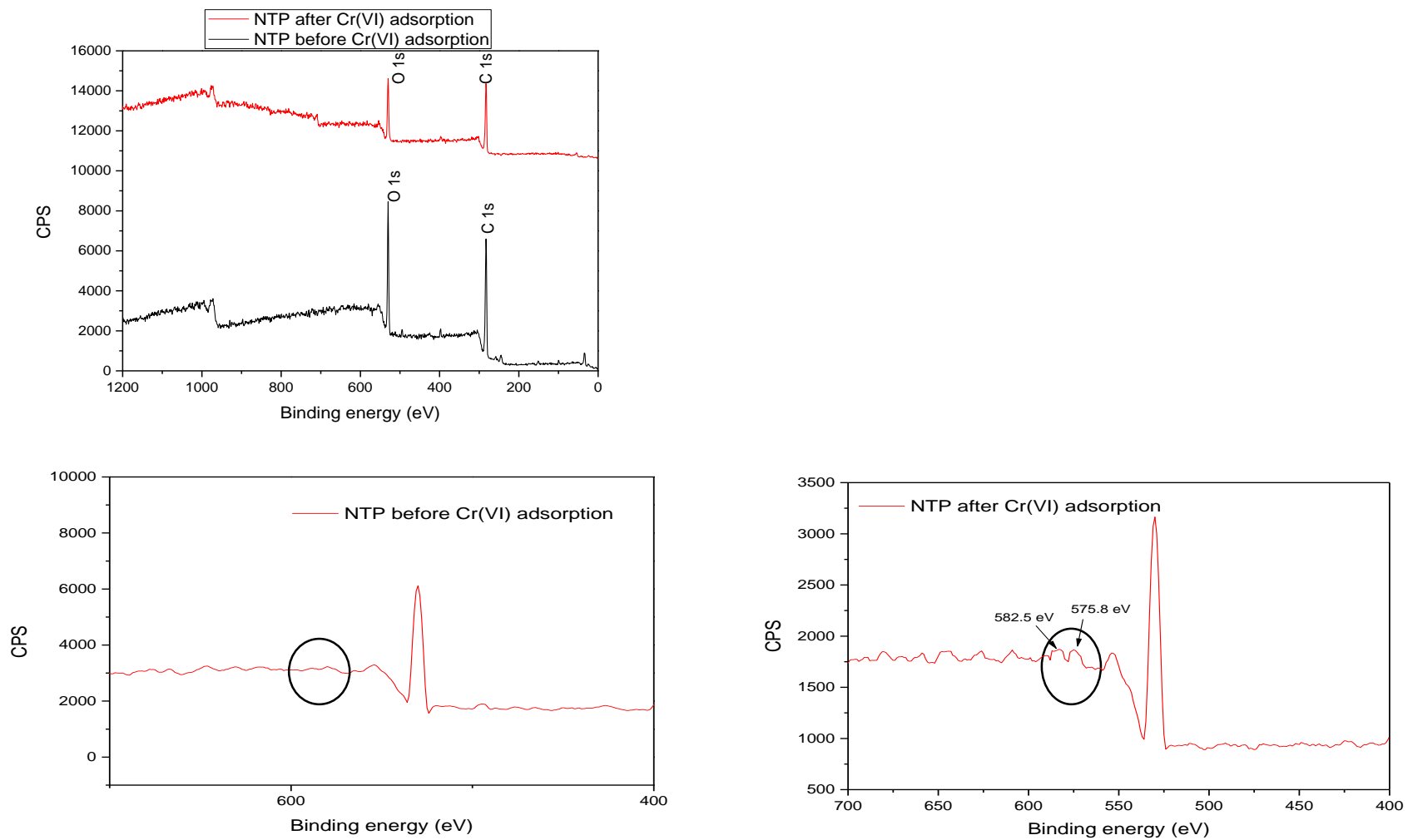
Figure 5.13: XPS profile of NTP biosorbent (a) Full spectra of NaOH treated pine cone before and after Cr(VI) adsorption, (b) Cr 2p core level before adsorption, (c) Cr 2p core level after adsorption.
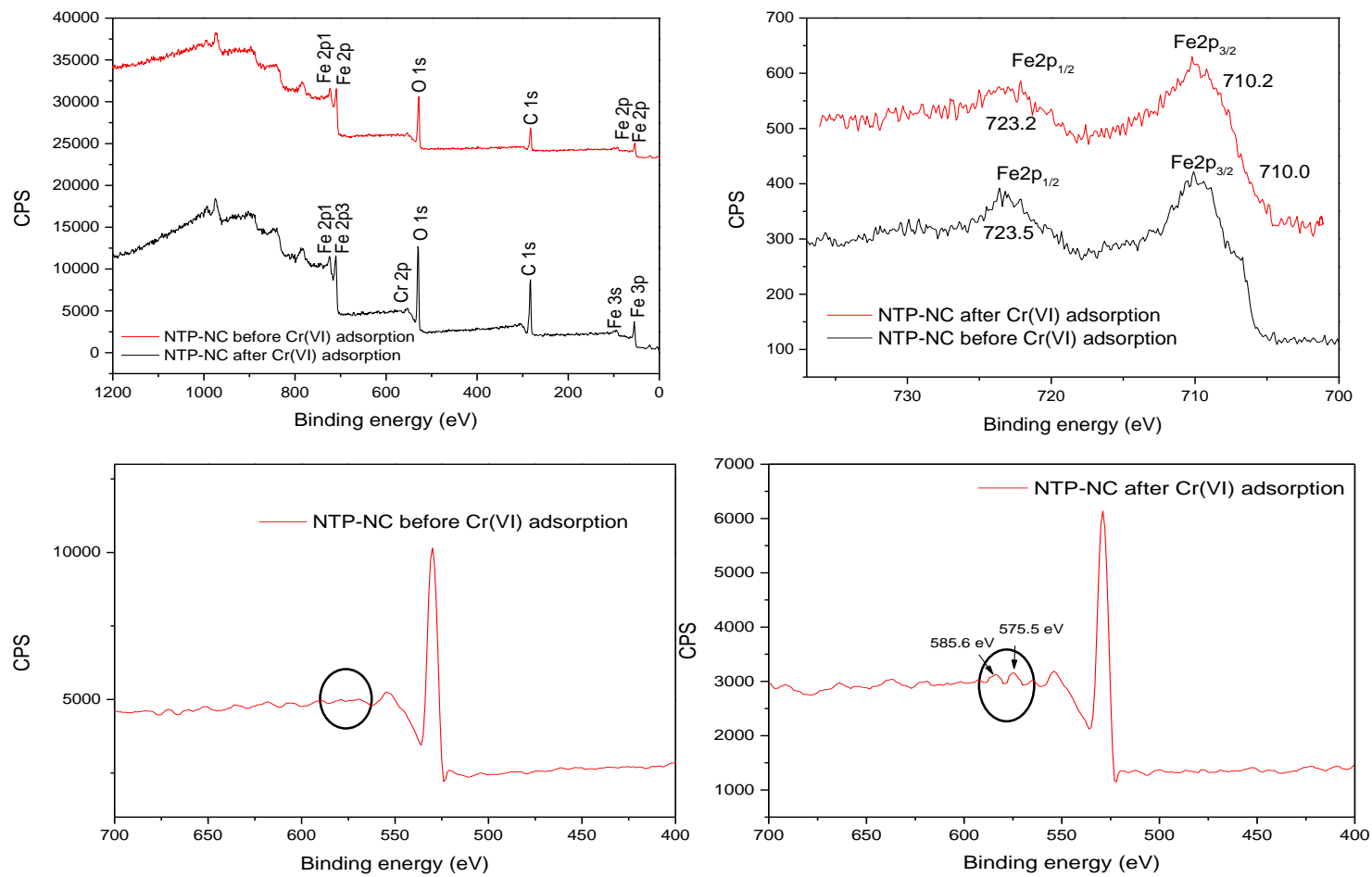
Figure 5.14: XPS profile of NTP-NC nanocomposite (a) Full spectra of NaOH treated pine cone-magnetite nanocomposite before and after Cr(VI) adsorption, (b) Fe 2p core levels before and after Cr(VI) removal, (c) Cr 2p core level before adsorption, (d) Cr 2p core level after adsorption.

### 5.2.8 Ionic strength effect

The effect of ionic strength on the uptake of Cr(VI) onto NTP and NTP-NC was performed using NaNO$_3$ in the concentration range of 0.01 to 0.2 mol/dm$^3$ and at solution pH 3. 6 and 8. The thickness of the electric double layer and the interface potential are known to be affected by ionic strength of the solution, which in turn determines the nature of the binding of adsorbent to adsorbate (Ajouyed et al., 2010). The results of the effect of ionic strength shown in Fig. 5.15 A and B reveal that the Cr(VI) adsorption capacity of both NTP and NTP-NC increased slightly with increase in ionic strength of the solution at all solution pH's. The reason for the slight increase in adsorption capacity may be due to compression of the electric double layer which neutralizes the repulsion between Cr(VI) and the adsorbent surface (Zhang et al., 2012). It was also observed that solution pH did not alter the effect of ionic strength on Cr(VI) uptake significantly, as the solution pH was increased from 3 to 8 the Cr(VI) capacity was only slightly reduced. These results therefore suggest that Cr(VI) interaction with NTP and NTP-NC may not be by electrostatic interaction or through outer-sphere complex formation, since outer-sphere complex formation occurs via electrostatic attraction (Cheng et al., 2016a). Therefore inner-sphere complex formation which proceeds via covalent bond formation is likely predominant in the adsorption process (Sun et al., 2014).

### 5.2.9 Effect of competing anions

Removal of Cr(VI) from natural and industrial wastewater is usually challenged by the co-existing anions present in the environment or effluents competing for adsorbent active sites. The effect of anion competing for NTP and NTP-NC adsorption sites was therefore determined by performing the adsorption experiments in the presence of naturally occurring anions in water such as $PO_4^{3-}$, $CO_3^{2-}$, $SO_4^{2-}$ and $Cl^-$ anions. The results of competition for adsorption sites between Cr(VI) and some selected anions on NTP and NTP-NC at different pH are shown in Fig. 5.16 a and b. The results reveal that $PO_4^{3-}$, $CO_3^{2-}$, $SO_4^{2-}$ anions in solution were able to reduce Cr(VI) capacity of both

 NTP and NTP-NC while $Cl^-$ anion increased the Cr(VI) capacity slightly. Several factors such as charge density, molecular dimension, degree of hydration, ionic radii and reactivity with

adsorbent surface have been known to control anion competition onto magnetic biomaterials (Duranoğlu et al., 2012). The order of reduction in Cr(VI) adsorption capacity amongst the competing anions in this study was $PO_4^{3-} > CO_3^{2-} > SO_4^{2-}$ for both NTP and NTP-NC at all solution pH. The order can be attributed to the charge densities of the anions as compared with $HCrO_4^-$. Since the charge densities of the competing anions are all higher than that of $HCrO_4^-$, they compete strongly with $HCrO_4^-$ for adsorption sites on NTP and NTP-NC and reduce the capacity in the order of their increasing charge density (Gheju et al., 2016). $PO_4^{3-}$ with the highest charge density, similar molecular dimension and ionic radii as $HCrO_4^-$ exhibits the most inhibitive effect (Qi et al., 2016). $CO_3^{2-}$ anion also exhibited a strong inhibitive effect of Cr(VI) adsorption which can be attributed to the consumption of some of the active sites on NTP-NC by $CO_3^{2-}$ anion forming siderite and/or (oxy)hydroxy carbonates of Fe(III)/Fe(II) on the adsorbent surface (Shang et al., 2017). $SO_4^{2-}$ anions also showed intense competition with $HCrO_4^-$ for NTP and NTP-NC active sites which can be attributed to high charge density, similar ionic radii and lower $pK_{a2}$ of $SO_4^{2-}$ over $HCrO_4^-$ anions (Álvarez-Ayuso et al., 2007). Only $Cl^-$ anion was observed to slightly increase the $HCrO_4^-$ uptake among the applied anions. Although $Cl^-$ and $HCrO_4^-$ have singular negative charge, the charge density of $Cl^-$ is higher than that of $HCrO_4^-$, but the smaller size of the ion gives $Cl^-$ a higher degree of hydration over $HCrO_4^-$ hence the carbon surface in NTPNC have higher selectivity for $HCrO_4^-$ over $Cl^-$ (Duranoğlu et al., 2012).
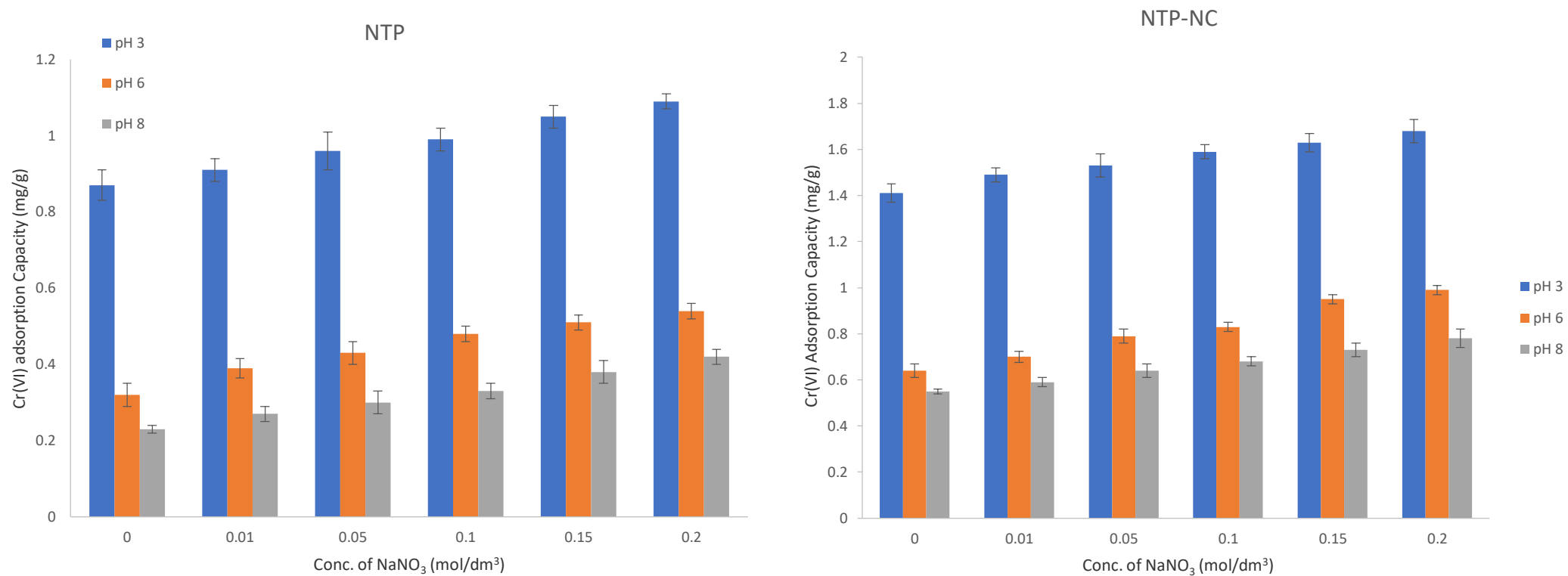
Figure 5.15: Effect of Ionic strength for Cr(VI) uptake onto (a) NTP and (b) NTP-NC
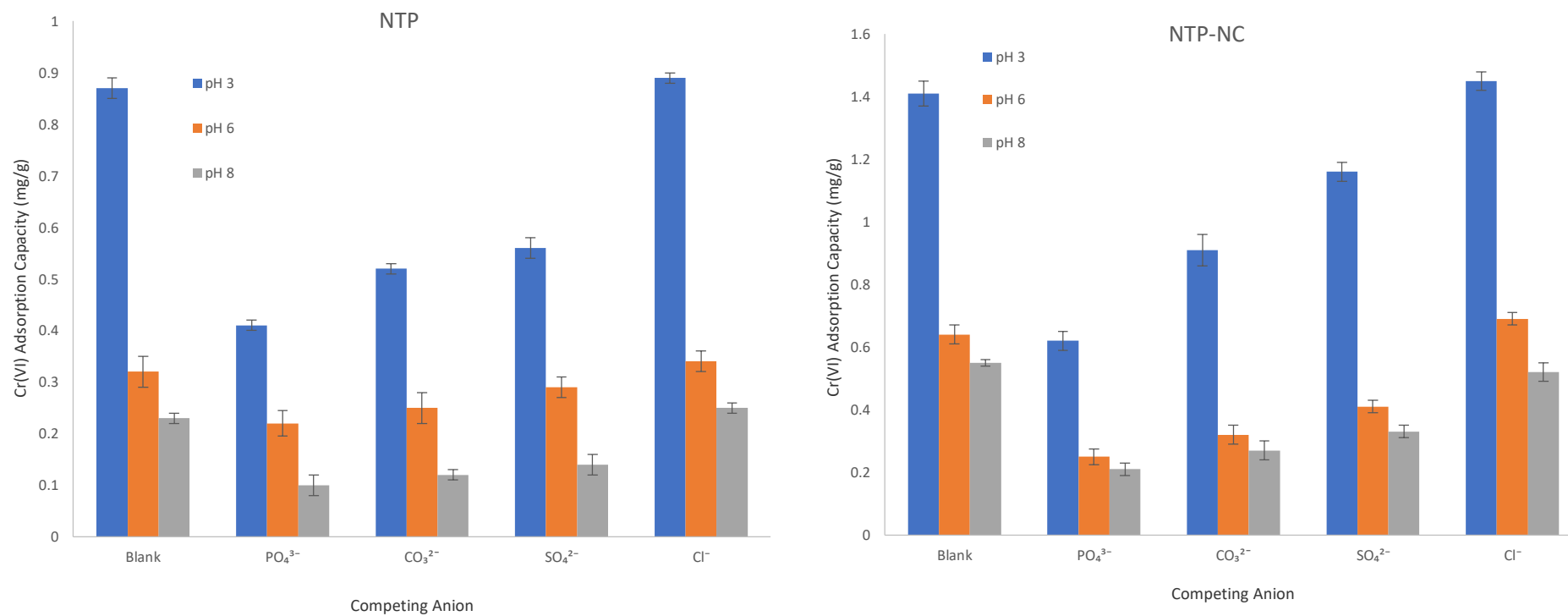
Figure 5.16: Effect of competing anions on Cr(VI) uptake onto NTP and NTP-NC

## 5.2.10 Desorption studies

To design and optimize a biosorption process for industrial application, it is important to elucidate the adsorption-desorption behavior of the biosorbent. A pollutant can be desorbed by a suitable desorbing solvent so that the biosorbent can be re-used in multiple adsorption-desorption cycles. To determine which eluate may efficiently desorb Cr(VI) and to evaluate the mechanism of biosorption process, desorption experiments were performed using 100 $cm^3$ of 0.5 mol $dm^{-3}$ of each of the desorbing solvents (HCl, NaOH, $CH_3COOH$) and $H_2O$. Fig 5.17 shows the percentage Cr(VI) desorbed using different desorbing solvents. From the results, it was observed that NaOH was the most efficient desorbing agent followed by acetic acid, HCl and water. The sample extracted with 0.5 mol/$dm^3$ of NaOH had the highest Cr(VI) desorption percentage of 51.27 % for NTP and 87.64 % for NTP-NC, followed by the sample extracted by acetic acid desorbing 16.67 % for NTP and 45.91 % for NTP-NC. HCl and $H_2O$ were less efficient with the lowest Cr(VI) desorption percentage of 1.76 and 1.19 % for NTP and 3.86 and 3.12 % for NTP-NC. Park et al. 2005 also observed that NaOH was more effective in desorbing Cr from the fungal biomass of *Aspergillus niger*. The results suggest that ion-exchange is the predominant and possible mechanism for Cr(VI) adsorption for both NTP and NTP-NC, followed by chemisorption while physical adsorption is not playing a significant role in Cr(VI) removal by both NTP and NTP-NC.
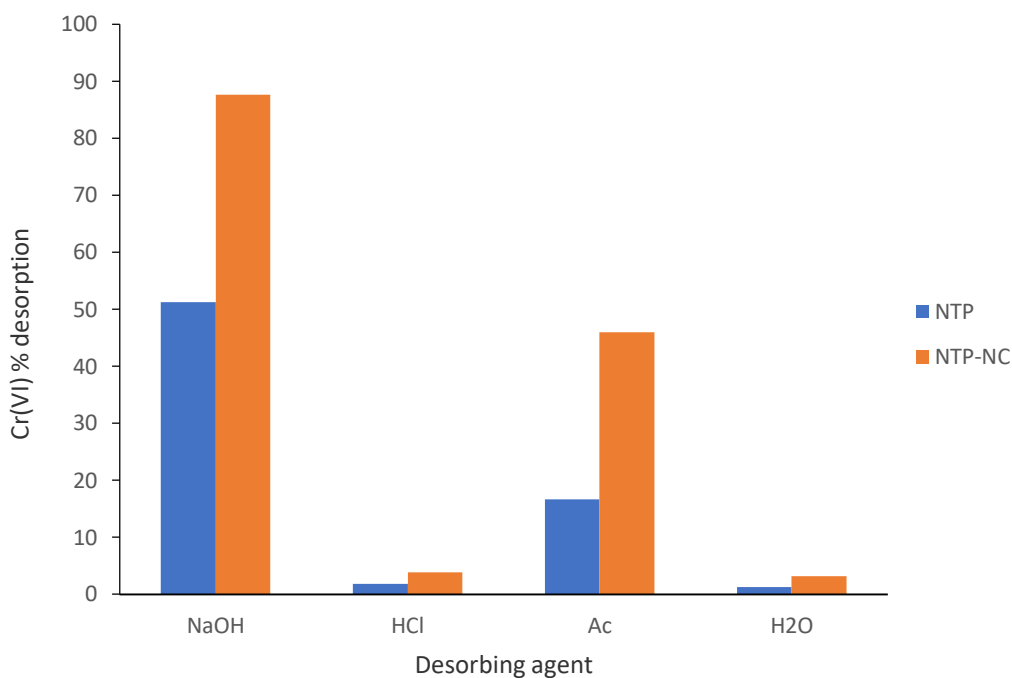
Figure 5.17: Desorption profile of Cr(VI) onto NTP and NTP-NC using different desorbing agents.


## 5.2.11 Regeneration

To determine the possibility of regeneration and reusability of NTP and NTP-NC as adsorbents, Cr(VI) adsorption-desorption cycle was repeated 4 times using NaOH as the desorbing solvent and the results are shown in Fig.5.18. Cr(VI) adsorption capacity was observed to be 15.75 mg/g for NTP and 17.97 mg/g for NTP-NC. Cr(VI) adsorption capacity reduced gradually from 15.75, to 15.11, 14.98 and 14.95 mg/g for NTP and from 19.97 to 17.45, 17.31 to 16.96 mg/g for NTP-NC after the fourth cycle. The adsorption capacity of both NTP and NTP-NC for Cr(VI) adsorption did not give a significant change during the repeated adsorption-desorption cycles indicating that both adsorbents could be applied repeatedly without any significant loss of its initial adsorption capacity. It was also observed that the adsorption capacity for NTP-NC was higher than NTP biosorbent for all cycles. The higher adsorption capacity and good reproducibility make the NTP-NC bio-composite a significant potential adsorbent for removal of Cr(VI) from aqueous solution.
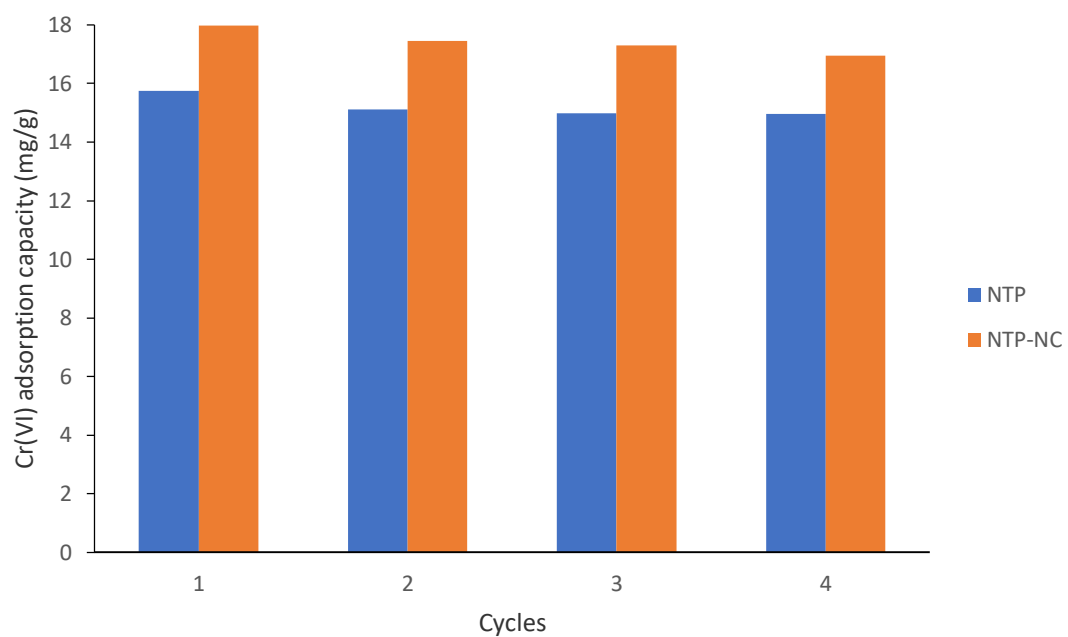
Figure 5.18: Recycling of NTP and NTP-NC after four cycles of adsorption/desorption

## 5.3   BATCH ADSORPTION STUDIES FOR ARSENIC

### 5.3.1   Effect of solution pH

The effect of solution pH on arsenic removal using NaOH treated pine cone and magnetite coated pine cone was examined over the solution pH range 1.0 to 10.0 using 0.1 $dm^3$ of As(III) solution with an initial concentration of 100 $mg/dm^3$, stirred at 200 rpm for 2 hours, and the results are shown in Fig.5.19. The results in Fig. 5.19 reveal that As(III) adsorption onto NTP-NC were higher than that of NTP and the variation of As(III) removal with pH were wider for NTP than for NTP-NC. In the range of pH 1 to 6, As(III) removal was observed to increase from 8.19 to 11.79 mg/g for NTP and from 15.07 to 23.60 mg/g for NTP-NC respectively. The highest values of As(III) capacities for both adsorbents were observed between pH 7 to 8 (the pH range for drinking water) which were 11.35 and 12.42 mg/g for NTP and 25.069 and 27.73 mg/g for NTP-NC respectively. Above pH 8, the As(III) capacities were observed to drop to 10.34 mg/g for NTP and 25.09 mg/g for NTP-NC.
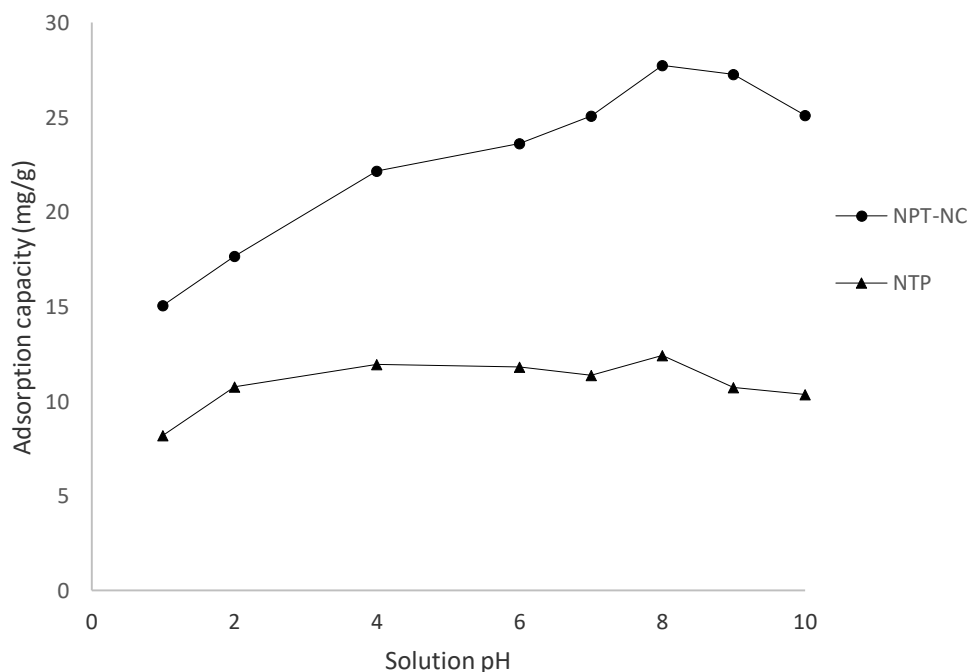


Figure 5.19: Effect of solution pH on the adsorption of arsenic using NaOH treated pine and magnetite coated pine cone biosorbents.

This may be explained by the arsenic speciation. It has been reported that the species of As(III) considered to be responsible for adsorption are $H_3AsO_3$ and $H_2AsO_3^-$ (Saleh et al., 2016). Between the pH range of 2 and 9, As(III) exists in the non-ionic form ($H_3AsO_3$), while at solution pH greater than 9, As(III) exists in the anionic form ($H_2AsO_3^-$) (Yadav et al., 2016). The As(III) speciation with the corresponding equilibrium constants can be expressed as follows (Xu et al., 2007):

$$H_3AsO_3 \leftrightarrow H_2AsO_3{}^- + H^+; pKa_1 = 9:23 \tag{5.18}$$

$$H_2AsO_3{}^- \leftrightarrow HAsO_3{}^{2-} + H^+; pKa_2 = 12:1 \tag{5.19}$$

$$HAsO_3{}^{2-} \leftrightarrow AsO_3{}^{3-} + H^+; pKa_1 = 12:7 \tag{5.20}$$

At low solution pH, there is an abundance of $H^+$ in solution which coordinates with lone pair of electrons on the oxygen of iron oxide in NTP-NC and also oxygenated groups on NTP to form positive charges $Fe-OH_2^+$ and $R-OH_2^+$, these groups cannot bind with non-ionic As(III) (Aryal et al., 2010). At solution pH between 7 and 8, the $H^+$ ions in solution is greatly reduced and groups such as $Fe-OH_2^+$ and $R-OH_2^+$ are deprotonated to form $Fe-OH$ and $R-OH$. $Fe-OH$ on magnetite can form both physical and ligand (ion) exchange (inner and outer sphere complexes) bonds with non-ionic As(III) (Vatutsina et al., 2007) while the hydroxyl functions on cellulose and hemicellulose form coordination bonds with non-ionic As(III) (Vinh et al., 2015). This will account for the higher adsorption of As(III) between pH 7 and 8. Finally, at solution pH above 9, $Fe-OH$ and $R-OH$ groups are totally deprotonated to form $Fe-O^-$ and $R-O^-$ which will electrostatically repel As(III) anions from the adsorbent surface leading to decrease in As(III) adsorption. Similar results were observed by Sansuri, et al. 2013 when using Fe-coated empty fruit bunch biochar and Fe-coated rice husk biochar as adsorbents for As(III) adsorption and Sahu et al. 2017 for the adsorption of As(III) and As(V) by cigarette soot activated carbon with $Fe_3O_4$ nanoparticles.

### 5.3.2 Effect of adsorbent dose

The effect of adsorbent dose on the uptake of As(III) onto NTP and NTP-NC was conducted from 0.05 to 1.5 g in a batch system maintained at optimum solution pH of 8 and the results are illustrated in Fig 5.20.a and b. From the graph, it was observed that the As(III) uptake percentages of NTP and NTP-NC increased with increasing adsorbent dose in the range of adsorbent doses considered. The As(III) uptake percentage were higher for NTP-NC than for NTP at any dose. The increase in As(III) uptake percentage can be attributed to increased adsorption sites as adsorbent dose is increased and the higher surface area imparted by magnetite in NTP-NC (Saleh et al., 2016). The observed increase in adsorption percentage from 0.05 to 1.5 g were 9.39 to 14.78 % for NTP and 18.456 to 96.75 % for NTP-NC respectively. At adsorbent dose, higher than 0.5 g, the percentage uptake increased only slightly and therefore 0.5 g was taken as the optimum dose when the adsorbents were contacted with 100 mg/dm$^3$ of As(III) solution at pH 8 for 2 hrs.

### 5.3.3 Kinetics studies - effect of concentration

#### 5.3.3.1 Kinetic modelling

5.3.3.1.1 Pseudo first and pseudo second order model

The effect of As(III) initial concentration on the uptake of As(III) from aqueous solution onto NTP and NTP-NC was studied by conducting batch kinetic experiments and plotting the kinetic data of the amount of As(III) adsorbed (mg/g) versus time (min). The kinetic data were then modelled according to the Lagergren's (1989) pseudo first-order and the Ho and Ofomaja (2006) pseudo second-order models expressed by Eqs. (5.6) and (5.9) respectively. In the model equations, the parameters $q_e$ (mg/g) are the maximum (equilibrium) capacities per gram of adsorbent and $k_1$ (min$^{-1}$) and $k_2$ (g/mg min) are the kinetic rate constants. The parameters obtained are presented in Table 5.7 a and b. Results from error determination for pseudo first-order shows a coefficient of determination, $r^2 > 0.988$ and % variable error < 34.08 for NTP and $r^2 > 0.987$ and % variable error < 65.13 for NTP-NC (Table 5.7a and b). For the pseudo second-order NTP had coefficient of determination, $r^2 > 0.996$ and % variable error < 5.70 and NTP-NC had $r^2 > 0.994$ and % variable error < 12.28 for NTP-NC (Table 5.7a and b).
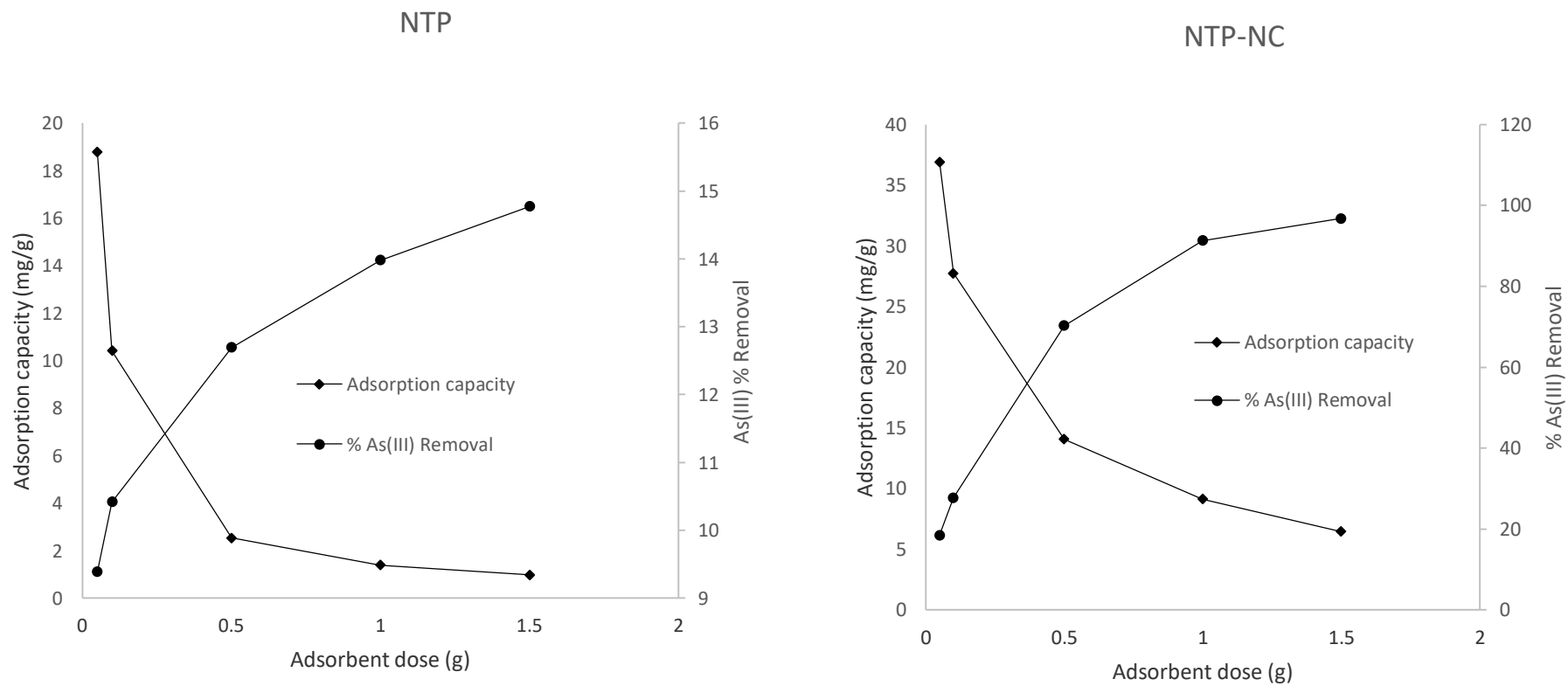
Figure 5.20: The effect of As(III) adsorbent dose for (a) NTP and (b) NTP-NC

Table 5.7 a: Kinetic data for As(III) adsorption onto NTP

| Kinetic model | 25 mg/dm$^3$ | 50 mg/dm$^3$ | 75 mg/dm$^3$ | 100 mg/dm$^3$ | 150 mg/dm$^3$ |
|---|---|---|---|---|---|
| NTP | | | | | |
| **Pseudo first-order** | | | | | |
| *Model q* (mg/g) | 1.97 | 4.13 | 5.89 | 9.19 | 13.06 |
| $k_1$ (min$^{-1}$) | 0.0409 | 0.0829 | 0.1286 | 0.2581 | 0.3460 |
| $r^2$ | 0.9941 | 0.9947 | 0.9927 | 0.9887 | 0.9872 |
| %Variable Error | 0.39 | 1.93 | 5.02 | 16.68 | 34.08 |
| | | | | | |
| **Pseudo second-order** | | | | | |
| *Model q* (mg/g) | 2.42 | 4.80 | 6.69 | 9.96 | 13.89 |
| $k_2$ (g mg/min) | 0.0176 | 0.0197 | 0.0219 | 0.0328 | 0.0347 |
| *h* (mg/g min) | 0.103 | 0.454 | 0.980 | 3.254 | 6.694 |
| $r^2$ | 0.9956 | 0.9994 | 0.9970 | 0.9961 | 0.9988 |
| Variable Error | 0.29 | 1.91 | 2.06 | 5.70 | 3.14 |

Table 5.7 b: Kinetic data for As(III) adsorption onto NTP-NC

| Kinetic model | 25 mg/dm$^3$ | 50 mg/dm$^3$ | 75 mg/dm$^3$ | 100 mg/dm$^3$ | 150 mg/dm$^3$ |
|---|---|---|---|---|---|
| NTP-NC | | | | | |
| **Pseudo-first order** | | | | | |
| *Model q* (mg/g) | 4.61 | 8.58 | 10.95 | 13.32 | 15.88 |
| $k_1$ (min$^{-1}$) | 0.0852 | 0.1847 | 0.2816 | 0.3689 | 0.5053 |
| $r^2$ | 0.9926 | 0.9899 | 0.9906 | 0.9943 | 0.9876 |
| % Variable Error | 3.22 | 12.74 | 19.50 | 15.97 | 65.13 |
| | | | | | |
| **Pseudo-second order** | | | | | |
| *Model q* (mg/g) | 5.35 | 8.99 | 11.81 | 11.81 | 16.74 |
| $k_2$ (g mg/min) | 0.0182 | 0.0246 | 0.0306 | 0.0363 | 0.0451 |
| *h* (mg/g min) | 0.521 | 1.948 | 4.268 | 7.278 | 12.638 |
| $r^2$ | 0.9939 | 0.9968 | 0.9976 | 0.9964 | 0.9979 |
| Variable Error | 2.67 | 3.91 | 5.04 | 12.28 | 7.52 |

These results reveal that both the pseudo-first and second-order models can describe the kinetic data but the pseudo second-order model can better describe the kinetic data. The fit of the kinetic models to the experimental data was also tested by plotting the predicted adsorption capacities for each model against the experimental data. Figs. 5.21 a and b shows the predicted adsorption capacities at different time intervals (at 150 mg/dm$^3$ As(III)) compared with the experimental data for pseudo first and second-order models. The results were shown to be in line with that predicted by the error measurement methods. Tables 5.7 a and b shows the kinetic model constants of the pseudo-first and second-order models for As(III) adsorption onto NTP and NTP-NC. The results indicate higher adsorption capacities for NTP-NC than for NTP at all initial concentrations. The As(III) adsorption capacities increased rapidly for both adsorbents at the beginning of the adsorption period up to the first 30 min and thereafter the rapid uptake reduced and became almost constant probably due to site saturation (Nashine and Tembhurkar, 2016). Increase in initial As(III) concentrations produced an increase in As(III) adsorption for both adsorbents. This suggests that As(III) adsorption may be driven by concentration driving force to the adsorbent surfaces (Vieira et al., 2017a). Higher pseudo second-order rate constants and initial adsorption rate were observed for NTP-NC than for NTP. This can be attributed to additional adsorption sites created by iron oxide on the adsorbent surface and the higher affinity of Iron oxide for As(III) interaction. He at al. (2018) observed a rapid increase in As adsorption rate and capacity in the adsorption of As onto biochar modified with magnetite nanoparticles, as compared with the native biochar. The authors, He et al. (2018), also noted that an increase in the % magnetite in the composite lead to increased adsorption rate and capacity which they attributed to adsorption sites on magnetite nanoparticles.

### 5.3.3.2   *Intraparticle model*

#### 5.3.3.2.1   Intraparticle diffusion

The rate determining step of many As(III,V) adsorption systems employing iron oxide modified adsorbents have been tested using the intraparticle diffusion model (Cheng et al., 2016b, Liu et al., 2018a). The intraparticle equation according to Weber and Morris (1963) is given in Eq.(5.11) and the intraparticle diffusion plots for the adsorption of As(III) onto NTP and NTP-NC are shown in Figs.5.22 a and b while the model parameters shown in Tables 5.8.a and b.
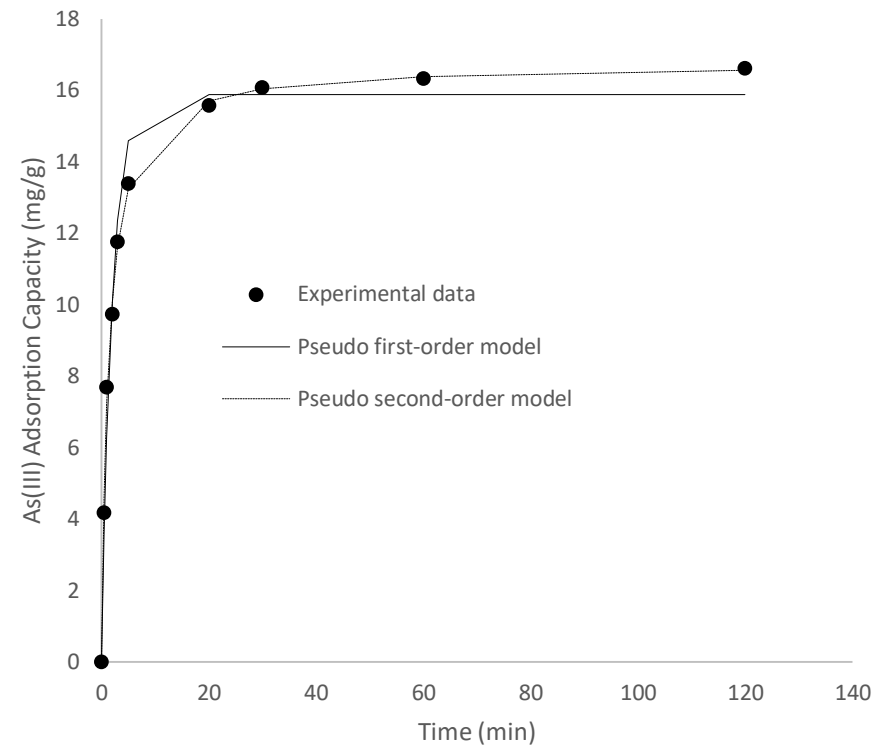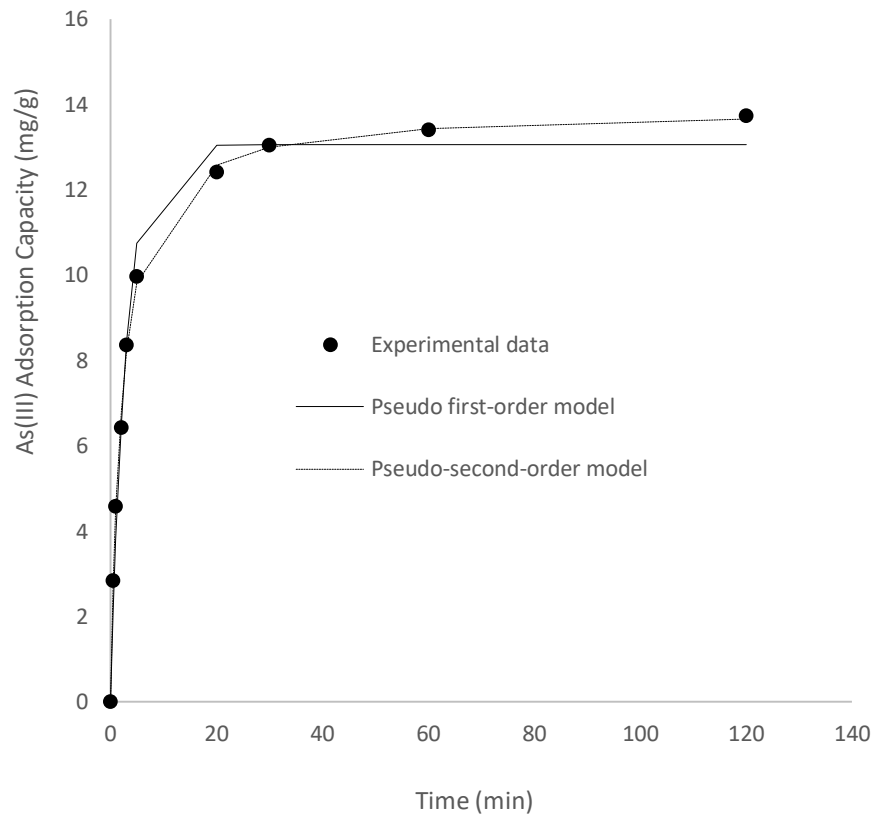
Figure 5.21: Kinetics models for As(III) adsorption using NTP and NTP-NC.

Figs.5.22 A and B shows that the adsorption profile for As(III) adsorption onto NTP and NTP-NC did not pass through the origin, indicating that intraparticle diffusion is not solely rate limiting but can be separated into two stages. The first initial rapid step represents external surface adsorption in which surface adsorption is rate-determining while the second almost horizontal step represents the adsorption equilibrium stage. Table 5.8A and B shows that the values of $k_i$ were higher for NTP-NC than for NTP and also the values of $k_i$ increased with increasing As(III) concentration for NTP but decreased with increasing As(III) concentration for NTP-NC. The higher $k_i$ values for NTP-NC can be attributed to the larger surface and higher number of active sites produced by the incorporation of magnetite nanoparticles on NTP. This then increases As(III) to penetrate into the adsorbent.

This explanation is supported by the higher pseudo second-order rate constant, initial sorption rate and higher adsorption capacity of NTP-NC over NTP. As As(III) concentration is increased from 25 to 150 mg/dm$^3$, the value of $k_i$ for NTP-NC was observed to reduce. The decrease in $k_i$ with increase in concentration can be due to (i) rapid uptake rate leading to exhaustion of adsorption sites within pores, (ii) the repulsion on magnetite due to surface saturation and (iii) rapid reduction of As(III) concentration in solution (Leone et al., 2018). On the other hand, the slower As(III) uptake rate onto NTP led to faster diffusion into pores which caused an increase in $k_i$ with increase in concentration in bulk solution. Iron oxide nanoparticles are known to have dominant external surfaces over internal surface and most of its adsorption sites are located on its external surface (Mejia-Santillan et al., 2018). Therefore, NTP-NC will have high magnitude of surface reactions and compared with NTP and as As(III) concentration increases in solution, the magnitude of surface reaction will increase

### 5.3.3.2.2  Pore and film diffusion

Because of the double nature of intra-particle diffusion which confirms the presence of both film and pore diffusion, in order to determine the actual rate determining step for As(III) adsorption onto NTP and NTP-NC bio-composite, kinetic data were further analyzed using the fractional uptake and Boyd model.
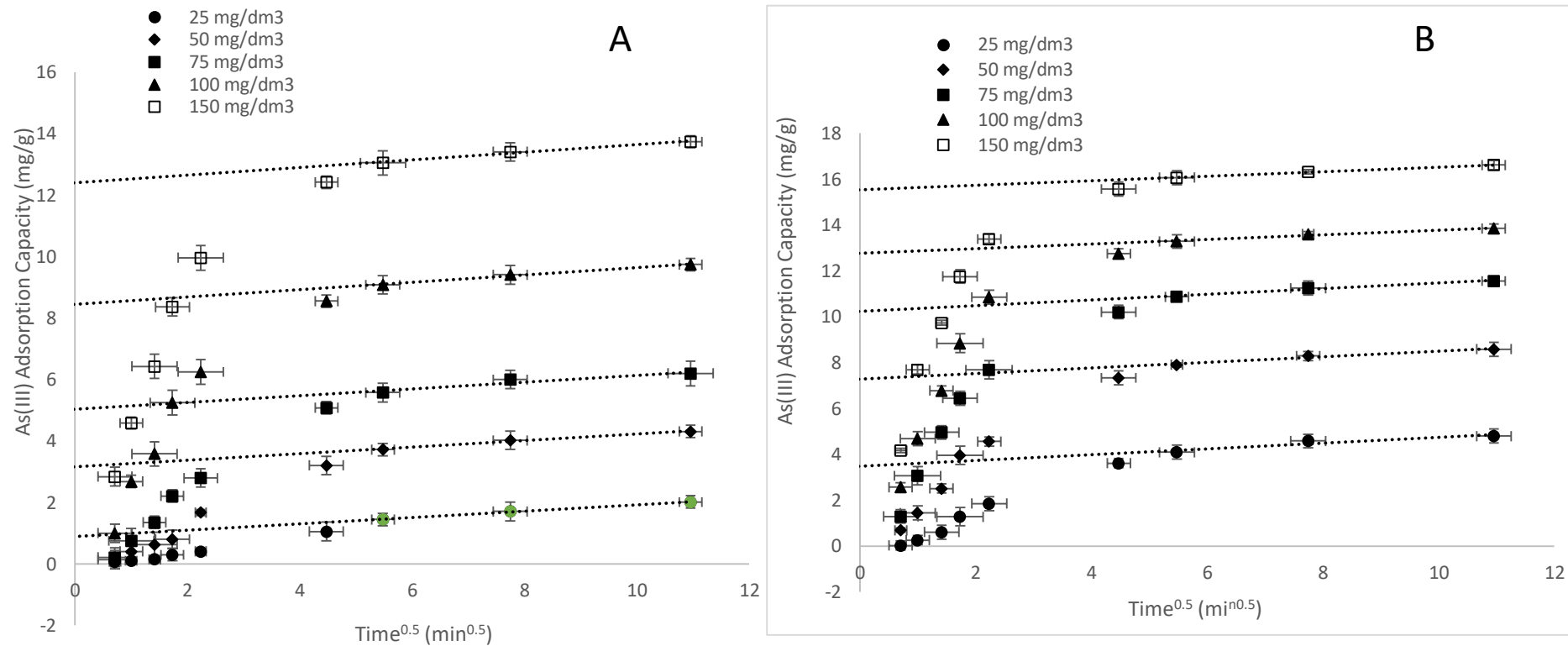
Figure 5.22: Intraparticle diffusion of As(III) adsorption onto (a) NTP and (b) NTP-NC at different concentration

Table 5.8 a: Intraparticle model data for As(III) adsorption onto NTP

| Kinetic model | 25 mg/dm$^3$ | 50 mg/dm$^3$ | 75 mg/dm$^3$ | 100 mg/dm$^3$ | 150 mg/dm$^3$ |
|---|---|---|---|---|---|
| NTP | | | | | |
| **Intraparticle Diffusion model** | | | | | |
| $k_i$ (mg g$^{-1}$ min$^{-0.5}$) | 0.1028 | 0.1065 | 0.1103 | 0.1187 | 0.1240 |
| $C$ | 0.896 | 3.160 | 5.036 | 8.453 | 12.396 |
| $r^2$ | 0.9975 | 0.9880 | 0.9119 | 0.9985 | 0.9841 |
| **Film Diffusion** | | | | | |
| $D_1$ (cm$^2$/s) | 1.43 x10$^{-14}$ | 1.63 x10$^{-14}$ | 1.72 x10$^{-14}$ | 1.82 x10$^{-14}$ | 1.93 x10$^{-14}$ |
| $r^2$ | 0.9932 | 0.9532 | 0.9632 | 0.9854 | 0.9125 |
| **Pore Diffusion** | | | | | |
| $D_2$ (cm$^2$/s) | 1.16 x10$^{-13}$ | 1.19 x10$^{-13}$ | 2.12 x10$^{-13}$ | 2.23 x10$^{-13}$ | 2.30 x10$^{-13}$ |
| $r^2$ | 0.9884 | 0.9124 | 0.9822 | 0.9425 | 0.93335 |

Table 5.8 b: Intraparticle model data for As(III) adsorption onto NTP-NC

| Kinetic model | 25 mg/dm$^3$ | 50 mg/dm$^3$ | 75 mg/dm$^3$ | 100 mg/dm$^3$ | 150 mg/dm$^3$ |
|---|---|---|---|---|---|
| NTP-NC | | | | | |
| **Intraparticle Diffusion model** | | | | | |
| $k_i$ (mg/ g min) | 0.1250 | 0.1242 | 0.1230 | 0.1021 | 0.0991 |
| $C$ | 3.481 | 7.245 | 10.233 | 12.758 | 15.529 |
| $r^2$ | 0.9043 | 0.9851 | 0.9964 | 0.9687 | 0.9981 |
| | | | | | |
| **Film Diffusion** | | | | | |
| $D_1$ (cm$^2$/s) | 2.22 x10$^{-14}$ | 2.26 x10$^{-14}$ | 2.33 x10$^{-14}$ | 2.35 x10$^{-14}$ | 2.36 x10$^{-14}$ |
| $r^2$ | 0.9477 | 0.9631 | 0.9278 | 0.9129 | 0.9099 |
| | | | | | |
| **Pore Diffusion** | | | | | |
| $D_2$ (cm$^2$/s) | 1.59 x10$^{-13}$ | 1.61 x10$^{-13}$ | 1.75 x10$^{-13}$ | 1.76 x10$^{-13}$ | 1.83 x10$^{-13}$ |
| $r^2$ | 0.9681 | 0.9294 | 0.9778 | 0.9394 | 0.9449 |

The fractional plots of $q_t/q_e$ against $t_{0.5}$ in Fig. 5.23 A and B for As(III) adsorption onto NTP and NTP-NC, show two sections in the curves. The plots show the initial rapid stage followed by a slow uptake with time. The film diffusion coefficient ($D_1$) values for both the NTP and NTP-NC bio-composite different initial concentrations of As(III) were calculated from the gradient of the plots of $q_t/q_e$ against $t_{0.5}$ and the values are presented in Table 5.8 a and b, respectively.

The $Bt$ values at different contact times were calculated using the Eq.(5.17) and the calculated $Bt$ values were plotted against time $t$ as shown in Fig.5.24 A and B. The plots from Fig. 5.24 a and b were observed to be linear but did not pass through the origin, confirming that external mass transport mainly governs the sorption process for the studies initial concentrations. The calculated values of the film diffusion coefficients, $D_1$, were observed to increase from $1.43 \times 10^{-14}$ to $1.9 \times 10^{-14}$ cm$^2$/s for NTP and from $2.22 \times 10^{-14}$ to $2.36 \times 10^{-14}$ cm$^2$/s for NTP-NC with increase in initial concentration. The pore diffusion coefficients, $D_2$ were also seen to increase from $1.16 \times 10^{-13}$ to $2.30 \times 10^{-13}$ cm$^2$/s for NTP and from $1.59 \times 10^{-13}$ to $1.83 \times 10^{-13}$ cm$^2$/s for NTP-NC as the initial concentration was increased from 25 to 150 mg/dm$^3$. Both the film and pore diffusion coefficient increased with increase in initial concentration of As(III) for both NTP and NTP-NC, due to the increase in concentration gradient between the bulk solution and biosorbents surface. NTP-NC bio-composite was seen to have higher film diffusion coefficients than NTP suggesting that surface modification enhanced diffusion across the boundary. Pore diffusion coefficient values for NTP-NC on the other hand, were seen to be higher than values for NTP biosorbent only at lower concentration (25 and 50 mg/dm$^3$) and lower as initial concentration increases from 75 to 150 mg/dm$^3$ concentrations. Higher pore diffusion coefficient, $D_2$, values were observed for both NTP and NTP-NC suggesting that pore diffusion controls the adsorption process.
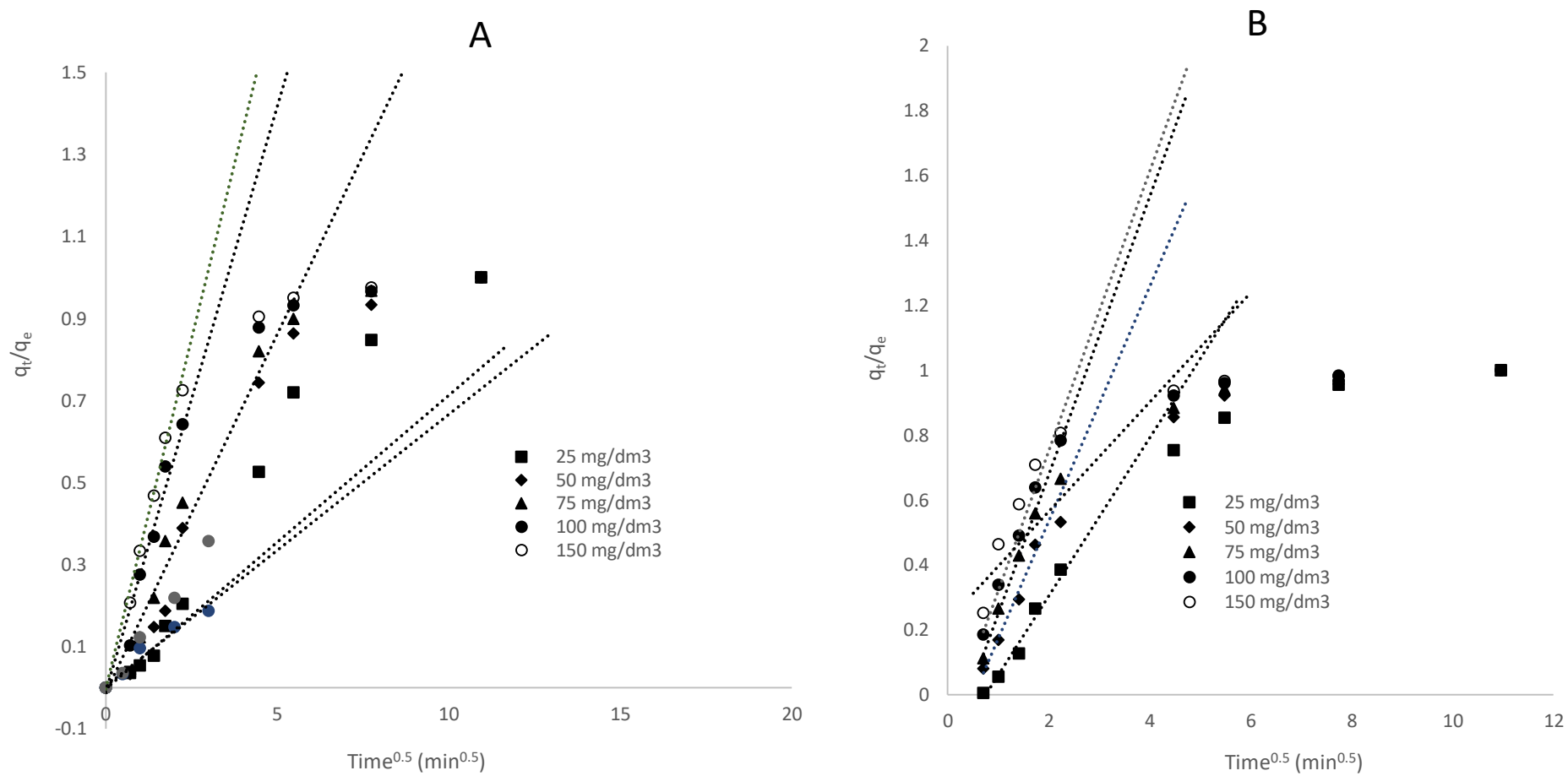
Figure 5.23: Fractional uptake of As(III) adsorption onto (A) NTP and (B) NTP-NC at different concentrations.
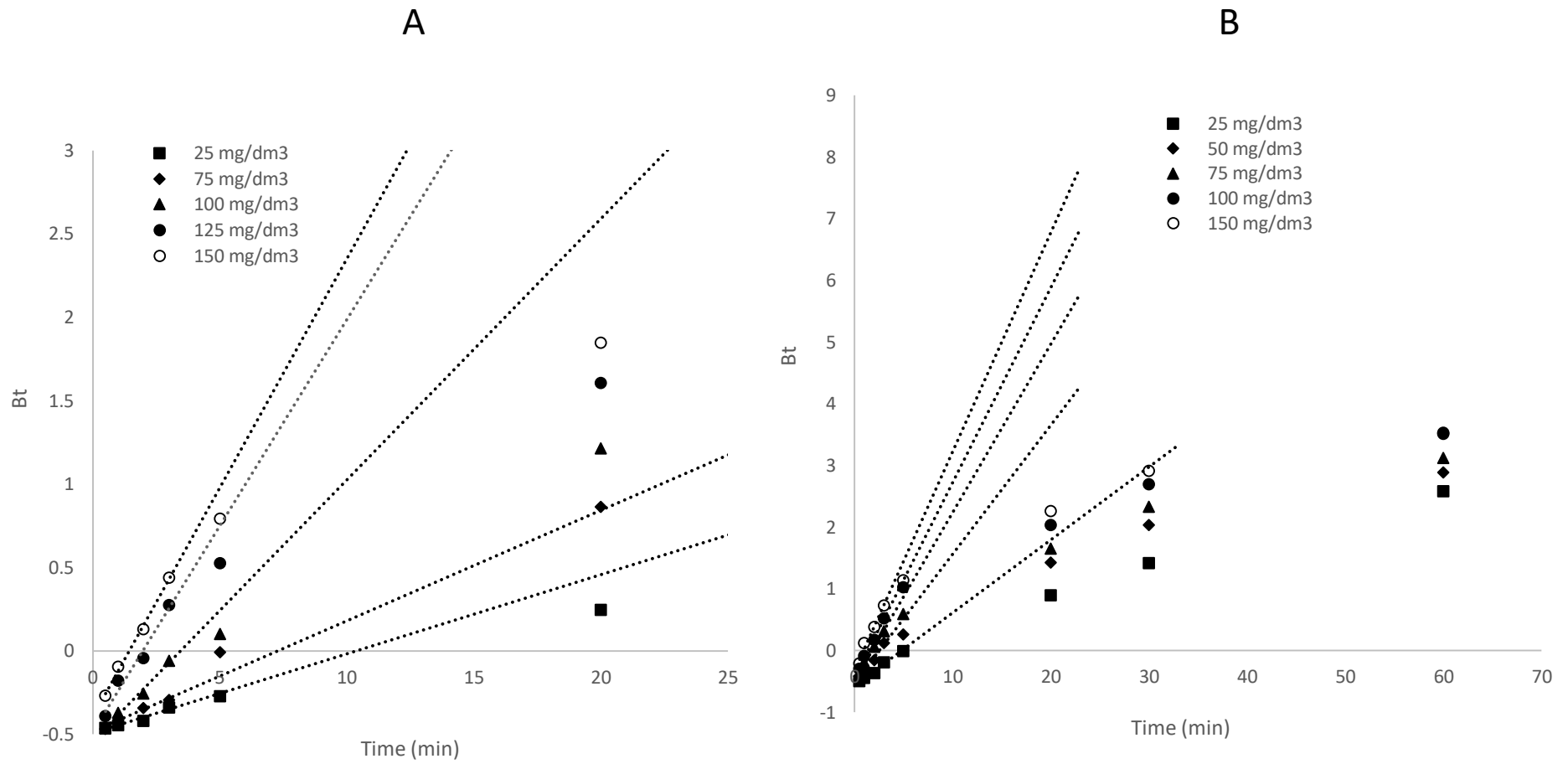
Figure 5.24: Boyd plot for As(III) adsorption onto (A) NTP and (B) NTP-NC at different concentration.

### 5.3.4  Kinetics studies - Effect of temperature

#### 5.3.4.1  *Kinetic modelling*

##### 5.3.4.1.1  Pseudo first and pseudo second order kinetic models

The kinetics of As(III) adsorption onto NTP and NTP-NC was performed at different temperatures and modelled using the non-linear forms of the pseudo first and pseudo-second order kinetic models: The results in Table 5.9 a and b shows the error determination as measured by correlation coefficient, $r^2$ and % variable error for As(III) adsorption onto NTP and NTP-NC bio-composite. Error measurements for pseudo first-order model were $r^2 > 0.953$ and % variable error $< 248$ for NTP and $r^2 > 0.95$ and % variable error $< 290$ for NTP-NC, while for pseudo second-order, $r^2 > 0.995$ and % variable error $< 24.76$ for NTP and $r^2 > 0.996$ and % variable error $< 25$ for NTP-NC were observed. These results indicate that the pseudo-second order model describes the adsorption of As(III) better than the pseudo first order model for both NTP and NTP-NC.  The pseudo-second-order rate constant, $k_2$ and initial sorption rates, $h$ were observed to increase with an increase in temperature from 299 to 319 K for both NTP and NTP-NC. The increase in As(III) capacity, pseudo second-order rate and initial sorption rate constant with temperature can be attributed to increased mobility of As(III) ions in solution with increasing temperature and the larger surface area (Karthick et al., 2017). Increasing temperature may produce a swelling effect within the internal structure of the NTP enabling As(III) ions to penetrate through. Increasing the temperature would also decrease the viscosity of the solution which enhanced the rate of diffusion of the As(III) ions across the external boundary layer of the NTP resulting in higher biosorption efficiency (Nassar, 2010).

Table 5.9 a: Kinetic data for As(III) adsorption onto NTP

| Kinetic model | 299 K | 304 K | 309 K | 313 K | 319 K |
|---|---|---|---|---|---|
| **PCP** | | | | | |
| **Pseudo first-order** | | | | | |
| *Model q* (mg/g) | 13.06 | 14.38 | 16.83 | 18.88 | 20.58 |
| $k_1$ (min$^{-1}$) | 0.3460 | 0.4057 | 0.5138 | 0.6675 | 0.8975 |
| $r^2$ | 0.9872 | 0.9654 | 0.9598 | 0.9572 | 0.9535 |
| %Variable Error | 34.08 | 102.73 | 155.76 | 200.85 | 248.45 |
| | | | | | |
| **Pseudo second-order** | | | | | |
| *Model q* (mg/g) | 13.89 | 15.15 | 17.66 | 19.83 | 21.66 |
| $k_2$ (g/mg min) | 0.0347 | 0.0405 | 0.0461 | 0.0545 | 0.0672 |
| $h$ (mg/g min) | 6.694 | 9.296 | 14.377 | 21.431 | 31.527 |
| $r^2$ | 0.9988 | 0.9938 | 0.9919 | 0.9943 | 0.9954 |
| %Variable Error | 3.14 | 18.47 | 31.51 | 26.43 | 24.76 |

Table 5.9 b: Kinetic data for As(III) adsorption onto NTP-NC

| Kinetic model | 299 K | 304 K | 309 K | 313 K | 319 K |
|---|---|---|---|---|---|
| **NTP-NC** | | | | | |
| **Pseudo first-order** | | | | | |
| *Model q* (mg/g) | 15.58 | 18.63 | 21.76 | 23.39 | 25.68 |
| $k_1$ (min$^{-1}$) | 0.5013 | 0.6362 | 0.8636 | 0.0932 | 1.2957 |
| $r^2$ | 0.9822 | 0.9506 | 0.9672 | 0.9573 | 0.9654 |
| % Variable Error | 65.13 | 99.64 | 217.35 | 290.33 | 278.88 |
| | | | | | |
| **Pseudo second-order** | | | | | |
| *Model q* (mg/g) | 16.74 | 19.58 | 22.33 | 24.62 | 27.01 |
| $k_2$ (g/mg min) | 0.0451 | 0.0512 | 0.0636 | 0.0726 | 0.0789 |
| $h$ (mg/g min) | 12.638 | 19.629 | 31.713 | 44.006 | 57.561 |
| $r^2$ | 0.9975 | 0.9964 | 0.9962 | 0.9966 | 0.9979 |
| Variable Error | 7.52 | 16.58 | 24.63 | 25.19 | 16.69 |

## 5.3.4.1.2  Activation energy

The increase in As(III) capacity with temperature also suggests that the adsorption process is endothermic. Since the relationship between the pseudo second-order rate constant, $k_2$ and reaction temperature was linear, $k_2$ was then plotted as a function of temperature using the Arrhenius expression (eq 5.20). The activation energy was then obtained from the slope of the plot of $\ln(k_2)$ versus $1/T$. The plot was observed to be linear with $r^2$ of 0.9922 and activation energy of 26.24 kJ/mol for NTP and $r^2$ of 0.9922 and activation energy of 23.78 kJ/mol for NTP-NC. The rate limiting step of a heterogeneous reaction can be chemical reaction at the surface or diffusion of the reactant (Lien and Zhang, 2007). Surface controlled reactions in solutions have activation energies that are greater than 29 kJ/mol while diffusion-controlled reactions have lower activation energies between 8 to 21 kJ/mol (Cheng et al., 1997). The results show activation energy to be between 21 and 29 kJ/mol, meaning the rate-limiting step for NTP and NTP-NC is complex, a mixture between surface and diffusion control. The activation energies of NTP-NC were closer to diffusion controlled (23.78 kJ/mol).

## 5.3.4.2   Diffusion modelling

## 5.3.4.2.1  Intraparticle diffusion

Intraparticle plot of $q_t$ versus $t^{0.5}$ in Fig 5.25 a and b was rapid at the initial rapid stage followed by slower stage at which adsorption was almost constant. The straight line did not pass through the origin, indicating that intraparticle diffusion was not solely rate-limiting. The nature of the intraparticle diffusion plots suggests that both film and particle diffusion influences As(II) adsorption (Banerjee and Chattopadhyaya, 2017). The values of $k_i$ and $C$ were obtained from the slope and the intercept of the linear plot of $q$ versus $t^{0.5}$ (Fig. 5.25 A and B) and are shown in Table 5.10 a and b. The value of $k_i$ was observed to increase from 0.1240 mg g$^{-1}$ min$^{-0.5}$ to 0.1411 mg g$^{-1}$ min$^{-0.5}$ as temperature rise from 299 to 319 K for NTP and decrease from 0.0969 mg g$^{-1}$ min$^{-0.5}$ to 0.0689 mg g$^{-1}$ min$^{-0.5}$ for NTP-NC.
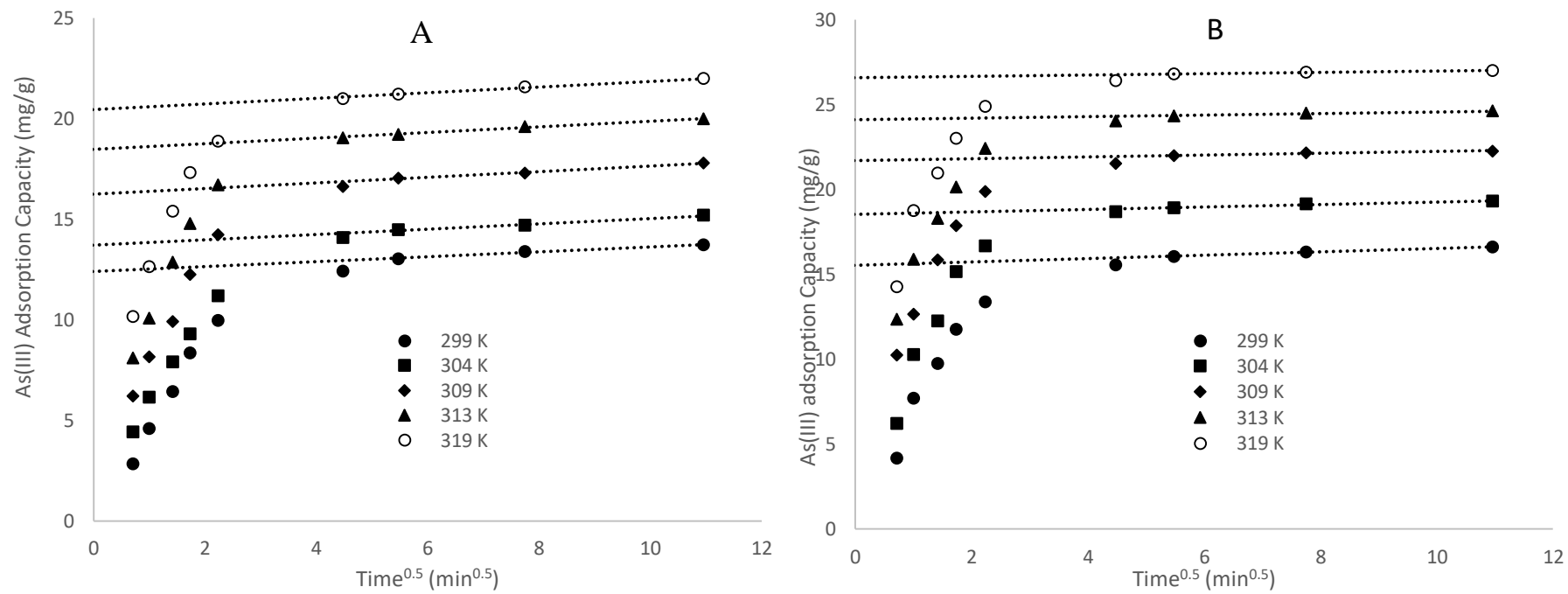
Figure 5.25: Intraparticle diffusion of As(III) adsorption onto (A) NTP and (B) NTP-NC

Table 5.10 a: Intraparticle model data for As(III) adsorption onto NTP

| Kinetic model | 299 K | 304 K | 309 K | 313 K | 319 K |
|---|---|---|---|---|---|
| **NTP** | | | | | |
| **Intraparticle Diffusion model** | | | | | |
| $K_p$ (mg g$^{-1}$ min$^{-0.5}$) | 0.1240 | 0.1327 | 0.1395 | 0.1406 | 0.1411 |
| $C$ | 12.396 | 13.723 | 16.251 | 18.476 | 20.449 |
| $r^2$ | 0.9841 | 0.9905 | 0.9957 | 0.9914 | 0.9958 |
| **Film Diffusion** | | | | | |
| $D_1$ (cm$^2$/s) | 1.43 x10$^{-14}$ | 1.57 x10$^{-14}$ | 1.74 x10$^{-14}$ | 1.90 x10$^{-14}$ | 1.96 x10$^{-14}$ |
| $r^2$ | 0.9932 | 0.9864 | 0.9929 | 0.9909 | 0.9751 |
| **Pore Diffusion** | | | | | |
| $D_2$ (cm$^2$/s) | 1.66 x10$^{-13}$ | 1.60 x10$^{-13}$ | 1.47 x10$^{-13}$ | 1.43 x10$^{-13}$ | 1.37 x10$^{-13}$ |
| $r^2$ | 0.9884 | 0.9908 | 0.9938 | 0.9853 | 0.9669 |

Table 5.10 b: Intraparticle model data for As(III) adsorption onto NTP-NC

| Kinetic model | 299 K | 304 K | 309 K | 313 K | 319 K |
|---|---|---|---|---|---|
| **NTP-NC** | | | | | |
| **Intraparticle Diffusion model** | | | | | |
| $k_i$ (mg g$^{-1}$ min$^{-0.5}$) | 0.0998 | 0.0719 | 0.0518 | 0.0704 | 0.0689 |
| $C$ | 15.529 | 18.542 | 21.720 | 23.960 | 26.357 |
| $r^2$ | 0.9981 | 0.9715 | 0.9286 | 0.9997 | 0.9997 |
| | | | | | |
| **Film Diffusion** | | | | | |
| $D_1$ (cm$^2$/s) | 2.22 x10$^{-14}$ | 2.32 x10$^{-14}$ | 2.38 x10$^{-14}$ | 2.41 x10$^{-14}$ | 2.48 x10$^{-14}$ |
| $r^2$ | 0.9477 | 0.9422 | 0.9776 | 0.9650 | 0.9304 |
| | | | | | |
| **Pore Diffusion** | | | | | |
| $D_2$ (cm$^2$/s) | 1.59 x10$^{-13}$ | 1.57 x10$^{-13}$ | 1.43 x10$^{-13}$ | 1.36 x10$^{-13}$ | 1.32 x10$^{-13}$ |
| $r^2$ | 0.9681 | 0.9949 | 0.9938 | 0.9918 | 0.9783 |

The increasing values of $k_i$ with temperature have been reported to be attributed to increased mobility of As(III) into the inner structure of pine cone biosorbent (Ofomaja et al., 2010a). On the other hand, the decreasing value of $k_i$ with temperature for NTP-NC is attributed to rapid surface reaction with increasing temperature (Hao et al., 2014). The magnitude of the constant, $C$ increased with temperature for both NTP and NTP-NC suggesting greater participation of surface adsorption and activation of adsorption sites with increase in temperature.

### 5.3.4.3   Film and Pore diffusion

According to (Mittal et al., 2007), the participation of film diffusion is greater when external transport becomes greater than internal transport and pore diffusion participates more when internal diffusion is greater than external diffusion. To evaluate the extent of the participation of film and pore diffusion in the adsorption process, fractional uptake and Boyd plot were conducted. The plots of fractional uptake of As(III) onto NTP and NTP-NC versus $t^{0.5}$ are shown in Fig. 5.26a and b, respectively. The plot can be separated into two sections which are the initial rapid period and a slow and almost constant stage which is similar to the intraparticle diffusion profile. The values of the film diffusion constant, $D_1$ at different temperatures were then calculated from the slope of the plot of $q_t/q_e$ versus time and recorded in Table 5.10 a and b.

The value of $Bt$ at different temperatures was calculated from Eq.(5.17) and plotted against $t$ for the different temperatures to identify if the rate of As(III) adsorption onto NTP and NTP-NC is controlled by external or pore diffusion. The plots in Fig. 5.27 did not pass through the origin suggesting that external mass transfer is rate-limiting at the initial stages of the adsorption process. The lines were close to the intercept suggesting greater participation of external mass transfer at the initial stage of adsorption. The values of $B$ at different temperatures was calculated from the slope of the plot of $B_t$ versus t and the pore diffusion coefficient, $D_2$ determined using Eq.(5.18).
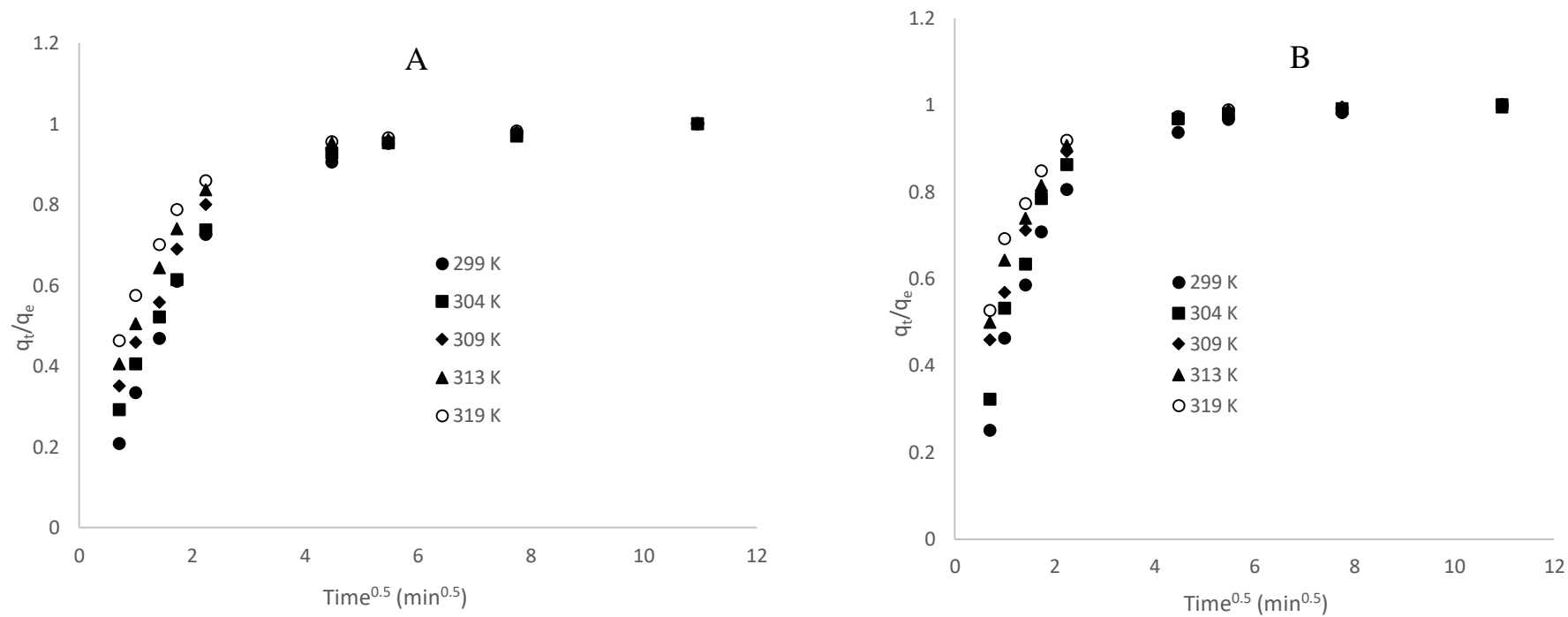
Figure 5.26: Fractional uptake of As(III) onto (A) NTP and (B) NTP-NC versus $t^{0.5}$ at different temperature.

The calculated values of film diffusion, $D_1$ and pore diffusion, $D_2$ coefficients for NTP and NTP-NC at different temperatures are shown in Table 5.10 a and b, respectively. The results show that the coefficient of film diffusion, $D_1$ increased from 1.43 x10$^{-14}$ to 1.96 x10$^{-14}$ cm$^2$/s for NTP and from 2.22 x10$^{-14}$ to 2.48 x10$^{-14}$ cm$^2$/s NTP-NC with increasing temperature. The increase in $D_1$ with temperature can be attributed to increase in the mobility of As(III) ions due to retarding forces acting on the As(III) diffusion (Banerjee and Chattopadhyaya, 2017). Santra and Sarkar. 2016 also observed an increase in $D_1$ with temperature in the adsorption of As onto cerium oxide loaded cellulose nanoparticle beads. The values of pore diffusion coefficients $D_2$ also shown in Tables 5.10 a and b, respectively, were found to reduce with increasing temperature from 1.66 x10$^{-13}$ to 1.37 x10$^{-13}$ cm$^2$/s for NTP and from 1.59 x10$^{-13}$ to 1.32 x10$^{-13}$ cm$^2$/s for NTP-NC. The reduction of $D_2$ with temperature can be attributed to increased surface reaction as temperature is increased. Though the pore diffusion coefficient values were observed to reduce with temperature, they were seen to be higher than the film diffusion coefficients.
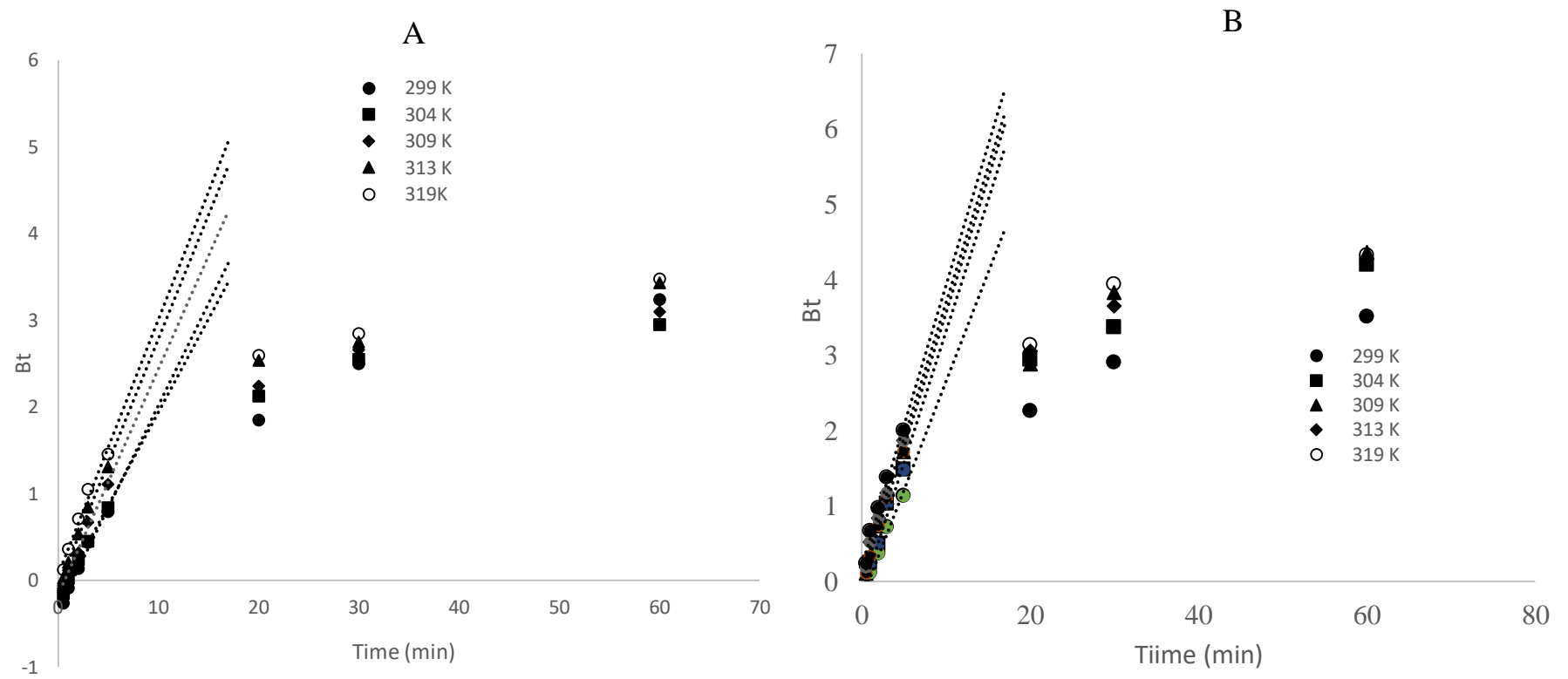
Figure 5.27: Boyd plot for As(III) adsorption onto (A) NTP and (B) NTP-NC at different temperature.

### 5.3.5    Equilibrium isotherm of As(III) adsorption

The adsorption type and the description of the relationship between the adsorbate in solution and that on the adsorbent surface were obtained using three isotherm models, Langmuir, Freundlich, and Dubinin-Radushkevish isotherm models. Tables 5.11 a and b shows results for error analysis and isotherm constants for the isotherms applied at different temperatures in this study. It was observed that the Langmuir isotherm had coefficient of determination, $r^2$ values > 0.999 and percentage variable < 7.44 and Freundlich isotherm had $r^2$ > 0.920 and percentage variable < 665.09 for As(III) adsorption onto NTP. Langmuir isotherm for NTP-NC had coefficient of determination, $r^2$ values > 0.996 and percentage variable < 41.15, while Freundlich isotherm had $r^2$ > 0.908 and percentage variable < 1042.88. These results suggest that the Langmuir isotherm model provided better fitting of the experimental data than the Freundlich isotherm for As(III) adsorption onto both NTP and NTP-NC at all temperatures. This implies that the adsorption of As(III) onto NTP and NTP-NC follows monolayer adsorption of As(III) on the adsorption sites on the adsorbent surfaces. A plot of experimental data and equilibrium model capacities versus equilibrium concentration at 319 K were made to compare the fit of the predicted data to the experimental data and is shown in Figs. 5.28 A and B. The results in Figs. 5.28 A and B confirms the better fitting of the Langmuir isotherm model to the experimental data suggesting that the incorporation of magnetite to NTP provided increased number of sites for reaction to take place.

The magnitude of $K_a$, is determined largely by the heat of adsorption, high $K_a$ values indicates high heat of adsorption and therefore stronger bonds formed (Ofomaja et al., 2010). From the results, it was observed that $K_a$ values for NTP-NC were all higher than for NTP and the values for $K_a$ increased with increasing solution temperature. These results indicate that the bonding between NTP-NC and As(III) were stronger than those found between NTP and As(III). The adsorption type between As(III) and the various adsorbents was determined by applying the D-R isotherm. The coefficient of correlation, $r^2$ > 0.99 and the percentage variable error < 50.33 shows that the isotherm model described the experimental data to a reasonable extent. The calculated values for the isotherm constants can be seen in Tables 5.11 A and B. The saturation capacities were observed to be higher for NTP-NC than for NTP and both increased with increasing solution temperatures. The values of adsorption energies were higher for NTP than for NTP-NC and both reduced with increasing solution temperatures.

Table 5.11 a: Equilibrium data for As(III) adsorption onto NTP

| Isotherm model | 299 K | 303 K | 309 K | 313 K | 319 K |
|---|---|---|---|---|---|
| **NTP** | | | | | |
| **Langmuir** | | | | | |
| $q$ (mg/g) | 14.83 | 16.44 | 19.75 | 20.79 | 22.33 |
| $K_a$ (dm$^3$/mg) | 0.1025 | 0.2217 | 0.3238 | 0.5114 | 0.8745 |
| $r^2$ | 0.9997 | 0.9988 | 0.9993 | 0.9990 | 0.9991 |
| % Variable Error | 0.93 | 4.93 | 3.82 | 7.05 | 7.44 |
| | | | | | |
| **Freundlich** | | | | | |
| $n$ | 3.28 | 4.07 | 4.17 | 4.38 | 4.73 |
| $K_F (mg/g)(dm^3/mg)^{1/n}$ | 3.661 | 5.762 | 7.280 | 8.870 | 10.777 |
| $r^2$ | 0.9711 | 0.9493 | 0.9440 | 0.9323 | 0.9208 |
| % Variable Error | 85.21 | 210.80 | 332.80 | 480.29 | 665.09 |
| | | | | | |
| **Dubinin–Radushkevich** | | | | | |
| $q_s$ (mol/g) | $2.01 \times 10^{-4}$ | $2.89 \times 10^{-4}$ | $3.10 \times 10^{-4}$ | $2.77 \times 10^{-4}$ | $3.42 \times 10^{-4}$ |
| $\beta$ (mol$^2$/J$^2$) | $3.62 \times 10^{-9}$ | $2.59 \times 10^{-9}$ | $2,86 \times 10^{-9}$ | $2.66 \times 10^{-9}$ | $2.40 \times 10^{-9}$ |
| $E$ (kJ/mol) | 11.7 | 13.0 | 13.2 | 13.7 | 14.4 |
| $r^2$ | 0.9962 | 0.9965 | 0.9972 | 0.9966 | 0.9977 |
| % Variable Error | 9.36 | 8.88 | 9.35 | 8.44 | 7.98 |

Table 5.11 b: Equilibrium data for As(III) adsorption onto NTP-NC

| Isotherm model | 299 K | 303 K | 309 K | 313 K | 319 K |
|---|---|---|---|---|---|
| **NTP-NC** | | | | | |
| **Langmuir** | | | | | |
| $q$ (mg/g) | 18.02 | 20.53 | 22.11 | 24.04 | 26.98 |
| $K_a$ (dm$^3$/mg) | 0.1845 | 0.3587 | 0.6382 | 0.8881 | 1.6673 |
| $r^2$ | 0.9991 | 0.9960 | 0.9991 | 0.9992 | 0.9964 |
| % Variable Error | 4.21 | 26.99 | 7.18 | 7.66 | 41.15 |
| | | | | | |
| **Freundlich** | | | | | |
| $n$ | 3.57 | 4.01 | 4.28 | 4.40 | 4.49 |
| $K_F (mg / g)(dm^3 / mg)^{1/n}$ | 5.508 | 7.840 | 9.763 | 11.435 | 14.730 |
| $r^2$ | 0.9591 | 0.9372 | 0.9466 | 0.9227 | 0.9089 |
| % Variable Error | 195.82 | 419.07 | 434.56 | 729.52 | 1042.88 |
| | | | | | |
| **Dubinin–Radushkevich** | | | | | |
| $q_s$ (mol/g) | $2.54 \times 10^{-4}$ | $2.89 \times 10^{-4}$ | $3.39 \times 10^{-4}$ | $3.63 \times 10^{-4}$ | $3.74 \times 10^{-4}$ |
| $\beta$ (mol$^2$/J$^2$) | $3.31 \times 10^{-9}$ | $2.88 \times 10^{-9}$ | $2.42 \times 10^{-9}$ | $2.33 \times 10^{-9}$ | $2.14 \times 10^{-9}$ |
| $E$ (kJ/mol) | 12.13 | 13.30 | 14.40 | 14.60 | 15.30 |
| $r^2$ | 0.9987 | 0.9980 | 0.9979 | 0.9985 | 0.9981 |
| % Variable Error | 7.76 | 7.68 | 7.88 | 8.07 | 8.55 |
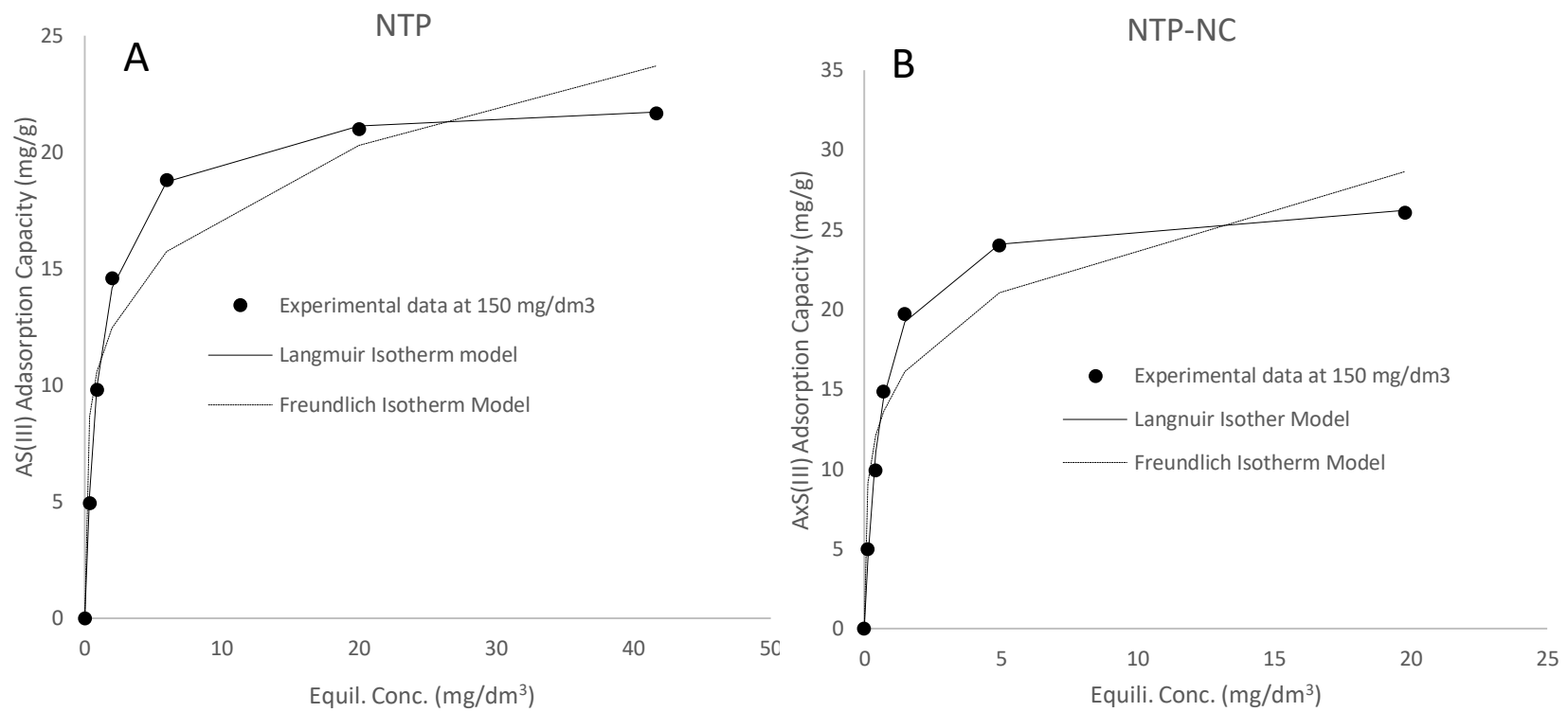
Figure 5.28: Comparison of predicted Equilibrium model data with experimental data for (A) NTP and (B) NTP-NC.

Finally, the mean free energy of adsorption, $E$, were higher for NTP-NC than for NTP and both increased with increasing solution temperatures. The values of $E$ were found to be between 11.7 to 14.4 kJ/mol for NTP and between 12.13 to 15.30 kJ/mol for NTP-NC indicating that the adsorption process was ion-exchange for As(III) adsorption onto both adsorbents and the ion-exchange was stronger for NTP-NC than for NTP. Several studies have also shown the As(III) adsorption onto other magnetic materials followed ion-exchange process (Hu et al., 2017, Huo et al., 2018, Saleh et al., 2016). A comparison of monolayer adsorption capacities of NTP and NTP-NC with other adsorbents for As(III) is shown in Table 5.12 and both adsorbents seem to be comparable with other adsorbents applied for As(III) removal.

Table 5.12: Comparison of As(III) adsorption capacity onto different adsorbents

| Adsorbents | Conc. (mg/dm$^3$) | pH | Dose | Adsorption capacity | Reference |
|---|---|---|---|---|---|
| Saccharum officinarum bagasse | 50 -500 µg/dm$^3$ | 7 | 1.5 g/dm$^3$ | 1.20 mg/g | Gupta et al., 2015 |
| *Azadirachta indica* (neem) bark powder | 50 – 500 µg/dm$^3$ | 7 | 1.5 g/dm$^3$ | 0.17 mg/g | Roy et al., 2017 |
| Sugarcane Bagasse | 50 -75 mg/dm$^3$ | 7 | 1.5 g/dm$^3$ | 11.90 mg/g | Tajernia et al., 2014 |
| *Hydrilla verticilata* | 100 µg/dm$^3$ | 7 | 1.5 g/dm$^3$ | 11.65 mg/g | Nigam et al., 2013 |
| Raw pine cone biochar | 100 µg/dm$^3$ | 4 | 5.0 g/dm$^3$ | 0.0075 mg/g | Vinh et al., 2015 |
| NTP | 25 -150 mg/dm$^3$ | 8 | 5.0 g/dm$^3$ | 9.74 mg/g | This study |
| | | | | | |
| Magnetic Wheat Straw | 1 – 28 mg/dm$^3$ | 8 | 5.0 g/dm$^3$ | 3.90 mg/g | Tian et al., 2011 |
| Iron/Olivine composite | 1-10 mg/dm$^3$ | 7 | 3.0 g/dm$^3$ | 2.83 mg/g | Ghosal et al., 2018 |
| Fe(III)-treated Staphylococcus xylosus | 10 – 300 mg/dm$^3$ | 7 | 3.0 g/dm$^3$ | 5.93 mg/g | Aryal et a., 2010 |
| Iron oxide coated seed | 1 – 40 mg/dm$^3$ | 7 | 10.0 g/dm$^3$ | 4.00 mg/g | Vieira et al., 2017 |
| Magnetite-Reduced Graphene Oxide | 3 – 7 mg/dm$^3$ | 7 | 0.2 g/dm$^3$ | 13.01 mg/g | Chandra et al., 2010 |
| NTP-NC | 25 -150 mg/dm$^3$ | 8 | 5.0 g/dm$^3$ | 13.86 mg/g | This study |

## 5.3.6 Thermodynamics of As(III) adsorption onto NTP and NTP-NC

The thermodynamics of As(III) adsorption onto NTP and NTP-NC space was determined using the expressions. The calculated values of free energy, $\Delta G$, ranged from -22.2 to -29.7 kJ/mol for NTP and between -23.7 to -31.1 kJ/mol for NTP-NC with increasing solution temperature respectively (Table 5.13). The results show that the values of $\Delta G$ for both samples were negative at all temperatures indicating the thermodynamic feasibility and spontaneous nature of the adsorption. The feasibility of the adsorption process was also found to be higher for NTP-NC than for NTP meaning that the adsorptive forces for NTP-NC are stronger than those of NTP to overcome the potential barrier. The values of $\Delta H$ for NTP and NTP-NC were calculated to be 81.34 and 84.27 kJ/mol suggesting that the adsorption process is endothermic in nature at the reaction temperatures investigated. The values of $\Delta S$ for NTP and NTP-NC were calculated to be 347.19 and 361.57 J/mol K indicating a release of orderly structured hydration water and increase in the randomness at the solid/solution interface during the adsorption process (Meng et al., 2017a).

## 5.3.7 Adsorption mechanism

Several results obtained from these experiments points to the probable mechanism of As(III) adsorption onto NTP and NTP-NC. These results include (1) the higher As(III) removal capacity at solution pH of 8 at which both the predominant arsenic species and the surface charge on the adsorbent were close or actually neutral, (2) the value of the Dubinin-Radushkevish mean free Energy, $E$ which was in the range of 8 and 16 kJ/mol. Therefore, to confirm this mechanism, (i) the FTIR spectra before and after As(III) adsorption, (ii) XPS before and after As(III) adsorption, (iii) point zero charge before and after As(III) adsorption and the displacement of adsorbed nitrate ions on NTP-NC were performed.

Table 5.13: Thermodynamics parameters of As(III) adsorption onto NTP and NTP-NC

| Adsorbent | Temperature (K) | $\Delta G$ (kJ/mol) | $\Delta H$ (kJ/mol) | $\Delta S$ (J/mol K) |
|---|---|---|---|---|
| NTP | 299 | -22.2 | | |
| | 301 | -24.6 | | |
| | 309 | -25.9 | 81.34 | 347.19 |
| | 314 | -27.6 | | |
| | 319 | -29.7 | | |
| NTP-NC | 299 | -23.7 | | |
| | 301 | -25.8 | | |
| | 309 | -27.7 | 84.27 | 361.57 |
| | 314 | -29.0 | | |
| | 319 | -31.1 | | |

### 5.3.7.1  FTIR before and after As(III) adsorption

FTIR spectrum of NTP before and after As(III) adsorption in Fig.5.29 a. shows shifting, increase and reduction of several peaks. The asymmetrical stretching vibration at 3330 cm$^{-1}$ was observed to have slightly increased in intensity and shifted to 3328 cm$^{-1}$. The C-O-C stretching of alcohols and carboxylic acids at 1021 cm$^{-1}$ and the aliphatic acid group due to deformation vibration of C=O at 1263 cm$^{-1}$ were observed to have reduced in intensity and shifted to 1004 and 1268 cm$^{-1}$, respectively. A peak representing As-O stretching at 809 cm$^{-1}$ was observed to have slightly shifted to 811 cm$^{-1}$ after As(III) adsorption (Meng et al., 2017a). The results indicated that the carbonyl and hydroxyl groups on PCP biomaterial were mainly involved in the adsorption of As(III) and ion-exchange may be the possible biosorption mechanism that took place. Similar results were reported by Sari et al. (2009) for As(III) and As(V) biosorption from aqueous solution by macrofungus (*Inonotus hispidus)* biomass.

Fig.5.29 b shows the FTIR spectra of NTP-NC before and after As(III) adsorption. The spectrum shows peaks at 3338, 2881, 1633, 1598, and 1052 cm$^{-1}$ representing hydrogen bond stretching of α-cellulose, methylene -CH$_3$, -CH$_2$-, of cellulose (Subramanian et al., 2005) and C=O, C-O, C-O-C in lignin (Gupta and Nayak, 2012a). The peaks at 1027, 548 and 477 cm$^{-1}$ are attributed to Fe-O and Fe-OH (Reza and Ahmaruzzaman, 2015b) groups in NTP-NC. After As(III) adsorption, reduction and shift in peak intensities were observed for -OH stretching of α-cellulose from 3338 to 3289 cm$^{-1}$, the C-O-C and Fe-O from 1052 and 1027 to 1021 and 1000 cm$^{-1}$ and Fe-OH peak from 477 to 448 cm$^{-1}$. The shift in peak at 812 to 814 cm$^{-1}$ have been attributed to the formation of As-O bond (Meng et al., 2017b). Several authors have concluded that this shift in peaks of oxygenated groups and especially to the peak at 814 cm$^{-1}$ accounts for the formation of As-O bonds (Meng et al., 2017b, Venkatesan and Narayanan, 2018).

### 5.3.7.2  XPS analysis before and after As(III) adsorption

Further investigation on the chemical state of elements present in the NTP and NTP-NC materials and for elucidation of the As(III) binding mechanism onto the NTP and NTP-NC can be analysed by XPS analysis. The XPS analysis of NTP and NTP-NC before and after As(III) adsorption was performed and results shown in Fig. 5.30 a-f and Fig 5.31a-h, respectively.
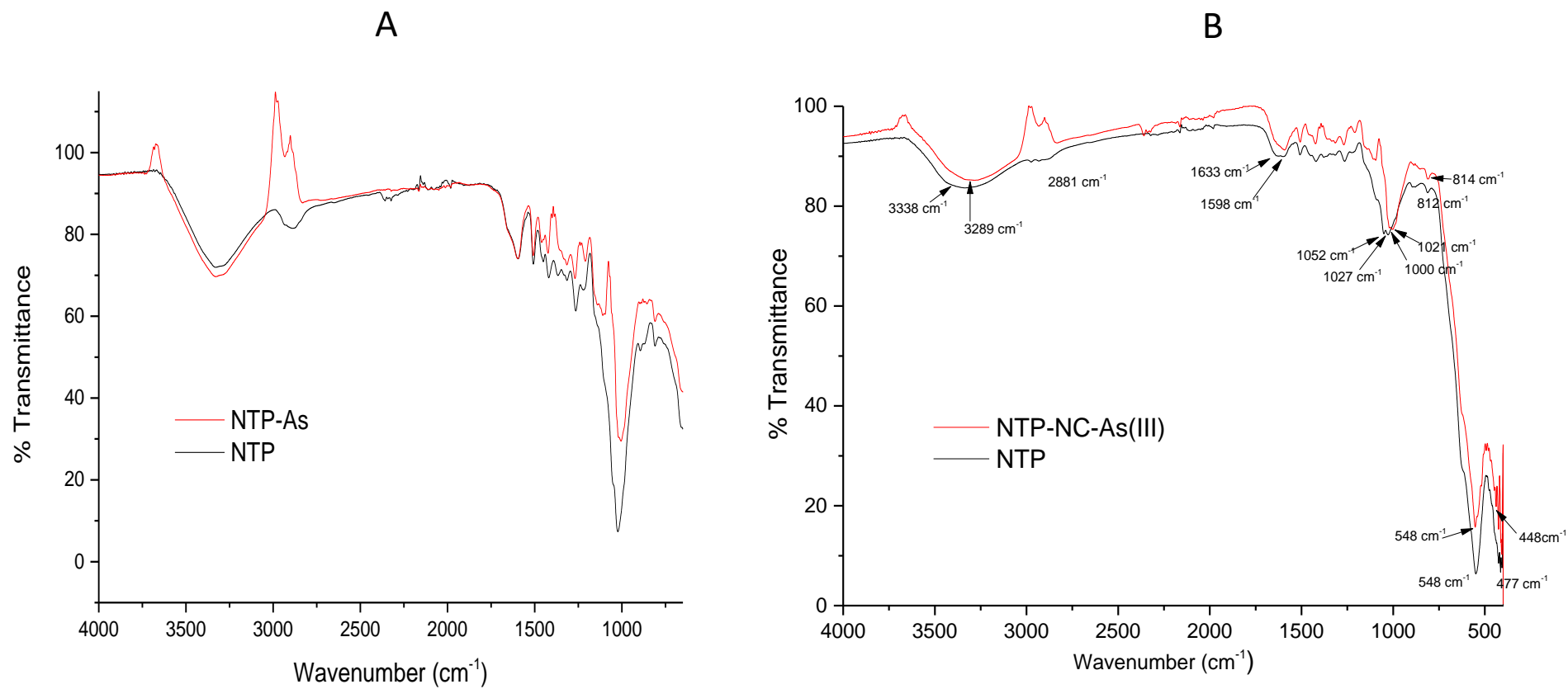
Figure 5.29: (A) FTIR spectra of NTP and (B) NTP-NC before and after As(III) adsorption

The full spectrum, carbon (C 1s) and oxygen (O 1s) of NTP biomaterial before and after As(III) adsorption are shown in Fig. 5.30. (A-G). The XPS survey spectrum of NTP before and after As(III) adsorption in Fig 5.30 A and B, indicates the presence of two major peaks at binding energies 282 and 530 eV, corresponding to C 1s and O 1s, respectively. The deconvolution of C 1s peak before As(III) adsorption (Fig. 5.30 C), produces three peaks with binding energy of 282.6, 284.3 and 285.9 eV, attributed to the carbon atoms in the forms of C-H, C-C (aromatic) and C-O (carbonyl), respectively (Zheng et al., 2009). The peaks were found to have shifted to higher binding energy after As(III) adsorption in Fig. 5.30 D. The C-H, C-C (aromatic) and C-O peaks were observed to have shifted from 282.6, 284.3 and 285.9 eV to 283.2, 284.9 and 287.2 eV, respectively, indicating that carbonyl groups are involved in As adsorption. From Fig. 5.30 E, the O 1s spectrum of the NTP before As(III) adsorption is composed of three component peaks at binding energies 529.1, 530.5 and 531.7 eV, which are respectively assigned to the M-O group, C-O functional group (Zheng et al., 2009) and C=O bonds (Toupin and Bélanger, 2008). The M-O peak may be due to the presence of Fe in the NTP biomaterial.

The spectra for O 1s peak after As(III) adsorption in Fig. 5.30 F, show a disappearance of a peak at 529.1 eV and shifting of peaks attributed to C-O and C=O from 530.5 and 531.7 eV to 530.8 and 531.8 eV. The shift in these peaks after As(III) adsorption confirm the inner-sphere adsorption of As(III) onto NTP. Similar observation has been reported by Cheng et al. (2016) using carbonaceous materials for As(V) and Cr(VI) adsorption. The authors reported a shift in binding energy after Cr(VI) adsorption and no shift after As(V) suggesting the inner sphere adsorption of Cr(VI) and outer sphere adsorption of As(V) on carbonaceous material. The O 1s peaks appear broader after As(III) adsorption representing the As-O formation. Similar results were observed by Lim et al. 2009 on the uptake of arsenate by an alginate-encapsulated magnetic sorbent. The NTP after As(III) adsorption spectrum in Fig 5.30 G, shows a new peak at binding energy 46 eV corresponding to As(III) 3d confirming the As(III) adsorption onto NTP biomaterial surface (Mahanta and Chen, 2013). The As 3d peak can be curve fitted into two peaks at binding energy 42.8 and 44.9 eV, with % concentration of 51.1 and 48.9 % corresponding to As(III) and As(V), respectively. This indicate that pine cone biomaterial was able to oxidize 48.9 % of As(III) to As(V).
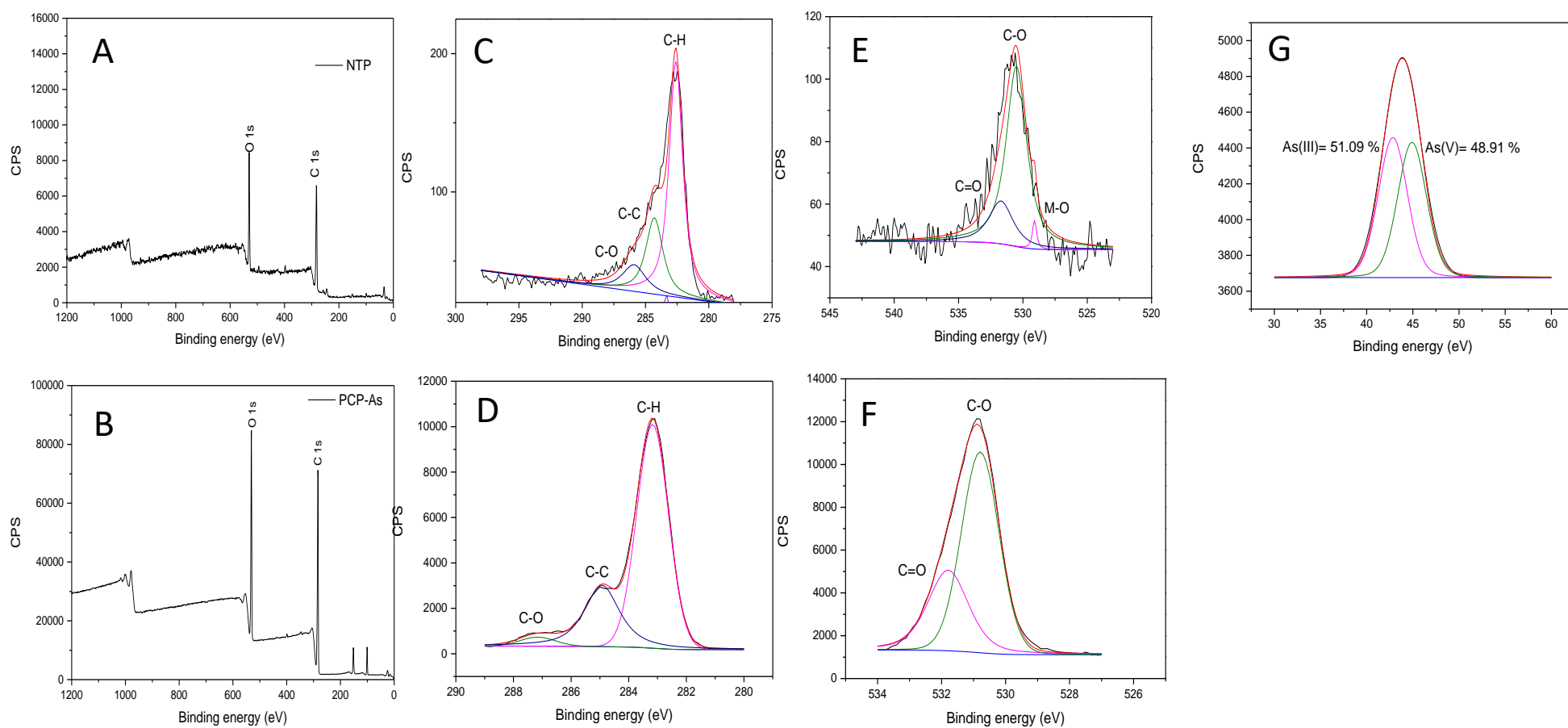
Figure 5.30: Full spectra of NTP (A) Before As(III) adsorption, (B) after As(III) adsorption, C 1s spectra of NTP (C) before As(III) adsorption, (D) After As(III) adsorption, O 1s spectra of PCP (E) before As(III) adsorption, (F) After As(III) adsorption (G) As 3d peak after As(III) adsorption.

XPS survey spectra of NTP-NC before and after As(III) adsorption in Fig 5.31 A and B shows three major peaks at binding energies 284, 530 and 710 eV corresponding to C 1s, O 1s and Fe 2p photoemissions, respectively. The spectrum for NTP-NC after As(III) adsorption was observed to have a new peak at binding energy 43.5 eV corresponding to As(III) 3d (Mahanta and Chen, 2013). The Fe 2p spectrum before and after As(III) adsorption are shown in Fig. 5.31 C and D. Fig. 5.31 A shows two strong peaks at binding energies of 709.9 and 723.5, eV corresponding to Fe $2p_{3/2}$ and Fe $2p_{1/2}$, respectively, which can be attributed to magnetite (Yoon et al., 2017). The peak at binding energy of 709.9 eV before and after As(III) adsorption was curve fitted into two peaks with binding energies at 709.73 and 713.48 eV, assigned to Fe(II) and Fe(III), respectively (Wilson and Langell, 2014). The % atomic concentration of Fe(II) and Fe(III) on the NTP-NC before adsorption was 74.2 % Fe(II) and 25.8 % Fe (III), while after adsorption was 57.2 % Fe(II) and 42.8 % for Fe (III) respectively indicating that Fe(II) was partially oxidized to Fe(III).

The O 1s spectrum of the NTP-NC adsorbent before As(III) adsorption (Fig. 5.31 E and F) is composed of three component peaks at 530.56 and 531.73 and 532.71 eV, which are respectively assigned to the Fe-O, the C-O group and the adsorbed water ($H_2O$). The presence of the As-O peak after As(III) adsorption (Fig. 5.31 F) confirms the As(III) adsorption onto NTP-NC surface (Zhang et al., 2010, Yu et al., 2013). The surface hydroxyl peak and the carbonyl peak reduced after As(III) adsorption, indicating the decrease in the amount of hydroxyl group on the adsorbent surface during arsenic adsorption. The results also show that there was a shift in the O 1s peak before and after As(III) adsorption (Fig. 5.31 G). The XPS spectrum of As(III) 3d (Fig. 5.31 H) was observed to be composed of two characteristic peaks with binding energies of 42.9 and 43.9 eV with % concentration on 57.17 and 42.8 % corresponding to As(III) and As(V), respectively.
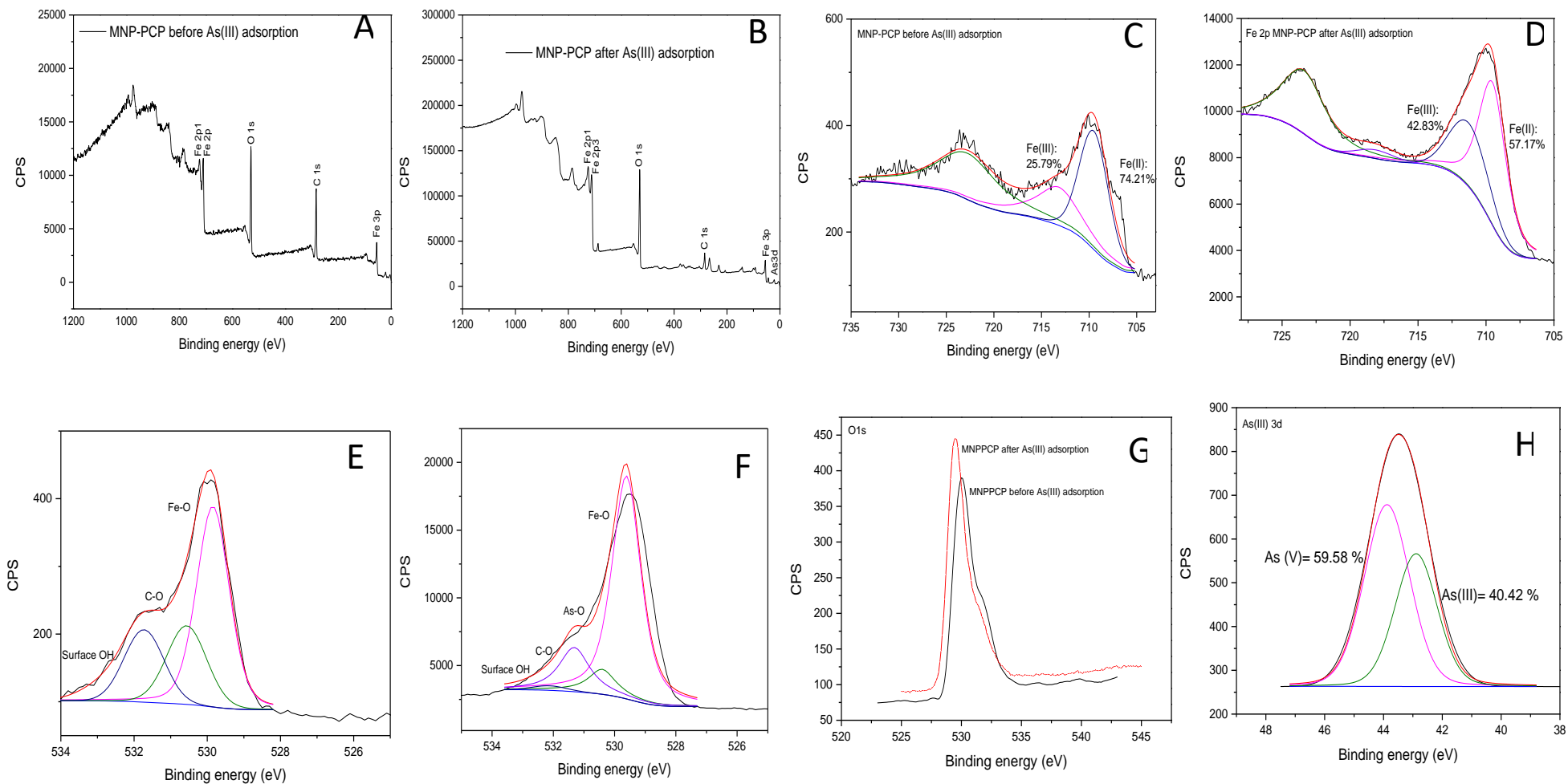
Figure 5.31: Full spectra of NTP-NC (A) Before As(III) adsorption, (B) after As(III) adsorption, Fe 2p spectra of NTP-NC (C) before As(III) adsorption, (D) After As(III) adsorption. O 1s spectra of NTP-NC (E) Before As(III) adsorption, (F) after As(III) adsorption, (G) O 1s spectra of NTP-NC before and after As(III) adsorption, (H) and As3d spectra of NTP-NC after As(III) adsorption.

### 5.3.7.3 Point of zero charge before and after As(III) adsorption

Since the adsorption of As(III) indicated the formation of inner sphere complex ion onto the NTP biomaterial and NTP-NC bio-composite, $pH_{pzc}$ of the PCP biomaterial before and after As(III) adsorption was conducted to confirm the mechanism and the results are shown in Fig. 5.32. The values for $pH_{pzc}$ were found to be 5.69, 5.86, 4.33 and 4.26 for NTP, NTP-NC, NTP-As(III) and NTP-NC-As(III) respectively. The shift of $pH_{pzc}$ to lower values when the adsorbent is As(III) loaded is typical of inner sphere complex ion-exchange reactions (Goldberg and Johnston, 2001). Therefore, the shift in $pH_{pzc}$ to lower values confirms the presence of inner sphere complex ion-exchange reactions in the adsorption of As(III) onto NTP and NTP-NC.
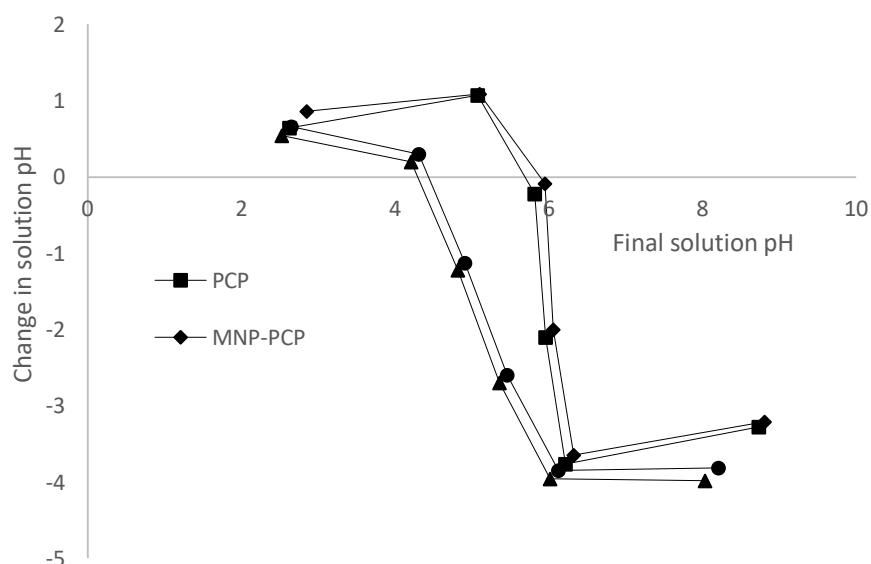


Figure 5.32: $pH_{pzc}$ graph of NTP and NTP-NC before and after As(III) adsorption.

### 5.3.7.4 As(III)/$NO_3^-$ exchange on $NO_3^-$-loaded NTP and NTP-NC

To confirm ion-exchange process as the adsorption mechanism, $NO_3^-$-loaded NTP and NTP-NC were prepared by adsorbing $NO_3^-$ ions onto NTP and NTP-NC and washing to remove excess $NO_3^-$ ions. About 0.1 g of the $NO_3^-$-loaded NTP-NC was then contacted with different concentrations (5, 25, 50 and 100 mg/dm$^3$) of As(III) solution. The amounts of $NO_3^-$ ions

released and the As(III) adsorbed were measured and the results are recorded in Table 5.14. The results show an increase in $NO_3^-$ ions released as the initial As(III) concentration and the As(III) capacity increases for both NTP and NTP-NC materials. This suggests that ligand exchange took place between the $NO_3^-$ and the As(III) anions. Similar observation between As(III) adsorbed and $SO_4^{2-}$ released were made by Burton et al. (2009) and Wu et al. (2013) in the adsorption of As(III) onto Schwertmannite and Fe-based backwashing sludge respectively. Both group of authors studied the molar ratios of $SO_4^{2-}$ released and As(III) adsorbed on Schwertmannite and Fe-based backwashing sludge defined as the As(III)/ $SO_4^{2-}$ exchange coefficient $(R_{As(III)/SO_4^{2-}})$. The values of the exchange coefficients were 0.16 to 0.31 for Schwertmannite and 0.11 to 0.25 for Fe-based backwashing sludge. In this study, the exchange coefficient $(R_{As(III)/NO_3^-})$ was determined as the ratio of $NO_3^-$ released to As(III) adsorbed. The values of exchange coefficient $(R_{As(III)/NO_3^-})$ ranged from 0.06 to 0.55 for NTP and from 0.11 to 0.74 for NTP-NC, which was comparable to the results of Burton et al. (2009) and (Wu et al., 2013). This suggested that $NO_3^-$ ions exchanged were located within the tunnels of NTP and NTP-NC and not only adsorbed on the surface.

### 5.3.8   Effect of ionic strength

The effect of ionic strength on the adsorption of As(III) onto NTP and NTP-NC was examined by contacting 0.5 g of NTP and NTP-NC with 100 mg/dm³ of As(III) containing 0, 0.01, 0.05, 0.10, 0.15 and 0.20 mg/dm³ of NaNO₃. The results shown in Fig. 5.33 reveal that there was a slight increase in the uptake of As(III) with increase in ionic strength of NaNO₃ from 0 to 0.20 mg/dm³. The increase in adsorption capacity was from 9.74 to 12.17 mg/g for NTP and 13.86 to 17.42 mg/g for NTP-NC. This weak dependence on increase in ionic strength is suggestive of inner-sphere adsorption mechanism (Goldberg and Johnston, 2001). According to Zhang et al. (2015), inner-sphere exchange reactions are favoured by increase in ionic strength because the reduced dissociation constant, $pK_a$, at higher ionic strength can cause surface hydroxyl to become more labile and easily displaced during exchange reactions (Selim and Sparks, 2001, Roy et al., 2017).

Table 5.14: Parameters for As(III)/$NO_3^-$ exchange processes for NTP and NTP-NC

| As(III) Init. Conc. (mg/dm$^3$) | Amt. of $NO_3^-$ released (mol/g) | As(III) adsorbed (mol/g) | As(III)/ $NO_3^-$ exchange coefficient $\left( R_{As(III)/NO_3^-} \right)$ |
|---|---|---|---|
| NTP | | | |
| 0 | 0.00 | 0.00 | 0.00 |
| 5 | 0,572488 | 0,033115 | 0,057845 |
| 25 | 0,711176 | 0,102082 | 0,14354 |
| 50 | 0,753104 | 0,234383 | 0,311223 |
| 100 | 0,809547 | 0,448345 | 0,553822 |
| | | | |
| NTP-NC | | | |
| 0 | 0.00 | 0.00 | 0.00 |
| 5 | 0.47411 | 0.054378 | 0.114693 |
| 25 | 0.62731 | 0.141324 | 0.225283 |
| 50 | 0.68376 | 0.304925 | 0.445953 |
| 100 | 0.84986 | 0.631741 | 0.743344 |

The increase in adsorption capacity for NTP-NC over NTP when the concentration of the electrolyte was increased from 0 to 0.20 mg/dm$^3$ suggests stronger participation of inner-sphere exchange reactions in NTP-NC than in NTP.
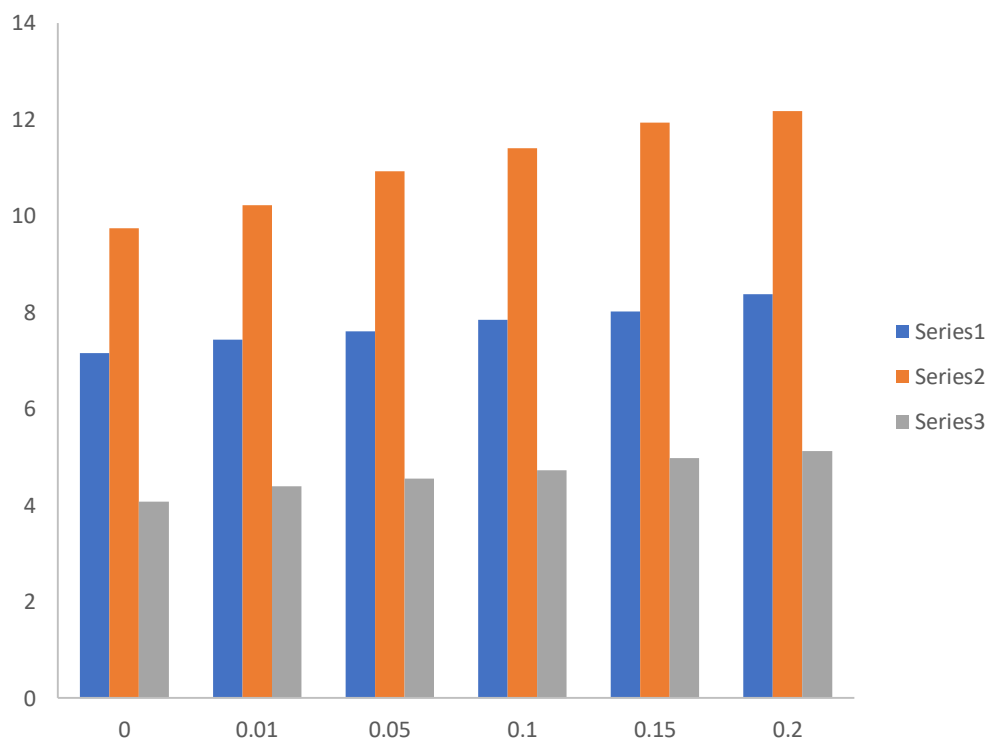


Figure 5.33: Effect of NaNO$_3$ ionic strength at different initial solution pH on the adsorption of As(III) onto NTP and NTP-NC nanocomposite.

## 5.3.9   Effect of competing anions on As(III) adsorption onto NTP and NTP-NC

Underground water polluted by As(III) usually contain along with it several other anions such as $PO_4^{3-}, SO_4^{2-}, CO_3^{2-}, NO_3^-$ and $Cl^-$ which can influence the adsorption of As(III). Therefore, in this study the influence of these anions on As(III) adsorption was investigated by contacting 0.5 g of NTP or NTP-NC with 100 mg/dm$^3$ of As(III) solution containing 0.1 mg/dm$^3$ of each anion. The results of the experiments for the influence of competing anions are shown in Fig. 5.34 for NTP and NTP-NC. The results revealed that for NTP, the presence of $SO_4^{2-}, CO_3^{2-}, NO_3^-$ and $Cl^-$ increased As(III) adsorption slightly from 9.74 mg/g to 11.34 mg/g with $SO_4^{2-}$, 11.22 mg/g with $CO_3^{2-}$, 10.22 mg/g with $NO_3^-$ and 11.76 mg/g with $Cl^-$ anion.

In the case of NTP-NC, various increases in the presence of anions were from 13.86 mg/g to 15.79 mg/g with $SO_4^{2-}$, 15.23 mg/g with $CO_3^{2-}$, 14.72 mg/g with $NO_3^-$ and 16.88 mg/g with $Cl^-$ anion. These results show that removal of As(III) with NTP and NTP-NC in the presence of $SO_4^{2-}$ and $Cl^-$ will aid the adsorption process. Wu et al. (2018) observed an increase in Arsenic adsorption onto graphene oxide/CuFe$_2$O$_3$ in the presence of $Cl^-$ anions and Wu et al. (2013) also observed an increase in As(III) adsorption onto Fe-based backwashing sludge in the presence of $SO_4^{2-}$. The adsorption capacities of NTP and NTP-NC for As(III) were found to reduce in the presence of $PO_4^{3-}$ from 9.74 to 3.65 mg/g for NTP and from 13.86 to 5.67 mg/g for NTP-NC. The reason for this observation is that $PO_4^{3-}$ has similar molecular structure with arsenic ions (Li et al., 2017) and retain multi-hydroxyl groups in solution. These hydroxyl groups react in the same way as the hydroxyl groups on As(III) with surface groups of FeOH, ROH and COOH on NTP and NTP-NC, therefore strongly competes with As(III) for adsorption sites (Cheng et al., 2016). The percentage reduction in As(III) adsorption was higher for NTP-NC (40.91%) than for NTP (37.47%) suggesting the greater contribution of ion-exchange reaction in As(III) adsorption for NTP-NC than for NTP.
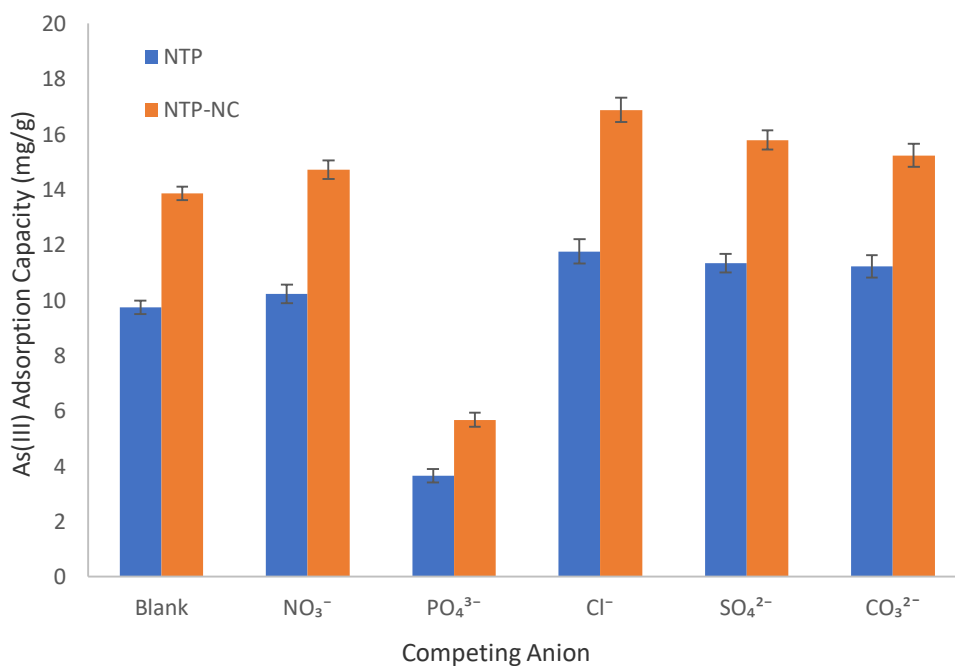


Figure 5.34: Effect of competing ions on the adsorption of As(III) onto (a) NTP and (b) NTP-NC bio-composite.

**5.3.10 Desorption**

In order to design and optimize a biosorption processes for industrial application, it is important to elucidate the adsorption-desorption behavior of the adsorbents. Fig. 5.35 shows the plot of percentage As(III) desorption from the metal loaded adsorbents against the various desorbing agents. The results revealed that water is a poor desorbing agent for As(III) from NTP and NTP-NC suggesting that physical adsorption only slightly explain the binding mechanism. When 0.1 mg/dm$^3$ of NaOH and HCl were applied as desorbing agents, the percentage As(III) desorbed was 68.34 % and 54.32 % for NTP, and 81.60 % and 65.98 % for NTP-NC respectively. Various studies have shown that NaOH and HCl are good desorbing agents for As(III) from magnetite modified adsorbents. Zhou et al. (2014) observed a 97 % desorption of As(III) from magnetic cellulose nanocomposite with 0.1 M HCl and  desorbed over 90 % of As(III) from $\gamma$-Fe$_2$O$_3$ modified SBA-15 using 0.1 M NaOH. These finding suggests that ion exchange reactions are responsible for As(III) binding onto NTP and NTP-NC.
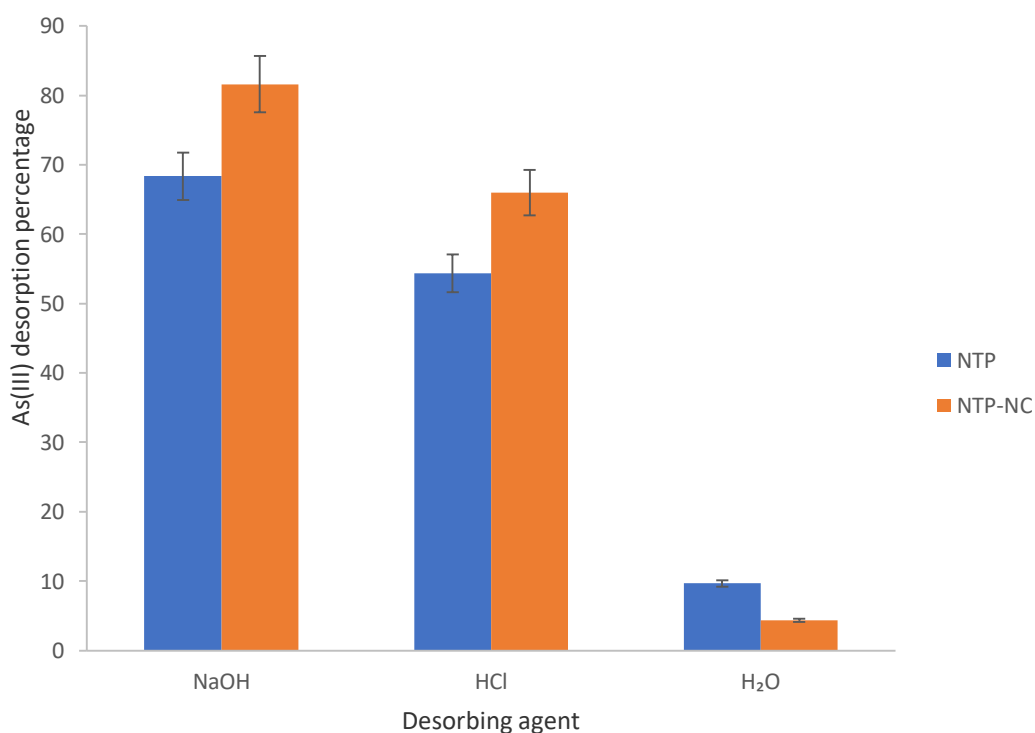


Figure 5.35: Desorption studies of As(III) from NTP and NTP-NC

### 5.3.11 Regeneration

The regeneration efficiency of NTP and NTP-NC after five adsorption-desorption cycles is shown in Fig. 5.36. The results show that the As(III) adsorption capacities of NTP and NTP-NC were observed to reduce gradually from 9.74 to 8.88, 7.99 and 6.02 mg/g for NTP and from 13.86 to 12.89, 12.49 and 12.09 mg/g for NTP-NC respectively. These results suggest that NTP-NC was more stable over five adsorption-desorption cycles than NTP which can be attributed to stronger bonds formed between As(III) and NTP-NC.
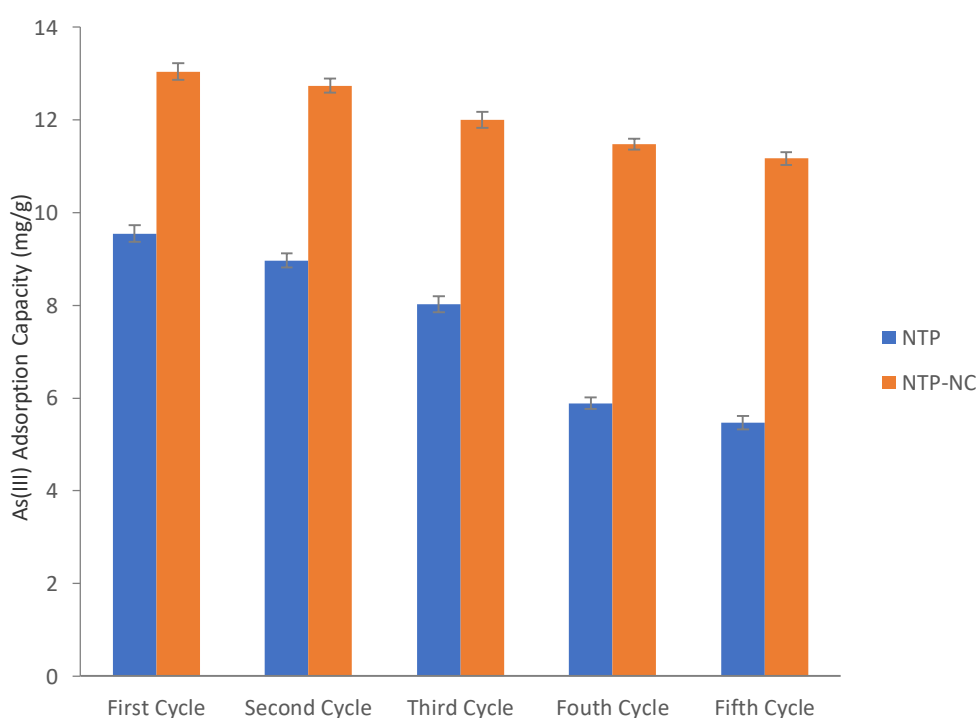


Figure 5.36: Recycling of NTP and NTP-NC after three cycles of adsorption/desorption

### 5.4 CONCLUSION

Application of the synthesized magnetite coated pine cone (NTP-NC) and its comparison with NaOH treated pine cone for Cr(VI) and As(III) adsorption is well reported in this chapter. From batch adsorption optimization study, Cr(VI) adsorption capacity of 6.48 and 13.88 mg/g were reached at optimum solution pH of 3 and adsorbent dose of 0.5 g while As(III) adsorption capacity of 9.74 and 13.86 mg/g was reached at an optimum solution pH of 8 and adsorbent dosed of 0.5 g for NTP and NTP-NC, respectively. The change in solution hydrogen ion

concentration ($\Delta H^+$) and amounts of total Cr, Cr(III) and Cr(VI) left in solution pointed to the fact that the mechanism of Cr(VI) removal was adsorption-coupled reduction mechanism which was slightly modified by the presence of magnetite coating. The good fit of the kinetic data to the pseudo-second-order model and the external mass transfer suggests that both external mass transfer and surface diffusion played an important role in the Cr(VI) adsorption process and their impact was stronger for NTP-NC than for NTP. The results of $\Delta H$ and $\Delta G$ indicate the exothermic and spontaneous nature of adsorption process on the surface of both NTP and NTP-NC bio-composite. For Cr(VI) adsorption results, $PO_4^{3-}$, $CO_3^{2-}$, $SO_4^{2-}$ had a negative effect while $Cl^-$ anion positively affected Cr(VI) adsorption onto both NTP and NTP-NC bio-composite. Cr(VI) was better desorbed by NaOH and acetic acid for both NTP and NTP-NC.

The results indicated that magnetite particles interacted with oxygenated groups of NaOH treated pine cone. Both the Langmuir and D-R isotherm showed that adsorption process was favourable at all temperatures, monolayer in nature and a ligand exchange process. Thermodynamic data indicated that the adsorption was spontaneous at all temperatures and endothermic in nature. FTIR evidence of ligand exchanged was observed as shifts in peaks at 814 cm$^{-1}$ representing As-O bonding while XPS confirms the formation As-O by the presence of As(III) and As(V) peaks after As(III) adsorption suggesting the oxidation of As (III) adsorbed on NTP and NTP-NC bio-composite. The reduction in pH$_{pzc}$ after As (III) adsorption, the trend in the displacement of $NO_3^-$ from $NO_3^-$-loaded NTP and NTP-NC with increasing concentrations of As (III) along with the values of anion-exchange coefficient confirmed ligand ion exchange as the adsorption mechanism. Effect of ionic strength positively affected As(III) adsorption suggesting inner sphere adsorption mechanism while $PO_4^{3-}$ had a negative effect on the adsorption process. HCl and NaOH effectively desorbed As(III) from both samples and NTP-NC had better stability in five cycles of adsorption-desorption than NTP. Magnetite coated pine cone bio-composite is a promising adsorbent for removal of Cr(VI) and As(III) ions from aqueous solution.

## 5.5    REFERENCE

AJOUYED, O., HUREL, C., AMMARI, M., ALLAL, L. B. & MARMIER, N. 2010. Sorption of Cr(VI) onto natural iron and aluminium (oxy)hydroxides: Effects of pH, ionic strength and initial concentration. *Journal of Hazardous Material,* 174**,** 616-622.

ÁLVAREZ-AYUSO, E., GARCÍA-SÁNCHEZ, A. & QUEROL, X. 2007. Adsorption of Cr(VI) from synthetic solutions and electroplating wastewaters on amorphous aluminium oxide. *Journal of Hazardous Material,* 142**,** 191-198.

ALBADARINA, A. B, AL-MUHTASEBB, A. H., AL-LAQTAHA, N.A., WALKER, G.M., ALLENA, S. J. & AHMED. M. N. M. 2011. Biosorption of toxic chromium from aqueous phase by lignin: mechanism, effect of other metal ions and salts. *Chemical Engineering Journal,* 169, 20–30

ARYAL, M., ZIAGOVA, M. & LIAKOPOULOU-KYRIAKIDES, M. 2010. Study on arsenic biosorption using Fe(III)-treated biomass of Staphylococcus xylosus. *chemical Engineering Journal,* 162**,** 178-185.

BANERJEE, S. & CHATTOPADHYAYA, M. 2017. Adsorption characteristics for the removal of a toxic dye, tartrazine from aqueous solutions by a low cost agricultural by-product. *Arabian Journal of Chemistry,* 10**,** S1629-S1638.

BURTON, E. D., BUSH, R. T., JOHNSTON, S. G., WATLING, K. M., HOCKING, R. K., SULLIVAN, L. A. & PARKER, G. K. 2009. Sorption of arsenic (V) and arsenic (III) to schwertmannite. *Environmental Science & Technology,* 43**,** 9202-9207.

CHANDRA, V., PARK, J., CHUN, Y., LEE, J. W., HWANG, I. C. & KIM, K. S. 2010. Water-Dispersible Magnetite-Reduced Graphene Oxide Composites for Arsenic Removal. *ACS NANOTECHNOLOGY,* 4**,** 3979-3986.

CHEN, C. Y., YANG, C. Y. & CHEN, A. H. 2011. Biosorption of Cu(II), Zn(II), Ni(II) and Pb(II) ions by cross-linked metal-imprinted chitosans with epichlorohydrin. *Journal of Environmental Management,* 92**,** 796-802.

CHENG, W., DING, C., WANG, X., WU, Z., SUN, Y., YU, S., HAYAT, T. & WANG, X. 2016a. Competitive sorption of As(V) and Cr(VI) on carbonaceous nanofibers. *Chemical Engineering Journal,,* 293**,** 311-318.

CHENG, W., ZHANG, W., HU, L., DING, W., WU, F. & LI, J. 2016b. Etching synthesis of iron oxide nanoparticles for adsorption of arsenic from water. *RSC Advances,* 6**,** 15900-15910.

CRANK, J. 1975. Diffusion in a cylinder. *The Mathematics of Diffusion*, 69-88.

DONG, X., MA, L. Q. & LI, Y. 2011. Characteristics and mechanisms of hexavalent chromium removal by biochar from sugar beet tailing. *J Hazard Mater,* 190, 909-915.

DURANOĞLU, D., TROCHIMCZUK, A. W. & BEKER, U. 2012. Kinetics and thermodynamics of hexavalent chromium adsorption onto activated carbon derived from acrylonitrile-divinylbenzene copolymer. *Chemical Engineering Journal* 187, 193-202.

FATHY, N. A., EL-WAKEEL, S. T. & EL-LATIF, R. R. A. 2015. Biosorption and desorption studies on chromium (VI) by novel biosorbents of raw rutin and rutin resin. *Journal of Environmental Chemical Engineering,* 3, 1137-1145.

GHEJU, M., BALCU, I. & VANCEA, C. 2016. An investigation of Cr(VI) removal with metallic iron in the co-presence of sand and/or MnO2. . *Journal of Environmental Management,* 170, 145-151.

GOLDBERG, S. & JOHNSTON, C. T. 2001. Mechanisms of arsenic adsorption on amorphous oxides evaluated using macroscopic measurements, vibrational spectroscopy, and surface complexation modeling. *Journal of Colloid and Interface Science,* 234, 204-216.

GUPTA, A., VIDYARTHI, S. R. & SANKARARAMAKRISHNAN, N. 2015. Concurrent removal of As(III) and As(V) using green low cost functionalized biosorbent – Saccharum officinarum bagasse. . *Journal of Environmental Chemical Engineering,* 3, 113-121.

GUPTA, V. & NAYAK, A. 2012. Cadmium removal and recovery from aqueous solutions by novel adsorbents prepared from orange peel and Fe2O3 nanoparticles. *Chemical Engineering Journal,* 180, 81-90.

HASAN, S., SINGH, K., PRAKASH, O., TALAT, M. & HO, Y. 2008. Removal of Cr (VI) from aqueous solutions using agricultural waste 'maize bran'. *Journal of Hazardous Materials,* 152, 356-365.

HE, R., PENG, Z., LYU, H., HUANG, H., NAN, Q. & TANG, J. 2018. Synthesis and characterization of an iron-impregnated biochar for aqueous arsenic removal. *Science of the Total Environment,* 612, 1177-1186.

HO, Y.-S. 1995. *Absorption of heavy metals from waste streams by peat.* University of Birmingham.

HO, Y., NG, J. & MCKAY, G. 2000. Kinetics of pollutant sorption by biosorbents. *Separation and Purification Methods,* 29, 189-232.

HO, Y. S. & OFOMAJA, A. E. 2005. Effects of calcium competition on lead sorption by palm kernel fibre. *Journal of Hazardous Material,* 120**,** 157-62.

HO, Y. S. & OFOMAJA, A. E. 2006. Pseudo-second-order model for lead ion sorption from aqueous solutions onto palm kernel fiber. *Journal of Hazardous Material,* 129**,** 137-42.

HU, Q., LIU, Y., GU, X. & ZHAO, Y. 2017. Adsorption behaviour and mechanism of different arsenic species on mesoporous MnFe2O4 magnetic nanoparticles. *Chemosphere,* 181**,** 328-336.

HUO, J. B., XU, L., YANG, J. C. E., CUI, H. J., YUAN, B. & FU, M. L. 2018. Magnetic responsive Fe3O4-ZIF-8 core-shell composite for efficient removal of As(III) from water. *Colloids and Surfaces A,* 539**,** 59-68.

KAMINS, T. 1998. Polycrystalline Silicon for Integrated Circuits and Displays.-Kluwer Academic Publishers.

KARTHICK, K., NAMASIVAYAM, C. & PRAGASAN, L. A. 2017. Removal of Direct Red 12B from aqueous medium by ZnCl 2 activated Jatropha husk carbon: Adsorption dynamics and equilibrium studies.

KRATOCHVIL, D., PIMENTEL, P. & VOLESKY, B. 1998. Removal of trivalent and hexavalent chromium by seaweed biosorbent. *Environmental Science & Technology,* 32**,** 2693-2698.

LAGERGREN, S. 1898. Zur theorie der sogenannten adsorption gelöster stoffe, Kungliga Svenska Vetenskapsakademiens. *Handlingar,* 24**,** 1-39.

LAZARIDIS, N. & ASOUHIDOU, D. 2003. Kinetics of sorptive removal of chromium (VI) from aqueous solutions by calcined Mg–Al–CO 3 hydrotalcite. *Water Research,* 37**,** 2875-2882.

LEONE, V. O., PEREIRA, M. C., AQUINO, S. F., OLIVEIRA, L. C. A., CORREA, S., RAMALHO, T. C., GURGEL, L. V. A. & SILVA, A. C. 2018. Adsorption of diclofenac on a magnetic adsorbent based on maghemite: experimental and theoretical studies. *New Journal of Chemistry,* 42**,** 437-449.

LI, J., GYOTEN, H., SONODA, A., FENG, Q. & XUE, M. 2017. Removal of trace arsenic to below drinking water standards using a Mn–Fe binary oxide. *Rsc Advances,* 7**,** 1490-1497.

LIEN, H.-L. & ZHANG, W.-X. 2007. Nanoscale Pd/Fe bimetallic particles: catalytic effects of palladium on hydrodechlorination. *Applied Catalysis B: Environmental,* 77**,** 110-116.

LIM, S. F., ZHENG, Y.-M., ZOU, S. W. & CHEN, J. P. 2009. Uptake of arsenate by an alginate-encapsulated magnetic sorbent: Process performance and characterization of adsorption chemistry. *Journal of Colloid and Interface Science,* 333**,** 33-39.

LIU, Z., CHEN, J., WU, Y., LI, Y., ZHAO, J. & NA, P. 2018. Synthesis of magnetic orderly mesoporous $\alpha$-$Fe_2O_3$ nanocluster derived from MIL-100(Fe) for rapid and efficient arsenic (III,V) removal. . *Journal of Hazardous Material,* 343**,** 304-314.

LUNGE, S., SINGH, S. & SINHA, A. 2014. Magnetic iron oxide ($Fe_3O_4$) nanoparticles from tea waste for arsenic removal. *Journal of Magnetism and Magnetic Materials,* 356**,** 21-31.

MAHANTA, N. & CHEN, J. P. 2013. A novel route to the engineering of zirconium immobilized nano-scale carbon for arsenate removal from water. *Journal of Materials Chemistry A,* 1**,** 8636-8644.

MAO, N., YANG, L., ZHAO, G., LI, X. & LI, Y. 2012. Adsorption performance and mechanism of Cr (VI) using magnetic PS-EDTA resin from micro-polluted waters. *Chemical engineering journal,* 200**,** 480-490.

MCKAY, G. & POOTS, V. J. 1980. Kinetics and diffusion processes in colour removal from effluent using wood as an adsorbent. *Journal of Chemical Technology and Biotechnology,* 30**,** 279-292.

MEJIA-SANTILLAN, M. E., PARIONA, N., BRAVO, J., HERRERA-TREJO, M., MONTEJO-ALVARO, F., ZARATE, A., PERRY, D. L. & I, M.-E. A. 2018. Physical and arsenic adsorption properties of maghemite and magnetite sub-microparticles. *journal of Magnetism and Magnetic Materials,* 451**,** 594-601.

MENG, F., YANG, B., WANG, B., DUAN, S., CHEN, Z. & MA, W. 2017a. Novel dendrimer like magnetic biosorbents based on modified orange peel waste: adsorption-reduction behaviour of arsenic. *ACS Sustainable for Chemical Engineers* 5**,** 9692-9700.

MENG, F., YANG, B., WANG, B., DUAN, S., CHEN, Z. & MA, W. 2017b. Novel Dendrimerlike Magnetic Biosorbent Based on Modified Orange Peel Waste: Adsorption–Reduction Behavior of Arsenic. *ACS Sustainable Chemistry & Engineering,* 5**,** 9692-9700.

MICHELSEN, D. L., GIDEON, J. A., GRIFFITH, G. P., PACE, J. E. & KUTAT, H. L. 1975. Removal of soluble mercury from waste water by complexing techmiques. *Bull Water Resour Res Cent Va Polytech Inst State Univ*.

MITTAL, A., KURUP, L. & MITTAL, J. 2007. Freundlich and Langmuir adsorption isotherms and kinetics for the removal of Tartrazine from aqueous solutions using hen feathers. *Journal of hazardous materials,* 146**,** 243-248.

NAMASIVAYAM, C. & SANGEETHA, D. 2006. Removal and recovery of vanadium (V) by adsorption onto ZnCl2 activated carbon: Kinetics and isotherms. *Adsorption,* 12**,** 103-117.

NASHINE, A. L. & TEMBHURKAR, A. R. 2016. Equilibrium, kinetic and thermodynamic studies for adsorption of As(III) on coconut (Cocos nucifera L.) fiber. . *Journal of Environmental Chemical Engineering,* 4**,** 3267-3273.

NASSAR, N. N. 2010. Rapid removal and recovery of Pb(II) from wastewater by magnetic nano adsorbents. *Journal of Hazardous Material,* 184**,** 538-546.

NIGAM, S., GOPAL, K. & VANKAR, P. S. 2013. Biosorption of arsenic in drinking water by submerged plant: Hydrilla verticilata. *Environmental Science & Technology,* 20**,** 4000-4008.

OFOMAJA, A. E., UNUABONAH, E. I. & OLADOJA, N. A. 2010. Competitive modeling for the biosorptive removal of copper and lead ions from aqueous solution by Mansonia wood sawdust. *Bioresour Technol,* 101**,** 3844-52.

ÖNAL, Y., AKMIL-BAŞAR, C. & SARıCı-ÖZDEMIR, Ç. 2007. Investigation kinetics mechanisms of adsorption malachite green onto activated carbon. *Journal of hazardous materials,* 146**,** 194-203.

ÖZER, A. 2007. Removal of Pb (II) ions from aqueous solutions by sulphuric acid-treated wheat bran. *Journal of Hazardous Materials,* 141**,** 753-761.

PARK, D., LIM, S. R., YUN, Y. S. & PARK, J. M. 2008. Development of a new Cr(VI)-biosorbent from agricultural biowaste. *Bioresour Technol,* 99**,** 8810-8.

PENG, X., ZHAO, Y., TANG, T., YANG, Y., JIANG, Y., MA, Z., LI, X., HOU, J., XI, B. & H, L. 2018. One-step and acid free synthesis of γ-Fe2O3/SBA-15 for enhanced arsenic removal. *Microporous and Mesoporous Materials,* 258**,** 26-32.

QI, W., ZHAO, Y., ZHENG, X. & JI, M. 2016. Zhang. Adsorption behavior and mechanism of Cr(VI) using Sakura waste from aqueous solution. *Applied Surface Science,* 360**,** 470-476.

REZA, R. A. & AHMARUZZAMAN, M. 2015. A novel synthesis of Fe 2 O 3@ activated carbon composite and its exploitation for the elimination of carcinogenic textile dye from an aqueous phase. *RSC Advances,* 5**,** 10575-10586.

ROY, P., DEY, U., CHATTORAJ, S., MUKHOPADHYAY, D. & MONDAL, N. K. 2017. Modeling of the adsorptive removal of arsenic(III) using plant biomass: a bioremedial approach. *Applied Water Sciences,* 7**,** 1307-1321.

SALEH, T. A., SARı, A. & TUZEN, M. 2016. Chitosan-modified vermiculite for As(III) adsorption from aqueous solution: Equilibrium, thermodynamic and kinetic studies. *Journal of Molecular Liquids,* 219**,** 937-945.

SANTRA, D. & SARKAR, M. 2016. Optimization of process variables and mechanism of arsenic (V) adsorption onto cellulose nanocomposite. *Journal of Molecular Liquids,* 224**,** 290-302.

SELIM, H. M. & SPARKS, D. L. 2001. *Heavy metals release in soils*, CRC Press.

SHANG, J., ZONG, M., YU, Y., KONG, X., DU, Q. & LIAO, Q. 2017. Removal of chromium (VI) from water using nanoscale zerovalent iron particles supported on herb-residue biochar. . *Journal of Environmental Management,* 197**,** 331-337.

SINGHA, B., NAIYA, T. K., BHATTACHARYA, A. K. & DAS, S. K. 2011. Cr(VI) Ions Removal from Aqueous Solutions Using Natural Adsorbents – FTIR Studies. *Journal of Environmental Protection,* 02**,** 729-735.

SUBRAMANIAN, K., KUMAR, P. S., JEYAPAL, P. & VENKATESH, N. 2005. Characterization of ligno-cellulosic seed fibre from Wrightia Tinctoria plant for textile applications—an exploratory investigation. *European Polymer Journal,* 41**,** 853-861.

SUKUMAR, C., JANAKI, V., KAMALA-KANNAN, S. & SHANTHI, K. 2014. Biosorption of chromium (VI) using Bacillus subtilis SS-1 isolated from soil samples of electroplating industry. *Clean Technologies and Environmental Policy,* 16**,** 405-413.

SUN, Y., LI, J. & WANG, X. 2014. The retention of uranium and europium onto sepiolite investigated by macroscopic, spectroscopic and modeling techniques. *Geochim. Cosmochim. Acta,* 140**,** 621-643.

TAJERNIA, H., EBADI, T., NASERNEJAD, B. & GHAFORI, M. 2014. Arsenic Removal from Water by Sugarcane Bagasse: An Application of Response Surface Methodology (RSM). *Water Air Soil Pollution,* 225**,** 2028.

TOUPIN, M. & BÉLANGER, D. 2008. Spontaneous functionalization of carbon black by reaction with 4-nitrophenyldiazonium cations. *Langmuir,* 24**,** 1910-1917.

VADIVELAN, V. & KUMAR, K. V. 2005. Equilibrium, kinetics, mechanism, and process design for the sorption of methylene blue onto rice husk. *Journal of Colloid and Interface Science,* 286**,** 90-100.

VATUTSINA, M., SOLDATOV, V. S., SOKOLOVA, V. I., JOHANN, J., BISSEN, M. & WEISSENBACHER, A. 2007. A new hybrid (polymer/inorganic) fibrous sorbent for arsenic removal from drinking water,. *Reactive and Functional Polymers,* 67**,** 184-201.

VENKATESAN, G. & NARAYANAN, S. L. 2018. Synthesis of Fe2O3-coated and HCl-treated bauxite ore waste for the adsorption of arsenic (III) from aqueous solution: Isotherm and kinetic models. *Chemical Engineering Communications,* 205**,** 34-46.

VIEIRA, B. R. C., PINTOR, A. M. A., BAVENTURA, R. A. R., BOTELHO, C. M. S. & SANTOS, S. C. R. 2017. Arsenic removal from water using iron-coated seaweeds. *Journal of Environmental Management,* 192**,** 224-233.

VINH, N. V., ZAFAR, M., BAHERA, S. K. & PARK, H. S. 2015. Arsenic(III) removal from aqueous solution by raw and zinc-loaded pine cone char: equilibrium, kinetics and thermodynamic studies. *International Journal of Environmental Science and Technology,* 12**,** 1283-1294.

WANG, S.-L. & LEE, J.-F. 2011. Reaction mechanism of hexavalent chromium with cellulose. *Chemical Engineering Journal,* 174**,** 289-295.

WEBER, W. J. & MORRIS, J. C. 1963. Kinetics of adsorption on carbon from solution. *Journal of the Sanitary Engineering Division,* 89**,** 31-60.

WILSON, D. & LANGELL, M. 2014. XPS analysis of oleylamine/oleic acid capped Fe3O4 nanoparticles as a function of temperature. *Applied Surface Science,* 303**,** 6-13.

WU, K., LIU, R., LI, T., LIU, H., PENG, J. & QU, J. 2013. Removal of arsenic (III) from aqueous solution using a low-cost by-product in Fe-removal plants—Fe-based backwashing sludge. *Chemical engineering journal,* 226**,** 393-401.

WU, L.-K., WU, H., ZHANG, H.-B., CAO, H.-Z., HOU, G.-Y., TANG, Y.-P. & ZHENG, G.-Q. 2018. Graphene oxide/CuFe2O4 foam as an efficient absorbent for arsenic removal from water. *Chemical Engineering Journal,* 334**,** 1808-1819.

XU, P., ZENG, G. M., HUANG, D. L., LAI, C., ZHAO, M. H., WEI, Z., LI, N. J., HUANG, C. & XIE, G. X. 2012. Adsorption of Pb (II) by iron oxide nanoparticles immobilized Phanerochaete chrysosporium: equilibrium, kinetic, thermodynamic and mechanisms analysis. *Chemical Engineering Journal,* 203**,** 423-431.

XU, T., CAI, Y. & O'SHEA, K. E. 2007. Adsorption and photocatalyzed oxidation of methylated arsenic species in TiO2 suspensions. *Environmental science & technology,* 41**,** 5471-5477.

YADAV, R., SHARMA, A. K. & BABU, J. N. 2016. Sorptive removal of arsenite [As(III)] and arsenate [As(V)] by fuller's earth immobilized nanoscale zero-valent iron

nanoparticles (F-nZVI): Effect of Fe0 loading on adsorption activity. *Journal of Environmental Chemical Engineering,* 4**,** 681-694.

YOON, Y., ZHENG, M., AHN, Y.-T., PARK, W. K., YANG, W. S. & KANG, J.-W. 2017. Synthesis of magnetite/non-oxidative graphene composites and their application for arsenic removal. *Separation and Purification Technology,* 178**,** 40-48.

YU, X., TONG, S., GE, M., ZUO, J., CAO, C. & SONG, W. 2013. One-step synthesis of magnetic composites of cellulose@ iron oxide nanoparticles for arsenic removal. *Journal of Materials Chemistry A,* 1**,** 959-965.

ZHANG, D., MA, Y., FENG, H. & HAO, Y. 2012. Adsorption of Cr(VI) from aqueous solution using carbon-microsilica composite adsorbent. *Journal of Chil Chem. Soc,* 57**,** 964-968.

ZHANG, S., LI, X.-Y. & CHEN, J. P. 2010. An XPS study for mechanisms of arsenate adsorption onto a magnetite-doped activated carbon fiber. *Journal of colloid and interface science,* 343**,** 232-238.

ZHENG, J.-C., FENG, H.-M., LAM, M. H.-W., LAM, P. K.-S., DING, Y.-W. & YU, H.-Q. 2009. Removal of Cu (II) in aqueous media by biosorption using water hyacinth roots as a biosorbent material. *Journal of Hazardous Materials,* 171**,** 780-785.

ZHOU, S., WANG, D., SUN, H., CHEN, J. & NA, S. 2014. Synthesis, characterization, and adsorptive properties of magnetic cellulose nanocomposites for arsenic removal. *Water Air Soil Pollution,* 225**,** 1945.

ZULFIKAR, M. A., SETIYANTO, H. & DJAJANTI, S. D. 2013. Effect of temperature and kinetic modelling of lignosulfonate adsorption onto powdered eggshell in batch systems. *Songklanakarin J. Sci. Technol.,* 35**,** 1-31.

# 6 RESULTS AND DISCUSSION

## 6.1 INTRODUCTION

This chapter is divided into two sections. The first section covers the optimization of crosslinking magnetite coated pine cone (NTP-NC) with beta cyclodextrin (β-CD) using epichlorohydrin (EPI) and hexamethylene diisocyanate (HMDI) by response surface methodology (RSM). Characterization of the synthesized NTPNC-EPI-CD and NTPNC-HMDI-CD using FTIR, TGA, XRD, TEM, VSM, $pH_{pzc}$ and BET surface area were conducted and discussed. The second part covers the application of NTPNC, NTPNC-EPI-CD and NTPNC-HMDI-CD for 4-nitrophenol (4-NP) adsorption from aqueous solution. Batch adsorption optimization, equilibrium studies, kinetic studies, and 4-nitrophenol mechanism were discussed.

## 6.2 RESPONSE SURFACE METHODOLODY (RSM)

Response surface methodology (RSM) is a collection of statistical and mathematical techniques useful for developing and optimizing processes in which a response of interest is influenced by several variables. The methodology generally involves three stages: (1) design and experiments, (2) response surface modelling via regression and (3) optimization. The model is mostly applied to reduce the number of experiments, save time and cost, determine the main effects of independent variables on response, and determine optimum conditions. RSM studies the effect of factors and their interactions involved in the optimization of the process (Hosseinpour et al., 2011). Central composite design (CCD), which is a proficient design utilized for sequential experimentation and offers realistic amount of data to test the goodness of fit and does not need remarkably huge number of design points, thus decreasing the total cost associated with the experiment, was used in designing the experiment. The method is suitable for fitting a quadratic surface and helps to optimize the effective parameters with a minimum number of experiments, as well as analysing the interaction between the parameters.

### 6.2.1 Optimization of working parameters on NTPNC-CD-HMDI synthesis

To synthesize an adsorbent that will be insoluble in nature, more effective for 4-NP adsorption and can be easily separated by a magnetic field, RSM technique was employed by design expert

software (version 10) to study the effects of experimental variables. Independent variables carefully chosen based on the synthesis procedure were the mass of cyclodextrin, catalyst (Dibutyltin dilaurate) volume, cross linker (HMDI) volume and the reaction temperature on cross linking of β-CD onto NTPNC using HMDI. % yield, % Fe in the nanocomposite and the 4-nitrophenol adsorption capacity were selected as responses. 30 runs of experiment were designed including factorial, axial, and replications of centre point (that were used to determine the errors of design). The experimental design matrix and their responses are shown in Table 6.1. Results were analysed using the software and a quadratic polynomial equation (Eq. 6.1) was used to study the interaction between the independent and dependent variables.

$$Y = b_0 + \sum_{i=1}^{3} b_i x_i + \sum_{i=1}^{3} b_i x_i^2 + \sum_{i=1}^{3} \sum_{j=i1}^{3} b_{ij} x_i x_j \qquad (6.1)$$

Where Y is the response variable, $x_i$ and $x_j$ are the coded variables which determine $Y$, $b_0$ is the constant coefficient, $b_i$ is the linear coefficient, $b_{ij}$ is the interaction coefficient and $b_{ii}$ is the quadratic coefficient. The relationship between the responses and the independent variables, dibutyltin dilaurate volume (A), Cyclodextrin mass (B), temperature (C) and hexamethylene diisocyanate volume (D) and calculated as the sum of a constant, four first-order effects (terms in A, B, C and D), six interaction effects (AB, AC, AD, BC, BD and CD) and four second-order effects ($A^2$, $B^2$, $C^2$ and $D^2$) are expressed.

The mechanism that governs the β-CD crosslinking onto NTPNC may be of importance in explaining the effect of the synthesis variables on responses. β-CD have high chemically reactive hydroxyl groups in the glucose unit which can form number of linkages (Gallego et al., 2013b, Morin-Crini and Crini, 2013). Crosslinking of β-CD onto magnetite coated pine cone by 1,6 hexamethylene diisocyanate (HMDI) take place on the reactive hydroxy group on the CD and NTP-NC and the isocyanate group on HMDI. However, the reaction requires the initial activation of the nanocomposite which causes a swelling to allow access of the HMDI cross-linker to the matrix surface (Gafurov et al., 1970, Rozman et al., 2001). The isocyanate group (-N=C=O) will react with the OH nucleophile on the β-CD and NTPNC to form two amide linkages (-NH-C(O)-O-) because of its ability to co-ordinate with the hydrogen of the nucleophile according to the reaction in scheme 6.1. Catalysts are more effective in promoting this reaction and their activity have been reported to increase with basicity of the material (Silva and Bordado, 2004). The hydroxyl groups will allow direct substitution reactions to different

positions yielding various polymerized derivatives. The yield of the polymer is known to increase with the amount of diisocyanate content relative to β-CD.
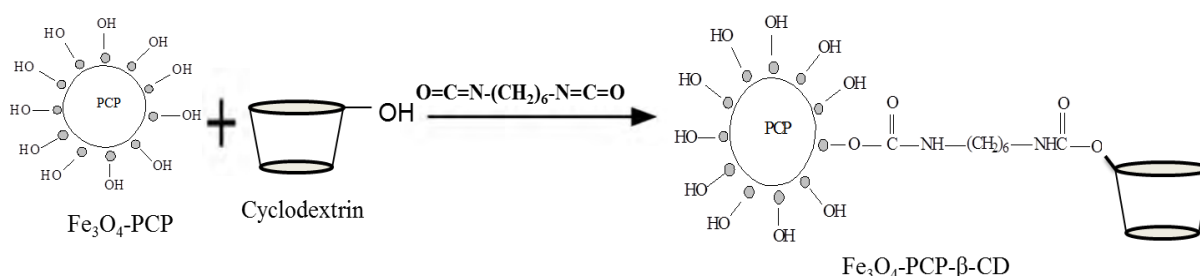


Scheme 6.1: Reaction pathway for the crosslinking of β-CD onto NTPNC using HMDI as a cross linker.

### 6.2.1.1 Yield of the NTPNC-HMDI-CD nanocomposite

To determine the efficiency of the crosslinking method and to estimate the cost of production of the nanocomposite, it is very important to take into consideration the % yield of the nanocomposite synthesised. The percentage yield of the NTPNC-HMDI-CD nanocomposite of 30 experimental runs ranged from 20.96 to 48.09 % as shown in Table 6.1. The quadratic model was selected based on the highest order polynomial where the addition term is significant. After the data was subjected to multiple regression analysis of CCD, the quadratic equation describing the relationship between % iron and the synthesis variables (β-CD mass, HMDI volume, DBTDL volume and the reaction temperature) is shown in Eq.6.2:

$$\% \text{ Yield} = + 35.66 + 2.09 \text{ A} + 1.13 \text{ B} + 3.53 \text{ C} + 1.92 \text{ D} + 11.53 \text{ A}^2 + 1.99 \text{ B}^2 - 11.88 \text{ C}^2 + 4.02 \text{ D}^2 - 0.81 \text{ AB} - 0.49 \text{ AC} - 0.71 \text{ AD} + 0.67 \text{ BC} + 3.26 \text{ BD} + 0.72 \text{ CD} \qquad (6.2)$$

Table 6.1: Experimental design matrix and the response results

| Run | Variables | | | | Responses | | |
|-----|-----------|---|---|---|-----------|---|---|
| | DBTDL volume (ml) | CD mass (g) | Temp (°C) | HMDI volume (ml) | % Yield | Adsorption capacity (mg/g) | % Fe |
| 1 | 0.50 | 0.15 | 40.00 | 2.00 | 30.77 | 17.92 | 18.9 |
| 2 | 0.50 | 0.15 | 60.00 | 2.00 | 39.93 | 21.6 | 23.9 |
| 3 | 1.00 | 0.10 | 50.00 | 2.50 | 37.01 | 20.36 | 16.9 |
| 4 | 1.50 | 0.05 | 40.00 | 2.00 | 42.75 | 12.56 | 32 |
| 5 | 0.50 | 0.15 | 40.00 | 3.00 | 41.31 | 20.06 | 23.8 |
| 6 | 1.00 | 0.10 | 60.00 | 2.50 | 26.21 | 20.62 | 16.5 |
| 7 | 1.00 | 0.05 | 50.00 | 2.50 | 37 | 21.2 | 22.5 |
| 8 | 1.00 | 0.15 | 50.00 | 2.50 | 37.92 | 20.94 | 14.1 |
| 9 | 1.00 | 0.10 | 50.00 | 2.50 | 37.49 | 20.68 | 19.7 |
| 10 | 0.50 | 0.10 | 50.00 | 2.50 | 45.9 | 10.86 | 19.5 |
| 11 | 1.50 | 0.15 | 60.00 | 2.00 | 41.95 | 12.18 | 14.9 |
| 12 | 0.50 | 0.05 | 40.00 | 2.00 | 35.63 | 7.9 | 22.8 |
| 13 | 1.50 | 0.05 | 60.00 | 3.00 | 44.02 | 16.8 | 24 |
| 14 | 0.50 | 0.15 | 60.00 | 3.00 | 52.55 | 9.38 | 22.1 |
| 15 | 1.50 | 0.15 | 40.00 | 3.00 | 44.35 | 22.74 | 18.2 |
| 16 | 1.00 | 0.10 | 50.00 | 2.50 | 32.86 | 18.1 | 15.7 |
| 17 | 1.00 | 0.10 | 50.00 | 2.50 | 33.89 | 22 | 17.6 |
| 18 | 1.50 | 0.10 | 50.00 | 2.50 | 48.09 | 12.56 | 20.21 |
| 19 | 1.00 | 0.10 | 50.00 | 3.00 | 40.82 | 24.62 | 21.1 |
| 20 | 0.50 | 0.05 | 60.00 | 2.00 | 39.29 | 21.64 | 30.2 |
| 21 | 1.00 | 0.10 | 50.00 | 2.00 | 38.15 | 26.38 | 21.9 |
| 22 | 1.50 | 0.15 | 60.00 | 3.00 | 52.99 | 6.42 | 10.7 |
| 23 | 0.50 | 0.05 | 40.00 | 3.00 | 32.19 | 12.36 | 23.8 |
| 24 | 1.00 | 0.10 | 40.00 | 2.50 | 20.96 | 22.02 | 15.1 |
| 25 | 1.00 | 0.10 | 50.00 | 2.50 | 36.38 | 21.24 | 19.7 |
| 26 | 1.50 | 0.15 | 40.00 | 2.00 | 36.5 | 16.62 | 16 |
| 27 | 1.50 | 0.05 | 40.00 | 3.00 | 37.99 | 22 | 29.6 |
| 28 | 0.50 | 0.05 | 60.00 | 3.00 | 41.23 | 11.92 | 23 |
| 29 | 1.50 | 0.05 | 60.00 | 2.00 | 47.85 | 22.74 | 33.5 |
| 30 | 1.00 | 0.10 | 50.00 | 2.50 | 37.45 | 20.96 | 18.5 |

After discarding the insignificant terms, the quadratic equation reflecting the empirical relationship between % yield and the synthesis variables (only significant terms with $p < 0.05$ at 95% confidence level) are shown below:

% Yield = + 35.66 + 2.09 A + 1.13 B + 3.53 C + 1.92 D + 11.53 $A^2$ + 1.99 $B^2$ + 4.02 $D^2$ - 0.81 AB + 3.26 BD

The coefficient with larger amount controls the variable over the response while the sign before the coefficient indicate the nature of influence of variables on the response. Positive terms in the equation indicate a synergistic effect implying a direct proportionality between factor and response while negative terms indicate the antagonistic effect implying inverse proportionality (Sarkar and Majumdar, 2011). The model equation obtained suggested that the catalyst volume (A), β-CD mass (B), temperature (C) and HMDI volume (D), second order effect of $A^2$, $B^2$ and $D^2$, and interaction between β-CD mass and HMDI volume (BD) positively correlated to the NTPNC-HMDI-CD % yield. The interaction between the catalyst volume and the mass of β-CD was observed to have a negative correlation with the NTPNC-HMDI-CD % yield. DBTDL volume was observed to be the most influential parameter to the NTPNC-HMDI-CD % yield indicated by the highest coefficient.

The goodness of fitted model was assessed by coefficient of determination ($R^2$). A high $R^2$ value, close to 1, implies the good statistical model. The $R^2$ value of 0.9779 was obtained indicating that only 2.21 % of the total variation were not explained by the regression model. The adjusted $R^2$ value of 0.9572 was obtained which is said to correct the $R^2$ value for the sample size and the number of terms in the model (Yetilmezsoy et al., 2009). The lower value of the adjusted-$R^2$ compared to $R^2$ value indicate the goodness of data fit. The predicted $R^2$ value was obtained to be 0.9348 which was found to be in a reasonable agreement with the adjusted $R^2$ of 0.9572.

Table 6.2:. F-values and Prob > F from analysis of variance for all responses

| Response | % Yield | | 4-NP adsorption | | % Iron | |
|---|---|---|---|---|---|---|
| | F value | Prob > F | F value | Prob > F | F value | Prob > F |
| Model | 47.38 | < 0.0001 | 62.74 | < 0.0001 | 49.08 | < 0.0001 |
| A | 38.63 | < 0.0001 | 7.28 | 0.0165 | 3.70 | 0.0735 |
| B | 11.23 | 0.0044 | 0.096 | 0.7611 | 291.02 | < 0.0001 |
| C | 109.89 | < 0.0001 | 7.15 | 0.0173 | 0.092 | 0.7660 |
| D | 32.61 | < 0.0001 | 10.59 | 0.0053 | 14.85 | 0.0016 |
| $A^2$ | 168.48 | < 0.0001 | 249.37 | < 0.0001 | 11.32 | 0.0043 |
| $B^2$ | 5.03 | 0.0405 | 6.701E-003 | 0.9358 | 1.13 | 0.3036 |
| $C^2$ | 179.09 | < 0.0001 | 0.11 | 0.7402 | 6.92 | 0.0189 |
| $D^2$ | 20.46 | 0.0004 | 54.07 | < 0.0001 | 33.60 | < 0.0001 |
| AB | 5.20 | 0.0376 | 66.49 | < 0.0001 | 122.49 | < 0.0001 |
| AC | 1.90 | 0.1883 | 33.13 | < 0.0001 | 26.93 | 0.0001 |
| AD | 3.95 | 0.0655 | 25.05 | 0.0002 | 6.15 | 0.0255 |
| BC | 3.48 | 0.0819 | 144.04 | < 0.0001 | 3.21 | 0.0935 |
| BD | 83.16 | < 0.0001 | 4.31 | 0.0556 | 19.44 | 0.0005 |
| CD | 4.10 | 0.0610 | 211.58 | < 0.0001 | 42.53 | < 0.0001 |
| Residual | | | | | | |
| Lack of Fit | 0.28 | 0.9591 | 0.28 | 0.9574 | 0.20 | 0.9850 |
| Pure Error | | | | | | |
| Cor Total | | | | | | |
| $R^2$ | 0.9779 | | 0.9832 | | 0.9786 | |
| Adjusted $R^2$ | 0.9572 | | 0.9675 | | 0.9587 | |
| Predicted $R^2$ | 0.9348 | | 0.9437 | | 0.9532 | |

The actual and predicted removal efficiency plot for NTPNC-HMDI-CD % yield is shown in Fig. 6.1 A. The actual values are observed to be distributed close to the straight line indicating that the predicted values of NTPNC-HMDI-CD % yield obtained from the model are in good agreement with the actual experimental data. The results of analysis of variance (ANOVA) for the crosslinking of β-CD to NTP-NC using HMDI are presented in table 6.2. The ANOVA is essential to identify and determine the most significant factors and the meaningful of the experimental results with the Fisher's F-values and the P-values being the most important factors to conduct the comparison (Kasiri and Khataee, 2012). The P-values are used as an indication to determine the significance of each coefficient, which will show the pattern of the interaction between different variables. The coefficient with P-values less than 0.05 are significant and insignificant if greater than 0.1. It can be observed from Table 6.2, that the coefficients of A, B, C, D, $A^2$, $B^2$, $B^2$, $D^2$, AB, and BD were significant for NTPNC-HMDI-CD % yield as indicated by the p-values less than 0.05.

The higher F-values for each coefficient suggest the significance of that term in the model. The model F-values of 47.38 for NTPNC-HMDI-CD % yield was observed, implying that the model is significant and there is only a 0.01% chance that an F-Value this large could occur due to noise. The F-values and probability-values showed that second-order effect of DBTDL volume ($A^2$) followed by the reaction temperature (C) greatly influenced the NTPNC-HMDI-CD nanocomposite % yield while DBTDL (A), HMDI volume (D) and interaction between β-CD mass and HMDI volume moderately influenced the % yield. Lack of Fit (LOF) F-test which describes the variation of the data around the fitted model was also analysed. The non-significance of Lack of Fit is favourable and specifies the high predictability of the model while the significance of Lack of Fit implies that the model does not fit the data well (Sohrabi and Akhlaghian, 2016). Lack of Fit F-values was observed to be 0.28 for NTPNC-HMDI-CD % yield, which implies that the Lack of Fit is not significant relative to the pure error.

Three-dimensional surfaces and their corresponding contour graphs can facilitate the most significant interaction effect of significant experimental variables on the NTPNC-HMDI-CD nanocomposite % yield. In each plot, the response model is mapped against two experimental factors while the third factor is held constant at its central level. Two-dimensional contour plots are important in the determination of variable interactions, different types of interactions are explained by different shapes of contours. The elliptical shape of the contour plot demonstrates the strong interaction between independent variables (Muralidhar et al., 2001), the circular

contour shape shows no interaction between two variables and the linear contour shape indicate that there is a direct relationship between the independent variables (Makareviciene et al., 2014). Fig.6.2 A depicts the 3D surface plot of the simultaneous influence of amount of β-CD mass and DBTDL volume on % yield while maintaining HMDI volume and temperature at 2.5 ml and 50 °C, respectively. From Fig.6.2 a, it has been observed that at both low and high amount of β-CD, higher NTPNC-HMDI-CD % yield was obtained at low catalyst (DBTDL) volume of 0.5 ml, which resulted in a reduction in % yield up to a minimum followed by a steady increase with an increase in the catalyst volume. It was also noticed that at both low and high volume of DBTDL, an increase in β-CD mass did not have any noticeable effect on NTPNC-HMDI-CD nanocomposite % yield. A circular contour plot shows no interaction effect between β-CD mass and the catalyst (DBTDL) volume on NTPNC-HMDI-CD nanocomposite % yield.

Fig.6.2 B depicts the 3D surface plot of the simultaneous influence of β-CD mass and HMDI volume while maintaining DBTDL volume and temperature at 1.0 ml and 50 °C, respectively. From Fig.6.2 B, at both low and high β-CD mass, increasing HMDI volume led to an increase in NTPNC-HMDI-CD nanocomposite % yield. Similarly, at both low and high HMDI volume, increasing β-CD mass led to an increase in NTPNC-HMDI-CD nanocomposite % yield. Both variables showed the enhancing effect on NTPNC-HMDI-CD nanocomposite % yield. The results show that increment of β-CD mass and the HMDI cross-linker favours the formation of NTPNC-HMDI-CD nanocomposite. The contour plot shows no interaction between β-CD mass and HMDI volume on NTPNC-HMDI-CD nanocomposite % yield. Nanocomposite yield was observed to be strongly controlled by DBTDL volume. DBTDL catalyst plays an important role in isocyanates reactions as it affects the rate of chemical reaction responsible for the formation of polymers and exert a considerable influence on their ultimate properties. Higher volume of DBTDL catalyst, HMDI volume and β-CD mass resulted in the high yield of NTPNC-HMDI-CD nanocomposite.

### 6.2.1.2   *4-nitrophenol adsorption trend by NTPNC-HMDI-CD*

The adsorption capability of the NTPNC-HMDI-CD nanocomposite was demonstrated using 4-nitrophenol which is a toxic pollutant used in various industries. Since the nanocomposite is synthesised for organic pollutants removal from aqueous solution, its adsorption behaviour towards the targeted organic pollutant is of importance when optimizing synthesis variables.
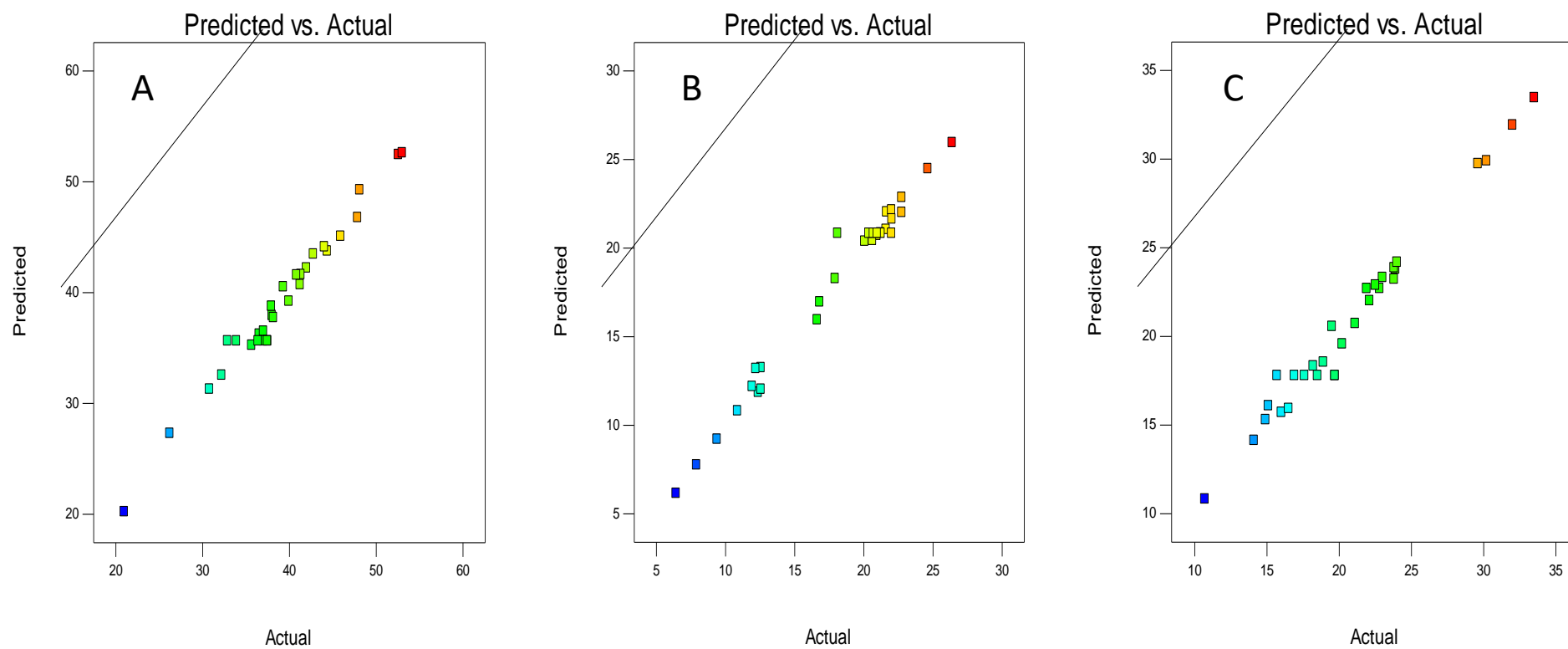
Figure 6.1: The predicted response versus actual response for (A) % yield, (B) 4-Nitrophenol adsorption capacity and (C) % Iron for the synthesis of NTPNC-HMDI-CD.
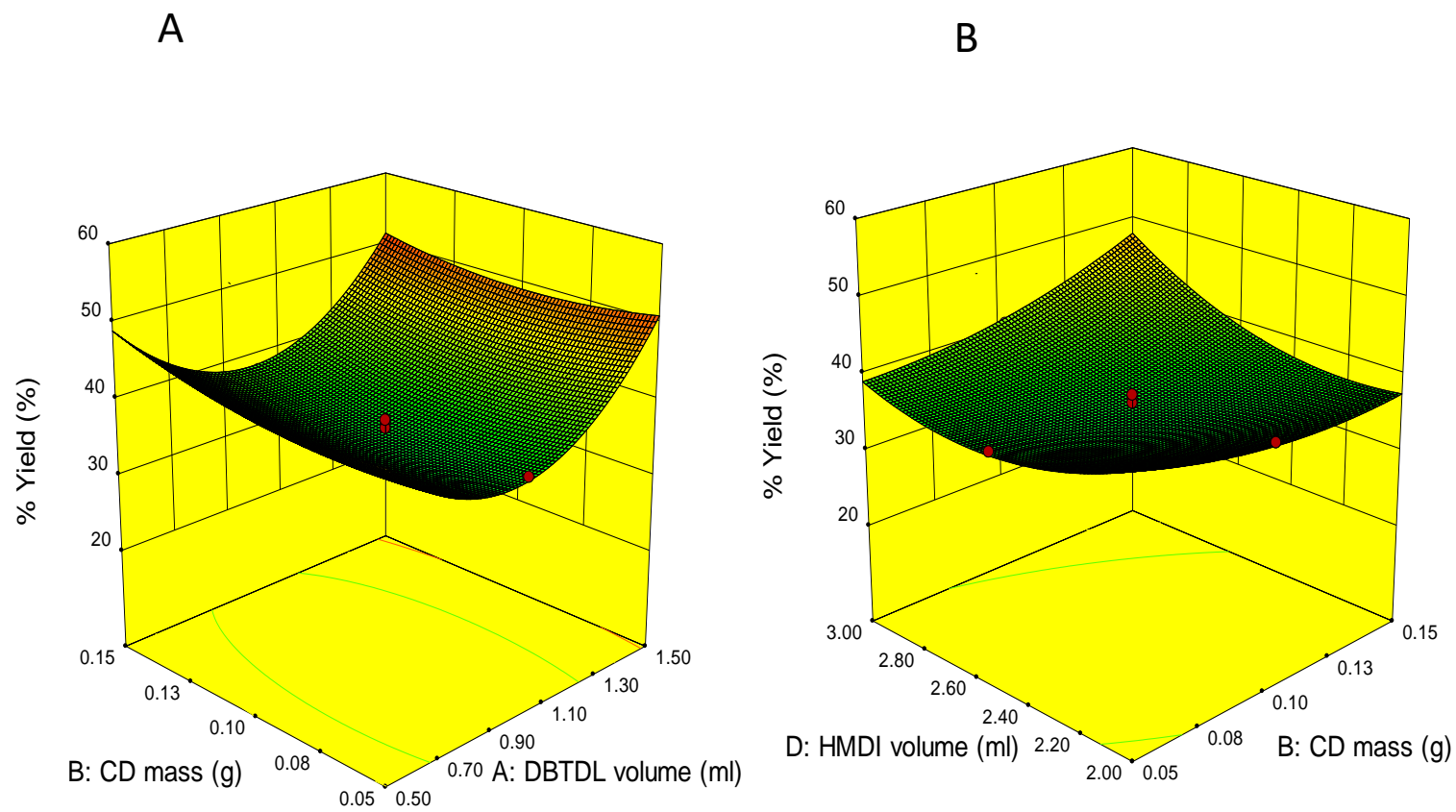
Figure 6.2: 3D surface plot showing the effect of independent variabled (C) β-CD mass versus DBTDL volume (D) HMDI volume versus β-CD mass for % yield.

The adsorption capacity of 4-nitrophenol using NTPNC-HMDI-CD nanocomposite of 30 experimental runs is shown in Table 6.1 and it is observed to range from 6.42 to 26.38 mg/g. The fitted model for the 4-nitrophenol adsorption capacity can be expressed as follows:

Adsorption capacity = + 20.84 + 0.61 A - 0.070 B - 0.60 C - 0.74 D- 9.41 $A^2$ - 0.049 $B^2$ + 0.20 $C^2$ + 4.38 $D^2$ - 1.96 AB - 1.38 AC + 1.20 AD - 2.88 BC- 0.50 BD - 3.49 CD     (6.3)

After discarding the insignificant terms, the fitted model in Eq.6.3 is represented as:

Adsorption capacity = + 20.84 + 0.61 A - 0.60 C - 0.74 D- 9.41 $A^2$ + 4.38 $D^2$ - 1.96 AB - 1.38 AC + 1.20 AD - 2.88 BC - 3.49 CD     (6.4)

4-nitrophenol adsorption capacity model equation obtained suggests that the DBTDL volume (A), the second order effects of HMDI volume ($D^2$) and the interaction between the catalyst volume and HMDI volume positively correlate to the 4-NP adsorption capacity. An increase in temperature (C), HMDI volume (D), the second order effect of the catalyst volume ($A^2$), the interaction between the catalyst volume and CD mass (AB), the catalyst volume and temperature (AC), CD mass and temperature (BC) and temperature and HMDI volume (CD) led to a reduction in 4-NP adsorption capacity. The $R^2$ value of 0.9832 and the adjusted $R^2$ value of 0.9675 for were obtained. Goodness of the data fit was indicated by the lower value of the adjusted-$R^2$ compared to $R^2$ while the predicted $R^2$ value of 0.9437 was found to be in a reasonable agreement with the adjusted $R^2$ of 0.9675 showing the difference of less than 0.2 indicating the applicability of the model in the prediction of the experimental results.

The actual and predicted removal efficiency plot for 4-NP adsorption capacity is shown in Fig. 6.1 B. The actual values are observed to be distributed close to the straight line indicating that the predicted values obtained from the model are in good agreement with the actual experimental data. The results of analysis of variance (ANOVA) for the crosslinking of β-CD to NTP-NC using HMDI are presented in Table 6.2. It can be observed from Table 6.2, that the coefficients of A, C, D, $A^2$, $D^2$, AB, AC, AD, BC, CD have p-values less than 0.05 hence they are significant model terms for 4-NP adsorption capacity. The model F-values of 62.74 for 4-NP adsorption capacity was observed, implying that the model is significant and there is only a 0.01% chance that an F-Value this large could occur due to noise. The F-values and probability-values showed that the second-order effect of DBTDL volume ($A^2$) is the most influential factor for 4-NP adsorption capacity. Lack of Fit F-value of 0.20 was observed implying that the Lack of Fit is not significant relative to the pure error.

3D surface plot and the corresponding contour plot of the simultaneous influence of DBTDL volume and β-CD mass while keeping HMDI volume and temperature fixed at 2.5 ml and 50 ºC on 4-NP adsorption capacity, respectively is shown in Fig.6.3 A. At both low and high β-CD mass, increasing DBTDL volume led to an increase in 4-NP adsorption capacity up to a maximum then a slight reduction in 4-NP adsorption capacity was observed as DBTDL volume increases. On the other hand, at low DBTDL volume, increasing β-CD mass resulted in a slight increase in the adsorption capacity while at high DBTDL volume, increasing the amount of β-CD resulted in a decrease in the adsorption capacity. The contour plot was seen to be linear in shape indicating that there is a direct relationship between the DBTDL volume and β-CD mass.

Fig.6.3 B, shows the 3D surface plot of the simultaneous influence of DBTDL volume and temperature while keeping β-CD mass and HMDI volume at 0.5 g and 2.5 ml on 4-NP adsorption capacity, respectively. From the 3D surface plot on Fig. 6.3 B, at both low and high temperature, an increase in DBTDL volume resulted in an increase in 4-NP adsorption capacity up to a maximum value then slightly decreased until the highest DBTDL volume of 1 ml. On the other hand, at low DBTDL volume, increase in temperature led to a slight increase in adsorption capacity while at high DBTDL volume, increasing reaction temperature led to a slight reduction in 4-NP adsorption capacity. This trend was observed to be similar to the trend observed for the interaction between DBTDL volume and β-CD mass in Fig.6.3 A. The contour plot shows that there is a direct relationship between the DBTDL volume and temperature.

Fig.6.3 C, shows the 3D surface plot of the simultaneous influence of HMDI volume and DBTDL volume while keeping β-CD mass and temperature fixed at 0.5 g and 50 ºC on 4-NP adsorption capacity, respectively. The 3D surface plot shows that at both low and high HMDI volume, increasing DBTDL volume led to an increase in adsorption capacity up to a maximum value then a decrease in adsorption capacity was observed as DBTDL volume is further increased. At both low and high DBTDL volume, adsorption capacity was observed to be almost constant then increased steadily up to a maximum value of about 15 mg/g as HMDI volume was increased. The contour plot shows a strong interaction between DBTDL and HMDI volume. DBTDL was observed to greatly influence the 4-Nitrophenol adsorption and high removal was obtained at moderate amount.
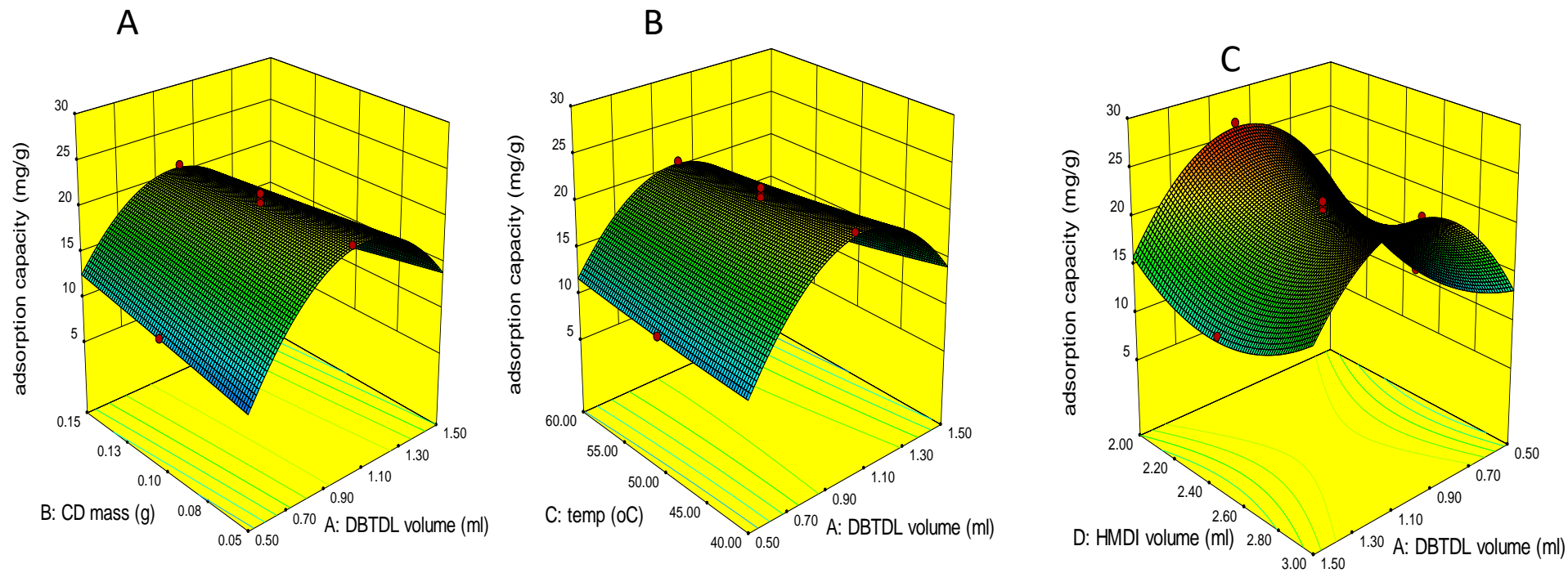
Figure 6.3: 3D surface plots showing the effect of independent variables (A) β-CD mass versus DBTDL volume (B) temperature versus DBTDL volume, (C) HMDI volume versus DBTDL volume for adsorption capacity.

### 6.2.1.3　Percentage iron in the NTPNC-HMDI-CD nanocomposite

To synthesize a nanocomposite material that will have magnetic properties for easy separation through a magnetic field, percentage magnetite in the nanocomposite need to be considered. Magnetic functionality of the nanocomposite originates from the presence of magnetite in their chemical composition which was measured as a function of % iron content.The % iron on the NTPNC-HMDI-CD nanocomposite of the 30 experimental runs is shown in Table 1 and it is observed to range from 10.7 to 33.5 %. The fitted model for the % iron can be expressed as:

% Iron = +17.80 - 0.49 A - 4.38B - 0.078 C - 0.99 D + 2.28 $A^2$ + 0.72 $B^2$ - 1.78 $C^2$ + 3.92 $D^2$ - 3.01 AB - 1.41 AC - 0.67 AD - 0.49 BC + 1.20 BD - 1.77 CD　　　　　　　(6.6)

After discarding the insignificant terms, the quadratic equation reflecting the empirical relationship between % iron and the synthesis variables (only significant terms with p < 0.05 at 95% confidence level) are shown below:

% Iron = +17.80 - 4.38 B - 0.99 D + 2.28 $A^2$ + 0.72 $B^2$ - 1.78 $C^2$ + 3.92 $D^2$ -3.01 AB - 1.41 AC - 0.67 AD + 1.20 BD - 1.77 CD　　　　　　　　　　(6.7)

The % iron model equation (eq. 6.7) suggested that the second order effect of catalyst volume ($A^2$), CD mass ($B^2$), HMDI volume ($D^2$), and the interaction between the CD mass and HMDI volume (BD) positively correlate to the 4-NP adsorption capacity while β-CD mass (B), HMDI volume (D), the second order effects of temperature ($C^2$), the interaction between the catalyst volume and CD mass (AB), the catalyst volume and temperature (AC), catalyst volume and HMDI volume (AD) and temperature and HMDI volume (CD) led to a reduction in % iron present in the NTPNC-HMDI-CD material. The $R^2$ value of 0.9786 and the adjusted $R^2$ value of 0.9587 were obtained. Goodness of the data fit was indicated by the lower value of the adjusted-$R^2$ compared to $R^2$ while the predicted $R^2$ value of 0.9532 was found to be in a reasonable agreement with the adjusted $R^2$ of 0.9587 showing the difference of less than 0.2 indicating the applicability of the model in the prediction of the experimental results.

The actual and predicted removal efficiency plot for 4-NP adsorption capacity is shown in Fig.6.1 C. The actual values are observed to be distributed close to the straight line indicating that the predicted values obtained from the model are in good agreement with the actual experimental data.
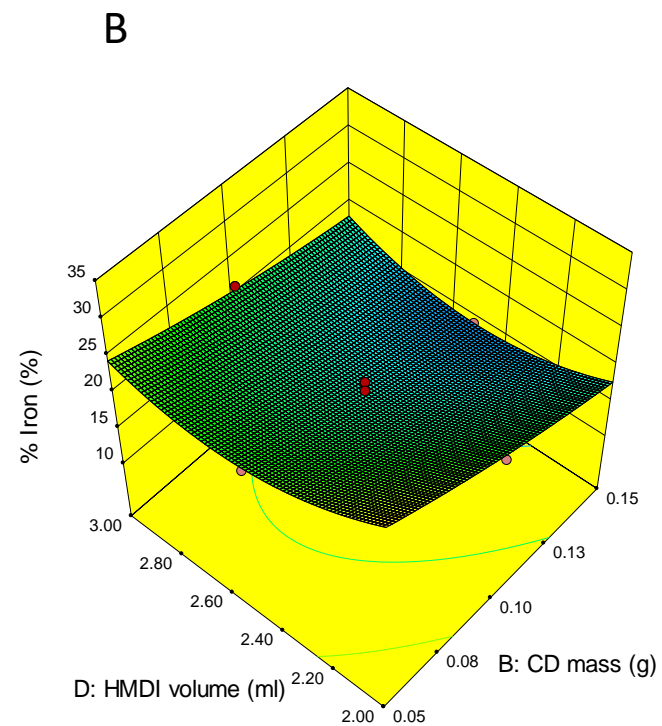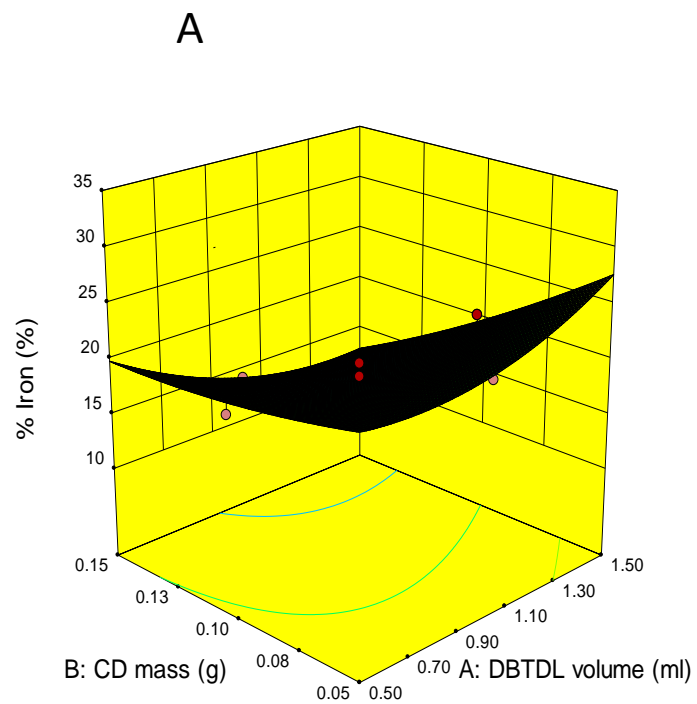
Figure 6.4: 3D surface plot showing the effect of independent variabled (A) β-CD mass versus DBTDL volume (B) HMDI volume versus β-CD mass for % Iron.

The results of analysis of variance (ANOVA) for the crosslinking of β-CD to NTP-NC using HMDI are presented in table 6.2. It can be observed from Table 6.2, that the coefficients of B, D, $A^2$, $C^2$, $D^2$, AB, AC, AD, BD, CD. have p-values less than 0.05 hence they are significant model terms for % iron. The model F-value of 49.08 was observed, implying that the model is significant and there is only a 0.01% chance that an F-Value this large could occur due to noise. The F- values and probability-values showed that the second-order effect of DBTDL volume (B) is the most influential factor for 4-NP adsorption capacity. Lack of Fit F-value of 0.28 was observed implying that the Lack of Fit is not significant relative to the pure error. Fig.6.4a show the 3D surface plot of the simultaneous influence of β-CD mass and DBTDL volume while keeping temperature and HMDI volume at 50 ºC and 2.5 ml on % iron, respectively. It has been observed that at low DBTDL volume, increasing β-CD mass didn't have any effect on % iron while increasing β-CD mass at high DBTDL volume caused a reduction in % iron. DBTDL volume was also shown to have a similar trend as mass of β-CD on % iron present in the nanocomposite. % iron was observed to reduce as DBTDL volume increases at high β-CD mass, and no effect in % Iron was observed at low β-CD mass. The contour plot shows a circular shape implying that there is no strong interaction between mass of β-CD and DBTDL volume along with % iron.

Fig.6.4 B, shows the 3D surface plot of the simultaneous influence of HMDI volume and β-CD mass while keeping reaction temperature and DBTDL volume at 50 ºC and 1.0 ml on % iron, respectively. The 3D surface plot shows that at both low and high β-CD mass, increasing HMDI volume led to a slight decrease in % iron up to a minimum value followed by a slight increase as HMDI volume was further increased. At both low and high HMDI volume, increasing β-CD mass led to a slight decrease in % iron of the NTPNC-HMDI-CD nanocomposite. A circular contour shape was observed indicating no strong interaction between β-CD mass and HMDI volume. It has been observed that the nanocomposite with higher % Iron was formed when high amount of the DBTDL catalyst and low amount of β-CD are added. Higher % Iron in the nanocomposite was obtained at low β-CD amount due to higher amount of NTPNC in the nanocomposite contributing to higher % iron.

Optimization of the process variables was conducted after multiple fitting of the regression by deploying algorithm of the RSM software. Setting of goals for optimum parameters were selected according to the application of the nanocomposite material. Goals may be set at

maximum, minimum, in range, target or be equals to the specific value when optimizing the response. Optimum conditions for NTPNC-HMDI-CD are presented in Table 6.3. From Table 6.3, optimum parameters were observed to be DBTDL volume,1.39 ml, β-CD mass of 0.15 g, HMDI volume of 3 ml at reaction temperature of 42 ºC yielding 44.57 % of the NTPNC-HMDI-CD nanocomposite that will have 18 % of iron and can remove 24.39 mg/g of 4-nitrophenol from aqueous solution. The optimum conditions were observed by keeping the DBTDL volume in range, maximised β-CD mass and HMDI volume while keeping reaction temperature at minimal values.

Table 6.3: Optimum results for NTPNC-HMDI-CD

| Variables | | | | Responses | | | |
|---|---|---|---|---|---|---|---|
| DBTDL vol (ml) | β-CD mass (g) | Temp (º C) | HMDI vol (ml) | % Yield | Adsorption Capacity (mg/g) | % Fe | Desirability |
| 1.39 | 0.15 | 42 | 3 | 44.57 | 24.39 | 18.00 | 0.861 |

## 6.3 OPTIMIZATION OF WORKING PARAMETERS ON NTPNC-EPI-CD SYNTHESIS

With an effort to synthesize an insoluble and highly selective cyclodextrin crosslinked to magnetite coated pine cone using epichlorohydrin (NTPNC-EPI-CD) nanocomposite material for 4-Nitrophenol adsorption from aqueous solution, carboxymethyl-beta-cyclodextrin (CM-β-CD) polymer was synthesized and crosslinked onto NTPNC previously synthesized. Response surface methodology (RSM) and central composite design (CCD) were used to determine the interaction between the working condition variables and the response. Four parameters (CM-β-CD-EPI mass, NTP-NC mass, temperature and reaction time) that may have an influence on 4-NP removal were selected along with three responses: 4-NP adsorption capacity, % Iron and surface area of the NTPNC-EPI-CD. The design matrix and the responses showing 30 experimental runs are given in Table 6.4.

### 6.3.1.1 Percentage iron in the NTPNC-EPI-CD nanocomposite

Percentage iron in the NTPNC-EPI-CD nanocomposite was measured with a Rigaku NEX-QC model X-ray fluorescence (XRF) instrument, using magnetite analysis application mode and the results are presented in Table 6.4. From Table 6.4, % Iron in the nanocomposite was observed to range from 50.8 to 92.47 %. The quadratic model was selected based on the highest order polynomial where the addition term is significant. After the data was subjected to multiple regression analysis of CCD, the quadratic equation describing the relationship between % iron and the synthesis variables (CM-β-CD-EPI mass, NTP-NC mass, temperature and reaction time) is given below:

% Iron= + 77.51 + 2.36 A - 5.02 B - 0.42 C - 0.85 D - 0.63 AB - 0.13 AC - 0.36 AD -0.19 BC - 0.79 BD + 0.43 CD - 3.41 $A^2$ - 12.26 $B^2$ - 17.16 $C^2$ + 14.94 $D^2$        (6.8)

Where A, B, C and D are the synthesis variables, NTP-NC mass, CM-β-CD mass, reaction temperature and reaction time, respectively. After discarding the insignificant terms, the resultant model is represented as:

% Iron= + 77.51 + 2.36 A - 5.02 B - 0.42 C - 0.85 D - 0.63 AB - 0.79 BD + 0.43 CD - 3.41 $A^2$ - 12.26 $B^2$ - 17.16 $C^2$ + 14.94 $D^2$        (6.9)

The quadratic equation obtained suggest that NTPNC mass (A) the interaction between reaction temperature and time (CD) and second-order effect of temperature ($D^2$) positively

228

correlated to the NTPNC-EPI-CD % yield while other factors negatively correlated to the % yield. CM-β-CD mass (B) was observed to be the most influential parameter to the NTPNC-EPI-CD yield seen by the highest coefficient. Correlation coefficient was evaluated to test the fit of the model. The value of the correlation coefficient ($R^2$) was obtained to be 0.9981 while the adjusted $R^2$ value of 0.9964 was obtained. The closeness of the adjusted $R^2$ values to the correlation coefficient ($R^2$) indicate a good agreement between the experimental and predicted values for all variables. The Predicted $R^2$ of 0.9866 is in reasonable agreement with the adjusted $R^2$ of 0.9964. The actual and predicted removal efficiency plot for % iron in NTPNC-EPI-CD nanocomposite is shown in Fig.6.5a. The actual values are observed to be distributed close to the straight line indicating that the predicted values obtained from the model are in good agreement with the actual experimental data.

To find the most important effects and interactions, analysis of variance (ANOVA) was analysed using the software Design Expert (10) and the results are given in Table.6.4, while the correlation coefficient results are given in Table.6.5. The statistical significance of all the model equations was evaluated by the Fisher's F-test and probability p-values. The Model F-values were observed to be of 570.35 implying that the model is significant and there is only a 0.01% chance that an F-value this large could occur due to noise. It is observed that the coefficients NTPNC mass (A), CM-β-CD mass (B), reaction temperature (C), time (D), interaction between NTPNC mass and CM-β-CD mass (AB), CM-β-CD mass and time (BD), reaction temperature and time (CD) and the quadratic effect of NTPNC mass ($A^2$), CM-β-CD mass ($B^2$), temperature ($C^2$), time ($D^2$) were significant for % iron in the NTPNC-EPI-CD nanocomposite, as it can be seen by the probability values less than 0.05 from the ANOVA table in Table.6.5. The F-values and probability-values showed that the second-order effect of temperature ($C^2$) greatly influenced % iron in the NTPNC-EPI-CD nanocomposite. The 2D contour plot and the 3D surface plots were analysed to optimise interaction between variable in respect to the response.

Chemical reaction governing the crosslinking of β-CD onto NTPNC is shown in scheme 6.2. The NTPNC-EPI-CD nanocomposite synthesis followed a 2 steps procedure where the first step involves the preparation of carboxymethyl-β-cyclodextrin followed by the crosslinking of CM-β-CD onto NTPNC bio composite surface. The carboxyl group of the CM-β-CD directly react with the active surface hydroxyl group on the magnetite to form Fe-carboxylate (Badruddoza et al., 2010).

Table 6.4: Experimental design matrix and the response results

| Runs | NTPNC mass (g) | CM-β-CD mass (g) | Temp (°C) | Time (hrs) | % Iron (%) | Adsorption capacity (mg/g) | Surface area (m²/g) |
|---|---|---|---|---|---|---|---|
| 1 | 2.00 | 2.00 | 30.00 | 3.00 | 60.1 | 16.12 | 262.71 |
| 2 | 2.00 | 0.50 | 90.00 | 24.00 | 67.1 | 11.31 | 433.78 |
| 3 | 0.50 | 2.00 | 90.00 | 3.00 | 53.9 | 15.096 | 365.55 |
| 4 | 1.25 | 1.25 | 60.00 | 13.50 | 77.6 | 17.608 | 347.44 |
| 5 | 1.25 | 1.25 | 60.00 | 3.00 | 92.7 | 21.12 | 230.96 |
| 6 | 0.50 | 2.00 | 30.00 | 24.00 | 50.8 | 10.874 | 361.24 |
| 7 | 2.00 | 0.50 | 90.00 | 3.00 | 68.4 | 13.95 | 341.46 |
| 8 | 0.50 | 1.25 | 60.00 | 13.50 | 71 | 11.874 | 292.32 |
| 9 | 1.25 | 1.25 | 60.00 | 13.50 | 77.32 | 17.216 | 350.00 |
| 10 | 0.50 | 0.50 | 30.00 | 3.00 | 61.4 | 17.292 | 270.50 |
| 11 | 1.25 | 1.25 | 60.00 | 24.00 | 92.3 | 17.43 | 350.02 |
| 12 | 0.50 | 0.50 | 90.00 | 24.00 | 62 | 12.798 | 364.12 |
| 13 | 1.25 | 1.25 | 60.00 | 13.50 | 77.3 | 17.924 | 399.40 |
| 14 | 1.25 | 1.25 | 30.00 | 13.50 | 60.7 | 18.336 | 420.61 |
| 15 | 1.25 | 1.25 | 90.00 | 13.50 | 60.1 | 18.798 | 323.71 |
| 16 | 1.25 | 1.25 | 60.00 | 13.50 | 77.8 | 17.924 | 351.49 |
| 17 | 0.50 | 2.00 | 90.00 | 24.00 | 50.8 | 14.24 | 291.61 |
| 18 | 2.00 | 2.00 | 90.00 | 3.00 | 56.4 | 14.146 | 267.15 |
| 19 | 2.00 | 2.00 | 30.00 | 24.00 | 55.1 | 10.506 | 343.90 |
| 20 | 2.00 | 2.00 | 90.00 | 24.00 | 54.8 | 12.444 | 238.06 |
| 21 | 1.25 | 1.25 | 60.00 | 13.50 | 77.7 | 17.506 | 376.35 |
| 22 | 0.50 | 2.00 | 30.00 | 3.00 | 54.9 | 16.562 | 292.21 |
| 23 | 1.25 | 0.50 | 60.00 | 13.50 | 70.4 | 15.456 | 634.68 |
| 24 | 1.25 | 1.25 | 60.00 | 13.50 | 77 | 16.772 | 379.82 |
| 25 | 0.50 | 0.50 | 30.00 | 24.00 | 62 | 10.31 | 542.20 |
| 26 | 2.00 | 0.50 | 30.00 | 24.00 | 66.8 | 10.892 | 654.78 |
| 27 | 2.00 | 1.25 | 60.00 | 13.50 | 77.3 | 10.798 | 298.18 |
| 28 | 2.00 | 0.50 | 30.00 | 3.00 | 69.2 | 16.608 | 356.70 |
| 29 | 1.25 | 2.00 | 60.00 | 13.50 | 60.2 | 15.506 | 524.59 |
| 30 | 0.50 | 0.50 | 90.00 | 3.00 | 60 | 15.07 | 291.80 |

Table 6.5: F-values and Prob > F from analysis of variance for all responses

| Response | % Iron | | 4-NP adsorption | | Surface area | |
|---|---|---|---|---|---|---|
| | F value | Prob > F | F value | Prob > F | F value | Prob > F |
| Model | 570.35 | < 0.0001 | 235 | < 0.0001 | 51.14 | < 0.0001 |
| A | 285.02 | < 0.0001 | 60.97 | < 0.0001 | 2.02 | 0.1760 |
| B | 992.12 | < 0.0001 | 9.25 | 0.0083 | 114.46 | < 0.0001 |
| C | 6.84 | 0.0195 | 0.44 | 0.5172 | 44.44 | < 0.0001 |
| D | 28.48 | < 0.0001 | 960.89 | < 0.0001 | 104.42 | < 0.0001 |
| $A^2$ | 66.02 | < 0.0001 | 1215.10 | < 0.0001 | 53.88 | < 0.0001 |
| $B^2$ | 853.04 | < 0.0001 | 109.67 | < 0.0001 | 215.89 | < 0.0001 |
| $C^2$ | 1671.09 | < 0.0001 | 89.27 | < 0.0001 | 1.91 | 0.1873 |
| $D^2$ | 1266.34 | < 0.0001 | 193.42 | < 0.0001 | 59.43 | < 0.0001 |
| AB | 13.96 | 0.0020 | 0.045 | 0.8350 | 38.69 | < 0.0001 |
| AC | 0.60 | 0.4493 | 15.58 | 0.0013 | 4.93 | 0.0422 |
| AD | 4.45 | 0.0522 | 0.35 | 0.5626 | 1.55 | 0.2325 |
| BC | 1.32 | 0.2694 | 11.53 | 0.0040 | 12.63 | 0.0029 |
| BD | 22.08 | 0.0003 | 8.70 | 0.0091 | 68.39 | < 0.0001 |
| CD | 6.52 | 0.0221 | 278.15 | < 0.0001 | 62.77 | < 0.0001 |
| Residual | | | | | | |
| Lack of Fit | 7.12 | 0.0214 | 0.58 | 0.7812 | 0.96 | 0.5536 |
| Pure Error | | | | | | |
| Cor Total | | | | | | |
| $R^2$ | 0.9981 | | 0.9744 | | 0.9795 | |
| Adjusted $R^2$ | 0.9964 | | 0.9506 | | 0.9603 | |
| Predicted $R^2$ | 0.9866 | | 0.9421 | | 0.9199 | |

Carboxymethyl cellulose was grafted onto cyclodextrin using epichlorohydrin to control the structure of the material while modifying the surface chemistry of the nanocomposite. It is important to understand the NTPNC-EPI-CD reaction mechanism so as to explain the variable interaction and their effect on respective responses. Reaction temperature, time, the amount of NTPNC and CM-β-CD added may influence the crosslinking of CM-β-CD onto NTPNC hence their optimization is of importance.
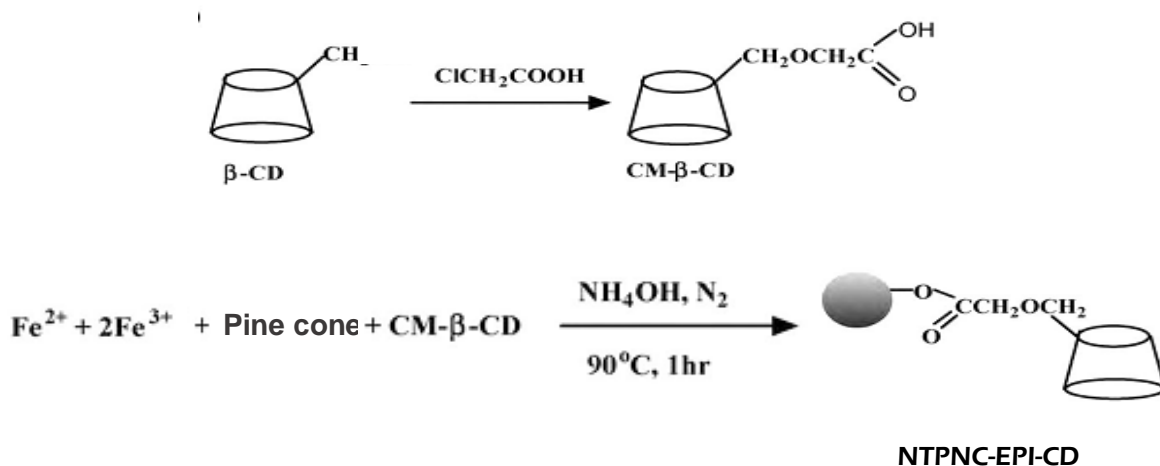


Scheme 6.2: Schematic presentation of CM-β-CD polymer crosslinked onto NTPNC bio-composite.
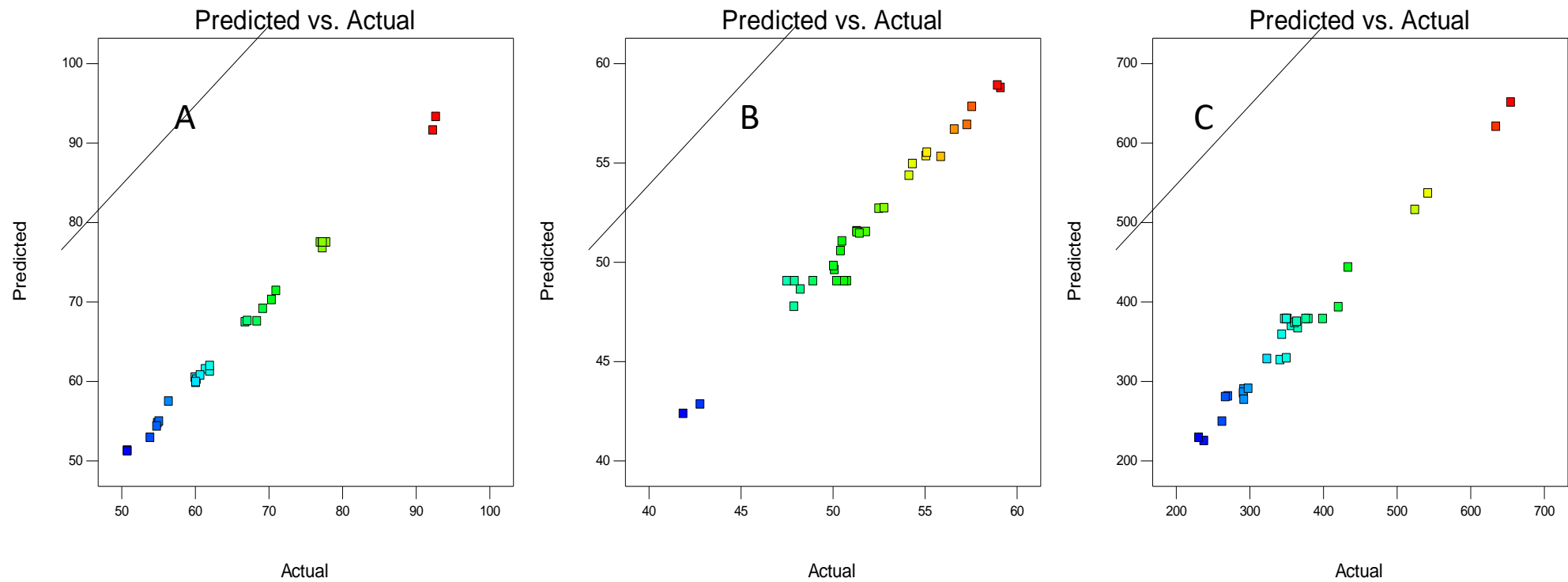
Figure 6.5: The predicted response versus actual response for (A) % iron, (B) 4-Nitrophenol adsorption capacity and (C) Surface area of NTPNC-EPI-CD nanocomposite.
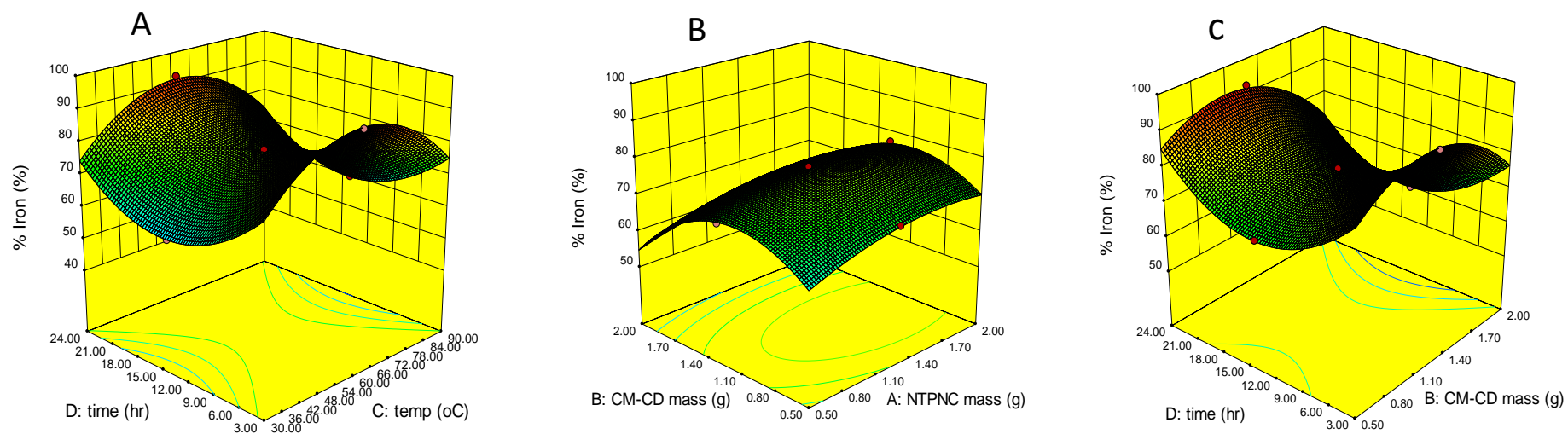
Figure 6.6:3D surface plots showing the effect of independent variables (A) Time versus temperature, (B) CM-β-CD mass versus NTPNC mass (C) reaction time versus CM-β-CD mass for % iron in the NTPNC-EPI-CD nanocomposite

Two-dimensional contour plots and three-dimensional surface plots are important in determining interaction between variables. and their plots are presented in Fig.6.6 (A-C). Interaction effect of reaction time and temperature on the % iron content in NTPNC-EPI-CD nanocomposite while keeping the CM-β-CD and NTPNC mass fixed at 1.25 g is presented in Fig.6.6 A. At both short and long time, increasing the reaction temperature resulted in an increase in % iron up to a maximum value which then reduced as temperature was increased. On the other hand, at both low and high temperature, increasing the reaction time resulted in a slight reduction in % iron up to a minimum value followed by a gradual increase in % iron at long reaction time. The elliptical line of the contour plot shows a strong interaction between temperature and time for % iron in the nanocomposite.

Interaction effect of CM-β-CD and NTPNC mass on % iron in NTPNC-EPI-CD while keeping the reaction temperature fixed at 60 °C and time at 1 hour is presented in Fig.6.6 b. It can be seen from the plot that at low amount of CM-β-CD, increasing NTPNC mass had a slight increase in % iron, but, at higher amount of CM-β-CD, increment in NTPNC mass had insignificance increase in % iron. At both low and high amount of NTPNC mass, initial increase in CM-β-CD resulted in an increase of % iron from 50.8 to 71 % when 1.4 g of CM-β-CD was added. Further increase in CM-β-CD mass to 2.0 g resulted in a slight reduction of % iron. This shows that more amount of NTPNC added at low amount of CM-β-CD will lead to higher % iron in the NTPNC-EPI-CD nanocomposite while CM-β-CD increment increases % iron up to a maximum value and reduced as more CM-β-CD is added to the nanocomposite. The circular line of the contour plot implies that there is no strong interaction between the CM-β-CD mass and NTPNC mass. The interaction between CM-β-CD and reaction time on % Iron in NTPNC-EPI-CD while keeping the reaction NTPNC mass fixed at 1.25 g and temperature at 60 °C is presented in Fig.6.6 c. Increase in the amount of CM-β-CD led to an increase in % iron up to a maximum value of 92.7 % which then reduced to 75 % as CM- β-CD mass was further increased to 2.0 g at all reaction time. At both low and high CM- β-CD mass, higher % iron was observed which reduced to a minimum value of 55 % then increase steadily with time. Reduction in % iron as more CM-β-CD is added is beause of the higher amount of CM-β-CD content in the nanocomposite resulting in lower amount of NTPNC hence a drop in % iron. Amount of CM-β-CD need to be considered to prepare a material that will have a moderate magnetite content for magnetic separation. The contour plot shows the elliptical shape implying

the strong interaction between CM-β-CD mass and the reaction time in the NTPNC-EPI-CD synthesis.

### 6.3.2   4-Nitrophenol adsorption trend by NTPNC-EPI-CD nanocomposite

The adsorption capacity of 4-NP using NTPNC-EPI-CD nanocomposite of 30 experimental runs is shown in Table 6.4 and it is observed to range from 10.29 to 21.82 mg/g. The fitted model for the 4-NP adsorption capacity can be expressed as follows:

Adsorption capacity = + 17.30 – 0.50 A+ 0.20 B -0.043 C -2.00 D+ 0.015 AB - 0.27 AC +- 0.041 AD + 0.23 BC + 0.20 BD + 1.14 CD – 5.93 $A^2$ – 1.78 $B^2$ + 1.61 $C^2$ + 2.36 D     (6.10)

After discarding the insignificant terms, the resultant model is represented as:

Adsorption capacity = + 17.30 – 0.50 A+ 0.20 B -2.00 D - 0.27 AC + 0.20 BD + 1.14 CD – 5.93 $A^2$ – 1.78 $B^2$ + 1.61 $C^2$ + 2.36 $D^2$                    (6.11)

The model equation obtained for 4-NP adsorption capacity suggested that the interaction between CM-β-CD mass and time (BD), reaction temperature an time (CD), CM-β-CD mass (B), the second order effect reaction temperature ($C^2$) and time ($D^2$) positively correlate to the 4-NP adsorption capacity. The NTPNC mass (A), reaction time (D), interaction between NTPNC mass and temperature (AC) and second order effect of CM-β-CD mass ($B^2$) were observed to have a negative influence on the 4-NP adsorption capacity. Second order effect of NTPNC mass ($A^2$), second order effect of time ($D^2$) and reaction time (D) were observed to be the most influential parameters to the 4-NP adsorption capacity as seen by the highest coefficient. The value of the correlation coefficient ($R^2$) was obtained to be 0.9744 while the adjusted $R^2$ value of 0.9506 was obtained. The closeness of the adjusted $R^2$ values to the correlation coefficient ($R^2$) indicate a good agreement between the experimental and predicted values for all variables. The Predicted $R^2$ of 0.9421 is in reasonable agreement with the adjusted $R^2$ of 0.9506. The actual and predicted removal efficiency plot for 4-NP adsorption by NTPNC-EPI-CD nanocomposite is shown in Fig. 6.5 B. The actual values are observed to be distributed close to the straight line indicating that the predicted values obtained from the model are in good agreement with the actual experimental data
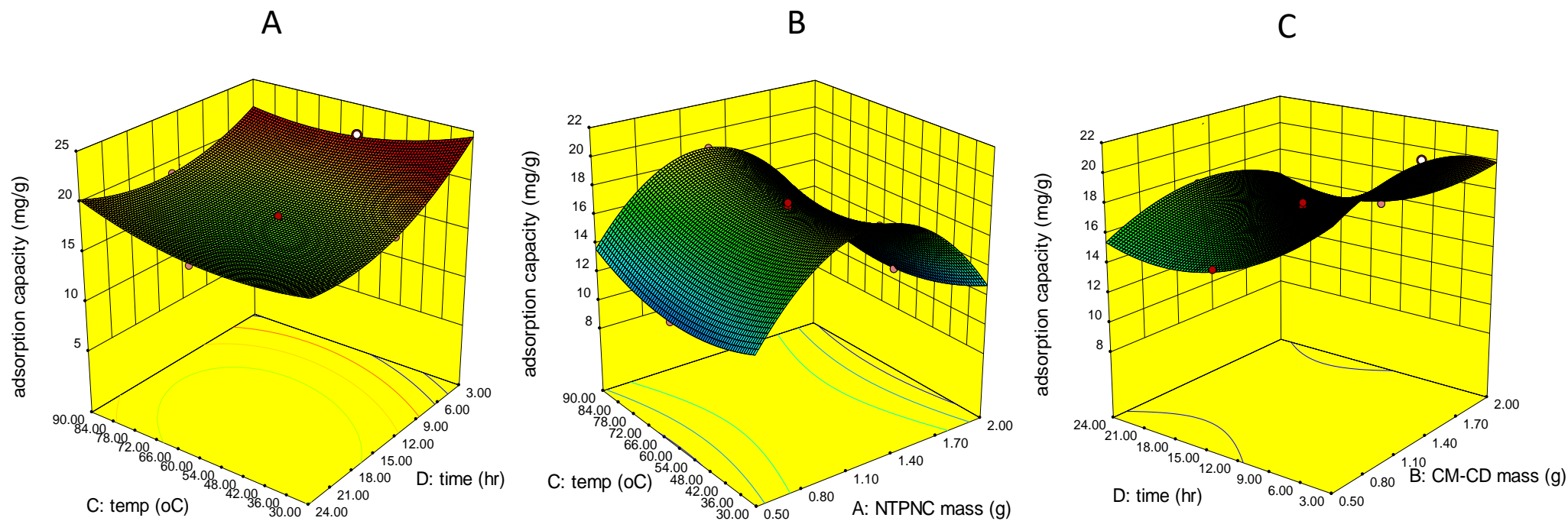
Figure 6.7:3D surface plots showing the effect of independent variables (A) temperature versus reaction time, (B) temperature versus NTPNC mass and (C) reaction time versus CM-β-CD mass for 4-NP adsorption onto NTPNC-EPI-CD nanocomposite.

The statistical significance of all the model equations was evaluated by the Fisher's F-test and probability p-values. The Model F-values were observed to be 40.85 implying the significance of the model. From the ANOVA table in Table.6.5, the coefficients a, B, D, AC, BD, CD second order effect of $A^2$, $B^2$, $C^2$, $D^2$ were significant as it can be seen by the probability values less than 0.05. From the F-values and probability-values, 4-NP adsorption capacity was observed to be greatly influenced by the second order effect of NTPNC mass ($A^2$) followed by the reaction time (D), the interaction between the reaction temperature and time and the second order effect of time ($D^2$).

The contour and the 3D surface plots of the most significant variables that influence the 4-NP adsorption onto NTPNC-EPI-CD nanocomposite is shown in Fig. 6.7 (A-C). Interaction effect of reaction time and temperature on the 4-NP adsorption capacity of NTPNC-EPI-CD while keeping CM-β-CD mass fixed at 1.25 g for 1hr is presented in Fig. 6.7 A. Fi. 6.7 A shows that, at short and long reaction time, increasing the reaction temperature did not have any noticeable change on the 4-NP adsoption capacity. At low and high temperatures, increasimg the reaction time resulted in an increase in 4-NP adsorption. Contour plot shows no strong interaction between reaction time and NTPNC mass for 4-NP adsorption onto NTPNC-EPI-CD nanocomposite. Fig.6.7 B shows interaction effect of reaction temperature and NTPNC mass while keeping CM-β-CD mass and time fixed at 1.25 g and 1 hr, respectively. The figure shows that at both low and high reaction temperature, an increase in NTPNC mass resulted in an increase in 4-NP adsorption capacity up to a maximum value followed by a slight reduction at higher amount of NTPNC. On the other hand, at both low and high NTPNC mass, increasing temperature resulted in a increase in 4-NP adsorption capacity. The elliptical shape suggest the strong interaction between NTPNC mass and temperature. Fig.6.7 C shows interaction effect of reaction time and CM-β-CD mass while keeping NTPNC mass and temperature fixed at 1.25 g and 60 ᵒC, respectively. It is noticed that at both low and high CM-β-CD mass, increasing reaction time led to a gradual reduction in adsorption capacity up to an almost constant capacity as time increases. At both short and long reaction time, increase in CM-β-CD mass resulted in an increase in adsorption capacity up to a minimum value followed by a slight reduction in as reaction time was increased. The contour plot shows strong interaction between reaction time and CM-β-CD mass for 4-NP adsorption onto NTPNC-EPI-CD nanocomposite. The adsorpion of 4-NP is highly favoured by the NTPNC-EPI-CD nanocomposite at short reaction time and when the amount of NTPNC is equivalent to the amount of CM-β-CD. A reduction in the amount of 4-NP adsorbed was observed as NTPNC amount is in excess. This shows that the

inclusion phenomena between CM-β-CD and 4-NP plays a major role in the adsorption mechanism.

### 6.3.3 Surface area of NTPNC-EPI-CD nanocomposite

Surface area values of the 30 experimental runs from tables.6.4 ranged from 230.96 to 654.78 $m^2/g$. The fitted model for the surface area of NTPNC-EPI-CD can be observed in eq. 6.12.

Surface area = + 378.70 + 6.95 A - 52.39 B - 32.64 C + 50.04 D - 32.31 AB -11.54 AC + 6.46 AD + 18.46 BC - 42.95 BD - 41.15 CD - 94.74 $A^2$ + 189.64 $B^2$ - 17.83 $C^2$ - 99.50 $D^2$ (6.12)

After discarding the insignificant terms the fitted model in eq. 6.12 is represented as:

Surface area = + 378.70 - 52.39 B - 32.64 C + 50.04 D - 32.31 AB -11.54 AC + 18.46 BC - 42.95 BD - 41.15 CD - 94.74 $A^2$ + 189.64 $B^2$ - 99.50 $D^2$ (6.13)

The model equation obtained suggested that the reaction time (D), interaction between CM-β-CD mass and temperature (BC) and the second order effect CM-β-CD mass (B) positively correlated to the surface area of NTPNC-EPI-CD while other factors negatively affected the surface area on the nanocomposite. The second order effect of CM-β-CD mass ($B^2$) had the highest coefficient, therefore the most influential variable for surface area. Correlation coefficient ($R^2$) was obtained to be 0.9795 while the adjusted $R^2$ value of 0.9603 was obtained. The closeness of the adjusted $R^2$ values to the correlation coefficient ($R^2$) indicate a good agreement between the experimental and predicted values for all variables. The Predicted $R^2$ of 0.9199 is in reasonable agreement with the adjusted $R^2$ of 0.9603. The actual and predicted removal efficiency plot for 4-NP adsorption by NTPNC-EPI-CD nanocomposite is shown in Fig.6.5 C. The actual values are observed to be distributed close to the straight line indicating that the predicted values obtained from the model are in good agreement with the actual experimental data The Model F-values were observed to be 51.14 implying that the model is significant and there is only a 0.01% chance that an F-value this large could occur due to noise.
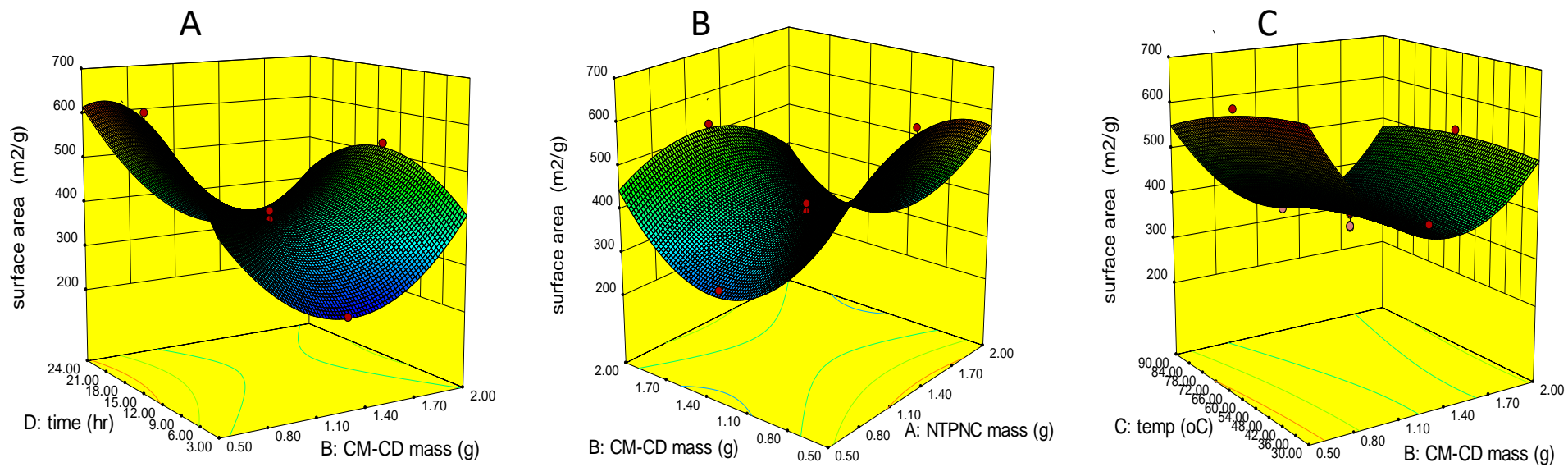
Figure 6.8:3D surface plots showing the effect of independent variables (A) Time versus CM-β-CD mass, (B) CM-β-CD mass versus NTPNC mass (C) reaction temperature versus CM-β-CD mass for 4-NP adsorption onto NTPNC-EPI-CD nanocomposite.

Coefficients, B, C, D, AB, AC, BC, BD, CD, $A^2$, $B^2$, $D^2$ were significant for surface area as they had the probability value less than 0.05. F-values shows that NTPNC-EPI-CD nanocomposite surface area was greatly influenced by CM-β-CD mass (B), the second order effect of CM-β-CD mass ($B^2$) and the reaction time (D). The actual and predicted removal efficiency plot in Fig. 6.5c shows that the actual values are seen to be distributed close to the straight line. The closeness of the actual values to the predicted values indicate that the predicted values of all responses obtained from the model are in good agreement with the actual experimental data. The 3D surface plot in Fig. 6.8 (A-C) show the influence of the synthesis variables on surface area of NTPNC-EPI-CD. Interaction between reaction time and CM-β-CD mass while keeping NTPNC mass and temperature fixed at 1.25 g and 60 °C, respectively is shown in Fig. 6.8 A. At low CM-β-CD mass, increasing the reaction time resulted in an increase in surface area of the nanocomposite while an increase in reaction time at high CM-β-CD led to an increase in surface area up to a maximum then a slight reduction of surface area with time was observed. In both short and long time, increase in CM-β-CD mass resulted in a decrease in surface area up to a minimum, which further increased with increasing CM-β-CD mass. Contour plot shows a strong interaction between CM-β-CD mass and time on the nanocompopsite surface area.

Interaction between NTPNC and CM-β-CD mass while keeping reaction time and temperature fixed at 1 hr and 60 °C, respectively is shown in Fig.6.8 B. The Fig show that an increasing NTPNC mass at both low and high amount of CM-β-CD mass, led to an increase in surface area up to a maximum value in which the surface area then reduced as NTPNC mass was further increased. On the other hand, increasing the amount of CM-β-CD at both low and higher amount of NTPNC resulted in a reduction of the surface area of the nanocomposite up to a minimum value which then increased as the amount of CM-β-CD was further increased. Higher surface area was observed at lower amount of CM-β-CD and high NTPNC mass. Interaction between reaction temperature and CM-β-CD  mass while keeping NTPNC time fixed at 1.25 g and 1 hr is shown in Fig.6.8 C. At both low and high temperature, increasing the amount of CM-β-CD led to a reduction in the nanocomposite surface area up to a minimum value which then increased as CM-β-CD mass was increased while an increase in temperature at both low and high amount of CM-β-CD did not show any noticeable change in the nanocomposite surface area. Surface area of the nanocomposite was mostly controlled by the amount of CM-β-CD in the material. Nanocomposite of high surface area was synthesised at low CM-β-CD mass, high NTPNC amount and longer reaction time while temperature didn't have any

influence on the surface area. Cyclodextrin functionalized polymers of low (Mahaninia et al., 2014) and medium (Huq and Mercier, 2001) surface area have been reported. Crosslinking β-CD onto NTPNC has been found to enhance the surface area of the material.

To obtain a nanocomposite that will have high selectivity towards targeted compounds and be easily separated by magnetic separation after pollutants adsorption, optimum conditions for NTPNC-EPI-CD are presented in Table 6.6. From Table 6.6, optimum conditions were observed to be 2.0 g of CM-β-CD, 0.83 g of NTPNC at reaction temperature of 30 $^{o}$C for 7.40 hrs yielding 47.55 % of the NTPNC-EPI-CD nanocomposite that will have 430.15 m$^2$/g surface area which can remove 15.32 mg/g of 4-nirophenol from aqueous solution.

Table 6.6: Optimum results for NTPNC-EPI-CD synthesis

| Variables | | | | Responses | | | |
|---|---|---|---|---|---|---|---|
| CM-β-CD mass (g) | NTPNC mass (g) | Temp ($^{o}$ C) | Time (hr) | % Yield | Adsorption Capacity (mg/g) | Surface area (m$^2$/g) | Desirability |
| 0.83 | 2 | 30 | 7.40 | 47.55 | 15.32 | 430.15 | 1 |

## 6.4 CHARACTERIZATION OF NTPNC-HMDI-CD AND NTPNC-EPI-CD NANOCOMPOSITES

### 6.4.1 Introduction

Characterization of the optimum NTPNC-HMDI-CD and NTPNC-EPI-CD nanocomposites were conducted using different techniques. The structures of the prepared NTPNC-HMDI-CD nanocomposite was studied by FTIR spectroscopy and X-ray diffractometer, thermal stability was determined using TGA/DTA, surface morphology was observed with a high-resolution transmission electron microscope (TEM), the magnetic property was determined using VSM, the surface area analysis was tested using BET surface area while surface charge was determined by conducting $pH_{pzc}$.

### 6.4.2 FTIR analysis of NTPNC-HMDI-CD and NTPNC-EPI-CD nanocomposites

FTIR spectra of NTPNC, NTPNC-EPI-CD and NTPNC-HMDI-CD nanocomposites were conducted to confirm the crosslinking of β-CD onto the surface of NTPNC nanocomposite and the results are reported in Fig.6.9. NTPNC nanocomposite spectra shown in Fig.6.9. shows that NTP-NC exhibited a broad O-H stretching vibration at 3307 $cm^{-1}$, symmetric C-H band at 2888 $cm^{-1}$, and C-O vibration at 1622 $cm^{-1}$ (Acisli et al., 2017, Subramanian et al., 2005). The band at 1027 $cm^{-1}$ indicating the antisymmetric glycosidic C-O-C vibration and the peak associated with Fe-O presenting the tetrahedral side of magnetite was observed at 560 $cm^{-1}$ (Chen et al., 2009). Certain groups were observed to have shifted, increased, and decreased in intensities and some new peaks appeared after crosslinking with both epichlorohydrin and hexamethylene diisocyanate. On crosslinking the CM-β-CD onto NTPNC with EPI, all significant peaks of CM-β-CD and NTPNC were present in the spectrum of the NTPNC-CD-EPI nanocomposite with reduction in intensities and shift in peaks confirming successful crosslinking. The broad OH stretching vibration and C-H groups were observed to have shifted from 3307 to 3343 $cm^{-1}$ and 2888 to 2883 $cm^{-1}$, respectively, and increased in intensities. The C-O peak at 1622 $cm^{-1}$ was observed to increase to 1636 $cm^{-1}$ which is characterized as the COOM group indicating the reaction between the COOH group of the CM-β-CD with the suraface of OH groups of magnetite surface resulting in the formation of iron carboxylate (Zhang et al., 2009). The C-O-C peak was also found to have increased in intensities and shifted to a lower wavenumber after crosslinking. The Fe-O peak slightly shifted to 555 $cm^{-1}$ confirming the presence magnetite

after crosslinking. Similar results were reported by Badroddoza et al. (2010) when synthesizing carboxymethyl-cyclodextrin conjugated magnetic nano-adsorbent.
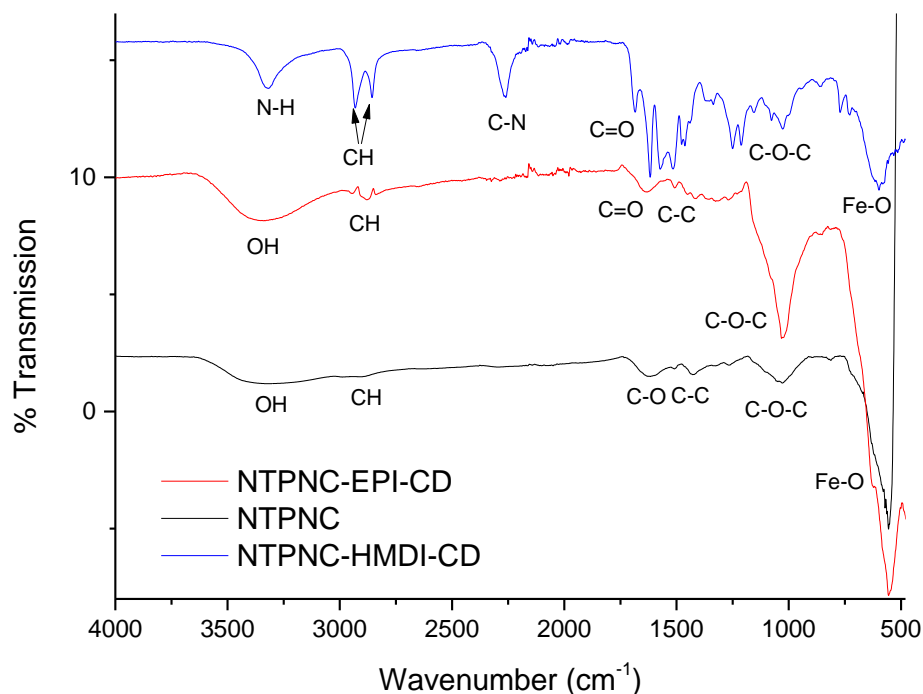


Figure 6.9: FTIR spectra of NTPNC, NTPNC-EPI-CD and NTPNC-HMDI-CD nanocomposites.

The broad OH group of NTP-NC (3307 $cm^{-1}$) was observed to have sharpened and shifted to 3318 $cm^{-1}$ after crosslinking with HMDI, which is indicative of the NH groups from the formation of the amide linkage. The C-H group increased in intensity and splitted into two peaks at 2932 $cm^{-1}$ and 2855 $cm^{-1}$ confirming the presence of the long hydrocarbon chain from the hexamethylene diisocyanate cross linker. New peaks appeared at 2261 $cm^{-1}$ and 1681 $cm^{-1}$ due to the unreacted isocyanate group (-N=C=O) from the isocyanate group and the C=O due to the carboxylic group from the amide linkage formed (Mohamed et al., 2011a). A sharp peak at 1624 $cm^{-1}$ corresponding to the amide bond due to the reaction of isocyanate and hydroxyl group was observed (Liu et al., 2017). The Fe-O stretching vibration corresponding to magnetite nanoparticle was also observed to have shifted from 560 to 598 $cm^{-1}$. Thus, it can be said that the β-CD has been successfully crosslinked onto the surface of NTPNC using HMDI via chemical bond formation.

### 6.4.3 Thermal gravimetric analysis (TGA)

Thermal gravimetric analysis was conducted on the NTP-NC, NTPNC-EPI-CD and NTPNC-HMDI-CD to determine how crosslinking affected the thermal stability of the materials and the results are reported on Fig. 6.10 A, while the DTA peaks corresponding to their thermal stability are shown in Fig.6.10 B. The decomposition profile of NTP-NC biocomposite is well explained in chapter 4 and is observed to show three weight loss processes. The first weight loss of 5 % due to loss of moisture is observed at the temperature range of 94 to 99 $^{o}$C corresponding to a DTA curve at 54 $^{o}$C. The second weight loss was observed at the temperature range between 250 and 380 $^{o}$C corresponding to DTA curve at 366 $^{o}$C, attributed to the decomposition of the cellulose and hemicellulose from the pine cone biomass. The third weight loss showing two peaks is observed at the temperature range of 660 to 820 $^{o}$C. The weight loss at 670 $^{o}$C corresponding to DTA curve at 681, has been attributed to the phase transition from $Fe_3O_4$ to FeO, and the last weight loss at around 786 $^{o}$C because of the deoxidation of FeO since the TGA/DTA analysis was achieved under the nitrogen atmosphere (Zhao et al., 2006).

TGA curve of the nanocomposite after cross-linking magnetite with β-cyclodextrin using EPI exhibits three steps of weight loss. The first weight loss of 1 % is observed at temperature between 34 to 100 $^{o}$C with a corresponding DTA curve of 68 $^{o}$C attributed to loss of water in the sample. The second weight loss was observed to have slightly shifted to temperatures between 260 to 340 $^{o}$C corresponding to the DTA peak at 325 which was due to the decomposition of CM-β-CD, hemicelluloses and cellulose degradation in the NTPNC-EPI-CD nano-composite. Finally, the third weight loss was observed at a temperature between 570 and 700 $^{o}$C due to decomposition of magnetite in the sample. The two DTA peaks observed around 577 and 615 $^{o}$C confirm the phase transition from $Fe_3O_4$ to FeO in the NTPNC-EPI-CD nano-composite. Epichlorohydrin cross-linker has been shown to have enhanced the nanocomposite adsorbent stability. The TGA plot of NTPNC-HMDI-CD nanocomposite showed three stages of weight loss while the DTA revealed the thermal curves corresponding to the mass loses. The initial weight loss of 3 % is seen at the temperature below 120 $^{o}$C due to the loss of the adsorbed water. Two overlapping steps occurred from 300 to 500 $^{o}$C. The first mass loss of 53% due to decomposition of cellulose and hemicellulose from the pine cone and the β-cyclodextrin moiety was observed between 300-370 $^{o}$C corresponding to the DTA peak at 340 $^{o}$C while the second step occurred from 370-500 $^{o}$C due to the oxidation of organic matter from HMDI and

magnetite corresponding to the DTA peak at 464 °C (Li et al., 2004, Okoli et al., 2015). Crosslinking of CD onto NTPNC nanocomposite led to the slight enhancement of thermal stability. Similar results have been reported by Okoli et al. (2015) when cross-linking starch using 1,6-hexamethylene diisocyanate. NTPNC-EPI-CD nanocomposite was observed to be more thermally stable than the NTPNC-HMDI-CD nanocomposite.
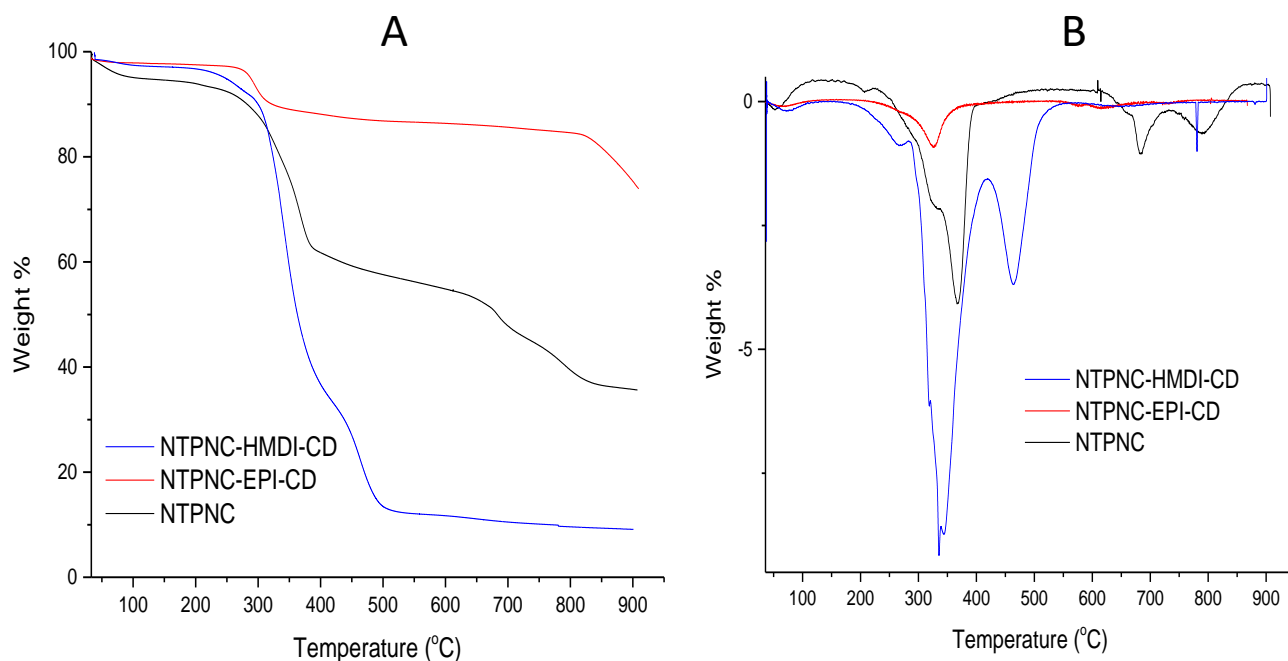


Figure 6.10: (A) TGA and (B) DTA of NTPNC, NTPNC-EPI-CD and NTPNC-HMDI-CD

## 6.4.4 Transmission electron microscopy (TEM) analysis

TEM analysis of NTPNC-EPI-CD and NTPNC-HMDI-CD was conducted to confirm crosslinking of β-CD onto NTPNC surface and the TEM image and size distribution of NTPNC, NTPNC-EPI-CD and NTPNC-HMDI-CD are shown in Fig.6.11 A-F. The TEM image of NTPNC on Fig. 6.11 A shows the spherical shape of the bio-composite with average size distribution of 8.23 nm (Fig. 6.11 D). On cross-linking NTPNC and CD with EPI, the image in Fig.6.11 B, shows the spherical shape with mean diameter of 9.77 nm (Fig.6.11 E). The increase in the nanocomposite size after crosslinking may be due to the addition of cyclodextrin and epichlorohydrin cross-linker. The NTPNC-HMDI-CD image in Fig.6.11 C shows the carbon with small spherical shape of magnetite nanoparticles with average size of 5.42 nm (Fig. 6.11 F). The results indicate that β-CD was successfully cross-linked onto the NTP-NC bio-composite surface and cross-linking did not significantly result in the change of

the nanoparticle shape. The results also confirmed XRD analysis which showed characteristics peaks of magnetite in the NTPNC-EPI-CD nanocomposite.
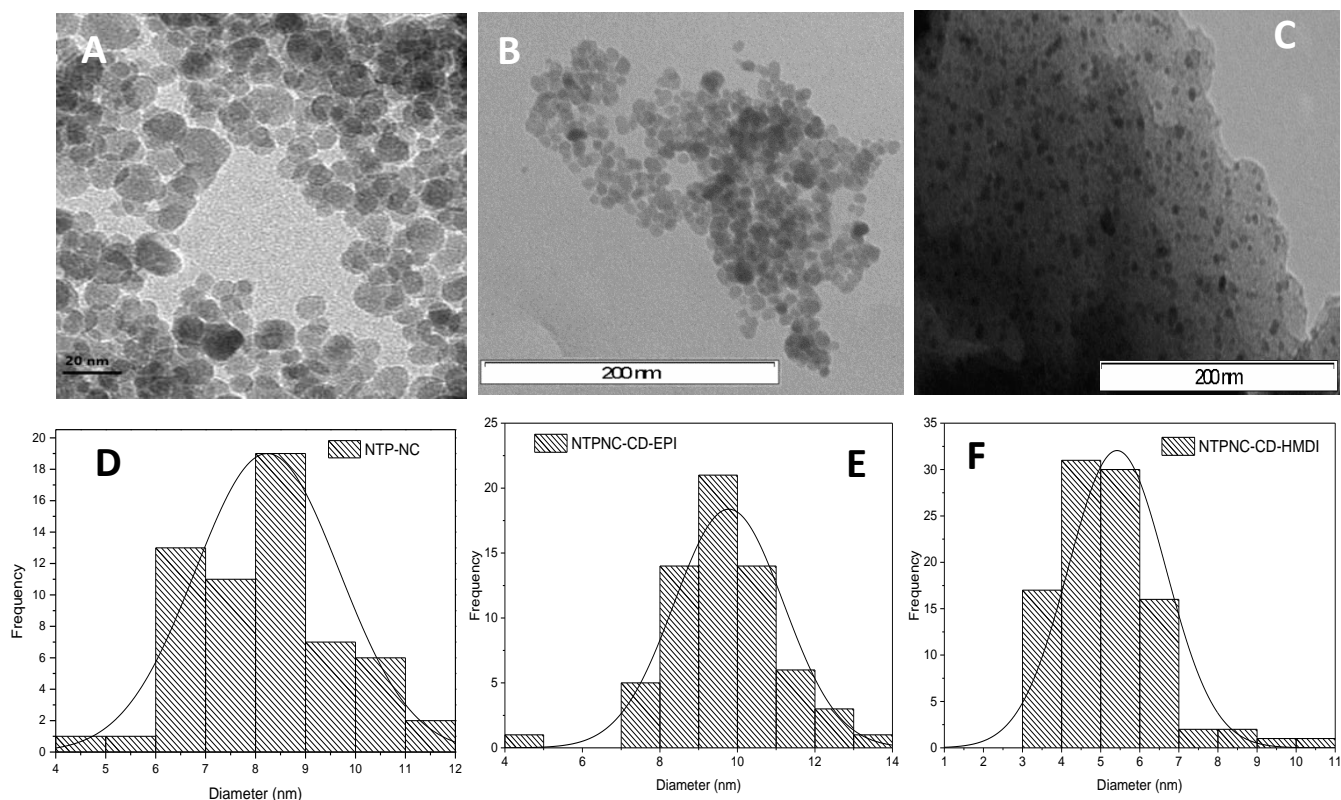


Figure 6.11: TEM images of (A) NTPNC, (B) NTPNC-EPI-CD and (C) NTPNC-HMDI-CD and size distribution of (D) NTPNC, (E) NTPNC-EPI-CD and (F) NTPNC-HMDI-CD

### 6.4.5   Vibrating scanning magnetometer (VSM) analysis

To understand the magnetic properties and confirm the cross-linking of β-CD onto magnetite coated pine cone, VSM technique was conducted and magnetization measurements were performed by measuring the applied field dependence of magnetization cycled between -15 and 15 kOe at room temperature. The VSM results of NTPNC, NTPNC-EPI-CD and NTPNC-HMDI-CD are presented in Fig.6.12. Magnetic saturation of pure magnetite from chapter 4 was observed to be 64.66 emu/g, which was seen to reduce to 37.50 emu/g as magnetite was coated with pine cone, and further reduced to 21.75 and 24.74 emu/g on crosslinking magnetite coated pine cone to cyclodextrin using EPI and HMDI, respectively. Low coercivity values of 10.64, 10.05 and 13.42 G for NTPNC, NTPNC-EPI-CD and NTPNC-HMDI-CD, respectively, showed the superparamagnetic behavior of materials confirming the crosslinking of β-CD onto

magnetite coated pine cone. Similar results were reported by Saeb et al. (2017) in the synthesis of functionalized magnetite with β-CD hydroxyl- rich precursor. Magnetization slightly reduced after cross-linking cyclodextrin with NTPNC and the effect was more for EPI crosslinked than HMDI. However, both nanocomposites exhibit magnetic properties.
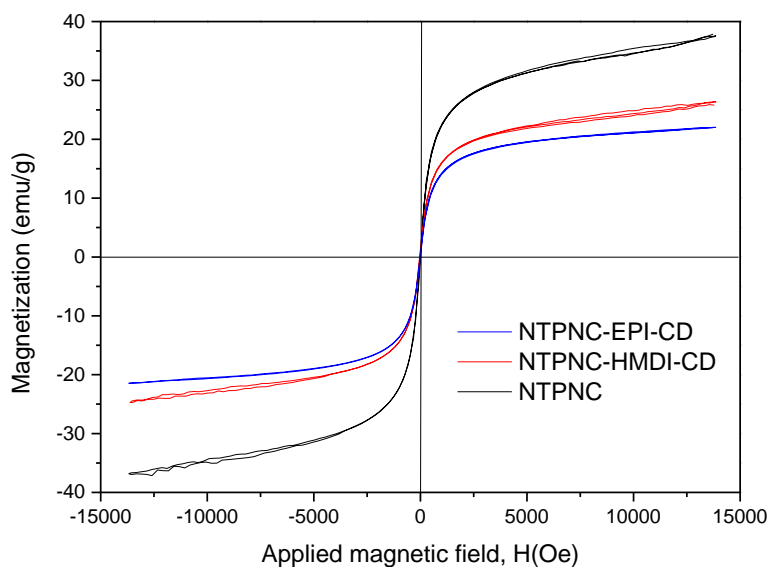


Figure 6.12: Magnetization curve of NTPNC, NTPNC-EPI-CD and NTPNC-HMDI-CD

### 6.4.6 pH at point zero charge

The ionic character of the NTPNC-EPI-CD and NTPNC-HMDI-CD nanocomposite and adsorption behaviour can be analyzed by the $pH_{pzc}$, which is the pH at which the net charge of the surface is zero. $pH_{pzc}$ of NTPNC and after β-CD crosslinking onto NTPNC was conducted and the results are given in Fig.6.13. $pH_{pzc}$ of NTPNC biocomposite was found to be 5.86. which was observed to slightly shift to a lower pH value of 4.00 after crosslinking with EPI while cross-linking with HMDI slightly increased the $pH_{pzc}$ to a higher value of 6.57. The shift in $pH_{pzc}$ to lower solution pH after cross-linking the CM-β-CD containing multi carboxyl groups with NTPNC using EPI occurred due to the introduction of acidic surface groups onto the NTPNC surface. Badruddoza et al. (2011) also obtained a shift in $pH_{pzc}$ from 6.8 to 4.7 after surface modification of $Fe_3O_4$ nanoparticles with CM-β-CD. On the other hand, an increase in $pH_{pzc}$ after crosslinking using HMDI may be attributed to the formation of urethane linkages which reduced acidic groups on the NTPNC and β-CD polymer. Similar results have been

reported by Choubey (2018) when crosslinking Fenton pre-treated pine cone using HMDI. The author observed an increase in $pH_{pzc}$ from 5.40 to 6.12 for the Fenton pre-treated cross-linked pine sample.
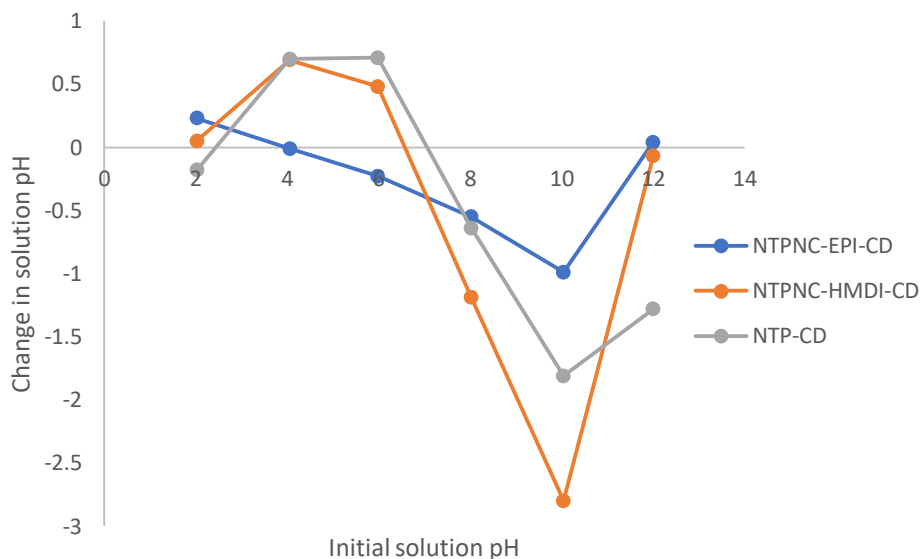


Figure 6.13: $pH_{pzc}$ of NTPNC, NTPNC-EPI-CD and NTPNC-HMDI-CD

### 6.4.7   X-Ray Diffraction analysis

The XRD analysis of NTPNC-EPI-CD and NTPNC-HMDI-CD nanocomposite were conducted to confirm crosslinking of β-CD onto NTPNC surface and the XRD pattern is shown in Fig 6.14. From the Fig and the discussion in chapter 4, the NTPNC depicts the crystalline structure of cellulose I peak at 2 theta 22.84° and five characteristic peaks at 30.09°, 35.42°, 43.05°, 56.94° and 62.51° corresponding to (220), (311), (400), (511) and (440) of magnetite crystalline structure (JCPDS Card no. 19-0629). The diffraction peaks at 30.2°, 35.7°, 43.2°, 53.6°, 57.2°,62.8° and 74.4° corresponding to the indices (220), (311), (400), (422), (511), (440) and (533) ascribed to $Fe_3O_4$ were observed for the NTPNC-EPI-CD nanocomposites. The NTPNC-HMDI-CD nanocomposite exhibit six characteristics peaks at 2 theta 30.37°, 35.7°, 43.37°, 53.81°, 57.48° and 63.12° corresponding to indices (220), (311), (400), (422), (511) and (440) confirming the cubic crystalline structure of magnetite (JCPDS Card no. 19-0629). Two crystalline structure of cellulose I peak at 12.39° and 22.73° due to the presence of pine cone and cyclodextrin was also observed for NTPNC-EPI-CD while NTPNC-HMDI-CD nanocomposite showed the crystalline structure of cellulose I peak at 22.78°. The XRD patterns

of NTPNC-EPI-CD and NTPNC-HMDI-CD shows that the resultant nanocomposites were crystalline, and crosslinking did not induce any phase change.
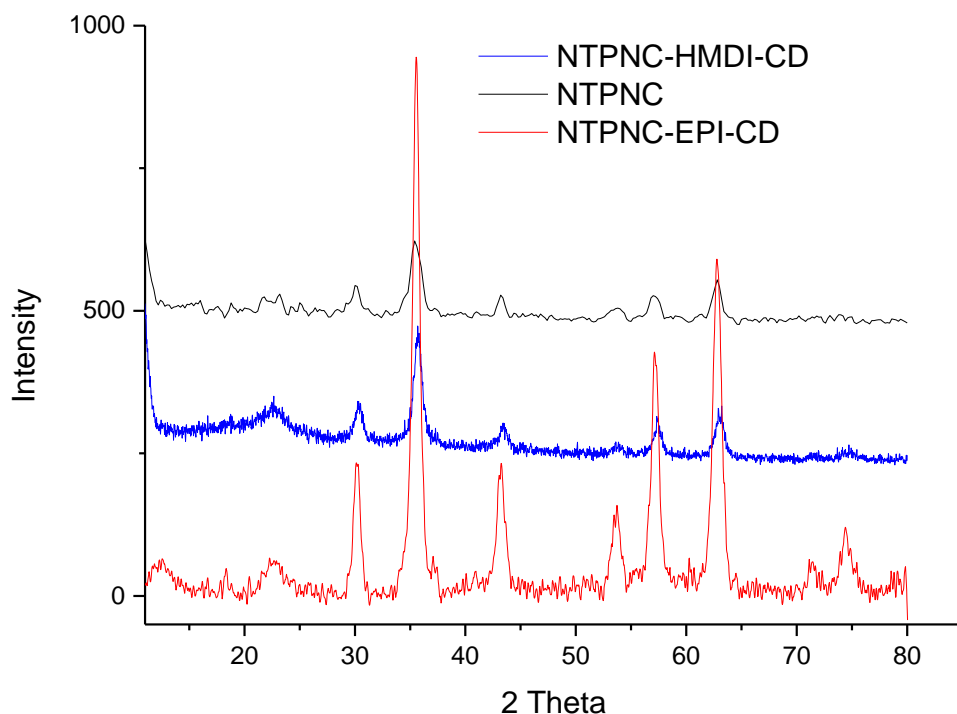


Figure 6.14: XRD pattern of NTPNC, NTPNC-EPI-CD and NTPNC-HMDI-CD nanocomposite.

### 6.4.8    BET Specific surface area

The surface properties and pore size distribution of NTPNC, NTPNC-EPI-CD and NTPNC-HMDI-CD were studied using BET technique by recording the adsorption-desorption isotherm under nitrogen and the results are shown in Fig.6.15 A and B while the surface properties are presented in Table 6.7. The adsorption–desorption isotherms for all nanocomposite adsorbents, exhibited a type IV isotherm with H3 type hysteresis loop at a relative pressure between 0.6-1.0, characteristic for mesopores. BET surface area of NTPNC reported in chapter 4 was observed to be 54.80 $m^2$/g. On crosslinking CD onto magnetite using EPI, the surface area was observed to reduce to 24.28 $m^2$/g and increased to 64.83 $m^2$/g after crosslinking using HMDI. NTPNC, NTPNC-EPI-CD and NTPNC-HMDI-CD nanocomposites were observed to have the pore volume of 0.1522, 0.0705 and 0.1882 $cm^3$/g and average pore size of 23.10, 11.86 and 11.64 nm, respectively. Cross-linking with EPI exhibited lower surface area while cross-

250

linking with HMDI slightly increased the nanocomposite surface area. This may be due to the fact that HMDI is a hydrophobic cross-linker which is susceptible to water while EPI is a hydrophillic cross-linker. Therefore, it can be said that the high surface area of NTPNC-HMDI-CD is due to the hydrophobic cross-linker that shows more affinity towards the organic phase, which give rise to a mesoporous architecture. Similar results were also observed by Anne et al. (2018) when using aromatic (2,4-toluene diisocyanate) and aliphatic (1,6-hexamethylene diisocyanate) cross-linker to form insoluble β-CD-TDI and β-CD-HDI. The particle size diameter curve of NTPNC-EPI-CD and NTPNC-HMDI-CD nanocomposite in Fig.6.15 B shows the pore diameters between 50-150 nm with peak value of 100 and 115 nm, respectively, indicating that the nanocomposites belongs to macroporous material.

Table 6.7: Surface Properties

| Properties | NTPNC | NTPNC-EPI-CD | NTPNC-HMDI-CD |
|---|---|---|---|
| Surface area ($m^2$/g) | 54.80 | 24.28 | 64.83 |
| Pore volume ($cm^3$/g) | 0.1522 | 0.0705 | 0.1882 |
| Ave. pore width (nm) | 23.10 | 11.86 | 11.64 |
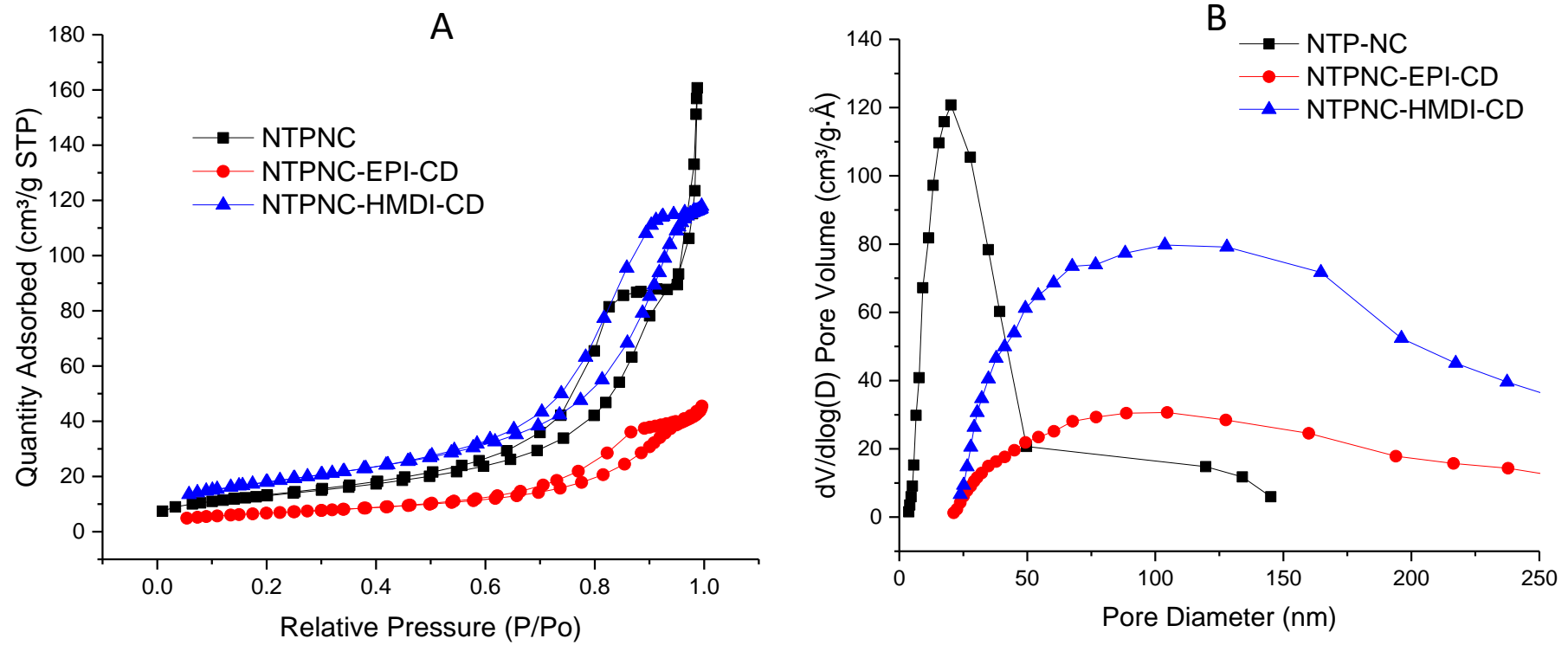
Figure 6.15: (A) Nitrogen adsorption isotherms and (B) Pore size distribution of NTPNC, NTPNC-EPI-CD and NTPNC-HMDI-CD.

## 6.5 BATCH ADSORPTION STUDIES FOR THE REMOVAL OF 4-NITROPHENOL USING NTP-NC, NTPNC-EPI-CD AND NTPNC-HMDI-CD NANOCOMPOSITES

### 6.5.1 Effect of solution pH

Effect of solution pH on the adsorption of 4-Nitrophenol by NTP-NC, NTPNC-EPI-CD and NTPNC-HMDI-CD was determined at the solution pH ranging from 2 to 9 and the results are presented in Fig.6.16. Results indicate that the removal of 4-Nitrophenol from aqueous solution depend highly on the solution pH and NTPNC-HMDI-CD nanocomposite was observed to have the highest 4-NP removal followed by NTPNC-EPI-CD then NTP-NC. Adsorption of 4-NP onto NTP-NC and NTPNC-EPI-CD were observed to have similar trend. The amount of 4-NP adsorbed was observed to increase from 8.08 to 8.36 mg/g and 13.34 to 15.12 mg/g as solution increases from pH 2 to pH 3 for NTP-NC and NTPNC-EPI-CD nanocomposite, respectively. Further increase in solution pH from pH 3 to pH 9 resulted in a decrease of 4-NP adsorbed for both NTP-NC and NTPNC-EPI-CD nanocomposite. On the other hand, it was observed that the amount of 4-NP adsorbed onto NTPNC-HMDI-CD increased from 20.52 to 23.1 mg/g with an increase in solution pH from pH 2 to 7 and steadily decreased from 23.1 to 18.01 as solution pH increased from pH 7 to pH 9.
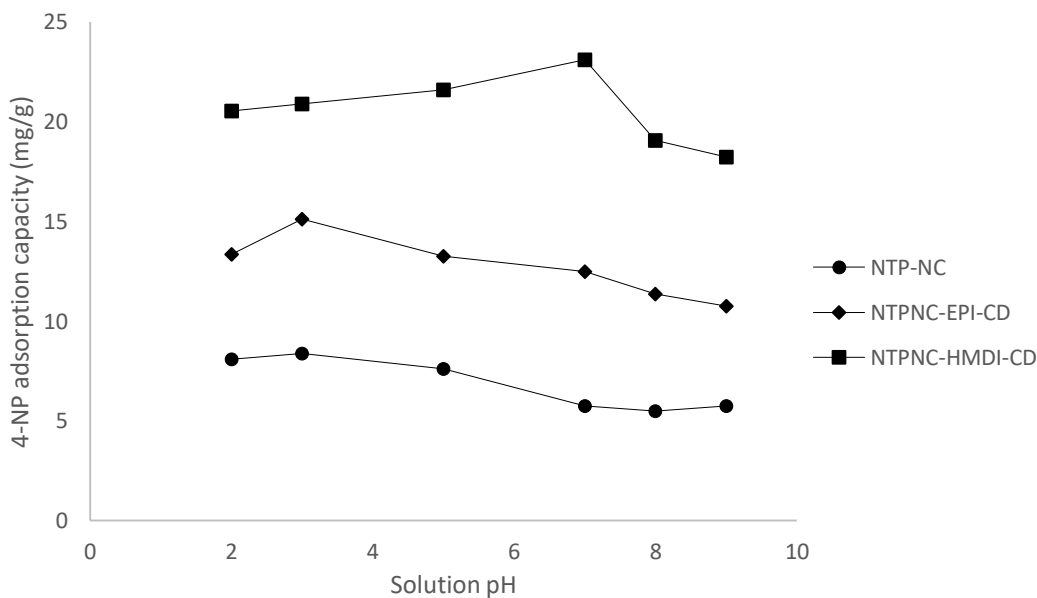


Figure 6.16: Effect of solution pH on the adsorption of 4-NP using NTP-NC, NTPNC-EPI-CD and NTPNC-HMDI -CD.

Effects of pH on 4-NP adsorption have been stated to reveal information about adsorption forces and mechanisms. Laszlo et al. ( 2003) suggested 4-types of interactions between the carbon surface and the phenols in solution: (1) electron donor–acceptor interactions between the phenolic ring and the basic surface oxygen; (2) electrostatic attraction; (3) van der Waals interactions and (4) dispersion effect between the phenolic ring and the $\pi$ electrons of the carbon. Adsorption of 4-nitrophenol onto the nanocomposites may be well explained by considering its pka value which is 7.2 and the pHpzc of the nanocomposite samples. pHpzc values of NTPNC, NTPNC-EPI-CD and NTPNC-HMDI-CD were observed to be 5.86, 4.00 and 6.57, respectively. Optimum solution pH values for all nanocomposite materials are observed to be below 4-nitrophenol pKa value. Adsorbent surface carry zero net charge at pHpzc, are positively charged at solution pH below $pH_{pzc}$ and negative charge at solution pH above $pH_{pzc}$. At low solution pH, pH below pKa, 4-Nitrophenol exist as molecules or in nonionized form while the adsorbent surface groups are protonated. The adsorption of 4-nitrophenol on both NTPNC and NTPNC-EPI-CD were favoured at low solution pH of 3. Higher 4-nitrophenol removal of NTPNC and NTPNC-EPI-CD at pH 3 may have occurred through 2 mechanisms. Hydrophobic interaction between pine cone in the NTPNC bio-composite and 4-nitrophenol and the hydrogen bonding between weakly acidic Fe-OH in the NTPNC bio-composite as pH is adjusted to solution pH of 3. NTPNC-EPI-CD had $pH_{pzc}$ value of 4.00, where the surface charge is neutral. As solution pH was reduced to 3, the NTPNC-EPI-CD nanocomposite accumulated $H^+$ ions and became weakly acidic, therefore hydrogen bonding between Fe-OH in solution and the OH of the aromatic ring in the 4-nitrophenol occurred. Hydrophobic interaction may also occur between (pine cone and 4-nitrophenol) and (cyclodextrin and 4-nitrophenol). Zhou et al. (2012) observed high p-nitrophenol removal at lower solution pH of 4 when using hypercrosslinked magnetic resin.

Adsorption of 4-nitrophenol onto NTPNC-HMDI-CD was observed to be favoured at solution pH of 7. The surface of NTPNC-HMDI-CD had pHpzc of 6.57 and start to build a partial negative charge as solution pH is increased to 7, while 4-nitrophenol was in a molecular form. Adsorption of 4-nitrophenol onto NTPNC-HMDI-CD at neutral solution may involve several mechanisms such as, interaction between ''$\pi$'' electrons that are delocalized on the N-C-O surface structure and ''$\pi$'' electrons of the benzene ring, hydrogen bonding between the OH of cyclodextrin and Fe-OH with 4-nitrophenol, and hydrogen bond and hydrophobic bonds between neutral form of 4-

nitrophenol and the carbon chains of the NTPNC-HMDI-CD. Hydrophobic bonding between OH of the aromatic ring in the 4-nitrophenol and OH on the cyclodextrin and pine cone may also occur. NTPNC-HMDI-CD may have interacted with 4-nitrophenol via several mechanisms which account for its highest removal than NTPNC and NTPNC-EPI-CD. Its high surface area may have also contributed to its higher 4-nitrophenol removal. Therefore, crosslinking with isocyanate groups have been found to have improved the 4-nitrophenol removal. Similar results have been reported by several reseachers on removal of 4-Nitrophenol by CD based adsorbent (Li et al., 2009). At high solution pH, pH higher than pKa value, 4-nitrophenol exist as phenolate ions. There will be electrostatic repulsion between phenolate ions in solution and the NTPNC, NTPNC-EPI-CD and NTPNC-HMDI-CD nanocomposite at higher solution pH, hence a reduction in the amount of 4-nitrophenol adsorbed for all adsorbents.

### 6.5.2   Effect of adsorbent dose on 4-nitrophenol adsorption

The effect of NTP-NC, NTPNC-EPI-CD and NTPNC-HMDI-CD nanocomposites adsorbent dose on adsorption of 4-nitrophenol was studied at the initial concentration of 100 mg/dm$^3$, at solution pH of 3 for NTPNC and NTPNC-EPI-CD and pH 7 for NTPNC-HMDI-CD at 26 $^o$C for 2 hrs and the results are presented in Fig.6.17 A-C. From the results, an increase in adsorbent dose from 0.05 to 1.5 g resulted in a decrease in adsorption capacity from 11.08 to 2.47 mg/g, 34.12 to 3.25 mg/g and 38.68 to 3.05 mg/g for NTPNC, NTPNC-EPI-CD and NTPNC-HMDI-CD, respectively. However, the percentage removal sharply increased with an increase in adsorbent dosage from 5.54 to 37.1 %, 17.06 to 48.78 % and 29.01 to 68.55 % for NTPNC, NTPNC-EPI-CD and NTPNC-HMDI-CD, respectively, due to the increase in the number of available active sites as adsorbent dosage increases. The amount of 0.1 g was then taken as the optimum dose for further 4-nitrophenol adsorption studies for all adsorbents.
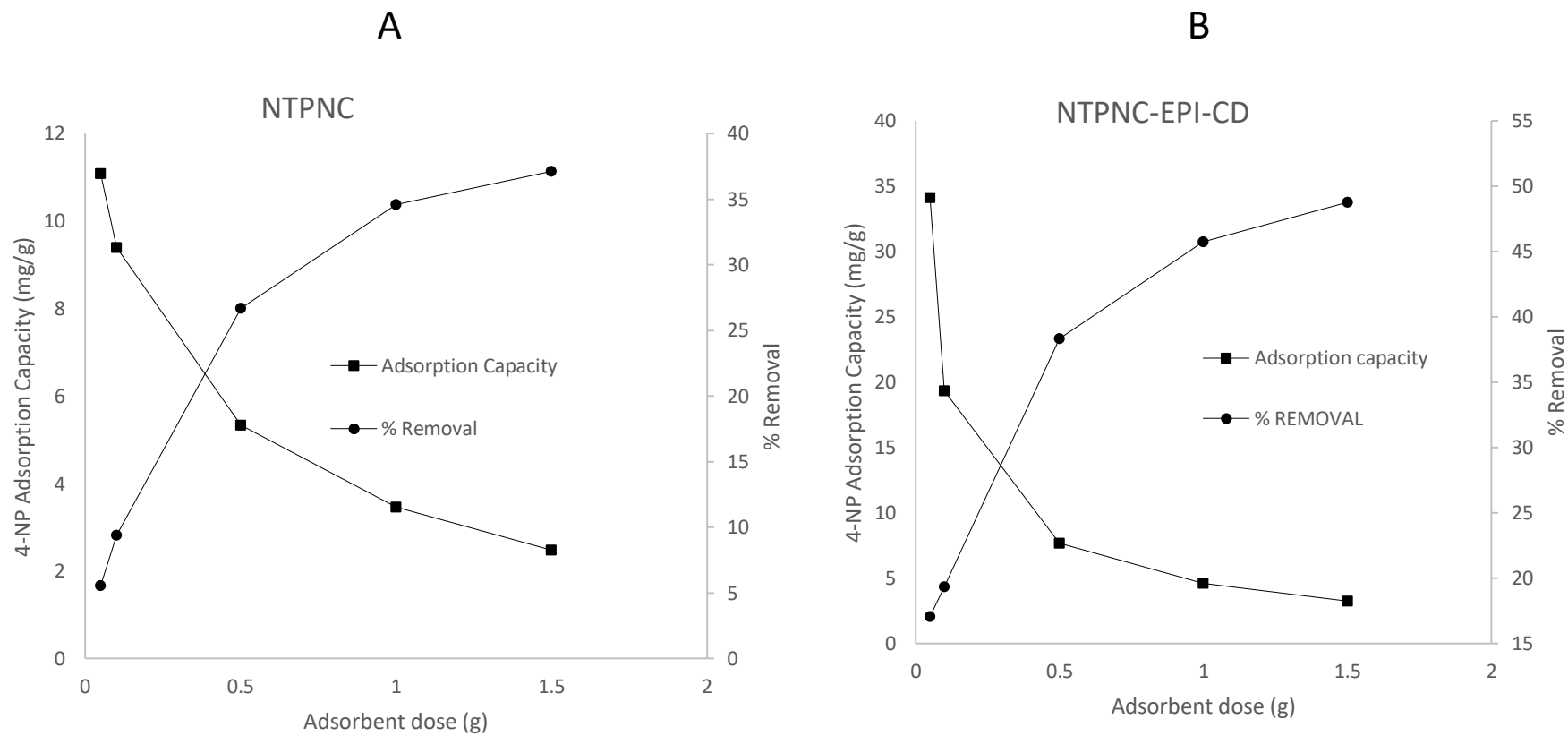
Figure 6.17: Effect of adsorbent dose for 4-nitrophenol using (A) NTP-NC and (B) NTPNC-EPI-CD nanocomposites.

C
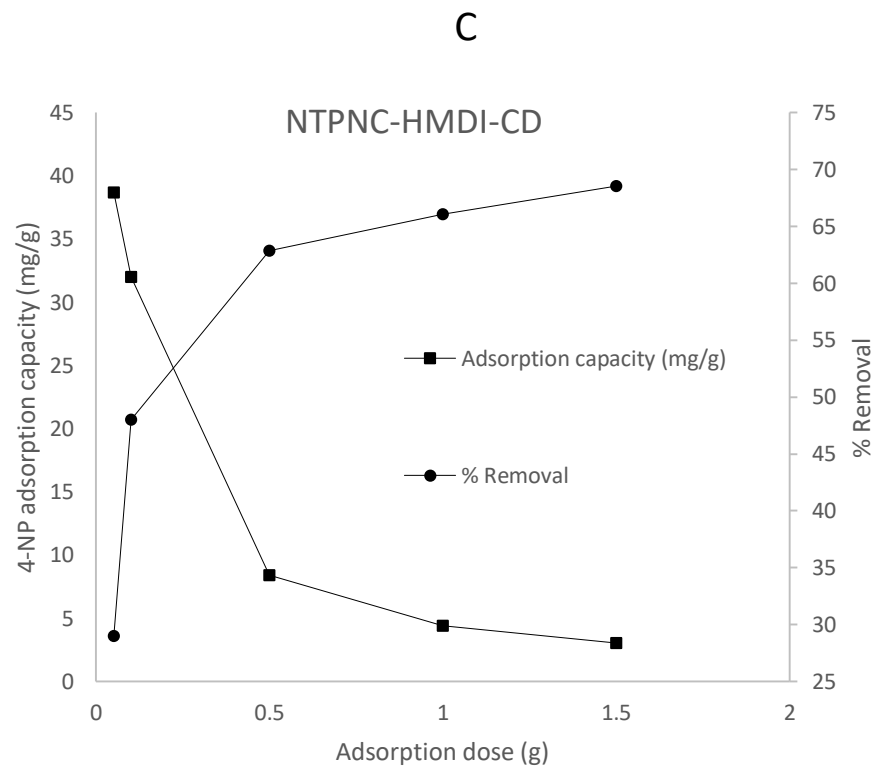
NTPNC-HMDI-CD

Figure 6.17 C: Effect of adsorbent dose for 4-nitrophenol using NTPNC-HMDI-CD nanocomposite.

### 6.5.3 Effect of contact time

The effect of contact time on the adsorption of 4-nitrophenol onto NTPNC, NTPNC-EPI-CD and NTPNC-HMDI-CD nanocomposite were investigated at different contact time of 0, 0.5, 1, 2, 5, 10, 20, 30, 60 and 120 min at initial concentration ranging from 25 to 125 mg/dm$^3$ for NTPNC and NTPNC-EPI-CD and 50 to 150 mg/dm$^3$ for NTPNC-HMDI-CD and the results are presented in Fig.6.18 a-c. All three adsorbent samples show a rapid increase in the amount of 4-nitrophenol adsorbed at the initial adsorption stage followed by a gradual increase until reaching an almost constant stage at the end of adsorption This is attributed to the fact that at the initial stage of adsorption process, the surface of the adsorbent materials was empty and the adsorption sites were free while at the end of adsorption process, the surface of the adsorbents were saturated with 4-nitrophenol molecules. The amount of 4-nitrophenol adsorbed for both nanocomposite adsorbents were observed to increase with increasing 4-nitrophenol initial concentration. This can be attributed to the extent of driving force of the concentration gradients with the increase in the 4-nitrophenol concentration. Although the optimum contact time for all three nanocomposites was achieved at 120 min, the 4-nitrophenol removal efficiency by NTPNC-HMDI-CD was the highest followed by NTPNC-EPI-CD and NTPNC. Therefore, 120 min was selected for further study for all nanocomposite adsorbents.

### 6.5.4 Kinetics studies - Effect of concentration

#### 6.5.4.1 Kinetic modelling

##### 6.5.4.1.1 Pseudo first and pseudo second order models

To further investigate the process and mechanism of 4-nitrophenol adsorption onto NTP-NC, NTPNC-EPI-CD and NTPNC-HMDI-CD nanocomposites surface, kinetic models were employed. The experimental kinetic data for the batch contact adsorption between 0.1 g of NTP-NC, NTPNC-EPI-CD and NTPNC-HMDI-CD nanocomposites and different concentrations (25, 50, 75, 100, and 125 mg/dm$^3$) for NTPNC and NTPNC-EPI-CD and concentrations (50, 75, 100, and 125 and 150 mg/dm$^3$) for NTPNC-HMDI-CD of 4-nitrophenol solutions were obtained and plotted according to the pseudo-first and pseudo-second order kinetic models and the kinetic parameters calculated are presented in Table 6.8 a-c.
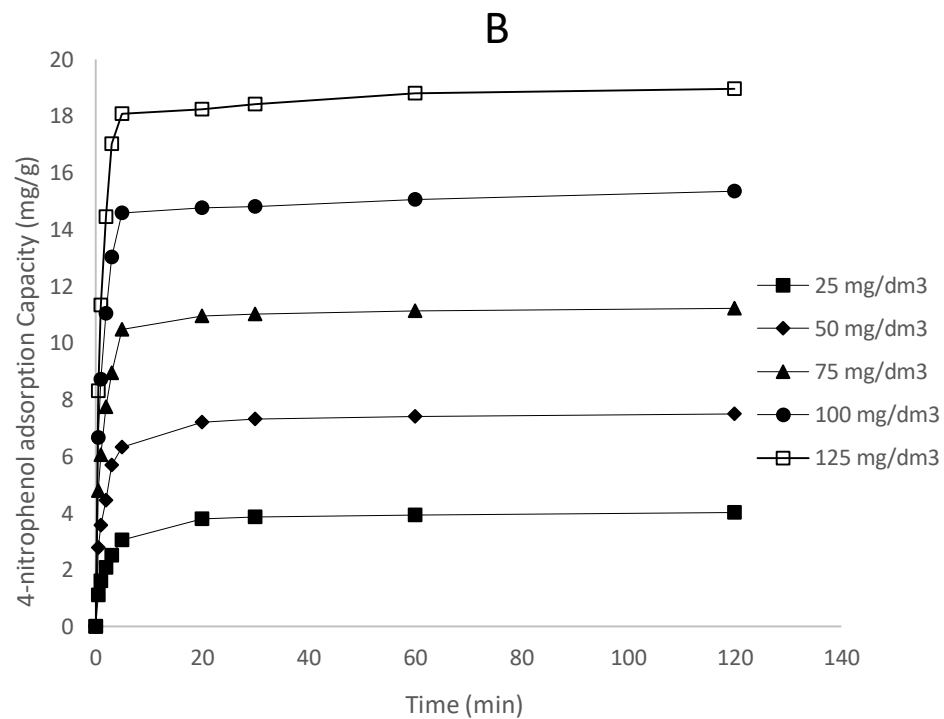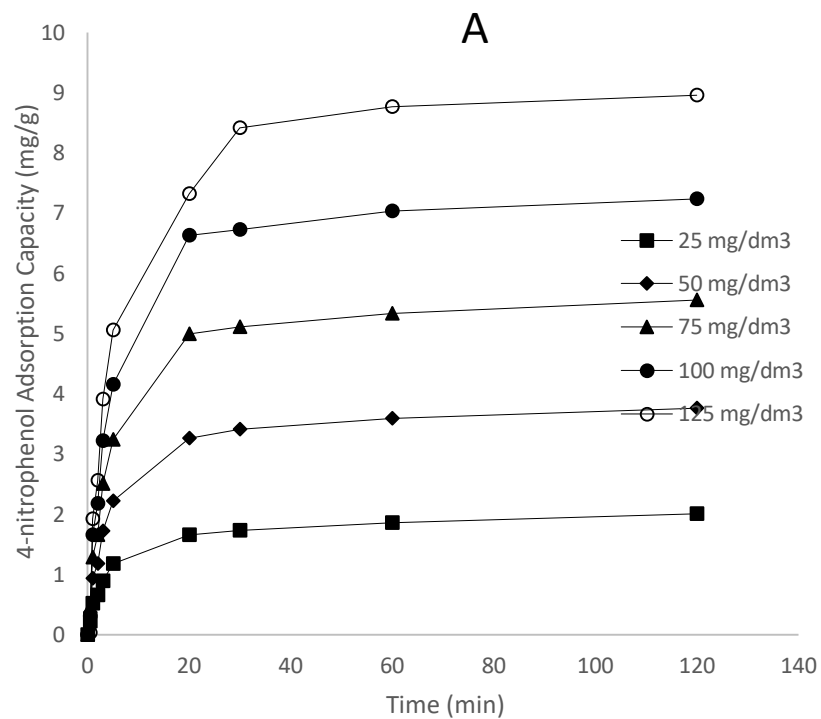
Figure 6.18: Effect of contact time on the adsorption of 4-nitrophenol onto (A) NTPNC and (B) NTPNC-EPI-CD at different initial concentration
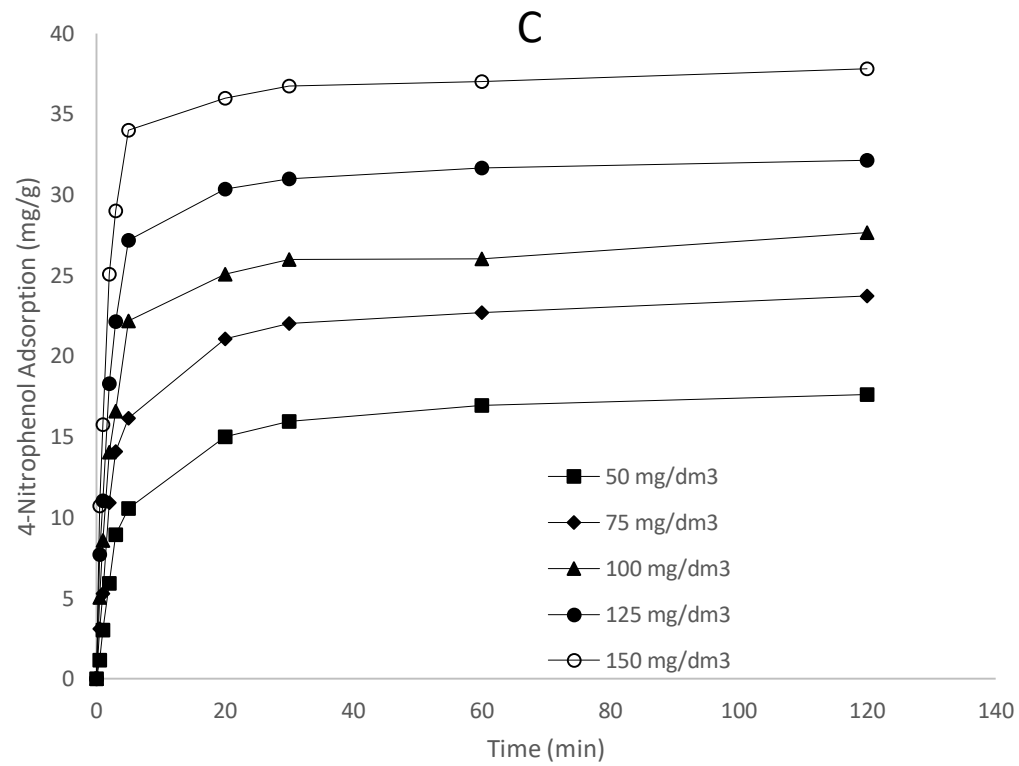
Figure 6.18 c: Effect of contact time on the adsorption of 4-nitrophenol onto NTPNC-HMDI-CD at different initial concentration

The results revealed that the experimental adsorption capacities for each adsorbent increased with increasing initial 4-nitrophenol concentration and NTPNC-HMDI-CD had the highest adsorption capacity followed by NTPNC-EPI-CD and NTP-NC for all initial concentrations. The adsorption capacity of NTPNC for pseudo first order model increased from 1.82 to 9.42 mg/g, from 4.02 to 18.96 mg/g for NTPNC-EPI-CD and from 15.45 to 36.68 mg/g for NTPNC-HMDI-CD as the initial concentration of 4-nitrophenol solution was increased. The adsorption capacity for pseudo second order model was observed to increase from 1.99 to 9.42 for NTPNC, 4.06 to 19.22 mg/g for NTPNC-EPI-CD and from 18.01 to 38.57 mg/g for NTPNC-HMDI-CD, as the initial concentration of 4-nitrophenol solution was increased.

Results from error determination for pseudo first-order from Table 6.8 a-c show coefficient of determination, $r^2 > 0.9930$ and % Variable error $> 0.06$ for NTPNC, $r^2 > 0.9887$ and % Variable error $> 1.53$ for NTPNC-EPI-CD and $r^2 > 0.9902$ and % Variable error $> 2.74$ for NTPNC-HMDI-CD. For the pseudo second-order, coefficient of determination of, $r^2 > 0.9972$ and % Variable error $> 0.15$ for NTPNC, $r^2 > 0.9979$ and % Variable error $> 0.37$ for NTPNC-EPI-CD and $r^2 > 0.9937$ and % Variable error $> 1.94$ for NTPNC-HMDI-CD were observed. The correlation coefficients, $r^2$, values for the adsorption process were higher for the pseudo-second order kinetic model than for the pseudo-first order model while the values of variable error for the pseudo second-order model were found to be lower than that of the pseudo first order for all samples. The predicted adsorption capacity values of pseudo second order model were closer to the experimental values than those of the pseudo first order model for all samples. Results, therefore, reveal that pseudo second-order kinetic model better described the adsorption process than the pseudo first order kinetic model. Pseudo second order kinetic model strongly suggest that the determining factor in the adsorption of 4-nitrophenol onto NTPNC, NTPNC-EPI-CD and NTPNC-HMDI-CD may be chemisorption involving valence forces through electrons sharing or exchange between p-nitrophenol and the nanocomposites such as hydrogen bond (Wu et al., 2016). Similar results were obtained by Shen et al. 2015 when using β-cyclodextrin grafted silica gel for fast adsorption of p-nitrophenol from aqueous solution.

Table 6.8 a: Kinetic data for 4-nitrophenol adsorption onto NTPNC

| Kinetic model | 25 mg/dm$^3$ | 50 mg/dm$^3$ | 75 mg/dm$^3$ | 100 mg/dm$^3$ | 125 mg/dm$^3$ |
|---|---|---|---|---|---|
| **NTPNC** | | | | | |
| **Pseudo-first order** | | | | | |
| Exp. $q$ (mg/g) | 2.01 | 3.76 | 5.56 | 7.24 | 8.96 |
| *Model q* (mg/g) | 1.82 | 3.52 | 5.27 | 6.95 | 9.42 |
| $k_1$ (min$^{-1}$) | 0.2265 | 0.2149 | 0.2025 | 0.1938 | 0.0226 |
| $r^2$ | 0.9804 | 0.9887 | 0.9930 | 0.9930 | 0.9795 |
| % Variable Error | 0.010 | 0.035 | 0.040 | 0.060 | 0.019 |
| | | | | | |
| **Pseudo-second order** | | | | | |
| Exp. $q$ (mg/g) | 2.01 | 3.76 | 5.56 | 7.24 | 8.96 |
| *Model q* (mg/g) | 1.99 | 3.86 | 5.80 | 7.66 | 9.42 |
| $k_2$ (g mg/ min) | 0.1370 | 0.0675 | 0.0421 | 0.0303 | 0.0226 |
| $h$ (mg/g min) | 0.5425 | 1.0057 | 1.4162 | 1.7779 | 2.0054 |
| $r^2$ | 0.9956 | 0.9972 | 0.9961 | 0.9932 | 0.9895 |
| % Variable Error | 0.003 | 0.006 | 0.02 | 0.05 | 0.15 |

Table 6.8 b: Kinetic data for 4-nitrophenol adsorption onto NTPNC-EPI-CD

| Kinetic model | 25 mg/dm$^3$ | 50 mg/dm$^3$ | 75 mg/dm$^3$ | 100 mg/dm$^3$ | 125 mg/dm$^3$ |
|---|---|---|---|---|---|
| **NTPNC-EPI-CD** | | | | | |
| **Pseudo-first order** | | | | | |
| Exp. $q$ (mg/g) | 4.02 | 7.49 | 11.23 | 15.36 | 18.96 |
| *Model q* (mg/g) | 3.88 | 7.20 | 10.86 | 14.77 | 18.37 |
| $k_1$ (min$^{-1}$) | 0.4011 | 0.5820 | 0.7586 | 0.8675 | 0.9574 |
| $r^2$ | 0.9748 | 0.9682 | 0.9726 | 0.9808 | 0.9887 |
| %Variable Error | 0.05 | 0.22 | 0.43 | 1.53 | 0.49 |
| | | | | | |
| **Pseudo-second order** | | | | | |
| Exp. $q$ (mg/g) | 4.02 | 7.49 | 11.23 | 15.36 | 18.96 |
| *Model q* (mg/g) | 4.06 | 7.55 | 11.37 | 15.46 | 19.22 |
| $k_2$ (g mg/ min) | 0.1480 | 0.124 | 0.1109 | 0.0942 | 0.0838 |
| $h$ (mg/g min) | 2.4396 | 7.0683 | 14.3368 | 22.5149 | 30.9564 |
| $r^2$ | 0.9959 | 0.9926 | 0.9931 | 0.9979 | 0.9915 |
| %Variable Error | 0.01 | 0.05 | 0.11 | 0.22 | 0.37 |

Table 6.8 c: Kinetic data for 4-mitrophenol adsorption onto NTPNC-HMDI-CD

| Kinetic model | 50 mg/dm$^3$ | 75 mg/dm$^3$ | 100 mg/dm$^3$ | 125 mg/dm$^3$ | 150 mg/dm$^3$ |
|---|---|---|---|---|---|
| **NTPNC-HMDI-CD** | | | | | |
| **Pseudo-first order** | | | | | |
| Exp. $q$ (mg/g) | 17.91 | 22.22 | 26.66 | 31.15 | 35.18 |
| *Model q* (mg/g) | 15.45 | 22.56 | 26.63 | 31.17 | 36.68 |
| $k_1$ (min$^{-1}$) | 0.2215 | 0.3035 | 0.3596 | 0.4365 | 0.5669 |
| $r^2$ | 0.9883 | 0.9906 | 0.9912 | 0.9918 | 0.9902 |
| %Variable Error | 0.60 | 0.81 | 1.00 | 1.63 | 2.74 |
| | | | | | |
| **Pseudo-second order** | | | | | |
| Exp. $q$ (mg/g) | 17.01 | 22.22 | 26.66 | 31.15 | 35.18 |
| *Model q* (mg/g) | 18.01 | 23.94 | 28.37 | 32.93 | 38.57 |
| $k_2$ (g mg/ min) | 0.0144 | 0.0164 | 0.0173 | 0.0192 | 0.0224 |
| $h$ (mg/g min) | 4.6708 | 9.3992 | 13.9240 | 20.8201 | 33.3232 |
| $r^2$ | 0.9937 | 0.9930 | 0.9929 | 0.9928 | 0.9915 |
| Variable Error | 0.30 | 0.60 | 0.81 | 1.03 | 1.94 |

*6.5.4.2   Diffusion processes*

6.5.4.2.1  Intraparticle diffusion model

Analysis of the rate controlling step in the adsorption process using Weber and Morris model is very beneficial for elaborating the adsorption mechanism. The plots of $q_t$ versus $t^{0.5}$ at different initial 4-nitrophenol concentrations are shown in Fig. 6.19 A-C for NTPNC, NTPNC-EPI-CD and NTPNC-HMDI-CD, respectively. From Fig. 6.19 A-C, the plots of $q_t$ versus $t^{0.5}$ at different initial 4-nitrophenol concentration show that two steps of adsorption process occurred. There was a rapid increase in the 4-nitrophenol adsorption at the initial stage followed by slower stage at which adsorption capacity was almost constant for all samples. The first rapid stage due to the external surface adsorption occurred because of the availability of large surface area and active adsorption site at the beginning of the adsorption process. The second stage which is the gradual adsorption stage where intraparticle diffusion is rate-controlled, was due to the decrease in concentration gradient leading to low adsorption capacity. The plot of $q_t$ versus $t^{0.5}$ did not pass through the origin, indicating that intraparticle diffusion was not solely rate-limiting but rather a complex process involving surface adsorption and intraparticle diffusion for all three nanocomposite adsorbents. The intraparticle diffusion constant, $k_i$ and the boundary layer constant, C were calculated from the slope and intercept of the plot of $q_t$ versus $t^{0.5}$ and are shown in Tables 6.9 a-c for NTPNC, NTPNC-EPI-CD and NTPNC-HMDI-CD, respectively. The intraparticle rate constant, $k_i$, was observed to increase from 0.0535 to 0.1023 mg/ g min for NTPNC and from 0.0339 to 0.1110 mg/ g min for NTPNC-EPI-CD with increasing 4-nitrophenol concentration but reduced from 0.3787 to 0.2449 mg/ g min with increasing concentration for NTPNC-HMDI-CD. An increase in the value of $k_i$ with initial concentration was attributed to formation of higher concentration gradient which causes faster diffusion and quicker adsorption. Reduction of $k_i$ with concentration on the other hand, has been reported to be due to smaller total surface area of the NTPNC-HMDI-CD as 4-nitrophenol concentration was increased thereby resulting in an increase in boundary layer resistance causing a reduction in external diffusion rates (Kupeta et al., 2018). The magnitude of the constant, *C* was observed to increase with increasing 4-nitrophenol initial concentration for all adsorbents indicating that as intraparticle diffusion rate increased, more solutes were being adsorbed at the boundary.
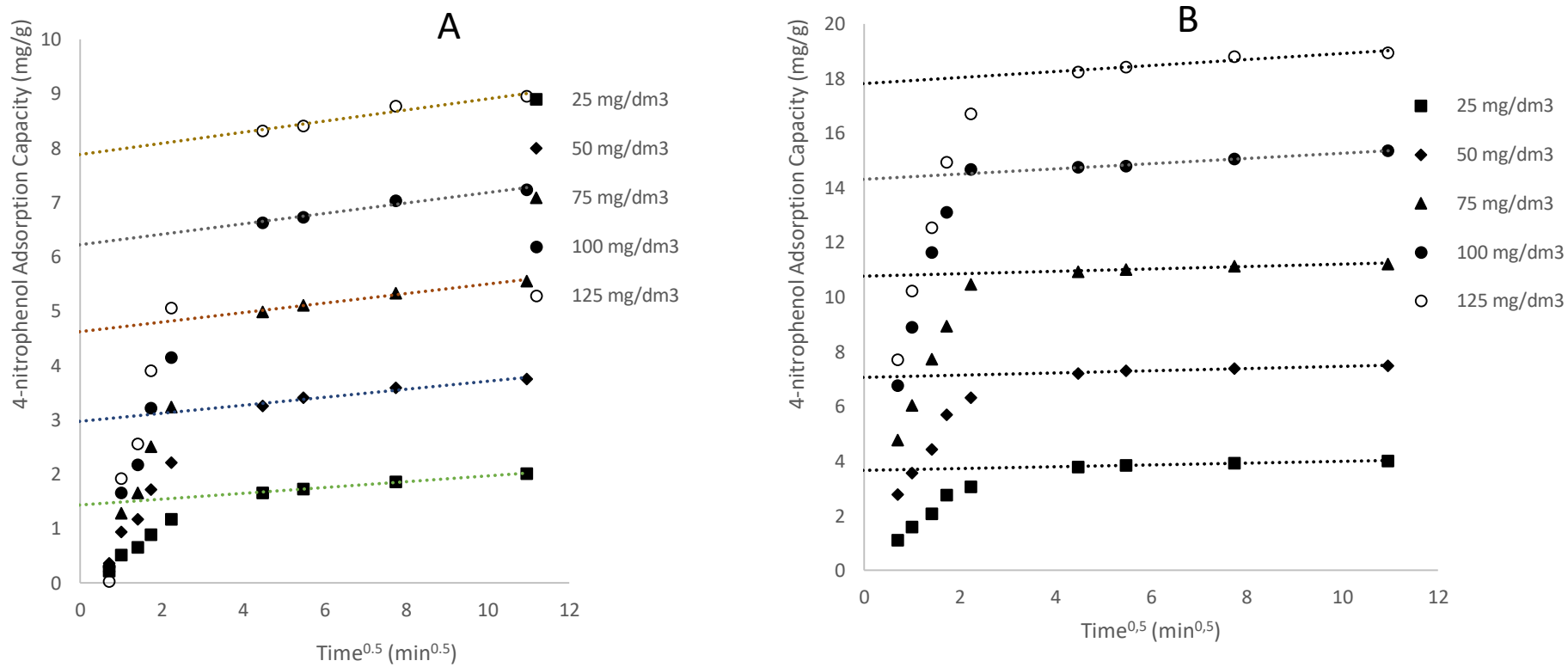
Figure 6.19: Intraparticle diffusion plots of 4-nitrophenol adsorption by (a) NTPNC and (b) NTPNC-EPI-CD at different concentrations.
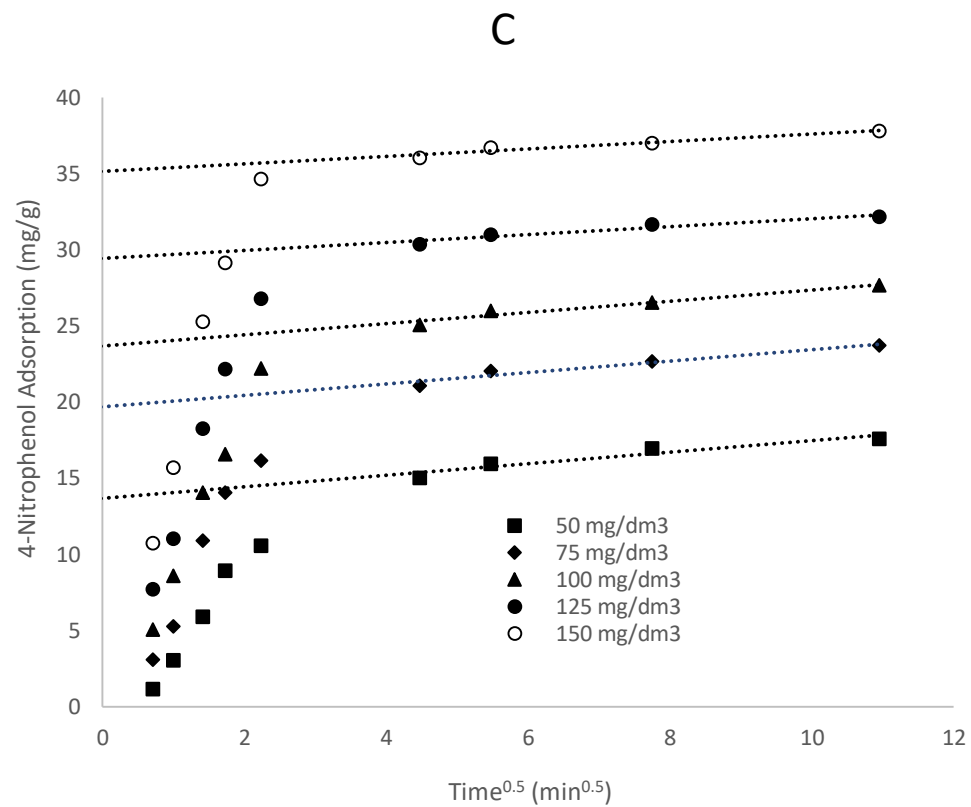
Fig. 6.19: (c) Intraparticle diffusion plots of 4-nitrophenol adsorption by NTPNC-HMDI-CD at different concentrations.

Table 6.9 a: Intraparticle model data for 4-nitrophenol adsorption onto NTPNC

| Kinetic model | 25 mg/dm$^3$ | 50 mg/dm$^3$ | 75 mg/dm$^3$ | 100 mg/dm$^3$ | 125 mg/dm$^3$ |
|---|---|---|---|---|---|
| **NTPNC** | | | | | |
| **Intraparticle Diffusion model** | | | | | |
| $k_i$ (mg/ g min) | 0.0535 | 0.0740 | 0.0870 | 0.0959 | 0.1023 |
| $C$ | 1.432 | 2.975 | 4.624 | 6.221 | 7.882 |
| $r^2$ | 0.9944 | 0.9618 | 0.9898 | 0.9748 | 0.9545 |
| | | | | | |
| **Film Diffusion** | | | | | |
| $D_1$ (cm$^2$/s) | 1.46 x10$^{-13}$ | 1.50 x10$^{-13}$ | 1.51 x10$^{-13}$ | 154 x10$^{-13}$ | 1.58 x10$^{-13}$ |
| $r^2$ | 0.9944 | 0.9618 | 0.9898 | 0.9742 | 0.9545 |
| | | | | | |
| **Pore Diffusion** | | | | | |
| $D_2$ (cm$^2$/s) | 1.08 x10$^{-14}$ | 1.13 x10$^{-14}$ | 1.14 x10$^{-14}$ | 1.16 x10$^{-14}$ | 1.17 x10$^{-14}$ |
| $r^2$ | 0.9833 | 0.9798 | 0.9795 | 0.9685 | 0.9671 |

Table 6.9 b: Intraparticle model data for 4-nitrophenol adsorption onto NTPNC-EPI-CD

| Kinetic model | 25 mg/dm$^3$ | 50 mg/dm$^3$ | 75 mg/dm$^3$ | 100 mg/dm$^3$ | 125 mg/dm$^3$ |
|---|---|---|---|---|---|
| **NTPNC-EPI-CD** | | | | | |
| **Intraparticle Diffusion model** | | | | | |
| $k_i$ (mg/ g min) | 0.0339 | 0.0405 | 0.0435 | 0.0954 | 0.1110 |
| $C$ | 3.659 | 7.063 | 10.770 | 14.314 | 17.810 |
| $r^2$ | 0.9635 | 0.9395 | 0.9957 | 0.9950 | 0.9224 |
| **Film Diffusion** | | | | | |
| $D_1$ (cm$^2$/s) | 1.50 x10$^{-13}$ | 1.52 x10$^{-13}$ | 1.55 x10$^{-13}$ | 157 x10$^{-13}$ | 1.58 x10$^{-13}$ |
| $r^2$ | 0.9957 | 0.9763 | 0.9945 | 0.9956 | 0.9433 |
| **Pore Diffusion** | | | | | |
| $D_2$ (cm$^2$/s) | 1.60 x10$^{-14}$ | 2.13 x10$^{-14}$ | 3.13 x10$^{-14}$ | 3.59 x10$^{-14}$ | 3.76 x10$^{-14}$ |
| $r^2$ | 0.9969 | 0.9969 | 0.933 | 0.9977 | 0.9834 |

Table 6.9 c: Intraparticle model data for 4-nitrophenol adsorption onto NTPNC-HMDI-CD

| Kinetic model | 50 mg/dm$^3$ | 75 mg/dm$^3$ | 100 mg/dm$^3$ | 125 mg/dm$^3$ | 150 mg/dm$^3$ |
|---|---|---|---|---|---|
| **NTPNC-HMDI-CD** | | | | | |
| **Intraparticle Diffusion model** | | | | | |
| $k_i$ (mg/ g min) | 0.3787 | 0.3753 | 0.3677 | 0.2619 | 0.2449 |
| $C$ | 13.665 | 19.697 | 23.681 | 29.409 | 35.143 |
| $r^2$ | 0.9191 | 0.9512 | 0.9588 | 0.9417 | 0.9417 |
| | | | | | |
| **Film Diffusion** | | | | | |
| $D_1$ (cm$^2$/s) | 1.62 x10$^{-13}$ | 1.66 x10$^{-13}$ | 1.70 x10$^{-13}$ | 171 x10$^{-13}$ | 1.72 x10$^{-13}$ |
| $r^2$ | 0.9771 | 0.9598 | 0.9954 | 0.9881 | 0.9704 |
| | | | | | |
| **Pore Diffusion** | | | | | |
| $D_2$ (cm$^2$/s) | 1.29 x10$^{-14}$ | 1.54 x10$^{-14}$ | 2.38 x10$^{-14}$ | 2.38 x10$^{-14}$ | 2.90 x10$^{-14}$ |
| $r^2$ | 0.9622 | 0.9488 | 0.9948 | 0.9987 | 0.9965 |

### 6.5.4.2.2 Film and Pore diffusion

Since intraparticle diffusion plot confirmed the presence of both film and pore diffusion, kinetic data were further analysed using the Boyd kinetic expression to predict the actual slow step involved in the adsorption process. The plots of $q_t/q_e$ versus $t^{0.5}$ for 4-nitrophenol adsorption onto NTPNC, NTPNC-EPI-CD and NTPNC-HMDI-CD are shown in Fig. 6.20 a-c, respectively, and the values of the film diffusion constant, $D_1$ at different concentrations were then calculated from the slope of the plot and the results are presented in Table 6.9 a-c. Fig. 6.20 a-c, show the initial rapid stage followed by a slow and almost constant stage similar to the intraparticle diffusion plot for all samples. The values of the film diffusion constant, $D_1$ were observed to increase with an increase in concentration for all adsorbent sample but was higher for NTPNC-HMDI-CD followed by NTPNC-EPI-CD and NTPNC. The increase in $D_1$ with concentration may be attributed to an increase in concentration gradient between the bulk solution and nanocomposites surface.

Plots of $B_t$ against t at different 4-nitrophenol initial concentrations is shown in Fig. 6.21 a-c to identify whether external transport or intraparticle transport control the rate of adsorption for NTPNC, NTPNC-EPI-CD and NTPNC-HMDI-CD, respectively (Boyd et al., 1947, Sarkar et al., 2003). The values of the constant B are taken from the slope and are used to calculate the pore diffusion coefficient, $D_2$ (since from eq. 5.16, $B = D_2\pi^2/a^2$) and the values are presented in Table 6.9 a-c for NTPNC, NTPNC-EPI-CD and NTPNC-HMDI-CD, respectively. The plot in Fig.6.21 a-c shows a rapid initial stage of 4-nitrophenol showing linear relationship for all adsorbent samples. The plot for NTPNC in Fig. 6.21 a, did not pass through the origin but cut the y-axis between -0.413 and -0.496 suggesting that external mass transfer is rate-limiting at the initial stages of the adsorption process. As NTPNC was crosslinked to CD using both EPI and HMDI, the intercept shifted towards the positive values signifying an increase in external mass transfer process because of cross-linking.

The lines were close to the intercept for NTPNC-EPI and NTPNC-HMDI confirming greater participation of external mass transfer at the initial stage of adsorption. The values of pore diffusion coefficients, $D_2$ in Tables 6.9 a-c, were found to increase with increasing concentration from 1.08 x$10^{-14}$ to 1.17 x$10^{-14}$ cm$^2$/s for NTPNC and from 1.60 x$10^{-14}$ to 3.76 x$10^{-14}$ cm$^2$/s for NTPNC-EPI-CD and 1.29 x$10^{-14}$ to 2.90 x$10^{-14}$ cm$^2$/s for NTPNC-HMDI-CD. NTPNC-EPI-CD and NTPNC-

HMDI-CD nanocomposites had higher $D_1$ and $D_2$ values than NTPNC bio-composite indicating that cyclodextrin cross-linking onto magnetite coated pine cone improved the adsorbent surface resulting in faster diffusion across the boundary layer and into the pores. The values of film diffusion coefficients, $D_1$, were also seen to be higher than those of pore diffusion coefficients, $D_2$ for all nanocomposites, indicating that film diffusion may be the overall rate determining process at this stage of the adsorption process
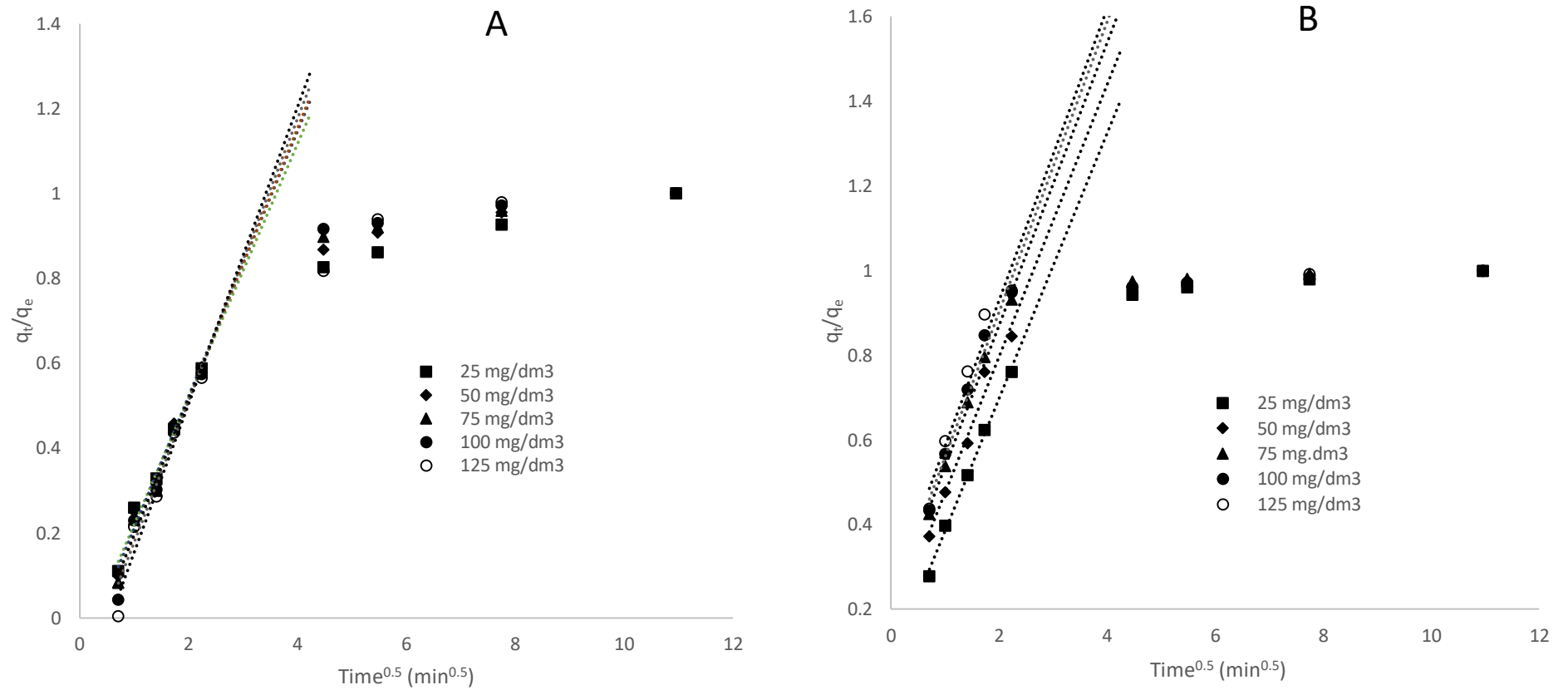
Figure 6.20: Fractional uptake plots of 4-nitrophenol adsorption by (a) NTPNC and (b) NTPNC-HMDI-CD at different concentration.
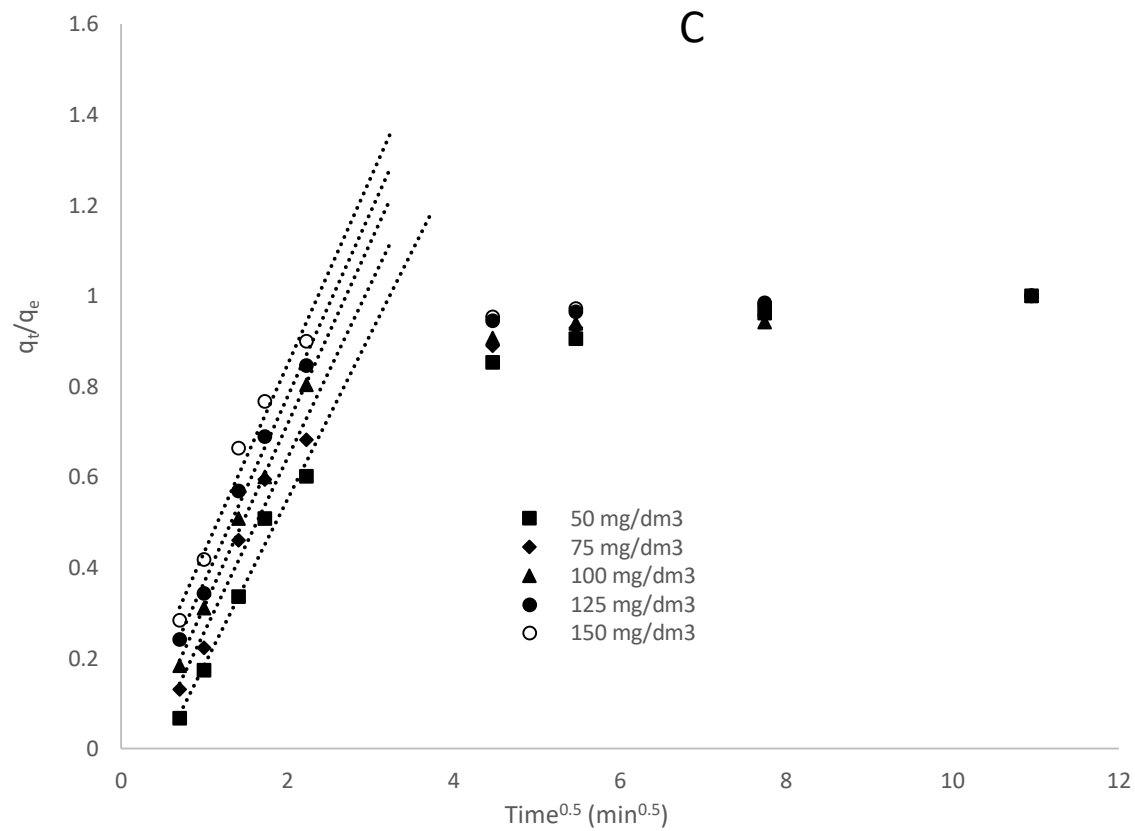
Fig. 6.20: (c) Fractional uptake plots of 4-nitrophenol adsorption by NTPNC-HMDI-CD at different concentrations.
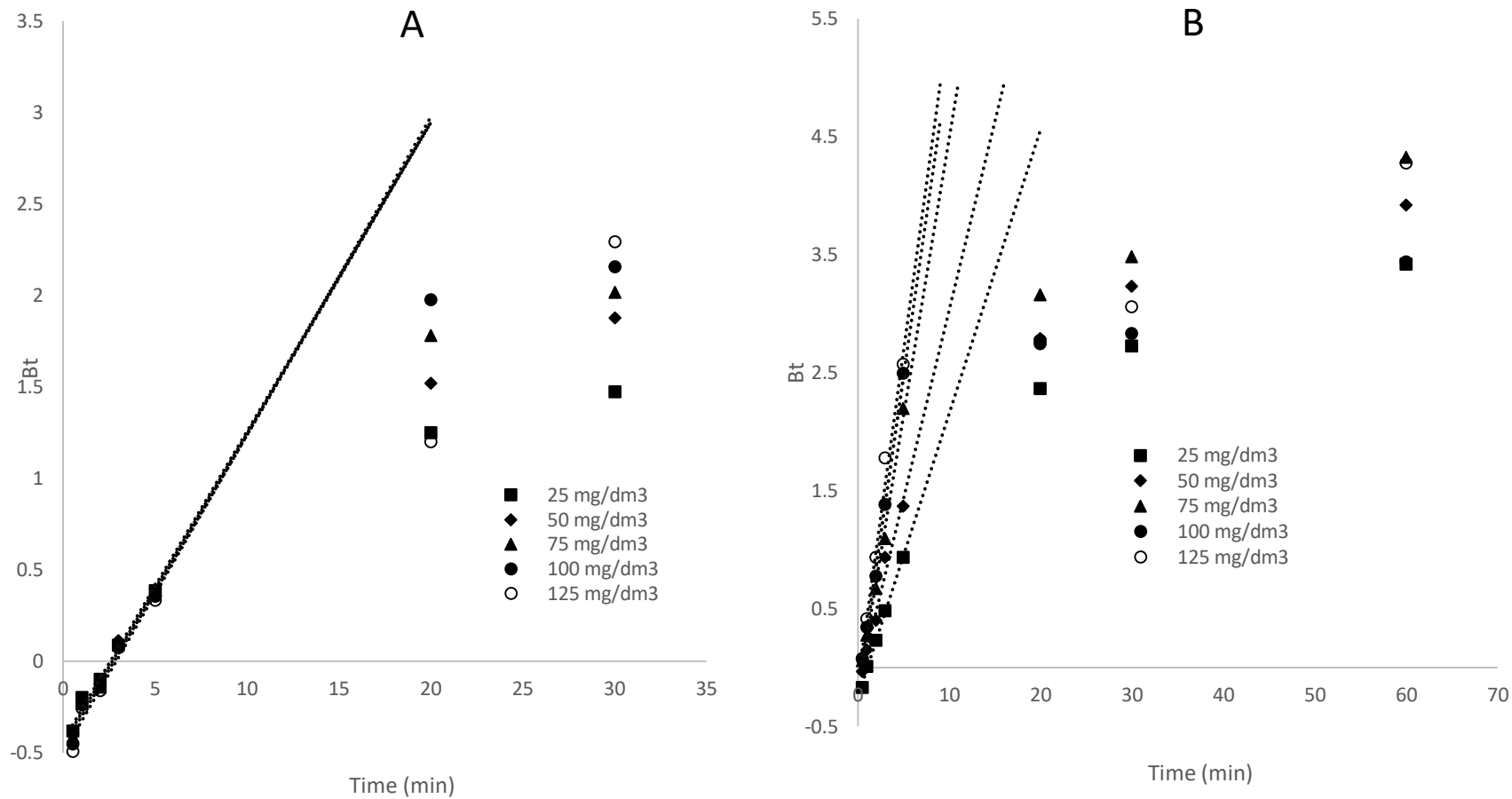
Figure 6.21: Boyd plot for 4-nitrophenol adsorption onto (a) NTPNC and (b) NTPNC-EPI-CD at different concentrations.
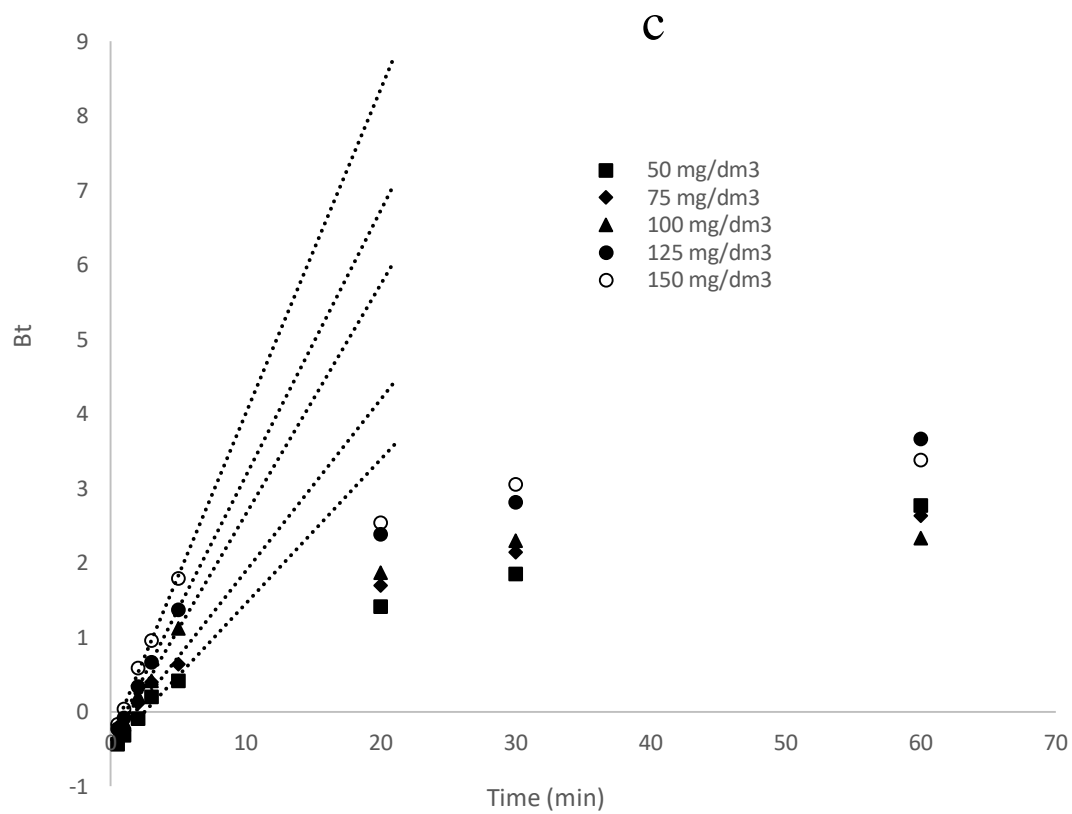
Fig. 6.21: (c) Boyd plot for 4-nitrophenol adsorption onto NTPNC-HMDI-CD at different concentrations.

### 6.5.5 Kinetic studies - Effect of Temperature

Temperature plays an important role in the adsorption process because it affects the diffusion rate of adsorbate molecules and surface physicochemical properties of adsorbents. The effect of temperature on the kinetics models and diffusion models were conducted and discussed in this section.

### 6.5.5.1 *Kinetic modelling*

#### 6.5.5.1.1 Pseudo first and pseudo second order models

Kinetics studies of 4-nitrophenol adsorption onto NTPNC-EPI-CD and NTPNC-HMDI-CD were performed with a constant initial 4-nitrophenol concentration of 100 mg/dm$^3$ and 0.1 g at five different temperatures (299, 301, 304, 306 and 309 K) and modelled using the linear forms of the pseudo first and pseudo-second order kinetic models. The effect of contact time at different temperatures on the amount of 4-nitrophenol removed by NTPNC, NTPNC-EPI-CD and NTPNC-HMDI-CD is shown in Fig.6.22 a-c, while the kinetics data at different temperatures are presented in Table 6.10 a-c, respectively. From Fig. 6.22 a-c, it has been observed that the amount of 4-nitrophenol adsorbed increased rapidly for the first 5 min, followed by a slower adsorption rate until reaching a saturation of adsorption capacity due to the full occupation of available active sites. The amount of 4-nitrophenol adsorbed was observed to increase with increase in temperature from 299 to 309 K for all nanocomposite adsorbents and NTPNC-HMDI-CD had the highest removal followed by NTPNC-EPI-CD and NTPNC. An increase in adsorption capacity with increasing temperature is due to the increase in mobility of the phenolate ions and a decrease in the retarding forces acting on the diffusing ions. It is reported that the adsorption capacity will increase with an increase in temperatures if the adsorption process is controlled by the diffusion process (intraparticle transport-pore diffusion). However, it has been observed that the diffusion of adsorbate into pores of the adsorbent is not the only rate-controlling step for all nanocomposite adsorbents. Therefore, the increase in adsorption capacity with an increase in temperature may be attributed to chemisorption.
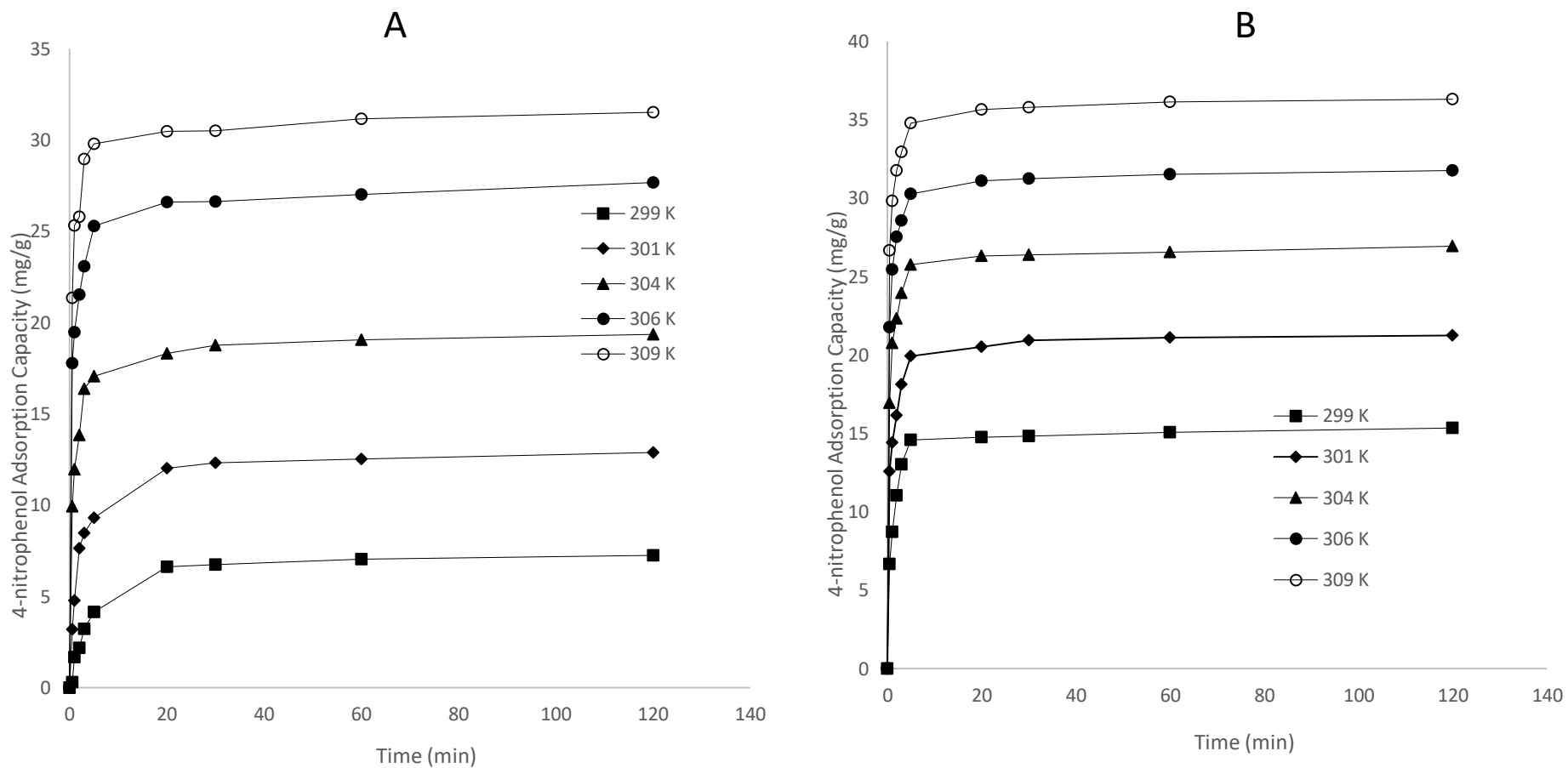
Figure 6.22: Effect of contact time at different temperature for 4-nitrophenol adsorption onto (a) NTPNC and (b) NTPNC-EPI-CD.
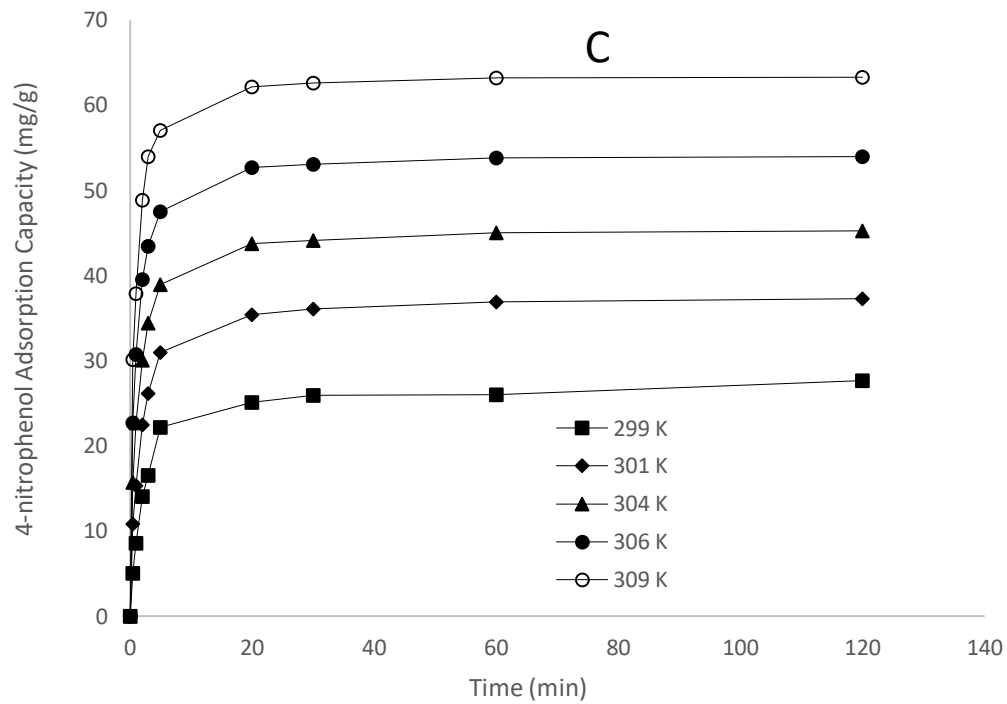
Fig. 6.22: (c) Effect of contact time at different temperature for 4-nitrophenol adsorption onto NTPNC-HMDI-CD.

The results in Table 6.10 a-c show the error determination as measured by correlation coefficient, $r^2$ and % variable error for 4-nitrophenol removal using NTPNC, NTPNC-EPI-CD and NTPNC-HMDI-CD. Error measurements for pseudo first-order model were $r^2 > 0.9930$ and % variable error $< 4.470$ for NTPNC, $r^2 > 0.9809$ and % variable error $< 3.070$ for NTPNC-EPI-CD and $r^2 > 0.9912$ and % variable error $< 11.952$ for NTPNC-HMDI-CD. Pseudo second-order gave the $r^2 > 0.9972$ and % variable error $< 0.934$ for NTPNC, $r^2 > 0.9987$ and % variable error $< 0.449$ for NTPNC-EPI-CD and $r^2 > 0.9995$ and % variable error $< 0.723$ for NTPNC-HMDI-CD. From the correlation coefficient and % variable error results, pseudo second order model was observed to have high $r^2$ values and low % variable error indicating that pseudo second order model better described the kinetic data for all three nanocomposite adsorbents. The adsorption capacities of both NTPNC-EPI-CD and NTPNC-HMDI-CD nanocomposites increased with an increase in temperature indicating the endothermic nature of adsorption. The pseudo-second-order rate constant, $k_2$ and initial sorption rates, $h$ were observed to increase with an increase in temperature from 299 to 309 K for both NTPNC-EPI-CD and NTPNC-HMDI-CD nanocomposites. This increase may be due to the fact that at higher temperatures, the increase in heat and the subsequent kinetic energy leads to increased mobility of the solute, which results to higher adsorption rates.

### 6.5.5.1.2 Activation energy

The activation energy provides information about the nature of the adsorption process. If the activation energy values are in the range 5-40 kJ/mol, adsorption process is said to be physical adsorption with relation to weak van der Waals forces such as hydrogen bonding. Adsorption process is considered to be through chemical bonds between the surface of the adsorbent and the adsorbate molecules formed if activation energy values are in the range 40-800 kJ/mol (Zhang et al., 2017). The pseudo second order activation energy of 4-nitrophenol onto NTPNC, NTPNC-EPI-CD and NTPNC-HMDI-CD were calculated to be 96.76 with $r^2$ value of 0.7279, 31.94 with $r^2$ value of 0.9583 and 31.87 with $r^2$ value of .9583, respectively. From the results, it can be said that the adsorption of 4-nitrophenol onto NTP-NC was through chemisorption but physisorption occurred for NTPNC-EPI-CD and NTPNC-HMDI-CD.

Table 6.10 a: Kinetic data for 4-mitrophenol adsorption onto NTP-NC

| Kinetic model | 299 K | 301 K | 304 K | 306 K | 309 K |
|---|---|---|---|---|---|
| **NTP-NC** | | | | | |
| **Pseudo-first order** | | | | | |
| Exp. *q* (mg/g) | 7.42 | 12.87 | 19.34 | 26.66 | 31.52 |
| *Model q* (mg/g) | 6.95 | 12.21 | 19.10 | 25.53 | 29.77 |
| $k_1$ (min$^{-1}$) | 0.1938 | 0.4294 | 1.0953 | 1.8167 | 2.2314 |
| $r^2$ | 0.9930 | 0.9764 | 0.9528 | 0.9422 | 0.9715 |
| % Variable Error | 0.064 | 0.524 | 1.915 | 4.470 | 2.905 |
| | | | | | |
| **Pseudo-second order** | | | | | |
| Exp. *q* (mg/g) | 7.42 | 12.87 | 19.34 | 26.66 | 31.52 |
| *Model q* (mg/g) | 7.66 | 12.91 | 19.03 | 26.81 | 30.96 |
| $k_2$ (g mg/min) | 0.0303 | 0.0486 | 0.0952 | 0.1130 | 0.1349 |
| *h* (mg/g min) | 1.7779 | 8.1001 | 34.4758 | 81.2216 | 129.3045 |
| $r^2$ | 0.9932 | 0.9972 | 0.9927 | 0.9679 | 0.9945 |
| % Variable Error | 0.062 | 0.063 | 0.297 | 0.934 | 0.561 |

Table 6.10 b: Kinetic data for 4-nitrophenol adsorption onto NTPNC-EPI-CD

| Kinetic model | 299 K | 301 K | 304 K | 306 K | 309 K |
|---|---|---|---|---|---|
| **NTPNC-EPI-CD** | | | | | |
| **Pseudo-first order** | | | | | |
| Exp. $q$ (mg/g) | 15.36 | 21.25 | 26.94 | 31.76 | 36.32 |
| *Model q* (mg/g) | 14.77 | 20.03 | 25.59 | 30.39 | 34.66 |
| $k_1$ (min$^{-1}$) | 0.8673 | 1.4253 | 1.8677 | 2.2277 | 2.5950 |
| $r^2$ | 0.9809 | 0.9479 | 0.9739 | 0.9782 | 0.9775 |
| % Variable Error | 0.537 | 2.517 | 1.9948 | 0.9897 | 3.070 |
| | | | | | |
| **Pseudo-second order** | | | | | |
| Exp. $q$ (mg/g) | 15.36 | 21.25 | 26.94 | 31.76 | 36.32 |
| *Model q* (mg/g) | 15.46 | 21.05 | 26.71 | 31.46 | 35.89 |
| $k_2$ (g mg/min) | 0.0942 | 0.1141 | 0.1250 | 0.1360 | 0.1463 |
| $h$ (mg/g min) | 22.5148 | 50.5580 | 89.1780 | 134.6035 | 188.4479 |
| $r^2$ | 0.9919 | 0.9907 | 0.9977 | 0.9987 | 0.9976 |
| % Variable Error | 0.226 | 0.449 | 0.176 | 0.155 | 0.324 |

Table 6.10 c: Kinetic data for 4-nitrophenol adsorption onto NTPNC-HMDI-CD

| Kinetic model | 299 K | 301 K | 304 K | 306 K | 309 K |
|---|---|---|---|---|---|
| **NTPNC-HMDI-CD** | | | | | |
| **Pseudo-first order** | | | | | |
| Exp. $q$ (mg/g) | 27.66 | 37.32 | 45.28 | 53.98 | 63.30 |
| *Model q* (mg/g) | 26.62 | 35.97 | 43.55 | 51.79 | 60.81 |
| $k_1$ (min$^{-1}$) | 0.3569 | 0.49.8 | 0.6399 | 0.8714 | 0.9994 |
| $r^2$ | 0.9912 | 0.9866 | 0.9799 | 0.9743 | 0.9734 |
| % Variable Error | 1.000 | 2.490 | 5.194 | 9.223 | 11.952 |
| | | | | | |
| **Pseudo-second order** | | | | | |
| Exp. $q$ (mg/g) | 27.66 | 37.32 | 45.28 | 53.98 | 63.30 |
| *Model q* (mg/g) | 28.37 | 37.87 | 45.78 | 54.41 | 63.89 |
| $k_2$ (g mg/ min) | 0.0173 | 0.0197 | 0.0221 | 0.0249 | 0.0257 |
| $h$ (mg/g min) | 13.9240 | 28.2525 | 46.3174 | 73.7152 | 104.9057 |
| $r^2$ | 0.9929 | 0.9984 | 0.9894 | 0.9995 | 0.9987 |
| Variable Error | 0.182 | 0.300 | 0.136 | 0.134 | 0.723 |

*6.5.5.2  Diffusion modelling*

6.5.5.2.1  Intraparticle diffusion

The plots of $q_t$ versus $t^{0.5}$ in Fig 6.23 a-c were rapid at the initial rapid stage followed by slower stage at which adsorption was almost constant. The straight line did not pass through the origin, indicating that intraparticle diffusion was not solely rate-limiting. Therefore, the plots suggest that both film and particle diffusion influenced the adsorption of 4-nitrophenol onto all three nanocomposite adsorbents. The values of $k_i$ and $C$ obtained from the slope and the intercept of the linear plot of $q$ versus $t^{0.5}$ are presented in Table 6.11 a-c. The value of $k_i$ was observed to increase from 0.0959 mg g$^{-1}$ min$^{-0.5}$ to 0.1763 mg g$^{-1}$ min$^{-0.5}$ for NTPNC, and 0.0954 mg g$^{-1}$ min$^{-0.5}$ to 0.1036 mg g$^{-1}$ min$^{-0.5}$ for NTPNC-EPI-CD as temperature was increased from 299 to 309 K and decrease from 0.3677 mg g$^{-1}$ min$^{-0.5}$ to 0.1675 mg g$^{-1}$ min$^{-0.5}$ for NTPNC-HMDI-CD. The magnitude of C increased with temperature for both NTPNC-EPI-CD and NTPNC-HMDI-CD nanocomposites suggesting greater participation of surface adsorption and activation of adsorption sites with increase in temperature.

6.5.5.2.2  Pore and film diffusion

The effect of pore and film diffusion on intraparticle diffusion at different temperatures was examined. Both the film diffusion, $D_1$, and the pore diffusion, $D_2$, were determined as they control the intraparticle diffusion process. The plots of fractional uptake of 4-nitrophenol onto NTPNC, NTPNC-EPI-CD and NTPNC-HMDI-CD nanocomposite versus $t^{0.5}$ are shown in Fig. 6.24 a-c, respectively. It was seen that the adsorption process tends to be followed by two phases, which are the initial rapid linear period followed by a slow and almost constant stage. The values of the film diffusion constant, $D_1$ at different temperatures were then calculated from the slope of the plot of $q_t/q_e$ versus time and recorded in Table 6.11 a-c for NTPNC, NTPNC-EPI-CD and NTPNC-HMDI-CD nanocomposite, respectively. The calculated values of $B_t$ *vs*. t were plotted to identify whether external transport or intraparticle diffusion controls the rate of adsorption and are shown in Fig. 6.25 a-c.
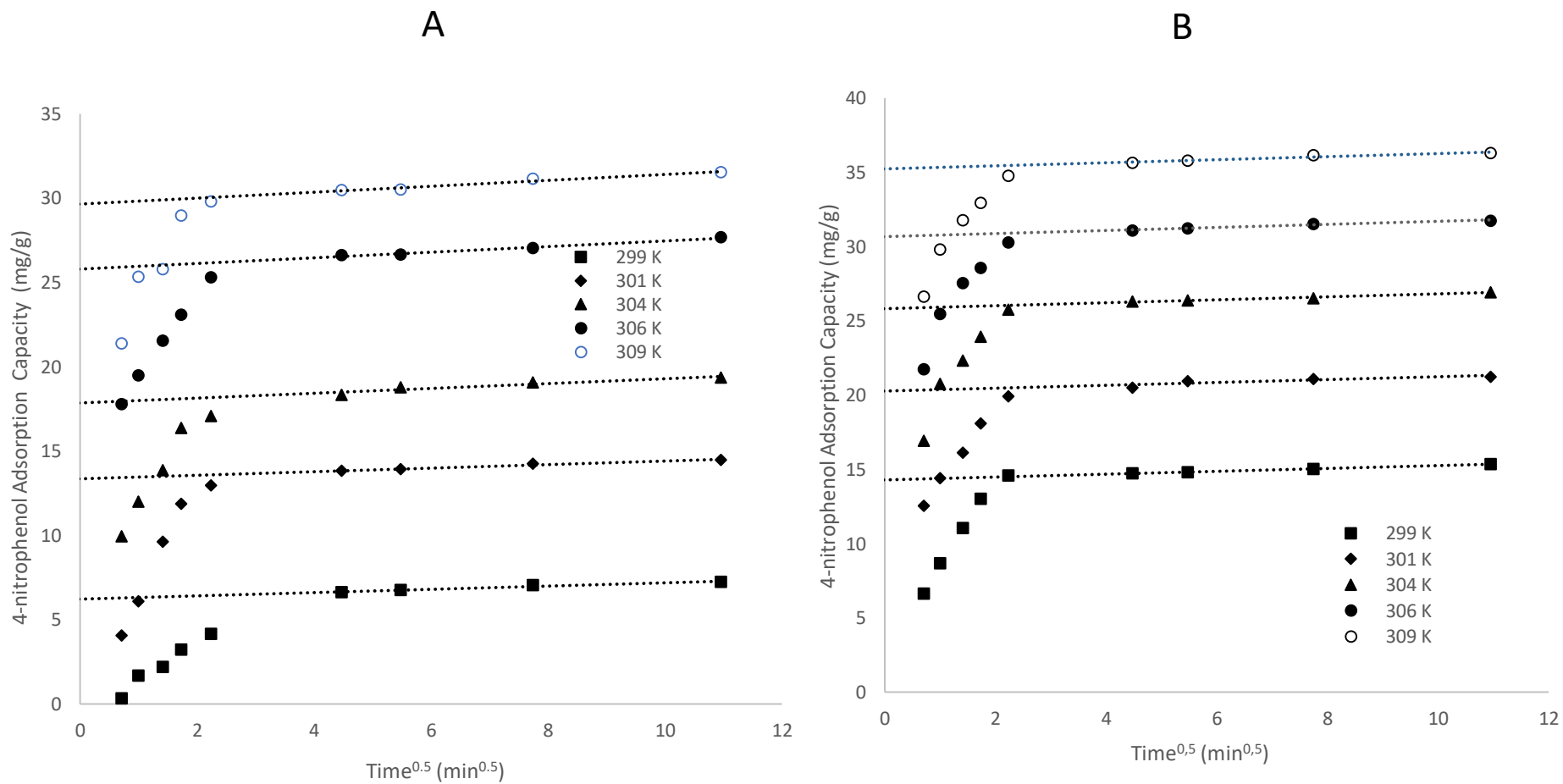
Figure 6.23: Intraparticle diffusion of 4-nitrophenol adsorption onto (a) NTPNC and (b) NTPNC-EPI-CD at different temperatures.
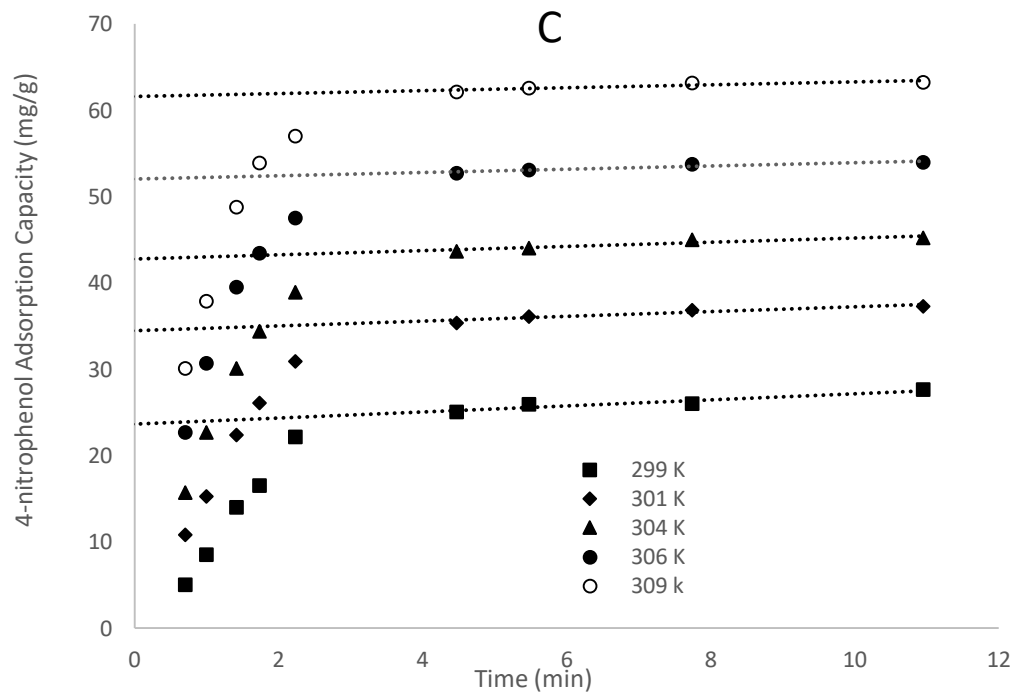
Fig. 5.23: (c) Intraparticle diffusion of 4-nitrophenol adsorption onto NTPNC-HMDI-CD at different temperatures.

Table 6.11 a: Intraparticle model data for 4-mitrophenol adsorption onto NTP-NC.

| Kinetic model | 299 K | 301 K | 304 K | 306 K | 309 K |
|---|---|---|---|---|---|
| **NTP-NC** | | | | | |
| **Intraparticle Diffusion model** | | | | | |
| $k_i$ (mg/ g min) | 0.0959 | 0.1040 | 0.1437 | 0.1684 | 0.1763 |
| $C$ | 6.221 | 13.360 | 17.839 | 25.779 | 29.642 |
| $r^2$ | 0.9742 | 0.9795 | 0.9871 | 0.9805 | 0.9532 |
| **Film Diffusion** | | | | | |
| $D_1$ (cm$^2$/s) | $1.54 \times 10^{-13}$ | $1.52 \times 10^{-13}$ | $1.34 \times 10^{-13}$ | $114 \times 10^{-13}$ | $1.09 \times 10^{-13}$ |
| $r^2$ | 0.9694 | 0.9689 | 0.9497 | 0.9974 | 0.9847 |
| **Pore Diffusion** | | | | | |
| $D_2$ (cm$^2$/s) | $1.14 \times 10^{-14}$ | $1.15 \times 10^{-14}$ | $2.16 \times 10^{-14}$ | $2.29 \times 10^{-14}$ | $2.36 \times 10^{-14}$ |
| $r^2$ | 0.9688 | 0.9737 | 0.9381 | 0.9881 | 0.9243 |

Table 6.11 b: Intraparticle model data for 4-nitrophenol adsorption onto NTPNC-EPI-CD

| Kinetic model | 299 K | 301 K | 304 K | 306 K | 309 K |
|---|---|---|---|---|---|
| **NTPNC-EPI-CD** | | | | | |
| **Intraparticle Diffusion model** | | | | | |
| $k_i$ (mg/ g min) | 0.0954 | 0.0965 | 0.0979 | 0.1004 | 0.1036 |
| $C$ | 14.314 | 20.268 | 25.841 | 30.691 | 36.238 |
| $r^2$ | 0.9950 | 0.9657 | 0.9828 | 0.9781 | 0.9469 |
| Diffusion model | | | | | |
| **Film Diffusion** | | | | | |
| $D_1$ (cm$^2$/s) | $1.57 \times 10^{-13}$ | $1.28 \times 10^{-13}$ | $1.2 \times 10^{-13}$ | $1.09 \times 10^{-13}$ | $9.97 \times 10^{-14}$ |
| $r^2$ | 0.9454 | 0.9832 | 0.9642 | 0.9416 | 0.9284 |
| **Pore Diffusion** | | | | | |
| $D_2$ (cm$^2$/s) | $3.59 \times 10^{-14}$ | $2.99 \times 10^{-14}$ | $2.78 \times 10^{-14}$ | $2.66 \times 10^{-14}$ | $2.58 \times 10^{-14}$ |
| $r^2$ | 0.9948 | 0.9938 | 0.9944 | 0.9712 | 0.9459 |

Table 6.11 c: Intraparticle model data for 4-nitrophenol adsorption onto NTPNC-HMDI-CD

| Kinetic model | 299 K | 301 K | 304 K | 306 K | 309 K |
|---|---|---|---|---|---|
| **NTPNC-HMDI-CD** | | | | | |
| **Intraparticle Diffusion model** | | | | | |
| $k_i$ (mg/ g min) | 0.3677 | 0.2772 | 0.2431 | 0.1927 | 0.1675 |
| $C$ | 23.681 | 34.445 | 42.786 | 52.025 | 61.625 |
| $r^2$ | 0.9588 | 0.9036 | 0.9868 | 0.9649 | 0.9055 |
| Diffusion model | | | | | |
| **Film Diffusion** | | | | | |
| $D_1$ (cm$^2$/s) | $1.70 \times 10^{-13}$ | $1.60 \times 10^{-13}$ | $1.52 \times 10^{-13}$ | $1.50 \times 10^{-13}$ | $1.40 \times 10^{-13}$ |
| $r^2$ | 0.9454 | 0.9832 | 0.9642 | 0.9416 | 0.9284 |
| **Pore Diffusion** | | | | | |
| $D_2$ (cm$^2$/s) | $2.06 \times 10^{-14}$ | $2.15 \times 10^{-14}$ | $2.20 \times 10^{-14}$ | $2.40 \times 10^{-14}$ | $2.50 \times 10^{-14}$ |
| $r^2$ | 0.9948 | 0.9938 | 0.9944 | 0.9712 | 0.9459 |

The plots of $B_t$ vs. t for the adsorption of 4-nitrophenol onto NTPNC, NTP-NC-EPI-CD and NTPNC-HMDI-CD nanocomposites were found to be linear at the initial stage of the adsorption process (up to 5 min of contact) and did not pass through the origin at all temperatures investigated indicating that external mass transfer mainly governs the adsorption process at the initial stages (Ofomaja, 2010). The values of the intercepts of the plots cutting the y-axis for NTPNC were observed to shift towards the positive value as NTPNC was cross-linked to CD using both epichlorohydrin and 1.6-hexamethylene diisocyanate. This suggest that NTPNC-EPI-CD and NTPNC-HMDI-CD had stronger participation of external mass transfer in the rate determining step. The values of $D_1$ for NTPNC, NTP-NC-EPI-CD and NTPNC-HMDI-CD nanocomposites in Table. 6.11 a-c, were observed to reduce while $D_2$ values increased with increasing reaction temperature for all nanocomposite adsorbents. The reduction in the values of $D_1$ may be attributed to rapid saturation of active sites on the adsorbent surface leading to the reduction of mass transfer across the thin liquid film. On the other hand, an increase in $D_2$ with increasing temperature was observed which may be due to increased mobility of the 4-nitrophenol molecules in solution with increasing temperature. Higher values of $D_2$ over $D_1$ for all nanocomposites indicates that adsorption mechanism is controlled by pore diffusion.
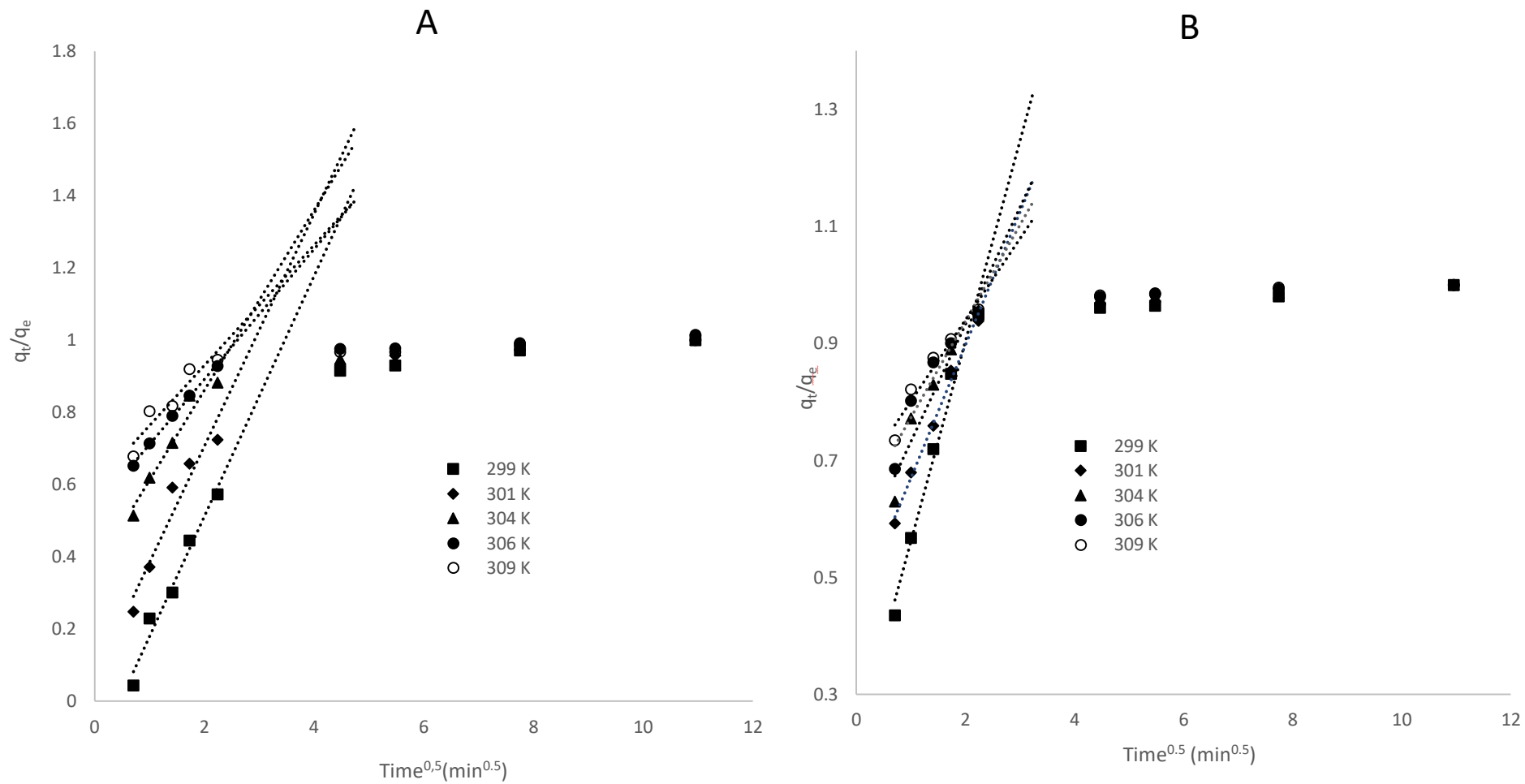
Figure 6.24: Fractional uptake of 4-nitrophenol adsorption onto (a) NTPNC and (b) NTPNC-EPI-CD at different temperatures.
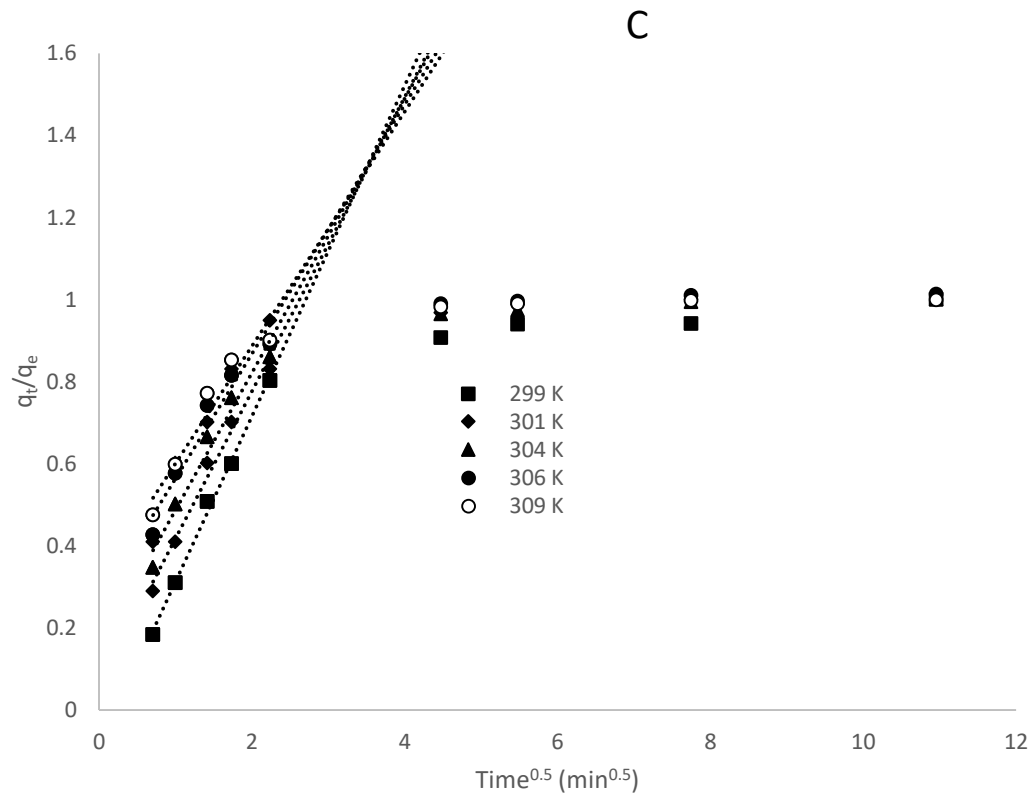
Fig. 6.24: (c) Fractional uptake of 4-nitrophenol adsorption onto NTPNC-HMDI at different temperatures-
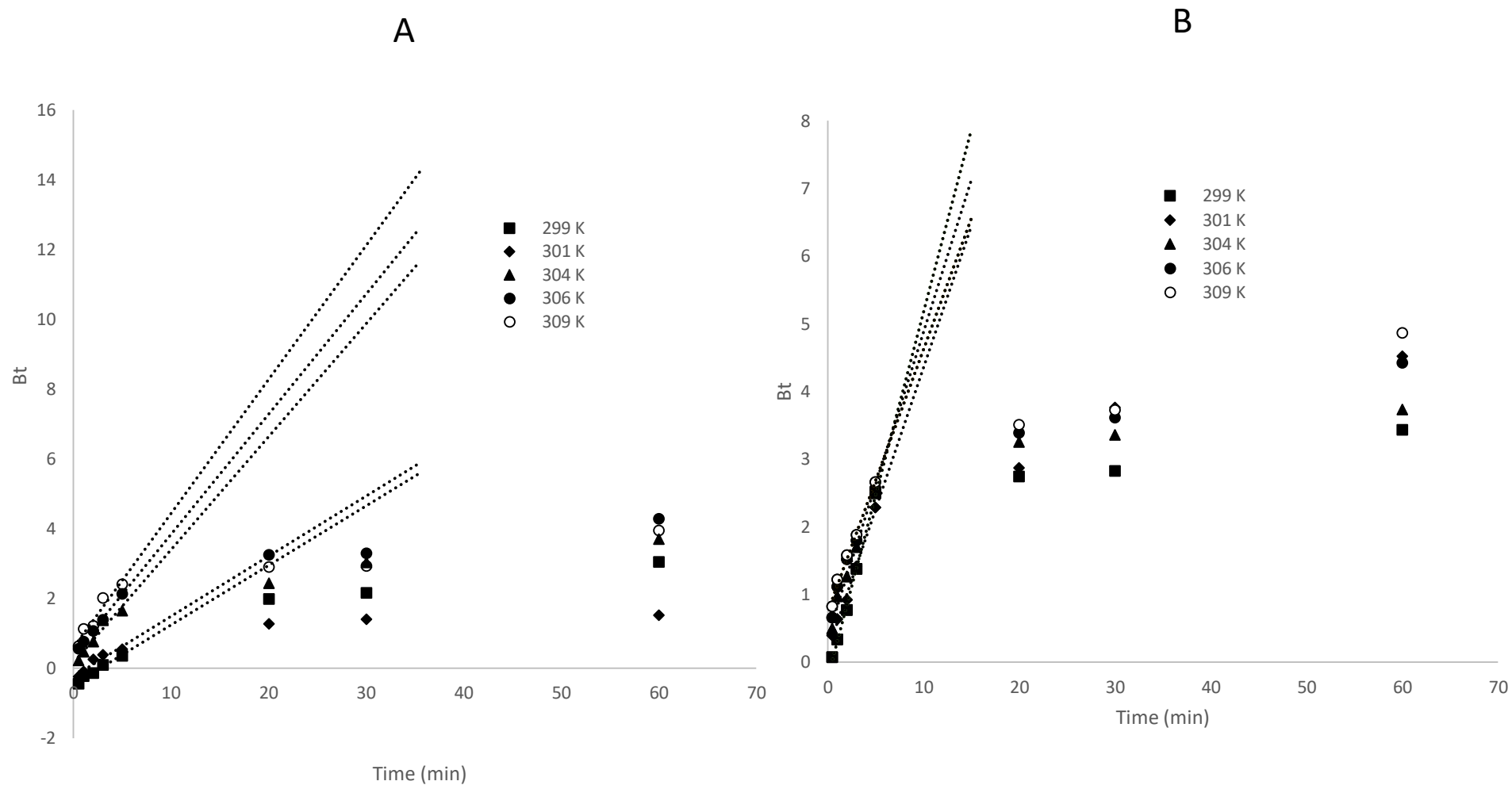
Figure 6.25: Boyd plot of 4-nitrophenol adsorption onto (a) NTPNC and (b) NTPNC-EPI-CD nanocomposite at different temperatures.
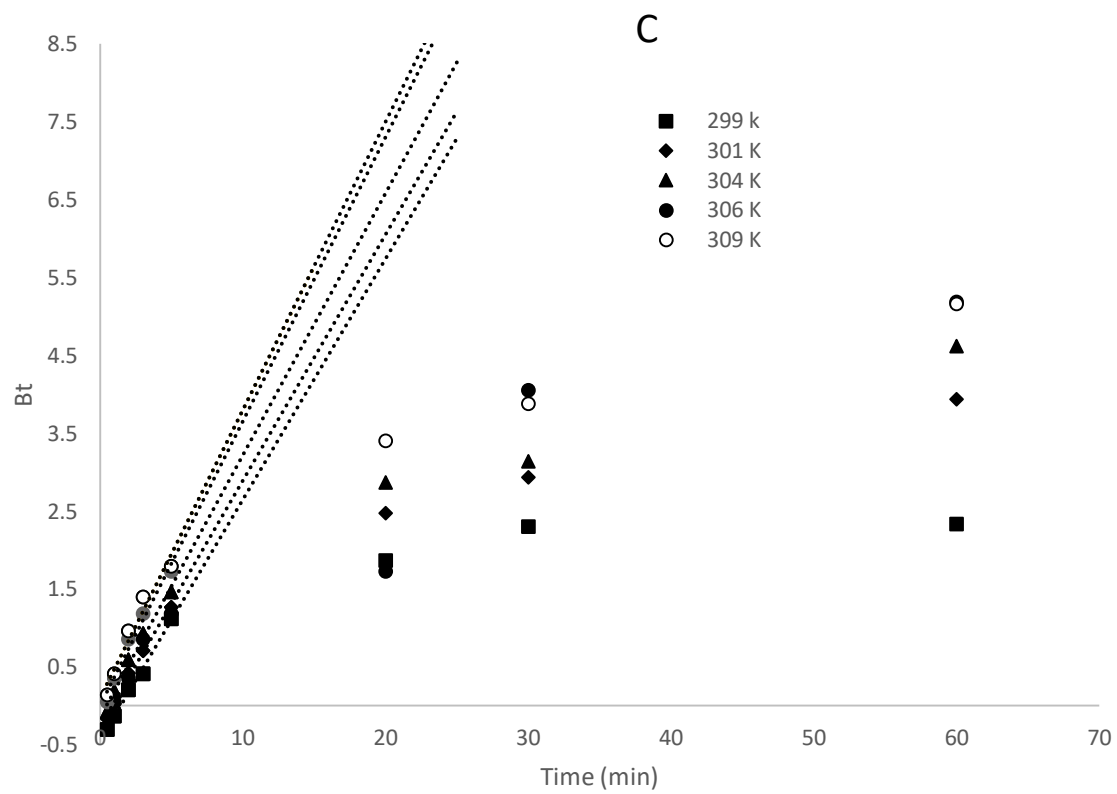
Fig. 6.25: (c) Boyd plot of 4-nitrophenol adsorption onto NTPNC-HMDI-CD nanocomposite at different temperatures.

## 6.5.6 Equilibrium isotherm

Equilibrium isotherm models give significant information about the adsorption mechanism and the nature of interaction between the biosorbent and adsorbate in solution. Equilibrium adsorption studies were conducted for the removal of 4-nitrophenol onto NTPNC, NTRPNC-EPI-CD and NTPNC-HMDI-CD nanocomposites from concentrations ranging from 25 to 125 mg/dm$^3$ for NTPNC and NTPNC-EPI-CD and 25 to 150 mg/dm$^3$ NTPNC-HMDI-CD at different temperatures from 299 to 309 K. The equilibrium plots of 4-nitrophenol adsorption capacity versus equilibrium concentration for NTPNC, NTRPNC-EPI-CD and NTPNC-HMDI-CD nanocomposites are shown in Fig. 6.26 A-C, respectively. The 4-nitrophenol adsorption capacity was observed to increase with increasing equilibrium concentration until attaining an almost constant value, due to increasing adsorption driving force for all adsorbents. The amount of 4-nitrophenol adsorption capacity was also seen to increase with increasing temperature from 299 to 309 K. Temperature of 309 K was taken as the highest temperature as 4-nitrophenol adsorption capacity was observed to reduce at higher temperature meaning that 4-nitrophenol adsorption is favoured at 309 K or lower temperatures. This might be due to the fact that 4-nitrophenol molecules escape from the solid phase to the bulk phase with an increasing temperature thereby weakening the forces of attraction between 4-nitrophenol and the nanocomposite adsorbent (Tang et al., 2007).

The values of the equilibrium constants obtained for the isotherm models along with values of correlation coefficient, $r^2$ and errors determination were calculated for all nanocomposites adsorbents and are shown in Table 6.12 a-c. The correlation coefficient, $r^2$ values for Langmuir model where in the range of 0.9982-0.9997, 0.9995-0.9999 and 0.9995-0.9998 while the errors determination, % variables were in the range of 0.02-0.1, 0.03-0.08 and 0.07-0.18 for NTPNC, NTRPNC-EPI-CD and NTPNC-HMDI-CD nanocomposites, respectively. Langmuir model gave good fit suggesting that adsorption sites on all nanocomposite adsorbents are homogeneous with monolayer coverage of 4-nitrophenol molecules on the surface. The equilibrium constant, $k_a$, for Langmuir isotherm had values increasing from 0.0222-0.0605, 0.0252-0.3080 and 0.505-0.0971 for NTPNC, NTRPNC-EPI-CD and NTPNC-HMDI-CD nanocomposites, respectively as temperature increases.
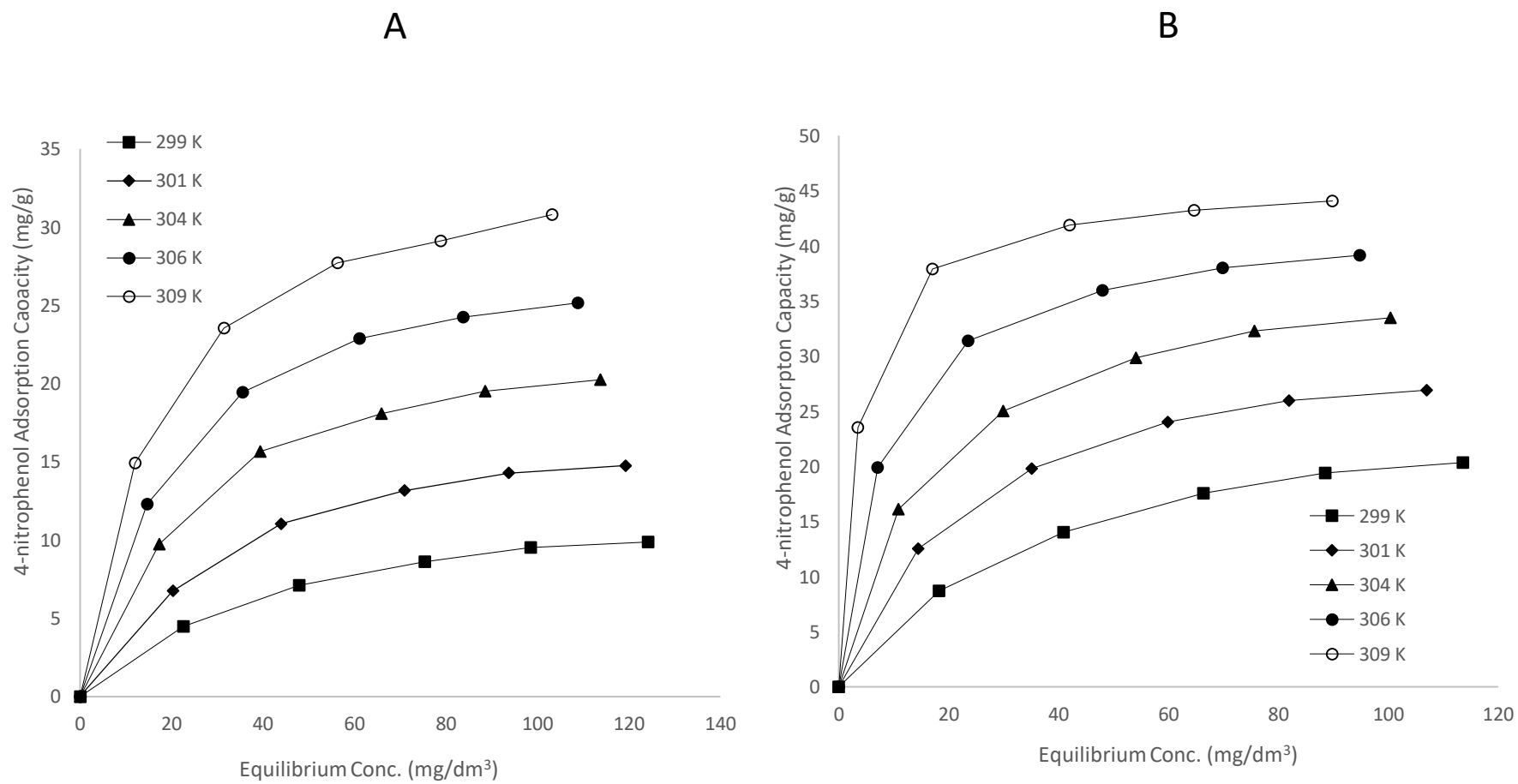
Figure 6.26: Equilibrium adsorption of 4-nitrophenol onto (a) NTPNC and (b) NTPNC-EPI-CD
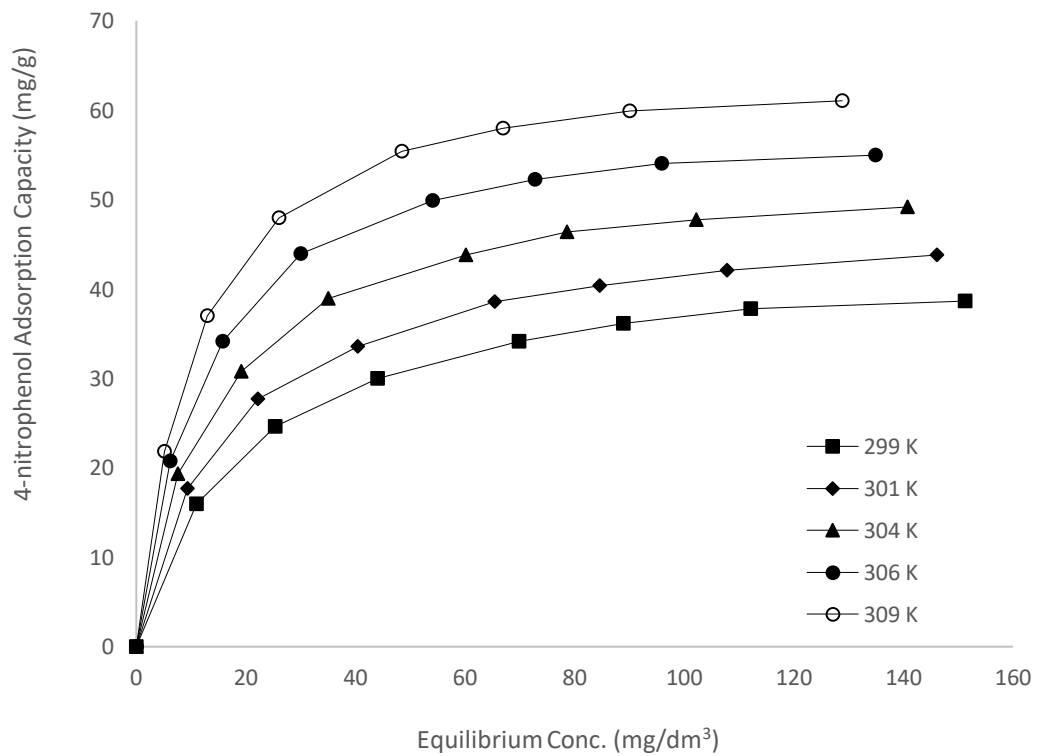
Figure 6.26: (c) Equilibrium adsorption of 4-nitrophenol onto NTPNC-HMDI-CD

Table 6.12 a: Equilibrium data for 4-nitrophenol adsorption onto NTPNC

| Isotherm model | 299 K | 301 K | 304 K | 306 K | 309 K |
|---|---|---|---|---|---|
| **NTPNC** | | | | | |
| **Langmuir** | | | | | |
| $q$ (mg/g) | 13.69 | 19.59 | 25.10 | 30.23 | 38.69 |
| $K_a$ (dm$^3$/mg) | 0.0222 | 0.0275 | 0.0389 | 0.0486 | 0.0608 |
| $r^2$ | 0.9991 | 0.9982 | 0.9986 | 0.9993 | 0.9997 |
| % Variable Error | 0.02 | 0.08 | 0.10 | 0.08 | 0.05 |
| | | | | | |
| **Freundlich** | | | | | |
| $n$ | 2.30 | 2.49 | 2.85 | 3.08 | 2.70 |
| $K_F (mg / g)(dm^3 / mg)^{1/n}$ | 1.263 | 2.273 | 4.008 | 5.720 | 7.702 |
| $r^2$ | 0.9914 | 0.9487 | 0.9878 | 0.9875 | 0.9897 |
| % Variable Error | 0.12 | 0.53 | 0.95 | 0.99 | 1.78 |
| | | | | | |
| **Dubinin–Radushkevich** | | | | | |
| $q_s$ (mol/g) | $3.32 \times 10^{-4}$ | $4.62 \times 10^{-4}$ | $6.17 \times 10^{-4}$ | $6.62 \times 10^{-4}$ | $7.17 \times 10^{-4}$ |
| $\beta$ (mol$^2$/J$^2$) | $9.90 \times 10^{-9}$ | $9.55 \times 10^{-9}$ | $9.55 \times 10^{-9}$ | $9.11 \times 10^{-9}$ | $8.90 \times 10^{-9}$ |
| $E$ (kJ/mol) | 7.11 | 7.24 | 7.31 | 7.41 | 7.50 |
| $r^2$ | 0.9821 | 0.9680 | 0.9655 | 0.9635 | 0.9721 |
| % Variable Error | 0.17 | 0.75 | 1.12 | 1.11 | 1.99 |

Table 6.12 b: Equilibrium data for 4-nitrophenol adsorption onto NTPNC-EPI-CD

| Isotherm model | 299 K | 301 K | 304 K | 306 K | 309 K |
|---|---|---|---|---|---|
| **NTPNC-EPI-CD** | | | | | |
| **Langmuir** | | | | | |
| $q$ (mg/g) | 27.83 | 33.23 | 38.68 | 42.33 | 45.39 |
| $K_a$ (dm$^3$/mg) | 0.0252 | 0.0424 | 0.0640 | 0.1234 | 0.3080 |
| $r^2$ | 0.9995 | 0.9997 | 0.9996 | 0.9999 | 0.9999 |
| %Variable Error | 0.04 | 0.04 | 0.08 | 0.03 | 0.05 |
| | | | | | |
| **Freundlich** | | | | | |
| $n$ | 2.69 | 5.36 | 8.40 | 13.78 | 21.20 |
| $K_F (mg/g)(dm^3/mg)^{1/n}$ | 2.292 | 2.818 | 3.243 | 4.195 | 5.794 |
| $r^2$ | 0.9921 | 0.9901 | 0.9924 | 0.9885 | 0.9835 |
| %Variable Error | 0.60 | 1.33 | 1.54 | 3.32 | 6.20 |
| | | | | | |
| **Dubinin–Radushkevich** | | | | | |
| $q_s$ (mol/g) | $6.89 \times 10^{-4}$ | $7.03 \times 10^{-4}$ | $7.17 \times 10^{-4}$ | $7.93 \times 10^{-4}$ | $8.76 \times 10^{-4}$ |
| $\beta$ (mol$^2$/J$^2$) | $9.70 \times 10^{-9}$ | $9.66 \times 10^{-9}$ | $9.56 \times 10^{-9}$ | $9.41 \times 10^{-9}$ | $9.38 \times 10^{-9}$ |
| $E$ (kJ/mol) | 7.18 | 7.19 | 7.23 | 7.29 | 7.30 |
| $r^2$ | 0.9869 | 0.9788 | 0.9840 | 0.9679 | 0.9486 |
| %Variable Error | 0.75 | 1.53 | 1.75 | 4.02 | 6.88 |

Table 6.12 c: Equilibrium data for 4-nitrophenol adsorption onto NTPNC-HMDI-CD

| Isotherm model | 299 K | 301 K | 304 K | 306 K | 309 K |
|---|---|---|---|---|---|
| **NTPNC-HMDI-CD** | | | | | |
| **Langmuir** | | | | | |
| $q$ (mg/g) | 44.00 | 48.52 | 54.35 | 60.57 | 66.89 |
| $K_a$ (dm$^3$/mg) | 0.0505 | 0.0594 | 0.0705 | 0.0842 | 0.0971 |
| $r^2$ | 0.9996 | 0.9995 | 0.9997 | 0.9997 | 0.9998 |
| %Variable Error | 0.07 | 0.12 | 0.10 | 0.18 | 0.13 |
| | | | | | |
| **Freundlich** | | | | | |
| $n$ | 3.34 | 3.48 | 3.64 | 3.80 | 3.86 |
| $K_F (mg/g)(dm^3/mg)^{1/n}$ | 9.179 | 11.015 | 13.523 | 16.319 | 18.779 |
| $r^2$ | 0.9839 | 0.9847 | 0.9773 | 0.9698 | 0.9667 |
| %Variable Error | 3.35 | 4.05 | 7.83 | 13.48 | 18.40 |
| | | | | | |
| **Dubinin–Radushkevich** | | | | | |
| $q_s$ (mol/g) | $7.93 \times 10^{-4}$ | $8.59 \times 10^{-4}$ | $9.68 \times 10^{-4}$ | $10.8 \times 10^{-4}$ | $12.1 \times 10^{-4}$ |
| $\beta$ (mol$^2$/J$^2$) | $9.44 \times 10^{-9}$ | $9.35 \times 10^{-9}$ | $9.30 \times 10^{-9}$ | $9.18 \times 10^{-9}$ | $9.08 \times 10^{-9}$ |
| $E$ (kJ/mol) | 7.28 | 7.31 | 7.33 | 7.38 | 7.42 |
| $r^2$ | 0.9719 | 0.9715 | 0.9603 | 0.9469 | 0.9430 |
| %Variable Error | 0.25 | 0.67 | 1.05 | 1.00 | 1.95 |

The increasing equilibrium constant values suggest that stronger bonds are formed between 4-nitrophenol and the nanocomposites adsorbents and the NTPNC-HMDI-CD had the highest values followed by NTPNC-EPI-CD and NTPNC. The monolayer capacity was also observed to increase with increasing temperature and NTPNC-HMDI-CD had higher values than those of NTPNC-EPI-CD and NTPNC indicating the participation of the hydrophobic NTPNC-HMDI-CD in the 4-nitrophenol adsorption process. The results also show that NTPNC-HMDI-CD nanocomposite has the higher affinity for 4-nitrophenol which can be due to the higher surface area and pore volume of the sample. The Freundlich isotherm showed the correlation coefficient, $r^2$ in the range 0.9487-0.9914, 0.9835-0.9924 and 0.9667-0.9847 while percentage variable error gave values in the range of 0.12-1.78, 0.60-6.20 and 3.35-18.40 for NTPNC, NTRPNC-EPI-CD and NTPNC-HMDI-CD nanocomposites, respectively. Both parameters, $n$ and $K_F$ were observed to increase in magnitude with increase in temperature suggesting that both affinity for 4-nitrophenol and adsorption capacity were favoured by increasing temperature.

Dubinin–Radushkevich isotherm gave correlation coefficient, $r^2$, in the range 0.9635-9.8721, 0.9486-.9869 and 0.9430-0.9719 and percentage variable error ranging from 0.17-1.99, 0.75-6.88 and 0.25-1.95 for NTPNC, NTRPNC-EPI-CD and NTPNC-HMDI-CD nanocomposites, respectively. The saturation capacity was also found to increase with increasing adsorption temperature for all nanocomposite adsorbents. The adsorption energy parameter, $\beta$ was found to decrease from $9.90 \times 10^{-9}$ to $8.90 \times 10^{-9}$ $mol^2/kJ^2$ for NTPNC and from $9.70 \times 10^{-9}$ to $9.38 \times 10^{-9}$ $mol^2/kJ^2$ for NTPNC-EPI-CD and from $9.44 \times 10^{-9}$ to $9.08 \times 10^{-9}$ $mol^2/kJ^2$ for NTPNC-HMDI-CD as temperature was increased from 299 to 309 K. The mean free energy of adsorption which gives an indication of the adsorption mechanism increased with adsorption temperature from 7.11 to 7.50 kJ/mol for NTPNC, from 7.18 to 7.30 kJ/mol for NTPNC-EPI-CD, and from 7.28 to 7.42 kJ/mol for NTPNC-HMDI-CD nanocomposite. The values of the mean free energy of adsorption, $E$, for all nanocomposite adsorbents obtained were below 8 kJ/mol indicated that physical process governed the 4-nitrophenol mechanism. Similar results have been reported by other researcher for adsorption of phenolic compounds (Kumar et al., 2018). Comparing the correlation coefficient, $r^2$ of the three isotherm models, (Table 6.12a-c), The results suggest that the Langmuir model provided better fit of the adsorption data followed by Freundlich the Dubinin-Radushkevich.

## 6.5.7  Thermodynamics studies

To gain insight into the adsorption behaviour of 4-nitrophenol onto NTPNC, NTPNC-EPI-CD and NTPNC-HMDI-CD, thermodynamics parameters such as Gibbs free energy change ($\Delta G$), enthalpy change ($\Delta H$) and entropy change ($\Delta S$) were calculated according to Eq.5.26 and the results are given in Table 6.13. The results show that the calculated values of $\Delta G$ for all 3 nanocomposite adsorbents were negative and reduced from -19.98 to -23.23 kJ/mol for NTPNC, from -20.29 to -27.46 kJ/mol for NTPNC-EPI-CD and from -22.02 to -24.43 kJ/mol for NTPNC-HMDI-CD with increasing temperature from 299 to 309 K implying that the adsorption process was spontaneous at all temperatures and spontaneity reduced with temperature. A reduction in $\Delta G$ with increasing temperature indicate a less driving force resulting in lesser adsorption capacity. The positive values of $\Delta H$ for all adsorbents (39.78 kJ/mol for NTPNC, 82.98 kJ/mol for NTPNC-EPI-CD and 29.23 kJ/mol for NTPNC-HMDI-CD) demonstrated that the 4-nitrophenol adsorption onto all three nanocomposite adsorbents was endothermic and thermodynamically favourable while the positive values of $\Delta S$ (94.85 J/mol K for NTPNC, 223.89 J/mol K for NTPNC-EPI-CD and 608.64 J/mol K for NTPNC-HMDI-CD) indicated the increase in number of species at the solid-liquid interface and greater stability of the adsorption process.

Table 6.13: Thermodynamics parameters of 4-nitrophenol adsorption onto NTPNC, NTPNC-EPI-CD and NTPNC-HMDI-CD

| Adsorbent | Temperature (K) | $\Delta G$ (kJ/mol) | $\Delta H$ (kJ/mol) | $\Delta S$ (J/mol K) |
|---|---|---|---|---|
| NTP-NC | 299 | -19.98 | | |
| | 301 | -20.67 | | |
| | 304 | -21.73 | 39.78 | 94.85 |
| | 306 | -22.44 | | |
| | 309 | -23.23 | | |
| NTPNC-EPI-CD | 299 | -20.29 | | |
| | 301 | -21.73 | | |
| | 304 | -22.99 | 82.98 | 223.89 |
| | 306 | -24.81 | | |
| | 309 | -27.40 | | |
| NTPNC-HMDI-CD | 299 | -22.02 | | |
| | 301 | -22.57 | | |
| | 304 | -23.23 | 29.23 | 608.64 |
| | 306 | -23.83 | | |
| | 309 | -24.43 | | |

## 6.6 ADSORPTION MECHANISM

From the results obtained from effect of solution pH and kinetics studies, the adsorption mechanism of p-nitrophenol onto NTPNC, NTPNC-EPI-CD and NTPNC-HMDI-CD was speculated. FTIR analysis before and after adsorption were conducted to confirm the mechanism that govern the 4-nitrophenol adsorption onto NTPNC, NTPNC-EPI-CD and NTPNC-HMDI-CD nanocomposites.

### 6.6.1 FTIR before and after 4-nitrophenol adsorption

Adsorption of 4-nitrophenol on carbon materials has been reported to be via several interactions such as polar, hydrophobic, electron donor acceptor and hydrogen bonding (Li et al., 2012). The involvement of various functional groups in 4-nitrophenol removal mechanism was elucidated based on the FTIR analysis in the wavelength range of 4000-500 $cm^{-1}$. FTIR spectra of NTPNC, NTPNC-EPI-CD and NTPNC-HMDI-CD nanocomposites before and after 4-nitrophenol adsorption are shown in. Fig. 6.27 a-c. The main difference in the NTPNC and NTPNC-EPI-CD spectra before and after 4-nitrophenol are observed to be the hydroxyl and carbonyl groups. The broad OH stretching vibration at 3307 $cm^{-1}$ on the NTPNC nanocomposite and 3343 on the NTPNC-EPI-CD were observed to have increased in intensity and shifted to 3334 $cm^{-1}$ and 3366 $cm^{-1}$ for NTPNC and NTPNC-EPI-CD after 4-nitrophenol adsorption, respectively. This may be due to the formation of hydrogen bond between 4-nitrophenol and the magnetite on the NTPNC and β-cyclodextrin units on the NTPNC-EPI-CD. The C-O vibration peak at 1622 $cm^{-1}$ for NTPNC and at 1639 $cm^{-1}$ for NTPNC-EPI-CD were found to have shifted to 1591 for NTPNC and splitted into two peaks at 1628 and 1583 $cm^{-1}$ on the NTPNC-EPI-CD nanocomposite. A new, very intense peak appeared at the wavenumber 1285 $cm^{-1}$ due to the asymmetry and symmetry stretching of N-O indicating the adsorption of 4-nitrophenol onto NTPNC-EPI-CD nanocomposite. The band at 1027 and 1034 $cm^{-1}$ indicating the antisymmetric glycosidic C-O-C vibration were observed to shift to 1022 and 1029 $cm^{-1}$ after 4-nitrophenol adsorption for NTPNC and NTPNC-EPI-CD nanocomposites, respectively. The changes in these peak positions indicate the important role of hydrogen bonding and π-π interactions formation between 4-nitrophenol and the nanocomposite adsorbents during the adsorption.
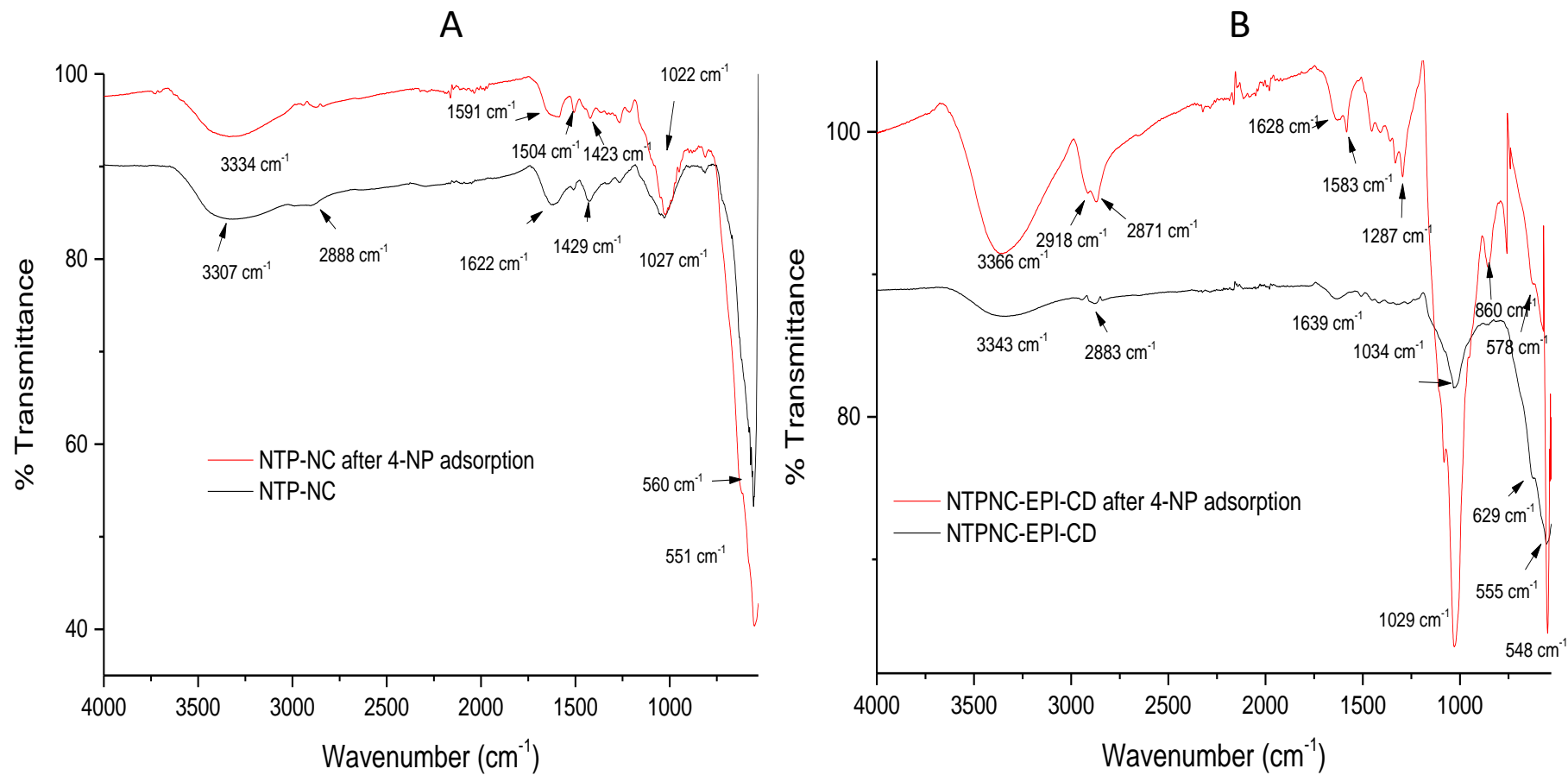
Figure 6.27: FTIR spectra of (a) NTP-NC and (b) NTPNC-EPI-CD, before and after 4-nitrophenol adsorption

Similar observation has been reported by other researchers (Shen et al., 2015; Salgin et al., 2016). On the other hand, the main difference in the FTIR spectra of NTPNC-HMDI-CD before and after 4-nitrophenol adsorption in Fig. 6.27c, are the shift in the region of 3318-3314, 1573-1542, 1024-933, 598-533 cm$^{-1}$ which represented the N-H bond stretching vibrations, the stretching vibration of the C=C in the phenyl ring, the C-O-C vibration and the Fe-O peaks, respectively. The sharp peak at 3318 cm$^{-1}$ due to N-H bond shifted to lower wavenumber and broadened indicating the presence of hydroxyl groups after 4-nitrophenol adsorption. Peaks at 2261, 1691. and 1624 cm$^{-1}$ due to the unreacted isocyanate group (-N=C=O), the C=O vibration and C-O stretching, were observed to disappear after 4-nitrophenol adsorption showing their participation in 4-nitrophenol adsorption. The N-O peak at 1255 cm$^{-1}$ was observed to increase in intensity and shifted to 1232 cm$^{-1}$ due to 4-nitrophenol adsorption (Salgin et al., 2016). The results suggest that 4-nitrophenol interacted with oxygen functions of the NTPNC-HMDI-CD nanocomposite. Oxygen groups like carboxylic and carbonyl groups on the adsorbent surfaces have been shown to enhance adsorption process by delocalizing the aromatic π-cloud of nitrophenols leading to π-hydrogen bonding between electron rich oxygen of the carboxyl and carbonyl groups and the hydrogen atoms of the 4-nitrophenol (Zheng et al., 2017).
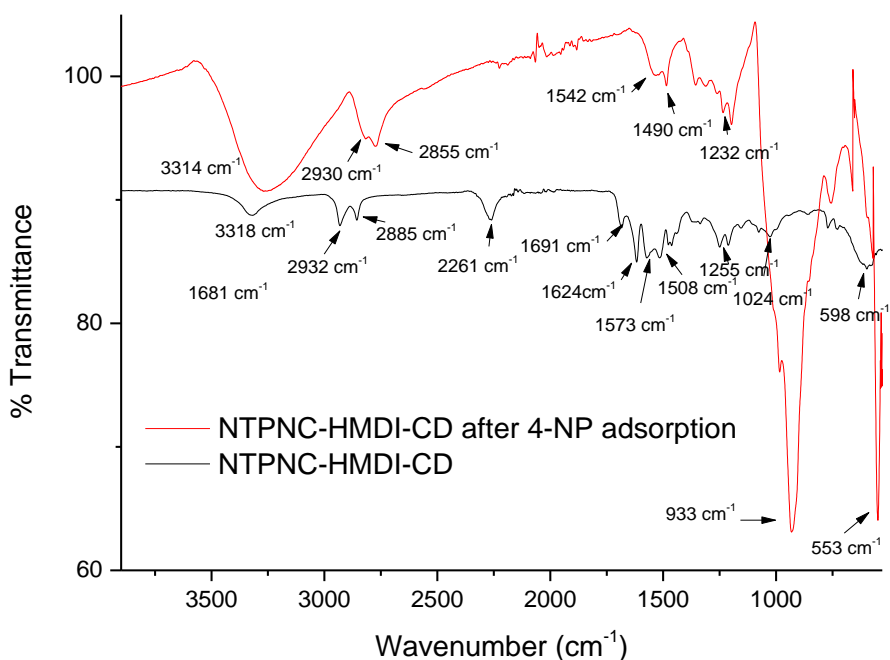


Fig. 6.27: (c) FTIR spectra of NTPNC-HMDI-CD before and after 4-nitrophenol adsorption

Therefore, based on the FTIR analysis above and the effect of solution pH results, the adsorption of 4-nitrophenol mechanism onto NTPNC may be due to hydrogen bonding between weakly acidic Fe-OH groups and the OH of the aromatic ring in the 4-nitrophenol. The mechanism that govern 4-nitrophenol adsorption onto NTPNC-EPI-CD may be hydrogen bonding, inclusion complex due to the presence of cyclodextrin in the nanocomposite and hydrophobic interaction. The adsorption of 4-nitrophenol onto NTPNC-HMDI-CD may be governed by inclusion complex, hydrogen bonding, interaction between $\pi$ electrons that are delocalized on the N-C-O surface structure of the hexamethylene diisocyanate and the $\pi$ electrons of the benzene ring in 4-nitrophenol and hydrophobic interaction. Because, cyclodextrin have electron rich hydrophobic cavities, they have the ability to form inclusion complexes with 4-NP by hydrogen bond formation as illustrated in scheme 6.3 (Zolfaghari, 2016).
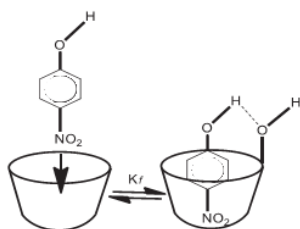


Scheme.6.3: The formation of CD-inclusion complex by CD with 4-Nitrophenol (Zolfaghari, 2016).

## 6.7    EFFECT OF IONIC STRENGTH

The effect of ionic strength on the uptake of 4-NP onto NTPNC, NTPNC-EPI-CD and NTPNC-HMDI-CD was performed using $NaNO_3$ in the concentration range of 0.01 to 0.2 mol/dm$^3$ and the results are shown in Fig.6.28 The results reveal that NTPNC-HMDI-CD had the highest 4-NP adsorption capacity than NTPNC-EPI-CD and NTPNC. For all three samples, 4-NP adsorption capacity reduced slightly with an increase in $NaNO_3$ ionic strength. This may be due to the fact that, when $NaNO_3$ salt was added, the sample solution became more viscous causing difficulty in mass transfer thereby lowering the 4-NP adsorption capacity (Anne et al., 2018). The reduction in interaction between 4-NP and the NTPNC, NTPNC-EPI-CD and NTPNC-HMDI-CD nanocomposite surface occurred on adding the salt, and the competition between $Na^+$ and 4-NP for the active sites was observed. According to Arafat et al. (1999), if phenols adsorbed onto

adsorbents were dissociated anions, $K^+$ in KCl would pair with the negative adsorbates and the ionic repulsion among molecules adsorbed on the surface would be reduced. Therefore, the adsorption capacity would increase with increasing concentration of additional KCl. However, from results in Fig. 6.28, the amount of 4-nitrophenol adsorbed was observed to reduce with an increase in effect of $NaNO_3$ ionic strength, implying that 4-nitrophenols adsorbed onto nanocomposites are molecules not dissociated anions. Similar observations were reported by Al-Ashes et al. 2004. The authors observed a decrease in 4-NP uptake in the presence of NaCl and KCl up to 0.025 M which was due to competition between the salt ions ($Na^+$ and $K^+$) and the adsorbate species for active sites.
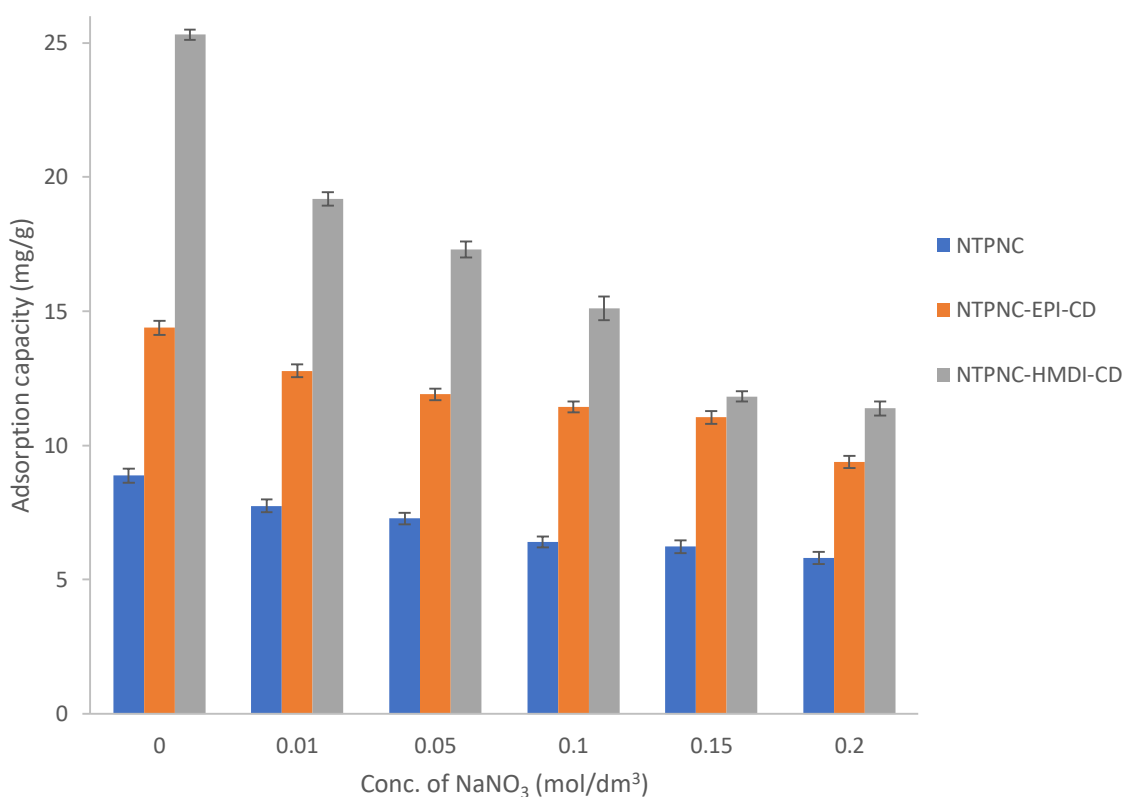


Figure 6.28: Effect of ionic strength for 4-nirophenol uptake onto NTPNC, NTPNC-EPI-CD and NTPNC-HMDI-CD

## 6.8    EFFECT OF COMPETING ANIONS

The influences of coexisting anions such as carbonate, sulphate, phosphate, chloride and nitrate on the 4-NP removal by NTPNC, NTPNC-EPI-CD and NTPNC-HMDI-CD nanocomposites are shown in Fig. 6.29. The results indicated that the presence of carbonate, sulphate, phosphate, chloride, and nitrate had some effect on the 4-NP adsorption. The amount of 4-NP adsorbed reduced from 8.80, 14.38 and 25.3 mg/g for NTPNC, NTPNC-EPI-CD and NTPNC-HMDI-CD, respectively. Phosphate was observed to have affected the 4-NP adsorption more than all other anions followed by chloride, nitrates, sulphates and carbonates. The effect of competing ions as shown in Fig 6. followed the order $CO_3^{2-} > SO_4^{2-} > NO_3^- > Cl^- > PO_4^{3-}$. The $CO_3^{2-}$ and $SO_4^{2-}$ are divalent anions with ionic radius of 178 and 258 pm, respectively while the monovalent electrolytes, $NO_3^-$ and $Cl^-$ have ionic radius of 179 and 167 pm, respectively. $PO_4^{3-}$ is a trivalent anion with ionic radius of 238 pm. The presence of these ions in solution may block active sites of the nanocomposites thus reducing 4-NP adsorption capacity. Results also show that higher valence and bigger ionic hydrated radius of the anions were not beneficial for the adsorption of 4-nitrophenol on all nanocomposite adsorbents. Ahmaruzzaman and Gayatri, 2010 also observed a reduction in p-nitrophenol adsorption capacity in the presence of competing anions when using activated tea waste as potential low cost adsorbent for p-nitrophenol removal.
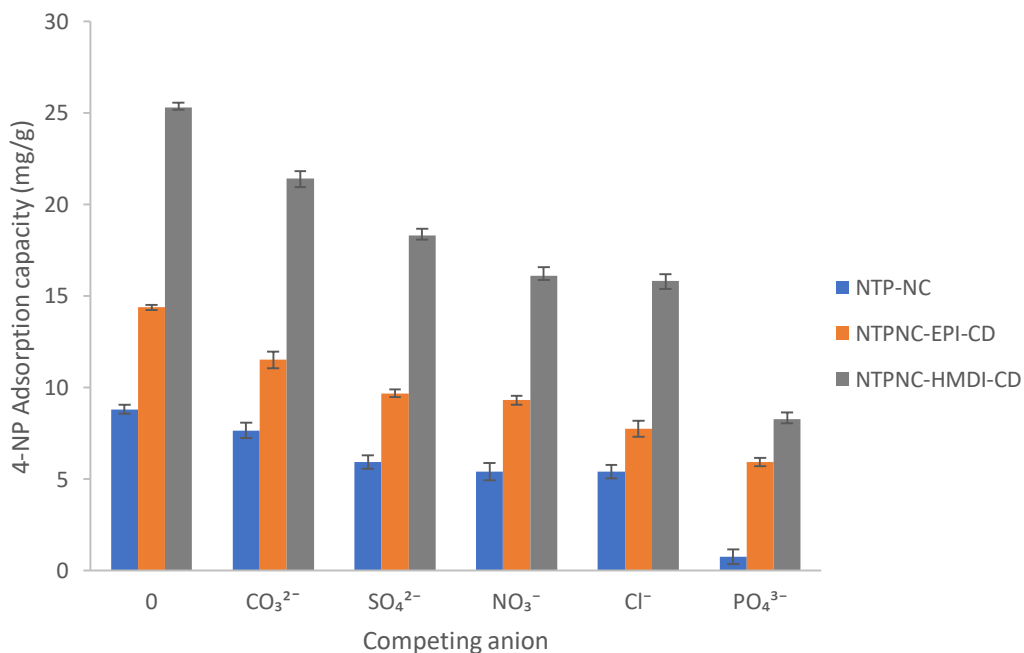


Figure 6.29: Effect of competing anions on 4-NP uptake onto NTPNC, NTPNC-EPI-CD and NTPNC-HMDI-CD nanocomposite

## 6.9 DESORPTION AND REGENERATION STUDIES

Desorption studies were performed to evaluate the possibility of reusability of the synthesized NTPNC, NTPNC-EPI-CD and NTPNC-HMDI-CD as efficient adsorbents. Adsorbent reusability is very important because it can greatly reduce the material cost which is significant for industrial application. Because phenols have shown high solubility in ethanol (Li et al., 2009), 4-NP adsorption-desorption cycle on NTPNC, NTPNC-EPI-CD and NTPNC-HMDI-CD was repeated 5 times using ethanol as the desorbing solvent and the results are shown in Fig.6.30 a and b. It can be observed from Fig.6.30 (a) that ethanol was effective in the desorption process, with the desorption efficiency of 84.69, 91.55 and 95.93 % for NTPNC, NTPNC-EPI-CD and NTPNC-HMDI-CD, respectively. Ethanol has been reported to desorb organic pollutants efficiently from some other cyclodextrin-based adsorbents (Zolfaghari, 2016). The adsorption capacity was observed to reduce gradually from 10.54, 10.00, 9.45, 7.25 and 6.00 mg/g for NTPNC, from 23.76, 22.64, 22.28, 18.20 and 16.25 mg/g for NTPNC-EPI-CD and from 31.56, 29.7, 25.66, 18.60 and 15.24 mg/g NTPNC-HMDI-CD. The reduction in adsorption capacity has been reported to be due to the decrease in active sites of the adsorbent as it is applied several times and the structural damage of surface functional groups on the adsorbent (Mohammadi and Veisi, 2018). The regeneration results, however, show that all adsorbents can be reused for at least three adsorption–desorption cycles without significant loss of its adsorption capacity.
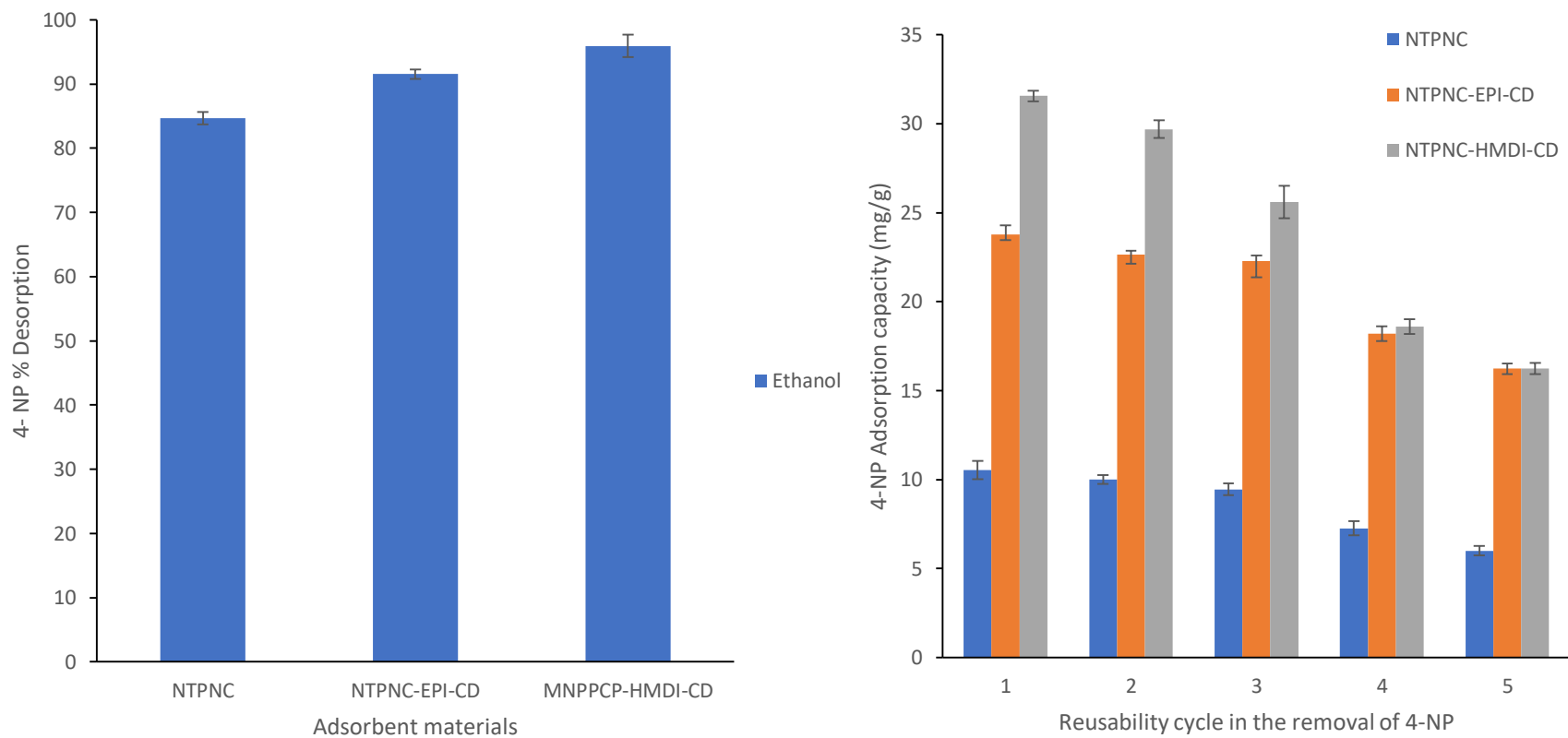
Figure 6.30: (a) Desorption profile and (b) Regeneration of 4-NP onto NTPNC, NTPNC-EPI-CD and NTPNC-HMDI-CD after 5 cycles of adsorption-desorption.

## 6.10  CONCLUSION

This study successfully applied response surface methodology, to optimize working conditions for the cross-linking of magnetite coated pine cone onto beta-cyclodextrin using both epichlorohydrin and 1,6-hexamethylene diisocyanate as cross-linking agents and their ability to remove 4-nitrophenol from aqueous solution was compared. A central composite design was effectively used for the experimental design and the analysis of the results. The optimum values predicted via response surface methodology showed that the NTPNC-EPI-CD and NTPNC-HMDI-CD nanocomposites were capable to remove 15.32 and 24.39 mg/g of 4-nitrophenol, respectively. The adsorption process was dependent on solution pH, adsorbent dose, initial concentration of temperature. The adsorption data were observed to follow pseudo second order kinetic model and the 4-nitrophenol uptake process was found to be controlled by external mass transfer at the earlier stage and by film diffusion at later stage. The proposed mechanism for 4-nitrophenol adsorption may be hydrogen bonding and hydrophobic interaction for NTPNC, hydrogen bonding, inclusion complex and hydrophobic interaction for NTPNC-EPI-CD while hydrogen bonding, hydrophobic interaction, inclusion complex and $\pi$-$\pi$ interaction mechanisms are proposed for 4-nitrophenol onto NTPNC-HMDI-CD nanocomposite. Compared with the magnetite coated pine cone (NTPNC) and the magnetite coated pine cone cross-linked to cyclodextrin using epichlorohydrin (NTPNC-CD-EPI), magnetite coated pine cone cross-linked to cyclodextrin using 1,6-hexamethylene diisocyanate (NTPNC-CD-HMDI) had higher adsorption capacity for the removal of 4-nitrophenol from aqueous solution and was comparable with other adsorbents. Results suggest that NTPNC-EPI-CD and NTPNC-HMDI-CD can be used as a reusable absorbent for easy, convenient, and efficient removal of 4-nitrophenol from aqueous solution.

## 6.11  REFERENCE

AL-ASHEH, S., BANAT, F. & MASAD, A. (2004). Kinetics and equilibrium sorption studies of 4-nitrophenol on pyrolyzed and activated oil shale residue. *Environmental Geology,* 45,1109-1117.

ABDOLMALEKI, A., MALLAKPOUR, S. & BORANDEH, S. 2015. Efficient heavy metal ion removal by triazinyl-bcyclodextrin functionalized iron nanoparticles. *RSC Advances,* 5**,** 90602-90608.

ACISLI, O., KHATAEE, A., KARACA, S., KARIMI, A. & DOGAN, E. 2017. Combination of ultrasonic and fenton processes in the presence of magnetite nanostructures prepared by high energy planetary ball mill *Ultrason Sonochemistry,* 34**,** 754-762.

AHMARUZZAMAN, M. 2008. Adsorption of phenolic compounds on low-cost adsorbents: a review *Advances in Colloid and Interface Science,* 143**,** 48-67.

AJOUYED, O., HUREL, C., AMMARI, M., ALLAL, L. B. & MARMIER, N. 2010. Sorption of Cr(VI) onto natural iron and aluminium (oxy)hydroxides: Effects of pH, ionic strength and initial concentration. *Journal of Hazardous Material,* 174**,** 616-622.

AL-AHMARI , S. D., WATSON, K., FONG, B. N., RUYONGA, R. M. & ALI, H. 2018. Adsorption kinetics of 4-n-nonylphenol on hematite and goethite. *Journal of Environmental Chemical Engineering,* 6**,** 4030-4036.

ALABA, P. A., OLADOJA, N. A., SANI, Y. M., AYODELE, O. B., MOHAMMED, I. Y., OLUPINLA, S. F. & DAUD, W. M. W. 2018. Insight into wastewater decontamination using polymeric adsorbents. *Journal of Environmental Chemical Engineering,* 6**,** 1651-1672.

ALTUNDOGAN, H. S., ALTUNDOGAN, S., TUMEN, F. & BILDIK, M. 2002. Arsenic adsorption from aqueous solutions by activated red mud. *Waste management,* 22**,** 357-363.

ÁLVAREZ-AYUSO, E., GARCÍA-SÁNCHEZ, A. & QUEROL, X. 2007. Adsorption of Cr(VI) from synthetic solutions and electroplating wastewaters on amorphous aluminium oxide. *Journal of Hazardous Material,* 142**,** 191-198.

ANASTOPOULOS, I., KARAMESOUTI, M., MITROPOULOS, A. C. & KYZAS, G. Z. 2017. A review for coffee adsorbents. *Journal of Molecular Liquids,* 229**,** 555-565.

ANASTOPOULOS, I., MASSAS, I. & EHALIOTIS, C. 2013. Composting improves biosorption of,$Pb^{2+}$ and $Ni^{2+}$ by renewable lignocellulosic materials. Characteristics and mechanisms involved. *Chemical Engineering Journal,* 231**,** 245-254.

ANNE, J. M., BOON, Y. H., SAAD, B., MISKAM, M., YUSOFF, M. M., SHAHRIMAN, M. S., ZAIN, N. N. M., LIM, V. & RAOOV, M. 2018. b-Cyclodextrin conjugated bifunctional isocyanate linker polymer for enhanced removal of 2,4-dinitrophenol from environmental waters. . *Royal Society Open Science,* 5**,** 180942.

ANSARI, M. I., MASOOD, F. & MALIK, A. 2011. Bacterial biosorption: a technique for remediation of heavy metals in microbes and microbial technology, in: I. Ahmad, F. Ahmad, J. Pichtel (Eds.). *Agricultural Environmental Applications.*

APHESTEGUY, J. C., KURLYANDSKAYA, G. V., DE CELIS, J. P., SAFRONOV, A. P. & SCHEGOLEVA, N. N. 2015. Magnetite nanoparticles prepared by co-precipitation method in different conditions, Materials Chemistry and Physics. *Materials Chemistry and Physics,* 161**,** 243-249.

ARIEF, V. O., TRILESTARI, K., SUNARSO, J., INDRASWATI, N. & ISMADJI, S. 2008. Recent progress on biosorption of heavy metals from liquids using low cost

biosorbents: characterization, biosorption parameters and mechanism studies, . *Clean Soil Air Water* 36**,** 937-962.

ARYAL, M., ZIAGOVA, M. & LIAKOPOULOU-KYRIAKIDES, M. 2010. Study on arsenic biosorption using Fe(III)-treated biomass of Staphylococcus xylosus. *chemical Engineering Journal,* 162**,** 178-185.

BABEL, S. & KURNIAWAN, T. A. 2003. Low-cost adsorbents for heavy metals uptake from contaminated water: a review. *Journal of Hazardous Material,* 97**,** 219-243.

BADRUDDOZA, A. Z. M., HAZEL, G. S. S., HIDAJAT, K. & UDDIN, M. S. 2010. Synthesis of carboxymethyl- -cyclodextrin conjugated magnetic nano-adsorbent for removal of methylene blue. *Colloids and Surfaces A: Physicochem. Eng. Aspects* 367**,** 85–95.

BADRUDDOZA, A. Z. M., TAY, A. S. H., TAN, P. Y., HIDAJAT, K. & UDDIN, M. S. 2011. Carboxymethyl- -cyclodextrin conjugated magnetic nanoparticles as nano-adsorbents for removal of copper ions: synthesis and adsorption studies. *Journal of Hazardous Material,* 185**,** 1177-1186.

BAIER, J., KOETZ, J., KOSMELLA, S., TIERSCH, B. & REHAGE, H. 2007. Polyelectrolyte-Modified Inverse Microemulsions and Their Use as Templates for the Formation of Magnetite Nanoparticles. *Journal of Physical Chemistry,* 111**,** 8612-1816.

BAILEY, S. E., OLIN, T. J., BRICKA, R. M. & ADRIAN, D. D. 1999. A review of potentially low-cost sorbents for heavy metals, . *Water Research,* 33**,** 2469-2479.

BANERJEE, S. & CHATTOPADHYAYA, M. 2017. Adsorption characteristics for the removal of a toxic dye, tartrazine from aqueous solutions by a low cost agricultural by-product. *Arabian Journal of Chemistry,* 10**,** S1629-S1638.

BANERJEE, S. S. & CHEN, D. H. 2007. Fast removal of copper ions by gum arabic modified magnetic nano-adsorbent, . *Journal of Hazardous Material,* 147**,** 174-179.

BANERJEE SS, J. M. & RV, J. 2004. *Separation and Purification Technology,* 39**,** 1611-.

BARBU, M., STOIA, M., STEFANESCU, O. & STEFANESCU, M. 2010. Thermal and FT-IR studies on the interaction between Cr(NO3)3.9H2O and some diols. *Chem. Bull. "Polltehnica" Uni. (Timisoara),* 55**,** 180-185.

BASSO, M. C., CERRELLA, E. G. & CUKIERMAN, A. L. 2002. Lignocellulosic materials as potential biosorbents of trace toxic metals from wastewater. *chemical resources,* 41**,** 3580-3585.

BASU, A., MUSTAFIZ, S., ISLAM, M. R., BJORNDALEN, N., RAHAMAN, M. S. & CHAALAL, O. 2006. A Comprehensive Approach for Modelling Sorption of Lead and Cobalt Ions through Fish Scales as an Adsorbent. *Chemical Engineering Communications,* 193**,** 580-605.

BENYOUCEF, S. & AMRANI, M. 2011. Adsorption of Phosphate Ions Onto Low Cost Aleppo Pine Adsorbent. *Desalination,* 275**,** 231-236.

BHATNAGARA, A. & SILLANPÄÄ, M. 2011. A review of emerging adsorbents for nitrate removal from water. *chemical Engineering Journal***,** 493-504.

BISHT, R., AGARWAL, M. & SINGH, K. 2016. Heavy metal removal from wastewater using various adsorbents: a review. *Journal of water Reuse and Desalination,* 7**,** 387-419.

BOYD, G. E., ADAMSON, A. W. & MYERS JR, L. S. 1947. The exchange adsorption of ions from aqeuous solutions by organic zeolites. II. Kinetics. *Jornal of the American Society,* 69**,** 2836-2848.

BRAIBANTI, A., PISICARO, E., GHIOZZI, A., COMPARI, C. & BOVIS, G. 1998. Host-guest interactions between β-cyclodextrin and piroxicam. *Reactive and Functional Polymers,* 36**,** 251-255.

BREZONIK, P. L. & ARNOLD, W. A. 2012. Water chemistry: Fifty years of change and progress. *Environmental Science and Technology,* 46**,** 5650-5657.

BRIJMOHAN, S. B. & SHAW, M. T. 2007. Magnetic ion-exchange nanoparticles and their application in proton exchange membranes. *Journal of Membrane Science,* 303**,** 64-71.

BURTON, E. D., BUSH, R. T., JOHNSTON, S. G., WATLING, K. M., HOCKING, R. K., SULLIVAN, L. A. & PARKER, G. K. 2009. Sorption of arsenic (V) and arsenic (III) to schwertmannite. *Environmental Science & Technology,* 43**,** 9202-9207.

CAO, F., YIN, P., LIU, X., LIU, C. & QU, R. 2014. Mercury adsorption from fuel ethanol onto phosphonated silica gel prepared by heterogeneous method. *Renewable Energy***,** 61-68.

CHAN, Y. J., CHONG, M. F., LAW, C. L. & HASSELL, D. G. 2009. A review on anaerobic-aerobic treatment of industrial and municipal wastewater. *Chemical Engineering Journal,* 155**,** 1-18.

CHANDRA, V., PARK, J., CHUN, Y., LEE, J. W., HWANG, I. C. & KIM, K. S. 2010. Water-Dispersible Magnetite-Reduced Graphene Oxide Composites for Arsenic Removal. *American Chemical Society Nanotechnology,* 4**,** 3979-3986.

CHANG, Y. C. & CHEN, D. H. 2005. Preparation and adsorption properties of monodisperse chitosan-bound $Fe_3O_4$ magnetic nanoparticles for the removal of Cu(II) ions,. *Journal of colloid Interface Science,* 283**,** 446-451.

CHEN, C. Y., YANG, C. Y. & CHEN, A. H. 2011. Biosorption of Cu(II), Zn(II), Ni(II) and Pb(II) ions by cross-linked metal-imprinted chitosans with epichlorohydrin. *Journal of Environmental Management,* 92**,** 796-802.

CHEN, J., WANG, Y. G., LI, Z. Q., WANG, C., LI, J. F. & GU, Y. J. Synthesis and characterization of magnetic nanocomposites with $Fe_3O_4$ core.  Journal of Physics: Conference Series, 2009. IOP Publishing, 012-041.

CHENG, W., DING, C., WANG, X., WU, Z., SUN, Y., YU, S., HAYAT, T. & WANG, X. 2016a. Competitive sorption of As(V) and Cr(VI) on carbonaceous nanofibers. *Chemical Engineering Journal,,* 293**,** 311-318.

CHENG, W., ZHANG, W., HU, L., DING, W., WU, F. & LI, J. 2016b. Etching synthesis of iron oxide nanoparticles for adsorption of arsenic from water. *RSC Advances,* 6**,** 15900-15910.

CHIBBAN, M., ZERBET, M., CARJA, G. & SINAN, F. 2012. Application of low cost adsorbents for Arsenic removal-A review. *Journal of Environmental Chemistry and Ecotoxicology,* 4**,** 91-102.

CHOUBEY, S. 2018. Kinetics and equilibrium study of 2-nitrophenol adsorption onto polyurethane cross-linked pine cone biomass. *Journal of Cleaner Production* 179**,** 191-209.

CIFUENTES, T., CAYUPI, J., CELIS-BARROS, C., ZAPATA-TORRES, G., BALLESTEROS, R. & BALLESTEROSGARRIDO, R. 2016. Spectroscopic studies of the interaction of 3-(2-thienyl)-[1,2,3]triazolo[1,5-a]pyridine with 2,6-dimethyl-beta-cyclodextrin and ctDNA. *Organic & Biomolecular Chemistry,* 14**,** 9760-9767.

COSIC, I. 1994. Macromolecular bioactivity: is it resonant interaction between macromolecules? - Theory and application. *IEEE Transactions On Biomedical Engineering,* 41**,** 1101-1114.

CRANK, J. 1975. Diffusion in a cylinder. *The Mathematics of Diffusion***,** 69-88.

CRINI, G. 2005a. Recent developments in polysaccharide-based materials used as adsorbents in wastewater treatment. *Progress in Polymer Science,* 30**,** 38-70.

CRINI, G. 2005b. Recent developments in polysaccharide-based materials used as adsorbents in wastewater treatment. *Progress in Polymer Science,* 30**,** 38-70.

CRINI, G. 2006. Non-conventional low-cost adsorbents for dye removal: a review. *Bioresource Technology,* 97**,** 1061-1085.

CUSHING, B. L., KOLESNICHHENKO, V. L. & O'CONNOR, C. J. 2004. Recent advances in the liquid phase synthesis of inorganic nanoparticles. *Chemical Reviews,* 104**,** 3893-3946.

DAI, J., REN, F., TAO, C. & 2012. Adsorption of Cr(VI) and speciation of Cr(VI) and Cr(III) in aqueous solutions using chemically modified chitosan, . *Internation Journal of Environmental Research and Public Health,* 9**,** 1757-1770.

DANESHFOZOUN, S., ABDULLAH, M. A. & ABDULLAH, B. 2017. Preparation and characterization of magnetic biosorbent based on oil palm empty fruit bunch fibers, cellulose and Ceiba pentandra for heavy metal ions removal. *Industrial Crops & Products,* 105**,** 93-103.

DAOU, T. J., POURROY, G., COLIN, S. B., GRENECHE, J. M., BOUILLET, C. U., LEGARE, P., BERNHARDT, P., LEUVREY, C. & ROGEZ, G. 2006. Hydrothermal Synthesis of Monodisperse Magnetite Nanoparticles. *Chemistry of materials,* 18**,** 4399-4404.

DAWOOD, S. & SEN, T. K. 2012. Removal of anionic dye Congo red from aqueous solution by raw pine and acid-treated pine cone powder as adsorbent: Equilibrium, thermodynamic, kinetics, mechanism and process design. *Water research* 46**,** 1933-1946.

DELVAL, F., CRINI, G., MORIN, N. O., VEBREL, J., BERTINI, S. & TORRI, G. 2002. The sorption of several types of dye on crosslinked polysaccharides derivatives. *Dyes and Pigments* 53**,** 79-92.

DEMIRAL, H., DEMIRAL, I., TUMSEK, F. & KARABACAKOGLU, B. 2008. Adsorption of chromium (VI) from aqueous solution by activated carbon derived from olive bagasse and applicability of different adsorption models, . *Chemical Engineering Journal,* 144**,** 188-196.

DEMIRBAS, E. 2008. Heavy metal adsorption onto agro-based waste materials: A review. *Journal of Hazardous Materials* 157**,** 220-229.

DODZIUK, H. 2006. Cyclodextrins and Their Complexes. *Ed.; Wiley-VCH: Weinheim.*

DONG, X., MA, L. Q. & LI, Y. 2011. Characteristics and mechanisms of hexavalent chromium removal by biochar from sugar beet tailing. *J Hazard Mater,* 190**,** 909-915.

DURANOĞLU, D., TROCHIMCZUK, A. W. & BEKER, U. 2012. Kinetics and thermodynamics of hexavalent chromium adsorption onto activated carbon derived from acrylonitrile-divinylbenzene copolymer. *Chemical Engineering Journal* 187**,** 193-202.

EL-KAMASH, A. M., ZAKI, A. A. & ABED EL GELEEL, M. A. 2005. Modeling batch kinetics and thermodynamics of zinc and cadmium ions removal from waste solutions using synthetic zeolite. *Journal of Hazardous Material,* B127**,** 211-220.

EL-SAID, A. G., BADAWAY, N. A., ABDEL-AAL, A. & GARAMAN, S. E. 2011. Optimization parameters for adsorption and desorption of Zn(II) and Se(IV) using rice husk:kinetic and equilibrium. *Ionics* 17**,** 263-270.

ESMERALDO, M. A., BARRETO, A. C. H., FREITAS, J. E. B., FECHINE, P. B. A., SOMBRA, A. S. B., CORRADINI, E., MELE, G., MAFFEZZOLI, A. & MAZZETTO, S. E. 2010. Dwarf-green coconut fibers: a versatile natural renewable raw bioresource. Treatment, morphology, and physicochemical properties. *BioResources,* 5**,** 2478-2501.

FAN, J., GUO, Y., WANG, J. & FAN, M. 2009. Rapid decolonization of azo dye methyl orange in aqueous solution by nanoscale zerovalent iron. *Journal of Hazardous Material,* 166**,** 904-910.

FATHY, N. A., EL-WAKEEL, S. T. & EL-LATIF, R. R. A. 2015. Biosorption and desorption studies on chromium (VI) by novel biosorbents of raw rutin and rutin resin. *Journal of Environmental Chemical Engineering,* 3**,** 1137-1145.

FENG, L., CAO, M., MA, X., ZHU, Y. & HU, C. 2012. Superparamagnetic high-surface-area $Fe_3O_4$ nanoparticles as adsorbents for arsenic removal. *Journal of Hazardous Material,* 227-228**,** 439-446.

FENG, N., GUO , X., LIANG, S., ZHU, Y. & LIU, J. 2011. Biosorption of heavy metals from aqueous solutions by chemically modified orange peel. *Journal of Hazardous Material,* 185**,** 49-54.

FENG, Q., LIN, Q., GONG, F., SUGITA, S. & SHOYA, M. J. 2004. *Journal of colloid Interface Science,* 278**,** 1.

FERNÁNDEZ, M., VILLALONGA, M. L., FRAGOSO, A., CAOB, B. N., M & VILLALONGA, R. 2004. α-Chymotrypsin stabilization by chemical conjugation with O-carboxymethyl- poly-cyclodextrin. *Process Biochemistry,* 39**,** 535-539.

FOMINA, M. & GADD, G. M. 2014. Biosorption: Current perspective on concept, definition and application. . *Bioresource Technology,* 160**,** 3-14.

GAFUROV, T. G., PILOSOV, M., ADYLOV, A., MANNANOVA, D., SUVOROVA, V., TASHPULATOV, G. V. & USMANOV, V. 1970. The reaction of cellulose with hexamethylene diisocyanate *Vysokomol soyed,* A12**,** 2515-2519.

GALLEGO, R., ARTEAGA, J. F., VALENCIA, C. & FRANCO, J. M. 2013a. Chemical modification of methyl cellulose with HMDI to modulate the thickening properties in castor oil. *Cellulose,* 21**,** 495-507.

GALLEGO, R., ARTEAGA, J. F., VALENCIA, C. & FRANCO, J. M. 2013b. Isocyanate-Functionalized Chitin and Chitosan as Gelling Agents of Castor Oil**.** *Molecules* 18**,** 6532-6549.

GARCIA-RIO, L., MEJUTO, J. C., RODRIGUEZ-DAFONTE, P. & HALL, R. W. 2010. The role of water release from the cyclodextrin cavity in the complexation of benzoyl chlorides by dimethyl-beta-cyclodextrin. *Tetrahedron,* 66**,** 2529-2537.

GENG, B. Y., MA, J. Z. & YOU, J. H. 2008. Controllable synthesis of single-crystalline Fe3O4 polyhedra possessing the active basal facets,. *Crystal Growth and Design,* 8**,** 1443-1447.

GHANBARI, D. S.-N., MASOUD GHASEMI-KOOCH, MAJID 2014. A sonochemical method for synthesis of Fe3O4 nanoparticles and thermal stable PVA-based magnetic nanocomposite. *Journal of Industrial and Engineering Chemistry,* 20**,** 3970-3974.

GHEJU, M., BALCU, I. & VANCEA, C. 2016. An investigation of Cr(VI) removal with metallic iron in the co-presence of sand and/or MnO2. . *Journal of Environmental Management,* 170**,** 145-151.

GHOSH, R., PRADHAN, L., DEVI, Y. P., MEENA, S. S., TEWARI, R. K. & UMAR, A. 2011. Induction heating studies of Fe3O4 magnetic nanoparticles capped with oleic acid and polyethylene glycol for hyperthermia. *Journal of Material Chemistry,* 21**,** 13388-13398.

GOLDBERG, S. & JOHNSTON, C. T. 2001. Mechanisms of arsenic adsorption on amorphous oxides evaluated using macroscopic measurements, vibrational spectroscopy, and surface complexation modeling. *Journal of  Colloid and Interface Science,* 234**,** 204-216.

GONG, J., CHEN, L., ZENG, G., LONG, F., DENG, J., NIU, Q. & HE, X. 2012. Shellac-coated iron oxide nanoparticles for the removal of cadmium(II) ions from aqueous solution. *Journal of environmental Sciences,* 24**,** 1165-1173.

GOYA, G., BERQUO, T., FONSECA, F. & MORALES, M. 2003. Static and dynamic magnetic properties of spherical magnetite nanoparticles. *Journal of Applied Physics,* 94**,** 3520-3528.

GRASSI, M., KAYKIOGLU, G., BELGIORNO, V. & LOFRANO, G. 2012. Removal of emerging contaminants from water and wastewater by adsorption process. In: Lofrano, G. (Ed.), Emerging Compounds Removal from Wastewater,. *Springer Briefs in Green Chemistry for Sustainability.*

GUPTA, A., VIDYARTHI, S. R. & SANKARARAMAKRISHNAN, N. 2015a. Concurrent removal of As(III) and As(V) using green low cost functionalized biosorbent – Saccharum officinarum bagasse. . *Journal of Environmental Chemical Engineering,* 3**,** 113-121.

GUPTA, S. & BABU, B. V. 2009. Removal of toxic metal Cr(VI) from aqueous solutions using sawdust as adsorbent: equilibrium, kinetics and regeneration studies. *Chemical Engineering Journal,* 150**,** 352-365.

GUPTA, V. & NAYAK, A. 2012a. Cadmium removal and recovery from aqueous solutions by novel adsorbents prepared from orange peel and Fe2O3 nanoparticles. *Chemical Engineering Journal,* 180**,** 81-90.

GUPTA, V. K., CARROTT, P. J. M., RIBEIRO CARROTT, M. M. M. & SUHAS 2009. Low cost adsorbents: growing approach to wastewater treatment - a review. *Critical Reviews in Environmental Science and Technology,* 39**,** 783-842.

GUPTA, V. K., MORADI, O., TYAGI, I., AGARWAL, S., SADEGH, H., GHOSHEKANDI, R. S., MAKHLOUF, A. S. H., GOODARZI, M. & GARSHASBI, A. 2015b. Study on the removal of heavy metal ions from industry waste by carbon nanotubes: effect of the surface modification: a review,. *Critical Reviews in Environmental Science and Technology.*

GUPTA, V. K. & NAYAK, A. 2012b. Cadmium removal and recovery from aqueous solutions by novel adsorbents prepared from orange peel and $Fe_2O_3$ nanoparticles. *Chemical Engineering Journal,* 180**,** 81-90.

GUPTA, V. K. & SUHA, S. 2009. Application of low-cost adsorbents for dye removal - a review. *Journal of Environmental Management,* 90**,** 2313-2342.

HASAN, S., SINGH, K., PRAKASH, O., TALAT, M. & HO, Y. 2008. Removal of Cr (VI) from aqueous solutions using agricultural waste 'maize bran'. *Journal of Hazardous Materials,* 152**,** 356-365.

HASHEM, A., AKASHA, R. A., GHITH, A. & HUSSEIN, D. A. 2007. Adsorbent based on agricultural wastes for heavy metal and dye removal: A Review,. *Energy Education Science and Technology,* 19**,** 69-86.

HE, R., PENG, Z., LYU, H., HUANG, H., NAN, Q. & TANG, J. 2018. Synthesis and characterization of an iron-impregnated biochar for aqueous arsenic removal. *Science of the Total Environment,* 612**,** 1177-1186.

HO, Y.-S. 1995. *Absorption of heavy metals from waste streams by peat.* University of Birmingham.

HO, Y. S. & MCKAY, G. 1998. Kinetic models for the sorption of dye from aqueous solution by wood. *Process Safety and Environmental Protection,* 76 B**,** 183-191.

HO, Y. S. & MCKAY, G. 2000. The kinetics of sorption of divalent metal ions onto sphagnum moss peat. *Water Research,* 34**,** 735-742.

HO, Y. S. & OFOMAJA, A. E. 2005. Effects of calcium competition on lead sorption by palm kernel fibre. *J Hazard Mater,* 120**,** 157-62.

HO, Y. S. & OFOMAJA, A. E. 2006. Pseudo-second-order model for lead ion sorption from aqueous solutions onto palm kernel fiber. *J Hazard Mater,* 129**,** 137-42.

HOSSEINPOUR, V., KAZEMEINI, M. & MOHAMMADREZAEE, A. 2011. Optimization of Ru-promoted Ir-catalysed methanol carbonylation utilising response surface methodology. *Applied Catalysis A: General,* 394**,** 166-175.

HU, F. X., NEOH, K. G. & KANG, E. T. 2006. Synthesis and in vitro anti-cancer evaluation of tamoxifen-loaded magnetite/PLLA composite nanoparticles. *Biomaterials,* 27**,** 5725-5733.

HU, J., CHEN, G. & LO, I. M. C. 2005. Removal and recovery of Cr(VI) from wastewater by maghaemite nanoparticles. *Water Research,* 39**,** 4528-4536.

HU, Q., LIU, Y., GU, X. & ZHAO, Y. 2017. Adsorption behaviour and mechanism of different arsenic species on mesoporous MnFe2O4 magnetic nanoparticles. *Chemosphere,* 181**,** 328-336.

HU, Z., LEI, L., YIJIU, L. I. & NI, Y. 2003. Chromium adsorption on high performance activated carbons from aqueous solution. *Separation and Purification Technology,* 31**,** 13-18.

HUANG, S. H. & CHEN, D. H. 2009. Rapid removal of heavy metal cations and anions from aqueous solutions by an amino-functionalized magnetic nano-adsorbent. *Journal of Hazardous Material,* 163**,** 174-179.

HUANG, Z., ZHANG, B. & FANG, G. 2013. Adsorption behavior of Cr(VI) from aqueous solutions by microwave modified porous larch tannin resin. *Bioresources,* 8**,** 4593-4609.

HUBER, D. L. 2005. Synthesis, properties and application of iron nanoparticles. *small,* 1**,** 482-501.

HUO, J. B., XU, L., YANG, J. C. E., CUI, H. J., YUAN, B. & FU, M. L. 2018. Magnetic responsive Fe3O4-ZIF-8 core-shell composite for efficient removal of As(III) from water. *Colloids and Surfaces A,* 539**,** 59-68.

HUQ, R. & MERCIER, L. 2001. Incorporation of cyclodextrin into mesostructured silica. *Chemistry of Material,* 13**,** 4512-4519.

IHSANULLAH, A. A., AL-AMER, A. M., LAOUI, T., AL-MARRI, M. J., NASSER, M. S. & ATIEH, M. A. 2016. Heavy metal removal from aqueous solution by advanced carbon nanotubes: Critical review on adsorption applications. *Separation and Purification Technology,* 157**,** 141-161.

ISAH, A. U., GIWA, A., SALISU, B., SALLAHUDEEN, M. & MUSTAPHA, A. 2015. Kinetics, equilibrium and thermodynamics studies of C.I. Reactive Blue 19 dye adsorption on coconut shell based activated carbon. *International Biodeterioration & Biodegradation,* 102**,** 262-273.

IZATT, R. M., BRADSHAW, J.S., BRUENING, R.L. AND BRUENING, M.L 1994. Solid phase extraction of ions of analytical interest using molecular recognition technology. *Am Lab,* 26**,** 28-38.

JANG, J. H. & LIM, H. B. 2010. Characterization and analytical application of surface modified magnetic nanoparticles. *Microchemical Journal,* 94**,** 148-158.

JARAMILLO, J., ALVAREZ, P. M. & GOMEZ-SERRANO, V. 2010. Oxidation of activated carbon by dry and wet methods: Surface chemistry and textural modifications. *Fuel Processing Technology,* 91**,** 1768-1775.

JIANG, C., LIU, R., SHEN, X., ZHU, L. & SONG, F. 2011. Ni0.5Zn0.5Fe2O4 nanoparticles and their magnetic properties and adsorption of bovine serum albumin,. *Powder Technology,* 211**,** 90-94.

JIMÉNEZ-CEDILLO, M. J., OLGUÍN, M. T., FALL, C. H. & COLÍN, A. 2011. Adsorption capacity of iron- or iron–manganese-modified zeolite-rich tuffs for As(III) and As(V) water pollutants. *Applied Clay Science,* 54**,** 206-216.

JIN, X., YU , B., CHEN, Z., AROCENA, J. M. & THRING, R. W. 2014. Adsorption of Orange II dyein aqueous solution onto surfactant-coated zeolite: characterization, kineticand thermodynamic studies. *Journal of colloid Interface Science*, 15-20.

KAMINS, T. 1998. Polycrystalline Silicon for Integrated Circuits and Displays.-Kluwer Academic Publishers.

KARTHICK, K., NAMASIVAYAM, C. & PRAGASAN, L. A. 2017. Removal of Direct Red 12B from aqueous medium by ZnCl 2 activated Jatropha husk carbon: Adsorption dynamics and equilibrium studies.

KASIRI, M. B. & KHATAEE, A. R. 2012. Removal of organic dye by UV/$H_2O_2$ process: modelling and optimization. *Environmental Technology,* 33, 1417-1425.

KIM, D., ZHANG, Y., VOIT, W., RAO, K. & MUHAMMED, M. 2001. Synthesis and characterization of surfactant-coated superparamagnetic monodispersed iron oxide nanoparticles. *Journal of Magnetism and Magnetic Materials,* 225, 30-36.

KONG, S., WANG, Y., ZHAN, H., LIU, M., LIANG, L. & HU, Q. 2014. Competitive adsorption ofhumic acid and arsenate on nanoscale iron-manganese binary oxide-loadedzeolite in groundwater. *Journal of Geochemical Exploration,* 87, 220-225.

KRATOCHVIL, D., PIMENTEL, P. & VOLESKY, B. 1998. Removal of trivalent and hexavalent chromium by seaweed biosorbent. *Environmental Science & Technology,* 32, 2693-2698.

KULSHRESHTHA, S. N. 1998. A global outlook for water resources to the year 2025. *Water Resources Management,* 12, 167-184.

KUMAR, P. S., RAMALINGAM, S., DINESH KIRUPHA, S., MURUGESAN, A., VIDHYADEVI, T. & SIVANESAN, S. 2011. Adsorption behavior of nickel(II) onto cashew nut shell: Equilibrium, thermodynamics, kinetics, mechanism and process design. *Chemical Engineering Journal,* 167, 122-131.

KUMARI, P. & PARASHARA, S. H. 2018. β-cyclodextrin modified magnetite nanoparticles for efficient removal of eosin and phloxine dyes from aqueous solution. *Materials Today: Proceedings,* 5, 15473-15480.

KUPETA, A. J. K., NAIDOO, E. B. & OFOMAJA, A. E. 2018. Kinetics and equilibrium study of 2-nitrophenol adsorption onto polyurethane cross-linked pine cone biomass. *Journal of Cleaner Production* 179, 191-209.

KURNIAWAN, T. A. & BABEL, S. 2003. A research study on Cr(VI) removal from contaminated wastewater using low-cost adsorbents and commercial activated carbon. In: Second Int. Conf. on Energy Technology towards a Clean Environment (RCETE). *Thailand,* 2, 1110-1117.

LAGERGREN, S. 1898. Zur theorie der sogenannten adsorption gelöster stoffe, Kungliga SvenskaVetenskapsakademiens. *Handlingar,* 24, 1-39.

LASZLO, K., PODKOSCIELNY, P. & DABROWSKI, A. 2003. Heterogeneity of Polymer-Based Active Carbons in Adsorption of Aqueous Solutions of Phenol and 2,3,4-Trichlorophenol. *Langmuir,* 19, 5287-5294.

LAURENT, S., FORGE, D., PORT, M., ROCH, A., ROBIC, C., L, V. E. & MULLER, R. N. 2008. Magnetic iron oxide nanoparticles: Synthesis, stabilization, vectorization, physicochemical characterizations and biological applications. *Chemical Rewiews,* 108, 2064-2110.

LEE, M. H., YOON, K. J. & KO, S. W. 2001. Synthesis of a vinyl monomer containing β-cyclodextrin and grafting onto cotton. *Journal of Applied Polymer and Science,* 80, 438-446.

LEONE, V. O., PEREIRA, M. C., AQUINO, S. F., OLIVEIRA, L. C. A., CORREA, S., RAMALHO, T. C., GURGEL, L. V. A. & SILVA, A. C. 2018. Adsorption of

diclofenac on a magnetic adsorbent based on maghemite: experimental and theoretical studies. *New Journal of Chemistry,* 42**,** 437-449.

LEUNG, W. C., WONG, M. F., CHUA, H., LO, W. & LEUNG, C. K. 2000. Removal and recovery of heavy metals by bacteria isolated from activated sludge treating industrial effluents and municipal wastewater. *Water Science and Technology* 41**,** 233-240.

LI, J., CHEN, B., WANG, X. & GOH, S. H. 2004. Preparation and characterization of inclusion complexes formed by biodegradebale poly ( -caprolactone)–poly(tetrahydrofuran)– poly( -caprolactone) triblock copolymer and cyclodextrins. *Polymers,* 45**,** 1777-1785.

LI, J., GYOTEN, H., SONODA, A., FENG, Q. & XUE, M. 2017. Removal of trace arsenic to below drinking water standards using a Mn–Fe binary oxide. *Rsc Advances,* 7**,** 1490-1497.

LI, J. M., MENG, X. G., HU, C. W. & DU, J. 2009. Adsorption of phenol, p-chlorophenol and p-nitrophenol onto functional chitosan. *Bioresource Technology* 100**,** 1168-1173.

LI, W. G., GONG, X. J., WANG, K., ZHANG, X. R. & FAN, W. B. 2014. Adsorption characteristics of arsenic from micro-polluted water by an innovative coal-based mesoporous activated carbon. *Bioresource Technology***,** 166-173.

LIDA, H., TAKAYANAGI, K., NAKANISHI, T. & OSAKA, T. 2007. Synthesis of Fe3O4 nanoparticles with various sizes and magnetic properties by controlled hydrolysis. *Journal of Colloid and Interface Science* 314**,** 274-280.

LIEN, H.-L. & ZHANG, W.-X. 2007. Nanoscale Pd/Fe bimetallic particles: catalytic effects of palladium on hydrodechlorination. *Applied Catalysis B: Environmental,* 77**,** 110-116.

LIM, S. F., ZHENG, Y.-M., ZOU, S. W. & CHEN, J. P. 2009. Uptake of arsenate by an alginate-encapsulated magnetic sorbent: Process performance and characterization of adsorption chemistry. *Journal of  Colloid and Interface Science,* 333**,** 33-39.

LIN, C.-R., CHU, Y.-M. & WANG, S.-C. 2006. Magnetic properties of magnetite nanoparticles prepared by mechanochemical reaction. *Materials Letters,* 60**,** 447-450.

LIU, H. B., CHEN, T. H., CHANG, D. Y., CHEN, D. H., LIU, Y., HE, H. P., YUAN, P. & FROST, R. 2012. Nitrate reduction over nanoscale zero-valent iron prepared by hydrogen reduction of goethite. *Materials Chemistry and Physics,* 133**,** 205-211.

LIU, J., GUO, D., ZHOU, Y., WU, Z., LI, W., ZHAO, F. & ZHENG, X. 2011. Identification of ancient textiles from Yingpan, Xinjiang, by multiple analytical techniques,. *Journal of Archaeology Sciences* 38**,** 1763-1770.

LIU, J. F., ZHAO, Z. S. & JIANG, G. B. 2008. Coating Fe₃O₄ magnetic nanoparticles with humic acid for high efficiency removal of heavy metals in water,. *Environmental Science and Technology,* 42**,** 6949-6954.

LIU, X., MA, Z., XING, J., AND LIU, H 2004. Preparation and characterization of amino-silane modified superparamagnetic silica nanospheres. *Journal of Magnetism and Magnetic Materials,* 270**,** 1-6.

LIU, Y., CHEN, M. & HAO, Y. 2013. Study of the adsorption of Cu(II) by EDTA functionalized Fe₂O₄ magnetic nano-particles. *Chemical Engineering Journal,* 218**,** 46-54.

LIU, Z., CHEN, J., WU, Y., LI, Y., ZHAO, J. & NA, P. 2018a. Synthesis of magnetic orderly mesoporous α-Fe₂O₃ nanocluster derived from MIL-100(Fe) for rapid and efficient arsenic (III,V) removal. . *Journal of Hazardous Material,* 343**,** 304-314.

LIU, Z., CHEN, J., WU, Y., LI, Y., ZHOO, J. & NA, P. 2018b. Synthesis of magnetic orderly mesoporous α-Fe₂O₃ nanocluster derived from MIL-100 (Fe) for rapid and efficient arsenic(III,V) removal *Journal of Hazardous Material,* 343**,** 304-314.

LOPEZ-CABEZA, R., GAMIZ, B., CORNEJO, J. & CELIS, R. 2017. Behavior of the enantiomers of the herbicide imazaquin in agricultural soils under different application regimes. *Geoderma,* 293**,** 64-72.

LÓPEZ-TÉLLEZ, G., BARRERA-DÍAZ, C. E., BALDERAS-HERNÁNDEZ, P., ROA-MORALES, G. & BILYEU, B. 2011. Removal of hexavalent chromium in aquatic solutions by iron nanoparticles embedded in orange peel pith. *Industrial Engineering Chemical Resources,* 50**,** 2488-2494.

LU, F. & ASTRU, D. 2018. Nanomaterials for removal of toxic elements from water. *Coordination Chemistry Reviews,* 356**,** 147-164.

LUNGE, S., SINGH, S. & SINHA, A. 2014. Magnetic iron oxide ($Fe_3O_4$) nanoparticles from tea waste for arsenic removal. *Journal of Magnetism and Magnetic Materials,* 356**,** 21-31.

MA, Z. & LIU, H. 2007. Synthesis and surface modification of magnetic particles for application in biotechnology and biomedicine. *China Particuology,* 5**,** 1-10.

MAHANINIA, M. H., KAGHAZCHI, T. & SOLEIMANI, M. 2014. Immobilization of betacyclodextrin onto the activated carbon. *International Review of Chemical Engineering,* 6**,** 73-76.

MAHANTA, N. & CHEN, J. P. 2013. A novel route to the engineering of zirconium immobilized nano-scale carbon for arsenate removal from water. *Journal of Materials Chemistry A,* 1**,** 8636-8644.

MAHDAVI, M., AHMAD, M., HARON, M. J., NAMVAR, F., NADI, B., RAHMAN, M. Z. & AMIN, J. 2013. Synthesis, Surface Modification and Characterisation of Biocompatible Magnetic Iron Oxide Nanoparticles for Biomedical Applications. *Molecules***,** 7533-7548.

MAHMOODI, N. M., HAYATI, B., ARAMI, M. & LAN, C. 2011. Adsorption of Textile Dyes on Pine Cone From Colored Wastewater: Kinetic, Equilibrium and Thermodynamic Studies. *Desalination,* 268**,** 117-125.

MAKAREVICIENE, V., SKORUPSKAITE, V., LEVISAUSKAS, D., ANDRULEVICIUTE, V. & KAZANCEV, K. 2014. The optimization of biodiesel fuel production from microalgae oil using response surface methodology. *International Journal of Green Energy,* 11**,** 527-541.

MALKOC, E. 2006. Ni(II) removal from aqueous solutions using cone biomass of Thuja orientalis. *Journal of Hazardous Material,* B137**,** 899-908.

MALLARD, I., STADE, L. W., RUELLAN, S., JACOBSEN, P. A. L., LARSEN, K. L. & FOURMENTIN, S. 2015. Sythesis, characterization and sorption capacities toward organic pollutants of new cyclodexrin modified zeolite derivatives, . *Colloids Surf A Physicochem. Eng. Asp,* 482**,** 50-57.

MANNING, B. A., KISER, J. R., KWON, H. & KANEL, S. R. 2007. Spectroscopic investigation of Cr(III)- and Cr(VI)-treated nanoscale zerovalent iron. *Environmental Science and Technology,* 41**,** 586-592.

MAO, N., YANG, L., ZHAO, G., LI, X. & LI, Y. 2012. Adsorption performance and mechanism of Cr (VI) using magnetic PS-EDTA resin from micro-polluted waters. *Chemical engineering journal,* 200**,** 480-490.

MARTÍNEZ-CABANAS, M., LÓPEZ-GARCÍA, M., BARRIADA, J. L., HERRERO, R. & SASTRE DE VICENTE, M. E. 2016. Green synthesis of iron oxide nanoparticles. Development of magnetic hybrid materials for efficient As(V) removal. *Chemical Engineering Journal,* 301**,** 83-91.

MCKAY, G. & POOTS, V. J. 1980. Kinetics and diffusion processes in colour removal from effluent using wood as an adsorbent. *Journal of Chemical Technology and Biotechnology,* 30**,** 279-292.

MEJIA-SANTILLAN, M. E., PARIONA, N., BRAVO, J., HERRERA-TREJO, M., MONTEJO-ALVARO, F., ZARATE, A., PERRY, D. L. & I, M.-E. A. 2018. Physical and arsenic adsorption properties of maghemite and magnetite sub-microparticles. *journal of Magnetism and Magnetic Materials,* 451**,** 594-601.

MENG, F., YANG, B., WANG, B., DUAN, S., CHEN, Z. & MA, W. 2017a. Novel dendrimer like magnetic biosorbents based on modified orange peel waste: adsorption-reduction behaviour of arsenic. *ACS Sustainable for Chemical Engineers* 5**,** 9692-9700.

MENG, F., YANG, B., WANG, B., DUAN, S., CHEN, Z. & MA, W. 2017b. Novel Dendrimerlike Magnetic Biosorbent Based on Modified Orange Peel Waste: Adsorption–Reduction Behavior of Arsenic. *ACS Sustainable Chemistry & Engineering,* 5**,** 9692-9700.

MERA, K., NAGAI, M., BROCK, J. W. C., FUJIWARA, Y., MURATA, T., MARUYAMA, T., BAYNES, J. W., OTAGIRI, M. & NAGAI, R. 2008. Glutaraldehyde is an effective cross-linker for production of antibodies against advanced glycation end-products,. *Journal of Immunological Methods,* 334**,** 82-90.

MEYER, E. E., ISLAM, M. F., LAU, W. & OU-YANG, H. D. 2000. Complexation kinetics of cyclodextrin with hydrophobic molecules confined in an isolated droplet in water. *Langmuir,* 16**,** 5519-5522.

MICHELSEN, D. L., GIDEON, J. A., GRIFFITH, G. P., PACE, J. E. & KUTAT, H. L. 1975. Removal of soluble mercury from waste water by complexing techmiques. *Bull Water Resour Res Cent Va Polytech Inst State Univ*.

MITTAL, A., KRISHNAN, L. & GUPTA, V. K. 2005. Removal and recovery of malachite green from wastewater using an agricultural waste material, de-oiled soya. *Separation and Purification Technology,* 43**,** 125-133.

MITTAL, A., KURUP, L. & MITTAL, J. 2007. Freundlich and Langmuir adsorption isotherms and kinetics for the removal of Tartrazine from aqueous solutions using hen feathers. *Journal of hazardous materials,* 146**,** 243-248.

ABD EL.-LATIF, M. M., IBRAHIM, A. & EI-KADY, M. 2010. Adsorption equilibrium, kinetics and thermodynamics of methylene blue from aqueous solutions using biopolymer oak sawdust composite. *J. Am. Sci,* 6**,** 267-283.

MOHAMED, M. H., WILSON, L. D. & HEADLEY, J. V. 2011a. Design and characterization of novel b-cyclodextrin based copolymer materials. *Carbohydrate Research,* 346**,** 219-229.

MOHAMED, M. H., WILSON, L. D. & HEADLEY, J. V. 2011b. Design and characterization of novel β-cyclodextrin based copolymer materials. *Carbohydrate Research,* 346**,** 219-229.

MOHAMMAD, M., MAITRA, S., AHMAD, N., BUSTAM, A., SEN, T. K. & DUTTA, B. K. 2010. Metal ion removal from aqueous solution using physic seed hull. *Journal of Hazardous Material,* 179**,** 363-372.

MOHAMMADI, A. & VEISI, P. 2018. High adsorption performance of β-cyclodextrin-functionalized multi-walled carbon nanotubes for the removal of organic dyes from water and industrial wastewater *journal of Environmental Chemical Engineering,* 6**,** 4634-4643.

MOMČILOVIĆ, M., PURENOVIĆ, M., BOJIĆ, A., ZARUBICA, A. & RANĐELOVIĆ, M. 2011. Removal of lead(II) ions from aqueous solutions by adsorption onto pine cone activated carbon. *Desalination* 276**,** 53-59.

MONTAZER-RAHMATI, M. M., RABBANI, P., ABDOLALI, A. & KESHTKAR, A. R. 2011. Kinetics and equilibrium studies on biosorption of cadmium, lead, and nickel ions from aqueous solutions by intact and chemically modified brown algae. *Journal of Hazardous Material,* 185**,** 401-407.

MORIN-CRINI, N. & CRINI, G. 2013. Environmental applications of water-insoluble β-cyclodextrin–epichlorohydrin polymers. *Progress in Polymer Science,* 38**,** 344-368.

MORNET, S., GRASSET, F. & PORTIER, J. 2002. Maghemite @silica nanoparticle for nanoparticle for biological applications. *European Cells and Materials,* 3**,** 10-113.

MOUZDAHIR, Y. E., ELMCHAOURI, A., MAHBOUB, R., GIL, A. & KORILI, S. 2010. Equilibrium modeling for the adsorption of methylene blue from aqueous solutions on activated clay minerals. *Desalination***,** 335-338.

MOYO, C. M., MUTARE, E., CHIGONDO, F. & NYAMUNDA, B. C. 2012. Removal of phenol from aqueous solution by adsorption on yeast, sacchromyces cerevisiae. *International journal of Recent Research and Applied Studies,* 11**,** 486-494.

MTHOMBENI, N. H., ONYANGO, M. S. & AOYI, O. 2015. Adsorption of hexavalent chromium onto magnetic natural zeolite-polymer composite. *Journal of the Taiwan Institute of Chemical Engineers***,** 242-251.

MULANI, K., DANIELS, S., RAJDEO, K., TAMBE, S. & N, C. 2013. Adsorption of chromium (VI) from aqueous solutions by coffee polyphenol-formaldehyde/acetaldehyde resins. *Journal of Polymer,* 2013**,** 1-11.

MURALIDHAR, R. V., CHIRUMAMIL, R. R., MARCHANT, R. & NIGAM, P. 2001. A response surface approach for the comparison of lipase production by Candida cylindracea using two different carbon sources. *Biochemical Engineering Journal,* 9**,** 17-23.

MÜRBE, J., RECHTENBACH, A. & TÖPFER, J. 2008. Synthesis and physical characterization of magnetite nanoparticles for biomedical applications. *Materials Chemistry and Physics,* 110**,** 426-433.

NAMASIVAYAM, C. & SANGEETHA, D. 2006. Removal and recovery of vanadium (V) by adsorption onto ZnCl2 activated carbon: Kinetics and isotherms. *Adsorption,* 12**,** 103-117.

NASHINE, A. L. & TEMBHURKAR, A. R. 2016. Equilibrium, kinetic and thermodynamic studies for adsorption of As(III) on coconut (Cocos nucifera L.) fiber. . *Journal of Environmental Chemical Engineering,* 4**,** 3267-3273.

NASSAR, N. N. 2010. Rapid removal and recovery of Pb(II) from wastewater by magnetic nano adsorbents. *Journal of Hazardous Material,* 184**,** 538-546.

NIGAM, S., GOPAL, K. & VANKAR, P. S. 2013. Biosorption of arsenic in drinking water by submerged plant: Hydrilla verticilata. *Environmental Science & Technology,* 20**,** 4000-4008.

O'CARROLL, D., SLEEP, B., KROL, M., BOPARAI, H. K. & KOCUR, C. 2013. Nanoscale zero valent iron and bimetallic particles for contaminated site remediation. *Advanced Water Resources,* 51**,** 104-122.

OFOMAJA, A. E. 2010. Intraparticle diffusion process for lead(II) biosorption onto mansonia wood sawdust. *Bioresour Technol,* 101**,** 5868-76.

OFOMAJA, A. E. & HO, Y. S. 2007. Effect of pH on cadmium biosorption by coconut copra meal. *Journal of Hazardous Material,* B139**,** 356-362.

OFOMAJA, A. E. & NAIDOO, E. B. 2010. Biosorption of lead(II) onto pine cone powder: Studies on biosorption performance and process design to minimize biosorbent mass. *Carbohydrate Polymers,* 82**,** 1031-1042.

OFOMAJA, A. E., NAIDOO, E. B. & MODISE, S. J. 2009. Removal of copper (II) from aqueous solution by pine and base modified pine cone powder as biosorbent. *Journal of Hazardous Material,* 168**,** 909-917.

OFOMAJA, A. E., PHOLOSI, A. & NAIDOO, E. B. 2013. Kinetics and competitive modeling of cesium biosorption onto chemically modified pine cone powder. *Journal of the Taiwan Institute of Chemical Engineers* 44**,** 943-951.

OFOMAJA, A. E., PHOLOSI, A. & NAIDOO, E. B. 2015. Application of raw and modified pine biomass material for cesium removal from aqueous solution. *Ecological Engineering* 82**,** 258-266.

OFOMAJA, A. E., UNUABONAH, E. I. & OLADOJA, N. A. 2010a. Competitive modeling for the biosorptive removal of copper and lead ions from aqueous solution by Mansonia wood sawdust. *Bioresour Technol,* 101**,** 3844-52.

OFOMAJA, A. E., UNUABONAH, E. I. & OLADOJA, N. A. 2010b. Competitive modeling for the biosorptive removal of copper and lead ions from aqueous solution by Mansonia wood sawdust. *Bioresource Technology,* 101**,** 3844-3852.

OGUZ, E. 2005. Adsorption characteristics and the kinetics of the Cr(VI) on the Thuja oriantalis. *Colloids and Surfaces A: Physicochem. Eng. Aspects,* 252**,** 121-128.

OKOLI, C. P., ADEWUYI, G. O., ZHANG, Q., ZHU, G., WANG, C. & GUO, Q. 2015. Aqueous scavenging of polycyclic aromatic hydrocarbons using epichlorohydrin, 1,6-hexamethylene diisocyanate and 4,4-methylene diphenyl diisocyanate modified starch: Pollution remediation approach. *Arabian Journal of Chemistry,* xxx.

ÖNAL, Y., AKMIL-BAŞAR, C. & SARıCı-ÖZDEMIR, Ç. 2007. Investigation kinetics mechanisms of adsorption malachite green onto activated carbon. *Journal of hazardous materials,* 146**,** 194-203.

ÖNSTEN, A., STOLTZ, D., PALMGREN, P., YU, S., GÖTHELID, M. & KARLSSON, U. O. 2010. Water adsorption on ZnO (0001): Transition from triangular surface structures to a disordered hydroxyl terminated phase. *The Journal of Physical Chemistry C,* 114**,** 11157-11161.

OZMEN, E. Y., SEZGIN, M., YILMAZ, A. & YILMAZ, M. 2008. Synthesis of β-cyclodextrin and starch based polymers for sorption of azo dyes from aqueous solutions. *Bioresource Technology,* 99**,** 526-531.

PAGNANELLI, F., MAINELLI, S., VEGLI, F. & TORO, L. 2003. Heavy metal removal by olive pomace: biosorbent characterization and equilibrium modelling. *Chemical Engineering Science,* 58**,** 4709-4717.

PAJZDERSKA, A., CZARNECKI, P., MIELCAREK, J. & WASICKI, J. 2011. H-1 NMR study of rehydration/dehydration and water mobility in beta-cyclodextrin. *Carbohydrate Polymers,* 346**,** 659-663.

PALMA, C., LLORET, L., PUEN, A., TOBAR, M. & CONTRERAS, E. 2016. Production of carbonaceous material from avocado peel for its application as alternative adsorbent for dyes removal. *Chinese Journal of Chemical Engineering,* 24**,** 521-528.

PANKHURST, Q. A., CONNOLLY, J., JONES, S. K. & DOBSON, J. 2003. Applications of magnetic nanoparticles in biomedicine. *Journal of Physics D: Applied Physics,* 36**,** 167-181.

PANNEERSELVAM, P., MORAD, N. & TAN, K. A. 2011a. Magnetic nanoparticle ($Fe_3O_4$) impregnated onto tea waste for the removal of nickel(II) from aqueous solution. *Journal of Hazardous Material,* 186**,** 160-168.

PANNEERSELVAM, P., MORAD, N. & TAN, K. A. 2011b. Magnetic nanoparticle (Fe304) impregnated onto tea waste for the removal of nickel(II) from aqueous solution. *Journal of Hazardous Material,* 186**,** 160-168.

PAOLINO, M., ENNEN, F., LAMONI, S., CERNESCU, M., VOIT, B., CAPPELLI, A., APPELHANS, D. AND KOMBER, H 2013. Cyclodextrin-Adamantane host-guest interactions on the surface of biocompatible Adamantyl-modified glycodendrimers,. *Macromole,* 46**,** 3215-3227.

PARK, D., LIM, S. R., YUN, Y. S. & PARK, J. M. 2008. Development of a new Cr(VI)-biosorbent from agricultural biowaste. *Bioresour Technol,* 99**,** 8810-8.

PARK, Y. D., PARK, Y. S. & MOON, J. 2010. The past, present, and future trends of biosorption. *Biotechnology and Bioprocess Engineering,* 15**,** 86-102.

PENG, X., ZHAO, Y., TANG, T., YANG, Y., JIANG, Y., MA, Z., LI, X., HOU, J., XI, B. & H, L. 2018. One-step and acid free synthesis of γ-Fe2O3/SBA-15 for enhanced arsenic removal. *Microporous and Mesoporous Materials,* 258**,** 26-32.

PHOLOSI, A., OFOMAJA, A. E. & NAIDOO, E. B. 2013. Effect of chemical extractants on the biosorptive properties of pine cone powder: Influence on lead(II) removal mechanism. *Journal of Saudi Chemical Society,* 17**,** 77-86.

PRATT, A., MUIR, I. & NESBITT, H. 1994. X-ray photoelectron and Auger electron spectroscopic studies of pyrrhotite and mechanism of air oxidation. *Geochimica et Cosmochimica Acta,* 58**,** 827-841.

PUTRA, E. K., PRANOWO, R., SUNARSO, J., INDRASWATI, N. & ISMADJI, S. 2009. Performance of activated carbon and bentonite for adsorption of amoxicillin from wastewater: Mechanisms, isotherms and kinetics. *Water Research,* 43**,** 2419-2430.

QAISER, S., SALEEMI, A. R. & AHMAD, M. M. 2007. Heavy metal uptake by agro based waste materials. *Environmental Biotechnology,* 10**,** 409-416.

QI, W., ZHAO, Y., ZHENG, X. & JI, M. 2016. Zhang. Adsorption behavior and mechanism of Cr(VI) using Sakura waste from aqueous solution. *Applied Surface Science,* 360**,** 470-476.

RAHMAN, I. M. M., BEGUM, Z. A. & HASEGAWA, H. 2013. Selective separation of elements from complex solution matrix with molecular recognition plus macrocycles attached to a solid,. *Microchemical Journal,* 110**,** 485-493.

RAKHSHAEE, R. & PANAHANDEH, M. 2011. Stabilization of a magnetic nano-adsorbent by extracted pectin to remove methylene blue from aqueous solution: A comparative study between two kinds of cross-linked pectin. *Journal of Hazardous Material,* 189**,** 158-166.

RAMRAKHIANI, L., HALDER, A., MAJUMDER, A., MANDAL, A. K., MAJUMDAR, S. & GHOSH, S. 2017. Industrial waste derived biosorbent for toxic metal remediation: Mechanism studies and spent biosorbent management. *Chemical Engineering Journal,* 308**,** 1048-1064.

RATTANACHUESKUL, N., SANING, A., KAOWPHONG, S., CHUMHA, N. & CHUENCHOM, L. 2016. Magnetic carbon composites with a hierarchical structure for adsorption of tetracycline, prepared from sugarcane bagasse via hydrothermal carbonization coupled with simple heat treatment process. *Bioresource Technology,* 226**,** 164-172.

RAVIKUMAR, K., DEEBIKA, B. & BALU, K. 2005. Decolourization of aqueous dye solutions by a novel adsorbent: application of statistical designs and surface plots for the optimization and regression analysis. *Journal of Hazardous Material,* 122**,** 75-83.

REHAN, M., ABDEL-WAHED, N. A. M., FAROUK, A. & EL-ZAWAHRY, M. M. 2018. Extraction of Valuable Compounds from Orange Peel Waste for Advanced Functionalization of Cellulosic Surfaces. *ACS Sustainable Chem. Eng.*

REZA, R. A. & AHMARUZZAMAN, M. 2015a. A novel synthesis of Fe2O3@ activated carbon composite and its exploitation for the elimination of carcinogenic textile dye from an aqueous phase. *RSC Advances,* 5**,** 10575-10586.

REZA, R. A. & AHMARUZZAMAN, M. 2015b. A novel synthesis of Fe 2 O 3@ activated carbon composite and its exploitation for the elimination of carcinogenic textile dye from an aqueous phase. *RSC Advances,* 5**,** 10575-10586.

RIJSBERMAN, F. R. 2006. Water scarcity: Fact or fiction? . *Agricultural Water Management,* 80**,** 5-22.

ROY, P., DEY, U., CHATTORAJ, S., MUKHOPADHYAY, D. & MONDAL, N. K. 2017. Modeling of the adsorptive removal of arsenic(III) using plant biomass: a bioremedial approach. *Applied Water Sciences,* 7**,** 1307-1321.

ROZMAN, H. D., TAN, K. W., KUMAR, R. N. & ABUBAKAR, A. 2001. The effect of hexamethylene diisocyanate modified ALCELL lignin as a coupling agent on the flexural properties of oil palm empty fruit bunch-polypropylene composites. *Polymer International,* 50**,** 561-567.

SAEB, M. R., RASTIN, H., SHABANIAN, M., GHAFFARID, M. & BAHLAKEHE, G. 2017. Cure kinetics of epoxy/β-cyclodextrin-functionalized Fe3O4 nanocomposites: Experimental analysis, mathematical modeling, and molecular dynamics simulation. *Progress in Organic Coatings,* 110**,** 172-181.

SAFARIK, I., HORSKA, K., SVOBODOVA, B. & SAFARIKOVA, M. 2012. Magnetically modified spent coffee grounds for dyes removal. *Eur Food Research Technology* 234**,** 345-350.

SAHA, R., MUKHERJEE, K., SAHA, I., GHOSH, A., GHOSH, S. K. & SAHA, B. 2013. Removal of hexavalent chromium from water by adsorption on mosambi (Citrus limetta) peel. 39**,** 2245-2257.

SALEH, T. A., SARı, A. & TUZEN, M. 2016. Chitosan-modified vermiculite for As(III) adsorption from aqueous solution: Equilibrium, thermodynamic and kinetic studies. *Journal of Molecular Liquids,* 219**,** 937-945.

SALEM, N. A. & YAKOOT, S. M. 2016. Research article non-steroidal anti-inflammatory drug, ibuprofen Adsorption using rice straw based biochar. *Internation Journal of Pharmacy***,** 729-736.

SANTRA, D. & SARKAR, M. 2016. Optimization of process variables and mechanism of arsenic (V) adsorption onto cellulose nanocomposite. *Journal of Molecular Liquids,* 224**,** 290-302.

SAQIB, A. N. S., WASEEM, A., KHAN, A. F., MAHMOOD, Q., KHAN, A., HABIB, A. & KHAN, A. R. 2013. Arsenic bioremediation by low cost materials derived from Blue Pine (Pinus wallichiana) and Walnut (Juglans regia). *Ecological Engineering* 51**,** 88-94.

SARKAR, A. B. & KOCHAK, G. M. 2005. HPLC analysis of aliphatic and aromatic dicarboxylic acid cross-linkers hydrolyzed from carbohydrate polyesters for estimation of the molar degree of substitution. *Carbohydrate Polymers,* 59**,** 305-312.

SARKAR, M., ACHARYA, P. K. & BATTACHARYA, B. 2003. Modeling and adsorption kinetics of some priority organic pollutants in water from diffusion and activation energy parameters. *Journal of  Colloid and Interface Science,* 266**,** 28.

SARKAR, M. & MAJUMDAR, P. 2011. Application of response surface methodology for optimization of heavy metal biosorption using surfactant modified chitosan bead. *Chemical Engineering Journal,* 175 376-387.

SCIBAN, M., KLASNJA, M. & SKRBIC, B. 2006. Modified hardwood sawdust as adsorbent of heavy metal ions from water. . *Wood Science Technology,* 40**,** 217-027.

SELIM, H. M. & SPARKS, D. L. 2001. *Heavy metals release in soils*, CRC Press.

SHANG, J., ZONG, M., YU, Y., KONG, X., DU, Q. & LIAO, Q. 2017. Removal of chromium (VI) from water using nanoscale zerovalent iron particles supported on herb-residue biochar. . *Journal of Environmental Management,* 197**,** 331-337.

SHARMA, S. & GARG, S. 2014. A brief study of various adsorbents for removal of Ni metal ions from waste water. *International Journal of Engineering study***,** 201-208

SHEN, Y., TANG, J., NIE, Z., WANG, Y., REN, Y. & ZUO, L. 2009a. Preparation and application of magnetic Fe 3 O 4 nanoparticles for wastewater purification. *Separation and Purification Technology,* 68**,** 312-319.

SHEN, Y. F., TANG, J., NIE, Z. H., WANG, Y. D., REN, Y. & ZUO, L. 2009b. Preparation and application of magnetic Fe304 nanoparticles for wastewater purification. *Separation and Purification Technology,* 66**,** 312-319.

SHOUMAN, M. M., FATHY, N. A., KHEDR, S. A. & ATTIA, A. A. 2013. Comparative biosorption studies of hexavalent chromium ion onto raw and modified branches. *Advanced Physical Chemistry,* 2013**,** 1-9.

SIKDER, M. T., ISLAM, M. S., KIKUCHI, T., SUZUKI, J., SAITO, T. & KURASAKI, M. 2014. Removal of copper ions from water using epichlorohydrin cross-linked β-cyclodextrin polymer: characterization, isotherms and kinetics. *Water Environment Research,* 86**,** 296-304.

SILVA, A. L. & BORDADO, J. C. 2004. Recent Developments in Polyurethane Catalysis: Catalytic Mechanisms Review. *Catalytic Mechanisms Review, Catalysis Reviews,* 46**,** 31-51.

SIMÕES DOS REIS, G., HOFFMANN SAMPAIO, C. H., LIMA, E. C. & WILHELM, M. 2016. Preparation of novel adsorbents based on combinations of polysiloxanes and sewage sludge to remove pharmaceuticals from aqueous solutions. *Colloids and Surfaces A: Physicochem. Eng. Aspects* 497**,** 304-315.

SIMSEK, E. B., OZDEMIR, E. & BEKER, U. 2013. Zeolite supported mono- and bimetallic oxides: promising adsorbents for removal of As(V) in aqueous solutions. *Chemical Engineering Journal,* 220**,** 402-411.

SING, K. S. W., HAUL, R. A. W., PIEROTTI, R. A. & SIEMIENIEWSKA, T. 1985. Reporting physisorption data for gas/solid systems with special reference to the determination of surface area and porosity. . *Pure & Applied Chemistry,* 57**,** 603-619.

SINGH, N. B., NAGPAL, G., AGRAWAL, S. & RACHNA, A. 2018

Water purification by using Adsorbents: A Review. *Environmental Technology & Innovation*

SINGHA, B., NAIYA, T. K., BHATTACHARYA, A. K. & DAS, S. K. 2011. Cr(VI) Ions Removal from Aqueous Solutions Using Natural Adsorbents – FTIR Studies. *Journal of Environmental Protection,* 02**,** 729-735.

SOHRABI, S. & AKHLAGHIAN, F. 2016. Modeling and optimization of phenol degradation over copper-doped titanium dioxide photocatalyst using response surface methodology. *process Safety and Environmental Protection,* 99**,** 120-128.

SRIVASTAVA, V. C., MALL, I. D. & M, M. I. 2006. Characterization of mesoporous rice husk ash (RHA) and adsorption kinetics of metal ions from aqueous solution onto RHA *Journal of Hazardous Material,* B134**,** 257-267.

SUBHEDAR, P. B., RAY, P. & GOGATE, P. R. 2018. Intensification of delignification and subsequent hydrolysis for the fermentable sugar production from lignocellulosic biomass using ultrasonic irradiation. *Ultras. Sonochem,* 40**,** 140-150.

SUBRAMANIAN, K., KUMAR, P. S., JEYAPAL, P. & VENKATESH, N. 2005. Characterization of ligno-cellulosic seed fibre from Wrightia Tinctoria plant for textile applications—an exploratory investigation. *European Polymer Journal,* 41**,** 853-861.

SUD, D., MAHAJAN, G. & KAUR, M. P. 2008. Agricultural waste material as potential adsorbent for sequestering heavy metal ions from aqueous solutions - A review. *Bioresource Technology,* 14**,** 6017-6027.

SUKUMAR, C., JANAKI, V., KAMALA-KANNAN, S. & SHANTHI, K. 2014. Biosorption of chromium (VI) using Bacillus subtilis SS-1 isolated from soil samples of electroplating industry. *Clean Technologies and Environmental Policy,* 16**,** 405-413.

SUN, D., ZHANG, X., WU, Y. & LIU, X. 2010. Adsorption of anionic dyes from aqueous solution on fly ash. *Journal of Hazardous Material,* 181**,** 335-342.

SUN, S. 2006. Recent Advances in Chemical Synthesis, Self-Assembly, and Applications of FePt Nanoparticles. *Advanced Materilals,* 18**,** 393-403.

SUN, Y., LI, J. & WANG, X. 2014. The retention of uranium and europium onto sepiolite investigated by macroscopic, spectroscopic and modeling techniques. *Geochim. Cosmochim. Acta,* 140**,** 621-643.

SUTHERLAND, C. 2004. Removal of heavy metals from waters using low cost adsorbents process development. . *PhD Thesis. The University of the West Indies, Trinidad***,** 150-164.

SWARNKAR, V., AGRAWAL, N. & TOMAR, R. 2012. Sorption of chromate and arsenate by Surfactant Modified Erionite (E-SMZ). *Journal of Dispersion Science and Technology,* 33**,** 919-927.

SZEJTLI, J. 2004. Past, present and futute of cyclodextrin research. *Pure Applied Chemistry,* 76**,** 1825-1845.

TAJERNIA, H., EBADI, T., NASERNEJAD, B. & GHAFORI, M. 2014. Arsenic Removal from Water by Sugarcane Bagasse: An Application of Response Surface Methodology (RSM). *Water Air Soil Pollution,* 225**,** 2028.

TALBOT, D., ABRAMSON, S., GRIFFETE, N. & BÉE, A. 2018. pH-sensitive magnetic alginate/γ-Fe2O3 nanoparticles for adsorption/desorption of a cationic dye from water. *Journal of Water Process Engineering,* 25**,** 301-308.

TANG, R. X., DAI, C., LI, C., LIU, W. H., GAO, S. T. & WANG, C. 2017. Removal of methylene blue from aqueous solution using agricultural residue walnut shell: equilibrium, kinetic, and thermodynamic studies. *Journal of Chemistry***,** 1-10.

TOUPIN, M. & BÉLANGER, D. 2008. Spontaneous functionalization of carbon black by reaction with 4-nitrophenyldiazonium cations. *Langmuir,* 24**,** 1910-1917.

TRUJILLO, E. M., SPRINTI, M. & ZHUANG, H. 1995. Immobilized biomass: a new class of heavy metal bioexchangers. In: Senguptal, A.K. *ed. Ion Exchange Technology: Advances in Pollution Control. Technomic Publishing Company Inc***,** 225-271.

TU, Y. J., YOU, C. F. & CHANG, C. K. 2012. Kinetics and thermodynamics of adsorption of Cd on green manufactured nano-particles. *Journal of Hazardous Material,* 235**,** 116-122.

TZVETKOV, G., KANEVA, N. & SPASSOV, T. 2017. Room-temperature fabrication of core-shell nano-ZnO/pollen grain biocomposite for adsorptive removal of organic dye from water. *Applied Surface Science,* 400**,** 481-491.

UCUN, H., BAYHAN, Y. K., KAYA, Y., CAKICI, A. & ALGUR, O. F. 2003. Biosorption of lead (II) from aqueous solution by cone biomass of pinussylvestris. *Desalination,* 154**,** 233-238.

UCUN, H., BAYHAN, Y. K., KAYA, Y., CAKICI, A. & F, A. O. 2002. Biosorption of chromium(VI) from aqueous solution by cone biomass of Pinus *Bioresource Technology,* 85**,** 155-158.

UGOCHUKWU, U. C., JONES, M. D., HEAD, I. M., MANNING, D. A. & FIALIPS, C. I. 2014. Biodegradation and adsorption of crude oil hydrocarbons supported on homo ionic montmorillonite clay minerals. *Applied Clay Science*, 84-86.

UTOMO, H. D. & HUNTER, K. A. 2010. Particle concentration effect: adsorption of divalent metal ions on coffee grounds. *Bioresource Technology,* 101**,** 1482-1486.

VADIVELAN, V. & KUMAR, K. V. 2005. Equilibrium, kinetics, mechanism, and process design for the sorption of methylene blue onto rice husk. *Journal of    Colloid and Interface Science,* 286**,** 90-100.

VATUTSINA, M., SOLDATOV, V. S., SOKOLOVA, V. I., JOHANN, J., BISSEN, M. & WEISSENBACHER, A. 2007. A new hybrid (polymer/inorganic) fibrous sorbent for arsenic removal from drinking water,. *Reactive and Functional Polymers,* 67**,** 184-201.

VAZQUEZ, G., ALONSO, R., FREIRE, S., GONZALEZ-ALVAREZ, J. & ANTORRENA, G. 2006. Uptake of Phenol From Aqueous Solutions by Adsorption in a Pinus pinaster Bark Bed. *Journal of Hazardous Material,* 133**,** 61-67.

VELAZQUEZ-JIMENEZ, L. H. 2013. Chemical characterization of raw and treated agave bagasse and its potential as adsorbent of metal cations from water. *Water Research,* 41.

VENKATESAN, G. & NARAYANAN, S. L. 2018. Synthesis of Fe2O3-coated and HCl-treated bauxite ore waste for the adsorption of arsenic (III) from aqueous solution: Isotherm and kinetic models. *Chemical Engineering Communications,* 205**,** 34-46.

VIEIRA, B. R. C., PINTOR, A. M. A., BAVENTURA, R. A. R., BOTELHO, C. M. S. & SANTOS, S. C. R. 2017a. Arsenic removal from water using iron-coated seaweeds. *Journal of Environmental Management,* 192**,** 224-233.

VIEIRA, B. R. C., PINTOR, A. M. A., BOAVENTURA, R. A. R., BOTELHO, C. M. S. & SANTOS, S. C. R. 2017b. Arsenic removal from water using iron-coated seaweeds. *Journal of Environmental Management* 192**,** 224-233.

VINH, N. V., ZAFAR, M., BAHERA, S. K. & PARK, H. S. 2015. Arsenic(III) removal from aqueous solution by raw and zinc-loaded pine cone char: equilibrium, kinetics and thermodynamic studies. *International Journal of Environmental Science and Technology,* 12**,** 1283-1294.

VOLESKY, B. & HOLAN, Z. R. 1995. Biosorption of heavy metals *Biotechnology Progress,* 11**,** 235-250.

WAN NGAH, W. S. & HANAFIAH, M. A. K. M. 2008. Removal of heavy metal ions from wastewater by chemically modified plant waste as adsorbents: A review. *Bioresource Technology,* 99**,** 3935-3948.

WAN NGAH, W. S., HANAFIAH, M.A.K.M 2008. Removal of heavy metal ions from wastewater by chemically modified plant wastes as adsorbents: A review. *Bioresource Technology,* 99**,** 3935-3948.

WANG, C., LI, J., SUN, X., WANG, L. & X, S. 2009. Evaluation of zeolites synthesized from fly ash as potential adsorbents for wastewater containing heavy metals. *Journal of environmental Sciences,* 21**,** 127-136.

WANG, S.-L. & LEE, J.-F. 2011. Reaction mechanism of hexavalent chromium with cellulose. *Chemical Engineering Journal,* 174**,** 289-295.

WANG, S. J., ZHANG, M. X. & YAO, Q. L. 2015. A novel biosorbent formed of marine-derived Penicillium janthinellum mycelial pellets for removing dyes from dye-containing wastewater. *Chemical Engineering Journal,* 259**,** 837-844.

WARTELLE, L. H. & MARSHALL, W. E. 2000. Citric acid modified agricultural by-products as copper ion adsorbents,. *Advances in Environmental Research,* 4**,** 1-7.

WILSON, D. & LANGELL, M. 2014. XPS analysis of oleylamine/oleic acid capped Fe3O4 nanoparticles as a function of temperature. *Applied Surface Science,* 303**,** 6-13.

WU, K., LIU, R., LI, T., LIU, H., PENG, J. & QU, J. 2013. Removal of arsenic (III) from aqueous solution using a low-cost by-product in Fe-removal plants—Fe-based backwashing sludge. *Chemical engineering journal,* 226**,** 393-401.

WU, L.-K., WU, H., ZHANG, H.-B., CAO, H.-Z., HOU, G.-Y., TANG, Y.-P. & ZHENG, G.-Q. 2018. Graphene oxide/CuFe2O4 foam as an efficient absorbent for arsenic removal from water. *Chemical Engineering Journal,* 334**,** 1808-1819.

WU, Z., YUAN, X., ZHONG, H., WANG, H., ZENG, G., CHEN, X., WANG, H., ZHANG, L. & SHAO, J. 2016. Enganced adsorptive removal of p-nitrophenol from water by aluminum metal-organic framework/reduced graphene oxide composite *Scientific Reports,* 6**,** 25638.

XU, P., ZENG, G. M., HUANG, D. L., LAI, C., ZHAO, M. H., WEI, Z., LI, N. J., HUANG, C. & XIE, G. X. 2012. Adsorption of Pb (II) by iron oxide nanoparticles immobilized Phanerochaete chrysosporium: equilibrium, kinetic, thermodynamic and mechanisms analysis. *Chemical Engineering Journal,* 203**,** 423-431.

XU, T., CAI, Y. & O'SHEA, K. E. 2007. Adsorption and photocatalyzed oxidation of methylated arsenic species in TiO2 suspensions. *Environmental science & technology,* 41**,** 5471-5477.

XU, X., SONG, W., HUANG, D., GAO, B., SUN, Y., YUE, Q. & FU, K. 2015. Performance of novel biopolymer-based activated carbon and resin on phosphate elimination from stream,. *Colloids Surf. A,* 476**,** 68-75.

YADAV, R., SHARMA, A. K. & BABU, J. N. 2016. Sorptive removal of arsenite [As(III)] and arsenate [As(V)] by fuller's earth immobilized nanoscale zero-valent iron nanoparticles (F-nZVI): Effect of Fe0 loading on adsorption activity. *Journal of Environmental Chemical Engineering,* 4**,** 681-694.

YAMAMURA, A. P. G., YAMAURAM, M. & COSTA, C. H. 2011. Magnetic biosorbent for removal of uranyl ions. *International Journal of Nuclear Energy Science and Technology,* 6**,** 8-16.

YANG, G. C. C. & LEE, H. L. 2005. Chemical reduction of nitrate by nanosized iron: kinetics and pathways,. *Water Research,* 39**,** 884-894.

YANG, J., PARK, S. B., YOON, H.-G. H., Y M & HAAM, S. 2006. Preparation of poly ε-caprolactone nanoparticles containing magnetite for magnetic drug carrier. *International Journal of Pharmaceutics,* 324**,** 185-190.

YANG, M., LIN, J., ZHAN, Y. & ZHANG, H. 2014. Adsorption of phosphate from water onlake sediments amended with zirconium-modified zeolites in batch mode. *Ecological Engineering***,** 223-233.

YAO, Z., WANG, L. & QI, J. 2009. Biosorption of methylene blue from aqueous solution using a bioenergy forest waste: Xanthoceras sorbifolia seed coat. *Clean Soil Air Water,* 37**,** 642-648.

YARGıÇ, A. S., YARBAY SAHIN, R. Z., OZBAY, N. & ONAL, E. 2014. Assessment of toxic copper(II) biosorption from aqueous solution by chemically-treated tomato waste (Solanum lycopersicum). *Journal of clean Production.*

YETILMEZSOY, K., DEMIREL, S. & VANDERBEI, R. J. 2009. Response surface modeling of Pb (II) removal from aqueous solution by Pistacia vera L.: Box–Behnken experimental design. *Journal of Hazardous Material,* 171**,** 551-562.

YOON, Y., ZHENG, M., AHN, Y.-T., PARK, W. K., YANG, W. S. & KANG, J.-W. 2017. Synthesis of magnetite/non-oxidative graphene composites and their application for arsenic removal. *Separation and Purification Technology,* 178**,** 40-48.

YU, X., TONG, S., GE, M., ZUO, J., CAO, C. & SONG, W. 2013. One-step synthesis of magnetic composites of cellulose@ iron oxide nanoparticles for arsenic removal. *Journal of Materials Chemistry A,* 1**,** 959-965.

ZHA, L. F., CHANG, S. & YUE YAN, J. 2008. Preparation and adsorption kinetics of porous γ-glycidoxypropyltrimethoxysilane crosslinked chitosan–β-cyclodextrin membranes. *Journal of Membrane Science,* 321**,** 316-323.

ZHANG, D., MA, Y., FENG, H. & HAO, Y. 2012. Adsorption of Cr(VI) from aqueous solution using carbon-microsilica composite adsorbent. *Journal of Chil Chem. Soc,* 57**,** 964-968.

ZHANG, G., QU, J., LIU, H., COOPER, A. T. & WU, R. 2007. CuFe2O4/activated carbon composite: a novel magnetic adsorbent for the removal of acid orange II and catalytic regeneration. *Chemosphere,* 68**,** 1058-1066.

ZHANG, M., GAO, B., VARNOOSFADERANI, S., HEBARD, A., YAO, Y. & INYANG, M. 2013. Preparation and characterization of a novel magnetic biochar for arsenic removal. *Bioresource Technology,* 130**,** 457-462.

ZHANG, S., LI, X.-Y. & CHEN, J. P. 2010. An XPS study for mechanisms of arsenate adsorption onto a magnetite-doped activated carbon fiber. *Journal of colloid and interface science,* 343**,** 232-238.

ZHANG, W. 2003. Nanoscaleiron particles for environmental remediation: an overview. *Journal of Nanoparticles Reseach,* 5**,** 323-332.

ZHANG, W., ZHUANG, L., SHEN, H., XIE, H., HU, Z. & HE, H. 2009. Controlled synthesis and properties of carboxymethyl chitosan-bound magnetic nanoparticles. *Journal of Scientific Conference Proceedings* 1**,** 211-214.

ZHANG, X. & WANG, C. 2011. Supra molecular amphiphiles. *Chem. Soc. Rev,* 40**,** 94-101.

ZHAO, D., QIU, Q., WANG, Y., HUANG, M., WU, Y., LIU, X. & JIANG, T. 2016. Efficient removal of acid dye from aqueous solutions via adsorption using low-cost blast-furnace slag. *Desalination Water Treatment,* 57**,** http://dx.doi.org/10.1080/19443994.2016.1179225.

ZHENG, J.-C., FENG, H.-M., LAM, M. H.-W., LAM, P. K.-S., DING, Y.-W. & YU, H.-Q. 2009. Removal of Cu (II) in aqueous media by biosorption using water hyacinth roots as a biosorbent material. *Journal of Hazardous Materials,* 171**,** 780-785.

ZHOU, Q., QIN LI, Z. Q., SHUANG, C. D., LI, A. M., WANG, M. Q. & ZHANG, M. C. 2012. Preparation of acid-resistant magnetic adsorbent for effective removal of p-nitrophenol. *Chinese Chemical Letters,* 23**,** 1079-1082.

ZHOU, S., WANG, D., SUN, H., CHEN, J. & NA, S. 2014. Synthesis, characterization, and adsorptive properties of magnetic cellulose nanocomposites for arsenic removal. *Water Air Soil Pollution,* 225**,** 1945.

ZHOU, Y., ZHANG, L. & CHENG, Z. J. 2015. Removal of organic pollutants from aqueous solution using agricultural wastes: a review. *Journal of Molecular Liquids,* 212**,** 739-762.

ZHU, J., WEI, S., RYU, J., SUN, L., LUO, Z. & GUO, Z. 2010. Magnetic epoxy resin nanocomposites reinforced with core- shell structured Fe@FeO nanoparticles: fabrication and property analysis. *ACS Appl. Mater. Interfaces,* 2**,** 2100-2107.

ZOLFAGHARI, G. 2016. β-Cyclodextrin incorporated nanoporous carbon: Host–guest inclusion for removal of p-Nitrophenol and pesticides from aqueous solutions. *Chemical Engineering Journal,* 283**,** 1424-1434.

ZULFIKAR, M. A., SETIYANTO, H. & DJAJANTI, S. D. 2013. Effect of temperature and kinetic modelling of lignosulfonate adsorption onto powdered eggshell in batch systems. *Songklanakarin J. Sci. Technol.,* 35**,** 1-31.

# 7 Conclusion and recommendations

Surface properties improvement of pine cone by NaOH treatment and adsorption properties improvement of magnetite and NaOH treated pine by coating magnetite with NaOH treated pine was examined in the first part of the study. Magnetite coated pine cone bio-composite was successfully synthesised, optimized, characterized and applied for toxic Cr(VI) and As(III) adsorption from aqueous solution. A novel biosorbent magnetite-nanomaterial cross-linked to cyclodextrin using epichlorohydrin and hexamethylene diisocyanate was synthesised in the second part of the study and its application for 4-nitrophenol removal from aqueous solution was studied. The conclusion on the findings of the present research are summarised and some recommendations for future work are proposed.

## 7.1 CONCLUSION

The following conclusion was drawn based on the results obtained.

The first part of the thesis focused on the synthesis and characterization of magnetite nanoparticles coated pine cone using co-precipitation method. The magnetite coated pine cone was successfully synthesized, characterized and applied for Cr(VI) and As(III) removal from aqueous solution. VSM results showed that the magnetite retained its magnetic properties after pine cone coating which allowed easy separation of the nanocomposite adsorbent after Cr(VI) and As(III) adsorption. Both structural and morphological analysis showed the spherically shaped magnetite nanoparticles with average particle size of 8.1 nm. FTIR and XPS techniques were conducted to elucidate the adsorption mechanism. Thermodynamics results indicated that the adsorption process of both Cr(VI) and As(III) onto NTP and NTPNC was endothermic and spontaneous in nature. Removal of Cr(VI) and As(III) was governed by ionic exchange mechanism as confirmed by shifting of the hydroxyl and carboxylate groups in the FTIR peaks. XPS spectra after Cr(VI) and As(III) adsorption confirmed that the toxic Cr(VI) was reduced to the less toxic Cr(III) and As(III) was oxidised to the less toxic As(V) after adsorption. Cr(VI) was found to bind to the surface of both NTP and NTPNC by the adsorption coupled reduction mechanism while As(III) bounded by ligand ion exchange and formation of inner-sphere complexes. The desorption results showed that ion-exchange is the predominant mechanism followed by chemisorption for Cr(VI) adsorption for both NTP and NTP-NC while the

predominant mechanism for As(III) adsorption was ion-exchange. Both NTP and NTPNC adsorbent were stable over five adsorption-desorption cycles for As(III) and 4 cycles for Cr(VI) adsorption-desorption process.

On the second part of the thesis, magnetite coated pine cone bio-composite was successfully cross-linked to β-CD using epichlorohydrin and 1,6 Hexamethylene diisocyanate. Synthesis conditions using both cross-linking agents were successfully optimized using response surface methodology, characterized and applied for 4-nitrophenol adsorption from aqueous solution. RSM results showed the most influential synthesis variables that control the investigated variables and the optimum values were obtained. The binding of β-CD onto the magnetite bio-composite surface was confirmed by FTIR, TGA, XRD, VSM, $pH_{pzc}$ and BET surface area analysis. Cross-linking process led to improvement in surface characteristics, level of hydrophobicity, and incorporation of relevant functional groups. The 4-nitrophenol adsorption on the nanocomposite adsorbents was observed to be pH, adsorbent amount, concentration and temperature dependant. The kinetics of 4-nitrophenol adsorption onto all three nanocomposite adsorbents followed the pseudo-second-order model and intraparticle diffusion. It can be concluded that the magnetite coated pine cone crosslinked to cyclodextrin using hexamethylene diisocyanate is considered a promising, effective and alternative adsorbent for the removal of 4-nitrophenol from aqueous solution, because of its high surface area, adsorption capacity, availability, and low cost. 1,6-hexamethylene diisocyanate is proposed as better cross-linker for the removal of 4-nitrophenol than epichlorohydrin.

## 7.2 RECOMMENDATIONS

➢ Based on the findings of this research, it is therefore, recommended that the magnetite coated pine cone crosslinked to cyclodextrin using epichlorohydrin be explored for heavy metals removal from wastewater since it is hydrophilic and did not perform very well for 4-nitrophenol adsorption.

➢ Other organic pollutants such as dyes and other phenolic derivatives may be explored using the magnetite coated pine crosslinked to cyclodextrin using 1,6-hexamethylene diisocyanate.

➢ The research has focused only on the batch adsorption studies for Cr(VI), As(III) and 4-nitrophenol removal, it is therefore recommended that the upscaling be taken into

consideration. A continuous separation system may be designed which will measure the feasibility of the nanocomposite adsorbents in real and practical application. It is capable to treat large volumes of pollutants and reach high removal efficiency and minimize time required for the adsorbent to reach equilibrium and also improve the adsorption process.

➢ More kinetic models and isotherms may be determined for better understanding of the adsorption mechanism for all pollutants investigated.